THE UNIVERSITY
of ADELAIDE

Faculty of Sciences
School of Physical Sciences

Triggering and Reconstructing Hadronic Jets in the Search for Dark Matter and Supersymmetry with the ATLAS Experiment

Maximilian Alexander Amerl

MPhil Thesis

25 August 2022

Contents

Abstract

Precision tests of the Standard Model of Particle Physics and searches for phenomena beyond the Standard Model are the focus for the ATLAS experiment at the Large Hadron Collider (LHC) over the next decade. The beginning of Run 3 of the LHC in 2022 and the eventual commissioning of the detector for High Luminosity operations with an upgraded LHC from 2029 provides a unique opportunity to extend the coverage of Beyond the Standard Model searches to new and hard to reach particle properties (parameter space). Many signatures of both Standard Model and Beyond the Standard Model physics involve the production of hadronic jets, sprays of composite particles called hadrons.

Low-mass searches for new particles using hadronic jets are limited by extremely high-rate background processes – there are significant limitations on the amount of LHC data that can be saved for analysis. The application of novel techniques for data acquisition and selection (triggering) plays an important role in collecting datasets with sufficient statistical power and high sensitivity to the production of low-mass particles. This thesis describes studies of different triggers that could be used in Run 3 searches for multi-jet resonances from supersymmetric particles in the mass range between 100 GeV and 400 GeV. Additional discussions of early studies to project the sensitivity of these analyses in the conditions of the High-Luminosity LHC (HL-LHC) are also included.

In the high-mass and high-momentum region of parameter space the decay products of hypothetical particles can be highly collimated and reconstructed within a single large jet (a "cone" around the decay products). The identification of the "parent particle" of these jets is an important aspect of selecting data to analyse. The jet identification (tagging) focus of this thesis consists of the development of top quark identification algorithms for use in HL-LHC simulations. Basic tagging algorithms are developed and compared to more complex Run 2 taggers to provide a first set of recommendations for identifying hadronic top quark decays in HL-LHC simulations.

Statement of Originality

I certify that this work contains no material which has been accepted for the award of any other degree or diploma in my name, in any university or other tertiary institution and, to the best of my knowledge and belief, contains no material previously published or written by another person, except where due reference has been made in the text. In addition, I certify that no part of this work will, in the future, be used in a submission in my name, for any other degree or diploma in any university or other tertiary institution without the prior approval of the University of Adelaide and where applicable, any partner institution responsible for the joint-award of this degree.

I give permission for the digital version of my thesis to be made available on the web, via the University's digital research repository, the Library Search and also through web search engines, unless permission has been granted by the University to restrict access for a period of time.

I acknowledge the support I have received for my research through the provision of an Australian Government Research Training Program Scholarship.

The University of Adelaide,
25 August 2022

Maximilian Amerl

Acknowledgements

It would not have been possible for me to complete my MPhil and this thesis without the support and guidance of many members of the University of Adelaide Physics Department and ATLAS collaborators. Firstly, I would like to thank my supervisor, Paul Jackson, for his support, suggestions, and feedback throughout my MPhil. I would also like to thank my co-supervisor, Gary Hill, for his support and feedback throughout my degree.

The support of Caterina Doglioni, Claire Antel, and Marco Montella was instrumental for the work addressing triggering and data acquisition in this thesis (Chapters 5 and 6). I would like to thank each of them for their assistance, answering my many questions, and various suggestions for the studies. In Chapter 6, the code used to generate the datsets for analysis optimisation drew on existing code from a Run 2 ATLAS analysis. I would like to thank Lea Halser for providing detailed information about the truth-matching framework considered for the Run 2 analysis and for answers to troubleshooting questions.

I would also like to thank Caterina Doglioni for providing feedback on this thesis and suggestions for modifications to the text.

Furthermore, without the support of Maximilian Swiatlowski (my technical supervisor), Dag Gillberg, Josu Cantero Garcia, Takuya Nobe, Reina Coromoto Camacho Toro, Chris Malena Delitzsch, Jennifer Roloff, Cecilia Tosciri, and Matt LeBlanc the HL-LHC boosted jet tagging studies (Chapter 7) would not have been possible. I thank them for their guidance, many suggestions, and answers to my multitude of questions about the work.

Finally, I would like to thank my fellow graduate students at the University of Adelaide whom I have shared this experience with and learnt from, especially members of the ATLAS group.

Chapter 1

Introduction

The Standard Model of Particle Physics correctly describes a wide range of phenomena in the visible Universe yet does not account for the prevalence of dark matter and dark energy. Combined, dark matter and dark energy make up approximately 95% of the total energy density of the Universe, while visible matter accounts for a mere 5% of the matter-energy density [1]. Clearly, our models of fundamental physics are incomplete – we need extensions to the standard model to describe new phenomena. The ATLAS Experiment at the Large Hadron Collider (LHC) is at the forefront of tests of the Standard Model and searches for signatures of new physics. In proton-proton (pp) collisions at the LHC, hadronic jet production (collimated sprays of particles called hadrons) is common and is also a prevalent feature of many Beyond the Standard Model (BSM) physics processes. As further constraints are placed on the production of new high-mass particles in hadronic processes, it remains important to explore the boundaries of low-mass parameter space.

This thesis focuses on triggering and reconstructing jets in both boosted (high-momentum, resulting from the decays of heavy particles) and low-mass (and therefore low-energy/low-momentum) topologies. The high-momentum particles produced by decays of massive particles (or simply produced with large momenta) are sufficiently boosted so that their decay products are enclosed in a single jet (a "cone" around the particles). The work on triggering focuses on preparations for the application of novel data-taking techniques involving (nearly) real-time analysis in searches for multi-jet resonances predicted by R-parity violating (RPV) supersymmetry (SUSY). While many searches have been conducted for R-parity conserving SUSY, extending consideration to RPV models removes requirements on the stability of the lightest supersymmetric particle allowing greater flexibility in the model parameters. The application of these novel data-taking techniques will be instrumental in overcoming trigger bandwidth limitations in searches for low-mass SUSY particles. These studies are undertaken in preparation for both Run 3 of the LHC (2022-2026) and the eventual transition to the High-Luminosity LHC (HL-LHC) (2029-). The challenging conditions resulting from the increased luminosity of the HL-LHC will lead to a significant increase in the low-momentum hadronic activity in pp events, degrading the performance of existing jet reconstruction and calibration methods. Thus, the consideration of low-mass ($m \approx 100 - 400$ GeV) signal searches is important to

identify a way forward to maintain and increase sensitivity to such low-momenta signatures that can benefit many other physics scenarios in the ATLAS physics program.

For boosted particles, the consideration of the substructure of jets containing some or all decay products of the parent particle plays a pivotal role in identifying that particle. In HL-LHC conditions, as for low-mass searches, increased pile-up levels will degrade the performance of jet identification techniques applied in previous LHC runs. The jet reconstruction studies in this thesis focus on the identification of top quark jets in HL-LHC conditions where the top quark has sufficient momentum for its decay products to be completely enclosed within a single large jet – *boosted jet tagging*. These studies focus on using selections on variables that describe the substructure of the jets to discriminate between top quark jets and other commonly produced hadronic radiation. The focus of these *tagging* algorithms (taggers) is limited to two-variable selections involving both the mass of the jet and another substructure-sensitive variable. However, an existing machine learning tagger used for Run 2 analyses is also studied to evaluate its performance in HL-LHC conditions. The final set of tagging recommendations is chosen based on the stability of the tagger performance in different conditions and different kinematic regimes for the jets in question.

The structure of this thesis is as follows:

- Chapter 2 provides an introduction to elementary particle physics, the Standard Model of Particle Physics, and extensions to the Standard Model through BSM physics.
- Chapter 3 introduces the LHC systems and the ATLAS Experiment.
- Chapter 4 provides a detailed introduction to the reconstruction of events in pp collisions with the ATLAS detector.
- Chapters 5 and 6 describe the results of studies for the application of Trigger-object Level Analysis in Run 3 of the LHC and at the HL-LHC, respectively.
- Chapter 7 discusses the development of simple top quark taggers for implementation in HL-LHC simulations of the ATLAS detector.

Finally, concluding remarks and future directions are discussed in Chapter 8.

Chapter 2

The Standard Model of Particle Physics and its extensions

The following Chapter presents a basic overview of our existing understanding of elementary particle physics in addition to extensions of our current models – physics beyond the Standard Model.

The basis of the Standard Model of Particle Physics is presented in Section 2.1. Later, beyond the Standard Model physics is discussed through the lens of dark matter physics with emphasis on models involving supersymmetry in Section 2.2.

2.1 The Standard Model of Particle Physics

The Standard Model of Particle Physics is one of the most significant theories of physics that explains a wide range of phenomena observed on the scale of elementary particles. There are four fundamental forces (that we know of) in nature:

1. gravity,
2. the strong force,
3. the weak force,
4. the electromagnetic force.

The latter three forces are described in the Standard Model, but not gravity. The detection of gravitational waves [2] motivates the existence of an associated force carrier for gravity, the graviton, which is typically massless, but discussion of massive gravitons does exist in the literature [3]. Nonetheless, the unification of gravity and the Standard Model, or the underlying quantum field theory to be specific, is challenging. The trouble in these theories lies in their ability to be renormalised[1] [1]. The unification of gravity and the Standard Model is an ongoing area of study in fundamental physics.

[1] Renormalisation is used to avoid divergences in theoretical calculations yielding finite, measurable quantities [4].

The Standard Model correctly accounts for the existence of a range of fundamental particles: quarks, leptons, and bosons. Quarks and leptons have half-integer spin and are classified as fermions, which must obey Fermi-Dirac statistics (most importantly the Pauli exclusion principle) [5]. Bosons have integer spin and obey Bose-Einstein statistics [5]. Within the SM, every charged fermion has an associated anti-particle with identical mass but opposite electric charge (and other quantum numbers) [6]. A pictorial overview of the particle constituents of the Standard Model is shown in Figure 2.1, while a more detailed discussion is presented in Section 2.1.1.

The mathematical picture of the strong, weak, and electromagnetic forces discussed earlier originates from the interpretation of the Standard Model as a *gauge field theory*. In this framework, the Standard Model is represented by a symmetry group, $SU(3)_c \times SU(2)_L \times U(1)_Y$, that governs the behaviour of these interactions [1]. The $SU(3)_c$ term is associated with quark-gluon (or gluon-gluon) interactions in quantum chromo-dynamics (QCD). Its generators give rise to the eight gluons of the QCD theory that mediate the strong force [1]. The $SU(2)_L \times U(1)_Y$ group governs electroweak physics and possesses its own generators, which make up the electroweak gauge bosons (the W- and Z-bosons, in addition to the photon) [1]. The breaking of the Standard Model group symmetry through the introduction of the Higgs field (and the associated Higgs boson) conrtibutes to the masses of the electroweak bosons and other fermions. The process of this symmetry breaking and its consequences are discussed further in Section 2.1.2.

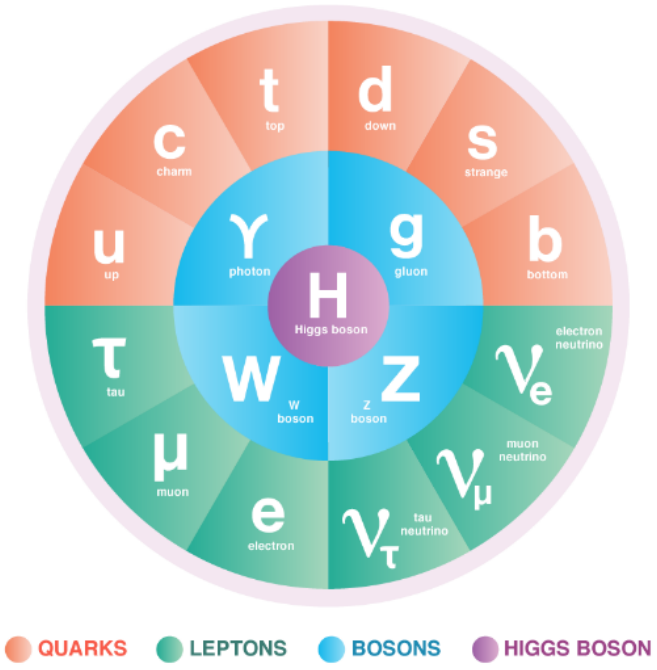

Figure 2.1: A visual representation of the particles that make up the Standard Model. Taken from [7].

2.1.1 Standard Model particles

Quarks

In the Standard Model there are three (approximately mass ordered) generations of quarks organised with one up-type (u, c, t) and one down-type (d, s, b) quark per generation. The generations are summarised as [6]:

$$\begin{pmatrix} u \\ d \end{pmatrix}, \begin{pmatrix} c \\ s \end{pmatrix}, \begin{pmatrix} t \\ b \end{pmatrix}. \tag{2.1}$$

Quarks (q)[2] carry a *colour charge* [6]. This colour charge can be either red, green, or blue, but quarks can also carry anti-colour charge (e.g. anti-red, etc.). They interact with other colour-charged particles through the exchange of gluons (massless bosons) [6]. Gluons themselves can self interact and carry both a unit of colour and anti-colour charge [6]. The interactions of quarks and gluons are described by QCD, which governs the strong force [6].

In nature, we do not observe states with colour – only colour neutral states are seen as a result of *colour confinement* [6]. Colour confinement results from the varying strength of the strong force as a function of the separation of two colour-charged particles [6]. As the separation of two quarks (e.g. in a quark/anti-quark pair) increases, the magnitude of the strong force increases. Eventually, it becomes energetically favourable for the quark pair to split into two different quark/anti-quark pairs (i.e. producing two separate q-$\bar{q}$ pairs). Thus, only colour neutral states called hadrons are observed [6].

The properties of the three quark generations are summarised in Table 2.1. The weak hypercharge, representative of the $U(1)$ component of the Standard Model, is also included – this encapsulates a representation of both the electric charge and the third "isospin"[3] component of particles [6].

Quark (hadronic) matter is broadly categorised into baryons and mesons. Baryons consist of three quarks (qqq) and having half-integer spin are fermions (e.g. the proton [uud] and neutron [udd]). Mesons consist of quark anti-quark pairs ($q\bar{q}$), which have integer spin (e.g. pions; π^0, $\pi^{\pm}$).

In the Standard Model, the quark fields transform under the $SU(3)$ gauge group as triplets (i.e. 3×1 column vectors) [1]. The left-handed chirality quarks transform under $SU(2)$ as doublets (2×1 column vectors containing a single up-type and down-type quark) (i.e. the weak interactions) [1]. The right-handed chirality fields

[2]The anti-particle of the quark is denoted $\bar{q}$.

[3]The isospin 3-vector, $\vec{T}$, is derived from the isospin generator $\vec{\tau}$, defined in terms of the Pauli spin matrices [6]. The "component isospin", T^3, is used to calculate the hypercharge Y in a linear combination of Q (electric charge) and T^3 (e.g. with $Y = 2(Q - T^3)$, but the factor of 2 normalisation varies) [1, 6].

Table 2.1: Standard Model quark properties separated by family taken from [8]. The electric charge is denoted as Q. The *Type* column refers to whether the quark is down (D) or up (U) type – important for electroweak interactions involving the W-boson. The weak hypercharge is taken from Ref. [4] and varies depending on the handedness (L- or R-handed) of the particles.

Quark	Type	Spin (J)	Q (units of e)	Y (weak hypercharge)	Mass
u (up)	U	1/2	2/3	1/6 (L-handed) 2/3 (R-handed)	2.16 MeV/c^2
d (down)	D	1/2	−1/3	1/6 (L-handed) −1/3 (R-handed)	4.67 MeV/c^2
c (charm)	U	1/2	2/3	1/6 (L-handed) 2/3 (R-handed)	1.27 GeV/c^2
s (strange)	D	1/2	−1/3	1/6 (L-handed) −1/3 (R-handed)	93 MeV/c^2
t (top)	U	1/2	2/3	1/6 (L-handed) 2/3 (R-handed)	172.76 GeV/c^2
b (bottom)	D	1/2	−1/3	1/6 (L-handed) −1/3 (R-handed)	4.18 GeV/c^2

transform as singlets (individual states) under $SU(2)$ [1]. All the quarks couple to $U(1)$ and have non-zero weak hypercharge [1].

Leptons

Like quarks, leptons are broadly categorised into three generations (or families), one for each lepton flavour. Each of these families includes a fermionic, charged lepton, ℓ, and its anti-particle, $\bar{\ell}$ [6]. The final constituent of each lepton family is a neutral, light neutrino, ν_ℓ (and its associated anti-particle $\bar{\nu}_\ell$) [6]. The Standard Model lepton flavours include the electron, muon, and tau [6]. Table 2.2 provides a summary of the key properties of these particles.

The leptons interact *only* electromagnetically (charged particles) and through the weak interactions (W- and Z-boson exchange). The left-handed chirality leptons transform as doublets containing a single neutrino and charged lepton (in the same family) under $SU(2)$ [1]. The right-handed chirality lepton fields (including anti-neutrinos) transform as singlets under $SU(2)$ [1, 6]. All the lepton fields except the right-handed ν fields have non-zero (weak) hypercharge [1, 6]. Originally neutrinos were thought to be massless, like the photon and gluon. However, evidence for neutrino oscillations where neutrinos change flavour as they travel over long distances led to the discovery that they indeed have a non-zero mass [4, 8].

Table 2.2: Standard Model lepton properties separated by family. Properties are taken from [8]. The electric charge is denoted as Q. Neutrino masses are quoted as upper limits from [8] with the confidence level of the limit in brackets (both the $\bar{\nu}_e$ and ν_e mass limits are given). The weak hypercharge is taken from Ref. [4] and varies depending on the handedness (L- or R-handed) of the particles.

Lepton	Spin (J)	Q (units of e)	Y (weak hypercharge)	Mass
e (electron/ positron)	1/2	± 1	$-1/2$ (L-handed) -1 (R-handed)	~ 0.511 MeV/c^2
ν_e (electron neutrino)	1/2	0	$-1/2$ (L-handed) 0 (R-handed)	$m_{\bar{\nu}} < 1.1$ eV/c^2 (90% CL) $m_{\nu} < 225$ eV/c^2 (95% CL)
μ (muon/ anti-muon)	1/2	± 1	$-1/2$ (L-handed) -1 (R-handed)	~ 105.66 MeV/c^2
ν_μ (muon neutrino)	1/2	0	$-1/2$ (L-handed) 0 (R-handed)	< 0.19 MeV/c^2 (90% CL)
τ (tau/ anti-tau)	1/2	± 1	$-1/2$ (L-handed) -1 (R-handed)	~ 1776.86 MeV/c^2
ν_τ (tau neutrino)	1/2	0	$-1/2$ (L-handed) 0 (R-handed)	< 18.2 MeV/c^2 (90% CL)

Bosons

Bosons mediate the interactions between fundamental (and composite) particles in the Standard Model. In QCD and electroweak (EWK) physics, certain force carriers (including the gluon and the Higgs boson) can also self interact. As discussed in earlier Sections, the W- and Z-bosons interact both with the leptons and quarks, while the gluon interacts only with colour charged particles. The photon only interacts with electrically charged particles. Conversely, the Higgs boson [9–11] is a scalar boson unlike the other Standard Model vector bosons, and it interacts with all the Standard Model particles, except the right-handed neutrinos and photons or gluons. Additionally, the Higgs boson has small couplings to low-mass particles – interactions involving heavy particles are more common [6, 12]. The properties of Standard Model bosons are summarised in Table 2.3.

The nature and origin of the masses for these particles is explained by the interpretation of the Standard Model as a gauge field theory with important implications for the existence of the Higgs boson discussed in the next Section.

2.1.2 The Standard Model as a gauge field theory

The interpretation of the Standard Model as a gauge field theory leads to a mathematical understanding of the fundamental interactions between leptons, quarks, and bosons. The *Lagrangian* ($\mathcal{L}$) of the Standard Model determines the interactions

Table 2.3: Standard Model boson properties. Properties are taken from [8]. The electric charge is denoted as Q. Only the Higgs *field* (not the boson itself) has a non-zero weak hypercharge (1/2), the other bosons do not couple to $U(1)$ [4].

Gauge boson	Spin (J)	Q (units of e)	Mass (GeV/c^2)
Photon (γ)	1	0	0
Gluon (g)	1	0	0
Z-boson (Z^0)	1	0	91.1876 ± 0.0021
W-boson ($W^{\pm}$)	1	± 1	80.379 ± 0.012
Higgs boson (H^0)	0	0	125.10 ± 0.14

and inherently the mass of each fundamental particle. In this interpretation, each particle is described by a *field* with varying properties depending on its bosonic or fermionic nature. The complete Lagrangian is lengthy, but can be summarised in terms of contributions from different interactions and fields as [1]:

$$\mathcal{L} = \mathcal{L}_G + \mathcal{L}_f + \mathcal{L}_H + \mathcal{L}_{fH} \tag{2.2}$$

where:

- $\mathcal{L}_G$ describes the behaviour of the QCD gluons and EWK W- and Z-bosons.
- $\mathcal{L}_f$ describes the behaviour of fermions – leptons and quarks.
- $\mathcal{L}_H$ describes the Higgs boson – and its mass.
- $\mathcal{L}_{fH}$ describes the interactions of fermions with the Higgs boson field.

The Higgs field interactions generate the masses of the EWK bosons and contribute to the masses of fermions through the *Higgs mechanism* involving *spontaneous symmetry breaking* (SSB) of the Standard Model gauge symmetry. The nature of SSB was studied by Brout, Englert, Higgs, and others in the 1960s leading to our current understanding of how the Standard Model gauge bosons gain their mass [9, 13].

The Standard Model $SU(2) \times U(1)$ symmetry group alone, without the Higgs mechanism, leads to massless gauge bosons – necessary to maintain the gauge symmetry [14]. Terms that predict the masses of particles (mass terms) in $\mathcal{L}$ *must* be *gauge invariant*. This refers to the fact that under as *gauge transformation* the mass terms should not change, they must remain the same. For the case of the Standard Model, a non-Abelian[4] gauge theory, the gauge transformation has the generic form

[4]In an Abelian theory $A \times B = B \times A$ for two (complex) numbers but this is not the case for a non-Abelian theory where A and B are represented by matrices that multiply vectors of fields.

[1]:

$$\psi(x) \to V(x)\psi(x) \tag{2.3}$$

where $\psi(x)$ is a particle field and $V(x)$ is a matrix in the Standard Model symmetry group $SU(3) \times SU(2) \times U(1)$ (or $SU(2) \times U(1)$ if only the EWK symmetry breaking is being considered). Both the field (ψ) and complex transformation matrix (V) are functions of the space-time coordinate x [1]. The definition of the "derivative" is modified to have the same transformation property as in Equation (2.3), and is called a covariant derivative. Restricting our consideration to the EWK symmetry, the covariant derivative is defined in terms of the individual gauge fields prescribed for each of the groups in the $SU(2) \times U(1)$ product [1]. The fields for $SU(2)$ are denoted W_μ^i ($i = 1,\ 2,\ 3$; or $\vec{W}_\mu$ in vector form) and the single field for $U(1)$ is denoted B_μ[5]. The covariant derivative accounts for the change in the fields under a gauge transformation and is then written as [1]:

$$D_\mu\psi(x) = \left(\partial_\mu + \frac{ig}{2}\vec{\tau}\cdot\vec{W}_\mu + \frac{ig'}{2}B_\mu\right)\psi(x) \tag{2.4}$$

such that it transforms as [1]:

$$D_\mu\psi \to V(x)D_\mu\psi. \tag{2.5}$$

In Equation (2.4), g and g' are the respective couplings to each gauge group, and $\vec{\tau} = \vec{\sigma}/2$ are the group generators of $SU(2)$ defined in terms of the Pauli matrices ($\vec{\sigma}$).

The Higgs field is introduced into the theory as a complex scalar doublet of the form [1]:

$$\phi = \begin{pmatrix}\phi^+\\ \phi^0\end{pmatrix}. \tag{2.6}$$

where ϕ^+ is a charged scalar field and ϕ^0 is a neutral scalar field. The Higgs portion of the Lagrangian is written [1]:

$$\mathcal{L}_H = (D^\mu\phi)^\dagger(D_\mu\phi) - V(\phi) \tag{2.7}$$

where $(D^\mu\phi)^\dagger$ is a Hermitian conjugate. The function $V(\phi)$ represents the Higgs potential [1]:

$$V(\phi) = \mu^2\phi^\dagger\phi + \lambda(\phi^\dagger\phi)^2, \tag{2.8}$$

which describes a Mexican-hat shape in the complex plane defined by the real and imaginary parts of ϕ^0 with a classical minimum (vacuum expectation value) $\nu = \sqrt{-\mu^2/\lambda}$ [1]. A convenient choice of the "unitary gauge" (where $\phi^+ = 0$) leads to an alternate form of the Higgs doublet (in practice, there may be extra exponential

[5]The fields themselves also change under gauge transformations! Furthermore, note that for each of the $SU(N)$ symmetry groups there are $N^2 - 1$ different generators, and therefore $N^2 - 1$ different gauge fields that represent the bosons.

terms multiplying the column vector below [4]) [1, 4]:

$$\phi = \frac{1}{\sqrt{2}} \begin{pmatrix} 0 \\ \nu + H \end{pmatrix} \tag{2.9}$$

where H is an additional quantum field that describes fluctuations around the classical value, ν.

The incorporation of the Higgs doublet in $\mathcal{L}_H$ leads to an expression for the $(D^\mu\phi)^\dagger(D_\mu\phi)$ term [1]:

$$(D^\mu\phi)^\dagger(D_\mu\phi) = \frac{1}{2}\begin{pmatrix} 0 & \nu \end{pmatrix}\left[\frac{g}{2}\vec{\tau}\cdot\vec{W}_\mu + \frac{g'}{2}B_\mu\right]^2\begin{pmatrix} 0 \\ \nu \end{pmatrix} + \text{other terms.} \tag{2.10}$$

In Equation (2.10), the $\vec{W}_\mu$ and B_μ fields combine into various superpositions to form four different fields [1]:

$$W_\mu^\pm = \frac{W_\mu^1 \mp iW_\mu^2}{\sqrt{2}} \tag{2.11}$$

$$Z_\mu^0 = \frac{gW_\mu^3 - g'B_\mu}{\sqrt{g^2 + (g')^2}} \tag{2.12}$$

$$A_\mu = \frac{g'W_\mu^3 + gB_\mu}{\sqrt{g^2 + (g')^2}} \tag{2.13}$$

which after rearrangement of Equation (2.10) gives [1, 4]:

$$(D^\mu\phi)^\dagger(D_\mu\phi) = \left(\frac{g\nu}{2}\right)^2 W_\mu^+ W^{\mu,-} + \frac{1}{2}\left(\frac{\sqrt{g^2 + (g')^2}\nu}{2}\right)^2 Z^\mu Z_\mu + (0)A_\mu. \tag{2.14}$$

The coefficients multiplying the fields are squares of the particle masses: the W-boson mass is $m_W = g\nu/2$ and the Z-boson mass is $m_Z = (\sqrt{g^2 + (g')^2}\nu)/2$, leaving A_μ as the massless photon field [1]. Thus, the introduction of a scalar doublet to describe the Higgs boson leads to SSB where the EWK $SU(2) \times U(1)$ group symmetry breaks to a $U(1)$ (electromagnetic) symmetry, resulting in massive gauge bosons [1].

The Higgs field also plays a role in the generation of fermion masses, which is not discussed further here. Interactions of Standard Model leptons and quarks with the Higgs boson lead to the generation of terms in the Lagrangian that are products of both left- and right-handed fields (opposite chirality products), representing mass terms [1, 4]. Higher-order terms in the Lagrangian also lead to (self-)interactions between the W, Z, and Higgs bosons [1]. The Higgs boson itself has a mass term, which appears in the Lagrangian of the theory [4].

2.1.3 The interactions of the W and Z bosons with fermions

Interactions of the W- and Z- bosons occur between both quarks and leptons, however, the charge of the W-boson allows it to engage in flavour changing interactions. In W-boson (charged current) interactions the incoming quark/lepton changes flavour/family during the interaction [14]. An example of a charged current interaction, the decay of a top quark, is illustrated in Figure 2.2a.

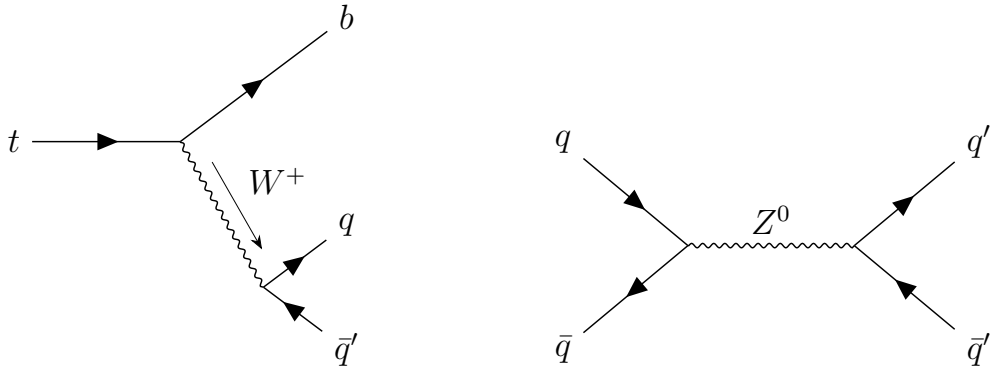

(a) The hadronic decay of a top quark through a weak interaction producing a b quark (the flavour changed component) in addition to two other quarks from the W-boson decay.

(b) The production of a Z-boson from a quark-anti quark pair. The Z-boson decays to quarks of a different flavour compared to the initial $q\bar{q}$ pair.

Figure 2.2: Feynman diagrams for common hadronic weak interactions.

Neutral current interactions preserve the flavour of particles and occur when the Z-boson mediates weak interactions [14] – see Figure 2.2b for an example. Note that the charged current interactions change the quark flavour such that up-type (e.g. t) quarks are converted to down-type (e.g. b) quarks. The probability for the decay of each of the up-type quarks into any down-type quark is governed by the Cabibbo-Kobayashi-Maskawa (CKM) matrix [4]. The Standard Model CKM matrix is unitary[6] – any deviation from unitarity is evidence of BSM physics. The matrix is written [4]:

$$V = \begin{pmatrix} V_{ud} & V_{us} & V_{ub} \\ V_{cd} & V_{cs} & V_{cb} \\ V_{td} & V_{ts} & V_{tb} \end{pmatrix} \tag{2.15}$$

where each element V_{ij} is defined so that it describes the mixing between quark flavours i and j in charged current interactions.

The next Section addresses key downfalls of the Standard Model and extensions that can be used to explain fundamental questions, including the nature of dark matter.

[6] A unitary matrix, V, satisfies $VV^\dagger = V^\dagger V = \mathbb{I}$ where $V^\dagger = (V^*)^T$ (i.e. transpose of the complex conjugate of the matrix) and $\mathbb{I}$ is the identity matrix.

2.2 Beyond the Standard Model

The Standard Model correctly explains a wide range of phenomena, but fails to account for some other experimental observations. In a cosmological context, the most striking flaw is the lack of a candidate for *dark matter* and *dark energy* in the Standard Model. A combination of cosmological measurements have shown that normal matter[7] accounts for only about 5% of the total matter-energy density of the Universe [1]. The remainder of the Universe is made up of dark matter (between 26% and 27%) and dark energy (between 68% and 69%) [1]. A model of fundamental physics should be able to explain these constituents of the Universe. Hence, the focus on collider searches for new physics that can explain the questions left unanswered by the Standard Model in its current form. Other ambiguities in the Standard Model raise questions about the origin of neutrino masses, the asymmetry between matter and anti-matter in the Universe, and the unification of the fundamental forces including gravity in a Grand Unified Theory (GUT) [1, 15].

A significant factor that motivates *supersymmetry* (SUSY) is the existence of the *hierarchy problem* [1]. Theoretically, the Higgs boson mass can be written as [1]:

$$m_H^2 = m_{H,0}^2 + \Delta m^2 \tag{2.16}$$

where m_H is the observed mass, $m_{H,0}$ is called the bare mass, and Δm^2 consists of corrections that originate from higher-order Feynman diagrams where the Higgs boson interacts with other particles (e.g. containing fermion loops) [1]. The correction terms diverge, and are much larger than the experimental 125 GeV mass of the Higgs boson [1]. Thus, if the correction terms are large and negative then the bare Higgs mass must also be large enough to result in a small (positive) difference. This violates *naturalness*, which ultimately requires that measured observables are not impacted by large corrections modified to balance "bare" quantities [1].

2.2.1 Dark matter

Dark matter, introduced briefly at the start of this Section, interacts primarily through the gravitational force (from astronomical observations), and is essential to the evolution of galaxies, galaxy clusters, and the Universe as we know it [16]. The absence of observations of electromagnetic (and strong/QCD) interactions of dark matter led to the traditional description of dark matter as a stable and neutral (non-baryonic) particle [17]. The effect of cosmological dark matter on the structure and evolution of the Universe is governed by the ΛCDM cosmological model – CDM represents *cold (non-relativistic) dark matter* and Λ represents dark energy [17, 18].

Our understanding of dark matter originates from astronomical observations of galaxies and galaxy clusters. In the 1930s, Fritz Zwicky measured red-shifts of

[7] Matter that interacts via the EM/weak/strong forces and is visible to detectors and telescopes.

galaxies within the Coma cluster to determine the spread of their recessional velocities due to the expansion of the Universe [19]. He compared these results to an expected value calculated using the Virial theorem[8] – the measured values were much larger than the calculated value [19]. The discrepancy of these results led to the conclusion that there was an over-abundance of non-visible (dark) material compared to visible material in those galaxies [19].

Further studies of spiral galaxy rotation curves lead to similar conclusions [19, 20]. For instance, studies of the rotation curves of the Andromeda (M31), Pinwheel (M101), and M81 spiral galaxies show that the curve remains stable at large radii [19–21]. The rotational velocity of material gravitationally bound to the galaxies should decrease proportional to $\{\text{radius}\}^{-1/2}$ according to Kepler's laws, but shows a relatively flat trend with increasing distance from the galactic centre [20]. Thus, there must be a significant concentration of mass in the halo of these galaxies – a dark matter halo [19] – such that the galaxies extend beyond the region that is measurable with visual astronomy techniques [21]. This raises the question: what actually makes up dark matter? While many theories exist, ranging from primordial black-holes from the early Universe to less likely MACHOs[9], WIMPs (weakly interacting massive particles) are thought to be a more probable candidate [19].

If dark matter is particle-like then its nature can be probed at collider experiments that aim to produce dark matter candidates from Standard Model particles through interactions proposed in BSM theories [22]. Since dark matter is not observed to interact with Standard Model particles (except gravitationally) it must be non-baryonic and unlike any particle already introduced in the standard model. The WIMP (Weakly Interacting Massive Particle) description of dark matter typically involves a thermal[10] relic particle (e.g. a SUSY neutralino) [16]. This particle will have existed in thermal equilibrium (number density approximately constant through self-annihilation reactions) in the early Universe until the effect of the expansion of the Universe was sufficient to force the particle to freeze out of (exit from) equilibrium and remain at an approximately constant number density [16]. The "WIMP miracle" summarises this mechanism, which ultimately leads to the present day dark matter density provided that dark matter particles self-annihilate with a cross-section on the order of 10^{-26} cm^3/s/v (v is the magnitude of the relative velocity for the interacting particles) [16, 19]. The estimated interaction cross-section for these particles is on a similar scale to those in EWK interactions – hence the term WIMP [19, 23].

The particle candidate for dark matter could originate from models of SUSY or as an alternative particle such as a light axion [16]. Nonetheless, the nature of dark

[8] The Virial theorem provides a relationship between the kinetic and (gravitational) potential energy of a mass distribution required for stable orbits [20].
[9] Massive Astrophysical Compact Halo Objects – planets, stars, etc. in the galactic halo [19].
[10] This terminology arises from the fact that the particles were produced in thermal equilibrium (thermal production).

matter need not be described by a single particle, rather there may be a complete *dark sector* of particles that interacts with dark matter candidate(s) [23].

2.2.2 Supersymmetry

Additional symmetry between fermions and bosons

SUSY extends the gauge symmetries of the Standard Model with the addition of a new symmetry between fermions and bosons. This new symmetry is described mathematically by the supersymmetric algebra[11] in terms of an operator Q and its conjugate $Q^\dagger$ that act to annihilate or create states with spin differing by 1/2 relative to the initial state [1, 24]. To achieve this, the operators must satisfy [24]:

$$\{Q,\ Q^\dagger\} = -2\gamma_\mu P^\mu \tag{2.17}$$

$$[Q,\ P^\mu] = 0 \tag{2.18}$$

where P^μ generates translations in four-dimensional space-time and γ_μ are the Dirac matrices in the same space-time. Equations (2.17) and (2.18) encode the effect of the Q operators on different spin states, and their variation under space-time coordinate translations (via P^μ; Equation (2.18) implies that Q does not change under translations) [24, 25].

Acting with the respective generator on a fermion alters its spin to produce a bosonic state and vice versa. Consequently, every Standard Model fermion (spin-1/2) degree of freedom[12] has a corresponding bosonic (spin-0) SUSY degree of freedom [1]. Similarly, Standard Model boson degrees of freedom have accompanying spin-1/2 SUSY degrees of freedom. Ultimately, the Standard Model particles have a corresponding supersymmetric analogue referred to as a sparticle such that the number of particles described in the extended model doubles [1].

The fact that SUSY has not yet been observed in any form at colliders indicates the symmetry must be broken [1, 8]. Were this symmetry exact[13], then the masses of Standard Model particles and their superpartners would be identical [8]. Since this is evidently not the case, the symmetry cannot be exact.

Particle content

The particle content of a basic supersymmetric model includes [1, 24, 26]:

[11] The mathematical foundation of SUSY will not be the focus here, so this information is stated for completeness only.

[12] Fermionic particles have two degrees of freedom (spin-up and spin-down), whilst integer spin bosonic particles have a single degree of freedom.

[13] Under an exact symmetry generated by G the Lagrangian is invariant ($[G,\ \mathcal{L}] = 0$) and the action of the generator on the empty vacuum state leads to a vanishing result ($G\,|0\rangle = 0$) [1]. Where, $G\,|0\rangle \neq 0$ the symmetry is spontaneously broken by the generators [1].

- The superpartners of the left-handed and right-handed quarks ($\tilde{q}_L$ and $\tilde{q}_R$) referred to as squarks (e.g. stop, etc.).
- The superpartners of the left-handed and right-handed charged leptons ($\tilde{e}_L$ and $\tilde{e}_R$) referred to as sleptons (e.g. selectron, etc.).
- The superpartners of the left-handed neutrinos ($\tilde{\nu}_L$).
- Superpartners of the gauge bosons: winos $\tilde{W}^{\pm}$ and $\tilde{W}^0$, bino $\tilde{B}^0$.
- Superpartners of the Higgs boson(s).
- The superpartner of the gluon, $\tilde{g}$, the gluino.
- The original Standard Model particles (with a modified Higgs sector).

Notationally, the L or R sub-scripts for the SUSY particles *only* indicate the chirality of their corresponding Standard Model partner [1].

The fields for the winos and binos are written in an analogous form to the description of Standard Model EWK symmetry breaking – the three $\tilde{W}$ fields are representative of the three $SU(2)$ generators and the single $\tilde{B}$ field is representative of the $U(1)$ generator. Thus, every original Standard Model gauge field is assigned a superpartner (like before we introduced the linear combinations of fields for the $W^{\pm}$ in Section 2.1.2). However, unlike in the Standard Model, two different Higgs doublets are required to achieve the same effect of generating fermion masses [1]. One of the new doublets interacts with u quarks and neutrinos, while the other interacts with d quarks and charged leptons (e, μ, τ) [1]. In the MSSM (the Minimal Supersymmetric Standard Model) this leads to five different Higgs bosons with spin-0 [26]:

- h, H – neutral bosons with CP[14] eigenvalues of +1 (even).
- A – a neutral boson with a CP eigenvalue of −1 (odd).
- $H^{\pm}$ – two charged Higgs bosons.

The supersymmetric partners of the two Higgs doublets are referred to as higgsinos – each field in the doublets has a superpartner as for all other Standard Model particles [1, 26]. Linear combinations of the winos, binos, and higgsinos produce the mass-ordered electroweakinos: charginos $\tilde{\chi}_j^{\pm}$ ($j = 1,\ 2$ – two states) and the neutralinos $\tilde{\chi}_i^0$ ($i = 1, \ldots, 4$ – four states) [1, 26].

Further constraints, including the conservation (or violation) of R-parity symmetry, can be imposed on the theory to modify the complete Lagrangian. The phenomenological differences that arise in these scenarios are discussed next.

[14]The CP (charge-parity) eigenvalues relate to the effect of operators acting on quantum states. The C (charge conjugation) operator acts to reverse the charge of the state (and also other internal quantum numbers including but not limited to the baryon and lepton number [6]) and the P (parity) operator acts to reverse the spatial orientation of the state (i.e. $\vec{r} \to -\vec{r}$) [4, 5].

R-parity and dark matter candidates

In a supersymmetric model the baryon number (B) and lepton number (L)[15] are used to define a new discrete quantum number, R-parity. R-parity (R_p) is defined [1, 26]:

$$R_p = (-1)^{3(B-L)+2S} \tag{2.19}$$

where S is the spin of the particle. For fundamental particles this leads to $R_p = +1$ for Standard Model particles and $R_p = -1$ for their sparticle counterparts.

When R-parity is conserved *all* terms in the Lagrangian violating lepton number and baryon number conservation vanish. This provides a convenient way to eliminate proton decays in an R-parity conserving (RPC) theory [27]. Additionally, RPC SUSY models only allow the production of sparticles in pairs [27, 28]. Each pair-produced sparticle decays to another state, which contains an additional sparticle for R-parity conservation and other Standard Model particles allowed by the process [27]. Eventually, the decays of the sparticles will produce the lightest supersymmetric particle (LSP), which can be interpreted as a dark matter candidate provided it is stable and neutral (e.g. a neutralino) [1, 27, 28]. The addition of RPC constraints in models of SUSY including the phenomenological MSSM (pMSSM) significantly reduces the number of parameters needed to fully describe the theory [26].

However, evidence of SUSY has not yet been observed at any collider experiment. RPC constraints, while convenient for explaining the nature of dark matter, reduce the total parameter space accessible to SUSY searches [26]. In nature, it is not possible to predict with certainty that SUSY actually respects R-parity symmetry. Searching uncovered parameter space for evidence of RPV (R-parity violating) SUSY provides an avenue to further constrain our understanding of physics beyond the Standard Model. The added flexibility in RPV models allow both baryon number ($\mathcal{L}_{\Delta B \neq 0}$) and lepton number ($\mathcal{L}_{\Delta L \neq 0}$) violating processes encapsulated in the SUSY Lagrangian as [24, 27]:

$$\mathcal{L}_{\Delta L \neq 0} = \frac{1}{2}\lambda^{ijk} L_i L_j \bar{e}_k + (\lambda')^{ijk} L_i Q_j \bar{d}_k + (\mu')^i L_i H_u \tag{2.20}$$

$$\mathcal{L}_{\Delta B \neq 0} = \frac{1}{2}(\lambda'')^{ijk} \bar{u}_i \bar{d}_j \bar{d}_k \tag{2.21}$$

where λ^{ijk}, $(\lambda')^{ijk}$, $(\mu')^i$, and $(\lambda'')^{ijk}$ are the coupling constants for each family (leptons) or generation (quarks) of particles indicated by indices i, j, and k. The L_i fields represent leptons and the $\bar{e}_k$ fields their right-handed (chirality) counterparts [27]. The Higgs doublet interacting with the u quarks is included as H_u and the quark fields are denoted with Q_i, $\bar{u}_i$, and $\bar{d}_i$ (the latter fields are for the up-type and down-type quarks) [27].

[15] For B (L) a q (ℓ) contributes 1/3 (+1) and a $\bar{q}$ ($\bar{\ell}$) contributes −1/3 (−1).

The λ^{ijk} term in Equation (2.20) results in multi-lepton processes, while the other $(\lambda')^{ijk}$ and $(\mu')^{i}$ terms result in mixed quark and lepton, and lepton and Higgs sector final states, respectively [27]. Conversely, the lone $(\lambda'')^{ijk}$ term in Equation (2.21) allows for purely hadronic finals states containing quarks – this term is referred to as the λ'' UDD coupling [27]. One consequence of the baryon number violating term is that it allows the decays of sparticles to hadronic Standard Model finals states – e.g. $\tilde{g}\tilde{g} \to 6q$ (three quarks from each gluino). These processes will be explored further in Chapters 5 and 6 in the context of low-mass resonance searches.

A perceived disadvantage of RPV SUSY models is that the LSP is not necessarily stable [26, 27]. Thus, there is no clear dark matter candidate in the model. However, other descriptions of dark matter can solve this problem, including the existence of QCD axions from a $U(1)$ symmetry imposed to ensure unobserved CP violating terms in the QCD Lagrangian vanish [1].

2.3 Summary

The Standard Model of particle physics describes a range of phenomena from electroweak physics to QCD with great precision. However, the model cannot explain the nature of dark matter or dark energy, which combined make up a far greater amount of our Universe than normal matter alone. A range of extensions to the Standard Model are possible to explain these phenomena. SUSY introduces a broad spectrum of new particles and is a candidate for solving the hierarchy problem associated with large corrections to the Higgs boson mass. The search for SUSY and alternative models will continue at modern colliders to expand constraints on BSM theories and reach uncovered regions of parameter space, including those introduced by the relaxation of conditions such as R-parity conservation on models.

Chapter 3

The ATLAS experiment at the LHC

The ATLAS (A Toroidal LHC ApparatuS) detector [29] at the LHC (Large Hadron Collider) is a general-purpose physics detector that provides data for precision tests of the Standard Model of Particle Physics and searches for Beyond the Standard Model (BSM) physics. The ATLAS detector consists of several sub-detectors devoted to reconstructing the products of proton-proton (pp) and heavy-ion collisions using a combination of calorimetry and charged particle tracking. Additional trigger and data acquisition (TDAQ) systems are essential to collecting "interesting" data in an environment where pp collisions occur at a maximum rate of 40 MHz.

The following Chapter provides an overview of the LHC (Section 3.1) and ATLAS detector systems (Section 3.2). Future upgrades, are discussed in parallel with the existing configuration of the ATLAS experiment.

3.1 The LHC

The LHC (Large Hadron Collider) is designed to deliver high energy proton collisions from two counter-rotating beams up to a $\sqrt{s} = 14$ TeV centre-of-mass (CM) frame energy [29–31]. Early Run 1 collisions occurred at $\sqrt{s} = 7$ TeV or $\sqrt{s} = 8$ TeV, while Run 2 collisions occurred at energies up to $\sqrt{s} = 13$ TeV [31]. During Run 3, the LHC will be run at $\sqrt{s} = 13.6$ TeV, and at the High-Luminosity LHC (HL-LHC) the CM frame energy will reach $\sqrt{s} = 14$ TeV. The LHC is also capable of delivering heavy-ion collisions of lead ions at 2.8 TeV beam energies [30]. Collisions are delivered at various points around the LHC ring where detectors are situated – including ATLAS, CMS, ALICE, and LHCb. The configuration of the LHC ring is shown in Figure 3.1.

Protons are injected into the LHC ring at an energy of 450 GeV but first undergo a sequential acceleration procedure. Hydrogen anions are accelerated in the linear accelerators, *LINAC*, to reach an energy of 50 MeV [33]. Then the acceleration of the protons continues in the four rings of the *Proton Synchrotron Booster* (PS) to reach an energy of 1.4 GeV [33]. The *Super Proton Synchrotron* (SPS) proceeds

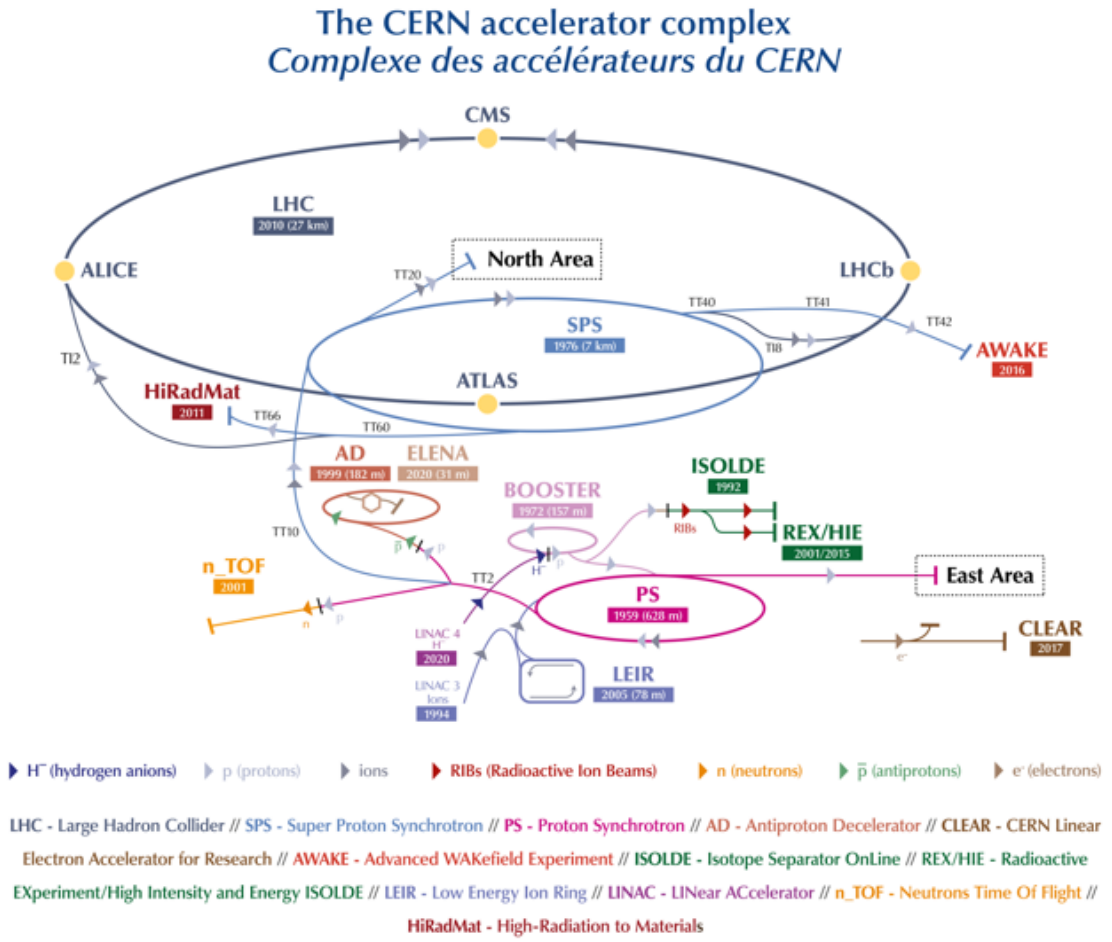

Figure 3.1: The CERN accelerator complex showing the various accelerators used to inject high-energy protons into the main LHC beam-line. The positions of the various experiments are also highlighted. Protons take the path indicated by grey arrows to reach the LHC, starting at the *Booster* from hydrogen ions accelerated at one of the linear accelerators, *LINAC*. Taken from [32].

to accelerate the particles to the energy at which they enter the LHC rings [33]. Further acceleration up to 7 TeV (for $\sqrt{s} = 14$ TeV pp collisions) is achieved with superconducting magnets and radio-frequency cavities in the LHC ring [33, 34].

Protons are collided in bunches of $\mathcal{O}(10^{11})$ protons to achieve a reasonable number of interactions per bunch crossing and therefore a sufficiently large data rate [30, 31]. The LHC is designed to deliver pp bunch crossings every 25 ns [31]. The collision rate is quantified using the luminosity for a Gaussian beam defined [30, 31]:

$$\mathcal{L} = \frac{N_b^2 n_b f_{\text{rev}} \gamma F}{4\pi \epsilon_n \beta^*} \tag{3.1}$$

where:

- N_b is the number of protons per bunch.
- n_b is the number of bunches per beam.
- f_{rev} is the revolution frequency of the beams ($f_{\text{rev}} = 11246$ Hz for proton beams [35]).
- γ is the Lorentz factor (from special relativity) of the beam (e.g. $\gamma = E_{beam}/m_p c^2$, m_p is the proton mass).
- β^* is the value of a "betatron" function that describes the squeezing of the beam through an aperture of the LHC magnets.
- ϵ_n is the normalised beam emittance ranging from 1 µm to 3.5 µm and describes the space that the beam occupies in combination with β^* [36].
- F is a scale factor accounting for increases in the relative angle between bunches at collision points – in these regions the beams travel through the same section of the beam pipe (and are not separated), which can lead to parasitic (unwanted) collisions [30].

The total *integrated* luminosity is given by integrating the instantaneous luminosity (measured at a particular instant in time) over the duration of data collection:

$$\mathcal{L} = \int \mathcal{L}_{\text{inst}} \, dt \tag{3.2}$$

where $\mathcal{L}_{\text{inst}}$ is the instantaneous luminosity in units of $\{\text{area}\}^{-1} \times \text{s}^{-1}$. The integrated luminosity has units that are the inverse of those for the cross-section for a given process (a measure of how often it occurs) and the expected yield (number of events) for a process can therefore be calculated as $N = \sigma \times \mathcal{L} \times \epsilon$ (where σ is the cross-section, $\mathcal{L}$ is the integrated luminosity, and ϵ is some efficiency for the detection/reconstruction of that process) [30]. An individual run of the LHC for a

duration T_{run} achieves an integrated luminosity of [30]:

$$L_{\text{int}} = L_0 \tau_L (1 - e^{-T_{\text{run}}/\tau_L}) \tag{3.3}$$

where L_0 is the initial luminosity and $\tau_L \approx 14.9$ h is the luminosity lifetime, which is a measure of how long it takes for the luminosity (and beam intensity) to fall due to beam losses associated with nuclear and machine effects. The optimal T_{run} value depends on the magnitude of τ_L in addition to the time taken to fill and clear the LHC beam pipes at the start and end of a run, respectively [30]. T_{run} typically takes on a value between 5.5 and 12 hours [30]. Consequently, if the LHC is operated for 200 days per year a total (integrated) luminosity of $80 - 200$ fb^{-1} is achieved for $L_0 \approx 10^{34}$ cm^{-2} s^{-1} [30].

Luminosity measurements are an essential part of monitoring data quality. The ATLAS experiment has several methods for measuring this quantity, including using the LUCID detector discussed later in Section 3.2.7. The cumulative integrated luminosity of collisions recorded by the ATLAS experiment in Run 2 is shown as a function of time in Figure 3.2a, which includes the 139 fb^{-1} of data usable for analyses.

An alternate formulation for Equation (3.1) is [35]:

$$\mathcal{L} = \sum_b \mathcal{L}_b \tag{3.4}$$

where $\mathcal{L}_b$ is the instantaneous luminosity for a single proton bunch [35]:

$$\mathcal{L}_b = \frac{\mu_{\text{vis}} f_{\text{rev}}}{\sigma_{\text{vis}}}. \tag{3.5}$$

In this Equation μ_{vis} is the number of visible interactions per bunch crossing and σ_{vis} is the cross-section for these visible interactions [35]. Importantly, μ_{vis} (and $\langle\mu\rangle$, the average number of interactions per bunch crossing) describe the number of extra inelastic pp interactions that take place every bunch crossing (in addition to the hard-scatter event that is useful for physics) [35]. These extra interactions are referred to as "pile-up" and produce challenging conditions for data collection. Reconstructed particles and objects originating from pile-up interactions might need to be rejected in favour of radiation from the hard-scatter interaction of interest as discussed in Chapter 4. Pile-up contamination levels will increase in Run 3 of the LHC and at the High Luminosity LHC (HL-LHC) where $\langle\mu\rangle$ will reach 200 interactions per bunch crossing compared to a value of 33.7 from Run 2. The $\langle\mu\rangle$ distribution for data taken at the ATLAS experiment during Run 2 of the LHC is shown in Figure 3.2b for the complete *ATLAS Recorded* dataset from Figure 3.2a.

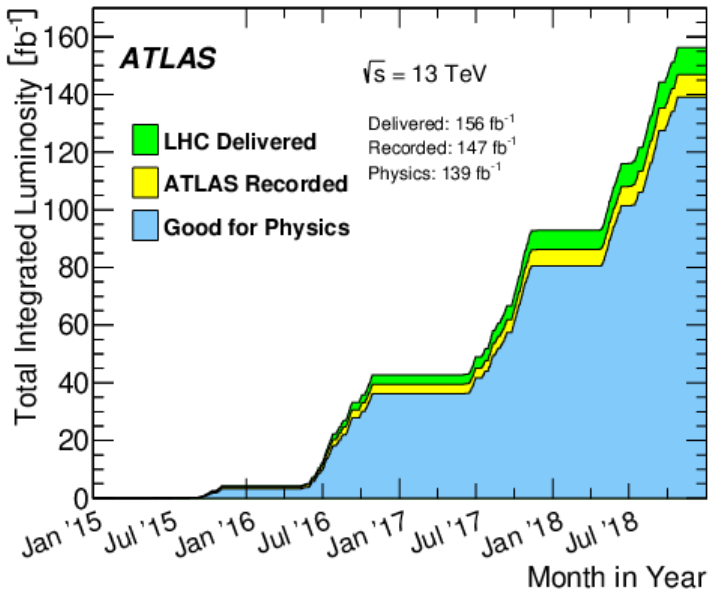

(a) The cumulative (integrated) luminosity as a function of time from stable beam conditions measured during Run 2 of the LHC. The *Good for Physics* luminosity in blue corresponds to data that can be used for physics analyses and totals 139 fb^{-1} for the Run 2 dataset. Taken from [37].

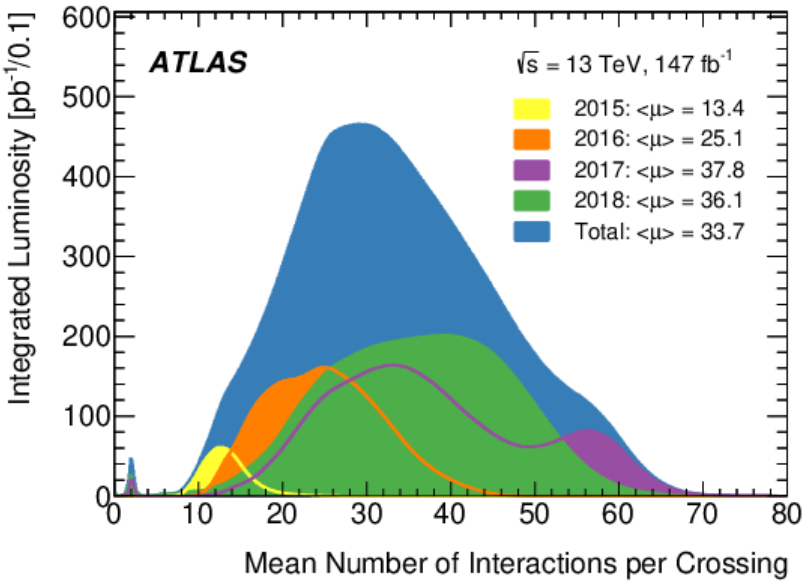

(b) The integrated luminosity as a function of the mean number of interactions per bunch crossing (μ) during Run 2 data-taking at $\sqrt{s} = 13$ TeV. The mean number of interactions per bunch crossing is a useful measure of the pile-up conditions in the detector and peaks between 30-40 interactions per bunch crossing for the final years of Run 2 data collection. Taken from [37].

Figure 3.2: ATLAS luminosity and pile-up results from Run 2 operations.

3.2 The ATLAS Detector

The ATLAS experiment sub-detectors provide a wide range of measurement capabilities and are also instrumented with hardware used to identify events of interest – trigger and data acquisition systems. The following Section introduces some of these detector systems and their purpose. A labelled diagram of the detector is shown in Figure 3.3.

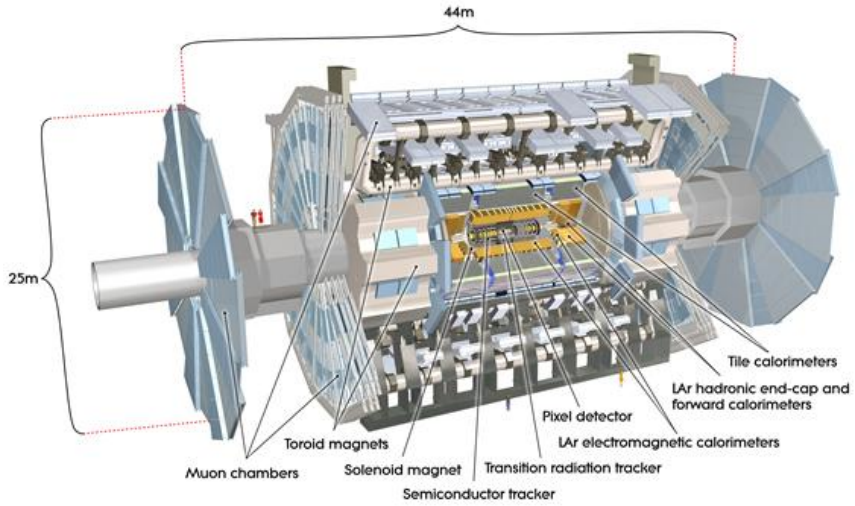

Figure 3.3: A labelled diagram showing the various sub-detectors that make up the ATLAS experiment. Taken from [38].

3.2.1 Detector Coordinate System

Events reconstructed in the ATLAS detector are described using a right-handed coordinate system where the origin lies at the nominal interaction point (IP) and the cartesian z-axis lies along the beam pipe. The x-axis and y-axis lie in the plane transverse to the beam such that the positive x-axis points towards the centre of the collider ring and the positive y-axis extends vertically [29]. The passage of a detected object is parametrised by coordinates (p_{T}, η, ϕ) [29]. Here, ϕ is the azimuthal angle of a cylinder around the IP, η is the pseudo-rapidity defined as $\eta = -\ln\tan\left(\frac{\theta}{2}\right)$ where θ is the polar angle relative to the beam, and p_T is the transverse momentum measured in the xy-plane ($p_{\mathrm{T}} = \sqrt{p_x^2 + p_y^2}$) [29]. A schematic of the η coordinate definition is shown in Figure 3.4. Distances in $\eta - \phi$ space are calculated as $\Delta R = \sqrt{\Delta\eta^2 + \Delta\phi^2}$ [29]. Since the pseudo-rapidity is an approximation for massless particles, the rapidity (y) is used for massive particles/detector objects, including hadronic jets [29]. The rapidity is substituted for η in the ΔR calculation for these objects, and is given by [29]:

$$y = \frac{1}{2}\ln\left(\frac{E + p_z}{E - p_z}\right) \tag{3.6}$$

where E is the energy of the object and p_z is the component of its momentum along the z-axis (beam-line).

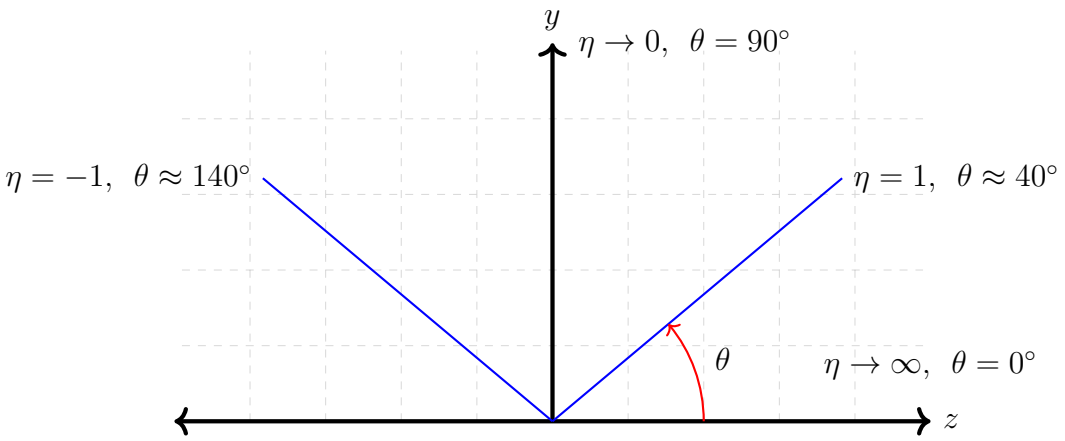

Figure 3.4: Pseudo-rapidity (η) diagram showing example values from the definition: $\eta = -\ln\tan\left(\frac{\theta}{2}\right)$. The η coordinate is defined in terms of the polar angle θ with respect to the z-axis. In this case, the x-axis lies perpendicular to the page and the coordinates are visualised in the yz-plane. Within the ATLAS detector, complete coverage up to $|\eta| \to \infty$ is not achieved because this would overlap with the beam pipe. The $|\eta|$ coverage of the detector terminates at $|\eta| = 4.9$ [29]. Adapted from [39].

The use of transverse coordinates is motivated by momentum conservation, to the extent that the net transverse component ($\vec{p}_{\mathrm{T}}$) of the total 3-momentum possessed by the interacting partons within the colliding protons is zero. Whereas, the total longitudinal component of their momentum is unknown, since the rest-frame of their interaction relative to the detector frame is not known. When the total $\vec{p}_{\mathrm{T}}$ of all collision products does not vanish, "missing transverse momentum" can be measured and attributed to undetected neutral particles, including undiscovered particles such as the lightest supersymmetric particle in R-parity conserving supersymmetry models [29, 40].

3.2.2 Magnet System

An extensive superconducting magnet system consisting of a solenoid magnet and three toroid magnets is used to deflect charged particle trajectories so that precision position and momentum measurements can be made by tracking detectors [29]. The inner detector (ID) discussed further in Section 3.2.3 is concentrically enclosed by a 2 T superconducting solenoid in the region defined by $|\eta| < 2.5$ [29].

The Muon Spectrometer (Section 3.2.5) relies on magnetic fields produced by superconducting air-core toroid magnets arranged parallel and perpendicular (aligned with the solenoid) to the beam axis in the barrel region and two end-caps, respectively [29]. The barrel and end-cap magnets provide coverage over $|\eta| < 1.4$ and $1.6 < |\eta| < 2.7$,

respectively, and both contain 8 symmetrically positioned (relative to the beam axis) coils [29]. Overlapping toroid magnetic fields in the region $1.4 < |\eta| < 1.6$ worsen the bending performance relative to other regions with a single dominant magnet [29].

3.2.3 The Inner Detector

The inner detector (ID) (ID) (Figure 3.5) provides essential charged particle tracking capabilities in the $|\eta| < 2.5$ region [29]. Measurements made with the ID contribute to momentum and vertex reconstruction, electron identification, and pattern recognition [29]. These capabilities are crucial for the rejection of pile-up tracks [41] and for identifying the decays of Beyond the Standard Model particles (e.g. dark matter signatures involving disappearing tracks or emerging jets [42, 43]). The tracking detectors in the barrel region are layered concentrically relative to the beam axis, and those in the end-caps are positioned perpendicular to the beam axis [29]. Several sub-detectors are used, including the semiconductor tracker (SCT), pixel (high granularity silicon) detectors, and transition radiation tracker (TRT) [29].

Innermost detectors, the SCT and pixel detectors, provide precision tracking capabilities, including for vertex identification. Impact parameter and vertex measurements for τ lepton and heavy-flavour particle identification[1] are performed with the SCT using silicon strips aligned parallel and radial to the beam direction in the barrel region and end-caps, respectively [29].

The transition radiation tracker (TRT) continues charged particle tracking up to $|\eta| < 2.0$ in the transition region between the inner detector and electromagnetic calorimeters [29]. Small-diameter straw tubes of varying lengths in the barrel and end-caps are used to provide tracking at large radii compared to the SCT and pixel detectors [29].

In the lead up to the commissioning of the HL-LHC, a new silicon tracking detector, the Inner Tracker (ITk), will be installed [45]. The $|\eta|$ coverage of the ITk will be much larger than the existing detectors allowing charged particle tracking up $|\eta| = 4$ [45]. This will improve particle reconstruction and identification in the forward region at large η, while also assisting in the rejection of radiation from pile-up interactions [45].

3.2.4 Calorimeters

Calorimeters (Figure 3.6) are responsible for measuring the energy deposits of both charged and neutral particles [29]. These detectors are one of the most important tools for measuring the energy of hadronic jets identified as energy clusters in the hadronic calorimeter [29]. Each calorimeter system is designed to ensure electromagnetic and

[1] For example, jets originating from b-quarks [44]

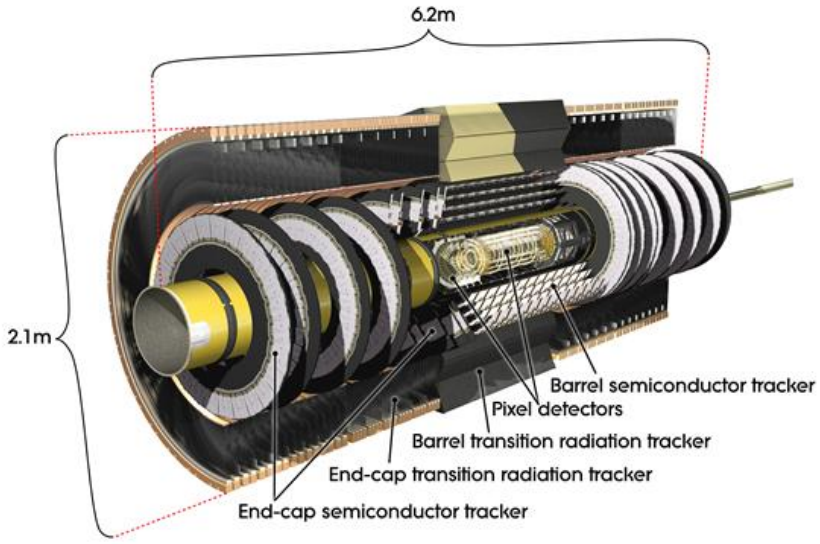

Figure 3.5: A labelled diagram of the inner detector. Taken from [46].

hadronic showers are contained within the detectors to a high degree while limiting the number of non-muon particles that reach the muon detectors [29, 47].

The calorimeter design depends on whether it is used for electromagnetic (EM) or hadronic particle detection. EM calorimeters are used to detect electrons and photons in EM showers, which do not penetrate as far into the calorimeter system as their hadronic counterparts (e.g. hadrons including pions) [29, 47]. Consequently, high granularity EM calorimeters are situated in the innermost region of the detector outside the tracking region [29]. Both barrel ($|\eta| < 1.475$) and endcap wheel ($1.375 < |\eta| < 3.2$) calorimeters immersed in liquid argon (LAr) cryostats (for cooling and to contain the LAr) are used for EM energy measurements [29].

Hadronic energy measurements are obtained with the Tile, LAr hadronic end-cap, and LAr forward calorimeters, with less granularity than those for EM measurements [29]. The Tile calorimeter is a three-layer sampling calorimeter, which provides coverage over $|\eta| < 1.0$ in the barrel and $0.8 < |\eta| < 1.7$ in the overlapping extended barrel [29]. A sampling calorimeter consists of one material (in this case steel) that produces detectable signals, and another *active* material (in this case scintillating tiles) that measures these signals [29, 47]. The scintillating tiles readout calorimeter signals into photomultiplier tubes [29]. The hadronic end-cap calorimeter uses copper wheels immersed in the same LAr cryostat as the EM end-cap calorimeter to cover $1.5 < |\eta| < 3.2$ [29]. The LAr forward calorimeter is also contained within the same LAr cryostat and comprises three components, the innermost component made from copper and the two outermost components made from tungsten [29]. The calorimeter granularity decreases in subsequent layers (and in the forward region for the EM calorimeter) [29], which has important implications for hadronic jet reconstruction discussed further in Chapter 4.

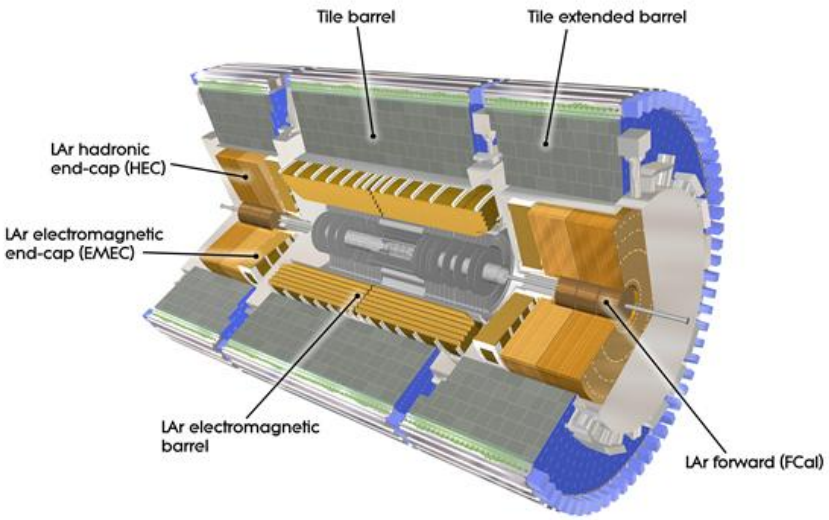

Figure 3.6: A labelled diagram of the ATLAS calorimeters. Taken from [48].

3.2.5 The Muon Spectrometer

The muon spectrometer (MS) provides measurements of muons, which do not deposit all of their energy in the calorimeters like other particles [29]. Magnetic fields provided by the toroid magnets introduced in Section 3.2.2 bend the paths of charged particles in order to identify muon tracks using various detection chambers [29]. Similar to other systems, detection chambers are positioned cylindrically around the beam axis in the barrel region, and perpendicular to the beam axis in the end-caps and transition regions [29]. Three layers of chambers are used in each of these regions [29].

The monitored drift tubes (MDTs) are used for precision tracking over $|\eta| < 2.7$ and $|\eta| < 2.0$ for the innermost layer [29]. Cathode strip chambers (CSCs) on the inner end-cap are used for tracking at larger $|\eta|$ in the $2.0 < |\eta| < 2.7$ region [29]. Resistive plate chambers (RPCs) are used in the barrel region ($|\eta| < 1.05$) for triggering and measurements of the second track angular coordinate [29]. Thin gap chambers (TGCs) serve the same purpose, and are situated in the end-cap regions $1.05 < |\eta| < 2.7$ and $1.05 < |\eta| < 2.4$ for the measurement and trigger chambers, respectively [29].

A key feature of the MS is that the alignment of the chambers in the magnetic field of the toroids must be very precise to accurately reconstruct muon candidates [29]. Consequently, alignment sensors are used in the MDTs to identify chamber positions and Hall sensors are used to monitor the toroid magnetic field [29]. Simulation comparisons are used to identify the toroid locations and the effects of other magnetic material in detector components [29].

During Run 3, the MS will include the two New Small Wheels (NSWs) installed during Long Shutdown 2. These detectors lie in the end-cap regions ($1.0 < |\eta| < 2.7$ (2.4) for tracking (triggering)) and consist of layers of small-strip TGCs and Micromegas, a gaseous particle detector [49].

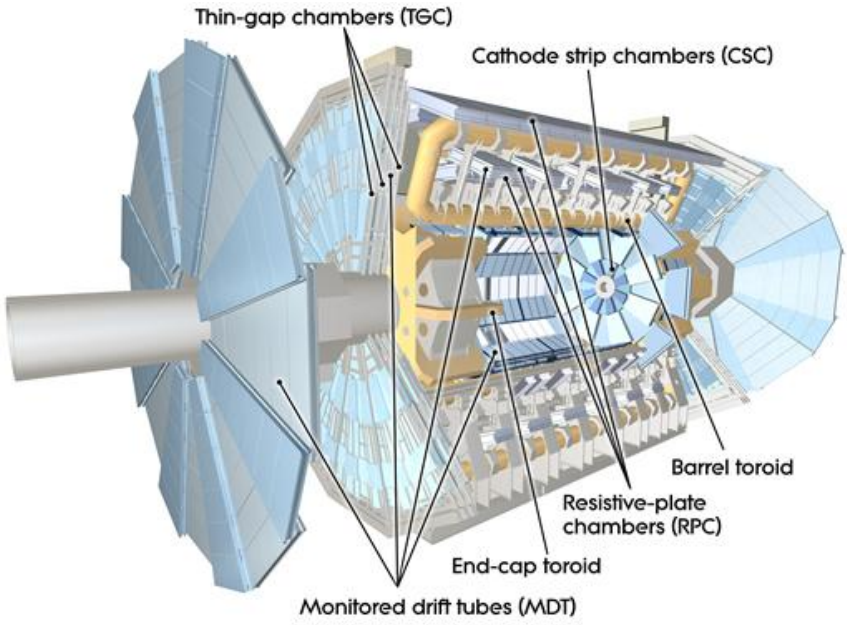

Figure 3.7: A labelled diagram of the ATLAS muon detection systems. Taken from [50].

3.2.6 Triggering and data acquisition

Architecture of ATLAS triggering and data acquisition systems

Triggering and data acquisition (TDAQ) is a significant focus of this thesis and plays a fundamental role in processing data readout by the ATLAS detector. The LHC provides collisions at a peak rate of 40 MHz – it is not possible to record all this data[2]. To reduce the rate at which data are recorded, the ATLAS experiment uses a two-level TDAQ system [51, 52]. A trigger menu comprising different signatures and selections on objects defines a set of "rules" that events must satisfy to be saved for analysis and broadly influences the phenomena that are studied [52].

The first level, the Level-1 (L1) trigger, is implemented as a hardware trigger that makes low-latency (2.5 µs) event selections using coarsely reconstructed detector information [29, 51]. Information from the calorimeter (L1Calo) and muon (L1Muon) hardware triggers is amalgamated in combination with information from the L1 topological (L1Topo) trigger in the Central Trigger Processor (CTP) to determine whether the event is passed on to the High-Level Trigger (HLT) [29, 51]. L1Topo information includes geometrical and kinematic selections involving quantities such

[2]Saving 1 MB of data per event for every event would lead to 40 TB of data being saved per second!

as the invariant masses and angular separations of objects. The L1Muon system passes information to the CTP through the Muon CTP Interface (MUCTPI) [29, 51]. During Run 3, the muon trigger systems will include hardware for both NSWs.

The L1 trigger identifies regions-of-interest (RoIs), which are readout by Front-End electronics at the L1 output rate of 100 kHz and transmitted to the HLT through Read-Out Drivers (RODs) and the Read-Out System [51]. The HLT consists of a CPU farm that makes software-based selections using offline-like reconstruction algorithms [51]. At the HLT, a trigger hypothesis decides whether an event passes a particular trigger signature(s). When this occurs, the Sub-Farm Output (SFOs) processors save data for later reconstruction [51]. This results in an output rate for the HLT on the order of 1 kHz (1.2 kHz during Run 2) [29, 51].

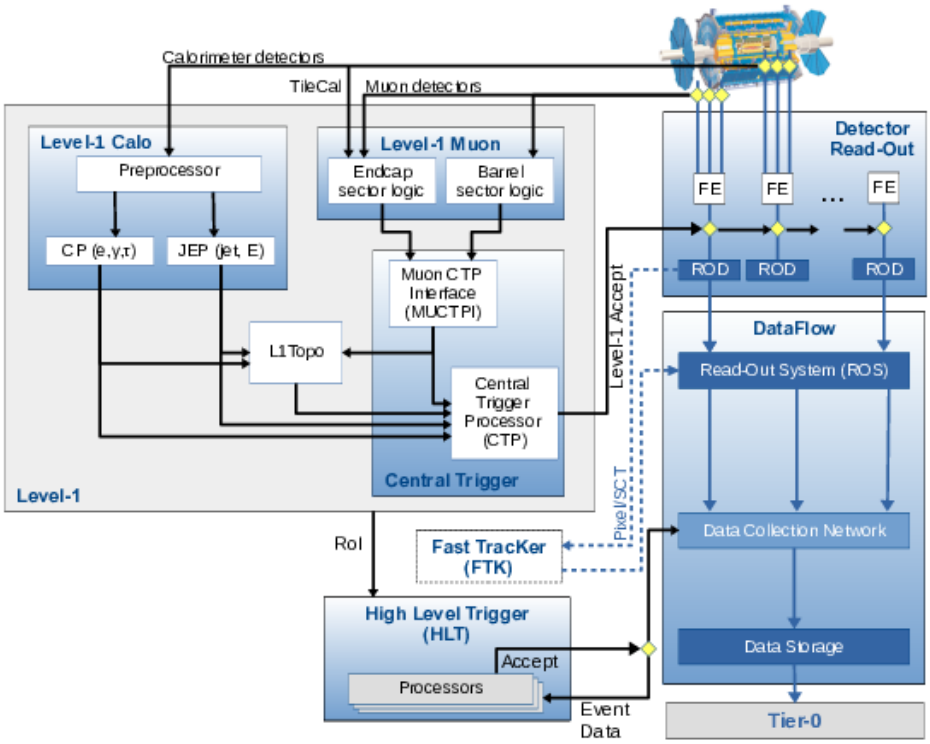

Figure 3.8: Configuration of the ATLAS trigger system in Run 2. The Fast TracKer (FTK) was not used during Run 2 and will not be used during Run 3 in favour of fast tracking algorithms at the HLT [53]. Taken from [51].

Trigger streams

A range of trigger streams are used to collect data for different purposes [52]. The *Physics-main* stream is devoted to data collection for all physics analyses [52]. However, this thesis will discuss the use of other streams with different applications. *Data-scouting* or *Trigger-object Level Analysis* (TLA) streams use high-rate triggers and small event sizes to overcome bandwidth limitations of the *Physics-main* stream [52] – this is discussed further in Chapter 5. During Run 3 of the LHC, a *Delayed*

Stream [54, 55] will also be used. This stream operates like the *Physics-main* stream with the exception that events saved to disk are not reconstructed immediately alongside other data. Rather, the data remain in storage until sufficient CPU resources are available for opportunistic reconstruction.

Resource usage and estimating trigger costs

TDAQ systems must consider both CPU costs and limitations on the amount of data that can be stored for analysis. A key quantity that encapsulates the rate at which data is saved and the size of events stored on disk is the bandwidth:

$$\{\text{bandwidth}\} = \{\text{event size}\} \times \{\text{trigger rate}\} \tag{3.7}$$

where the trigger rate[3] could be the rate of an individual trigger chain (consisting of an L1 trigger and/or HLT selection) or that of an entire trigger stream. During Run 2, the output bandwidth of the HLT reached 1.2 GB/s [51].

To estimate the trigger CPU and rate costs in preparation for the operation of the ATLAS detector, *enhanced bias* data is used to emulate real data-taking conditions [56]. In principle, the rate at which trigger chains fire is calculable with an unbiased event sample that is arbitrarily large [56]. However, this is unrealistic and impractical given the size of the dataset that would be required [56]. Instead, a suite of L1 triggers (5 different chains in Run 2) is used to collect a dataset with "enhanced bias" that favours events identified to contain many objects (high multiplicity) with large momenta [56]. The events are assigned an event weight indicative of the "true" probability of seeing such an event to remove the bias introduced by the L1 trigger selections [56]. Then the rates of any HLT (or L1) trigger signature can be estimated using the sum of the weights assigned to events passing the trigger divided by the time in which the dataset is collected [56].

There are several important factors relating to this estimation and data-collection procedure [56]:

- Trigger pre-scales: pre-scales are used to reduce event rates. A pre-scale of n corresponds to a probability $1/n$ of keeping an event that passes the pre-scaled trigger. By introducing this probability into the event weights during estimation one can determine the effect of pre-scales on any trigger.
- Estimates for trigger rates/CPU usage are only representative of run conditions at the *average* luminosity throughout the enhanced bias data-taking. If the conditions for data-taking change considerably (e.g. average number of interactions per bunch crossing, $\langle\mu\rangle$, or the collision CM energy, $\sqrt{s}$), then a new enhanced bias dataset is needed.

[3] For an individual trigger this is the number of times an event passes the selection in a particular time period. The trigger stream rate combines the rates of *all* trigger signatures assigned to the stream.

- Enhanced bias data are collected in parallel with data used for physics analyses. Consequently, the L1 selections used for data collection can be shared with the main physics trigger menu and therefore might have an existing pre-scale. Where this is the case, a random choice of L1 trigger (from a list of pre-defined L1 triggers for a complete L1 and HLT chain) is used to seed HLT triggers.

Changes towards high-luminosity operations

The ATLAS TDAQ systems will be upgraded to handle a significant increase in *pp* collision rates anticipated at the High-Luminosity LHC. This will include a significant change to the output rates of different trigger levels. The existing L1 trigger will transition to the Level-0 (L0) hardware trigger with an output rate of 1 MHz [45]. This system will include various components including the L0 calorimeter and muon triggers (L0Calo and L0Muon) in addition to other feature extraction electronics used for jet, electron, global, and forward (large $|\eta|$) reconstruction [45]. The *Global Trigger*, within the L0 trigger, will use offline-like reconstruction, apply topological selections, and calculate event-level observables with high-granularity detector information [45]. The *Central Trigger Processor*, like for the Run 2 and Run 3 TDAQ architecture, will make a collective decision on whether an event satisfies selections, and passing events will be readout and transmitted through a central DAQ system [45]. The HLT (*Event Filter*) will apply software-based reconstruction and selections to reduce the output rate of the detector to on average 10 kHz for storage [45].

3.2.7 Forward Detectors

The ATLAS detector systems include various sub-detectors situated in the forward region on either side of the primary detector, which are used for luminosity and heavy-ion collision measurements [29]. Each detector has two components positioned at an equal distance on either side of the IP (i.e. the centre of the ATLAS detector).

The LUCID (LUminosity measurement using Cerenkov Integrating Detector) is responsible for real-time (online) *pp* collision luminosity measurements at a position ± 17 m from IP [29]. The ALFA (Absolute Luminosity for ATLAS) detector also provides luminosity measurements at a location ± 240 m from the IP using a tracking detector equipped with scintillating material [29].

Measurements of centrality in heavy-ion collisions are provided by the ZDC (Zero Degree Calorimeter) ± 140 m from the IP [29]. However, since this thesis focuses on *pp* physics there will be no further discussion of this apparatus.

3.3 Summary

This Chapter provided a brief description of the LHC and its operation before discussing the ATLAS experiment in detail. The ATLAS detector draws on a complex

network of sub-detectors to precisely reconstruct *pp* and heavy-ion collisions. These sub-detectors include the calorimeters and inner detector, which are foundational for identifying the energy deposits and trajectories of particles contained in hadronic jets. The evolution of the detector systems to handle a more demanding collision environment at the HL-LHC will prove to be an essential component of extending existing measurements and searching for undiscovered phenomena.

Chapter 4

Hadronic final state reconstruction at the ATLAS experiment

Hadronic jets are an important feature in many Standard Model (SM) and Beyond the Standard Model (BSM) physics processes. The reconstruction of hadronic final states involves translating raw detector signals into the high-level information used to define the objects and observables used in physics analyses. A complete understanding of detector performance in the reconstruction of all objects – leptons, photons, jets, and missing transverse momentum – is therefore essential. After the initial stages of reconstruction, the calibration of physics objects brings their energy scales close to those of particle-level (truth) objects from simulations.

This Chapter introduces jet physics and provides an overview of the ATLAS reconstruction algorithms. Hadronic jets are introduced in Section 4.1 and their reconstruction is discussed further in Section 4.2 onwards. Lepton/photon and missing transverse momentum reconstruction are briefly discussed in Section 4.3 and Section 4.4, respectively. Section 4.5 provides an overview of jet calibration methods and Section 4.6 discusses reconstruction within the ATLAS trigger systems. The final Sections of this Chapter focus on boosted object reconstruction (Section 4.7) and jet identification (tagging) (Section 4.8).

4.1 Hadronic jets at collider experiments

Hadronic jet production is one of the most significant processes at modern hadron collider experiments and originates from the hadronisation of particle showers containing quarks (q) and gluons (g) into sprays of colour neutral hadrons [57]. Their formation is closely linked with asymptotic freedom and colour confinement in QCD (i.e. the strong force). A hard-scatter (HS) interaction of two protons leads to the interaction of one quark from each of the protons to produce another high energy q or g [4, 58]. As this particle propagates, it radiates gluons, which themselves radiate both $q\bar{q}$ pairs and additional gluons, producing a *parton*[1] *shower* [4, 58]. As the

[1] A collective term for quarks and gluons.

length scale of the interactions increases, the strong-force magnitude increases with the strong coupling, α_s [4, 58]. It eventually becomes energetically favourable to produce colourless hadrons from the parton shower (*hadronisation* linked to colour confinement) [4, 58], resulting in the spray of charged and neutral hadrons measured by tracking detectors and calorimeters.

Additional hadronic contributions to events include pile-up, additional simultaneous and inelastic pp interactions during a bunch crossing, and the *underlying event* [58]. If only one of the three quarks in the proton interacts in a hard-scatter interaction, the remaining quarks can continue to interact, contributing an additional low-energy background to the event, called the underlying event [57, 58]. Experimentally, the underlying event looks quite similar to low-p_{T} pile-up contributions [59]. Multi-jet events of interest later in this thesis arise when the "leftover" proton quarks interact in additional hard scatterings [58].

The experimental definition of a jet (in practice) is somewhat arbitrary compared to the QCD picture of a spray of hadrons originating from a q or g [57]. The "experimental" definition of a jet involves [57, 59]:

1. Detector measurements (*input objects*) that describe the jet 4-momentum (energy, 3-momentum, position) (e.g. calorimeter clusters, charged particle tracks,...).
2. A *jet clustering algorithm* that groups input objects into jets.
3. Some form of *size parameter* related to the "area" of a jet that determines the average (spatial) size of jets.

These definitions should be (relatively) easy to implement in experimental and theoretical scenarios, and they should produce measurements that are calculable (and do not diverge) in QCD perturbation theory results [57, 60]. A simple jet definition consists of a cone (initially) centred on some seed particle chosen as the hardest (highest p_{T}) particle in the event, clustering every particle within an angular distance, R, and iteratively re-defining the "seed" as the combined 4-momentum of the constituents until no additional jet constituents are found [57]. Iterative jet finding leads to issues associated with overlapping jets that share particles, and there are several approaches to resolve this [57]. However, with these modifications, the iterative algorithms fail to satisfy the requirements of *IRC (Infra-red [IR] and Collinear [C]) safety* defined in the next examples. For cone algorithms seeded by the hardest particle in an event, IR safety is violated when an alternative jet seed is identified after adding additional soft radiation [57]. If an algorithm is IR safe, then the jet clustering results do not change with the addition of soft radiation as described in Figure 4.1a [57]. Similarly, the prevention of jet overlap by removing the particles inside a "stable" (fully clustered) cone violates collinear safety [57]. If a high-p_{T} particle splits into two softer and nearly collinear particles, the choice of

seed for the next iteration might change as in Figure 4.1b, leading to a different set of jets being identified [57].

The IRC safe jet-finding algorithms currently used widely at hadron colliders (the LHC in particular) are *sequential recombination* algorithms. In certain cases they also yield useful information that is analogous to the QCD splitting behaviour [57]. These algorithms are discussed in detail in Section 4.2.

(a) An example of jet clustering failing IR safety requirements. Originally, two jets would be identified (left). After the addition of soft radiation (gluon in red), the jet clustering outcomes change – only a single jet is identified (right).

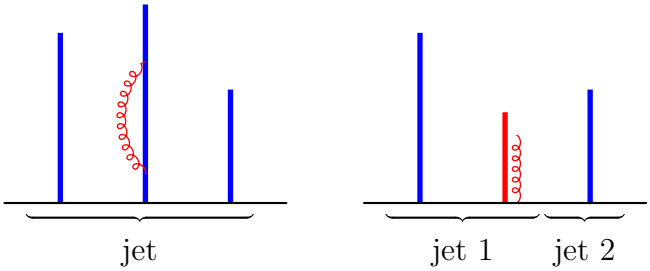

(b) An example of jet clustering failing collinear safety requirements. The splitting of a hard particle into two softer particles results in a new hard seed (right), altering the final jet(s) identified by the clustering algorithm.

Figure 4.1: Illustrative examples for both IR safety and collinear safety. Adapted from [57].

4.2 Building jets from detector information

Translating detector information into objects similar to the QCD definition of a jet requires the use of jet algorithms discussed in Section 4.1 and input objects built from detector information. For this purpose, the jet algorithm of choice at many collider experiments including the CMS and ATLAS experiments is a variation of a *sequential recombination algorithm* introduced in Section 4.2.1. At the ATLAS experiment these algorithms take as input: *topological clusters* (calorimeter clusters), charged particle tracks, or more complicated combinations of the two objects. These are discussed further in Section 4.2.2.

Besides the reconstruction of jets from real detector information, the execution of jet clustering algorithms on particles produced by Monte-Carlo (MC) event generators (generator-level particles) is used to identify truth- (or particle-) level jets. These are

essential to the calibration of the jet energy scale (Section 4.5 and Appendix A.3), which relies on information about the properties of "true" jets without detector effects. Beyond calibrations, the truth-level objects play an important role in representing the "true" properties of a particle or physics object (jet, etc.) to study detector or analysis performance.

4.2.1 Sequential recombination algorithms

Sequential recombination algorithms iteratively cluster jets using distance metrics to compare the separation of jet inputs from other jet inputs and the "beam". Like for other algorithms, these jets have a user-defined size parameter, R, involved in the angular part of the distance metric.

The distance measure between jet inputs is defined as [57]:

$$d_{ij} = \min(p_{\mathrm{T},i}^{2n}, p_{\mathrm{T},j}^{2n}) \left(\frac{\Delta R_{ij}}{R}\right)^2 \tag{4.1}$$

where $p_{\mathrm{T},i}$ and $p_{\mathrm{T},i}$ are the transverse momenta of the ith and jth jet input, while $\Delta R_{ij} = \sqrt{(\eta_i - \eta_j)^2 + (\phi_i - \phi_j)^2}$ is the angular distance between the two jet inputs in the (η, ϕ) plane.

Similarly, the beam-jet input distance is [57]:

$$d_{iB} = p_{\mathrm{T},i}^{2n} \tag{4.2}$$

where n is an integer that controls the behaviour of the algorithm.

Jet finding proceeds iteratively for *inclusive*[2] algorithms [57]:

1. All d_{ij} and d_{iB} are calculated.
2. The smallest d_{ij} and d_{iB} are compared to determine if the inputs are grouped: if $d_{ij} < d_{iB}$ the jet inputs i and j are nearby and clustered together into a jet. The algorithm then returns to step (1) with the exception that j is removed and i is now replaced by the "jet"[3] consisting of the clustered inputs.
3. If $d_{ij} > d_{iB}$ the jet inputs are sufficiently separated that they are not members of the same jet. In this case, i is classified as a (complete) jet and removed from the list of "jets"/inputs.

The *exclusive* variant of these algorithms continues clustering jets until a stopping condition, for instance on the number of jets found by the algorithm, is satisfied [57, 61]. This version of the clustering with the k_t variant (discussed next) of the algorithm ($n = 1$) is sometimes used to consider the substructure of large-R jets.

[2]These algorithms continue until no inputs for the jet reconstruction remain unclustered [57, 61].
[3]Not a complete jet!

The jet-finding procedure for the $n = 0$ and $n = 1$ algorithms is computationally expensive when many jet inputs exist – the runtime scales as $\mathcal{O}(N^3)$ for N jet inputs [57, 62]. After the application of computational geometry techniques in the `FastJet` package, the runtime of these algorithms scales as $\mathcal{O}(N \ln N)$ [57, 62].

The k_t algorithm

The k_t algorithm is a variant of the sequential recombination above with $n = 1$ [57]. Thus, the power of 2 in $d_{ij} = \min(p_{T,i}^{2n}, p_{T,j}^{2n})\frac{\Delta R_{ij}^2}{R^2}$ results in *soft* particles being clustered before hard particles [57]. This causes the final collection of jets to contain irregularly shaped jets as in Figure 4.2 [57].

An advantage of the k_t algorithm is that the clustering sequence is like what one may expect in QCD branchings of a parton shower [57]. This makes the algorithm useful for identifying smaller sub-jets (size parameter $R_0 < R$) within a jet, used extensively in the calculation and measurement of jet substructure observables. Additionally, since the algorithm favours soft radiation it has important implementations for the removal of pile-up radiation from jets, discussed in Section 4.5.

The Cambridge-Aachen (C/A) algorithm

Like the k_t algorithm, the Cambridge-Aachen (C/A) algorithm clustering sequence is a proxy for the QCD branching of a parton shower [57]. With $n = 0$ there is no dependence on jet input momentum in this variant of the clustering algorithm and the resulting jets are only dependent on the angular separation of the jet inputs [57]. Again, this is useful for exploring the substructure of large jets and results in irregularly shaped jets.

The anti-k_t algorithm

The anti-k_t algorithm uses $n = -1$ in the distance measures, which results in the clustering of *hard* jet inputs before soft jet inputs [57]. Unlike the cone algorithms discussed earlier in the Chapter, the anti-k_t *is* IRC safe due to the form of the distance metrics used for the clustering and their behaviour for collinear splittings (small ΔR) and soft (IR) radiation (the hardest radiation is clustered first) [57]. Importantly, the clustering sequence of the anti-k_t algorithm is such that circular jets (Figure 4.2) are produced like those from cone algorithms [57]. The benefit of the similarity between cone and anti-k_t jets becomes evident in jet calibration (Section 4.5) where a well-defined jet area [57] allows pile-up radiation subtraction and the consideration of detector effects.

4.2.2 Inputs for clustering

Inputs to jet reconstruction can consist of calorimeter only information, track-only information, or a combination of the two. Jet inputs with tracking information

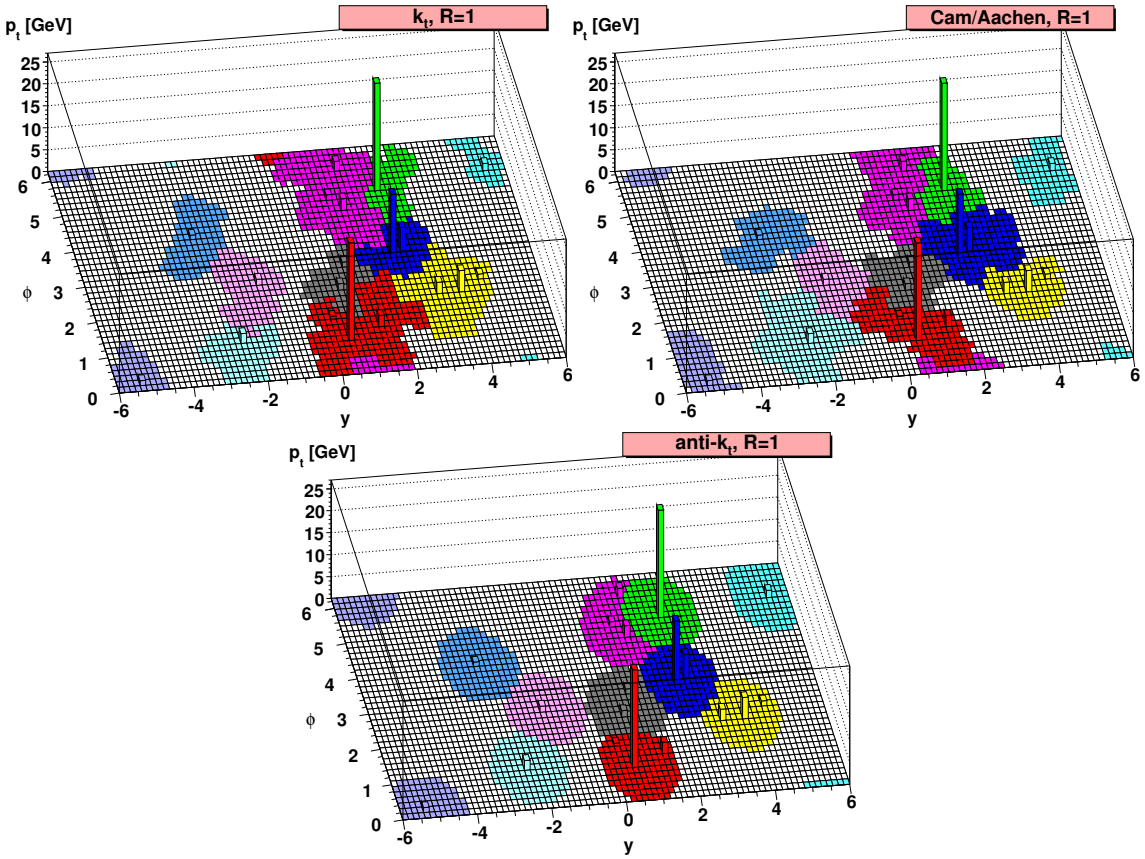

Figure 4.2: The shapes of $R = 1.0$ jets clustered with sequential recombination algorithms. Note the irregular shape of the k_t and C/A jets compared to the circular shapes of anti-k_t jets. Taken from [57].

are more robust against pile-up contamination – it is possible to reject pile-up radiation using charged particle tracking. Additionally, they are seen to improve the reconstruction performance of the jets in a *particle-flow* approach [63].

Topoclusters

Calorimeter clusters are the most basic input to jet reconstruction. They are built from the three-dimensional energy deposits of hadrons (and leptons/photons) in the calorimeters referred to as topological clusters, *topoclusters* [64]. A significance-based cell clustering algorithm is applied to build topoclusters [64]. First, the cell significance, ξ, is defined in terms of the measured calorimeter cell energy (E_{cell}) and the total calorimeter noise (σ_{total}) incorporating an electronic ($\sigma_{\text{electronic}}$) and pile-up ($\sigma_{\text{pile-up}}$) noise contribution (summed in quadrature) [64]:

$$\xi = \frac{E_{\text{cell}}}{\sigma_{\text{total}}}. \tag{4.3}$$

where [64]:

$$\sigma_{\text{total}} = \sqrt{\sigma_{\text{pile-up}} + \sigma_{\text{electronic}}}. \tag{4.4}$$

Since the cell energy, E_{cell}, can be negative, $|\xi|$ is used to calculate the cell significance. In practice, negative energy cells arise from pile-up and noise fluctuations [64]. There are three different clustering steps that use significance thresholds to ascertain the cells to group in clusters [64]. The progression of the clustering procedure is illustrated in Figure 4.3. The first clustering step identifies seed cells with $|\xi| > S$, where S is the significance threshold (see Figure 4.3a) [64]. Then the surrounding cells with significance, $|\xi|$, above a threshold N are added to the cluster (see Figure 4.3b) [64]. Finally, the cells surrounding the incomplete cluster with $|\xi| > P$ are added to obtain a complete topocluster (see Figure 4.3c). The typical configuration for offline reconstruction has thresholds: $S = 4$, $N = 2$, $P = 0$ [64]. The latter threshold means that *all* neighbouring cells are added to the cluster in the final step [64]. The combination of both positive and negative energy cells inside a single topocluster inherently results in noise (including pile-up!) suppression since the fluctuations (with different sign) effectively cancel each other [64].

By design, the ATLAS calorimeters are non-compensating, which means an electromagnetic energy deposit produces a larger calorimeter signal than a hadronic deposit [64]. Therefore, topoclusters produced from raw calorimeter cells are calibrated to an electromagnetic (EM) scale. Additional calibrations are needed to account for the non-compensation and correct the energies of hadronic deposits, so they are not systematically lower than their EM counterparts. This procedure is referred to as *Local Hadronic Cell Weighting* (LCW) [64]. Additional calibrations correct for effects including energy losses in dead (inactive) calorimeter material, the deposition of energy outside the topoclusters (out-of-cluster correction), and reconstruction thresholds imposed by the detector configuration (noise, etc.) that cause

signal losses [64]. Further details of the LCW calibration procedure are discussed in Appendix A.1.

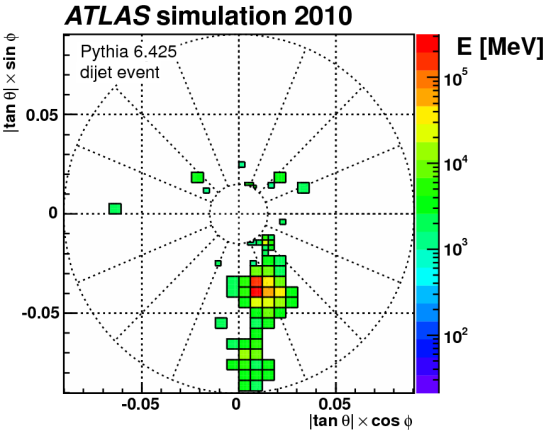

(a) Initial seeding of clusters with cells that have significance above S.

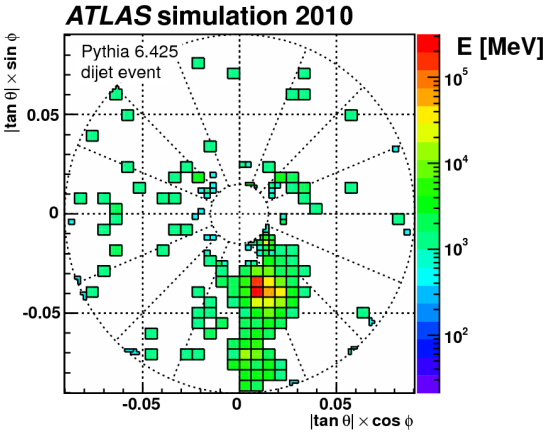

(b) Addition of neighbouring cells with significance above N.

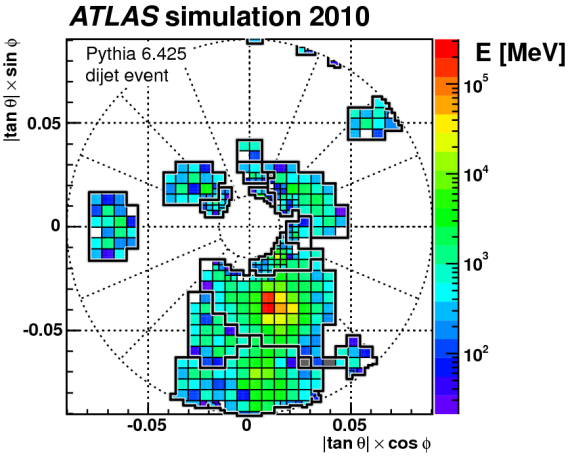

(c) Complete clusters formed after adding remaining cells with significance above P.

Figure 4.3: The procedure for the reconstruction of a dijet event in the forward calorimeter with topoclusters, displayed using polar angle θ and azimuthal angle ϕ. Taken from [64].

Charged particle tracks

Charged particle tracks are not just used for jet reconstruction, but to identify any charged particle produced in the detector. Hits from charged particles recorded by the semiconductor tracking detector and pixel detectors within the inner detector are used to produce clusters that define *space points*, and map out the trajectory a charged particle takes in the detector magnetic fields [65]. The tracking algorithms proceed iteratively to identify a wide variety of possible track candidates using many combinations of space points/clusters [65]. The combinatorial nature of these methods leads to track candidates that share clusters, which indicates that either

the candidate was mis-reconstructed, or it originates from a dense (high energy) environment where many objects are identified [65]. Track candidates are evaluated using an *ambiguity solver* that aims to distinguish between cases where hit clusters are correctly or incorrectly assigned [65]. First candidates must satisfy a series of quality criteria relating to their kinematics ($p_{\mathrm{T}} > 400$ MeV and $|\eta| < 2.5$), selections on measured values of impact parameters, and requirements on the number of assigned clusters and missing hits referred to as *holes* in different layers of the tracking detectors [65]. Candidates passing these requirements are assigned a score, which penalises poor reconstruction and determines the order they are processed in during ensuing steps – from highest to lowest score [65]. Neural networks are then used to continue the ambiguity solving steps only for track candidates with merged clusters (i.e. those candidates that share clusters) [65]. The final step in the track reconstruction for candidates passing all previous stages is a precision fit that draws on additional neural networks to predict the particle trajectory (track position) and uncertainties in measurements [65].

Particle-flow methods

The combination of tracking and calorimeter information provides an avenue to increase jet reconstruction performance – the resolution of objects and their pile-up stability (e.g. pile-up tracks can be rejected). Particle-flow (`PFlow`) jets are reconstructed from a combination of charged particle tracks and topoclusters using a track-cluster matching procedure [66, 67]. These objects implement a subtraction method to prevent double counting track and topocluster energy contributions at low-p_{T}, and have improved mass and energy resolution [63, 66, 67]. Recent developments in the reconstruction of large-R jets include the development of inputs that are more performant at high-p_{T} (Track Calo-Clusters) where the `PFlow` double-counting subtraction is disabled, and a combination of these and `PFlow` inputs to obtain good reconstruction performance across a wide p_{T} range (Unified Flow Objects) [66]. These inputs are discussed further in Appendix A.2.

4.2.3 Common jet definitions

A multitude of jet definitions (inputs, algorithm, size parameter) exist and are used in analyses. However, a select group of jet definitions are used for the studies and work presented in this thesis. These commonly used jet definitions and their abbreviations are summarised below:

- small-R `EMTopo` jets: anti-k_t $R = 0.4$ jets built from EM-scale topoclusters.
- small-R `EMPFlow` jets: anti-k_t $R = 0.4$ jets built from EM-scale particle-flow objects.
- large-R `LCTopo` jets: anti-k_t $R = 1.0$ jets built from LCW scale topoclusters.

The substructure of large-R (`LCTopo`) jets is typically probed by reclustering the original jet with the (exclusive) k_t algorithm (and a smaller size parameter) or the C/A algorithm.

4.3 Lepton and photon reconstruction

Charged leptons (e, μ, τ) and photons (γ) deposit energy in calorimeters and can produce charged particle tracks in the inner detector. These deposits may overlap with reconstructed hadronic jets, and jets (leptons) may be misidentified as leptons (jets) – the case of jets "faking" leptons is more common due to the abundance of jets. The reconstruction of these objects may be used to study hadronic processes by ensuring isolated jets are identified and vetoing events from (semi-)leptonic processes (e.g. semi-leptonic top quark decays).

Tau lepton reconstruction

Hadronic tau (τ) lepton decays are readily reconstructed from combined tracking and calorimeter information due to their relatively short lifetimes compared to the size of the detector [68]. Tau reconstruction historically draws on small-R jet(s), which are used to locate the decay vertex with the sum of the p_{T} for tracks within a $\Delta R < 0.2$ cone around the jet axis [68]. More recent reconstruction strategies rely on multivariate analysis algorithms referred to as *Boosted Decision Trees* (BDTs), which are trained to differentiate between background (quark/gluon) jet production and true τ leptons [68]. The charged pion decay products are reconstructed separately from neutral pions using a `PFlow`-like method compared to the BDT-only identification of their neutral counterparts [68]. The reconstruction of τ leptons in this *Tau Particle Flow* algorithm improves the energy and spatial resolution of the final τ candidates [68].

Muon reconstruction

Muons deposit little energy in calorimeters but can be identified from their charged particle tracks produced in the inner detector (ID) and the muon spectrometer (MS) surrounding the calorimeters and tracking region [69]. Candidate muons are reconstructed from a combination of ID tracks, MS tracks, and calorimeter deposits. The different types of muon candidates reconstructed in Run 2 include [69, 70]:

- Combined muons (CB) – combined track reconstruction from matched MS and ID tracks.
- Inside-out combined muons (IO) – built from extrapolated ID tracks associated with MS hits.
- Segment-tagged muons (ST) – extrapolated ID tracks are stringently matched to MS track segments using angular requirements.

- Calorimeter-tagged muons (CT) – ID tracks are extrapolated to the calorimeter and matched to energy deposits from *minimum ionising particles*[4] (mips). An additional $p_{\mathrm{T}} > 5$ GeV requirement is imposed for these candidates to mitigate contamination from other low-p_{T} radiation in the calorimeters.

Different reconstruction purity and identification efficiency working points are then defined by requirements on the track 4-momentum coordinates (i.e. ϕ, θ) and its fit, the charge to momentum (q/p) ratio of the track measured in the MS, impact parameter measurements from the ID, and ratios of the p_{T} for tracks identified with different reconstruction requirements [69–71].

Electron and photon reconstruction

Like other leptons, electrons and photons are reconstructed from both their calorimeter deposits and charged particle tracks [72]. The interaction of photons with detector material leads to the production of e^+e^- pairs that are identifiable with charged particle tracks (*photon conversion vertices*) despite the electrical neutrality of the original photon [72]. The electrons and photons are reconstructed from *superclusters* combining track or vertex matched (dependent on the photon/electron origin) topoclusters [72]. Photon conversion vertices are instead reconstructed with fixed-size calorimeter clusters that are loosely associated with tracks [72]. The reconstruction sequence solves ambiguities where photon/electron candidates may share clusters (a consequence of independent reconstruction)[5] and includes an energy calibration [72].

Like muon reconstruction, different working points are designed to yield different efficiencies for the identification of photon/electron candidates of varying purity [72]. Electron identification algorithms differentiate "prompt" electrons (i.e. electrons that do not originate from a background process) from background objects using ratios of individual likelihoods defined for prompt electron and background classification [72]. The *Loose* working point provides an efficiency (for electroweak processes) of 95%, which decreases to 88% for the *Medium* working point and is lowest for the 80% efficiency *Tight* working point [72]. The photon identification working points are defined by selections on one-dimensional distributions of variables sensitive to differences between prompt photons and backgrounds such as those from hadronic jet production [72]. These selections are binned in η (and E_{T} for the *Tight* working point) [72]. *Loose* working point selections are made on shower shape variables, and the *Medium* working point combines shower shape and EM LAr (first layer) calorimeter energy difference ratio[6] selections [72]. The *Loose* and *Medium* working points are primarily used for triggering, while the *Tight* working point is used for

[4] A particle with energy such that the ionisation density (energy lost per unit length of the path traversed by a particle) is minimised [47].

[5] In these cases, the photon (or electron) can also be identified as an electron (or photon) based on the reconstruction procedure implemented so far [72].

[6] The difference between the energy of the leading and second-leading energy deposits of a cluster normalised by their sum [72].

offline reconstruction and selects a subset of the *Medium* working point photons [72].

4.4 Missing transverse momentum reconstruction

Missing transverse momentum, ($\vec{E}_{\mathrm{T}}^{\mathrm{miss}}$), is used to infer the presence of weakly interacting neutral particles (including neutrinos in electroweak decays such as $W^{\pm} \to l^{\pm}\nu$) that do not deposit energy in calorimeters [73]. $\vec{E}_{\mathrm{T}}^{\mathrm{miss}}$ is also used to constrain models of BSM physics such as supersymmetry, where the lightest supersymmetric particle (LSP) is neutral and stable [73]. The calculation of the $\vec{E}_{\mathrm{T}}^{\mathrm{miss}}$ and its application in searches for new physics (or tests of the SM) relies on the conservation of the total momentum in the plane transverse to the beams [73].

The $\vec{E}_{\mathrm{T}}^{\mathrm{miss}}$ observable is unique in that it encapsulates the total energy of an event from both leptons/photons and hadrons [73]. Thus, the detector objects must be sequentially reconstructed to avoid mistaking the energy deposits from a lepton for those of a jet, for example [73]. The typical sequence for the reconstruction of the detector objects begins with muons (reconstructed primarily from tracks in the ID and MS) [73]. Then electrons, photons, and hadronically decaying τ leptons are reconstructed and identified [73]. Finally, either `EMTopo` or `PFlow` jets are reconstructed [73]. Overlap removal procedures are applied to prevent any double counting of contributions from nearby jets, leptons, or photons [73]. Any remaining calorimeter deposit or track contributes to the *soft* $\vec{E}_{\mathrm{T}}^{\mathrm{miss}}$ term from energy deposits not directly associated with the high-p_{T} leptons and jets [73]. The expression for the $\vec{E}_{\mathrm{T}}^{\mathrm{miss}}$ is broken into the *hard* term (leptons, jets, etc.) and the *soft* term in a two-dimensional (xy-plane) vectorial sum [73]:

$$\vec{E}_{\mathrm{T}}^{\mathrm{miss}} = \vec{E}_{\mathrm{T}}^{\mathrm{miss}(\mu)} + \vec{E}_{\mathrm{T}}^{\mathrm{miss}(e)} + \vec{E}_{\mathrm{T}}^{\mathrm{miss}(\tau)} + \vec{E}_{\mathrm{T}}^{\mathrm{miss}(\gamma)} + \vec{E}_{\mathrm{T}}^{\mathrm{miss}(\mathrm{jets})} + \vec{E}_{\mathrm{T}}^{\mathrm{miss}(\mathrm{soft})} \tag{4.5}$$

where the contribution of each type of object is calculated in terms of the transverse momentum as [73]:

$$\vec{E}_{\mathrm{T}}^{\mathrm{miss}(\mathrm{obj})} = -\sum_{\mathrm{objects}} \vec{p}_{\mathrm{T}}. \tag{4.6}$$

Pile-up contamination for the hadronic component of $\vec{E}_{\mathrm{T}}^{\mathrm{miss}}$ reconstruction negatively impacts the reconstruction performance. Therefore, a pile-up mitigation/rejection step is included to remove jets that originate from pile-up activity [73]. This is implemented as a Jet Vertex Tagger selection discussed further in Section 4.8.1 [73]. The different $\vec{E}_{\mathrm{T}}^{\mathrm{miss}}$ reconstruction working points (*Loose*, *Tight*) are defined in terms of these jet selection requirements [73]. The *Tight* working point provides a higher purity measurement with less pile-up contamination [73]. An additional reconstruction working point rejects forward pile-up jets (outside the tracking acceptance) to reduce pile-up contamination in $\vec{E}_{\mathrm{T}}^{\mathrm{miss}}$ distribution tails [73].

4.5 Small-R jet calibration

The small-R jet calibration modifies EM-scale jets such that their energy scale is similar to truth-level jets through a sequence of steps shown in Figure 4.4. The initial stages of the jet calibration[7] correct the angular coordinates of the jet 4-momentum to point from the reconstructed primary vertex rather than the centre of the detector (an origin correction) [74]. Next, contributions from pile-up radiation are estimated with a momentum density observable (momentum per unit area) calculated with k_t jets and subtracted from the anti-k_t jets after a measurement of their area (i.e. subtract the product of the momentum density and the jet area) [67, 74]. An additional step in the pile-up subtraction aims to eliminate the dependence of the jet p_{T} on other observables sensitive to pile-up – the number of primary vertices and the number of interactions per bunch crossing [74]. The motivation for this is linked to the calculation of the momentum density observable for central jets (within the tracking acceptance) such that very energetic jets or those with large η (forward jets) show residual pile-up dependence [67, 74].

The jet energy scale (JES) correction is then derived from MC simulation and aims to recover the truth-level jet energy scale [67, 74]. This correction applies a calibration scale factor derived from the jet energy response, the ratio of the reconstructed to truth jet energy, to the complete jet 4-momentum vector [67, 74]. Transitions between the sub-detectors in different detector regions lead to differences between the η coordinate of truth-level and reconstructed jets [67, 74, 75]. This necessitates a correction to the jet η using the difference between the truth-level and reconstructed jet η, and a correction to the jet p_{T} applied using a jet energy scale factor, but without modifying the complete 4-momentum [67, 74, 75].

The final calibration stages include the Global Sequential Calibration (GSC) and the *in situ* calibration. The GSC accounts for differences in the jets due to their initiating particle – quark-initiated jets penetrate further into calorimeters and the hadrons inside them carry a larger fraction of the jet p_{T} unlike gluon-initiated jets [74]. The correction derives scale factors (using similar methods to the JES correction) in terms of five different variables that encapsulate the differences between quark- and gluon-initiated jets [74]. Finally, the *in situ* correction uses both data and MC simulation to correct the energy scale of the jets to that seen in "real" jets by balancing[8] well-measured objects in data against jets under calibration [74].

Further details on the jet calibration procedures are provided in Appendix A.3.

[7] Unless this step is already done at the jet input level.
[8] Exploiting the conservation of momentum for different processes with recoiling objects.

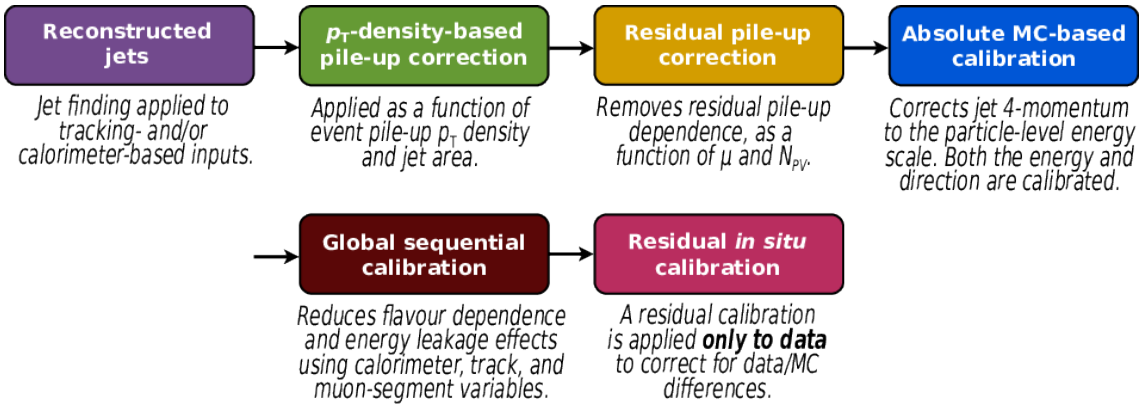

Figure 4.4: Small-R jet calibration sequence starting from jet inputs involving calorimeter or charged particle track inputs (or a combination of these). Taken from [67].

4.6 Trigger reconstruction

4.6.1 L1 reconstruction

L1 trigger reconstruction is quite different to offline reconstruction since the algorithms generally produce more coarse objects with a significant energy scale difference (electromagnetic-scale) compared to calibrated offline objects. The calorimeter trigger (L1Calo) identifies jets from coarse (in $\Delta\phi \times \Delta\eta$) calorimeter towers [76] and no tracking information is available, so additional pile-up mitigation steps (e.g. JVT in Section 4.8.1) are not possible. As discussed in Section 3.2.6, the principle of the L1 reconstruction is that the hardware trigger will readout information from the detectors and where the reconstructed objects are above reconstruction thresholds a region-of-interest (RoI) is defined [52]. The RoI information is carried through the TDAQ systems and used for further selections at the HLT where more complete reconstruction takes place [52].

The L1Calo reconstruction uses $\Delta\eta \times \Delta\phi = 0.1 \times 0.1$ granularity trigger (calorimeter) towers (the η granularity decreases for jets in the forward region) and sliding window algorithms for both lepton/photon and jet reconstruction [76]. The lepton/photon algorithms iterate over clusters of the EM calorimeter towers and identify an RoI where the $\sum E_{\mathrm{T}}$ in an inner 2×2 tower cluster shown in Figure 4.5 is at a local maximum (in case of overlapping windows) [52, 76]. Additional requirements are imposed on the isolation of energy deposits for lepton/photon reconstruction: all E_{T} deposits in a ring around the EM calorimeter 2×2 cluster and in/around the 2×2 "core" in the hadronic calorimeter must be below a certain threshold [76]. To identify tower clusters above reconstruction thresholds, an E_{T} sum is calculated for adjacent towers (that share an edge) in the 2×1 or 1×2 geometries indicated

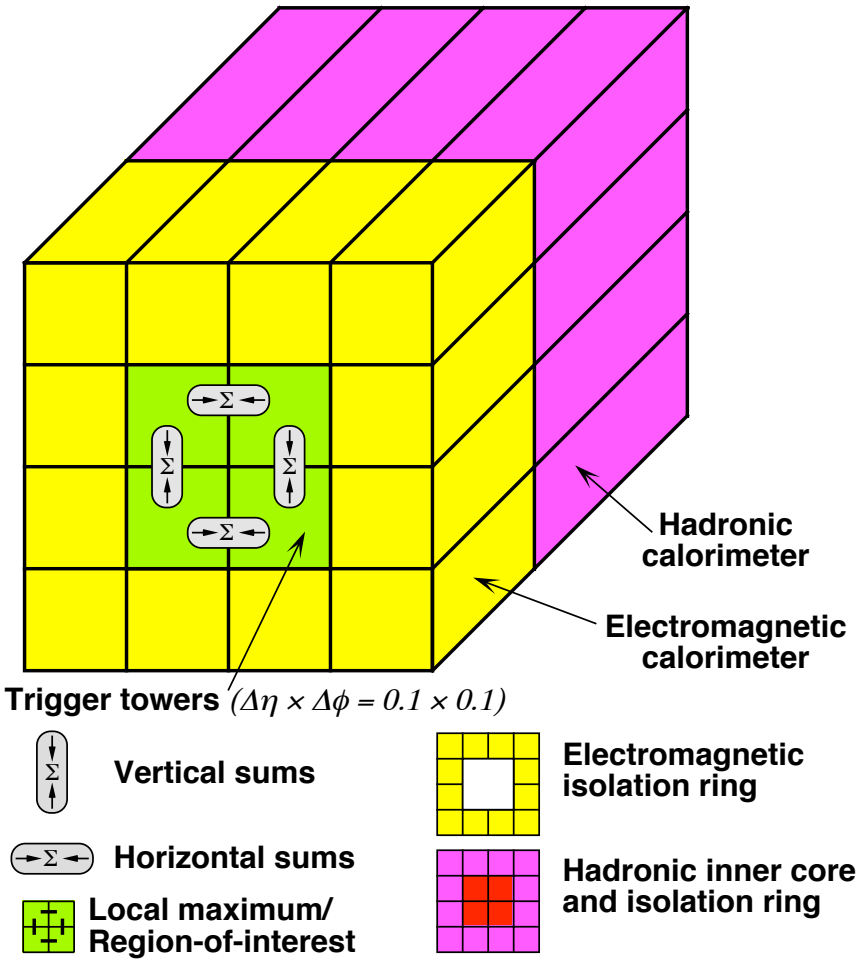

Figure 4.5: Diagram illustrating the energy-sum and calorimeter tower clustering procedure used in the L1Calo trigger. Taken from [52].

in Figure 4.5 [76]. When reconstructing τ leptons (their hadronic decays), the energy deposit in the hadronic calorimeter core is added to the four possible E_{T} sums from the EM calorimeter cluster [76]. This $\sum E_{\mathrm{T}}$ is then required to pass the reconstruction thresholds used to define RoIs discussed above [76]. The (L1) jet reconstruction relies on *jet elements*, 2×2 tower clusters combining the EM and hadronic calorimeter measurements, and considers whether the total $\sum E_{\mathrm{T}}$ in the "window" of the algorithm passes thresholds [76].

The Run 2 sliding window sizes for jet reconstruction included a 4×4 and an 8×8 trigger tower option, producing window sizes of 0.4×0.4 and 0.8×0.8 in $\Delta\eta \times \Delta\phi$, respectively [52]. Smaller windows lead to the identification of more jets compared to larger window sizes with higher reconstruction efficiency[9] [76]. Processing of the L1 jets proceeds using clusters of jet elements centred on a local maximum [76].

[9]It is more likely that $\sum E_{\mathrm{T}}$ calculations are above thresholds for reconstruction [76].

4.6.2 HLT reconstruction

High-Level Trigger (HLT) jet reconstruction uses similar algorithms to those applied for offline reconstruction, including calibrations [52]. HLT jets are commonly reconstructed with the anti-k_t algorithm and can be clustered from a combination of calorimeter and track inputs (e.g. topoclusters and `PFlow`[10] objects). The use of tracking information in the ATLAS HLT jet reconstruction in Run 3 will allow pile-up mitigation algorithms including the rejection of pile-up jets with the Jet Vertex Tagger (JVT) (introduced in Section 4.8). The flexibility of HLT jet reconstruction allows for only the regions of interest identified in the L1 trigger *or* all the detector information to be considered [52]. The latter case is necessary for the reconstruction of global event quantities (e.g. $\vec{E}_{\mathrm{T}}^{\mathrm{miss}}$) and full-detector tracking of charged particles [77]. Tracking algorithms in the HLT function similarly to those used offline and include a fast-tracking stage (important for fast decision-making and *pre-selections*[11]) that provides (lower precision) input to a precision (offline-like) tracking algorithm [52].

The energy scale differences between L1, HLT, and offline objects ultimately lead to a "turn-on" in trigger efficiency curves. Thus, a trigger will not necessarily have 100% efficiency above the kinematic thresholds used to define the trigger signature. Rather, there will be a smooth turn-on of the trigger efficiency to a plateau at (usually) 100% efficiency. These effects are most significant for L1 triggers where no calibrations are applied (EM-scale jets). However, HLT reconstructed jets have an energy scale comparable to objects reconstructed offline, resulting in sharper turn-on curves [52].

4.7 Techniques for boosted jets

Boosted jets are a consequence of the production (and decay) of high-mass or high-momentum particles. As the p_{T} of an object increases, its decay products become more collimated to the point that they can be reconstructed in a single large-R jet – in these cases, small-R (e.g. $R = 0.4$ jets) would overlap. For example, in Figure 4.6 the angular separation of the W-boson and b-quark in a t-quark decay is sufficiently small (less than 1.0) for the decay products of the t-quark to be reconstructed in a single $R = 1.0$ jet for $p_{\mathrm{T}}^{\text{top-quark}} > 350$ GeV.

The following Section will briefly introduce the reconstruction and calibration of large-R jets and related observables that are used to quantify the substructure of these jets.

[10] New for the trigger in Run 3!

[11] An object/event selection made before more costly (e.g. CPU usage) algorithms are applied.

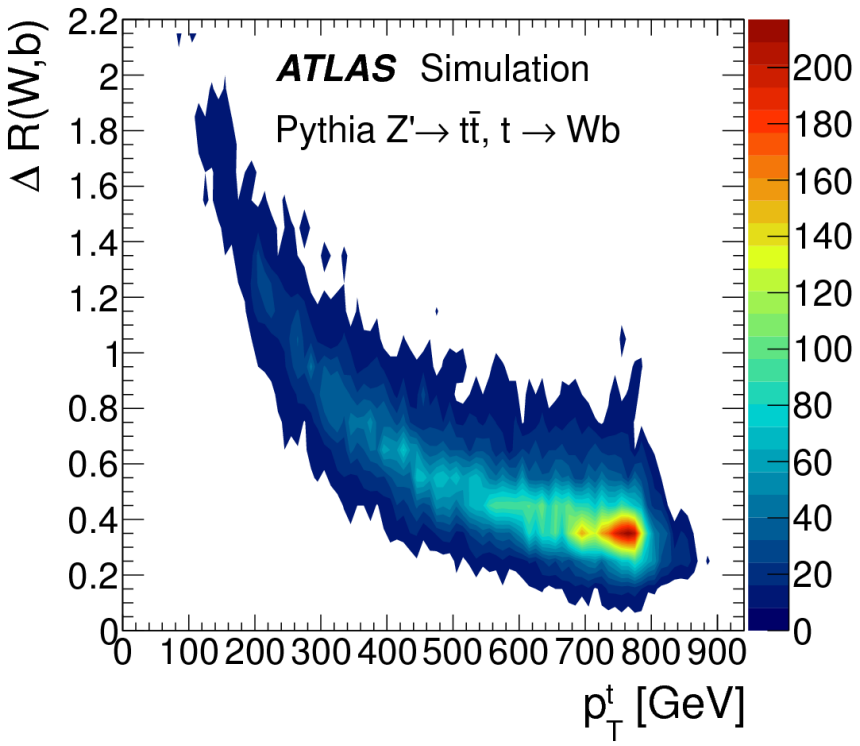

Figure 4.6: A two-dimensional histogram of the ΔR between the W-boson and b-quark originating from $t \to Wb$ decays. The ΔR is plotted as a function of the t-quark p_{T} to highlight the increasing containment of the Wb decay products with p_{T}. Taken from [78].

4.7.1 Pile-up removal

As for small-R jets, pile-up mitigation and subtraction algorithms are an important part of large-R jet reconstruction. The removal of pile-up radiation can take place at different stages in the reconstruction of jets. Some pile-up mitigation algorithms are applied at the level of jet inputs before jet clustering [66]. Whereas grooming algorithms are designed to be executed on jets after clustering – they remove constituents that are soft (low-p_{T}) or are emitted at wide-angles to the jet axis [66]. The soft and wide-angle nature of the removed radiation is a characteristic typical of pile-up.

While many algorithms exist, only those applied directly in the HL-LHC tagging studies in Chapter 7 will be discussed. Namely, grooming methods consisting of the trimming and soft-drop algorithms.

Trimming

The process of trimming involves re-clustering the constituents of the large-R jet using a jet clustering algorithm with a smaller size parameter (R_{sub}) favouring soft radiation – commonly the k_t algorithm (producing irregularly shaped sub-jets) [66]. The resulting sub-jets are tested to determine if they have a p_{T} that is smaller than $f_{\mathrm{cut}} \times p_{\mathrm{T}}^{\text{large-}R}$, where f_{cut} is a tunable parameter (between 0 and 1) and $p_{\mathrm{T}}^{\text{large-}R}$ is the original large-R jet p_{T} [66]. If this is the case, the sub-jet in question is removed from the large-R jet – removing soft radiation but not necessarily wide-angle radiation.

Soft-drop grooming

Soft-drop grooming eliminates both soft and wide-angle radiation from an ungroomed large-R jet. The original large-R jet is re-clustered with the C/A jet algorithm, and the QCD-like C/A clustering sequence is iterated over from the final clustered branch (i.e. reversing the sequence). At every 2-branch splitting, the soft-drop condition in Equation (4.7) is checked (subscripts 1 and 2 are indicative of the different branches) [66]. The grooming algorithm discards the softer branch when the condition is *not* satisfied, at which point it continues iterating through the clustering history along the harder of the two branches [66]. If the condition *is* satisfied, the grooming algorithm stops iterating over the branches, yielding the final groomed jet [66].

$$\frac{\min(p_{\mathrm{T},1},\ p_{\mathrm{T},2})}{p_{\mathrm{T},1} + p_{\mathrm{T},2}} < z_{\mathrm{cut}} \left(\frac{\Delta R_{12}}{R} \right)^{\beta}. \tag{4.7}$$

In Equation (4.7), β controls the acceptance of wide-angle jet radiation and z_{cut} controls the acceptance of soft jet radiation[12] [66]. Other variants of these algorithms

[12] A simple case: if $\beta = 0$ and z_{cut} is large then the condition is almost always satisfied. But, if z_{cut} is lowered, the softer emissions within the jet will gradually fail the condition.

(recursive and bottom-up soft-drop) exist to avoid problems associated with exiting the grooming algorithm early (at a hard splitting) when other soft branches may still exist in the clustering history [66].

4.7.2 Calibration

Large-R jet calibration (Figure 4.7) is similar to small-R jet calibration, but the pile-up subtraction step for small-R jets is substituted for a grooming step (trimming in Run 2) [79]. Additionally, there is no Global Sequential Calibration step for large-R jets [79]. The large-R jets are corrected with the JES calibration and an extra *in situ* correction, which is applied only to data, after grooming [79].

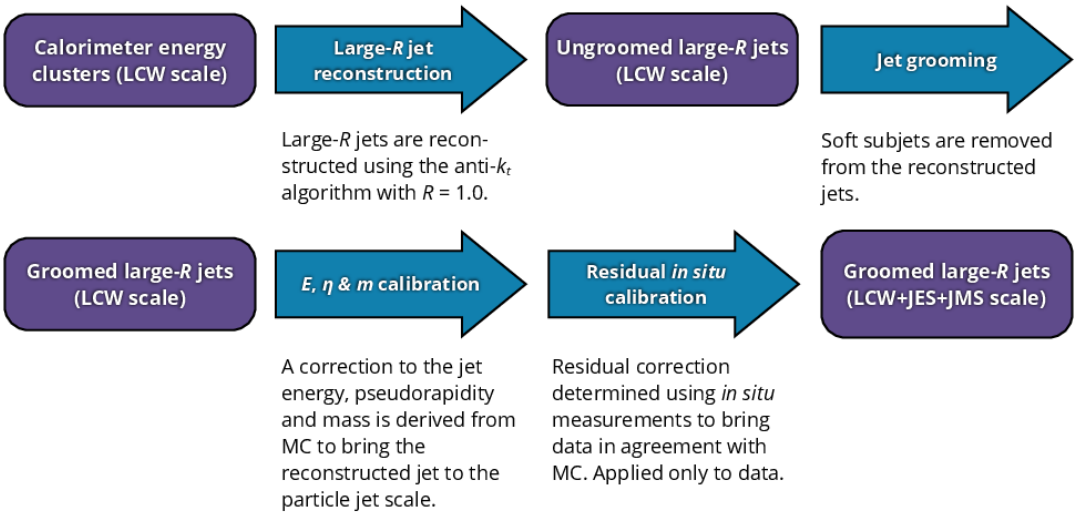

Figure 4.7: Large-R jet calibration sequence starting from calorimeter clusters (topo-clusters) calibrated to LCW scale. In principle, a similar procedure could be applied using alternative jet inputs. Taken from [79].

The JES calibration applies numerical inversion (discussed for small-R jets in Appendix A.3.3) to scale the reconstructed jet energy to that of truth-level jets [79]. An additional Jet Mass Scale (JMS) calibration corrects the reconstructed jet mass to the scale of truth-level jets [79]. This procedure exploits the jet mass response ($\mathcal{R}_m = \langle m_{\text{reco}} \,/\, m_{\text{truth}} \rangle$) in a numerical inversion correction after the JES correction, but only changes the jet p_{T} and mass [79]. The correction coefficient is determined

as a function of the reconstructed jet energy (after JES), η_{det}[13], and $\log(m_{\text{JES}}/E_{\text{JES}})$ (m_{JES}, E_{JES} are the jet mass and energy after JES) [79]. The complete correction is applied like so [79]:

$$E_{\text{JES+JMS}} = c_{\text{JES}} E_{\text{reco}} \tag{4.8}$$

$$m_{\text{JES+JMS}} = c_{\text{JES}} \times c_{\text{JMS}} \times m_{\text{reco}} \tag{4.9}$$

$$\eta_{\text{JES+JMS}} = \eta_{\text{reco}} + \Delta\eta \tag{4.10}$$

$$p_{\text{T}}^{\text{JES+JMS}} = c_{\text{JES}} \sqrt{E_{\text{reco}}^2 - c_{\text{JMS}}^2 m_{\text{reco}}^2} \tag{4.11}$$

where "JES+JMS" and "reco" refer to the calibrated and uncalibrated quantities, respectively.

The large-R jet *in situ* calibration begins by balancing well-measured objects against the large-R jet being calibrated (like for small-R jets). Some of these steps also use small-R jets including the *multi-jet balance*[14] step where a collection of small-R jets are balanced against the large-R jet. A second correction is derived with $t\bar{t}$ events where the top quarks decay to leptons and jets – a mixture of semi-leptonic and fully hadronic decays [79]. The mass response is measured with fits to peaks in the jet mass distribution characteristic of boosted W bosons (semi-leptonic events) and top quarks (fully hadronic events) [79]. The results of these measurements combined with a second[15] are used to produce the complete calibration coefficient for the jet mass calibration [79].

The HL-LHC boosted jet tagging studies in Chapter 7 do not use any calibration besides the LCW calibration applied to topoclusters since the studies explicitly focus on calorimeter based `LCTopo` jet tagging.

4.7.3 Jet substructure observables

Jet substructure observables parameterise the distribution of large-R jet constituents (individual jet inputs or sub-jets from the reclustering of jets with a certain algorithm) in both energy and space (angular coordinates). To discriminate between resonances from heavy particles and radiation from QCD jets or another hadronic process, the observables must be sensitive to decays with a certain number of hard prongs. In top quark identification, the observables must be sensitive to 3-prong decays (e.g. $t \to Wb \to q\bar{q}'b$), while in W/Z-boson decays they must be sensitive to 2-prong decays (e.g. $W \to q\bar{q}'$, $Z \to q\bar{q}$). Ultimately, different observables will provide different separation performance, dependent on the "signal" topology under consideration.

[13] The detector η measured with respect to the centre of the detector.
[14] More discussion of general in situ corrections is available in Appendix A.3.5, otherwise, the calibration is discussed in more detail within Ref. [79].
[15] Using ratios between calorimeter and track measured jet p_{T} in dijet events [79].

The jet mass (m_{jet}) is one commonly used discriminating variable and can be reconstructed from a combination of track and calorimeter information [80] – this thesis will only consider the calorimeter jet mass constructed from (LCW-scale) topoclusters. When the decay products of a boosted particle are fully contained in a jet, m_{jet} represents the invariant mass of the decaying particle.

More general observables used to identify N-prong decays include *N-subjettiness* variables [81–83], *(generalised) energy correlation functions* [82, 84, 85], and ratios of each of the latter observables. Further substructure variables are associated with jet shapes, and measure the symmetry of the distribution of jet constituents within the large-R jet – including *sphericity* and *aplanarity* [86]. Finally, combinations of constituents can be used to define variables such as the minimum invariant mass of sub-jet pairs, Q_W, used for top quark identification [87], or the distance metrics of the k_t algorithm can be considered to quantify the splittings between "particles" enclosed in the jet [87, 88].

This is by no means a complete collection of jet substructure observables. Most of these are suited to identifying W-bosons and top quarks (the focus of Chapter 7), but many more variables exist that are tailored to the identification of different particles. A complete introduction to a selection of these variables including those used for the tagging studies in Chapter 7 can be found in Appendix B.

4.8 Jet tagging

Jet *tagging* is the process of identifying the origin of a hadronic jet whether that is the nature of the initiating particle (a top quark, b-hadron, etc.), or the hard-scatter or pile-up association of the jet. This Section provides a brief introduction to several of these key applications including pile-up rejection in Section 4.8.1, b-jet (b-hadron) identification in Section 4.8.2, and boosted object tagging in Section 4.8.3.

4.8.1 Pile-up jet rejection with JVT

The small-R and large-R jet calibrations remove pile-up *within* jets, but pile-up interactions alone can produce additional jets. Identifying and rejecting jets that do not originate from the hard-scatter vertex is achieved with the likelihood-based *Jet Vertex Tagger* (JVT), which relies on information from tracks associated with jets [41]. The variables contributing to the likelihood are: corrJVF, the JVF (Jet Vertex Fraction, measuring the scalar sum of the p_{T} of tracks associated to the hard-scatter vertex relative to that from other vertices) corrected for dependence on the number of primary vertices, and R_{pT} [41]. The corrJVF variable is defined as [41]:

$$\text{corrJVF} = \frac{\sum_k p_{\text{T}}^{\text{trk},k}(\text{PV}_0)}{\sum_l p_{\text{T}}^{\text{trk},l}(\text{PV}_0) + \left(\sum_{n\geq 1}\sum_l p_{\text{T}}^{\text{trk},l}(\text{PV}_n)\right) / \left(k \times n_{\text{trk}}^{\text{PU}}\right)} \tag{4.12}$$

where PV_i is the ith primary vertex (PV_0 is the primary vertex with highest $\sum p_{\mathrm{T}}^2$), $n_{\mathrm{trk}}^{\mathrm{PU}}$ is the number of tracks from pile-up interactions, $p_{\mathrm{T}}^{\mathrm{trk},j}$ is the p_{T} of the jth track associated to a primary vertex. The k parameter, set to 0.01, represents an approximation of the slope of the average pile-up track p_{T} as a function of the number of tracks from pile-up interactions [41].

The R_{pT} variable is defined using ratios of the p_{T} of jet-matched tracks and the total jet p_{T} [41]:

$$R_{\mathrm{pT}} = \frac{\sum_k p_{\mathrm{T}}^{\mathrm{trk},k}(\mathrm{PV}_0)}{p_{\mathrm{T}}^{\mathrm{jet}}} \tag{4.13}$$

where $p_{\mathrm{T}}^{\mathrm{jet}}$ is the jet p_{T} from the sum of constituent 4-momenta.

The likelihood variables are correlated such that a hard scatter jet has large R_{pT} and corrJVF, while a pile-up jet has small R_{pT} and corrJVF [41]. The JVT discriminant is determined from a k-nearest neighbour algorithm, and for a region around each (R_{pT}, corrJVF) point determines the probability that the jet originates from the hard scatter interaction [41]:

$$\mathrm{JVT} = \frac{\text{number of hard scatter jets}}{\text{number of hard scatter + pile-up jets}}. \tag{4.14}$$

The JVT discriminant is skewed to 1 for hard scatter jets and skewed to zero for pile-up jets [41]. If a jet has no matched tracks the JVT discriminant is assigned a value of -0.1 [41].

The default JVT working point for `EMPFlow` jets is the *Tight* selection: $JVT > 0.5$ for jets within $|\eta| < 2.4$ and with $20 < p_{\mathrm{T}}\ (\mathrm{GeV}) < 60$. The selection on the jet p_{T} ensures that only jets with pile-up characteristics are considered for JVT selections to avoid rejecting hard-scatter jets[16]. Typically, the η selection is also made with the detector η measured with respect to the geometrical centre of the detector. As discussed in Section 4.6, JVT selections were not available for HLT jets in Run 1 and Run 2 of the LHC, but they will be in Run 3, allowing pile-up rejection to be used in trigger signatures.

4.8.2 *B*-hadron reconstruction and identification

The production of B-hadrons (and b-quarks) occurs in many SM and BSM processes – especially those involving the decays of top quarks or the Higgs boson [44]. The identification of B-hadrons in jets (*b-jets*) relies on the key differences between b-hadrons and lighter partons – especially the longer b-hadron lifetime, which leads to the production of a *secondary vertex* after they decay [44]. The prevalence of the secondary vertex in b-hadron decays motivates the use of tracking information for b-tagging, the reconstruction and identification of b-jets, combined with the reconstructed jet(s) themselves [44]. The b-tagging procedure begins with the

[16]The author thanks Caterina Doglioni for clarifying this.

application of likelihood methods to discriminate between the b-jet signal and light jet backgrounds (c-quarks, etc.) using low-level tracking information (for tracks matched to the b-jet candidate) including impact parameters and secondary vertex track fitting [44]. High-level algorithms that use both the discriminants for the low-level algorithms and additional tracking observables (including track multiplicities and ratios of the energies of all associated tracks to that of the jet) have been developed to provide a binary classification score (MV2, a Boosted Decision Tree tagger) and a multi-classification result (DL1, a deep neural network tagger) to produce the high-level tagger discriminant [44].

4.8.3 Large-R jet tagging for boosted particles

Since boosted object tagging is a significant focus of Chapter 7, large-R jet tagging will only be introduced briefly here. As described in Section 4.7, the decays of boosted particles permit the use of the substructure of jets to discriminate between boosted objects from signal and background processes. The most basic jet tagger consists of a set of selections (cut-based requirements) on suitable observables [80] – including those briefly introduced in Section 4.7.3 and Appendix B. To achieve sufficient discrimination power, selections on several variables can be combined to better isolate the kinematics of the signal object (e.g. a heavy boson or quark) [80].

The rise of machine learning (ML) in high-energy physics has led to the development of a range of ML-based taggers that take several variables as input and provide output in the form of a tagger score [80]. The tagger score is parametrised as a function of jet p_{T} to determine a smoothly varying selection that achieves stable performance across a wide kinematic regime [80]. Such techniques were applied to develop a DNN (deep neural network) tagger for trimmed large-R jets during Run 2 of the LHC [80]. The DNN takes several variables as input [80]:

- The combined jet mass – reconstructed from calorimeter and track-assisted jet mass measurements [80].
- The jet p_{T}.
- N-subjettiness variables: τ_1, τ_2, τ_3, τ_{21}, τ_{32}.
- (Generalised) Energy correlation functions and their ratios: e_3, C_2, and D_2.
- k_t splitting scales: $\sqrt{d_{12}}$ and $\sqrt{d_{23}}$.
- The Q_W observable – the minimum invariant mass of a pair of jet constituents.

These observables are defined in more detail in Appendix B. The DNN tagger has pre-defined working points at fixed 50% and 80% signal (top quark) efficiency for the identification of contained and inclusive top quark decays [80]. Contained top quark decays are those where all decay products are reconstructed in a single jet. Whereas, inclusive top quark decays correspond to cases where this may not occur

and only some decay products (e.g. the $W \to q\bar{q}'$ decay from the hadronic t quark decay) are contained in the jet.

4.9 Summary

This Chapter provided a brief overview of important techniques used at the ATLAS experiment for reconstructing, calibrating, and identifying objects in hadronic final states. Our ability to recognise these objects, most importantly hadronic jets, is imperative for the future of particle physics research, especially probing the decays of the Higgs boson in processes such as $HH \to b\bar{b}b\bar{b}$ or searches in other multi-jet final states. For the remainder of this thesis, this Chapter will provide a foundation for jet tagging and trigger performance studies oriented towards both Run 3 and the HL-LHC.

Chapter 5

Multi-jet Trigger-object Level Analyses during LHC Run 3

Trigger-object level analysis (TLA) is a non-standard data-taking and analysis method for increasing experimental sensitivity to rare physics signatures in regions of phase space where typical analyses are limited by trigger rate and bandwidth requirements. Rather than saving complete data for offline reconstruction, only objects reconstructed in the software trigger (jets, leptons, etc.) are saved, decreasing the size of stored events and therefore allowing higher rate data collection. In low-mass resonance searches where high-rate QCD jet production is most prevalent, this can produce a substantial benefit over standard data acquisition techniques. During Run 3 of the LHC, the ATLAS trigger menu will include a comprehensive stream devoted to TLA, to probe a range of physics signatures including exotic multi-jet and b-jet signals such as those arising from R-parity violating supersymmetry (RPV SUSY). When these searches are conducted in the higher luminosity conditions of the HL-LHC the aim is to be sensitive to electroweakino[1] production, which has a low cross-section for light electroweakino masses below 500 GeV [8, 89]. This is illustrated in Figure 5.1 where the gluino ($\tilde{g}$) pair-production cross-section is several orders of magnitude larger than the electroweakino ($\tilde{\chi}$) pair-production cross-sections.

This Chapter presents the findings of studies used to inform trigger choices for a Run 3 multi-jet TLA search focusing on RPV SUSY gluino pair-production signals. It should be noted that these studies were used to obtain an indicative and optimistic estimate of the sensitivity of a multi-jet TLA search, and therefore they do not present precision results that consider underlying systematic uncertainties.

A description of TLA and relevant background is provided in Section 5.1. Section 5.2 provides an overview of the RPV SUSY signal studied in addition to details on the generation of the MC samples used for these studies. The reconstruction of events for these studies is discussed in Section 5.3. The results of the trigger choice studies are described in detail in the following Sections:

[1] The supersymmetric partners to Standard Model gauge and Higgs bosons.

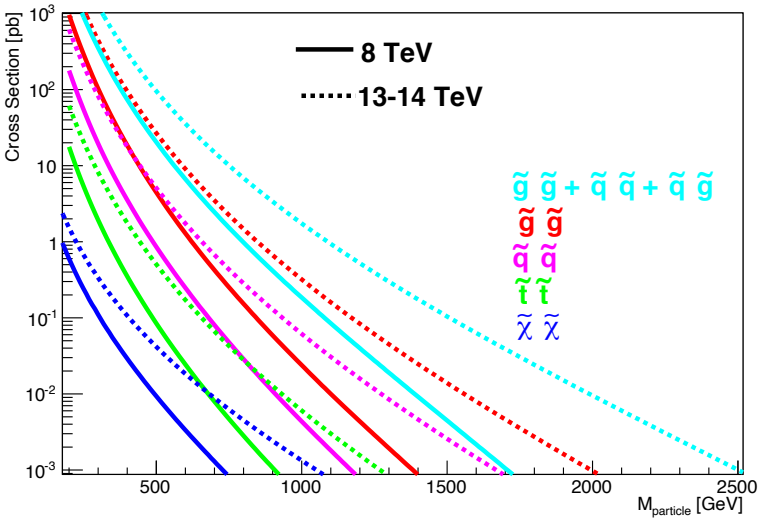

Figure 5.1: Cross-sections as a function of particle mass for different SUSY pair-production processes (here the focus is $\tilde{g}\tilde{g}$ and $\tilde{\chi}\tilde{\chi}$) taken from [89]. The cross-sections for $\tilde{g}\tilde{g}$ are evaluated at both $\sqrt{s} = 8$ TeV and $\sqrt{s} = 13$ TeV [89]. Whereas the $\tilde{\chi}\tilde{\chi}$ (electroweakino/higgsino) cross-sections are evaluated at $\sqrt{s} = 8$ TeV and $\sqrt{s} = 14$ TeV [89].

- Section 5.4 introduces the motivation for the studies and application of TLA for multi-jet searches.
- Section 5.5 introduces the trigger selections studied and provides a description of their naming conventions.
- Sections 5.6 and 5.7 outline the results of the signal acceptance studies for L1 triggers and the effects of different L1 selections on the kinematic distributions of both L1 trigger and calibrated (offline) jets.
- Section 5.8 discusses the signal acceptance studies for complete trigger chains involving kinematic selections.
- Section 5.9 briefly introduces pile-up mitigation strategies and their influence on the signal acceptances and p_{T} distributions for calibrated jets.

A summary of the results of the Run 3 studies and an outlook for the future is provided in Section 5.10.

5.1 Overview of Trigger-object Level Analysis

The analysis of trigger-level information is a technique used by all the LHC experiments that analyse pp collisions – *Data-scouting* at CMS [90] and the *Turbo stream* at LHCb [91]. Typical analyses (e.g. for high-momentum or high-mass final states)

rely on low-rate (and high-threshold) physics triggers to reject high-rate background processes and identify events that are stored for later (offline) reconstruction. Thus, many events with low-momentum objects can simply be discarded, which is not possible in searches for exotic low-mass particles. Where high-rate background processes dominate, low-mass searches are bandwidth limited. Recall from Section 3.2.6 that the trigger bandwidth is defined as:

$$\text{BW} = \{\text{rate}\} \times \{\text{event size}\}, \tag{5.1}$$

which has units MB/s, for an event size in MB. At ATLAS, trigger-object level analysis (TLA) is used to decrease the size of raw events by saving only the data for physics objects reconstructed in the High-Level Trigger (HLT). Thus, for a fixed bandwidth, a dramatic reduction in event size[2] allows for a significant increase in the rate of triggers used for data collection. It then becomes possible to search for rare processes in regions of parameter space that are otherwise inaccessible. In principle, a reduction in the event size by an order of magnitude allows for a complementary increase in the trigger rates, however, the maximum output rate for the L1 trigger (100 kHz) limits the increased rate that is feasible.

A Run 2 search for dijet resonances originating from models of dark matter involving Z' bosons [92] illustrates the power of TLA. The application of TLA allowed for high-rate data-taking utilising 1% of the bandwidth typical of non-TLA searches [92]. The benefits of TLA are evident upon inspection of the region of the dijet invariant mass distribution accessible to the search in Figure 5.2. A significant increase is seen in the number of events at low invariant masses, which is otherwise not seen with pre-scaled (offline analysis) triggers [92].

Other non-standard trigger strategies including partial event building (PEB) exist, but they are distinct from TLA. In PEB one saves a subset of the total raw detector information for analysis rather than only trigger-level objects. The remainder of this Chapter focuses solely on trigger strategies involving TLA.

For TLA to be a useful analysis strategy a range of requirements must be met. These include [93]:

- All algorithms must have fast execution times so as not to strain existing HLT resource usage (e.g. TLA data collection can then be run at the same time as that for the physics-main stream).
- The calibrated trigger-level objects should be comparable to offline reconstructed objects (energy scales, etc.) to avoid the duplication of reconstruction and calibration steps (and information) in the trigger and offline for analysis.
- TLA algorithms should perform well in high pile-up conditions – such as those at the HL-LHC.

[2] A Run 2 dijet TLA reduced the event size to less than 0.5% of the event size when complete data are saved for offline analysis [92].

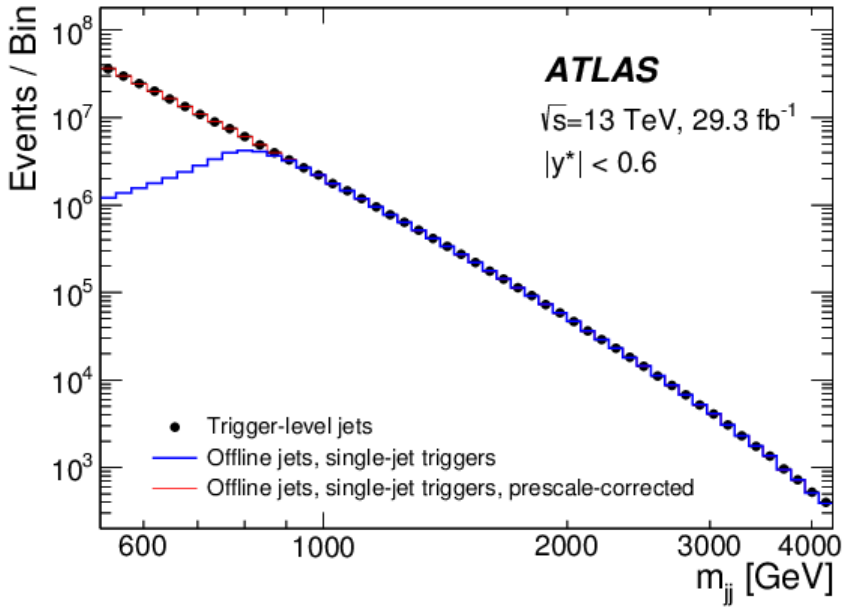

Figure 5.2: The dijet invariant mass distribution for trigger-level jets and offline jets from events collected with single-jet triggers [92]. The offline jet distribution only matches the trigger-level jet distribution after correcting for pre-scales applied to the single-jet triggers highlighting higher statistical power of trigger-level analyses [92]. Taken from [92].

For the studies discussed in this thesis the first and third requirements are considered.

5.2 Simulated event samples

5.2.1 Signal samples

These studies focused on the sensitivity of the ATLAS experiment to low-mass RPV SUSY multi-jet resonances. While the signal studied here may already be excluded (e.g. Ref. [94, 95]), it emulates the results we may see for electroweakinos, which have similar kinematic distribution shapes and smaller cross-sections. The signal process consists of gluino pair-production and decay to a fully hadronic final state containing six quarks, three from each gluino. The gluino decay occurs through the λ'' UDD coupling in the super-potential for the RPV SUSY model (see Section 2.2.2). A Feynman diagram for this process is shown in Figure 5.3. Two decays modes were considered: decays to a u, d, and s quark (UDS) and to a u, d, and b quark (UDB) for each gluino. The UDS and UDB decay modes produced similar results in our studies, so we focused primarily on the UDS decay mode but include results for the UDB decay mode for completeness in some Sections. The use of b-tagging could provide additional discrimination between signal and background processes for UDB decays but is not considered further in this work.

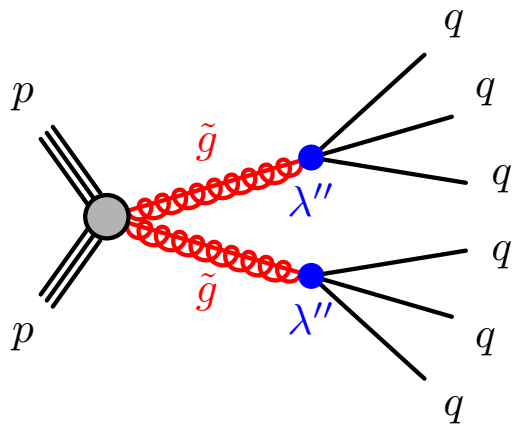

Figure 5.3: Feynman diagram for RPV SUSY gluino pair production from a proton collision. The gluinos each decay to three quarks via an RPV λ'' UDD coupling. Taken from [96].

Simulated MC samples officially produced by the ATLAS Collaboration were used to model the signal process. These samples mimic Run 2 data-taking conditions including pile-up levels (from the average number of interactions per bunch crossing, μ). The event samples were produced with MadGraph5_aMC@NLO (version 2.8.1) [97] (for the SUSY signal simulation), Pythia 8.244 [98], and EvtGen 1.7.0 [99], using the NNPDF23LO PDF sets [100]. The events were later passed through the ATLAS simulation framework, which emulates the complete response of the detector, to produce a collection of reconstructed signal events (with detector effects). Gluino masses between 100 GeV and 400 GeV in steps of 100 GeV were considered for these studies.

Run 2 ATLAS MC samples are separated into different campaigns configured to allow the combination of samples from different sub-campaigns to produce datasets with higher statistical power. Different sub-campaign samples emulate the different LHC data-taking conditions in each year during Run 2. Three different MC campaigns were used for these studies [101]:

- MC16a – with a pile-up profile that matches data taken in 2015 and 2016.
- MC16d – with the 2017 pile-up (μ) distribution.
- MC16e – with the expected (at the time of simulation) 2018 pile-up (μ) distribution.

Since the conditions between these samples vary, the results presented in the remainder of this Chapter incorporate both the MC16a (only) and MC16(a,d,e) combined samples. The size of the event samples used in these studies broken down by campaign is:

- MC16a (referred to as "MC16a" or "MC16a only"): 60000 events (UDS) and 70000 events (69000 for the $m_{\tilde{g}} = 200$ GeV sample) (UDB)

- MC16(a,d,e) combined (referred to as "combined MC16"): 230000 events (229000 for the $m_{\tilde{g}} = 100$ GeV and $m_{\tilde{g}} = 200$ GeV sample) (UDS) and 289000 events (290000 for the $m_{\tilde{g}} = 300$ GeV sample) (UDB)

The combined MC16(a,d,e) dataset required luminosity scaling to correctly account for the total number of (weighted) events processed for each sample. Thus, the event weights for the sample were scaled by:

$$\mathrm{SF} = \frac{\epsilon_f \times \sigma_{\mathrm{sample}} \times \mathcal{L}}{\sum_{\mathrm{event,\ i}} \mathcal{W}_i} \tag{5.2}$$

where SF is the event weight scale factor, ϵ_f is the filter efficiency of the MC generator, σ_{sample} is the cross-section for the sample, $\mathcal{L}$ is the integrated luminosity of the sample (set to 1.0 fb^{-1}), and the denominator represents the sum of the event weights for the complete sample (only those events processed).

Events from the MadGraph_aMC@NLO generator can have negative weights, which leads to un-physical negative values in histogram bins that only contain a few events (with large negative weights). This is most significant for two-dimensional histograms where the bin populations become important. No "special" handling was introduced to deal with negative weights in these studies. Where necessary, we ensured the axis limits of plots are physical (starting at 0.0 or 1.0) to adequately describe the results without complications from the bins with negative entries – the negative bin content issue rarely occurs in the most populated region of distributions. In a "real" analysis the negative event weights may need to be dealt with differently to avoid other code-based problems, however, for our purposes, it is sufficient to acknowledge their existence.

5.2.2 Background estimation

The background processes for RPV SUSY $\tilde{g}\tilde{g} \to 6q$ are dominated by QCD jet production, specifically dijet and multi-jet processes. Standard Model $t\bar{t}$ production also introduces a background from the top quark, a known low-mass resonance. For the Run 3 studies, no background estimation was conducted because expected trigger rates (in the absence of signal) were already available from "technical runs" of the HLT using enhanced bias[3] data collected in previous data-taking periods. Rather, the studies focused on the signal sensitivity for different Level-1 trigger and HLT chains.

5.3 Reconstructing events for analysis

This analysis considered small radius ($R = 0.4$) jets clustered from electromagnetic-scale particle-flow (`PFlow`) objects using the anti-k_t algorithm, referred to as `EMPFlow`

[3]The use of enhanced bias data is introduced in Section 3.2.6.

jets. The jets used to emulate decisions in the HLT were therefore offline[4] jets, *not* trigger-level jets. This allowed us to focus on an optimistic scenario for Run 3 TLA searches where tracking is expected to be available with an upgraded HLT CPU farm. The jets were calibrated by applying a Jet-Energy-Scale (JES) calibration based on recommendations for the ATLAS 2016 MC campaign. First an area correction was applied to remove pile-up contamination, then a residual pile-up and η correction were applied. The next calibration steps involved scaling the energy of the MC samples (JES – Jet Energy Scale) and corrections to mitigate differences between quark- and gluon-initiated jets (Global Sequential Calibration). Finally, a smearing was applied to the samples instead of the in-situ correction usually applied to data. If trigger-level jets were used, a dedicated trigger jet calibration would be applied.

No dedicated reconstruction algorithms were used to reconstruct (isolated) leptons since a fully hadronic final state was studied. It is possible for hadrons within jets to decay (semi-)leptonically whereby the charged particle tracks of leptons could be clustered into a jet and treated indistinguishably to another jet constituent. The rate at which this occurs depends on the branching fraction of the decay of a particular hadron to a final state containing leptons.

5.4 Motivation for Run 3 studies

Triggering and Data Acquisition (TDAQ) systems are fundamental for collecting data in collider searches for rare and exotic phenomena. Kinematic trigger selections should provide high acceptance for low cross-section signals even where background processes are dominant. The momentum and energy distributions for jets originating from low-mass resonances are shifted to lower values than those for higher mass resonances. Therefore, low-threshold triggers are needed to maximise the number of signal events passing selections.

An event measured in the ATLAS detector is first reconstructed at the Level-1 trigger (L1 trigger), which provides a coarse measurement of kinematic quantities. Events that pass L1 trigger selections progress to the HLT where additional selections are made before data is saved to disk. Past RPV SUSY searches have used the L1 trigger `L1J100` seed. This requires there to be at least one *electromagnetic-scale* jet in the event with $E_{\mathrm{T}} > 100$ GeV[5], which for low-mass signals cuts out many of the low-p_{T} events. Furthermore, analyses typically select events where triggers are fully efficient (have 100% efficiency), which for the `L1J100` corresponds to an approximate leading jet $p_{\mathrm{T}} > 220$ GeV cut for fully calibrated (offline) jets. It is evident from Figure 5.4 that this decimates the acceptance for low-mass resonances (e.g. $m_{\tilde{g}} = 100$ GeV gluinos). The `L1J100` selection eliminates most of the signal events, so clearly a more performant selection is required for very low mass resonances.

[4]Reconstructed as they would be for offline analysis.

[5]Level-1 jet triggers typically make selections on the E_{T} of jets identified in the calorimeter. Whereas the jet p_{T} is used in HLT selections.

The ideal trigger selection for low-mass signals has low momentum/energy thresholds and should not have stringent jet multiplicity requirements. For instance, consider the correlation between the offline and L1 trigger jet multiplicity shown in Figure 5.5 for all mass points of the UDS gluino decay mode. The signal events clearly contain many jets[6], and the core of the jet multiplicity distribution migrates to larger values as the gluino mass increases. Thus, a low threshold multi-jet or H_{T} (scalar sum of jet p_{T} or E_{T}) trigger could significantly improve the signal acceptance. For these studies, a H_{T} selection using the L1 Topological (L1Topo) trigger is considered since it is expected to be more performant than high-threshold single-jet selections and applicable to a wide range of signal topologies. Additional multi-jet triggers are also studied.

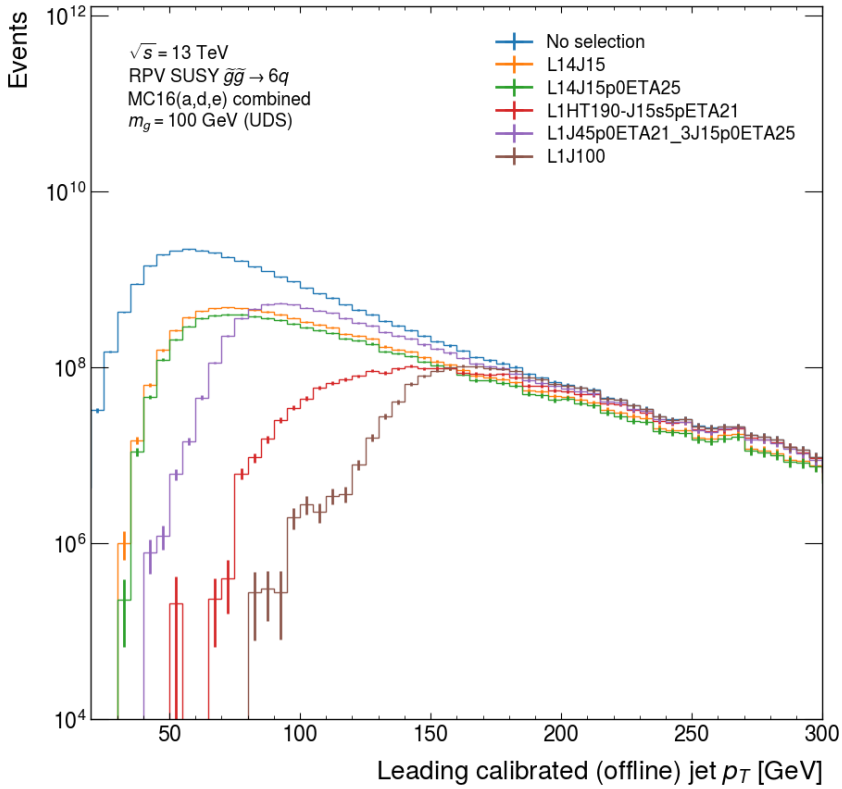

Figure 5.4: Offline calibrated leading jet transverse momentum distribution after different L1 trigger selections for a 100 GeV signal mass. The effect of different trigger thresholds is evident from the position of the lower edge of the p_{T} distributions after trigger selections compared to the *No selection* histogram.

[6]The higher offline jet multiplicity compared to the L1 trigger jet multiplicity in Figure 5.5 is a consequence of trigger and offline jet calibration and reconstruction differences. L1 trigger jets are uncalibrated and at a lower energy scale than offline jets. When reconstruction thresholds are applied to avoid reconstructing too many low-p_{T} L1 jets, the resulting L1 jet multiplicity is smaller than for the full offline event reconstruction.

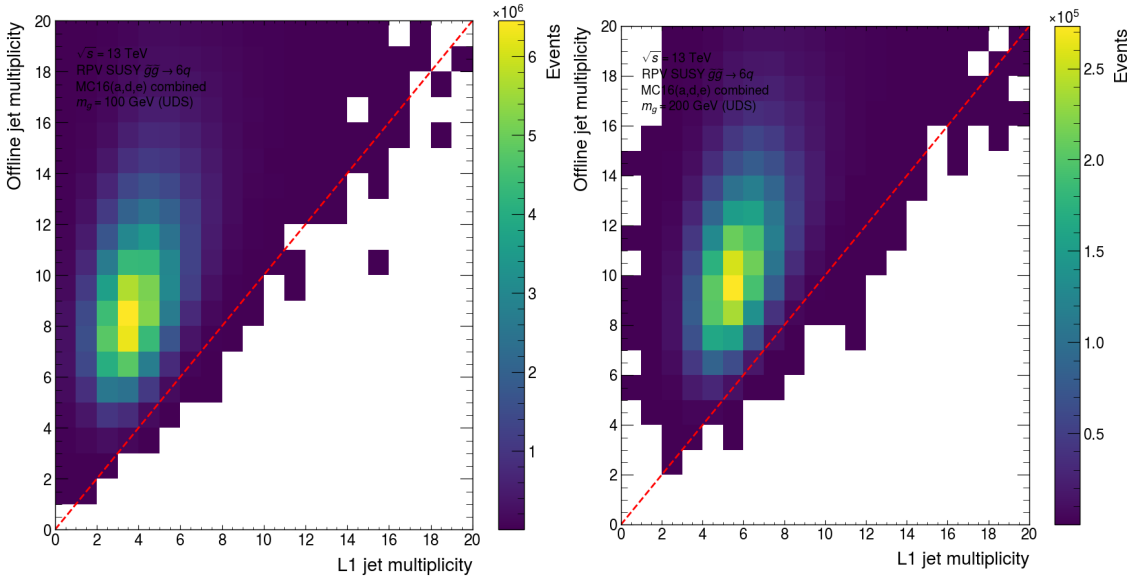

(a) $m_{\tilde{g}} = 100$ GeV (b) $m_{\tilde{g}} = 200$ GeV

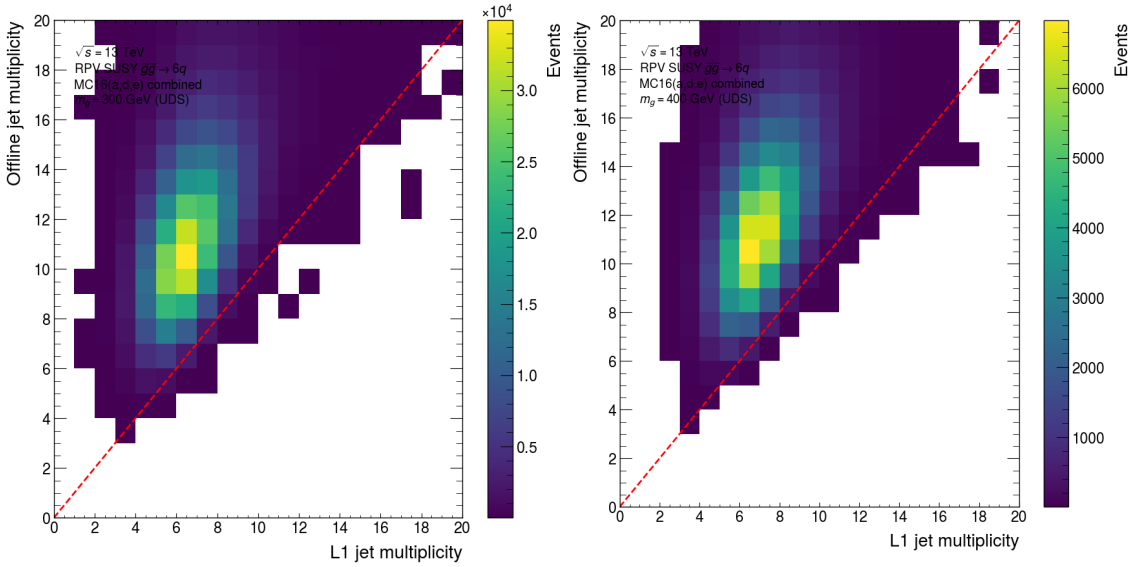

(c) $m_{\tilde{g}} = 300$ GeV (d) $m_{\tilde{g}} = 400$ GeV

Figure 5.5: Histograms showing correlations between the number of offline (calibrated) jets and L1 jets from the combined UDS MC16 event sample. The diagonal dashed line corresponds to the expectation of a one-to-one relationship between the number of offline and L1 jets. The bins on each axis are inclusive of the lower edge and exclude the upper edge. No p_{T} selections are made on jets, so these are the "raw" (untriggered) expectation of what might be seen in collision data. Without p_{T} selections the *offline jet multiplicity* will be larger than for the signal jets alone because pile-up jets are included.

5.5 Trigger chains studied

A standardized nomenclature is used to describe trigger chains. Since HLT chains are seeded by L1 trigger chains, L1 seed and L1 chain are used interchangeably here. HLT trigger chains are written in lower-case letters, while L1 trigger chain names are written in upper-case letters [52]. The naming schemes for L1 and HLT multi-jet and H_{T} triggers are described in more detail below. As noted briefly before, the L1 jet triggers make selections on the jet E_{T}, rather than the p_{T}, which is used in trigger chains at the HLT.

5.5.1 L1 trigger selections

The list below summarises multi-jet L1 triggers studied in preparation for Run 3:

- `L1J100`: requires at least 1 L1 jet with $E_{\mathrm{T}} > 100$ GeV.
- `L14J15`: requires at least 4 L1 jets with $E_{\mathrm{T}} > 15$ GeV.
- `L14J15p0ETA25`: same as above, but all L1 jets must be within $|\eta| < 2.5$.
- `L1J45p0ETA21_3J15p0ETA25`: requires at least 1 L1 jet with $E_{\mathrm{T}} > 45$ GeV within $|\eta| < 2.1$ and at least 3 jets with $E_{\mathrm{T}} > 15$ GeV within $|\eta| < 2.5$. The selection is inclusive, so the jet satisfying `J45p0ETA21` is also permitted to satisfy the `3J15p0ETA25` selection.

The `L1J45p0ETA21_3J15p0ETA25` L1 chain was considered as a seed for triggering on $HH \to 4b$ events in Run 3 and is referred to as the asymmetric seed herein.

L1Topo H_{T} selections impose both H_{T} and jet kinematic requirements [102]. For instance, `L1HT190-J15s5pETA21` consists of the following selections:

- `HT190`: requires $H_{\mathrm{T}} > 190$ GeV
- `J15`: only L1 jets with $E_{\mathrm{T}} > 15$ GeV are used to calculate the H_{T}.
- `s5`: only the first (leading; i.e. highest E_{T}) 5 L1 jets are considered in the H_{T} calculation.
- `ETA21`: only jets within $|\eta| \leq 2.1$ are used to calculate H_{T}.

The event-level H_{T} is calculated as the scalar sum of the transverse momentum of jets in the event satisfying selection criteria (e.g. `J15s5pETA21` described above). That is,

$$H_{\mathrm{T}} = \sum_{j} E_{\mathrm{T},j} \tag{5.3}$$

where j runs over the selected jets [102].

The lower edge of the L1Topo H_{T} distribution is influenced by the number of jets that contribute to the H_{T} calculation (after passing kinematic requirements). This behaviour was found to be most significant for the lowest mass signals and results in a departure from the typical distribution shape where the H_{T} rises smoothly to a peak and then decreases monotonically. This is illustrated in Figure 5.6 for both the UDS 100 GeV and 200 GeV signal points from the MC16a event sample. When only one jet contributes to the H_{T} calculation, a shape like a jet p_{T} (or E_{T}) distribution that falls as the H_{T} increases is produced. This caused an unexpected distribution shape (a low-H_{T} spike) for the 100 GeV signal but not the 200 GeV signal, which has fewer events where a single jet contributes to the H_{T}. The mass dependence of this feature results from the increasing jet E_{T} expected for higher mass signals. While the additional structure in the 100 GeV signal point H_{T} distributions seems odd at first, it would not be seen in "real-world" data-taking – such low-energy events would be discarded by H_{T} thresholds above 100 GeV.

In general, if a trigger chain is formatted with `...p...`, the section after `p` indicates an additional selection, often on $|\eta|$. Where a $|\eta|$ selection is not specified in a trigger chain, a default selection of $|\eta| < 3.1$ and $|\eta| < 3.2$ is used at the L1 trigger and HLT, respectively.

5.5.2 HLT selections

In complete trigger chains, events passing the L1 trigger selections from Section 5.5.1 are required to meet additional selection criteria at the HLT. In principle, a HLT chain may involve an initial pre-selection using calorimeter-only jets before more expensive selections involving tracking (including `PFlow` jets) or b-tagging are applied. Pre-selections are discussed further in Section 5.8.

These studies consider the HLT selections outlined below:

- `HLT_j20_L14J15`: at least one HLT jet must have $p_{\mathrm{T}} > 20$ GeV for events passing `L14J15`.

- `HLT_j20_L14J15p0ETA25`: at least one HLT jet must have $p_{\mathrm{T}} > 20$ GeV for events passing `L14J15p0ETA25`.

- `HLT_j20_L1J100`: at least one HLT jet must have $p_{\mathrm{T}} > 20$ GeV for events passing `L1J100`.

- `HLT_j20_L1HT190-J15s5pETA21`: at least one HLT jet must have $p_{\mathrm{T}} > 20$ GeV for events passing `L1HT190-J15s5pETA21`.

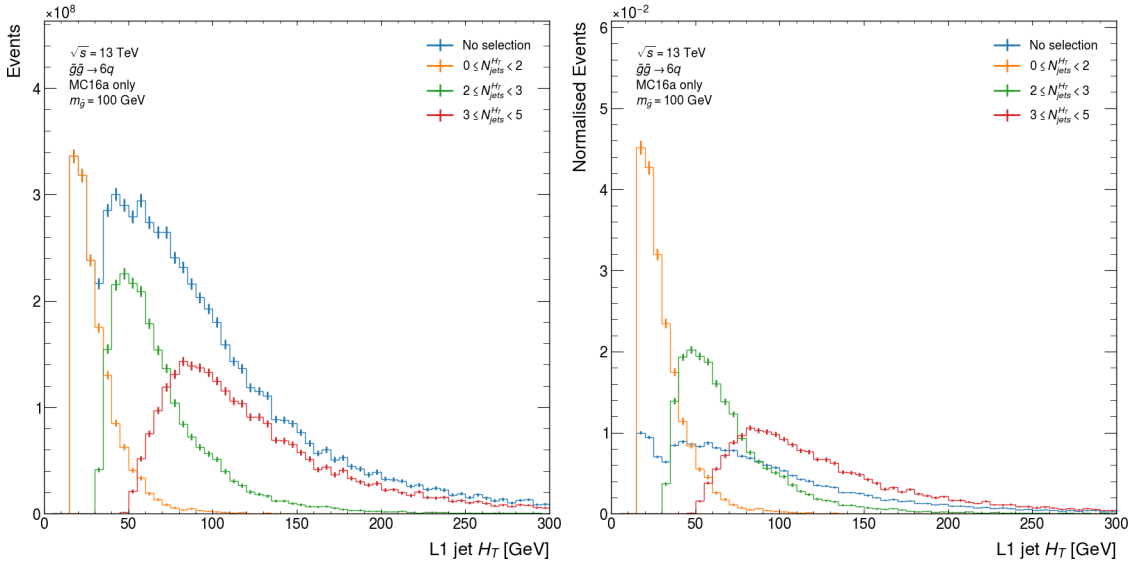

(a) $m_{\tilde{g}} = 100$ GeV un-normalised

(b) $m_{\tilde{g}} = 100$ GeV normalised

(c) $m_{\tilde{g}} = 200$ GeV un-normalised

(d) $m_{\tilde{g}} = 400$ GeV normalised

Figure 5.6: Shapes of the L1 H_{T} distributions for the `J15s5pETA21` selection in events where different numbers of jets contribute to the H_{T}. Results are included for only the UDS signal points. The *No selection* histogram is the complete H_{T} distribution. In the other legend entries $N_{\mathrm{jets}}^{H_{\mathrm{T}}}$ refers to the number of jets contributing to the H_{T} for each event. The normalised versions of the histograms (right) can be used to compare the shape of each contribution.

- `HLT_j80_j55_j28_j20_L1J45p0ETA21_3J15p0ETA25`: there must be at least 4 *different* HLT jets satisfying $p_{\mathrm{T}} > 80$ GeV, $p_{\mathrm{T}} > 55$ GeV, $p_{\mathrm{T}} > 28$ GeV, $p_{\mathrm{T}} > 20$ GeV for events passing `L1J45p0ETA21_3J15p0ETA25`.

- `HLT_j60_j45_2j20_L1J45p0ETA21_3J15p0ETA25`: the same as above but with different p_{T} thresholds for HLT jets; 4 different jets are required to have $p_{\mathrm{T}} > 60$ GeV, $p_{\mathrm{T}} > 45$ GeV, and $p_{\mathrm{T}} > 20$ GeV (for two jets).

- `HLT_4j120(_L1J100)`: at least 4 HLT jets must have $p_{\mathrm{T}} > 120$ GeV for events passing `L1J100`[7].

- `HLT_5j70_0eta240_L14J15`: at least 5 HLT jets must have $p_{\mathrm{T}} > 70$ GeV and be reconstructed within $|\eta| < 2.4$ for events passing `L14J15`.

- `HLT_ht1000_L1J100`: the HLT H_{T} (calculated from jets with $p_{\mathrm{T}} > 30$ GeV and $|\eta| < 3.2$) must be above 1000 GeV for events passing `L1J100`.

Further trigger selections will be introduced where necessary and involve variations of the selections presented above. The `HLT_j80_j55_j28_j20_L1J45p0ETA21_3J15p0ETA25` trigger chain proposed for the $HH \to 4b$ analysis normally involves additional b-jet tagging steps at the HLT. However, for the signal acceptance measurements here we focused primarily on the effects of simple kinematic selections involving the jet p_{T} or E_{T} and $|\eta|$ in addition to the H_{T}. All HLT jet selections use the $|\eta| < 3.2$ default η selection discussed in Section 5.5.1, unless a $|\eta|$ is otherwise specified.

The trigger chains outlined above include a range of conventional high-threshold triggers like those used in previous SUSY searches to provide a baseline measure of signal acceptance for comparison to TLA triggers. The `4j120` selection was motivated by previous searches for top squark pair-production that used 4-jet triggers requiring $p_{\mathrm{T}} > 100$ GeV and $p_{\mathrm{T}} > 120$ GeV (all within $|\eta| < 2.5$) in Ref. [103], and 4-jet triggers requiring $p_{\mathrm{T}} > 100$ GeV in Ref. [104] for a different signal topology[8]. The `5j70` selection appeared in SUSY searches for both R-parity conserving and violating gluino pair-production involving jets and $\vec{E}_{\mathrm{T}}^{\mathrm{miss}}$ [105–107]. Note that E_{T} triggers were used instead of p_{T} triggers in Ref. [107]. An additional high-threshold HLT H_{T} trigger, `HLT_ht1000_L1J100`, was included for comparisons. Although we do not

[7] In practice, a multi-jet L1 selection would likely be applied, but for the purpose of these studies the tight single-jet L1 selection serves to highlight the worst case acceptance for high-threshold triggers. A consideration of the efficiency turn-on curve would lead to a much lower analysis-level acceptance since `L1J100` becomes fully efficient for events where the leading jet has $p_{\mathrm{T}} > 200 - 220$ GeV and the `4j120` selection efficiency also needs to be considered (as a function of the fourth leading jet p_{T}).

[8] Keep in mind the caveats noted earlier about the choice of L1 trigger selection for use with the `4j120` selection in these studies.

consider HLT H_{T} selections in detail, the H_{T} for calibrated (HLT) jets describes the complete hadronic jet contribution to an event (like the L1 jet H_{T}) and should be considered in future studies for multi-jet signals.

5.5.3 Expected L1 seed rates

The rates of HLT and L1 triggers are constantly evaluated in ATLAS technical runs used to measure the performance (rate, resource usage, etc.) of different trigger chains. The rates for L1 seeds estimated recently using enhanced bias data during an official ATLAS technical run are summarised in Table 5.1.

Table 5.1: L1 trigger seed rates rounded to 2 decimal places from a recent technical run [Internal ATLAS technical run during May 2022]. The quoted rates are for unprescaled triggers.

Trigger	Rate (Hz)	Error (Hz)
`L1J100`	3616.64	24.14
`L14J15`	4157.69	37.35
`L14J15p0ETA25`	2961.47	22.02
`L1J45p0ETA21_3J15p0ETA25`	7561.38	64.38
`L1HT190-J15s5pETA21`	2205.39	18.79

Since existing triggers are severely rate-limited in data-taking conditions it is necessary to choose promising triggers that have a low rate or have a higher rate but are widely applicable for multiple analyses. If a trigger has a high (unaffordable but reasonable within the trigger menu) rate, then pre-selections (e.g. on calorimeter only information) may exist that reduce the rate to within an acceptable range to avoid significant CPU costs associated with charged particle tracking.

The asymmetric seed has the highest predicted rate of all the L1 seeds considered for the multi-jet TLA. Whereas the L1Topo H_{T} seed (`L1HT190-J15s5pETA21`) has the lowest rate. Also, note the reduction in rate for the `L14J15` trigger when a $|\eta|$ selection is applied to isolate the trigger to the region of the detector with charged particle tracking capabilities. The `L14J15` seed is more affordable than the asymmetric seed with an approximately 3 kHz lower rate. However, pre-selections can be explored to reduce the rate of the asymmetric (`L1J45p0ETA21_3J15p0ETA25`) seed, making it an affordable trigger choice. The asymmetric seed HLT pre-selections were not studied in this thesis but could be considered further for this signal topology in the future.

5.6 Signal acceptances for L1 seeds

Trigger selections were emulated for L1 seeds introduced in Section 5.5. The results of selections that existed in the Run 2 trigger menu (only a small sub-set of all triggers evaluated) were verified with independent results from the ATLAS Trigger Decision Tool implemented in `xAODAnaHelpers`, a Run 2 ATLAS analysis framework [108]. Percent-level agreement between these results was observed when all necessary default selections were imposed for L1 triggers. The HLT selections showed slightly more variation between the two methods likely because different jet collections were used for the emulation (e.g. topocluster jets versus `PFlow` jets). The signal acceptance fraction for L1 triggers was defined as the ratio of the number of events passing the L1 trigger to the total number of signal events for a given event sample. To correctly incorporate the event weights of the MC samples, the number of events in each case was calculated as a sum over the event weights.

To investigate the dependence of the signal acceptance on the L1 H_{T} trigger selections, the signal acceptance was plotted as a function of the H_{T} cut imposed by the trigger for several L1Topo jet selections. The results where the H_{T} was calculated from no more than 5 jets with low p_{T} thresholds and loose $|\eta|$ selections coinciding with the barrel/end-cap regions of ATLAS calorimeters are summarised in Figure 5.8 for all UDS decay mode mass points. A single plot for the $m_{\tilde{g}} = 100$ GeV UDB mass point is shown in Figure 5.7. Only the results derived from the MC16a event sample are included here.

For the 100 GeV gluino mass points in Figures 5.7 and 5.8a, the signal acceptances of L1 H_{T} seeds are small unless the H_{T} cut is quite low. This is a direct consequence of the shape of the L1 H_{T} distributions for these mass points, which are skewed to small values due to the lower p_{T} jets associated with the lowest signal masses. An appreciable increase in signal acceptance is seen for these triggers (with a $H_{\mathrm{T}} > 190$ GeV selection) at the 200 GeV gluino mass point in Figure 5.8b, where trigger acceptances increase to between 50% and 65% compared to 7% to 13% acceptances for the lowest mass point. Slightly smaller acceptances are seen for the individual UDB decay mode plot for the 100 GeV signal mass (Figure 5.7). This could be related to the higher mass b-quark produced in the decay and its effect on the kinematics of each jet produced by the quarks from the gluino decay. At gluino masses of 300 GeV and 400 GeV in Figures 5.8c and 5.8d, respectively, the triggers have above 85% signal acceptance with a $H_{\mathrm{T}} > 190$ GeV selection. One way to increase the acceptance of the low-mass gluino signals is to relax the thresholds on the H_{T} and jets used to calculate the H_{T}, leading to increased trigger rates and (likely) more background contamination. However, since there are significant limitations on trigger rates and CPU usage, lower rate triggers are preferred unless a dual-use scenario exists where a trigger is utilised for another analysis.

Alternative multi-jet trigger seed acceptances are shown alongside the H_{T} trigger acceptance curves in the Figures discussed above. All these multi-jet triggers, except

for the high threshold `L1J100` seed, achieve high signal acceptance. This is a result of their low p_{T} and jet multiplicity thresholds. The best performing trigger for all mass points in Figure 5.8 is the asymmetric seed, which achieves above 20% signal acceptance for the 100 GeV gluino mass and is close to fully efficient for the 400 GeV gluino mass. Since this trigger requires jets reconstructed within $|\eta| < 2.5$, the leading three jets passing the asymmetric seed (at the L1 trigger) would likely be reconstructed within the tracking acceptance of the detector at the HLT so various track-based pile-up mitigation procedures could be applied. The increased performance of `L1J45p0ETA21_3J15p0ETA25` relative to the 4-jet `L14J15` selection arises from the fact that L1 trigger selections are inclusive, so the asymmetric seed is actually a 3-jet selection, as mentioned in Section 5.5.1.

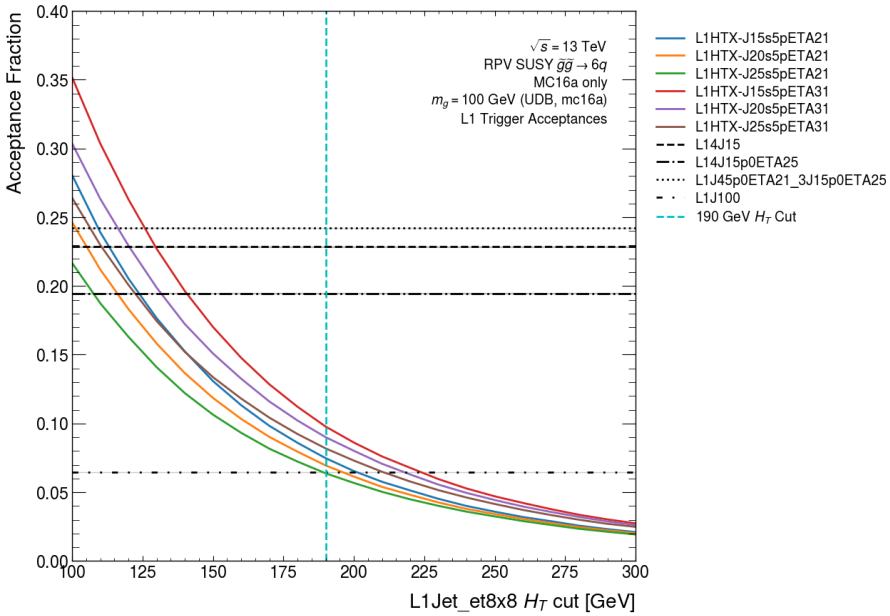

Figure 5.7: The acceptance of the UDB $m_{\tilde{g}} = 100$ GeV signal as a function of H_{T} for selected L1Topo H_{T} triggers. The vertical blue line indicates a 190 GeV H_{T} cut and horizontal lines indicate the acceptance of multi- and single-jet L1 seeds for comparison.

The requirements imposed on L1 jets for their contribution to the H_{T} calculation (e.g. `J15s5pETA21`) are constrained by the L1 trigger firmware. For instance, the Run 2 L1Topo system could only operate on 64 jets provided by L1Calo (the Level-1 calorimeter trigger), which was reduced to 6 or 10 jets after an initial sorting and selection step [102]. These limitations must be considered when choosing trigger signatures and algorithms, especially since it is not possible to change the L1Topo firmware while taking data [102]. Larger signal acceptances may be achieved by decreasing the E_{T} thresholds for jets used in the H_{T} calculation, but very low thresholds make the trigger more susceptible to low-E_{T} (and low-p_{T}) pile-up and background contamination. Similarly, loosening the $|\eta|$ selection will increase the signal acceptance for a fixed $H_{\mathrm{T}} > 190$ GeV selection. However, the increased pile-up

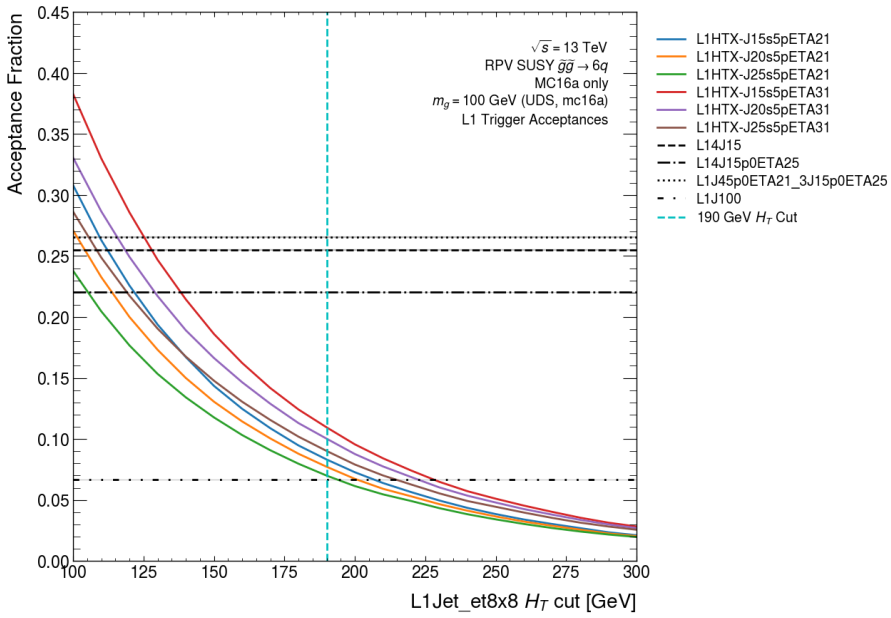

(a) $m_{\tilde{g}} = 100$ GeV

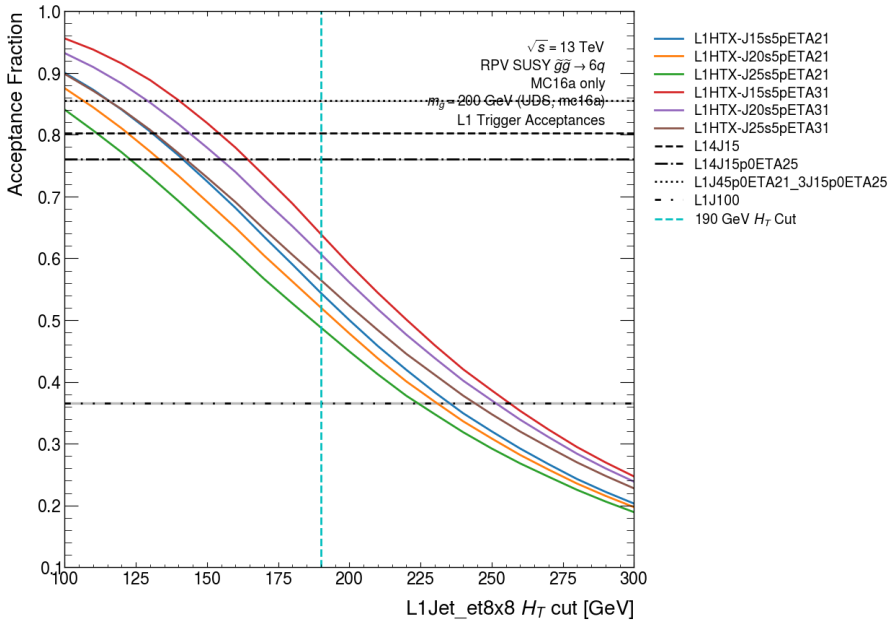

(b) $m_{\tilde{g}} = 200$ GeV

Figure 5.8: The acceptance of the UDS $\tilde{g}\tilde{g} \to 6q$ signals as a function of the H_{T} cut for selected L1Topo H_{T} triggers. The vertical blue line indicates a 190 GeV H_{T} cut and horizontal lines indicate the acceptance of multi- and single-jet L1 seeds for comparison.

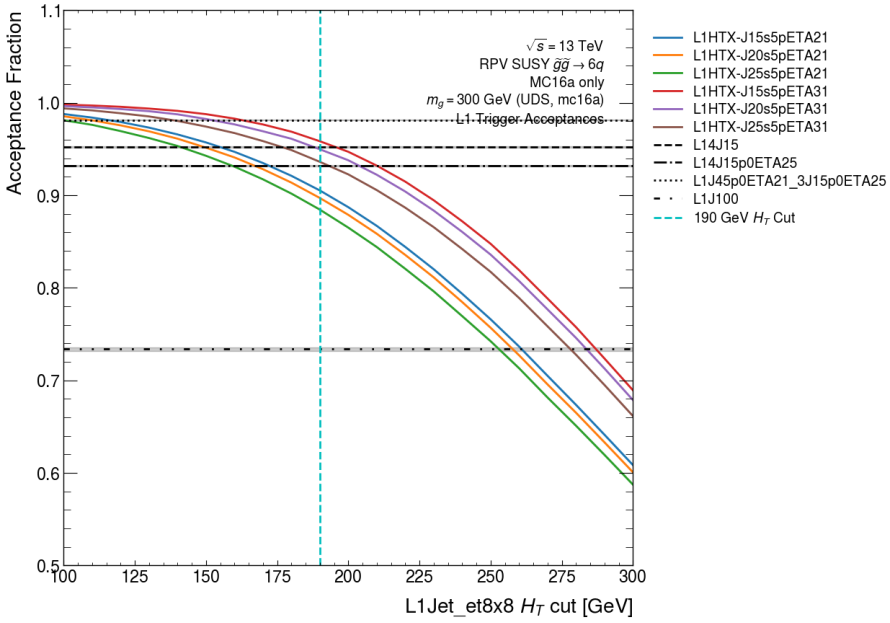

(c) $m_{\tilde{g}} = 300$ GeV

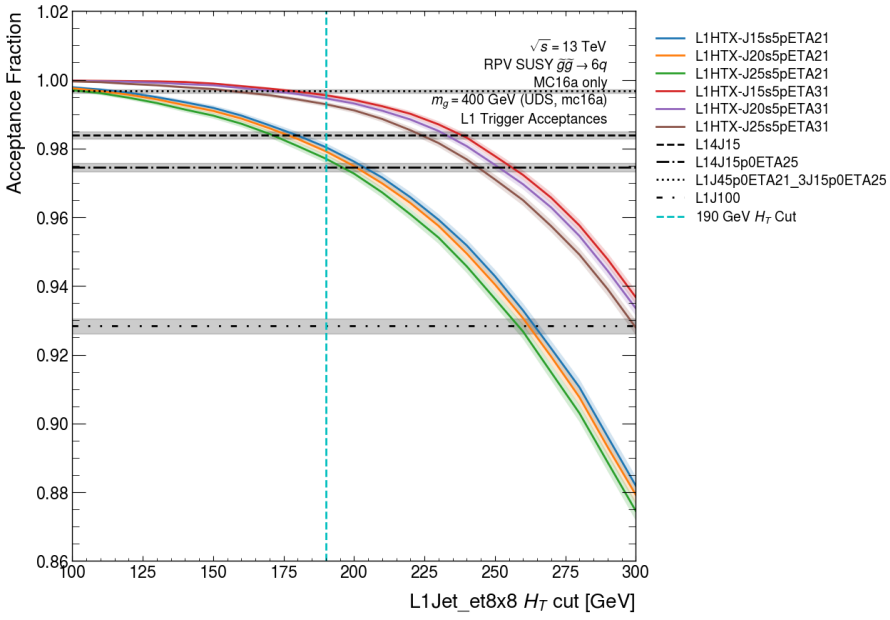

(d) $m_{\tilde{g}} = 400$ GeV

Figure 5.8 (cont.): The acceptance of the UDS $\tilde{g}\tilde{g} \to 6q$ signals as a function of the H_{T} cut for selected L1Topo H_{T} triggers. The vertical blue line indicates a 190 GeV H_{T} cut and horizontal lines indicate the acceptance of multi- and single-jet L1 seeds for comparison.

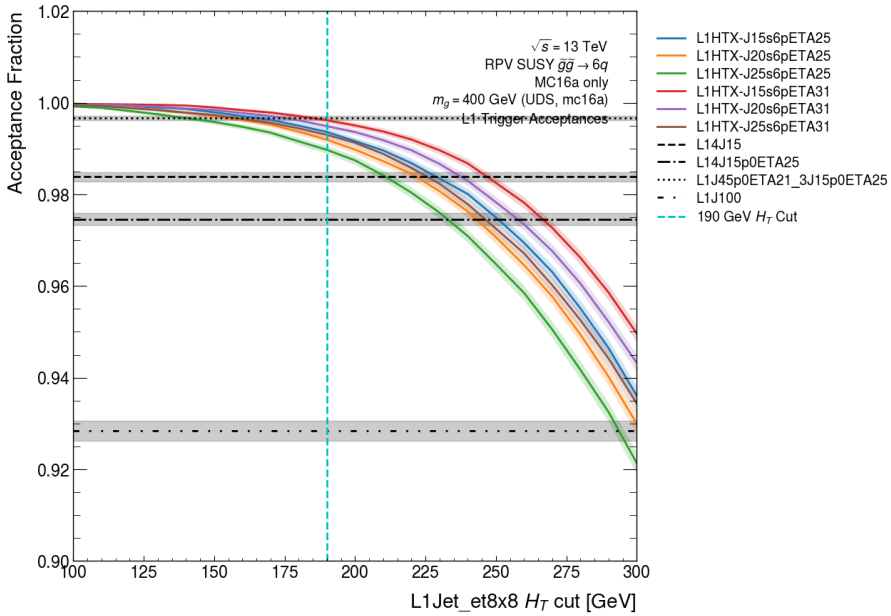

(a) Signal acceptances for the H_{T} calculated from six leading jets with looser $|\eta|$ thresholds ($|\eta| < 2.5$ in place of $|\eta| < 2.1$).

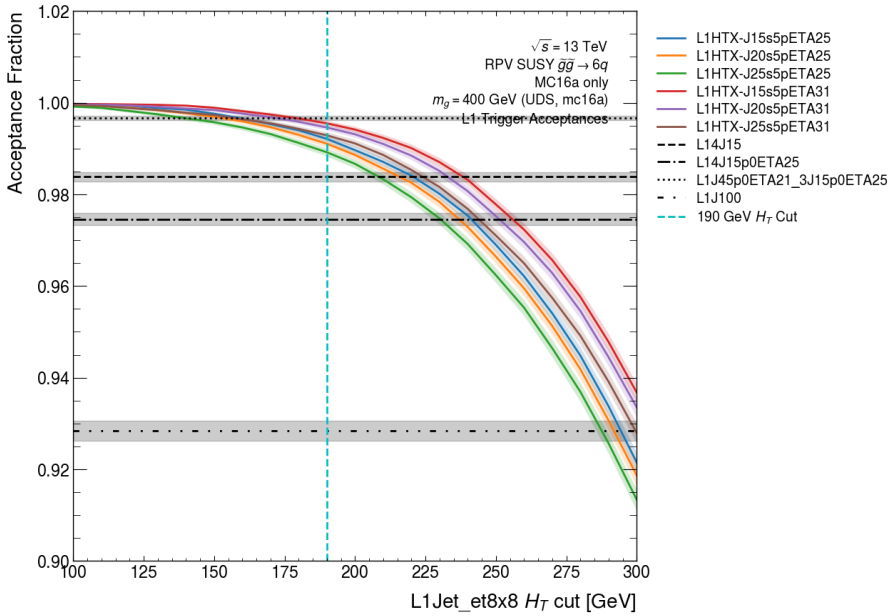

(b) Signal acceptances for the H_{T} calculated from five leading jets with looser $|\eta|$ thresholds ($|\eta| < 2.5$ in place of $|\eta| < 2.1$).

Figure 5.9: The acceptance of the UDS $m_{\tilde{g}} = 400$ GeV signal as a function of the H_{T} cut for selected L1Topo H_{T} triggers. The vertical blue line indicates a 190 GeV H_{T} cut and horizontal lines indicate the acceptance of multi- and single-jet L1 seeds for comparison. The selections shown in these plots involve looser (a, b) or tighter (c) thresholds on the selection used to identify jets for use in the H_{T} calculation.

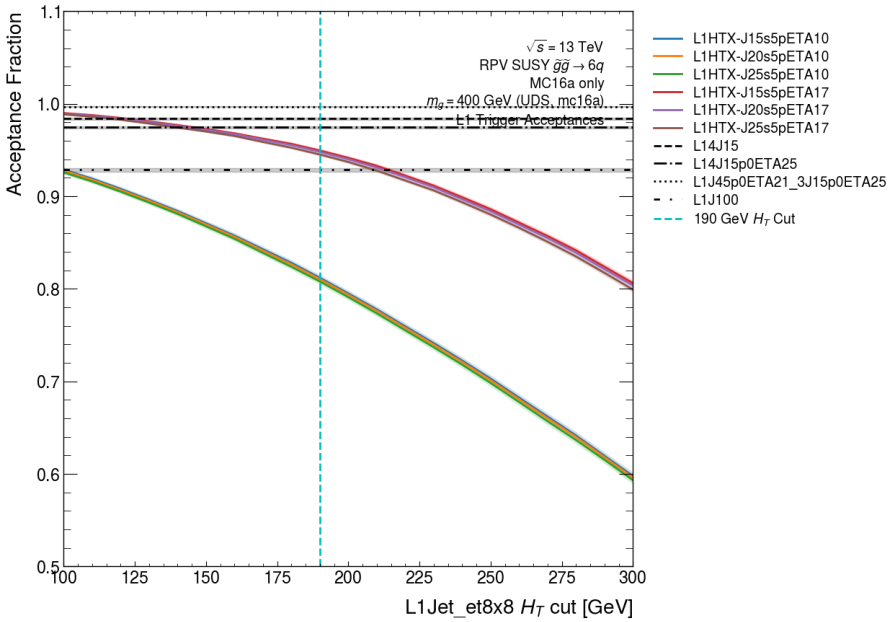

(c) Signal acceptances for the H_{T} calculated from five leading jets with tighter $|\eta|$ thresholds.

Figure 5.9 (cont.): The acceptance of the UDS $m_{\tilde{g}} = 400$ GeV signal as a function of the H_{T} cut for selected L1Topo H_{T} triggers. The vertical blue line indicates a 190 GeV H_{T} cut and horizontal lines indicate the acceptance of multi- and single-jet L1 seeds for comparison. The selections shown in these plots involve looser (a, b) or tighter (c) thresholds on the selection used to identify jets for use in the H_{T} calculation.

activity in the forward region (outside the tracking acceptance) could again saturate triggers with background events[9]. Thus, H_{T} calculations using L1 jets identified in the barrel/end-cap (i.e. not forward) region ($|\eta| < 2.1,\ 3.1$) are well motivated for triggering on central jets ($|\eta| < 2.5, 3.2$) at the HLT.

Nonetheless, the signal acceptance in Figure 5.9b and Figure 5.9a increases when 5- and 6-jet H_{T} calculations are used, respectively, and when looser $|\eta|$ selections ($|\eta| < 2.5$ instead of $|\eta| < 2.1$) are applied. Comparable signal acceptances are seen for both the 5- and 6-jet H_{T} calculations, but it is evident that the 6-jet H_{T} calculation produces higher H_{T} values and therefore a higher signal acceptance when the H_{T} selection is tightest. Tightening the $|\eta|$ selections with a 5-jet H_{T} calculation in Figure 5.9c causes the signal acceptance to fall significantly relative to looser selections as the H_{T} cut increased. These changes are expected as discussed above but are highlighted to illustrate the effects of modifications to the H_{T} distribution with different jet selections. The effects of different jet selections are discussed further in Section 5.7.

The numerical values of the signal acceptance using different trigger selections are shown in Tables 5.2 and 5.3 for the UDS and UDB signals, respectively. The `L1HT` seed included in these plots is that intended for use in Run 3, `L1HT190-J15s5pETA21`. While the `L1HT` trigger is not competitive with the low-threshold multi-jet triggers for the lowest (100 GeV) signal masses, it has high acceptance for higher mass signals and is overall a more flexible (and therefore useful!) alternative to the `L1J100` seed. As before, multi-jet triggers perform very well for both the UDS and UDB mass points relative to the `L1J100` and `L1HT` triggers. Thus, trigger chains with a low-threshold multi-jet selection or a H_{T} selection are most promising for the Run 3 multi-jet TLA. The tables for the trigger signal acceptance show an additional asymmetric threshold trigger, `L1J50_2J40p0ETA25_3J15p0ETA25`, that has similar thresholds to the `L1J45p0ETA21_3J15p0ETA25` trigger. The primary difference is that a higher-E_{T} jet ($E_{\mathrm{T}} > 50$ GeV) within $|\eta| < 3.1$ is required in addition to two jets with $E_{\mathrm{T}} > 40$ GeV within $|\eta| < 2.5$. This trigger also performs better than `L1J100` and `L1HT190-J15s5pETA21` for the lowest mass signals, which highlights the excellent performance of asymmetric triggers for certain multi-jet signatures. The `L1J50_2J40p0ETA25_3J15p0ETA25` was not studied further with additional HLT selections, only the `L1J45p0ETA21_3J15p0ETA25` trigger is included in further results throughout this Chapter.

When the trigger acceptances are evaluated for the combined MC16 sample, better performance for certain triggers (particularly multi-jet selections with low thresholds) is seen relative to the MC16a only sample in both Tables 5.2 and 5.3. The origin of this behaviour could be explained by the different pile-up conditions emulated by individual MC16 campaigns. For campaigns that simulate more significant levels

[9]Decreases in detector granularity in the forward region could also impact the resolution of signal-like jets reconstructed at large-η, but these jets would likely be rejected if tracking (within $|\eta| < 2.5$) is used.

of pile-up, a larger low-p_{T} hadronic jet contribution is expected, which leads to higher trigger acceptance values for lower mass signals (with lower p_{T} and E_{T} jets). Comparatively, the acceptance of higher mass signals, which contain higher p_{T} and E_{T} jets, will change little since many more events already pass trigger requirements.

The statistical uncertainty in all trigger acceptances (and the number of events passing triggers) was calculated assuming the trigger decision described a binomial variable. Thus, the uncertainty intervals in Tables 5.2 and 5.3 are quoted as 95% confidence intervals using quantiles of the F distribution [8]. The uncertainty calculation procedure is detailed in Appendix C and is used for all signal acceptance results in this Chapter. The use of a confidence interval occasionally results in different lower and upper values for the uncertainty relative to the central value after rounding the uncertainty estimates.

Table 5.2: L1 trigger acceptance fractions for UDS signal points with different event samples.

(a) MC16a event sample.

Trigger	$m_g = 100$ GeV	$m_g = 200$ GeV	$m_g = 300$ GeV	$m_g = 400$ GeV
L14J15	0.2552 ± 0.0001	0.8027 ± 0.0005	0.9521 ± 0.0008	0.9838 ± 0.001
L14J15p0ETA25	0.2205 ± 0.0001	0.7605 ± 0.0006	0.932 ± 0.001	0.9746 ± 0.001
L1J45p0ETA21_3J15p0ETA25	0.2657 ± 0.0001	0.8551 ± 0.0005	0.9812 ± 0.0005	0.9967 ± 0.0005
L1HT190-J15s5pETA21	0.0832 ± 0.0001	0.544 ± 0.0007	0.9052 ± 0.001	0.9804 ± 0.001
L1J50_2J40p0ETA25_3J15p0ETA25	0.1601 ± 0.0001	0.7233 ± 0.0006	$0.9597^{+0.0007}_{-0.0008}$	0.9933 ± 0.0007
L1J100	0.0668 ± 0.0001	0.3657 ± 0.0007	0.7336 ± 0.002	0.9284 ± 0.002

(b) Combined MC16 event sample.

Trigger	$m_g = 100$ GeV	$m_g = 200$ GeV	$m_g = 300$ GeV	$m_g = 400$ GeV
L14J15	0.2796 ± 0.0001	0.8161 ± 0.0003	0.9554 ± 0.0005	0.9851 ± 0.0006
L14J15p0ETA25	0.2404 ± 0.0001	0.7733 ± 0.0003	0.9361 ± 0.0005	0.9764 ± 0.0007
L1J45p0ETA21_3J15p0ETA25	0.2745 ± 0.0001	0.8585 ± 0.0003	0.9822 ± 0.0003	0.9967 ± 0.0003
L1HT190-J15s5pETA21	$0.084 \pm 4 \times 10^{-5}$	0.5504 ± 0.0004	0.9059 ± 0.0006	$0.9812^{+0.0006}_{-0.0007}$
L1J50_2J40p0ETA25_3J15p0ETA25	0.163 ± 0.0001	0.7293 ± 0.0004	0.9608 ± 0.0004	0.9936 ± 0.0004
L1J100	$0.0672 \pm 4 \times 10^{-5}$	0.3664 ± 0.0004	0.7339 ± 0.001	0.9277 ± 0.001

5.7 Kinematic shaping by L1 triggers

An additional consideration beyond the signal acceptance for L1 triggers is whether a given L1 trigger selection significantly shapes kinematic observables for jets in an event. Presumably, a trigger with high signal acceptance shapes distributions of jet p_{T} and η minimally as in Figure 5.4 for the leading offline jet p_{T}. We therefore expect more significant η and p_{T} shaping for triggers with tight selections on the jet kinematics. The shaping of the η and p_{T} distribution alters the 3-jet (triplet) invariant

Table 5.3: L1 trigger acceptance fractions for UDB signal points with different event samples.

(a) MC16a event sample.

Trigger	$m_g = 100$ GeV	$m_g = 200$ GeV	$m_g = 300$ GeV	$m_g = 400$ GeV
L14J15	0.2285 ± 0.0001	0.776 ± 0.0006	0.9441 ± 0.0009	0.9809 ± 0.001
L14J15p0ETA25	0.1947 ± 0.0001	0.7322 ± 0.0006	0.9223 ± 0.001	0.9718 ± 0.001
L1J45p0ETA21_3J15p0ETA25	0.2422 ± 0.0001	0.8332 ± 0.0005	0.9779 ± 0.0006	$0.996^{+0.0005}_{-0.0006}$
L1HT190-J15s5pETA21	0.0747 ± 0.0001	0.5127 ± 0.0007	0.8901 ± 0.001	0.9779 ± 0.001
L1J50_2J40p0ETA25_3J15p0ETA25	0.1431 ± 0.0001	0.6928 ± 0.0006	0.9503 ± 0.0008	$0.9919^{+0.0007}_{-0.0008}$
L1J100	0.0645 ± 0.0001	0.35 ± 0.0007	0.7127 ± 0.002	0.9177 ± 0.002

(b) Combined MC16 event sample.

Trigger	$m_g = 100$ GeV	$m_g = 200$ GeV	$m_g = 300$ GeV	$m_g = 400$ GeV
L14J15	0.2531 ± 0.0001	0.7904 ± 0.0003	0.9479 ± 0.0005	0.9824 ± 0.0006
L14J15p0ETA25	0.2162 ± 0.0001	0.7466 ± 0.0003	0.9271 ± 0.0006	0.973 ± 0.0008
L1J45p0ETA21_3J15p0ETA25	0.2527 ± 0.0001	0.8389 ± 0.0003	0.9786 ± 0.0003	0.9961 ± 0.0003
L1HT190-J15s5pETA21	$0.077 \pm 4 \times 10^{-5}$	0.5181 ± 0.0004	0.8908 ± 0.0007	0.9776 ± 0.0007
L1J50_2J40p0ETA25_3J15p0ETA25	0.1495 ± 0.0001	0.6994 ± 0.0004	0.9516 ± 0.0005	0.9922 ± 0.0004
L1J100	$0.0634 \pm 4 \times 10^{-5}$	0.3509 ± 0.0004	0.7134 ± 0.001	0.9165 ± 0.001

mass spectrum[10], and therefore affects the significance of any excess identified in a "bump hunt" analysis (e.g. Ref. [92]) including its ability to be identified against the background. The shaping of the following distributions was considered for these studies:

- Leading, sub-leading (second), and sixth-leading offline (calibrated) and L1 jet p_{T} (E_{T} for L1 jets),
- $|\eta|$ for the leading, sub-leading, and sixth-leading jets above.

The choice of these observables is linked to the 6-jet signal topology and their role in trigger selections. The same L1 trigger selections from Section 5.6 were applied, and various L1 H_{T} selections were tested. In these results, the L1 jet H_{T} calculation was limited to using no more than 5 jets with E_{T} thresholds of 15 GeV, 20 GeV, and 25 GeVand $|\eta|$ thresholds of 2.1 and 3.1. Also, only the effects of trigger selections on the UDS signal points were considered in detail. A comparison of the (offline/calibrated) jet p_{T} distributions for the UDS and UDB samples in Figure 5.10 illustrates that the UDB signal process leads to slightly lower p_{T} jets than for the UDS process. The separation is small, so we expect comparable results for the UDB signal points in this Section. Nonetheless, this explains the lower signal acceptances seen for UDB signals compared to UDS signals with the same trigger selections throughout this Chapter.

[10]This is most important for offline jets reconstructed with more granularity than L1 jets.

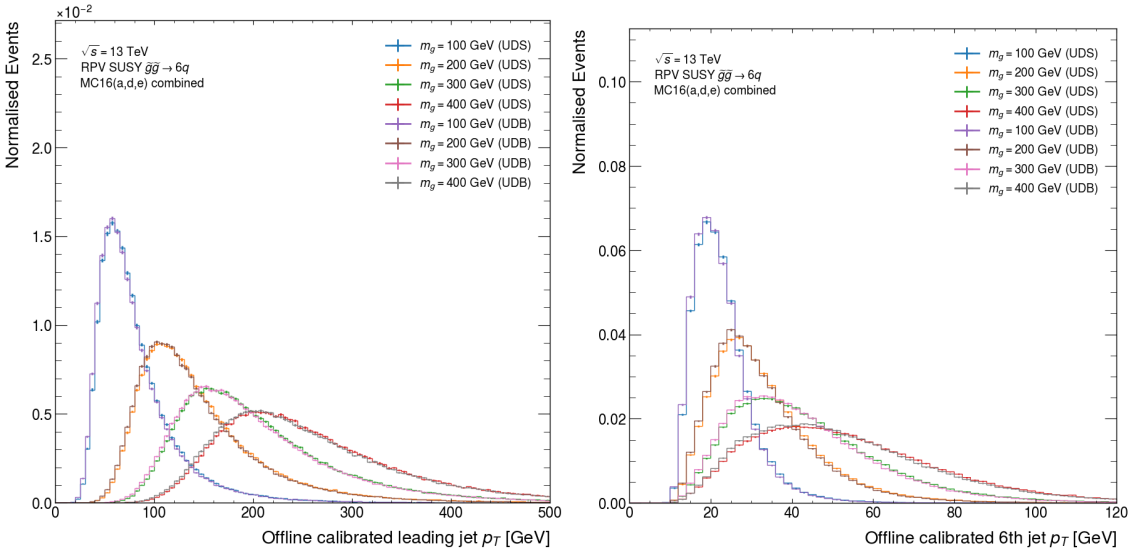

(a) Leading jet p_{T} comparison.

(b) Sixth jet p_{T} comparison.

Figure 5.10: Comparison of the calibrated offline jet p_{T} distributions for the UDS and UDB signal mass points. Slightly more separation is seen between UDS and UDB distributions for the sixth jet compared to the leading jet.

5.7.1 L1 jet p_{T}, H_{T}, and η shaping

L1 jet energy scales are far below that of calibrated offline jets as discussed in Section 4.6, which is evident in the L1 jet E_{T} (or offline jet p_{T}) and H_{T} distributions for all signal mass points. The 400 GeV signal mass point is shaped very little by all trigger selections – except for the `L1J100` trigger which selects events where the leading jet has $E_{\mathrm{T}} > 100$ GeV (provided it is also within $|\eta| < 3.1$). The most significant shaping is seen for the lower mass signals where the jet E_{T} is smaller – particularly the sub-leading jets for multi-jet triggers and where stringent selections are applied for the jets contributing to the H_{T} calculation.

Jet E_{T} spectra are shown in Figures 5.11 to 5.14 for the 100 GeV, 200 GeV, 300 GeV, and 400 GeV UDS signals, respectively. The effects of different trigger thresholds on the jet E_{T} distributions leads to a separation between low-threshold and high-threshold triggers. The `L1HT190-J15s5pETA21` selected leading jet E_{T} distribution clearly shows the benefit of event-level selections in comparison to the sharp edge at 100 GeV for the `L1J100` triggered leading jet. The other low-threshold multi-jet triggers display smaller degrees of shaping for the jet E_{T}. The asymmetric L1 trigger has a sharp edge at 45 GeV in the leading jet E_{T} distribution compared to the `L14J15` variations that have looser thresholds. Thus, even though the asymmetric threshold triggers have higher acceptance, the choice of their (higher first) thresholds leads to additional shaping compared to the other multi-jet selections. However, the threshold choice becomes a feasibility consideration at the point where the signal acceptance needs to be balanced with the total trigger rate as discussed throughout this Chapter. Similar results are seen for the second (sub-leading) and sixth jet: fewer

sharp edges (depending on jet multiplicity requirements for the trigger[11]) are seen for multi-jet triggers and the shape of the `L1J100` and `L1HT` selected distributions become more similar.

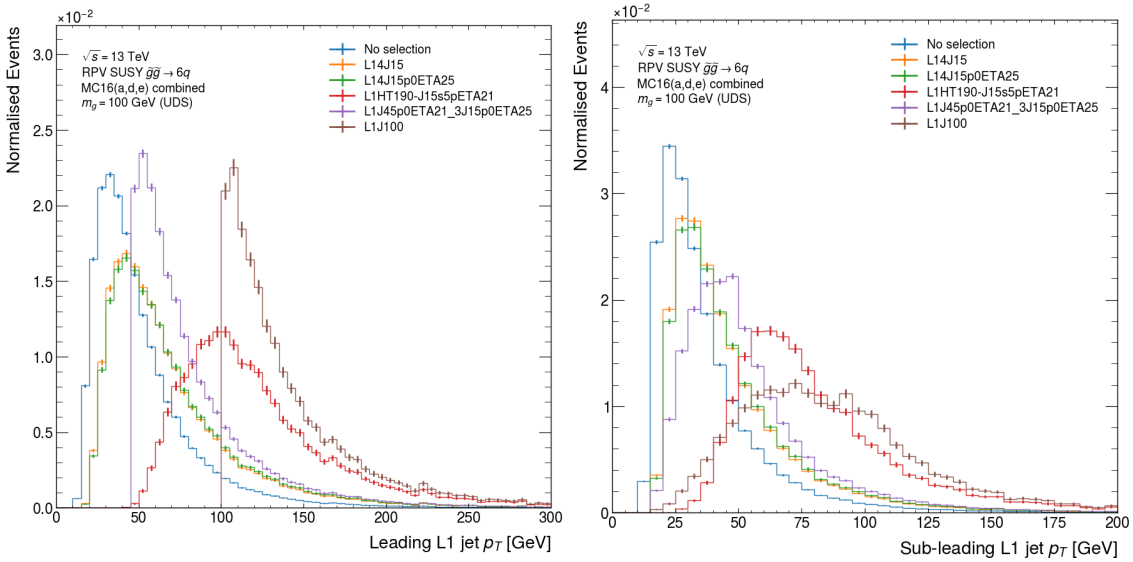

(a) Leading jet E_{T}

(b) Sub-leading (second) jet E_{T}

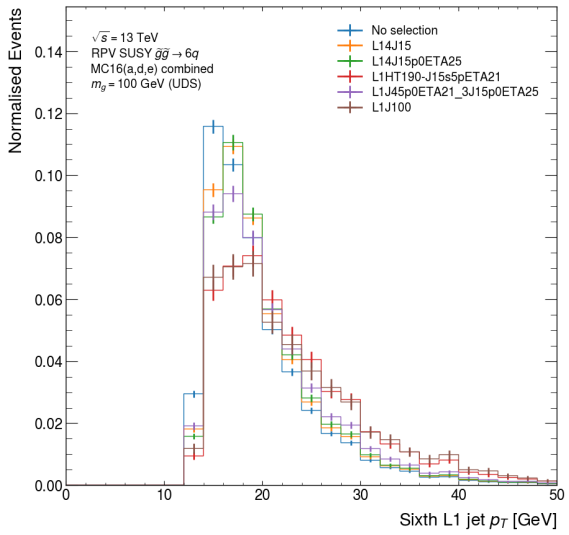

(c) Sixth jet E_{T}

Figure 5.11: L1 jet E_{T} (the axis labels are quoted as p_{T}, but actually display the E_{T}) and η distributions for the UDS $m_{\tilde{g}} = 100$ GeV combined MC16 event sample.

Jet η spectra are also shown in Figures 5.11 to 5.14 for the 100 GeV, 200 GeV, 300 GeV, and 400 GeV UDS signals, respectively. The η binning was chosen based on the granularity of L1Calo $\eta > 0$ trigger towers from Ref. [76]. A slightly different

[11]For example, if a trigger requires 4 jets with $E_{\mathrm{T}} > 15$ GeV then we would expect to see an approximate 15 GeV low-p_{T} edge in distributions up to and including the 4th leading jet (provided these jets pass the additional η selections).

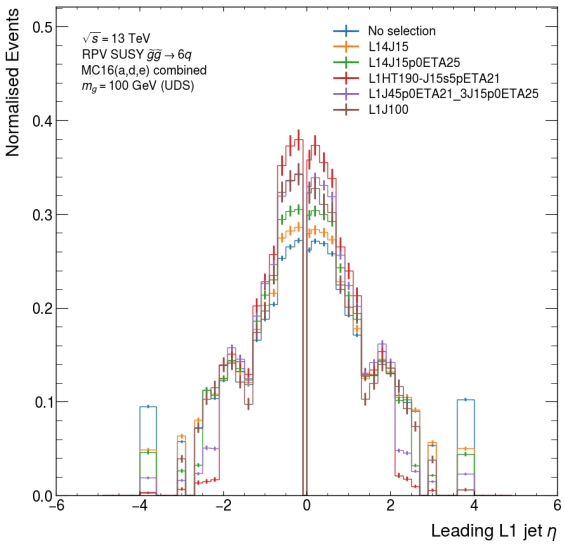

(d) Leading jet η

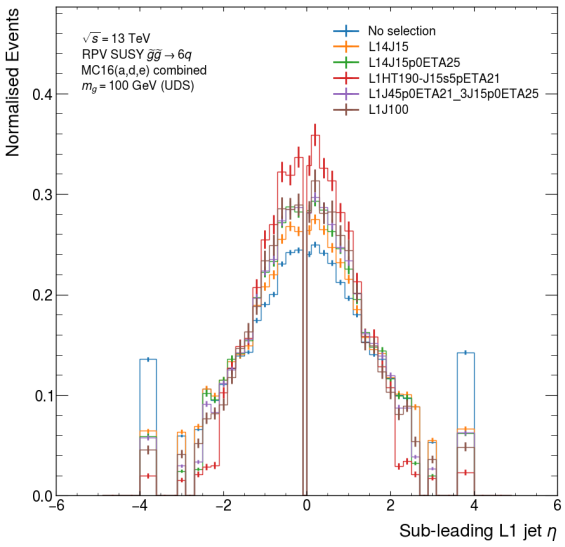

(e) Sub-leading (second) jet η

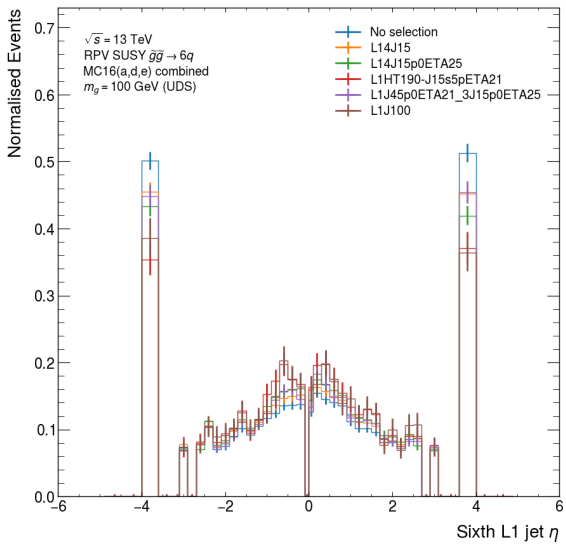

(f) Sixth jet η

Figure 5.11 (cont.): L1 jet E_{T} (the axis labels are quoted as p_{T}, but actually display the E_{T}) and η distributions for the UDS $m_{\tilde{g}} = 100$ GeV combined MC16 event sample.

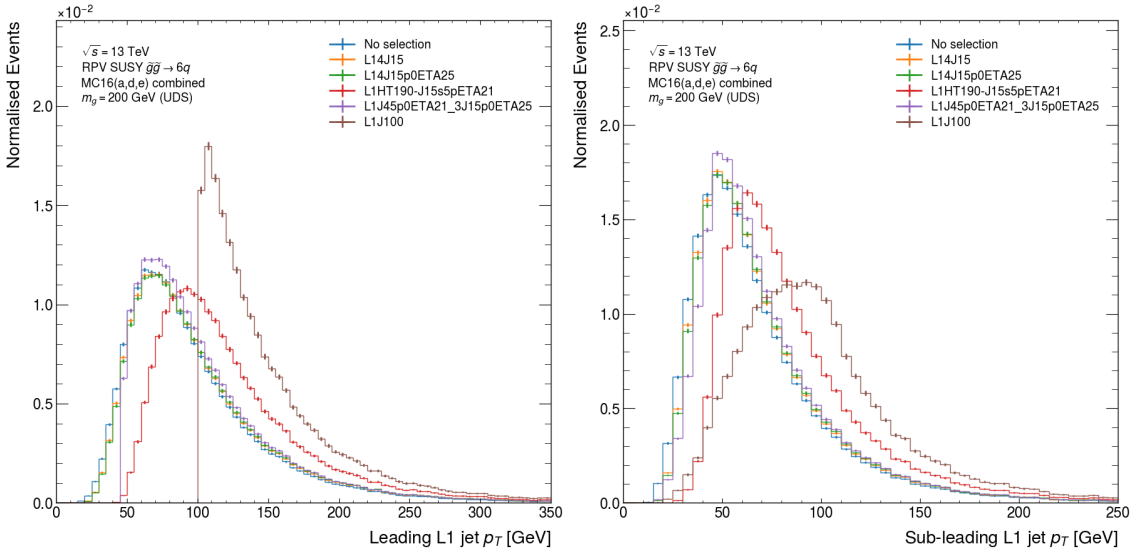

(a) Leading jet E_{T} (b) Sub-leading (second) jet E_{T}

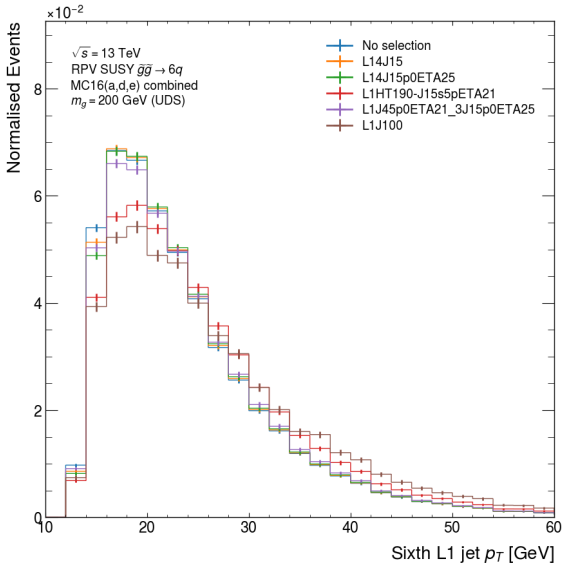

(c) Sixth jet E_{T}

Figure 5.12: L1 jet E_{T} (the axis labels are quoted as p_{T}, but actually display the E_{T}) and η distributions for the UDS $m_{\tilde{g}} = 200$ GeV combined MC16 event sample.

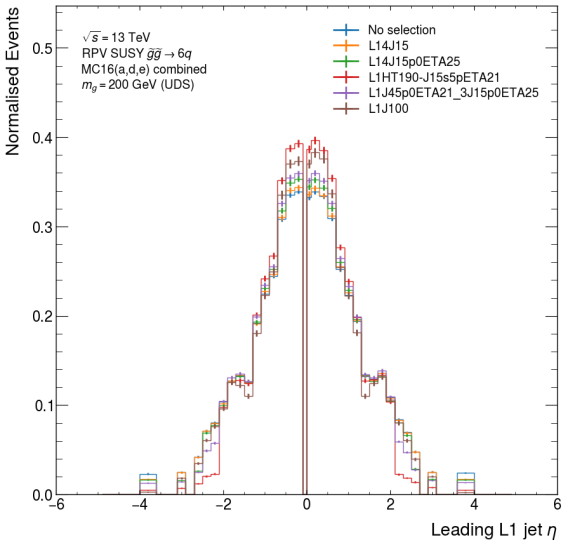

(d) Leading jet η

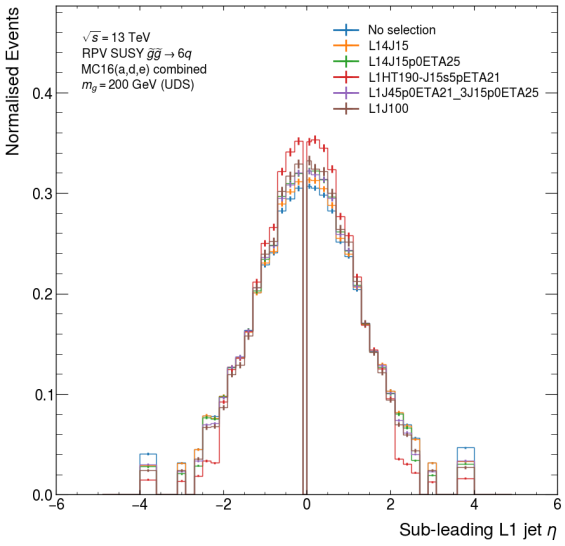

(e) Sub-leading (second) jet η

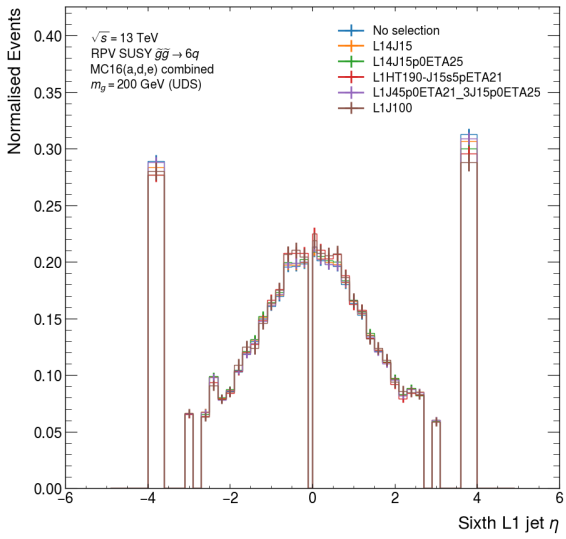

(f) Sixth jet η

Figure 5.12 (cont.): L1 jet E_{T} (the axis labels are quoted as p_{T}, but actually display the E_{T}) and η distributions for the UDS $m_{\tilde{g}} = 200$ GeV combined MC16 event sample.

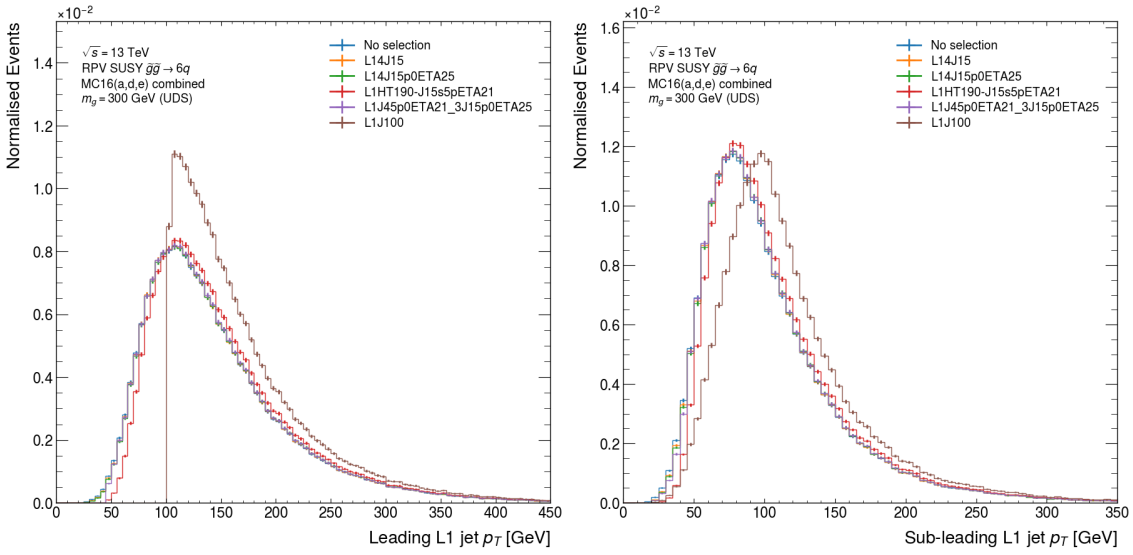

(a) Leading jet E_{T} (b) Sub-leading (second) jet E_{T}

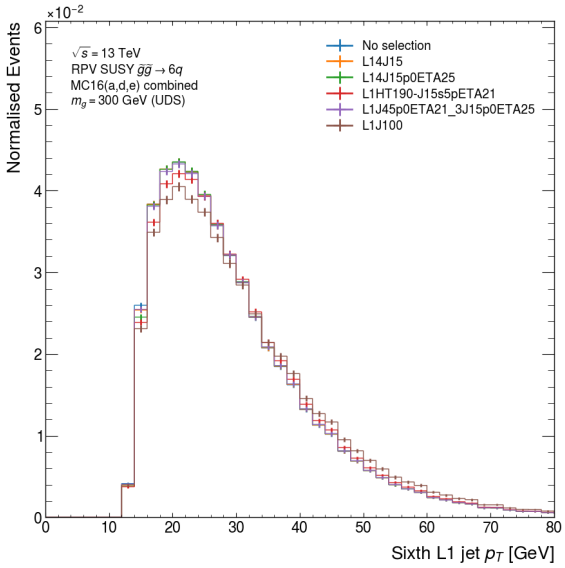

(c) Sixth jet E_{T}

Figure 5.13: L1 jet E_{T} (the axis labels are quoted as p_{T}, but actually display the E_{T}) and η distributions for the UDS $m_{\tilde{g}} = 300$ GeV combined MC16 event sample.

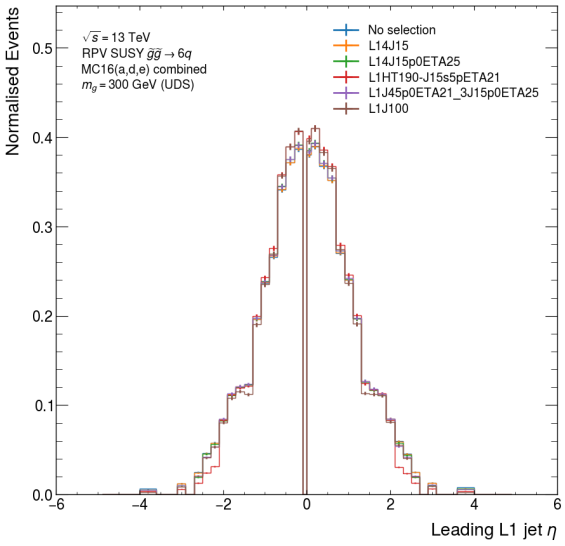

(d) Leading jet η

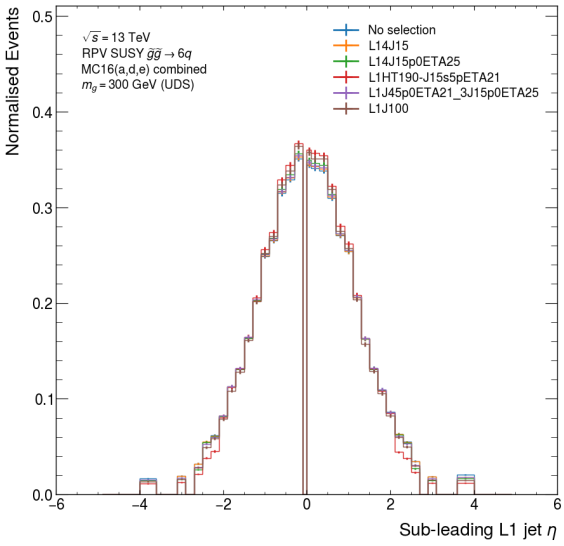

(e) Sub-leading (second) jet η

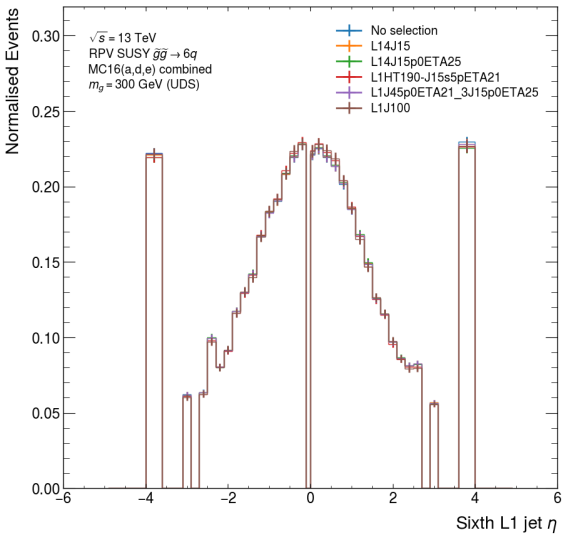

(f) Sixth jet η

Figure 5.13 (cont.): L1 jet E_{T} (the axis labels are quoted as p_{T}, but actually display the E_{T}) and η distributions for the UDS $m_{\tilde{g}} = 300$ GeV combined MC16 event sample.

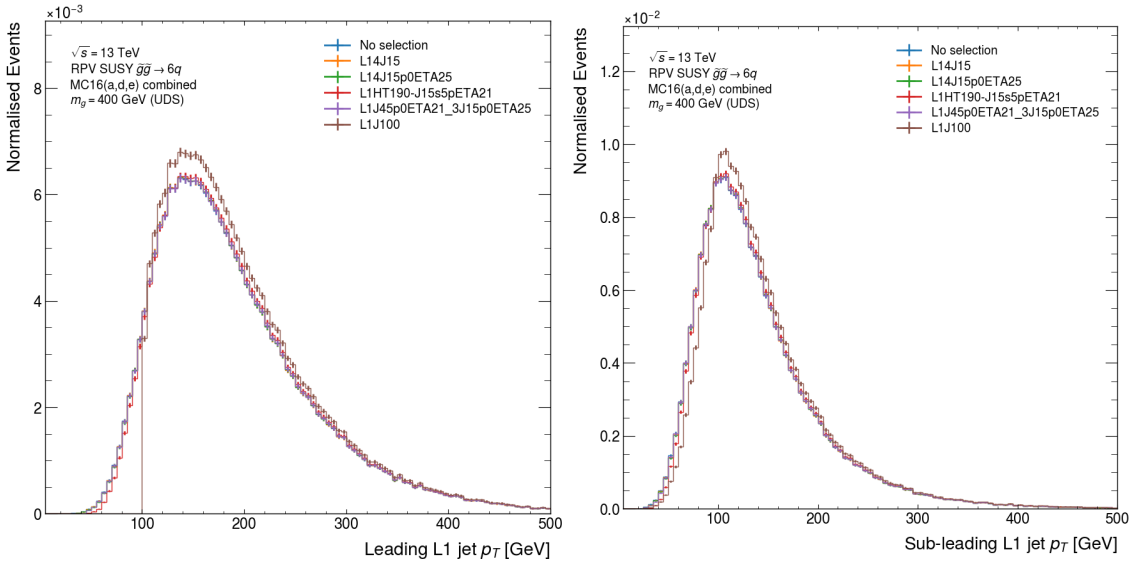

(a) Leading jet E_{T}

(b) Sub-leading (second) jet E_{T}

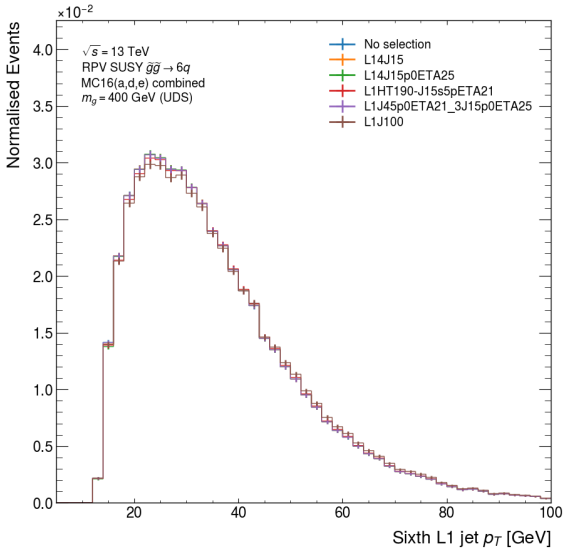

(c) Sixth jet E_{T}

Figure 5.14: L1 jet E_{T} (the axis labels are quoted as p_{T}, but actually display the E_{T}) and η distributions for the UDS $m_{\tilde{g}} = 400$ GeV combined MC16 event sample.

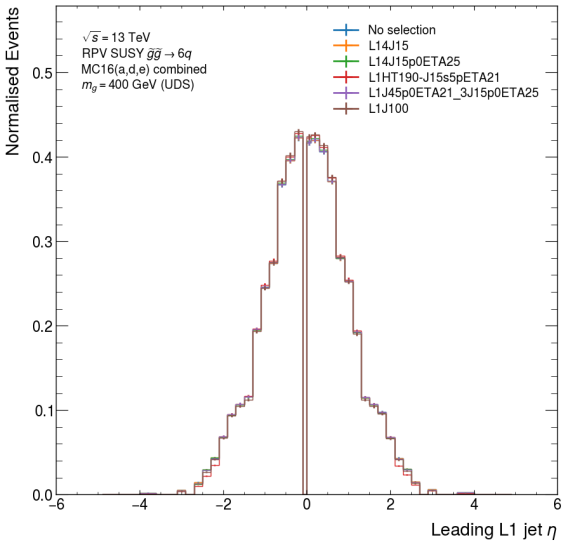

(d) Leading jet η

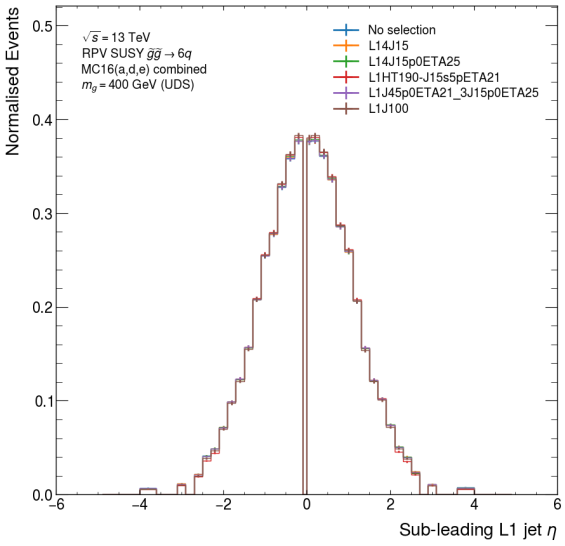

(e) Sub-leading (second) jet η

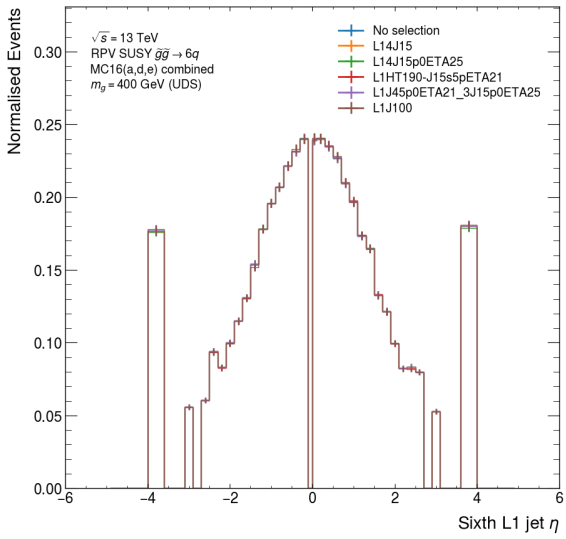

(f) Sixth jet η

Figure 5.14 (cont.): L1 jet E_{T} (the axis labels are quoted as p_{T}, but actually display the E_{T}) and η distributions for the UDS $m_{\tilde{g}} = 400$ GeV combined MC16 event sample.

normalisation procedure was used for the histograms to consider the bin widths in density calculations when an irregular binning is used. The offline jet η distributions presented later also use this normalisation scheme but have regular bin widths. The η distributions for L1 jets show features characteristic of transitions between different regions of the detector – notably the empty bin close to $\eta = 0$ where there is a break between the two halves of the detector. The η shaping is, however, not as extensive as the E_{T} shaping. Nonetheless, triggers with more stringent (central) η selections (e.g. `L1HT190-J15s5pETA21`) have more central η distributions.

Different variations of the jet selection used for the L1 H_{T} calculation lead to different H_{T} distribution shapes in Figure 5.20. When these different `L1HT` signatures are compared at a fixed 190 GeV H_{T} cut, the distributions of the jet E_{T} and η are shaped most when H_{T} calculations have tight jet E_{T} and η selections, as expected. As shown in Figures 5.15 to 5.17 and 5.19 for the different gluino signal masses, tighter E_{T} selections shift the E_{T} distributions of (H_{T} triggered) L1 jets to higher values. Similarly, tightening the η selection on the jets used for the H_{T} calculation leads to jet η distributions that are more central (smaller η).

Figures 5.21 to 5.24 illustrate the effect of different H_{T} cuts on the L1 jet E_{T} and η with a single `J15s5pETA21` jet selection. More stringent selections cause the E_{T} distributions to migrate to higher E_{T}, which is typical of all results in this Section. Interestingly, the more stringent H_{T} selections also shape the η distributions more than their looser counterparts – albeit in many bins the differences are within the range of statistical uncertainties. That is, the H_{T} selection *implicitly* requires central jets with the `J15s5pETA21` jet selection – higher values of H_{T} result from the contribution of 5 leading high-E_{T} *and* central ($|\eta| < 2.1$) jets.

One notable feature in the L1 jet η distributions (Figures 5.11 to 5.14) that is not prevalent in the distributions for offline jets (Figures 5.26 to 5.28) is an abundance of forward low-E_{T} jets (large $|\eta|$) and apparent "missing" bins. This could be a consequence of the L1 jet reconstruction algorithms and the granularity of the calorimeter towers used to identify L1 jets. A significant population of low-E_{T} jets (e.g. the sixth-leading jet) in the forward region could also be associated with pile-up radiation since the calorimeter occupancy increases at large $|\eta|$. For these studies and their translation into future analyses, only central jets within the tracking acceptance are important and the large-$|\eta|$ jets would be rejected. Since the η distribution in the central $|\eta| < 2.5$ region is continuous (after re-binning[12]), the forward jet features are not considered further.

[12] Without re-binning, 0.1 width bins in the central $|\eta| < 2.5$ region lead to additional "missing" bins, potentially explained by the granularity of L1 jets and their discreteness after reconstruction from fixed-size calorimeter towers.

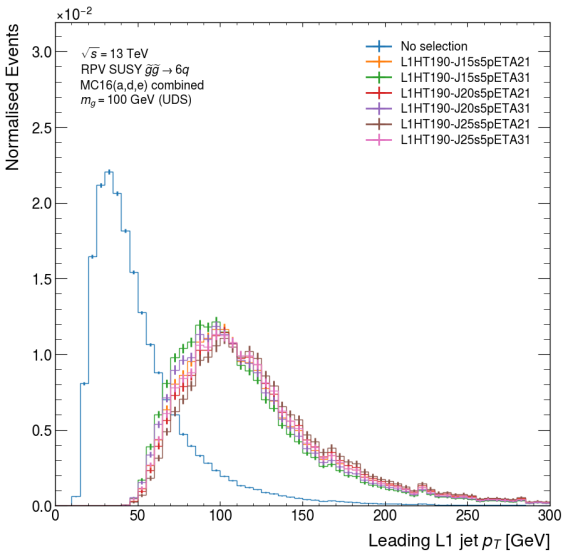

(a) Leading jet E_{T}

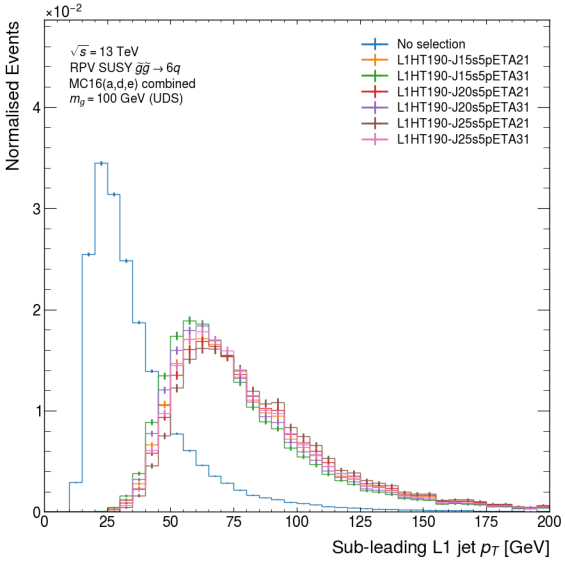

(b) Sub-leading (second) jet E_{T}

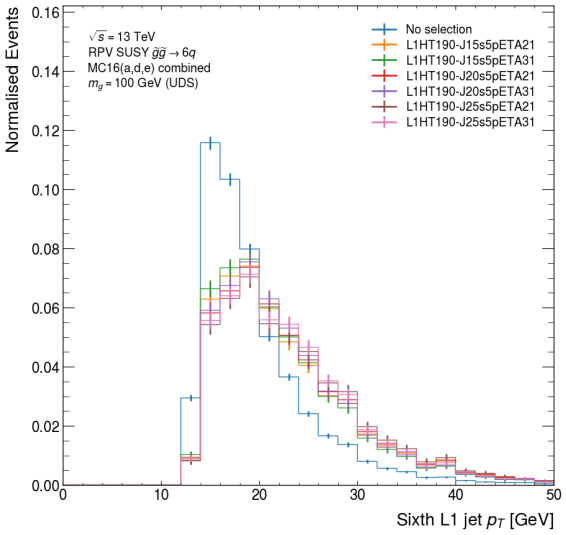

(c) Sixth jet E_{T}

Figure 5.15: L1 jet E_{T} (the axis labels are quoted as p_{T}, but actually display the E_{T}) and η distributions for the UDS $m_{\tilde{g}} = 100$ GeV combined MC16 event sample after a $H_{\mathrm{T}} > 190$ GeV selection when different jet selections are used for the H_{T} calculation.

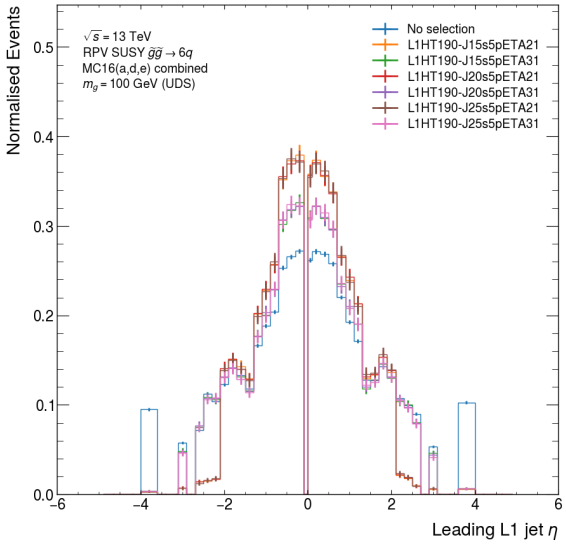

(d) Leading jet η

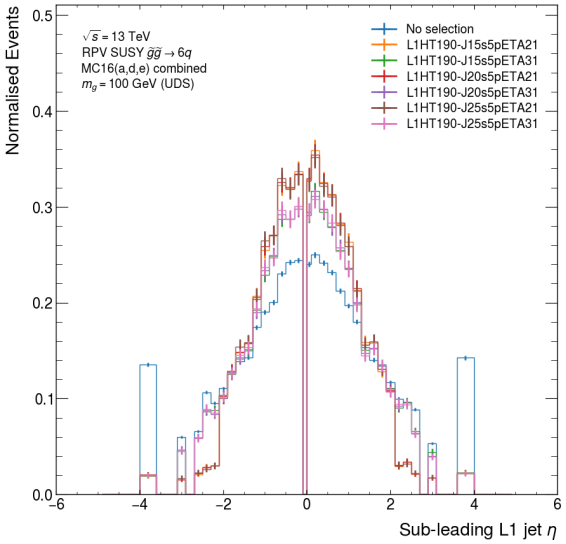

(e) Sub-leading (second) jet η

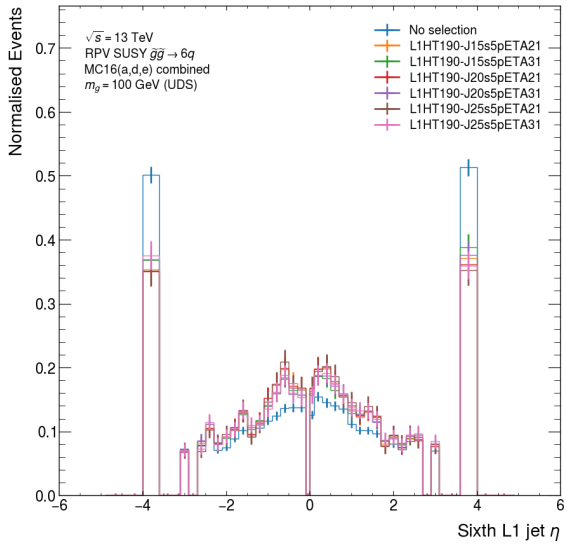

(f) Sixth jet η

Figure 5.15 (cont.): L1 jet E_{T} (the axis labels are quoted as p_{T}, but actually display the E_{T}) and η distributions for the UDS $m_{\tilde{g}} = 100$ GeV combined MC16 event sample after a $H_{\mathrm{T}} > 190$ GeV selection when different jet selections are used for the H_{T} calculation.

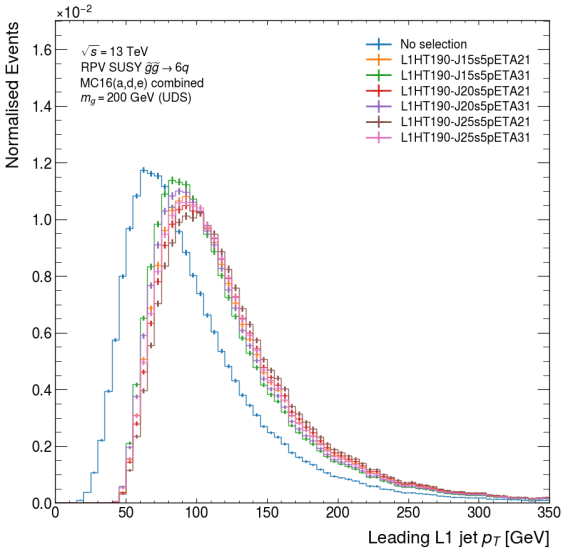

(a) Leading jet E_{T}

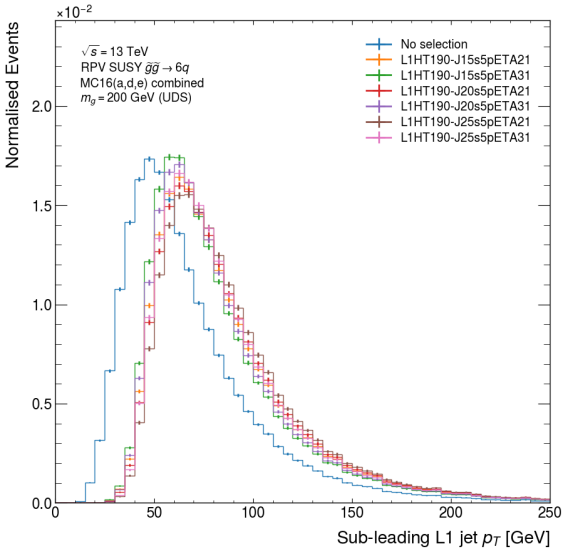

(b) Sub-leading (second) jet E_{T}

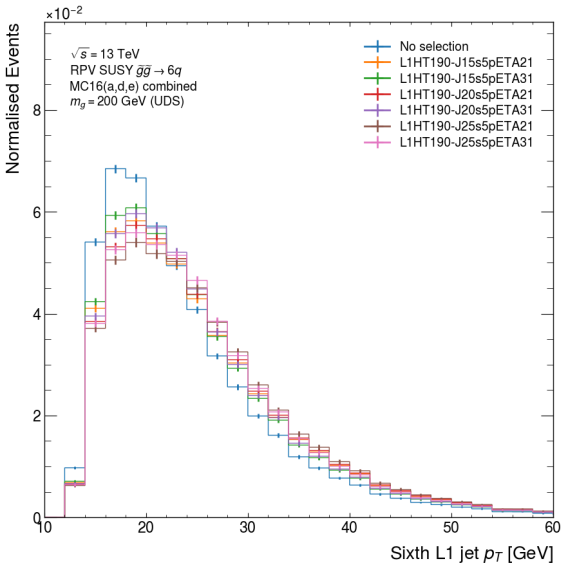

(c) Sixth jet E_{T}

Figure 5.16: L1 jet E_{T} (the axis labels are quoted as p_{T}, but actually display the E_{T}) and η distributions for the UDS $m_{\tilde{g}} = 200$ GeV combined MC16 event sample after a $H_{\mathrm{T}} > 190$ GeV selection when different jet selections are used for the H_{T} calculation.

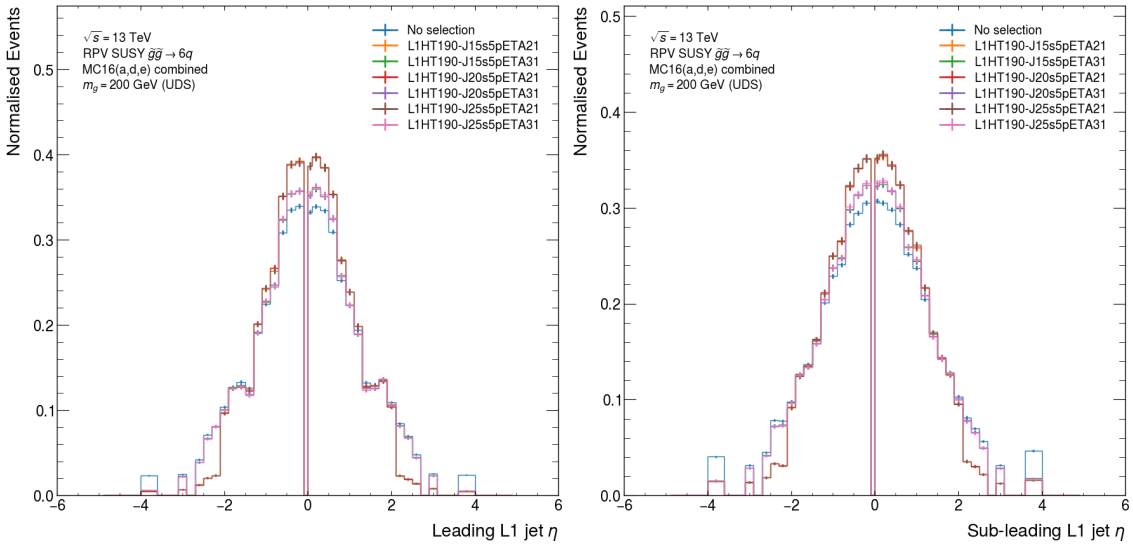

(d) Leading jet η (e) Sub-leading (second) jet η

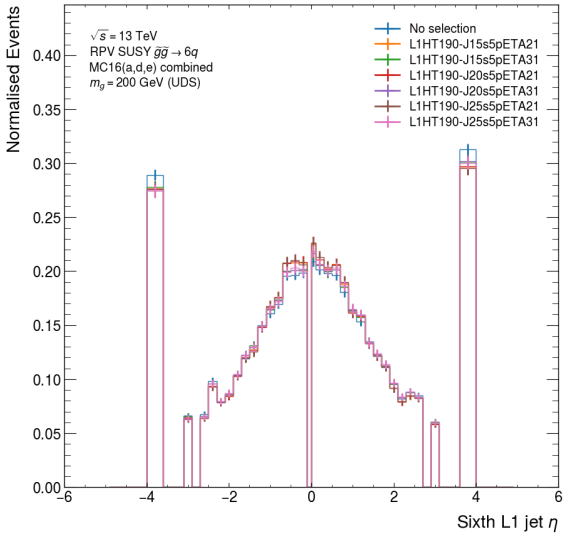

(f) Sixth jet η

Figure 5.16 (cont.): L1 jet E_{T} (the axis labels are quoted as p_{T}, but actually display the E_{T}) and η distributions for the UDS $m_{\tilde{g}} = 200$ GeV combined MC16 event sample after a $H_{\mathrm{T}} > 190$ GeV selection when different jet selections are used for the H_{T} calculation.

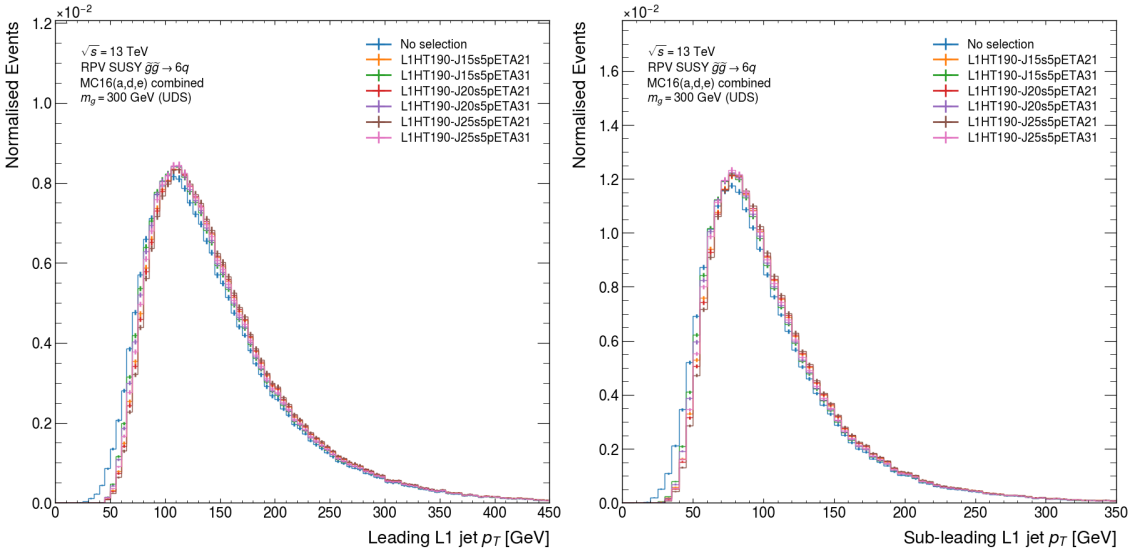

(a) Leading jet E_{T}

(b) Sub-leading (second) jet E_{T}

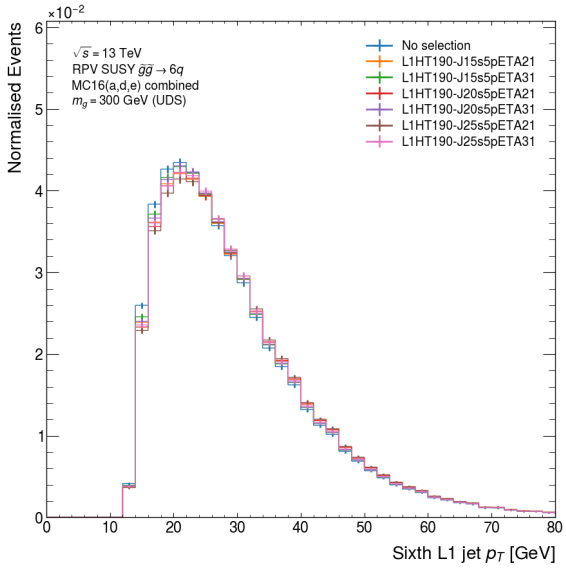

(c) Sixth jet E_{T}

Figure 5.17: L1 jet E_{T} (the axis labels are quoted as p_{T}, but actually display the E_{T}) and η distributions for the UDS $m_{\tilde{g}} = 300$ GeV combined MC16 event sample after a $H_{\mathrm{T}} > 190$ GeV selection when different jet selections are used for the H_{T} calculation.

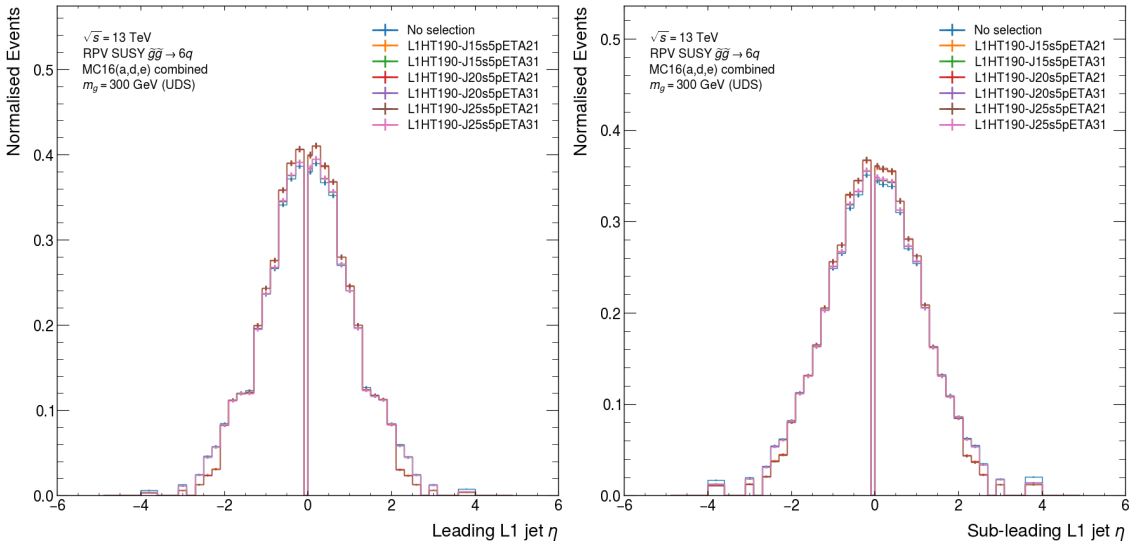

(a) Leading jet η (b) Sub-leading (second) jet η

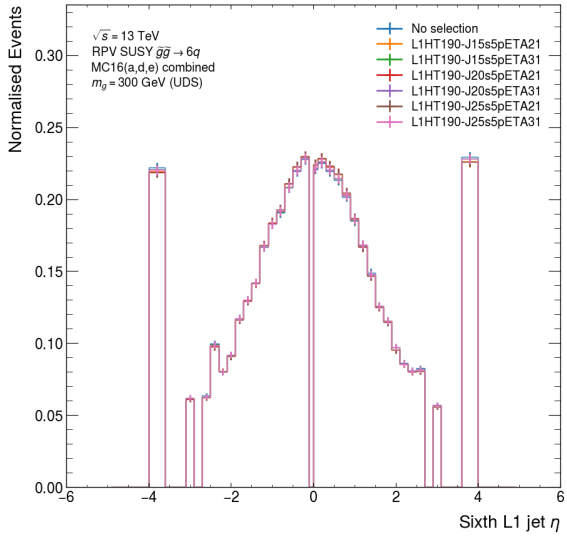

(c) Sixth jet η

Figure 5.18: L1 jet E_{T} (the axis labels are quoted as p_{T}, but actually display the E_{T}) and η distributions for the UDS $m_{\tilde{g}} = 300$ GeV combined MC16 event sample after a $H_{\mathrm{T}} > 190$ GeV selection when different jet selections are used for the H_{T} calculation.

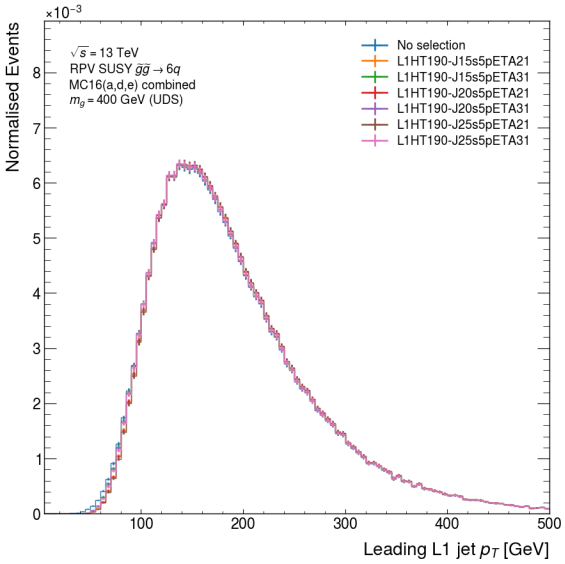

(a) Leading jet E_{T}

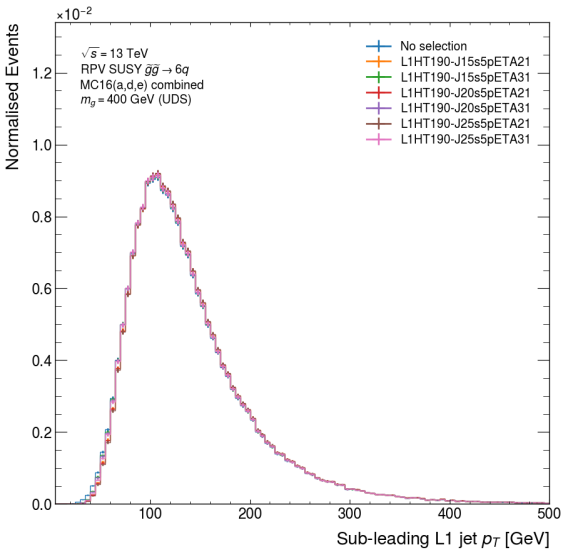

(b) Sub-leading (second) jet E_{T}

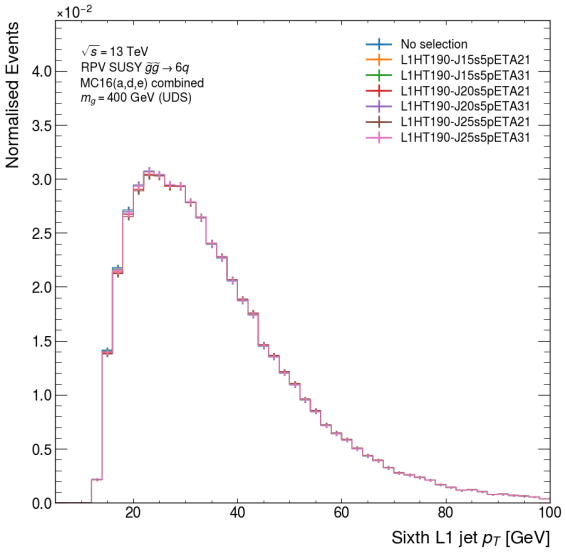

(c) Sixth jet E_{T}

Figure 5.19: L1 jet E_{T} (the axis labels are quoted as p_{T}, but actually display the E_{T}) and η distributions for the UDS $m_{\tilde{g}} = 400$ GeV combined MC16 event sample after a $H_{\mathrm{T}} > 190$ GeV selection when different jet selections are used for the H_{T} calculation.

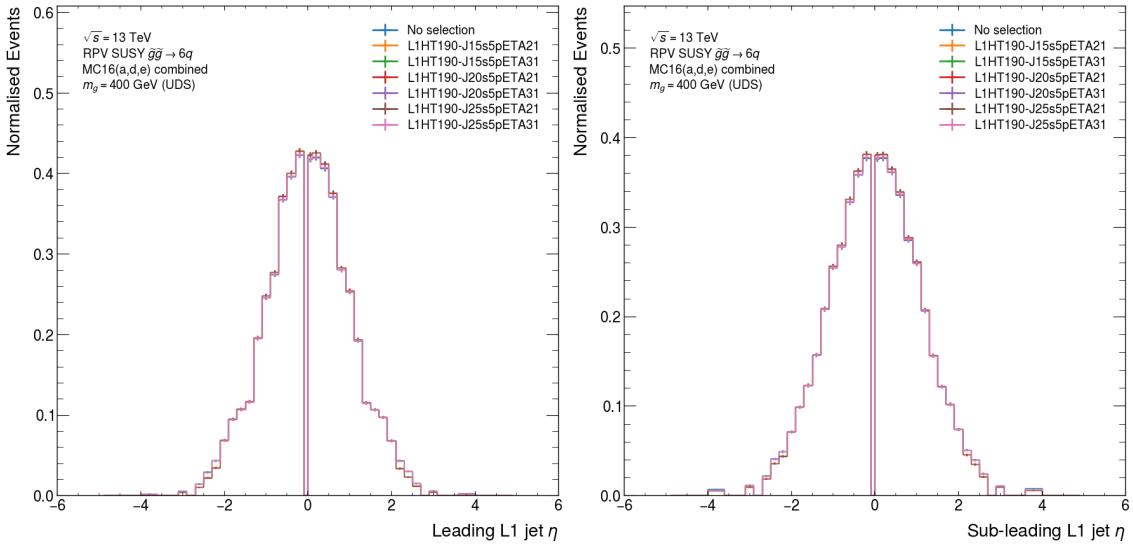

(d) Leading jet η (e) Sub-leading (second) jet η

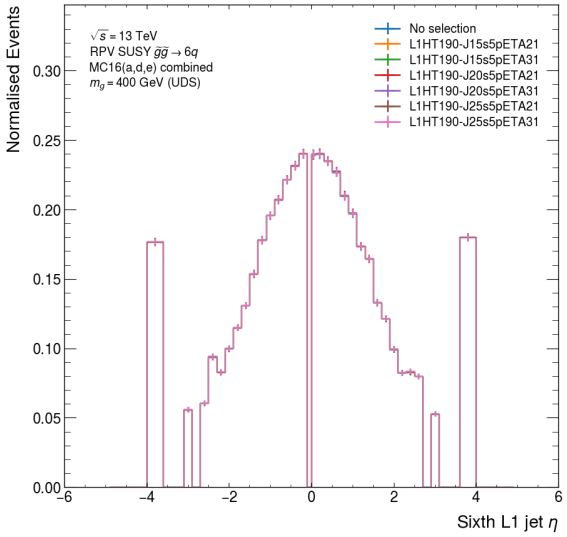

(f) Sixth jet η

Figure 5.19 (cont.): L1 jet E_{T} (the axis labels are quoted as p_{T}, but actually display the E_{T}) and η distributions for the UDS $m_{\tilde{g}} = 400$ GeV combined MC16 event sample after a $H_{\mathrm{T}} > 190$ GeV selection when different jet selections are used for the H_{T} calculation.

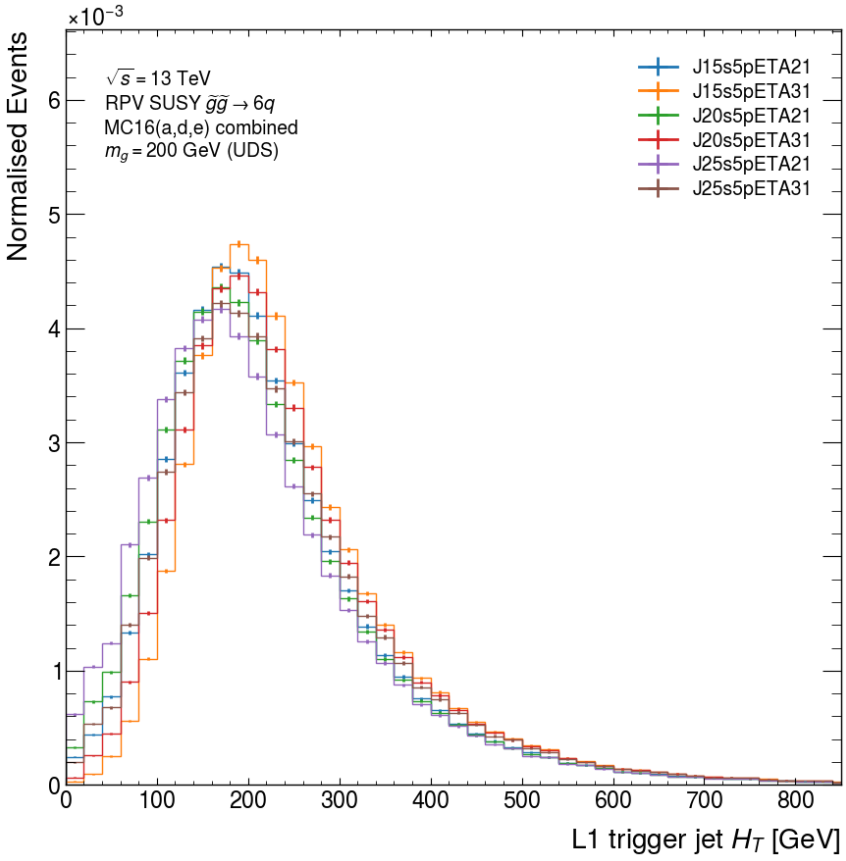

Figure 5.20: Comparisons of the L1 H_{T} distributions for the $m_{\tilde{g}} = 200$ GeV signal with different jet selections used in the H_{T} calculation. The most stringent jet selections result in distributions shifted to lower values of H_{T}, while, the looser jet selections produce distributions with larger values of H_{T}.

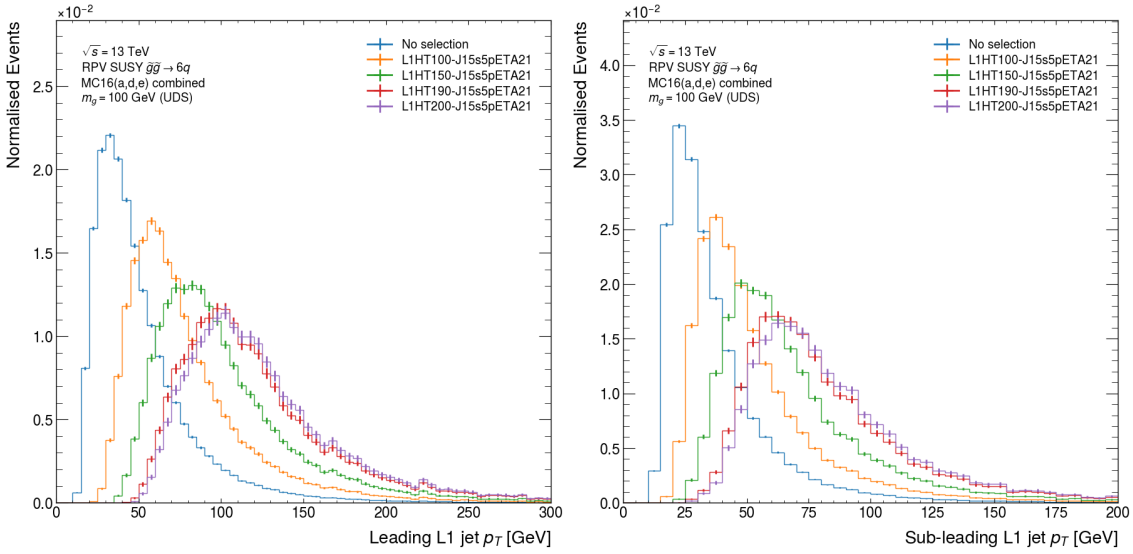

(a) Leading jet E_{T}

(b) Sub-leading (second) jet E_{T}

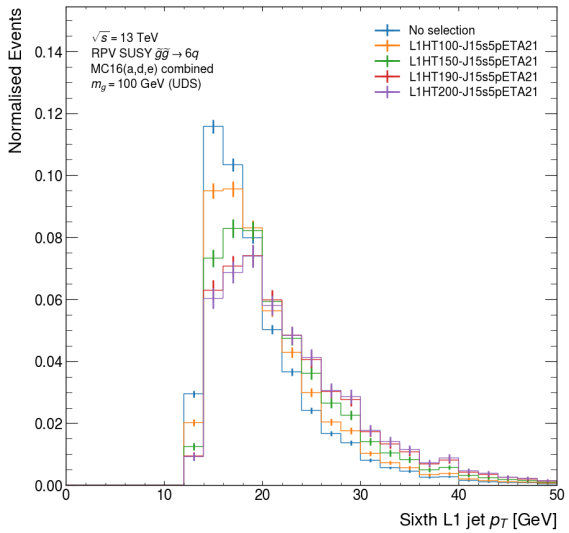

(c) Sixth jet E_{T}

Figure 5.21: L1 jet E_{T} (the axis labels are quoted as p_{T}, but actually display the E_{T}) and η distributions for the UDS $m_{\tilde{g}} = 100$ GeV combined MC16 event sample after various H_{T} selections for the `J15s5pETA21` jet selection.

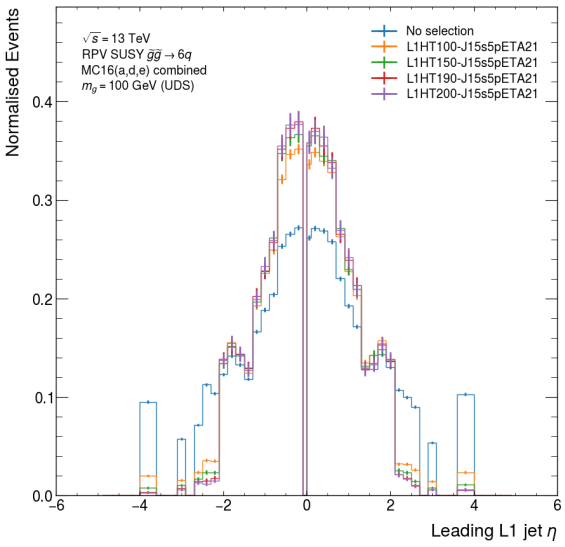

(d) Leading jet η

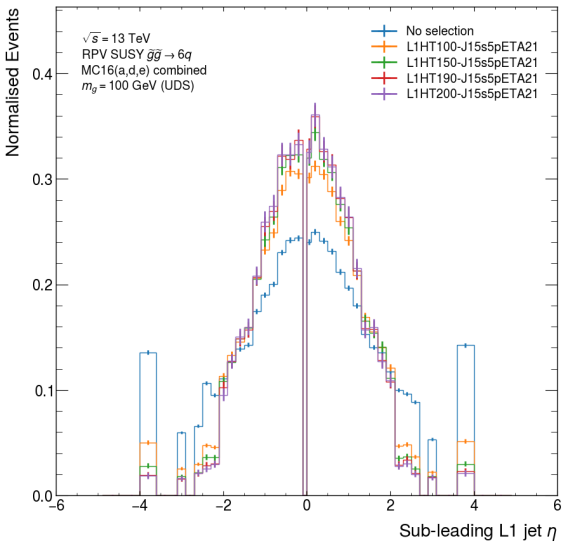

(e) Sub-leading (second) jet η

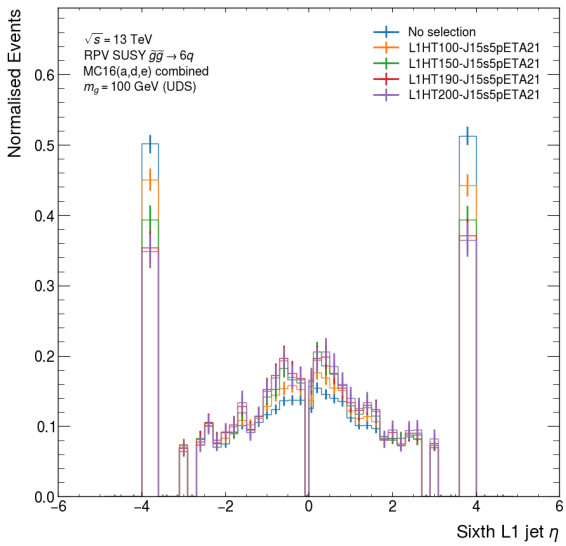

(f) Sixth jet η

Figure 5.21 (cont.): L1 jet E_{T} (the axis labels are quoted as p_{T}, but actually display the E_{T}) and η distributions for the UDS $m_{\tilde{g}} = 100$ GeV combined MC16 event sample after various H_{T} selections for the `J15s5pETA21` jet selection.

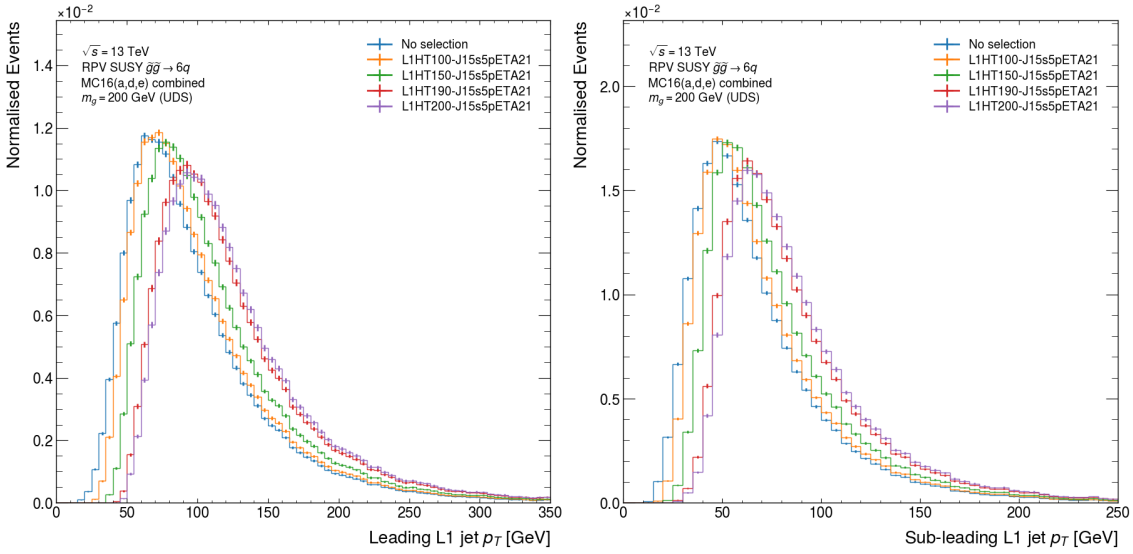

(a) Leading jet E_{T}

(b) Sub-leading (second) jet E_{T}

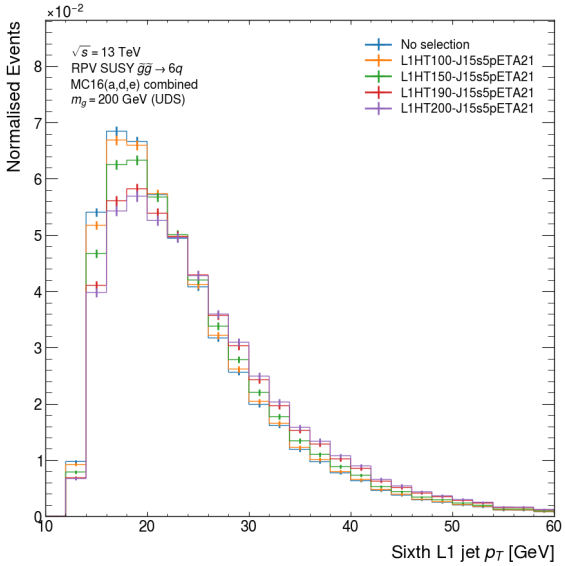

(c) Sixth jet E_{T}

Figure 5.22: L1 jet E_{T} (the axis labels are quoted as p_{T}, but actually display the E_{T}) and η distributions for the UDS $m_{\tilde{g}} = 200$ GeV combined MC16 event sample after various H_{T} selections for the `J15s5pETA21` jet selection.

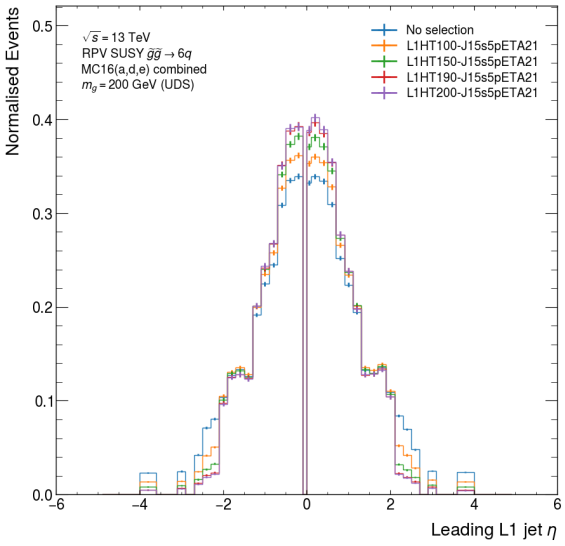

(d) Leading jet η

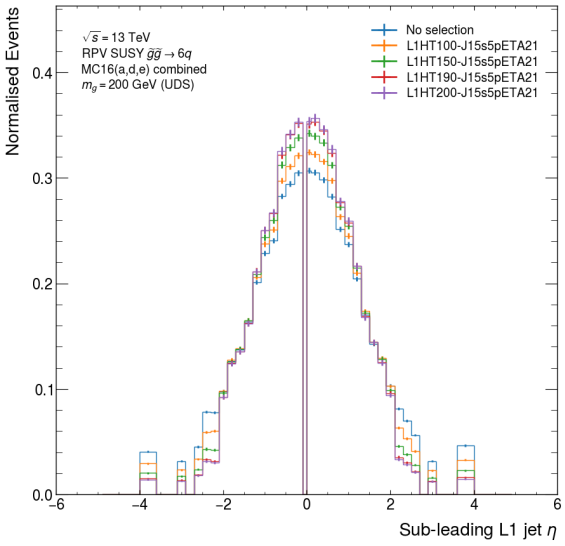

(e) Sub-leading (second) jet η

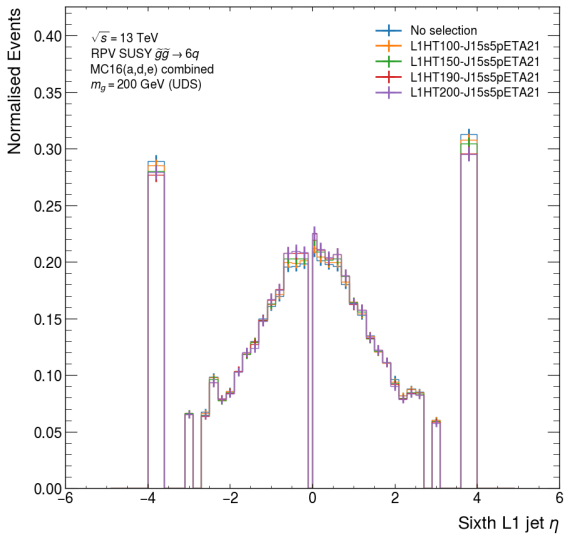

(f) Sixth jet η

Figure 5.22 (cont.): L1 jet E_{T} (the axis labels are quoted as p_{T}, but actually display the E_{T}) and η distributions for the UDS $m_{\tilde{g}} = 200$ GeV combined MC16 event sample after various H_{T} selections for the `J15s5pETA21` jet selection.

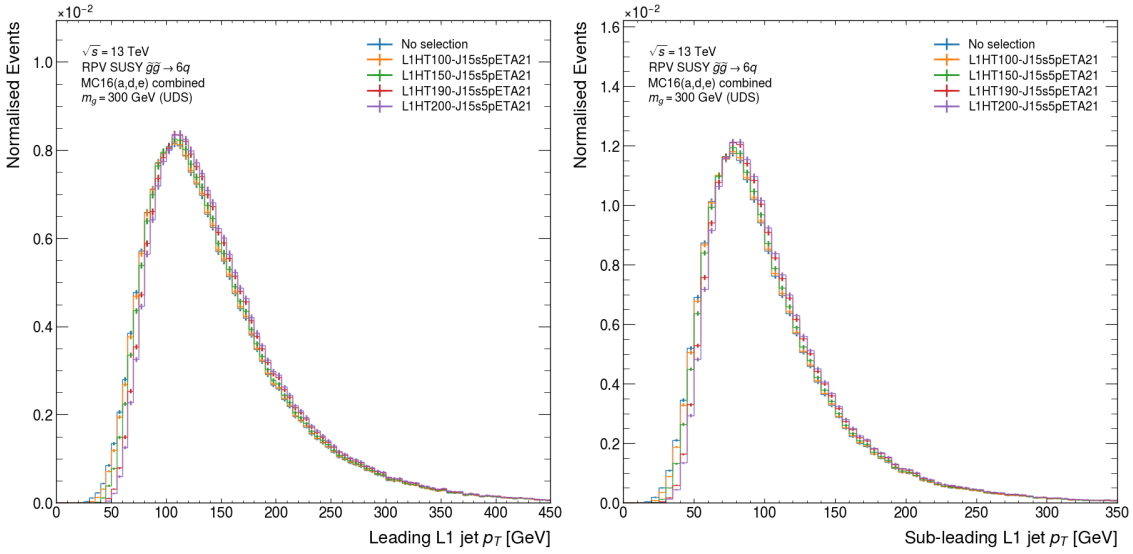

(a) Leading jet E_{T}

(b) Sub-leading (second) jet E_{T}

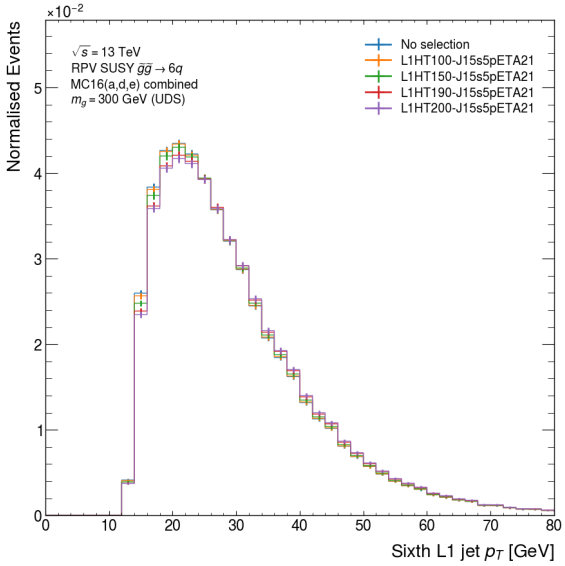

(c) Sixth jet E_{T}

Figure 5.23: L1 jet E_{T} (the axis labels are quoted as p_{T}, but actually display the E_{T}) and η distributions for the UDS $m_{\tilde{g}} = 300$ GeV combined MC16 event sample after various H_{T} selections for the `J15s5pETA21` jet selection.

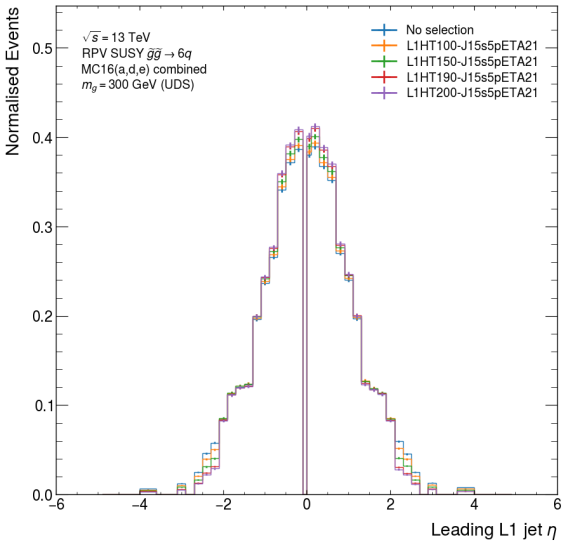

(d) Leading jet η

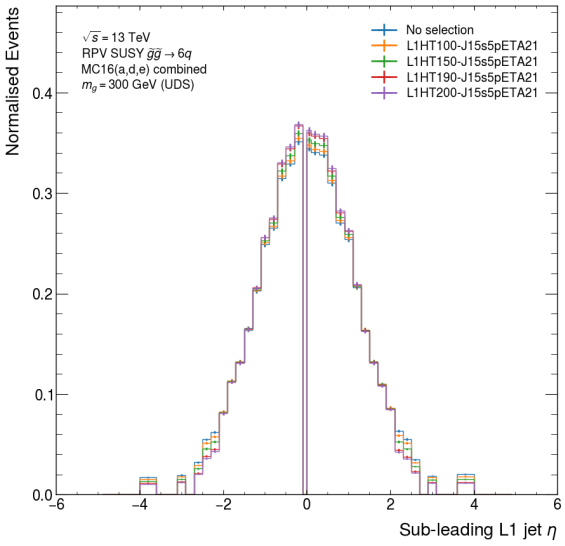

(e) Sub-leading (second) jet η

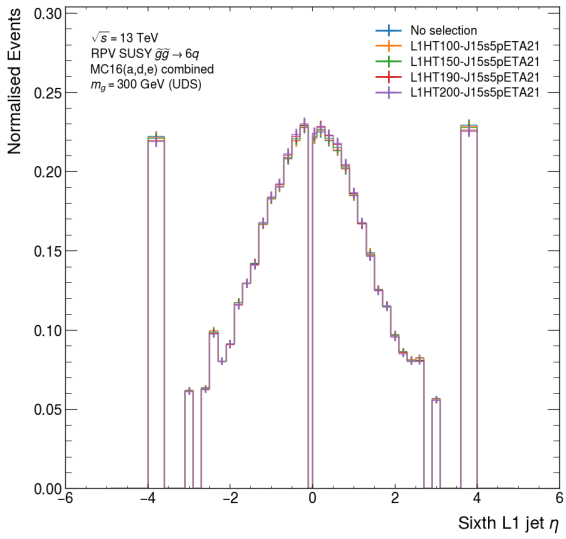

(f) Sixth jet η

Figure 5.23 (cont.): L1 jet E_{T} (the axis labels are quoted as p_{T}, but actually display the E_{T}) and η distributions for the UDS $m_{\tilde{g}} = 300$ GeV combined MC16 event sample after various H_{T} selections for the `J15s5pETA21` jet selection.

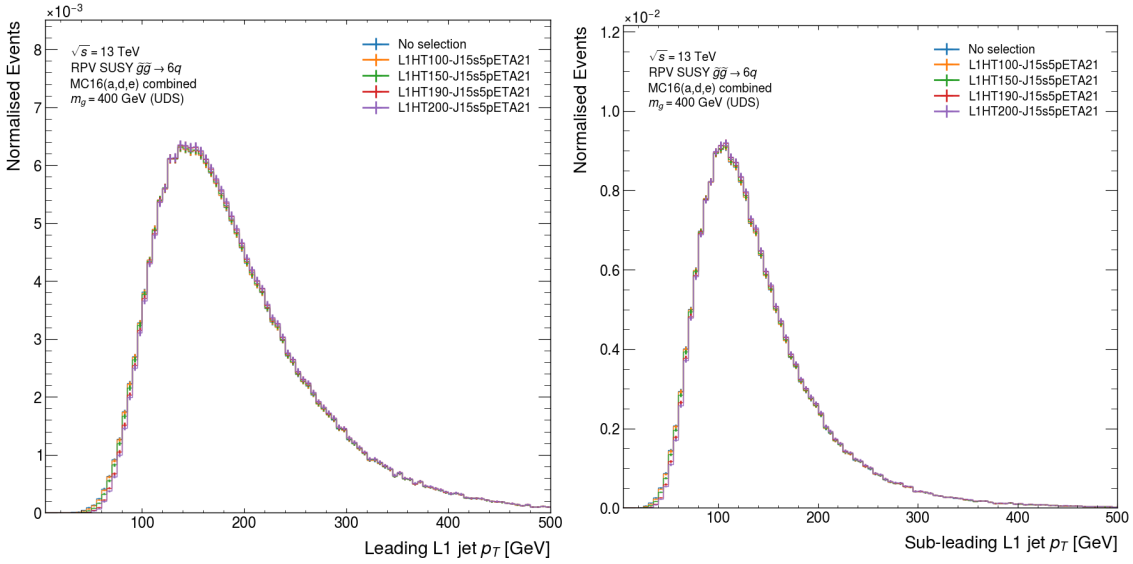

(a) Leading jet E_{T}

(b) Sub-leading (second) jet E_{T}

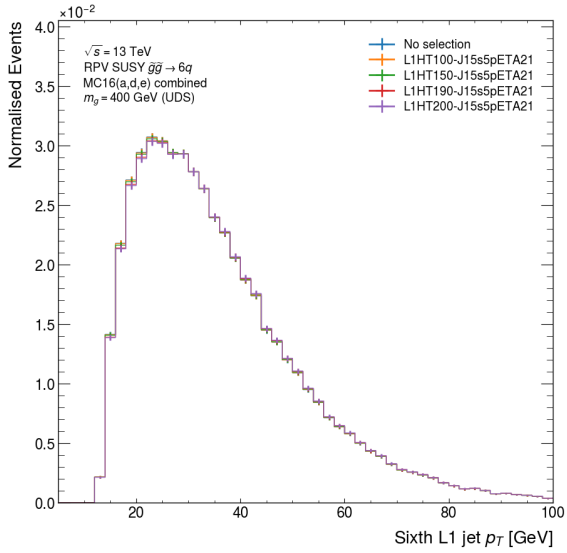

(c) Sixth jet p_{T}

Figure 5.24: L1 jet p_{T} (the axis labels are quoted as p_{T}, but actually display the E_{T}) and η distributions for the UDS $m_{\tilde{g}} = 400$ GeV combined MC16 event sample after various H_{T} selections for the `J15s5pETA21` jet selection.

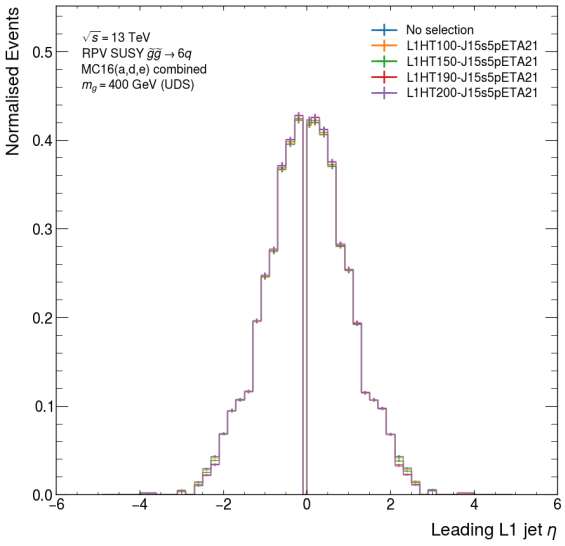

(d) Leading jet η

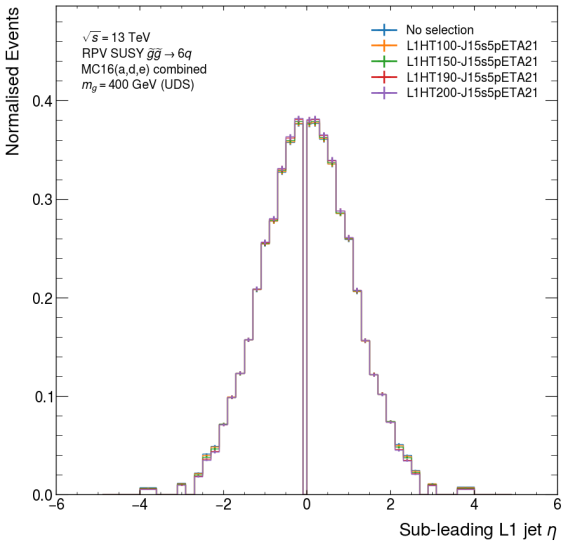

(e) Sub-leading (second) jet η

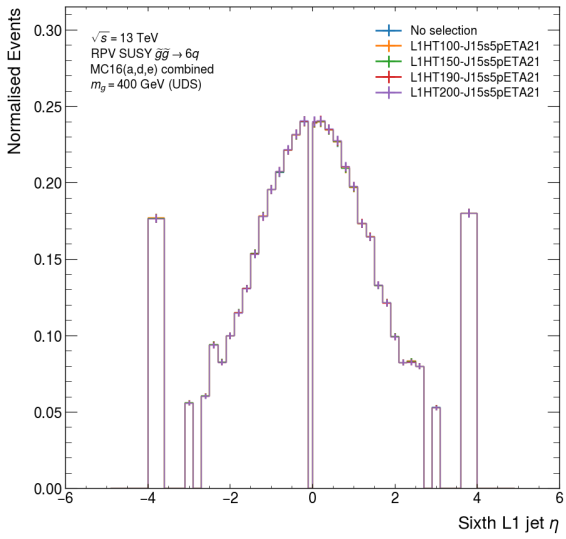

(f) Sixth jet η

Figure 5.24 (cont.): L1 jet p_{T} (the axis labels are quoted as p_{T}, but actually display the E_{T}) and η distributions for the UDS $m_{\tilde{g}} = 400$ GeV combined MC16 event sample after various H_{T} selections for the `J15s5pETA21` jet selection.

5.7.2 Offline jet p_{T} and η shaping

Only p_{T} and η shaping for the offline (calibrated) jets after L1 trigger selections was considered in detail, not the effects of different L1 H_{T} selections and calculation procedures, since these results largely reflect the same conclusions as for L1 jets, but at an energy scale closer to that of truth-level jets. The use of the offline jet information for a detailed study of the L1 trigger efficiency turn-on was not considered. The H_{T} distributions in Figure 5.25 illustrate the effect of making different trigger selections on quantities we use in trigger signatures at the HLT. The H_{T} distributions with L1 trigger selections applied are useful for determining appropriate HLT H_{T} (pre-)selections, which are not considered further in this thesis aside from these brief comments. For low-mass signals triggered with L1 multi-jet selections, a looser HLT H_{T} threshold can be used compared to when the `L1HT190-J15s5pETA21` selection is applied. The efficacy of different HLT H_{T} thresholds in terms of their signal acceptance is entirely dependent on the shapes of the H_{T} distribution in relation to whether the L1 trigger selection forces the H_{T} distribution to migrate to small or large values. Of course, the performance of the triggers for "background" events in relation to CPU costs and trigger rates is important and still being considered in preparation for Run 3.

Like for the L1 jet E_{T} and η distributions, the most stringent trigger thresholds lead to more p_{T} and η shaping in Figures 5.26 to 5.29. This is particularly true for the `L1HT` trigger where a narrowing of the η distribution for both offline and L1 jets is characteristic of the tighter $|\eta| < 2.1$ cut on L1 jets in the H_{T} calculation compared to other trigger η thresholds. Thus, like for L1 jets, the central η selection of the `L1HT` signature selects more central offline jets than those at large-η. For these studies, the binning in jet p_{T} is constrained to have $p_{\mathrm{T}} > 20$ GeV, but we do see cases for the sixth-leading jet p_{T} distributions where the jet p_{T} falls below 20 GeV. However, the calibration for very low p_{T} (< 20 GeV) jets does not perform as well as for higher p_{T} jets. Since we are interested primarily in the well-calibrated jets, realistic limits were placed on the jet p_{T} we considered. This is also evident in the use of HLT `j20` trigger selections rather than a lower jet p_{T} selection, although the background rate also affects choices of trigger thresholds.

5.8 Signal acceptances for HLT selections

The signal acceptance of complete trigger chains involving both an L1 trigger and HLT (kinematic) selection are shown in Tables 5.4 and 5.5 for the UDS and UDB signal points, respectively. While both the results for the UDS and UDB signal points are included we limit our discussion of results to the UDS signal points where the gluinos decay to light jets only. A small difference is seen between the UDS and UDB signal point trigger acceptances characteristic of the lower p_{T} of UDB signal jets relative to UDS signal jets in Figure 5.10, as noted before. Additional keywords (e.g. *JetDS*) in trigger names are used to denote the corresponding stream for the

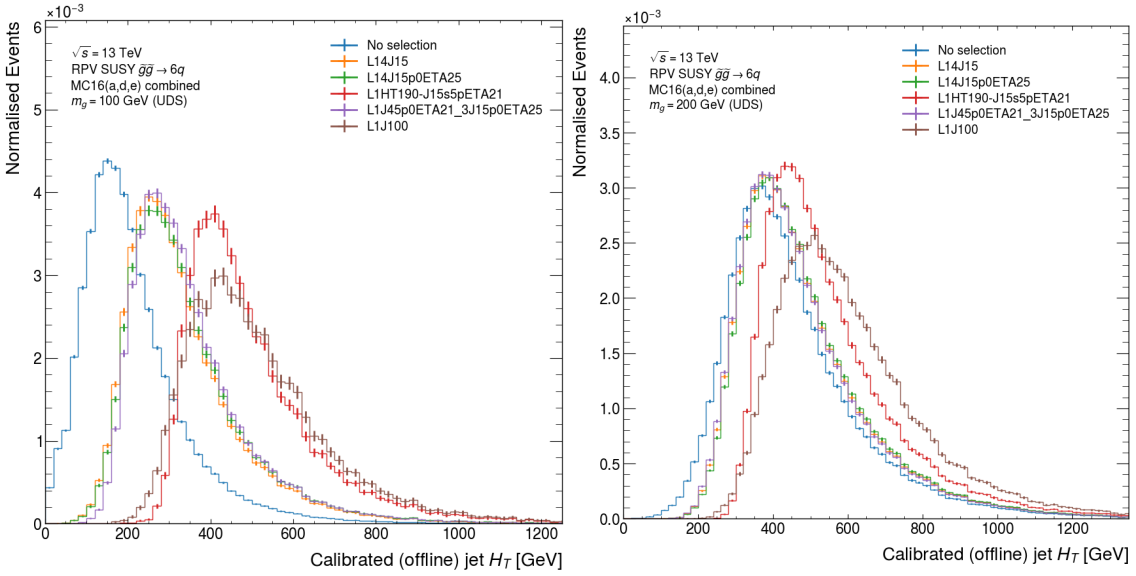

(a) $m_{\tilde{g}} = 100$ GeV

(b) $m_{\tilde{g}} = 200$ GeV

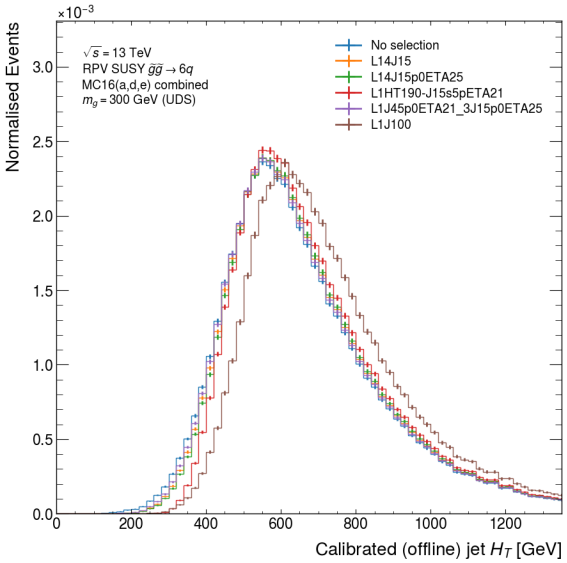

(c) $m_{\tilde{g}} = 300$ GeV

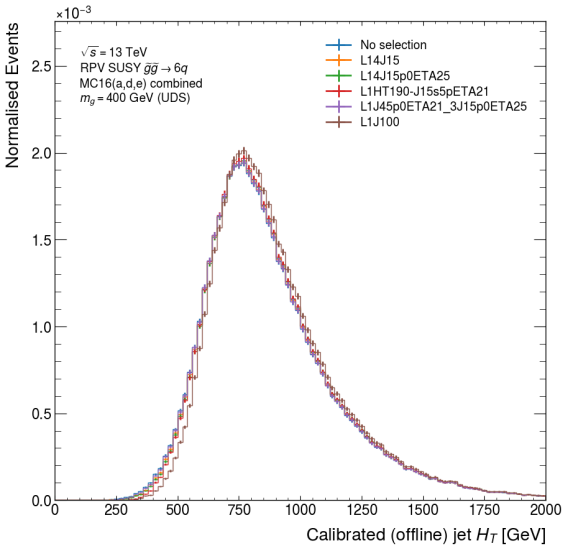

(d) $m_{\tilde{g}} = 400$ GeV

Figure 5.25: The offline/trigger H_{T} calculated from calibrated offline jets with $p_{\mathrm{T}} > 30$ GeV and $|\eta| < 3.2$ for the UDS signal points in the combined MC16 event sample after various L1 trigger selections.

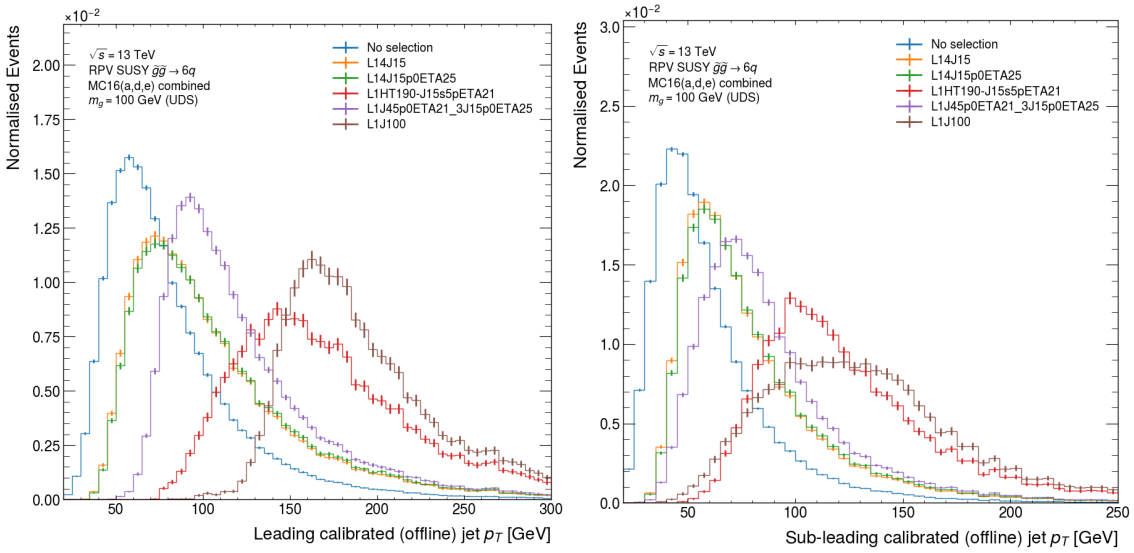

(a) Leading jet p_{T}

(b) Sub-leading (second) jet p_{T}

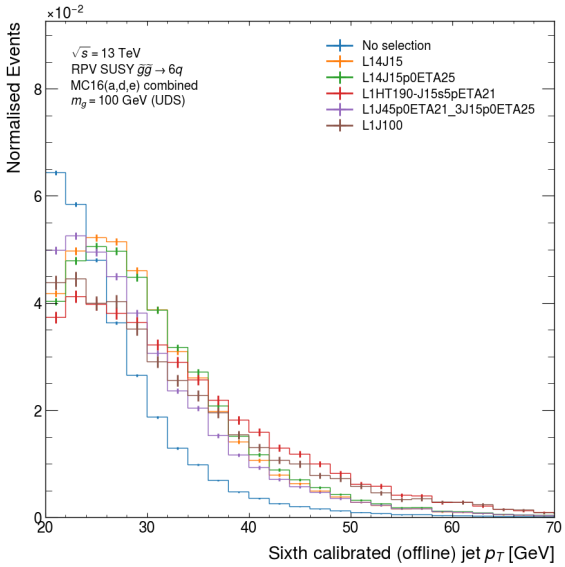

(c) Sixth jet p_{T}

Figure 5.26: Offline jet p_{T} and η distributions for the UDS $m_{\tilde{g}} = 100$ GeV combined MC16 event sample.

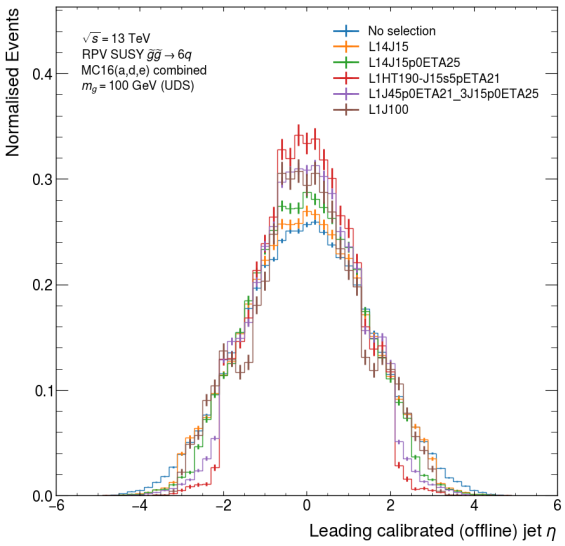

(d) Leading jet η

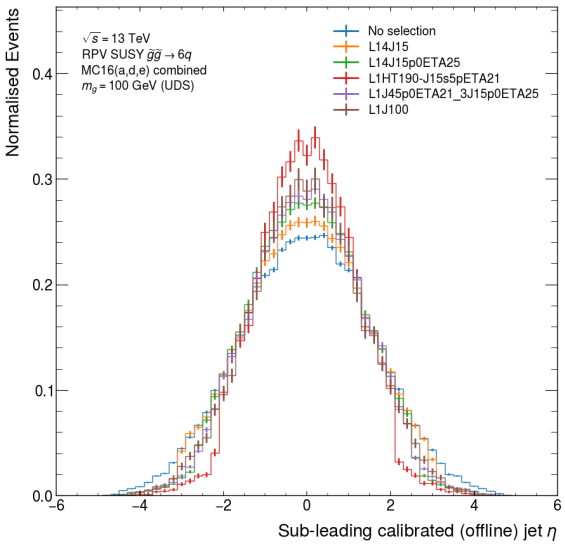

(e) Sub-leading (second) jet η

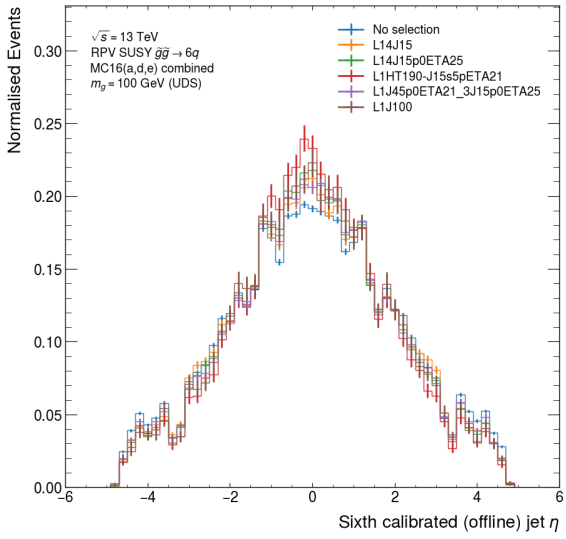

(f) Sixth jet η

Figure 5.26 (cont.): Offline jet p_{T} and η distributions for the UDS $m_{\tilde{g}} = 100$ GeV combined MC16 event sample.

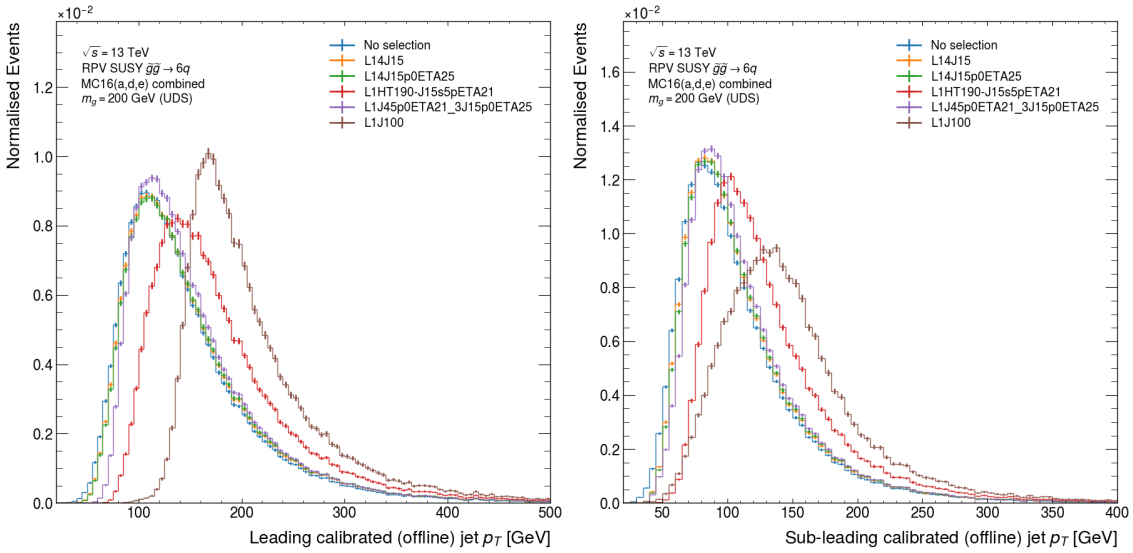

(a) Leading jet p_{T}

(b) Sub-leading (second) jet p_{T}

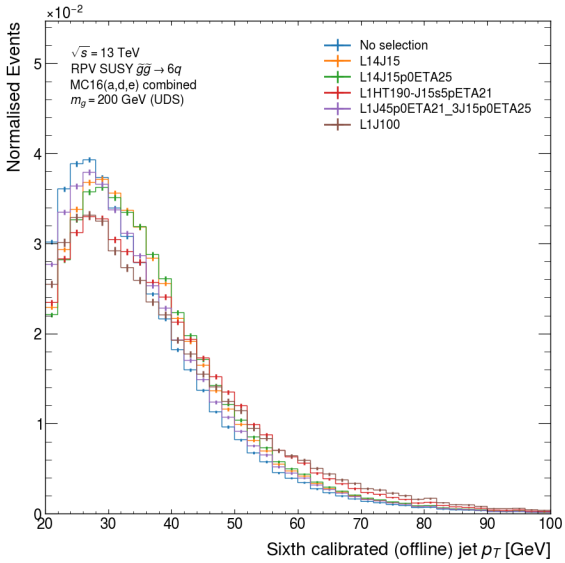

(c) Sixth jet p_{T}

Figure 5.27: Offline jet p_{T} and η distributions for the UDS $m_{\tilde{g}} = 200$ GeV combined MC16 event sample.

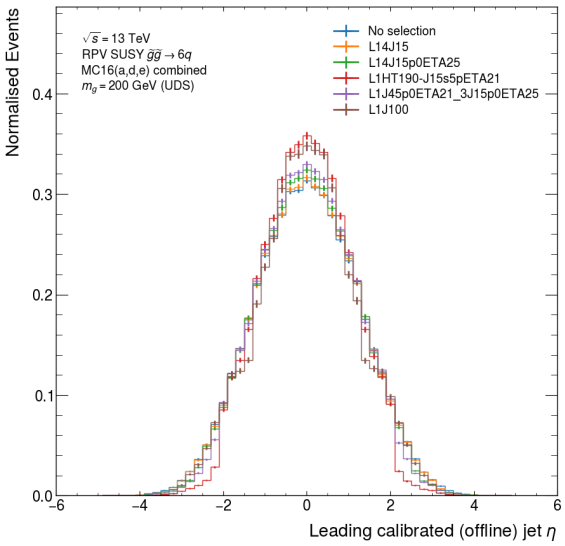

(d) Leading jet η

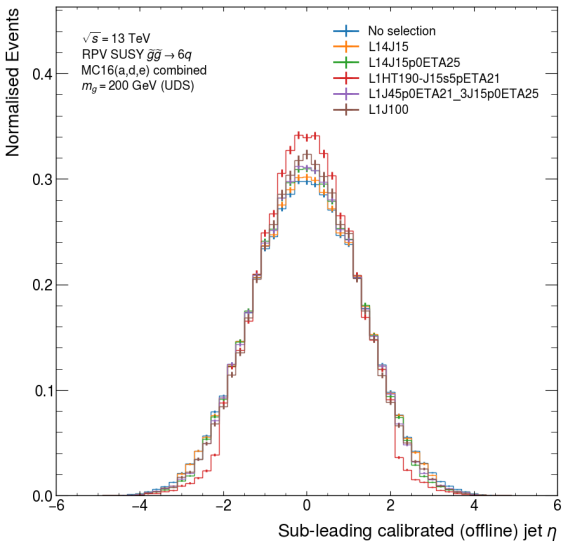

(e) Sub-leading (second) jet η

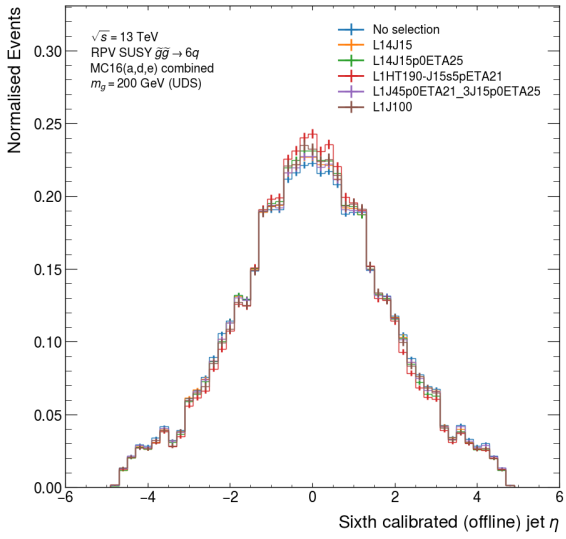

(f) Sixth jet η

Figure 5.27 (cont.): Offline jet p_{T} and η distributions for the UDS $m_{\tilde{g}} = 200$ GeV combined MC16 event sample.

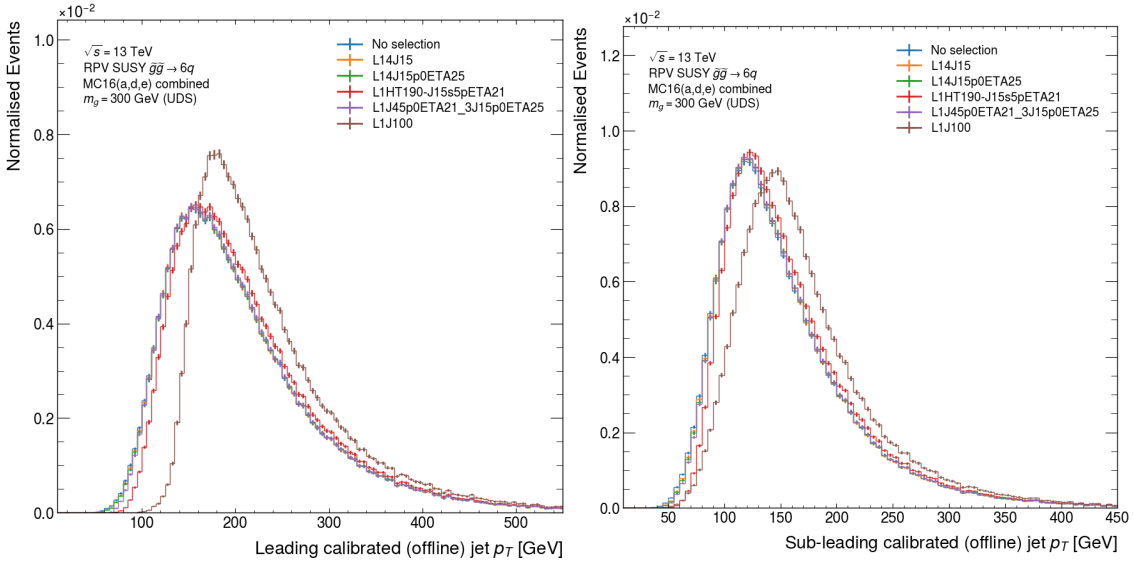

(a) Leading jet p_{T}

(b) Sub-leading (second) jet p_{T}

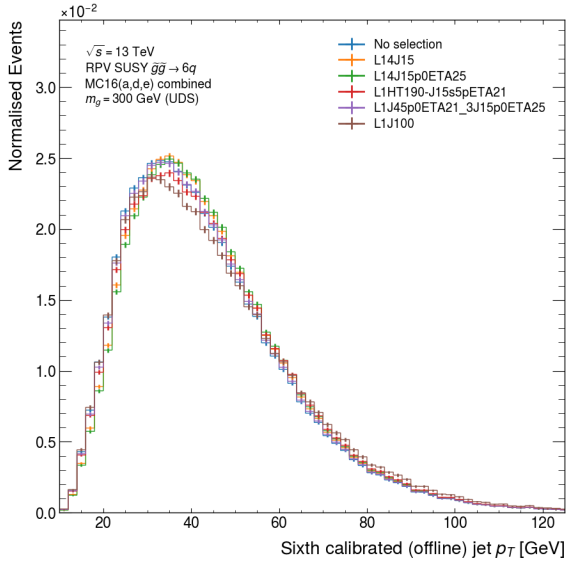

(c) Sixth jet p_{T}

Figure 5.28: Offline jet p_{T} and η distributions for the UDS $m_{\tilde{g}} = 300$ GeV combined MC16 event sample.

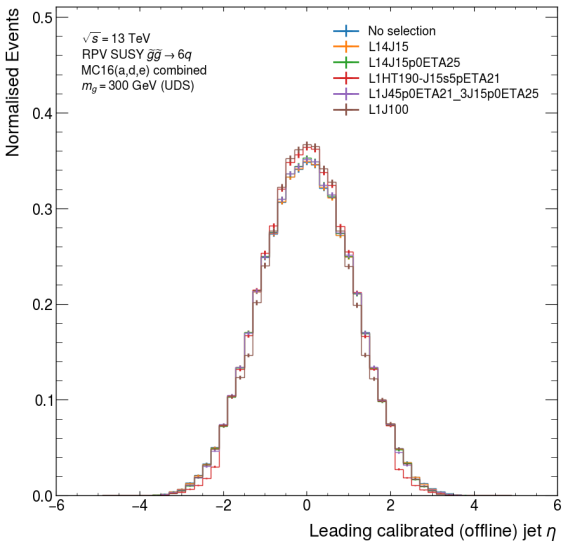

(d) Leading jet η

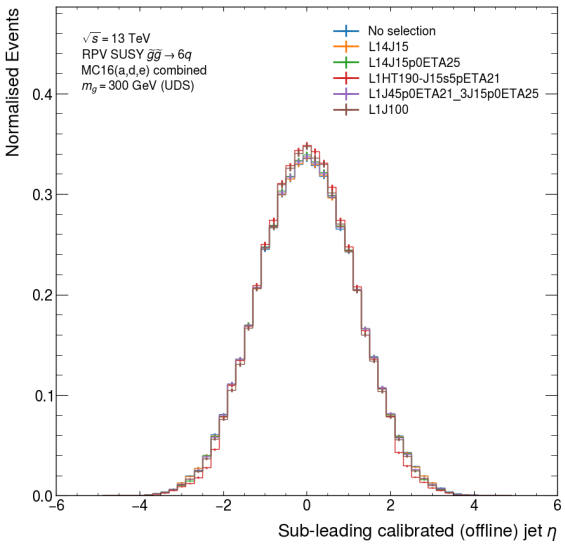

(e) Sub-leading (second) jet η

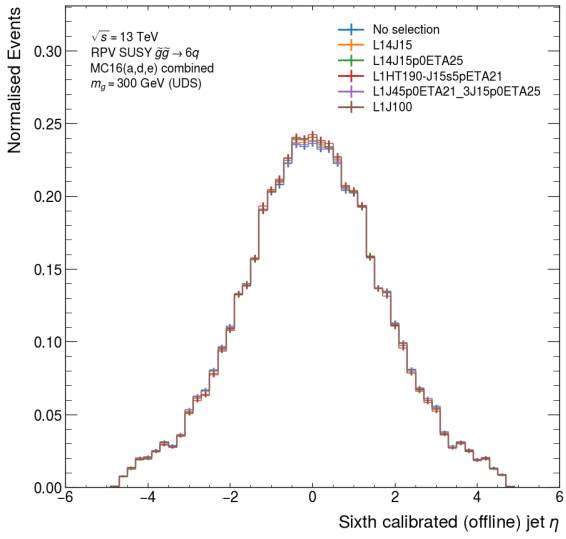

(f) Sixth jet η

Figure 5.28 (cont.): Offline jet p_{T} and η distributions for the UDS $m_{\tilde{g}} = 300$ GeV combined MC16 event sample.

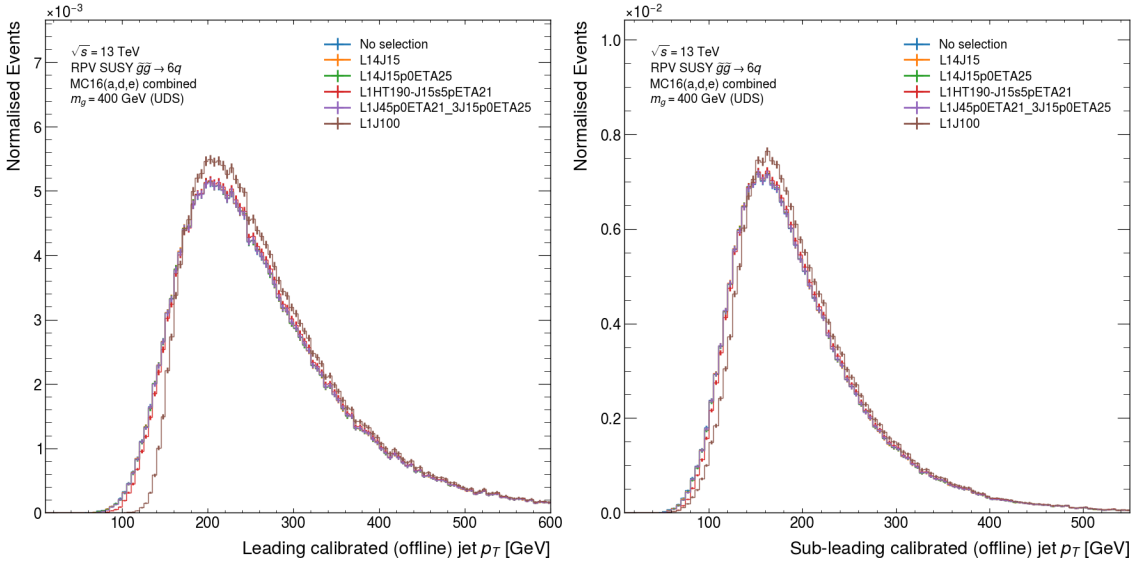

(a) Leading jet p_{T}

(b) Sub-leading (second) jet p_{T}

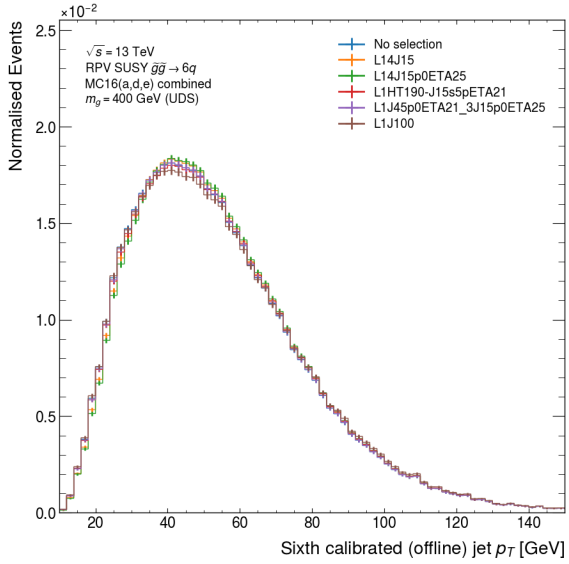

(c) Sixth jet p_{T}

Figure 5.29: Offline jet p_{T} and η distributions for the UDS $m_{\tilde{g}} = 400$ GeV combined MC16 event sample.

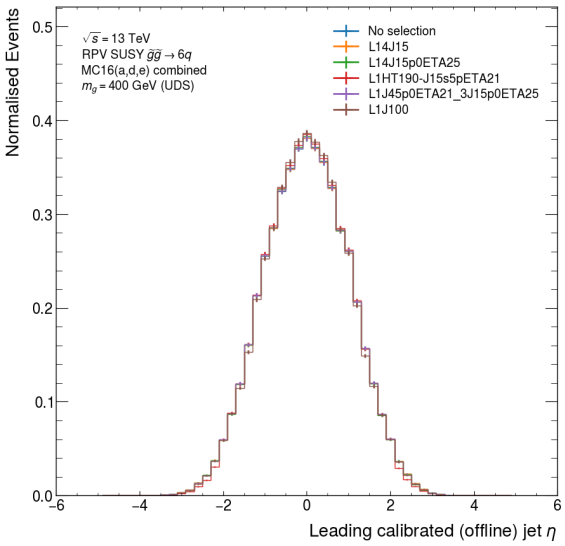

(d) Leading jet η

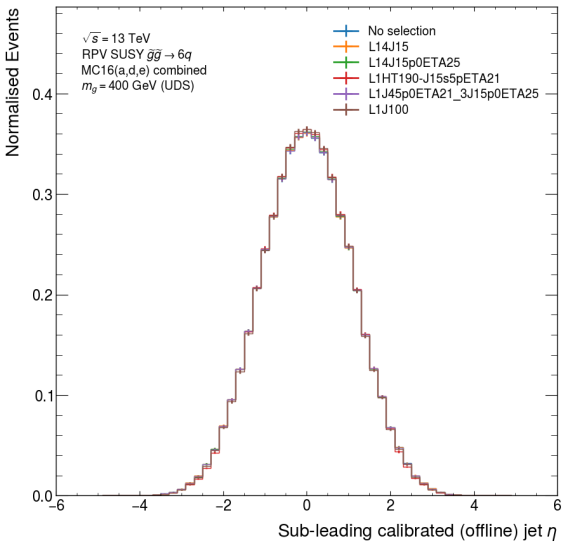

(e) Sub-leading (second) jet η

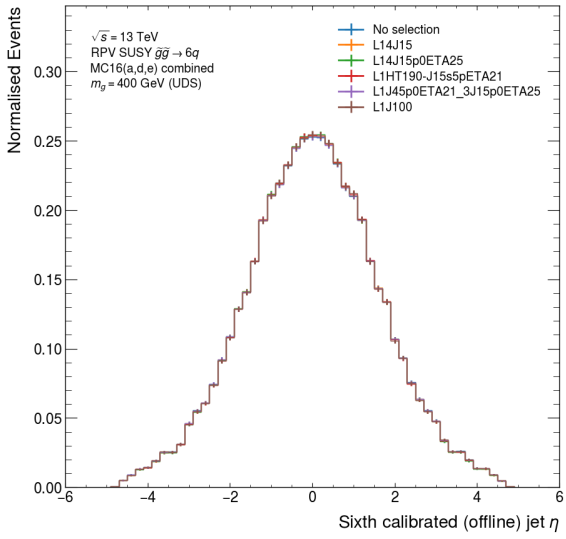

(f) Sixth jet η

Figure 5.29 (cont.): Offline jet p_{T} and η distributions for the UDS $m_{\tilde{g}} = 400$ GeV combined MC16 event sample.

trigger and have no impact on the event selection logic[13]. The same uncertainty estimation and trigger acceptance calculation procedure as for the L1 trigger studies was used.

Like for L1 trigger signal acceptances, the combined MC16 sample achieves larger acceptances for low-mass (100 GeV, 200 GeV) signals compared to the MC16a only sample – primarily for low-threshold multi-jet selections. Again, this could be a result of the different sample conditions – higher pile-up levels (more low-p_{T} jets, some which pass trigger thresholds) will lead to increased acceptances for lower mass signals.

From the wide variety of complete trigger chains studied, those with a multi-jet selection in both the HLT and L1 trigger are most performant. For instance, the `HLT_j20_L14J15` and `HLT_j20_L14J15p0ETA25` chain produces an acceptance above 20% acceptance compared to the `HLT_j20_L1J100` acceptance of 6-7%. The `L1HT190` seeded HLT selections clearly outperform `HLT_j20_L1J100`, but only produce small signal acceptance increases for the lowest mass signals (100 GeV). At higher signal masses up to 400 GeV, the `L1HT190` seeded trigger performance increases substantially relative to the `L1J100` triggers, leading to improved performance for the complete HLT+L1 chains. As expected, the higher threshold triggers in the final lines of the table (`HLT_4j120`[14], `HLT_5j70_0eta240_L14J15`, `HLT_ht1000_L1J100`) perform the worst. At the largest signal masses tested (400 GeV) the best-performing (low-threshold) triggers are almost fully efficient (i.e. 100% efficiency).

Triggers that exploit loose asymmetric thresholds perform comparably to the best-performing chains that use single-jet HLT selections and multi-jet L1 trigger selections. The `HLT_j60_j45_2j20` and `HLT_j80_j55_j28_j20` selections seeded by `L1J45p0ETA21_3J15p0ETA25` have lower signal acceptance than `HLT_j20_L14J15` for $m_{\tilde{g}} = 100$ GeV, but for higher mass (≥ 200 GeV) signals they provide the highest acceptances. The loose `HLT_j60_j45_2j20` selection has a 24-25% acceptance for $m_{\tilde{g}} = 100$ GeV but achieves a 99.6% acceptance for $m_{\tilde{g}} = 400$ GeV, at which point it is almost fully efficient. With larger uncertainties (greater than 1%) the performance of the asymmetric threshold triggers could agree to within uncertainties with the `HLT_j20_L14J15` acceptance for some higher mass (≥ 200 GeV) signals.

The limiting factor for TLA triggers in Run 3 has proven to be the rate of each chain and associated resource costs for tracking, primarily where chains should use `PFlow` jets. The `L1J45p0ETA21_3J15p0ETA25` trigger performs quite well but the kinematic selections alone lead to significant and unaffordable trigger rates for tracking as discussed throughout this Chapter. The candidate TLA triggers are still being finalised, but the trigger menu will initially include chains with both the `L1HT190` and `L1J100` seeds.

[13]The position and name of the stream in trigger chains has changed since early studies were conducted.

[14]Actually `HLT_4j120_L1J100`.

To mitigate the high rate of triggers used with tracking and PFlow reconstruction a calorimeter-only pre-selection can be applied using EMTopo jets. The results discussed here are primarily for illustrative purposes and show the effect of pre-selections on the signal acceptance of L1HT190 and L14J15p0ETA25 seeded chains[15]. The complete trigger selections were applied up to and including the pre-selection on EMPFlow jets, not EMTopo jets since only an indicative estimate of the signal acceptance was needed. In practice, these steps would take place *before* any expensive tracking/reconstruction algorithms are run at the HLT to reduce the number of events that require complete HLT reconstruction. The chosen pre-selection (regardless of the signature [e.g. multi-jet, H_{T}, etc.]) should reduce the trigger rate sufficiently using an appropriately stringent selection. We considered jet-based pre-selections including a baseline j180[16] L1HT selection, and looser 4-jet selections, 4jX[17], (where X is the jet p_{T} threshold) for both L1 triggers. The pre-selection results are included in the first eight rows of Tables 5.4 and 5.5. The limitation of the signal acceptance results presented here lies in the fact that they do not consider the trigger turn-on curves in detail and therefore very loose pre-selections may not be well motivated in terms of their reduction of trigger rates and resource costs.

When the j180 pre-selection is applied after a L1HT190 selection, the acceptance of the lowest mass signal ($m_{\tilde{g}} = 100$ GeV) events (where the jets originating from the gluino decay have low p_{T}) decreases considerably relative to the HLT_j20_L1HT190... chain without pre-selections. A looser multi-jet selection is one option to avoid high single-jet thresholds as seen for the TLA triggers in general. Four-jet selections (HLT_4jX_L1HT190...) with p_{T} thresholds between 20 GeV and 50 GeV obtain signal acceptances no less than half of the HLT_j20_L1HT190-J15s5pETA21 acceptance for the $m_{\tilde{g}} = 100$ GeV UDS and UDB signal in Tables 5.4 and 5.5, respectively. The HLT_4j20... selections will be satisfied by many low-p_{T} multi-jet QCD events, so more stringent selections (e.g. 40 GeV to 50 GeV p_{T} thresholds) might be optimal for limiting the rate of these chains sufficiently. The same is true for the multi-jet L1 seed, where more stringent pre-selections lead to $m_{\tilde{g}} = 100$ GeV acceptances approximately half that of the HLT_j20_L14J15p0ETA25 chain. In both Tables 5.4 and 5.5 these higher threshold selections maintain reasonably high sensitivity to the signals with gluino masses of at least 200 GeV. The more stringent pre-selections will always have a negative impact on sensitivity for the lowest mass 100 GeV signal, which is unavoidable. The tighter 4jX pre-selections (especially for the L1HT seeded trigger) provide an acceptable signal acceptance, which is lost with harsher (e.g.

[15] These studies were completed with input from Claire Antel and other members of the ATLAS trigger group to identify pre-selections for use in the main physics trigger stream (not TLA). However, since the L1HT190-J15s5pETA21 trigger will be used for TLA, the same pre-selection can be applied for the TLA trigger chains. Although only multi-jet pre-selections are included in these results, the final pre-selection chosen for the L1HT190 chain after further study by members of the ATLAS jet trigger group consists of a H_{T} selection for central $|\eta| < 2.4$ jets.

[16] A single jet with $p_{\mathrm{T}} > 180$ GeV is required to be reconstructed within $|\eta| < 3.2$.

[17] Four jets with $p_{\mathrm{T}} > X$ GeV are required to be reconstructed within $|\eta| < 3.2$.

j180) selections. Avenues for the use of PFlow reconstruction in TLA trigger chains, including pre-selections, are still being considered for Run 3.

Table 5.4: HLT chain acceptance fractions for UDS signal points with different event samples.

(a) MC16a event sample.

Trigger	$m_g = 100$ GeV	$m_g = 200$ GeV	$m_g = 300$ GeV	$m_g = 400$ GeV
HLT_4j45_L14J15p0ETA25	0.1044 ± 0.0001	0.6056 ± 0.0007	0.8836 ± 0.001	0.9597 ± 0.002
HLT_4j40_L14J15p0ETA25	0.1429 ± 0.0001	0.6836 ± 0.0006	0.9109 ± 0.001	$0.9684^{+0.001}_{-0.002}$
HLT_4j25_L14J15p0ETA25	0.2172 ± 0.0001	0.7596 ± 0.0006	0.9317 ± 0.001	0.9745 ± 0.001
HLT_j180_L1HT190-J15s5pETA21	$0.0316 \pm 5 \times 10^{-5}$	0.2145 ± 0.0006	0.5369 ± 0.002	0.8076 ± 0.003
HLT_4j50_L1HT190-J15s5pETA21	0.0449 ± 0.0001	0.3965 ± 0.0007	0.8043 ± 0.002	0.9412 ± 0.002
HLT_4j45_L1HT190-J15s5pETA21	0.0535 ± 0.0001	0.4424 ± 0.0007	0.8424 ± 0.001	0.9563 ± 0.002
HLT_4j40_L1HT190-J15s5pETA21	0.0613 ± 0.0001	0.479 ± 0.0007	0.8684 ± 0.001	0.9664 ± 0.002
HLT_4j20_L1HT190-J15s5pETA21	0.081 ± 0.0001	0.5417 ± 0.0007	0.904 ± 0.001	0.9799 ± 0.001
HLT_j20_L14J15	0.2552 ± 0.0001	0.8027 ± 0.0005	0.9521 ± 0.0008	0.9838 ± 0.001
HLT_j20_L14J15p0ETA25	0.2205 ± 0.0001	0.7605 ± 0.0006	0.932 ± 0.001	0.9746 ± 0.001
HLT_j20_JetDS_L1J100	0.0668 ± 0.0001	0.3657 ± 0.0007	0.7336 ± 0.002	0.9284 ± 0.002
HLT_j20_JetDS_L1HT190-J15s5pETA21	0.0832 ± 0.0001	0.544 ± 0.0007	0.9052 ± 0.001	0.9804 ± 0.001
HLT_j60_j45_2j20_JetDS_L1J45p0ETA21_3J15p0ETA25	0.2486 ± 0.0001	0.8488 ± 0.0005	0.9799 ± 0.0005	0.9963 ± 0.0005
HLT_j80_j55_j28_j20_L1J45p0ETA21_3J15p0ETA25	0.2088 ± 0.0001	0.8151 ± 0.0005	0.9768 ± 0.0006	$0.996^{+0.0005}_{-0.0006}$
HLT_4j120	$0.001 \pm 1 \times 10^{-5}$	0.0189 ± 0.0002	0.1002 ± 0.001	0.2701 ± 0.004
HLT_5j70_0eta240_L14J15	$0.0025 \pm 1 \times 10^{-5}$	0.0528 ± 0.0003	0.2275 ± 0.002	0.4585 ± 0.004
HLT_ht1000_L1J100	$0.0014 \pm 1 \times 10^{-5}$	0.0196 ± 0.0002	0.0925 ± 0.001	0.2546 ± 0.004

(b) Combined MC16 event sample.

Trigger	$m_g = 100$ GeV	$m_g = 200$ GeV	$m_g = 300$ GeV	$m_g = 400$ GeV
HLT_4j45_L14J15p0ETA25	0.1103 ± 0.0001	0.6186 ± 0.0004	0.8879 ± 0.0007	0.9615 ± 0.0009
HLT_4j40_L14J15p0ETA25	0.1523 ± 0.0001	0.6961 ± 0.0004	0.9155 ± 0.0006	0.9702 ± 0.0008
HLT_4j25_L14J15p0ETA25	0.2368 ± 0.0001	0.7722 ± 0.0003	0.9358 ± 0.0005	0.9763 ± 0.0007
HLT_j180_L1HT190-J15s5pETA21	$0.0329 \pm 3 \times 10^{-5}$	0.2161 ± 0.0003	0.5388 ± 0.001	0.8099 ± 0.002
HLT_4j50_L1HT190-J15s5pETA21	$0.0467 \pm 3 \times 10^{-5}$	0.4045 ± 0.0004	0.8092 ± 0.0009	0.9433 ± 0.001
HLT_4j45_L1HT190-J15s5pETA21	$0.0551 \pm 4 \times 10^{-5}$	0.4508 ± 0.0004	0.8454 ± 0.0008	0.9581 ± 0.001
HLT_4j40_L1HT190-J15s5pETA21	$0.063 \pm 4 \times 10^{-5}$	0.4877 ± 0.0004	0.8712 ± 0.0007	$0.9681^{+0.0008}_{-0.0009}$
HLT_4j20_L1HT190-J15s5pETA21	$0.0823 \pm 4 \times 10^{-5}$	0.5484 ± 0.0004	0.9051 ± 0.0006	0.9808 ± 0.0007
HLT_j20_L14J15	0.2796 ± 0.0001	0.8161 ± 0.0003	0.9554 ± 0.0005	0.9851 ± 0.0006
HLT_j20_L14J15p0ETA25	0.2404 ± 0.0001	0.7733 ± 0.0003	0.9361 ± 0.0005	0.9764 ± 0.0007
HLT_j20_JetDS_L1J100	$0.0672 \pm 4 \times 10^{-5}$	0.3664 ± 0.0004	0.7339 ± 0.001	0.9277 ± 0.001
HLT_j20_JetDS_L1HT190-J15s5pETA21	$0.084 \pm 4 \times 10^{-5}$	0.5504 ± 0.0004	0.9059 ± 0.0006	$0.9812^{+0.0006}_{-0.0007}$
HLT_j60_j45_2j20_JetDS_L1J45p0ETA21_3J15p0ETA25	0.2586 ± 0.0001	0.8528 ± 0.0003	0.9812 ± 0.0003	0.9963 ± 0.0003
HLT_j80_j55_j28_j20_L1J45p0ETA21_3J15p0ETA25	0.2169 ± 0.0001	0.8204 ± 0.0003	0.9782 ± 0.0003	0.996 ± 0.0003
HLT_4j120	$0.0011 \pm 1 \times 10^{-5}$	0.0205 ± 0.0001	0.1008 ± 0.0007	0.2756 ± 0.002
HLT_5j70_0eta240_L14J15	$0.0031 \pm 1 \times 10^{-5}$	0.0559 ± 0.0002	0.2332 ± 0.0009	0.4673 ± 0.002
HLT_ht1000_L1J100	$0.0016 \pm 1 \times 10^{-5}$	0.0204 ± 0.0001	0.0939 ± 0.0006	0.2635 ± 0.002

Table 5.5: HLT chain acceptance fractions for UDB signal points with different event samples.

(a) MC16a event sample.

Trigger	$m_g = 100$ GeV	$m_g = 200$ GeV	$m_g = 300$ GeV	$m_g = 400$ GeV
HLT_4j45_L14J15p0ETA25	0.0941 ± 0.0001	0.5775 ± 0.0007	0.8693 ± 0.001	0.9539 ± 0.002
HLT_4j40_L14J15p0ETA25	0.127 ± 0.0001	0.6567 ± 0.0006	0.8991 ± 0.001	0.9642 ± 0.002
HLT_4j25_L14J15p0ETA25	0.1921 ± 0.0001	0.7311 ± 0.0006	0.9222 ± 0.001	0.9718 ± 0.001
HLT_j180_L1HT190-J15s5pETA21	$0.0315 \pm 5 \times 10^{-5}$	0.2059 ± 0.0006	0.5175 ± 0.002	0.7957 ± 0.003
HLT_4j50_L1HT190-J15s5pETA21	0.041 ± 0.0001	0.3663 ± 0.0007	0.7833 ± 0.002	0.9324 ± 0.002
HLT_4j45_L1HT190-J15s5pETA21	0.0487 ± 0.0001	0.4099 ± 0.0007	0.8225 ± 0.002	0.9495 ± 0.002
HLT_4j40_L1HT190-J15s5pETA21	0.0556 ± 0.0001	0.4463 ± 0.0007	0.8498 ± 0.001	0.9613 ± 0.002
HLT_4j20_L1HT190-J15s5pETA21	0.0727 ± 0.0001	0.5094 ± 0.0007	0.8887 ± 0.001	0.9773 ± 0.001
HLT_j20_L14J15	0.2285 ± 0.0001	0.776 ± 0.0006	0.9441 ± 0.0009	0.9809 ± 0.001
HLT_j20_L14J15p0ETA25	0.1947 ± 0.0001	0.7322 ± 0.0006	0.9223 ± 0.001	0.9718 ± 0.001
HLT_j20_JetDS_L1J100	0.0645 ± 0.0001	0.35 ± 0.0007	0.7127 ± 0.002	0.9177 ± 0.002
HLT_j20_JetDS_L1HT190-J15s5pETA21	0.0747 ± 0.0001	0.5127 ± 0.0007	0.8901 ± 0.001	0.9779 ± 0.001
HLT_j60_j45_2j20_JetDS_L1J45p0ETA21_3J15p0ETA25	0.2265 ± 0.0001	0.825 ± 0.0005	0.9763 ± 0.0006	$0.9955^{+0.0005}_{-0.0006}$
HLT_j80_j55_j28_j20_L1J45p0ETA21_3J15p0ETA25	0.193 ± 0.0001	0.7902 ± 0.0006	0.9725 ± 0.0006	0.9951 ± 0.0006
HLT_4j120	$0.0009 \pm 1 \times 10^{-5}$	0.0188 ± 0.0002	0.0878 ± 0.001	0.2514 ± 0.004
HLT_5j70_0eta240_L14J15	$0.0028 \pm 1 \times 10^{-5}$	0.0502 ± 0.0003	0.2084 ± 0.002	0.4352 ± 0.004
HLT_ht1000_L1J100	$0.0013 \pm 1 \times 10^{-5}$	0.0179 ± 0.0002	0.0833 ± 0.001	0.2396 ± 0.004

(b) Combined MC16 event sample.

Trigger	$m_g = 100$ GeV	$m_g = 200$ GeV	$m_g = 300$ GeV	$m_g = 400$ GeV
HLT_4j45_L14J15p0ETA25	$0.1014 \pm 5 \times 10^{-5}$	0.591 ± 0.0004	0.8749 ± 0.0007	0.956 ± 0.001
HLT_4j40_L14J15p0ETA25	0.1384 ± 0.0001	0.669 ± 0.0004	0.9046 ± 0.0007	0.9658 ± 0.0009
HLT_4j25_L14J15p0ETA25	0.2131 ± 0.0001	0.7455 ± 0.0003	0.9269 ± 0.0006	0.9729 ± 0.0008
HLT_j180_L1HT190-J15s5pETA21	$0.0315 \pm 3 \times 10^{-5}$	0.2085 ± 0.0003	0.5223 ± 0.001	0.7945 ± 0.002
HLT_4j50_L1HT190-J15s5pETA21	$0.0427 \pm 3 \times 10^{-5}$	0.3765 ± 0.0004	0.7878 ± 0.0009	0.9346 ± 0.001
HLT_4j45_L1HT190-J15s5pETA21	$0.0504 \pm 4 \times 10^{-5}$	0.4196 ± 0.0004	0.8262 ± 0.0008	0.9513 ± 0.001
HLT_4j40_L1HT190-J15s5pETA21	$0.0577 \pm 4 \times 10^{-5}$	0.4551 ± 0.0004	0.8533 ± 0.0008	0.9626 ± 0.0009
HLT_4j20_L1HT190-J15s5pETA21	$0.0753 \pm 4 \times 10^{-5}$	0.5156 ± 0.0004	0.8898 ± 0.0007	0.9772 ± 0.0007
HLT_j20_L14J15	0.2531 ± 0.0001	0.7904 ± 0.0003	0.9479 ± 0.0005	0.9824 ± 0.0006
HLT_j20_L14J15p0ETA25	0.2162 ± 0.0001	0.7466 ± 0.0003	0.9271 ± 0.0006	0.973 ± 0.0008
HLT_j20_JetDS_L1J100	$0.0634 \pm 4 \times 10^{-5}$	0.3509 ± 0.0004	0.7134 ± 0.001	0.9165 ± 0.001
HLT_j20_JetDS_L1HT190-J15s5pETA21	$0.077 \pm 4 \times 10^{-5}$	0.5181 ± 0.0004	0.8908 ± 0.0007	0.9776 ± 0.0007
HLT_j60_j45_2j20_JetDS_L1J45p0ETA21_3J15p0ETA25	0.2378 ± 0.0001	0.8321 ± 0.0003	0.9774 ± 0.0003	0.9957 ± 0.0003
HLT_j80_j55_j28_j20_L1J45p0ETA21_3J15p0ETA25	0.2019 ± 0.0001	0.7985 ± 0.0003	0.9738 ± 0.0004	0.9953 ± 0.0003
HLT_4j120	$0.001 \pm 1 \times 10^{-5}$	0.0192 ± 0.0001	0.0914 ± 0.0006	0.2547 ± 0.002
HLT_5j70_0eta240_L14J15	$0.0028 \pm 1 \times 10^{-5}$	0.0517 ± 0.0002	0.217 ± 0.0009	0.4439 ± 0.002
HLT_ht1000_L1J100	$0.0015 \pm 1 \times 10^{-5}$	0.0193 ± 0.0001	0.0879 ± 0.0006	0.2459 ± 0.002

5.9 Effects of pile-up rejection

Searches for low-mass resonances that produce low-p_{T} jets are particularly susceptible to contamination from pile-up jets produced in the detector. The use of combinatorial techniques to identify the signal jets originating from each gluino decay could result in the mis-identification of a pile-up jet as a signal jet (relevant for HL-LHC projections in Chapter 6). To prevent this, some form of pile-up suppression is required such as the use of tracking capabilities in the trigger and JVT (the Jet Vertex Tagger introduced in Section 4.8.1).

These studies considered the effects of trigger- and analysis-level JVT selections in combination with multi-jet HLT selections on the acceptance of signal events and p_{T} spectra of signal jets, respectively. JVT selections corresponding to the *Tight* working point for `EMPFlow` jets were applied, and the p_{T} distributions of selected jets were compared to that with no selections. The *Tight* `EMPFlow` JVT working point requires jets with $|\eta| < 2.4$ and $20 < p_{\mathrm{T}}$ (GeV) < 60 to have JVT > 0.5. The JVT selection was applied to only the jet being considered: the leading, sub-leading (second), or sixth-leading jet. While analysis- or trigger-level JVT selections would be applied to all jets passing kinematic requirements in an event, the consideration of the performance for a limited set of jets allowed for the effects of JVT on a collection of both high- and low-p_{T} jets to be compared. Intermediate p_{T} jets (e.g. the third, fourth, or fifth leading jets) could be used to expand the p_{T} range under consideration but were not used in these studies. Multi-jet trigger selections were also applied before the JVT selection was made, including a `HLT_4j20_L1HT190-J15s5pETA21` (with a greater jet multiplicity requirement compared to the `j20` TLA trigger), `HLT_j80_j55_j28_j20`, and `HLT_j60_j45_2j20` selection – the asymmetric L1 seed is used for the final two triggers. For these initial results, the JVT selection acts as an "analysis selection" rather than a trigger-level selection because it was *not* applied to all jets considered by the trigger selection.

The UDS signal jet p_{T} spectra before and after trigger and JVT selections are shown in Figures 5.30 to 5.32 for the leading jet, sub-leading (2nd) jet, and sixth-leading jet, respectively. The bottom panel of the histograms shows the ratio of every distribution after selection to that without selections. Any bins where the ratio vanishes or blows up to ∞ are masked to avoid their impact on the ratio panel y-axis range. The effects of L1 trigger selections on these distributions are already well established and similar results are seen when HLT and L1 selections are combined. The jet p_{T} distributions after the application of high-acceptance triggers (with lower p_{T} thresholds) contain more low-p_{T} events where the spectrum does not cut-off at high-p_{T}, like for more stringent selections. The application of JVT alone indicates that *Tight* JVT selections have little effect on the highest p_{T} leading jet except for the $m_{\tilde{g}} = 100$ GeV signal. A more significant effect is seen for the second- and sixth-leading jets where jets from low-mass resonances inherently have quite low p_{T}. Events with very low-p_{T} sixth-leading jets are lost, while events with higher p_{T} sixth-leading jets are kept – in part due to the $20 < p_{\mathrm{T}}$ (GeV) < 60 requirement

required for JVT cut to be applied. Further plots illustrating the results for the MC16a only dataset and the UDB signal points are included in Appendix D.

Trigger-level JVT selections were emulated with JVT thresholds of 0.2, and 0.5 (like the offline Tight working point). Looser selections might be applied in the trigger to achieve an inclusive event selection before offline analysis where tighter selections are made with *all* information available. For the JVT selection to be considered part of the trigger selection, it must be applied to the *same* jets used to make the trigger decision. For multi-jet and single-jet triggers this is straightforward as the JVT selection can be applied at the same time as the kinematic selections, their order does not matter. However, for H_{T} triggers the JVT selection must be applied *before* calculating the H_{T} and making the H_{T} cut. The kinematic requirements for jets subject to JVT selections were applied to `EMPFlow` jets with the same selections as for the offline analysis recommendations – $|\eta| < 2.4$ and $20 < p_{\mathrm{T}}$ (GeV) < 60. The detector η coordinate measured with respect to the geometric centre of the detector is typically used for the kinematic selection before the JVT cut, but we used the jet η instead, so some differences between the jets to which JVT is applied can be expected.

The incorporation of JVT selections into the trigger selections leads to little variation in signal acceptances for the MC16a event sample results in Tables 5.6 and 5.7 for the UDS and UDB decay mode, respectively. For signal jets that originate from the hard-scatter vertex, the JVT likelihood is close to 1.0 [41] and in a sample where pile-up is not dominant (e.g. compared to later years of Run 2 or expectations for Run 3 and the HL-LHC) these effects lead to very small changes to the trigger acceptance with loose JVT cuts in Tables 5.6a and 5.7a. Tighter, JVT > 0.5, selections lead to more variation in the signal acceptance, but no change larger than 1% relative to the results with a looser selection is seen. Additionally, the trigger signatures most affected by the JVT selections have a significant jet multiplicity requirement (e.g. HLT asymmetric-threshold 4-jet triggers). It is more likely that a lower p_{T} jet fails the JVT requirement when multiple jets are considered in the trigger selection. Although the trigger chains from the pre-selection studies are included in these tables they should not be considered in detail – the pre-selection is only applied to calorimeter jets in practice so tracking (and JVT selections) would not be possible.

Similar outcomes are evident when the combined MC16 samples are evaluated, but those results are not included. Like for the MC16a event sample, triggers with multi-jet requirements at the HLT (i.e. not a single-jet `j20`) selection have larger differences (smaller than 1% for tighter JVT > 0.5 selections) in signal acceptances between the JVT selections considered. For both the MC16a and combined MC16 samples, the decrease in signal acceptance with a JVT selection is mass-dependent – the acceptance of higher mass signals is less affected by a JVT selection. These features are explained by the relative abundance of lower p_{T} jets from a low-mass resonance compared to that for a higher mass resonance.

Small changes in signal acceptances after emulating JVT cuts in trigger selections are expected given the relatively low level of pile-up in the MC16a event sample (compared to Run 3 expectations) and the fact that signal jets are known to originate from a hard-scatter interaction. Nonetheless, the offline JVT selection does not exactly reflect JVT selections applied at trigger-level, especially where different kinematic requirements may exist for the JVT selection. The use of a looser kinematic selection may lead to further decreases in the signal event acceptance where JVT selections are applied higher p_{T} jets. Nonetheless, since the signal jets originate from the hard-scatter interaction the change will likely still be small with the effect of rejecting any reconstructed events where pile-up jets contaminate the objects considered by trigger decisions. The impact of JVT selections on backgrounds including QCD jet production is more important for consideration but was not studied. Soft QCD jet radiation looks quite like pile-up and therefore its rejection with JVT provides another avenue to higher purity data containing background events from known resonances (e.g. $t\bar{t}$) and (hopefully!) events from an unobserved signal process.

Table 5.6: HLT chain acceptance fractions for MC16a UDS signal points with different JVT selections.

(a) JVT > 0.2 selection.

Trigger	$m_g = 100$ GeV	$m_g = 200$ GeV	$m_g = 300$ GeV	$m_g = 400$ GeV
HLT_4j45_L14J15p0ETA25	0.1028 ± 0.0001	0.602 ± 0.0007	0.8823 ± 0.001	0.9591 ± 0.002
HLT_4j40_L14J15p0ETA25	0.1397 ± 0.0001	0.6794 ± 0.0006	0.9097 ± 0.001	0.9679 ± 0.002
HLT_4j25_L14J15p0ETA25	0.213 ± 0.0001	0.7576 ± 0.0006	0.9312 ± 0.001	0.9744 ± 0.001
HLT_j180_L1HT190-J15s5pETA21	$0.0316 \pm 5 \times 10^{-5}$	0.2145 ± 0.0006	0.5369 ± 0.002	0.8076 ± 0.003
HLT_4j50_L1HT190-J15s5pETA21	0.0447 ± 0.0001	0.3952 ± 0.0007	0.8034 ± 0.002	0.9407 ± 0.002
HLT_4j45_L1HT190-J15s5pETA21	0.053 ± 0.0001	0.4404 ± 0.0007	0.8412 ± 0.001	0.9557 ± 0.002
HLT_4j40_L1HT190-J15s5pETA21	0.0607 ± 0.0001	0.4769 ± 0.0007	0.8672 ± 0.001	0.9658 ± 0.002
HLT_4j20_L1HT190-J15s5pETA21	0.0805 ± 0.0001	0.5408 ± 0.0007	0.9037 ± 0.001	0.9797 ± 0.001
HLT_j20_L14J15	0.2552 ± 0.0001	0.8027 ± 0.0005	0.9521 ± 0.0008	0.9838 ± 0.001
HLT_j20_L14J15p0ETA25	0.2205 ± 0.0001	0.7605 ± 0.0006	0.932 ± 0.001	0.9746 ± 0.001
HLT_j20_JetDS_L1J100	0.0668 ± 0.0001	0.3657 ± 0.0007	0.7336 ± 0.002	0.9284 ± 0.002
HLT_j20_JetDS_L1HT190-J15s5pETA21	0.0832 ± 0.0001	0.544 ± 0.0007	0.9052 ± 0.001	0.9804 ± 0.001
HLT_j60_j45_2j20_JetDS_L1J45p0ETA21_3J15p0ETA25	0.2449 ± 0.0001	0.847 ± 0.0005	0.9795 ± 0.0005	$0.9961^{+0.0005}_{-0.0006}$
HLT_j80_j55_j28_j20_L1J45p0ETA21_3J15p0ETA25	0.2058 ± 0.0001	0.8132 ± 0.0005	0.9763 ± 0.0006	$0.9958^{+0.0005}_{-0.0006}$
HLT_4j120	$0.001 \pm 1 \times 10^{-5}$	0.0189 ± 0.0002	0.1002 ± 0.001	0.2701 ± 0.004
HLT_5j70_0eta240_L14J15	$0.0025 \pm 1 \times 10^{-5}$	0.0528 ± 0.0003	0.2275 ± 0.002	0.4585 ± 0.004
HLT_ht1000_L1J100	$0.0013 \pm 1 \times 10^{-5}$	0.0194 ± 0.0002	0.0917 ± 0.001	0.2528 ± 0.004

(b) JVT > 0.5 selection.

Trigger	$m_g = 100$ GeV	$m_g = 200$ GeV	$m_g = 300$ GeV	$m_g = 400$ GeV
HLT_4j45_L14J15p0ETA25	0.1015 ± 0.0001	0.5985 ± 0.0007	0.8811 ± 0.001	0.9587 ± 0.002
HLT_4j40_L14J15p0ETA25	0.1376 ± 0.0001	0.6748 ± 0.0006	0.9084 ± 0.001	0.9674 ± 0.002
HLT_4j25_L14J15p0ETA25	0.2104 ± 0.0001	0.756 ± 0.0006	0.9308 ± 0.001	0.9743 ± 0.001
HLT_j180_L1HT190-J15s5pETA21	$0.0316 \pm 5 \times 10^{-5}$	0.2145 ± 0.0006	0.5369 ± 0.002	0.8076 ± 0.003
HLT_4j50_L1HT190-J15s5pETA21	0.0444 ± 0.0001	0.3941 ± 0.0007	0.8025 ± 0.002	0.9402 ± 0.002
HLT_4j45_L1HT190-J15s5pETA21	0.0527 ± 0.0001	0.4388 ± 0.0007	0.84 ± 0.001	0.9552 ± 0.002
HLT_4j40_L1HT190-J15s5pETA21	0.0604 ± 0.0001	0.4747 ± 0.0007	0.866 ± 0.001	0.9654 ± 0.002
HLT_4j20_L1HT190-J15s5pETA21	0.0802 ± 0.0001	0.5402 ± 0.0007	0.9033 ± 0.001	0.9796 ± 0.001
HLT_j20_L14J15	0.2552 ± 0.0001	0.8027 ± 0.0005	0.9521 ± 0.0008	0.9838 ± 0.001
HLT_j20_L14J15p0ETA25	0.2205 ± 0.0001	0.7605 ± 0.0006	0.932 ± 0.001	0.9746 ± 0.001
HLT_j20_JetDS_L1J100	0.0668 ± 0.0001	0.3657 ± 0.0007	0.7336 ± 0.002	0.9284 ± 0.002
HLT_j20_JetDS_L1HT190-J15s5pETA21	0.0832 ± 0.0001	0.544 ± 0.0007	0.9052 ± 0.001	0.9804 ± 0.001
HLT_j60_j45_2j20_JetDS_L1J45p0ETA21_3J15p0ETA25	0.2425 ± 0.0001	0.8454 ± 0.0005	$0.979^{+0.0005}_{-0.0006}$	$0.996^{+0.0005}_{-0.0006}$
HLT_j80_j55_j28_j20_L1J45p0ETA21_3J15p0ETA25	0.2042 ± 0.0001	0.8114 ± 0.0005	0.9759 ± 0.0006	$0.9957^{+0.0005}_{-0.0006}$
HLT_4j120	$0.001 \pm 1 \times 10^{-5}$	0.0189 ± 0.0002	0.1002 ± 0.001	0.2701 ± 0.004
HLT_5j70_0eta240_L14J15	$0.0025 \pm 1 \times 10^{-5}$	0.0528 ± 0.0003	0.2275 ± 0.002	0.4585 ± 0.004
HLT_ht1000_L1J100	$0.0013 \pm 1 \times 10^{-5}$	0.0193 ± 0.0002	0.0912 ± 0.001	0.2515 ± 0.004

Table 5.7: HLT chain acceptance fractions for MC16a UDB signal points with different JVT selections.

(a) JVT > 0.2 selection.

Trigger	$m_g = 100$ GeV	$m_g = 200$ GeV	$m_g = 300$ GeV	$m_g = 400$ GeV
HLT_4j45_L14J15p0ETA25	0.0929 ± 0.0001	0.5745 ± 0.0007	0.8681 ± 0.001	0.9535 ± 0.002
HLT_4j40_L14J15p0ETA25	0.1248 ± 0.0001	0.6529 ± 0.0007	0.8978 ± 0.001	0.9639 ± 0.002
HLT_4j25_L14J15p0ETA25	0.1888 ± 0.0001	0.7297 ± 0.0006	0.9219 ± 0.001	0.9716 ± 0.001
HLT_j180_L1HT190-J15s5pETA21	$0.0315 \pm 5 \times 10^{-5}$	0.2059 ± 0.0006	0.5175 ± 0.002	0.7957 ± 0.003
HLT_4j50_L1HT190-J15s5pETA21	0.0408 ± 0.0001	0.3654 ± 0.0007	0.7824 ± 0.002	0.932 ± 0.002
HLT_4j45_L1HT190-J15s5pETA21	0.0484 ± 0.0001	0.4084 ± 0.0007	0.8214 ± 0.002	0.9491 ± 0.002
HLT_4j40_L1HT190-J15s5pETA21	0.0552 ± 0.0001	0.4445 ± 0.0007	0.8487 ± 0.001	0.961 ± 0.002
HLT_4j20_L1HT190-J15s5pETA21	0.0722 ± 0.0001	0.5087 ± 0.0007	0.8884 ± 0.001	0.9772 ± 0.001
HLT_j20_L14J15	0.2285 ± 0.0001	0.776 ± 0.0006	0.9441 ± 0.0009	0.9809 ± 0.001
HLT_j20_L14J15p0ETA25	0.1947 ± 0.0001	0.7322 ± 0.0006	0.9223 ± 0.001	0.9718 ± 0.001
HLT_j20_JetDS_L1J100	0.0645 ± 0.0001	0.35 ± 0.0007	0.7127 ± 0.002	0.9177 ± 0.002
HLT_j20_JetDS_L1HT190-J15s5pETA21	0.0747 ± 0.0001	0.5127 ± 0.0007	0.8901 ± 0.001	0.9779 ± 0.001
HLT_j60_j45_2j20_JetDS_L1J45p0ETA21_3J15p0ETA25	0.2234 ± 0.0001	0.8233 ± 0.0005	0.9759 ± 0.0006	$0.9954^{+0.0005}_{-0.0006}$
HLT_j80_j55_j28_j20_L1J45p0ETA21_3J15p0ETA25	0.1906 ± 0.0001	0.7885 ± 0.0006	0.972 ± 0.0006	0.9949 ± 0.0006
HLT_4j120	$0.0009 \pm 1 \times 10^{-5}$	0.0188 ± 0.0002	0.0878 ± 0.001	0.2514 ± 0.004
HLT_5j70_0eta240_L14J15	$0.0028 \pm 1 \times 10^{-5}$	0.0502 ± 0.0003	0.2084 ± 0.002	0.4352 ± 0.004
HLT_ht1000_L1J100	$0.0013 \pm 1 \times 10^{-5}$	0.0177 ± 0.0002	0.0826 ± 0.001	0.2384 ± 0.004

(b) JVT > 0.5 selection.

Trigger	$m_g = 100$ GeV	$m_g = 200$ GeV	$m_g = 300$ GeV	$m_g = 400$ GeV
HLT_4j45_L14J15p0ETA25	0.0921 ± 0.0001	0.5719 ± 0.0007	0.8671 ± 0.001	0.9533 ± 0.002
HLT_4j40_L14J15p0ETA25	0.1232 ± 0.0001	0.65 ± 0.0007	0.8968 ± 0.001	0.9636 ± 0.002
HLT_4j25_L14J15p0ETA25	0.1871 ± 0.0001	0.7287 ± 0.0006	0.9216 ± 0.001	0.9715 ± 0.001
HLT_j180_L1HT190-J15s5pETA21	$0.0315 \pm 5 \times 10^{-5}$	0.2059 ± 0.0006	0.5175 ± 0.002	0.7957 ± 0.003
HLT_4j50_L1HT190-J15s5pETA21	0.0408 ± 0.0001	0.3645 ± 0.0007	0.7816 ± 0.002	0.9318 ± 0.002
HLT_4j45_L1HT190-J15s5pETA21	0.0482 ± 0.0001	0.4072 ± 0.0007	0.8206 ± 0.002	0.9488 ± 0.002
HLT_4j40_L1HT190-J15s5pETA21	0.0549 ± 0.0001	0.4432 ± 0.0007	0.8479 ± 0.001	0.9607 ± 0.002
HLT_4j20_L1HT190-J15s5pETA21	0.0719 ± 0.0001	0.5082 ± 0.0007	0.8881 ± 0.001	0.9771 ± 0.001
HLT_j20_L14J15	0.2285 ± 0.0001	0.776 ± 0.0006	0.9441 ± 0.0009	0.9809 ± 0.001
HLT_j20_L14J15p0ETA25	0.1947 ± 0.0001	0.7322 ± 0.0006	0.9223 ± 0.001	0.9718 ± 0.001
HLT_j20_JetDS_L1J100	0.0645 ± 0.0001	0.35 ± 0.0007	0.7127 ± 0.002	0.9177 ± 0.002
HLT_j20_JetDS_L1HT190-J15s5pETA21	0.0747 ± 0.0001	0.5127 ± 0.0007	0.8901 ± 0.001	0.9779 ± 0.001
HLT_j60_j45_2j20_JetDS_L1J45p0ETA21_3J15p0ETA25	0.2218 ± 0.0001	0.8219 ± 0.0005	0.9756 ± 0.0006	0.9953 ± 0.0006
HLT_j80_j55_j28_j20_L1J45p0ETA21_3J15p0ETA25	0.1893 ± 0.0001	0.7871 ± 0.0006	0.9718 ± 0.0006	0.9949 ± 0.0006
HLT_4j120	$0.0009 \pm 1 \times 10^{-5}$	0.0188 ± 0.0002	0.0878 ± 0.001	0.2514 ± 0.004
HLT_5j70_0eta240_L14J15	$0.0028 \pm 1 \times 10^{-5}$	0.0502 ± 0.0003	0.2084 ± 0.002	0.4352 ± 0.004
HLT_ht1000_L1J100	$0.0013 \pm 1 \times 10^{-5}$	0.0177 ± 0.0002	0.0823 ± 0.001	0.2375 ± 0.004

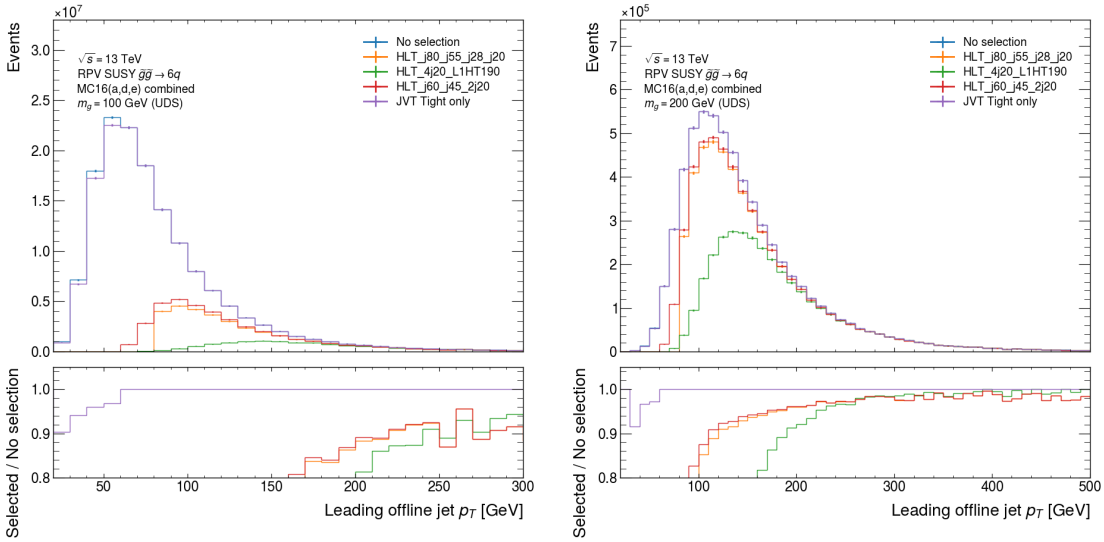

(a) $m_{\tilde{g}} = 100$ GeV

(b) $m_{\tilde{g}} = 200$ GeV

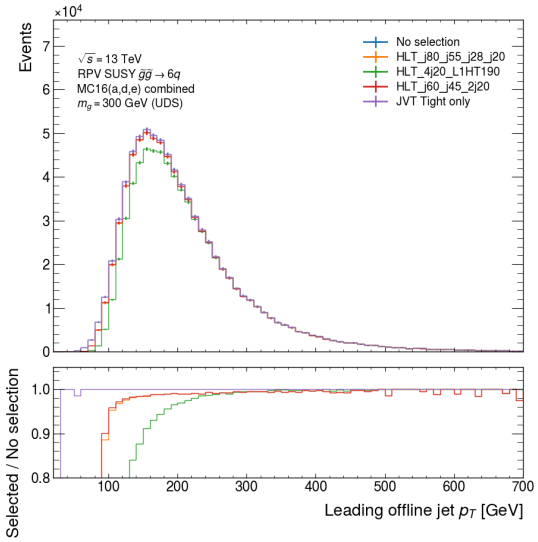

(c) $m_{\tilde{g}} = 300$ GeV

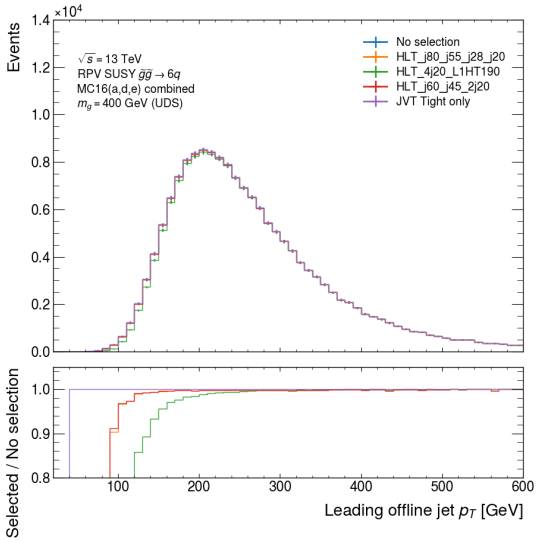

(d) $m_{\tilde{g}} = 400$ GeV

Figure 5.30: Plots of the leading jet p_{T} distributions for all UDS gluino pair-production signals without any selections (blue), with only JVT selections (purple), and with both JVT and trigger selections applied (orange, red, and green). The trigger selections are abbreviated such that `HLT_j80_j55_j28_j20` (orange) and `HLT_j60_j45_2j20` (red) are the two asymmetric threshold triggers with an `L1J45p0ETA21_3J15p0ETA25` seed. The final trigger selection (green) is the `HLT_4j20_L1HT190-J15s5pETA21` selection.

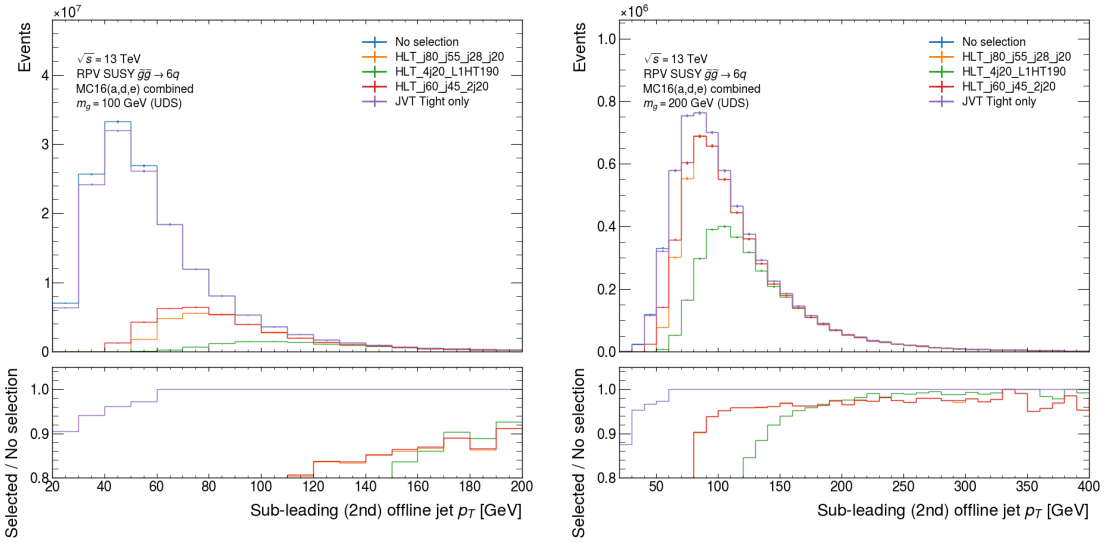

(a) $m_{\tilde{g}} = 100$ GeV

(b) $m_{\tilde{g}} = 200$ GeV

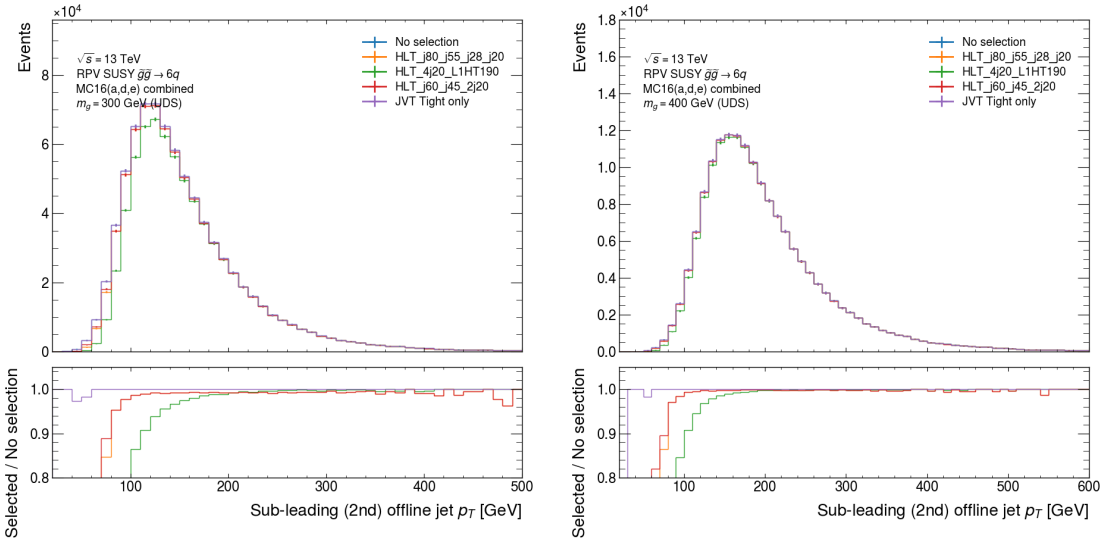

(c) $m_{\tilde{g}} = 300$ GeV

(d) $m_{\tilde{g}} = 400$ GeV

Figure 5.31: Plots of the sub-leading (2nd) jet p_{T} distributions for all UDS gluino pair-production signals without any selections (blue), with only JVT selections (purple), and with both JVT and trigger selections applied (orange, red, and green). The trigger selections are abbreviated such that `HLT_j80_j55_j28_j20` (orange) and `HLT_j60_j45_2j20` (red) are the two asymmetric threshold triggers with an `L1J45p0ETA21_3J15p0ETA25` seed. The final trigger selection (green) is the `HLT_4j20_L1HT190-J15s5pETA21` selection.

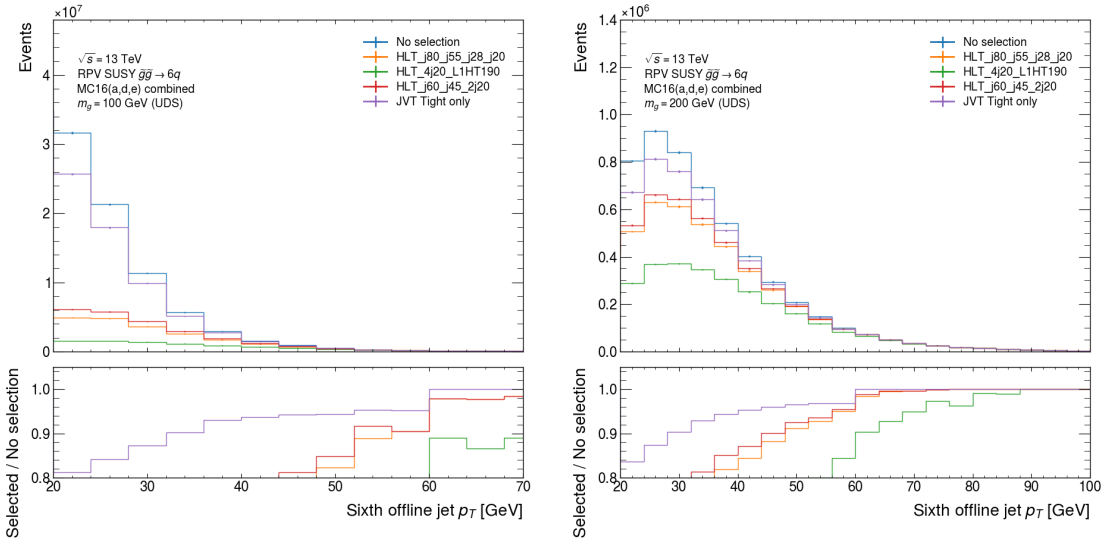

(a) $m_{\tilde{g}} = 100$ GeV (b) $m_{\tilde{g}} = 200$ GeV

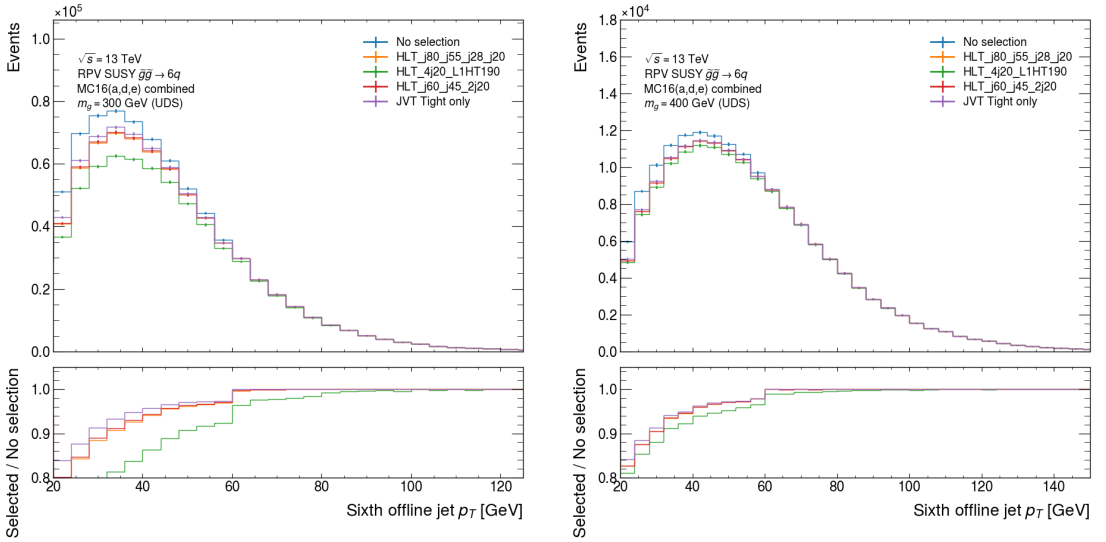

(c) $m_{\tilde{g}} = 300$ GeV (d) $m_{\tilde{g}} = 400$ GeV

Figure 5.32: Plots of the sixth-leading jet p_{T} distributions for all UDS gluino pair-production signals without any selections (blue), with only JVT selections (purple), and with both JVT and trigger selections applied (orange, red, and green). The trigger selections are abbreviated such that `HLT_j80_j55_j28_j20` (orange) and `HLT_j60_j45_2j20` (red) are the two asymmetric threshold triggers with an `L1J45p0ETA21_3J15p0ETA25` seed. The final trigger selection (green) is the `HLT_-4j20_L1HT190-J15s5pETA21` selection.

5.10 Summary and Run 3 Outlook

Run 3 of the LHC provides a unique and very exciting opportunity to continue the development of real-time analysis strategies and search for challenging signatures of new physics. This Chapter has provided an introduction to Trigger-object Level Analysis and some of its intricacies, expanding on the introduction to ATLAS TDAQ in Section 3.2.6. From our studies of the trigger acceptances for gluino pair-production signals it is evident that events from the lowest mass signal points are best identified with loose kinematic thresholds in trigger chains. Trigger signatures involving loose (asymmetric) multi-jet selections are therefore favoured. The use of Level-1 triggers with a H_{T} selection, but without explicit jet multiplicity or high single-jet E_{T} thresholds, produces a significant signal acceptance benefit compared to the baseline $E_{\mathrm{T}} > 100$ GeV single-jet trigger. The ability of these triggers to encapsulate an estimate of the total hadronic activity of events may prove useful for a wider range of signal processes than that studied in this work, so should be considered further.

While our results do not suggest that pile-up mitigation techniques penalise the acceptance of multi-jet signals considerably, further investigation into these techniques is necessary – especially because higher pile-up levels are anticipated in Run 3 and at the HL-LHC. Further studies should aim to emulate the complete trigger decision process from the L1 trigger to HLT event selections. Additional studies could explore new techniques (e.g. machine learning for fast pile-up rejection) currently proposed for use in the ATLAS trigger and consider their effect on both signal and background processes. The effect of JVT selections on signal events should also be explored further using dedicated trigger-level JVT recommendations rather than those tuned for offline analyses. A consideration of the overlap of different triggers (i.e. where the same event passes several different trigger selections) for the signal samples could also be useful. At analysis-level, performing a study of the frequency with which pile-up jets are mis-combined with signal jets using combinatorial techniques could provide an additional measure of pile-up contamination.

Chapter 6

Trigger-object Level Analysis Projections for the HL-LHC

The commissioning and operation of the HL-LHC will see the collection of 3000 fb^{-1} (integrated luminosity) of collision data with much higher instantaneous luminosities and therefore increased pile-up levels. High pile-up conditions at the HL-LHC will lead to a more significant low-momentum contribution to kinematic distributions than in Run 2 and Run 3 reducing sensitivity to low-mass resonances. This is an important consideration for "bump hunt" searches like Ref. [92, 109] where the invariant mass distributions of objects and their resolution governs the sensitivity of analyses. Therefore, to obtain meaningful results with TLA, high performance pile-up rejection techniques are imperative. This might involve using charged particle tracks to distinguish hard-scatter vertices from pile-up vertices, an existing technique used in Run 2 and 3 of the LHC.

Since the LHC and the ATLAS detector is not yet configured for data-taking in these conditions, we are limited to studying HL-LHC performance in simulation. This Chapter presents the initial results and preparations for studies to inform the development of ATLAS TDAQ frameworks for trigger-level analyses at the HL-LHC. This work is not yet complete, so the final Sections of this Chapter aim to address the future direction of these studies. The sensitivity of the ATLAS experiment to multi-jet signals from $\tilde{g}\tilde{g} \to 6q$ is considered foremost. However, the key results from these studies are relevant for any search for low-mass BSM physics with hadronic (multi-jet) signatures, including an extrapolation to electroweakino production cross-sections in Section 6.4.2.

The MC samples for these studies are introduced in Section 6.1. A discussion of the analysis workflow adopted from previous searches is discussed in Sections 6.2 and 6.3. A simple optimisation procedure for the analysis is detailed in Section 6.4. Finally, Sections 6.5 and 6.6 provides a discussion of future work that is necessary and a summary of the status of these studies.

6.1 Simulated event samples

6.1.1 Signal samples

The same $\tilde{g}\tilde{g} \to 6q$ signal process as used for the Run 3 TLA studies in Chapter 5 was considered, but a different (smaller) version of the samples was used (a note on the samples is included at the end of this Section). An extrapolation procedure is applied to the signal samples to scale the CM frame energy of the pp collision from $\sqrt{s} = 13$ TeV to $\sqrt{s} = 14$ TeV. No additional pile-up simulation was added, so these samples are limited to the comparatively low pile-up of Run 2 and the corresponding ATLAS detector geometry. Importantly, this means that the $|\eta|$ limit of the tracking acceptance is still $|\eta| = 2.5$ (not $|\eta| = 4.0$, anticipated for the ATLAS Inner-tracker at the HL-LHC). Therefore, these upgrade studies are limited to selections on central jets within the Run 2 tracking acceptance for consistency. The CM frame energy of the samples is scaled to $\sqrt{s} = 14$ TeV using ratios of PDFs (parton distribution functions). For these studies we used the `NNPDF23_lo_as_0130_qed` PDF with QED corrections [100], which was used in the simulation of the signal samples, accessible from LHAPDF6 [110]. The implementation for this scaling is based on the PDF re-weighting scheme implemented in the `SimpleAnalysis` [111] framework. The nominal event weights (we do not consider systematic variations) for the sample were scaled by:

$$\mathcal{W}_{\text{SF}} = \prod_{i=1,2} \frac{x_{i,\text{out}} f(x_{i,\text{out}}, q)}{x_{i,\text{in}} f(x_{i,\text{in}}, q)} \tag{6.1}$$

where x_i is the fraction of the proton momentum carried by the particles participating in the interaction [112] and f is the PDF evaluated at x_i and scale q. Every $x_{i,\text{out}}$ is calculated by multiplying the original $x_{i,\text{in}}$ by the ratio $\sqrt{s}_{\text{in}}/\sqrt{s}_{\text{out}} = 13/14$ [113]. Evidently, this means that the region where $x > 13/14 \approx 0.92857$ was not considered, and we lose a region of the parameter space where partons participating in the pp interaction carry a fraction of the proton momentum close to 100% [113]. An alternate extrapolation procedure may eventually need to be considered for this reason. After re-scaling the event weights using PDFs, the sum of the weights for each sample was recalculated to correctly scale the histograms/weights when different samples (MC16a,d,e as in Chapter 5) were combined and when signal yields were calculated. To combine the signal samples from the MC16 ATLAS sample production campaigns a luminosity weighting scheme was used like that applied for the signal samples from Chapter 5.

The $\sqrt{s} = 14$ TeV gluino pair-production cross-sections from Ref. [114, 115] were used to ensure the signal yields were correctly normalised. These cross-sections were calculated for models where the squarks are decoupled (i.e. no interactions considering squarks occur) by setting their masses to large values compared to the gluino mass [114, 115]. The signal cross-sections used for these studies are shown in Table 6.1, and are on the order of double the $\sqrt{s} = 13$ TeV cross-sections for the

samples used in Chapter 5. Thus, we could expect an enhancement in the rate at which gluinos are pair-produced at the HL-LHC (if RPV SUSY exists).

Table 6.1: Signal cross-sections at $\sqrt{s} = 14$ TeV used for the studies in this Chapter. No cross-section is currently available for the $m_{\tilde{g}} = 100$ GeV signal for these studies. The $\sqrt{s} = 13$ TeV cross-sections are taken from the meta-data for the original ATLAS MC samples. The $\sqrt{s} = 14$ TeV cross-sections are based on NLO+NLL (next-to-leading order and next-to-leading logarithm for higher-order corrections) calculations provided by the LHC Physics Working Group [114, 115]. Although uncertainties for the $\sqrt{s} = 14$ TeV cross-sections exist, they were not considered in these studies.

$m_{\tilde{g}}$ (GeV)	$\sigma_{\tilde{g}\tilde{g}}(\sqrt{s} = 13$ TeV) (pb)	$\sigma_{\tilde{g}\tilde{g}}(\sqrt{s} = 14$ TeV) (pb)
100	50100	–
200	2050	4277.01
300	264	568.096
400	55.500	123.307

Like for the Run 3 studies, negatively weighted events produced by the MadGraph generator were encountered in these samples. However, for the purposes of signal and background comparisons, we did not remove them and instead followed a similar approach to that mentioned in Section 5.2.1. It is possible that the negatively weighted events could lead to problems during a statistical analysis of the results (e.g. in code frameworks), so the incorporation of a method to deal with negative event weights is left for further studies if it becomes necessary.

A note on the signal samples

The signal samples used for the studies presented in this Chapter were different from those used for the earlier Run 3 TLA studies in Chapter 5. For these studies, the samples correspond to a smaller collection of events for each gluino mass point (before a statistics extension was completed). At the time of writing this thesis, these samples are being replaced due to an issue in their generation that affects the replicability of results. Thus, the results included in this Chapter will eventually be reprocessed with the newer datasets, and they should not be considered as a complete/precision analysis, but as a means to document the framework and procedure for these studies. The final Sections of this Chapter highlight further work that will be done to reach a final set of projections with the newest samples.

6.1.2 Background samples

Prominent fully hadronic background processes including $t\bar{t}$ and QCD dijet production are considered for the background estimation component of these studies. All the background samples were officially produced by the ATLAS Collaboration and simulated at $\sqrt{s} = 14$ TeV with μ between 190 and 210 to emulate the HL-LHC conditions.

QCD background samples

The QCD background contribution was estimated from MC simulations of QCD dijet production where the emission of extra jet radiation besides the two highest p_{T} jets was interpreted as a multi-jet process (as in Ref. [109]). The event samples were simulated in Pythia 8.240 [98] and EvtGen 1.7.0 [99] with the A14 PDF tune [116] and NNPDF23LO PDF set [117]. The dijet samples were sliced according to the p_{T} of truth-level jets to adequately sample the complete momentum range for jet production. For this reason, additional re-weighting steps were conducted using the cross-section, filter-efficiency (from the MC generator), and the weighted number of events processed for each slice[1]. This produced a p_{T} spectrum without un-physical fluctuations at the edges of each slice. Examples of some processes involving quarks (straight line) and gluons (curly lines) which can contribute to these events are shown in Figure 6.1.

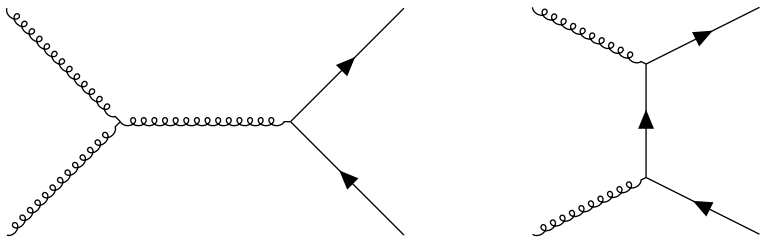

Figure 6.1: Examples of purely hadronic dijet processes seen at the LHC adapted from [118]. The inclusion of additional gluon or quarks in the final state leads to multi-jet processes with additional radiated jets. In principle, these diagrams can be modified by interchanging quarks and gluons provided each interaction vertex is permitted by QCD [118].

To reach the required pile-up levels of the HL-LHC, minimum-bias (pile-up) events were overlaid in the creation of the samples. Since the samples are sliced in the truth jet p_{T}, there are cases where the p_{T} of pile-up jets in low-momentum slices exceeds that of hard-scatter jets. The low-p_{T} slices contribute larger weights to the final distributions, which causes unphysical fluctuations in the jet p_{T} distribution where this occurs. To remedy this, an event selection was applied using truth information to determine whether the event contained spurious pile-up jets[2]. Events where the

[1] As for the combination of signal samples from different MC campaigns.

[2] The author thanks Dag Gillberg and Jeff Dandoy for providing feedback on methods for cleaning the dijet samples and suggesting this approach.

leading (highest p_{T}) jet from a collection of in-time pile-up (within a bunch crossing) jets has a p_{T} exceeding that of the leading hard-scatter jet in the event were vetoed. The leading jet p_{T} distributions for the QCD samples before and after applying this cleaning method are shown in Figure 6.2. From the ratio panel, it is clear that the event selection removes much of the contamination from pile-up overlay and produces a spectrum closer to that of truth (particle-level) jets but with inherent differences from the effects of pile-up.

A break-down of the efficiencies of the cleaning method for several dijet p_{T} slices is shown in Table 6.2. These values were calculated by determining the ratio of integrals over the leading truth jet p_{T} distribution before and after application of the cleaning method. Critically, the low-p_{T} and pile-up dominated `JZ0WithSW` slice contains events where the truth jets have insufficient p_T (lower than 5 GeV) for the jet-finder, and they are not saved in datasets. These events are skipped by default since they likely would not pass the cleaning requirements and are therefore not included in the efficiency calculation for `JZ0WithSW`. Consequently, the `JZ0WithSW` efficiency value is an estimate of the upper efficiency limit only. Since the `JZ0WithSW` sample contains such low-p_{T} jets we do not expect it to contribute to the analysis, the majority of the events would be removed by the cleaning method.

Table 6.2: Efficiencies estimated for the dijet sample cleaning procedure. The dijet slices `JZXWithSW` are sorted in order of increasing p_{T} for the truth jets in the samples. The higher p_{T} dijet slices are combined into a single entry since their cleaning efficiencies are identical.

Dijet slice	Estimated efficiency of cleaning selection
`JZ0WithSW`	< 0.0003
`JZ1WithSW`	0.1494
`JZ2WithSW`	0.9586
`JZ3WithSW`	0.9994
`JZ3WithSW`	$0.99997 \approx 1.0$
`JZXWithSW` $(X = 4, \ldots, 7)$	1.0

Top quark background

Standard Model top quark pair-production ($t\bar{t}$) is potentially an irreducible background in the search for a gluino pair production signal, particularly if the signal final state contains two b-jets like a Standard Model hadronic $t\bar{t}$ decay. Events containing b-jets could be vetoed to reduce the $t\bar{t}$ contribution in searches for gluino pair-production with light-jet (UDS) final states but this procedure is not explored in the results presented in this Chapter. Like the signal, the $t\bar{t}$ process produces six jets (3 from each top quark) and should appear as a resonance around $172 - 173$ GeV in the 3-jet invariant mass (m_{jjj}) distribution. This likely leads to a departure from smooth background distributions for low-mass searches [109] and is therefore

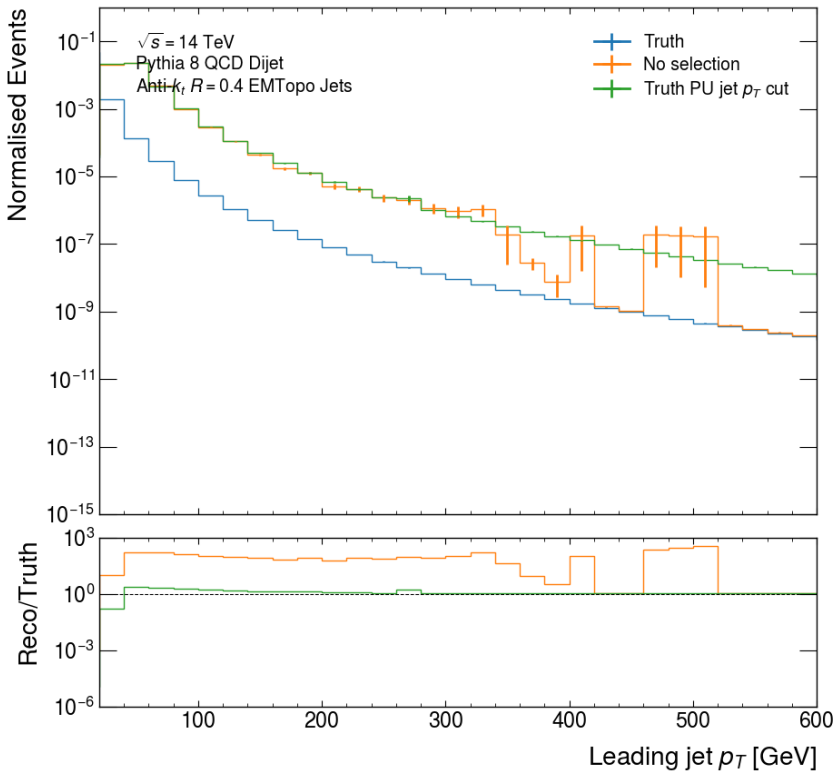

Figure 6.2: The leading jet p_{T} distribution for the combined QCD dijet slices after the application of the pile-up overlay cleaning technique. The ratio panel illustrates the agreement of reconstructed and truth jet information before and after the event selection. The legend entries correspond to truth particle-level jets (*Truth*), the uncorrected `EMTopo` (calibrated) jet p_T (*No selection*), and the corrected `EMTopo` jet distribution (*Truth PU jet* p_T *cut*). Note that the normalisation for the y-axis is actually the result of a density calculation.

a significant factor to consider. Standard Model $t\bar{t}$ production was simulated at $\sqrt{s} = 14$ TeV using Powheg (05–00 ATLAS version) [119–121], Pythia 8.245 [98], and EvtGen 1.7.0 [99] in a fully hadronic final state. The generator-level event sample was passed through the same reconstruction chain as for the QCD background samples to obtain a reconstructed event sample with the same detector conditions.

6.1.3 Event reconstruction and jet calibration

The event and jet reconstruction methods applied for these TLA upgrade studies were similar to those used for the Run 3 studies. Where necessary, different calibrations were applied, and since the HL-LHC jet energy scale calibration is currently only configured for `EMTopo`[3] jets we restricted our analysis to these objects. With the development of more performant `PFlow` and Unified Flow Object jet inputs it is possible (and likely) that jets reconstructed in the software trigger (that would be stored in trigger-level analyses) would not consist of calorimeter-only information. The use of tracking information in `PFlow`-like jets will be particularly important for the rejection of pile-up at the HL-LHC.

As in the Run 3 studies no lepton or photon reconstruction was considered for these studies since the final states for the signal and background consist purely of hadronic jets.

Signal jet reconstruction

The signal jet reconstruction applied for the upgrade studies was the same as that in Chapter 5 and no further modifications were made to the signal samples except for the event weight scaling discussed earlier. Importantly, the same calibration recommendations as for the Run 3 studies (albeit for `EMTopo` jets instead of `EMPFlow` jets) were used since the HL-LHC calibration discussed next is only configured for samples that use the expected HL-LHC ATLAS detector geometry.

Background jet reconstruction

The background jet (QCD and $t\bar{t}$) reconstruction differs from the signal jet reconstruction with respect to the jet calibrations. For the signal jets both the Global Sequential Calibration and a smearing step were applied. However, these steps were not taken for the background samples. Only the jet area and residual pile-up corrections in combination with the jet η and energy scale corrections were applied. The background jet calibration was derived in HL-LHC conditions, so it varies quite significantly compared to the version applied to signal jets.

[3] Jets reconstructed from calorimeter topoclusters with an electromagnetic energy scale (no calibrations for correcting the energy of hadronic deposits due to the non-compensating nature of the calorimeters).

6.2 Similarities with Run 2 CMS data-scouting searches

A recent search for pair-produced 3-jet resonances was conducted by CMS [109], with a focus on the same $\tilde{g}\tilde{g} \rightarrow 6q$ signal studied in this Chapter. The significance of this analysis for these studies is that the low-mass search used *Data Scouting* (another term for TLA). For the purposes of background estimation, the HL-LHC upgrade studies presented in this Chapter aim to follow the same method as that applied in the CMS search. Rather than using an alternate approach where various control and validation regions are defined, CMS used smooth functions validated in simulation and fitted to data to estimate the contribution of multi-jet QCD and $t\bar{t}$ background processes [109].

Discrimination between the signal and dominant QCD background process was achieved with *jet ensemble methods*, which consider the kinematic and topological properties of several jets [109]. The jet ensembles are defined both at event-level (a 6-jet event) and at triplet-level (3-jet "triplets" as would be expected from the gluino decays). Differences in the shape of triplet- and event-level variables between the signal and QCD background were exploited to identify a region with comparatively low background contamination [109]. The combinatorial analysis associated with this approach introduces an additional source of background – incorrectly combined signal jet triplets – modelled using the template functions fit to the background [109].

Similar analysis techniques (with key differences relating to the use of Dalitz variables in the more recent CMS search [109]) have been applied in several previous analyses by CMS [122, 123] at $\sqrt{s} = 7, 8$ TeV and by CDF in lower energy $p\bar{p}$ collisions [124]. A similar low-mass signal topology was considered for a multi-jet ATLAS search but a different background estimation method, not reliant on fitting smooth template functions, was used [95].

While the CMS analysis [109] was performed in Run 2 collision conditions, the exploration of these methods in HL-LHC conditions will yield important results associated with the impact of pile-up contamination on these searches. Jet ensemble methods and the observables used in the CMS analysis will be discussed further and defined as needed throughout this Chapter. For the remainder of these studies we will build upon the CMS analysis as a template for the background estimation procedure and selection of signal-like events in a HL-LHC setting.

6.3 Analysis procedure

This Section presents initial comparisons of signal and background distributions for each offline analysis variable that exploits jet-ensemble methods. Note that, where the signal is compared with different backgrounds the y-axis represents a

"Normalised" count, which is in fact a density calculation (the reason the y-axis limits are not always below 1.0). The inclusion of reconstructed and truth-level shapes of the analysis observables in this Section illustrates the impact of pile-up (primarily for the background) on the analysis observables. It is evident that the pile-up contributions to reconstructed jets cause the separation between signal and background distributions for the observables to fall.

These first results were derived with the same kinematic selections as Ref. [109] in Signal Region 1 (SR1, $m_{\tilde{g}} = 200$ GeV to $m_{\tilde{g}} = 400$ GeV). The kinematic pre-selection sequentially requires [109]:

1. At least 6 reconstructed jets ($N_{jets} \geq 6$) with $p_T > 30$ GeV and $|\eta| < 2.4$.
2. The sixth leading jet must have $p_T > 40$ GeV (i.e. the sixth leading jet passing (1))
3. The scalar sum of the p_{T} for the jets passing (1), the H_{T}, must exceed 650 GeV (i.e. $H_T > 650$ GeV).

A variation of this selection is used by CMS in Ref. [109] to ensure the Data-Scouting triggers are 100% efficient for any events passing all later analysis selections. To explore the analysis procedure and emulate the effect of a trigger selection, the same kinematic selections were used. The pre-selection must eventually be modified to study different trigger scenarios with varying trigger signatures.

Only the 4-momentum vectors of the leading 6 jets in events that pass the pre-selection were used for further analysis. From these 4-vectors all possible *distinct* 3-jet combinations (triplets) were determined. The jet triplets were then paired to form *distinct* triplet pairs representative of the topology of the gluino pair-production signal model. The triplet pairing method proceeded such that the first triplet pair contained the leading three jets in the event from the first triplet and the remaining lower-p_{T} jets from the second triplet (i.e. pairing triplets from the outside of the "triplet list" inwards). Alternate methods of pairing the triplets including minimising the invariant mass difference of the triplet pair were not considered but would produce a similar effect to later selections on the *mass asymmetry*. An example of the implementation of the analysis code is available in the MadAnalysis recast of the original CMS analysis, which we drew on for implementing the handling of triplet pairing and the analysis workflow [125].

The jet ensemble variables used throughout the analysis aim to distinguish between signal jet triplets with a symmetric distribution in the gluino CM frame, and the QCD background, which in the CM frame leads to asymmetrically distributed jets. Thus, the discriminating variables from Ref. [109] measure the deviation from a uniform three- (triplet-) or six-jet distribution in the CM frame. Of course, when $t\bar{t}$ backgrounds are considered, the 3-body (hadronic) top quark decay has symmetries that are very similar to the signal, which motivates the inclusion of a functional

form to describe Standard Model $t\bar{t}$ contributions in the background estimation [109].

Firstly, we considered a Dalitz variable defined in terms of the invariant mass of (distinct) pairs of jets taken from a triplet. Adopting the same notation used by CMS this has the form [109]:

$$\hat{m}^2(3,2)_{ij} = \frac{m_{ij}^2}{m_{ijk}^2 + \sum_l m_l^2} \tag{6.2}$$

where $(3,2)$ indicates that the variable is calculated for a triplet (3 jets) using jet pairs (2 jets) taken from the triplet. Here, m_{ij}, m_{ijk}, and m_l are the invariant masses of the jet pair, triplet, and individual jets in the triplet, respectively. The indices run over all three jets within the triplet ($i, j, k, l \in \{1,\ 2,\ 3\}$). Technically, in the context of the six-jet event (after the kinematic selection) these variables could have any indices from 0 to 5 (or 1 to 6 depending on where one specifies the starting point) provided i, j, k, and l are only taken from a sub-set of these indices (3 indices for the triplet) (e.g. 0, 3, 4 would be a valid combination of indices).

The denominator of Equation (6.2) is chosen to normalise the variables between 0 and 1 [109]. For a symmetric signal topology these variables should have values close to 1/3 [109]. However, a consequence of the pairing of jets from the triplet is that the variables do not all cluster around 1/3 in Figure 6.3. Of the three possible pairings, one pair produces the smallest m_{ij} ($\hat{m}^2_{lo}$), another produces the largest m_{ij} ($\hat{m}^2_{hi}$), and the final pairing has m_{ij} between that of the latter pairs ($\hat{m}^2_{mid}$). Plotting pairs of these variables, ($\hat{m}^2_{lo}$, $\hat{m}^2_{hi}$), ($\hat{m}^2_{lo}$, $\hat{m}^2_{mid}$), and ($\hat{m}^2_{mid}$, $\hat{m}^2_{hi}$) produces a *normalised Dalitz plot* [109] shown in Figure 6.4. This visualisation shows the clear discrimination power these variables can provide – the signal and QCD triplets cluster at the centre and edges of the plots in Figure 6.4, respectively [109].

Rather than make selections on individual Dalitz variables, they were incorporated into a *mass distance* observable [109]:

$$D^2_{[3,2]} = \sum_{i>j} \left(\hat{m}(3,2)_{ij} - \frac{1}{\sqrt{3}} \right)^2 \tag{6.3}$$

where the sum is forced to be over the distinct jet pairs by requiring $i > j$. The subtraction of $\frac{1}{\sqrt{3}}$ ensures that this variable is skewed towards (and peaks at) zero for a symmetric signal event topology as in Figure 6.5.

An additional triplet-level selection motivated by correlations between the triplet invariant mass (m_{ijk}) and the scalar sum of the p_{T} of jets in the triplet ($\sum_{\text{triplet}} p_{\mathrm{T}}$) was made [109]. In their analysis, CMS noted that the QCD (and combinatorial) background triplet invariant mass increases with the scalar sum of the p_{T} of jets in the triplet [109]. Whereas for correctly identified triplets originating from the signal resonance, no such correlation is seen [109]. A selection variable, Δ, is defined as

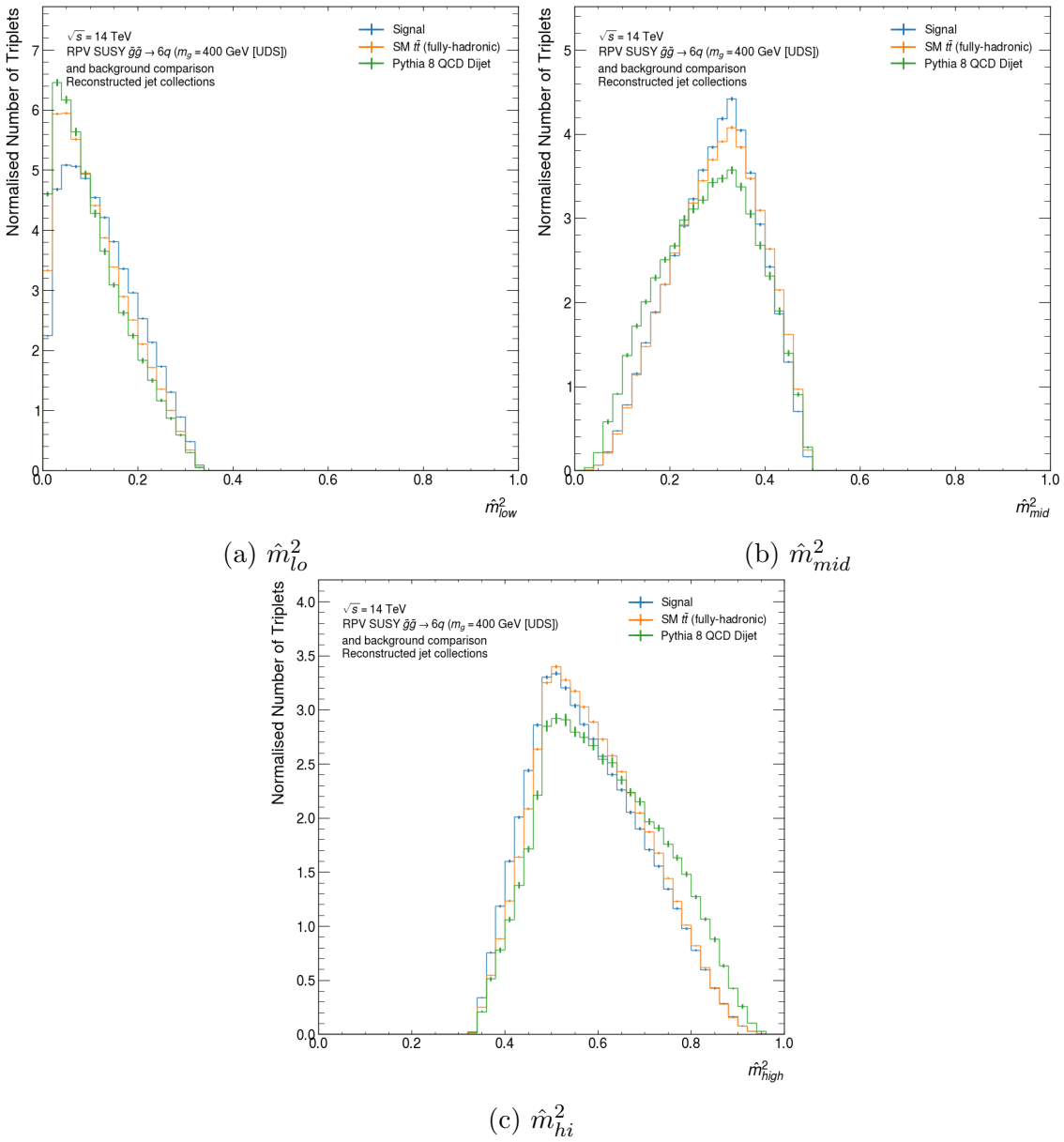

(a) $\hat{m}^2_{lo}$ (b) $\hat{m}^2_{mid}$

(c) $\hat{m}^2_{hi}$

Figure 6.3: The different Dalitz variables used to construct the triplet mass distance and the normalised Dalitz plots for the $m_{\tilde{g}} = 400$ GeV signal and both the QCD and $t\bar{t}$ backgrounds.

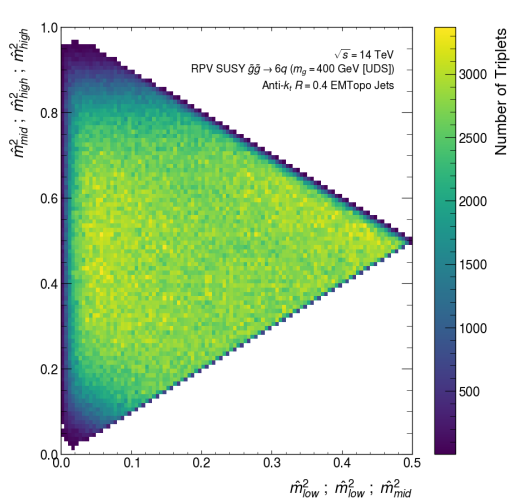

(a) $m_{\tilde{g}} = 400$ GeV $\tilde{g}\tilde{g} \to 6q$ signal (`EMTopo` jets).

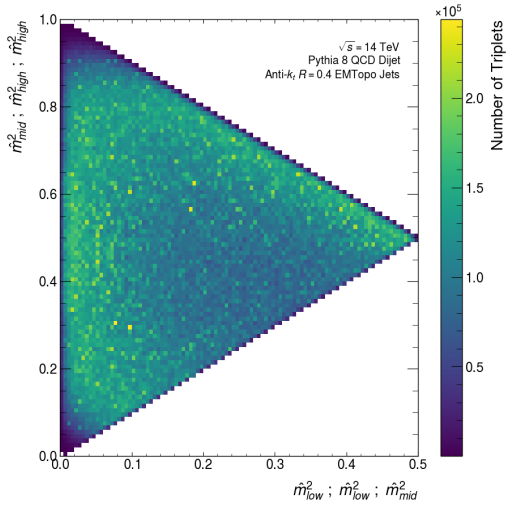

(b) QCD dijet background (`EMTopo` jets).

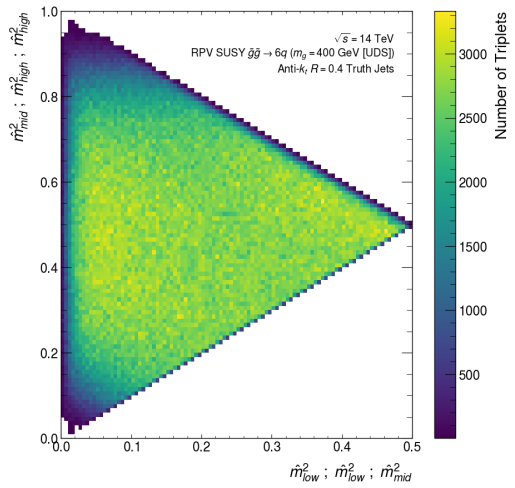

(c) $m_{\tilde{g}} = 400$ GeV $\tilde{g}\tilde{g} \to 6q$ signal (truth jets).

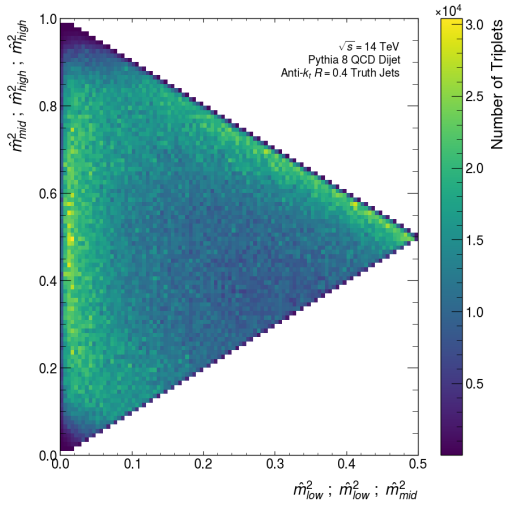

(d) QCD dijet background (truth jets).

Figure 6.4: Dalitz plot for signal and background jet triplets formed from (calibrated) `EMTopo` jets (top) and truth (particle-level) jets (bottom). Little difference is seen between the `EMTopo` and truth jets for the signal, but the QCD background shows slight differences likely resulting from the pile-up jets included in the `EMTopo` jet collection.

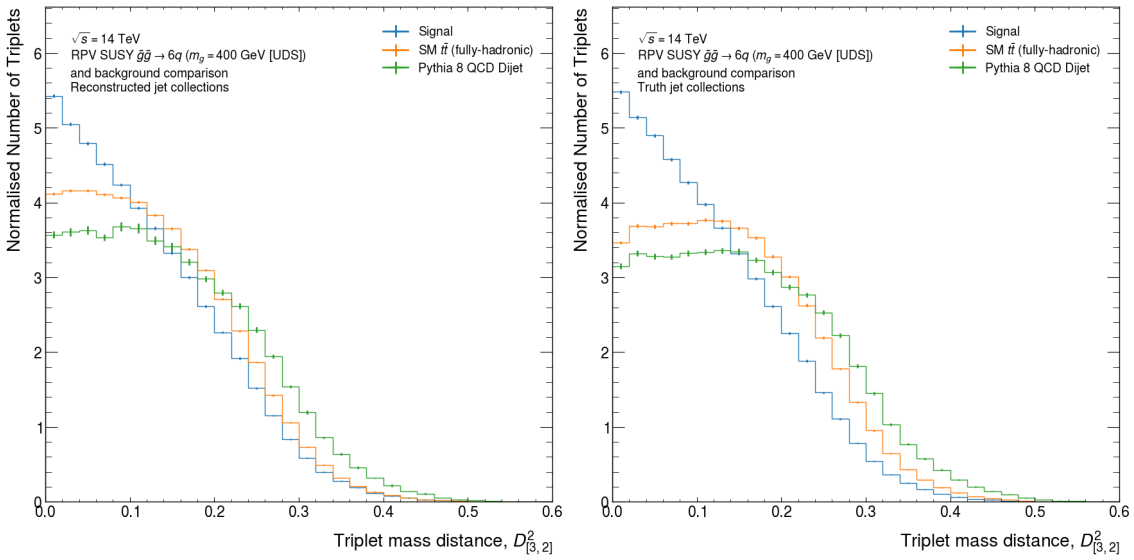

(a) Reconstructed (`EMTopo`) jets. (b) Truth jets.

Figure 6.5: Comparison of triplet mass distance distributions for the $m_{\tilde{g}} = 400$ GeV signal and the dominant background processes. The analysis variable is calculated with reconstructed jets on the left and truth-level jets on the right.

[109]:

$$\Delta = \left(\sum_{\text{triplet}} p_{\text{T}} \right) - m_{ijk}. \tag{6.4}$$

This selection can be interpreted by re-arranging the Equation above into the form:

$$m_{ijk} = \left(\sum_{\text{triplet}} p_{\text{T}} \right) - \Delta \tag{6.5}$$

where the equation now represents a line in the $(\sum_{\text{triplet}} p_{\text{T}},\ m_{ijk})$ plane. Then requiring the triplet to have $(\sum_{\text{triplet}} p_{\text{T}},\ m_{ijk})$ below this line [109]:

$$m_{ijk} < \left(\sum_{\text{triplet}} p_{\text{T}} \right) - \Delta \Rightarrow \left(\sum_{\text{triplet}} p_{\text{T}} \right) - m_{ijk} > \Delta. \tag{6.6}$$

If Δ is a tunable parameter, it can be chosen to eliminate a significant portion of the QCD and combinatorial background, which is evident from the relative positions of signal and background distribution shapes in Figure 6.6.

At the triplet pair level, the mass asymmetry A_m is used to select triplets with small differences in invariant mass, which is to be expected for triplets originating from particles with the same mass. This variable is defined as [109]:

$$A_m = \frac{|m_{ijk} - m_{lmn}|}{m_{ijk} + m_{lmn}} \tag{6.7}$$

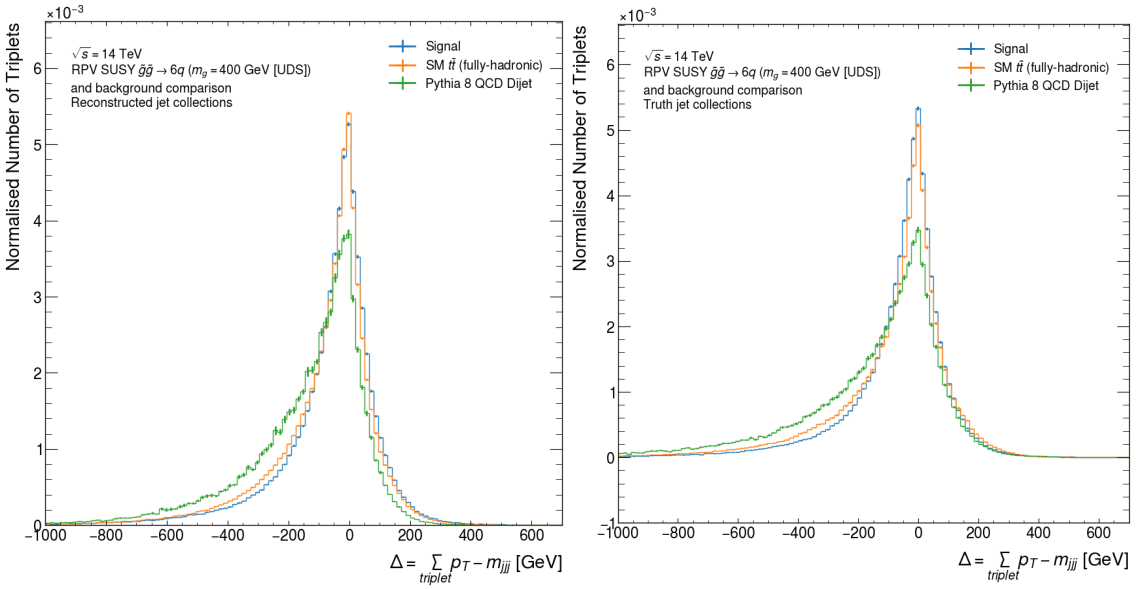

(a) Reconstructed (`EMTopo`) jets.

(b) Truth jets.

Figure 6.6: Comparison of the triplet Δ distributions for the $m_{\tilde{g}} = 400$ GeV signal and the dominant background processes. The analysis variable is calculated with reconstructed jets on the left and truth-level jets on the right. The negative axis for the truth jet histogram is a consequence of negative entries in the histogram tails (associated with negative weights) where the bin contents is not balanced by positively weighted contributions. Such events also impact the reconstructed jet histograms, which have a different axis range.

where m_{ijk} and m_{lmn} are the invariant masses of the triplets within a triplet pair. The absolute value in the numerator forces this variable, like the triplet mass distance, to be skewed towards zero as seen in Figure 6.7 for both the signal and background. The QCD background has more spread from zero (consistent with less symmetry between the triplets), whereas the $t\bar{t}$ background is shifted closer to the signal A_m distribution since it originates from an actual resonance. The differences between the signal and QCD jet distribution are explained by the fact that QCD background contributes two high-p_{T} jets (a dijet event) in addition to extra lower-p_{T} hadronic radiation. Thus, when triplets are created, we expect to see significant differences between the invariant mass of triplets created from a combination of the two high-p_{T} jets and the lower p_{T} jets.

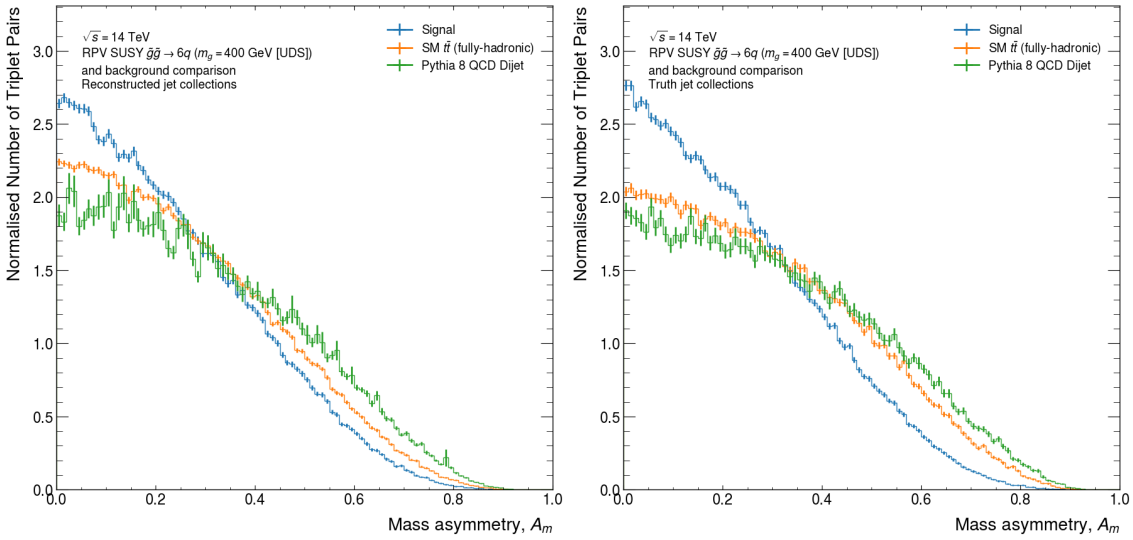

(a) Reconstructed (`EMTopo`) jets. (b) Truth jets.

Figure 6.7: A comparison of the mass asymmetry distributions for the $m_{\tilde{g}} = 400$ GeV signal and the dominant background processes. The analysis variable is calculated with reconstructed jets on the left and truth-level jets on the right.

The remaining selections are defined in terms of generalised event-level Dalitz variables[4] [109]:

$$\hat{m}^2(6,3)_{ijk} = \frac{m_{ijk}^2}{4m_{ijklmn}^2 + 6\sum_i m_i^2} \tag{6.8}$$

where m_{ijk} is the invariant mass of a triplet and m_{ijklmn} is the invariant mass of the leading 6 jets in the event such that i, j, k, l, m, and n run over indices 1 through 6 (or 0 through 5). Again, the denominator is chosen to normalise the variables between 0 and 1.

For a symmetric signal topology these variables cluster around 1/20 since there are 20 possible (distinct) triplets in a 6-jet event [109]. Rather than define a mass distance

[4]Like for the triplet-level case (6,3) refers to the 6-jet event and definition of the variable in terms of the 3-jet triplet invariant mass.

in the same way as the triplet-level expression in Equation (6.3), CMS combines both the $D^2_{[3,2]}$ and $D^2_{[6,3]}$ (the event-level mass distance) variables into a single generalised event-level variable [109]:

$$D^2_{[(6,3)+(3,2)]} = \sum_{i>j>k} \left(\sqrt{\hat{m}^2(6,3)_{ijk} + D^2_{[3,2],ijk}} - \frac{1}{\sqrt{20}} \right)^2 \tag{6.9}$$

This variable is not peaked at zero, but the mode of the distribution is closer to zero for signal events than QCD background events as seen in Figure 6.8, which is associated with the symmetry of the signal compared to the QCD background as for other observables [109].

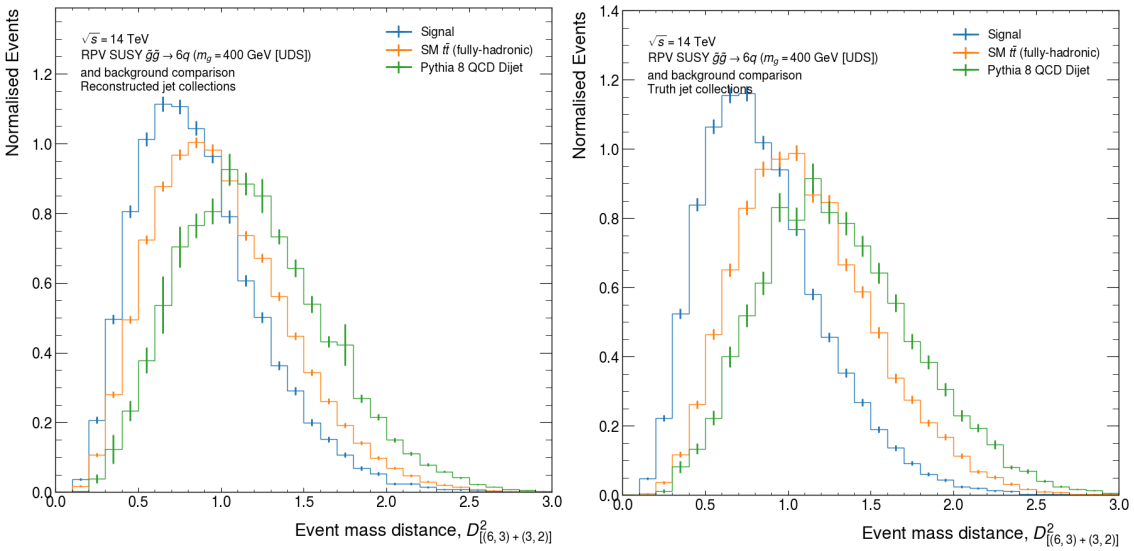

(a) Reconstructed (`EMTopo`) jets.

(b) Truth jets.

Figure 6.8: A comparison of the event-level mass distance distributions for the $m_{\tilde{g}} = 400$ GeV signal and the dominant background processes. The analysis variable is calculated with reconstructed jets on the left and truth-level jets on the right.

In our interpretation of the analysis, the selections were made starting from the event-level selections before making subsequent triplet-pair and triplet-level selections. The selections proceed as below (the selection criteria optimised by CMS for SR1 are included [109]):

1. The event-level mass distance selection was made requiring $D^2_{[(6,3)+(3,2)]} < 1.25$
2. Triplet pairs in events passing (1) were required to have $A_m < 0.25$
3. The triplets passing triplet pair selections were required to pass:
   - A delta cut, $\Delta > 250$ GeV
   - The triplet mass distance selection, $D^2_{[3,2]} < 0.05$

Only the triplets passing all of these selections were considered for further analysis and included in final histograms of the triplet invariant mass, where the signal appears as a "bump" against the QCD and $t\bar{t}$ background.

While only the $m_{\tilde{g}} = 400$ GeV signal was discussed in this Section, interesting results are seen for lower mass ($m_{\tilde{g}} = 200$ GeV) signals where the gluino mass is closer to the top quark mass. In these cases, the separation power of the jet-ensemble observables for discrimination between the symmetric signal topology and asymmetric QCD topology decreases, which is evident in the Dalitz plot shown in Figure 6.9. In this plot signal triplets are no longer uniformly distributed in the central region of the plot. Other comparisons of the analysis variables for the $m_{\tilde{g}} = 200$ GeV signal are illustrated in Figure 6.10. For brevity, only the `EMTopo` jet collection plots are included. Interestingly, since the $\tilde{g}$ mass is also quite close to the top quark mass the separation of the signal and $t\bar{t}$ background distributions decreases relative to the $m_{\tilde{g}} = 400$ GeV comparisons. Thus, searches for resonance masses near the top quark mass likely need to consider additional methods to either reduce the $t\bar{t}$ background or account for the presence of the top quark resonance in statistical analyses.

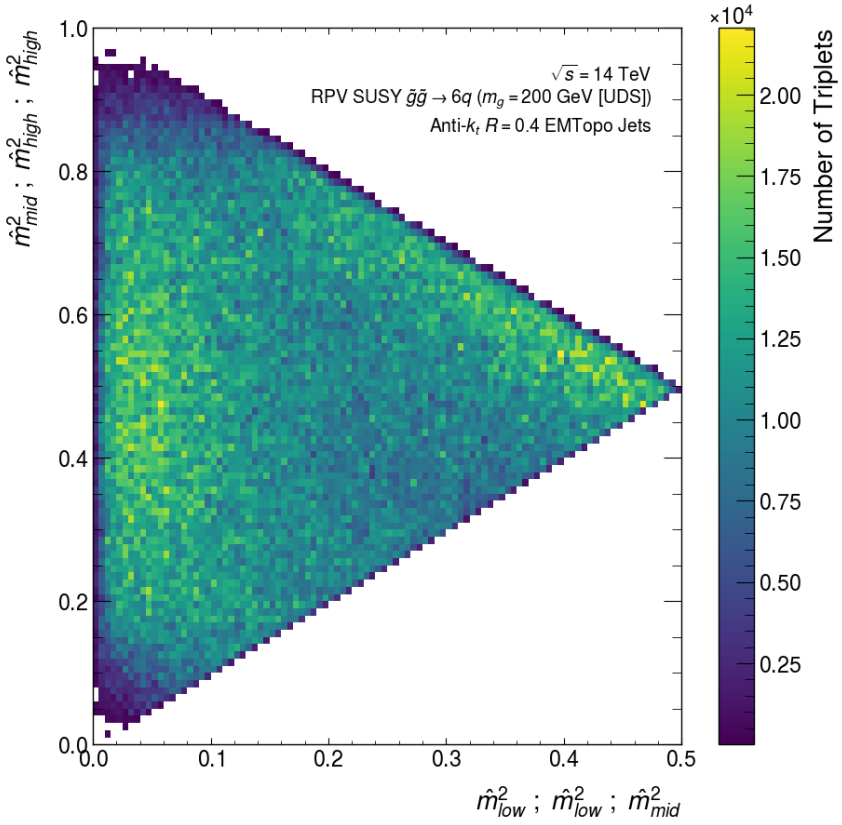

Figure 6.9: Normalised Dalitz plot for the $m_{\tilde{g}} = 200$ GeV signal sample using `EMTopo` jets.

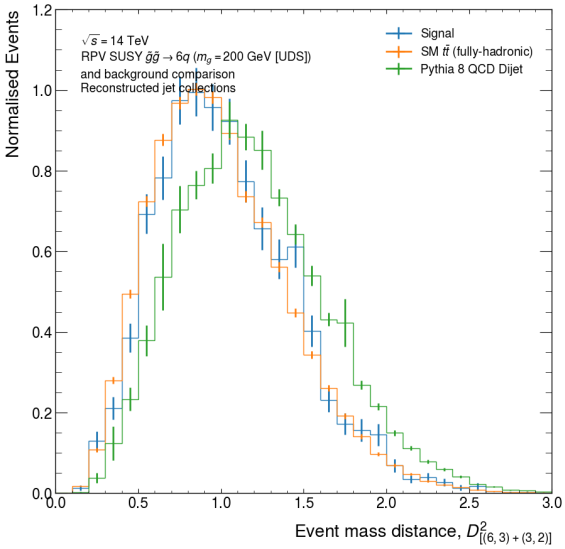

(a) Event-level mass distance.

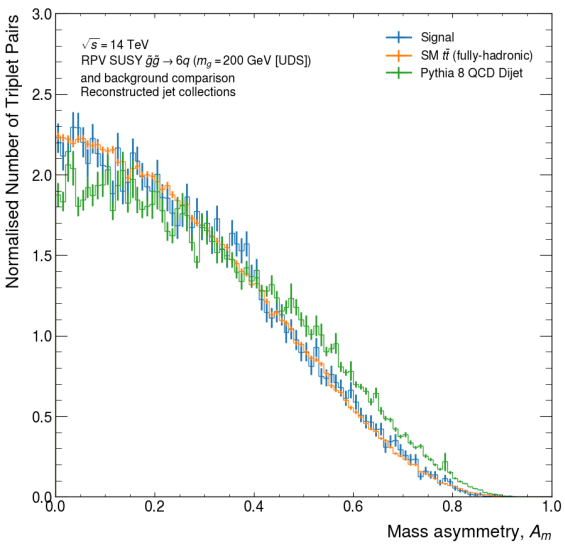

(b) Mass asymmetry.

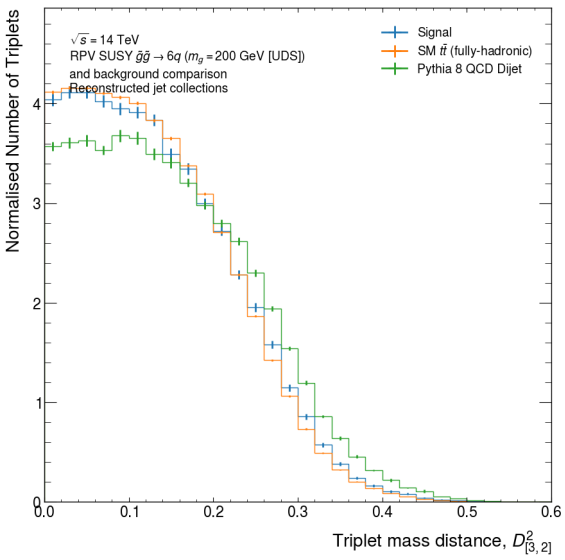

(c) Triplet-level mass distance.

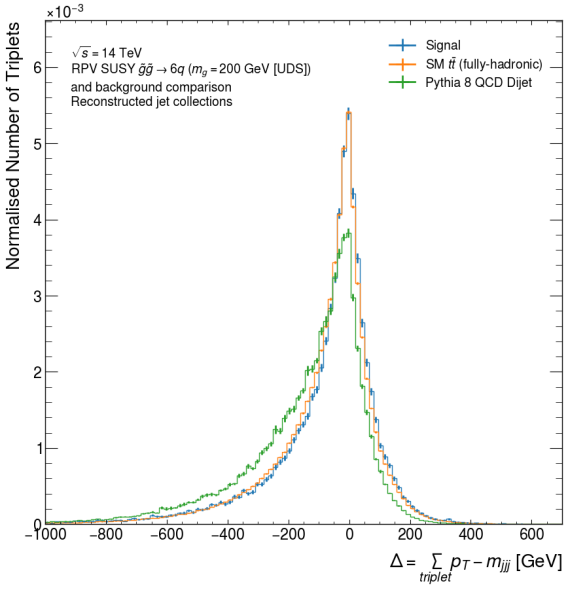

(d) Triplet $\Delta = \left(\sum_{\text{triplet}} p_{\text{T}}\right) - m_{\text{jjj}}$.

Figure 6.10: Analysis variable comparisons for the $m_{\tilde{g}} = 200$ GeV signal sample and dominant backgrounds using `EMTopo` jets.

6.4 Basic optimisation of analysis selections

A re-optimisation of the analysis implemented in Ref. [109] is warranted given the differences between the CMS and ATLAS detectors and the energy scales of fully-calibrated hadronic jets. While we may expect that the optimal selections are similar to those applied in the original analysis, they are ultimately determined by the analysis significance achieved with the full 3000 fb^{-1} integrated luminosity expected at the HL-LHC. Before considering a basic re-optimisation of the analysis we explored a truth-matching methodology similar to that used for an ongoing Run 2 ATLAS search for the same signal. The application of "truth-matching" to identify signal jets that originate from the gluino decays allows the "correct" signal yield (for correctly combined jet triplets and the events to which they belong) to be determined and used to calculate the analysis significance.

6.4.1 Truth matching and additional jet selections

To identify jet triplets originating from the decay products of the gluinos, a truth labelling scheme was used to match reconstructed jets to truth (generator-level) particles. This labelling procedure was evaluated using only the ATLAS MC16a event sample for the different signal mass points containing 10000 events. The truth-matching scheme closely follows that considered for the ATLAS Run 2 search for the same signal[5] [126].

The matching procedure involved matching truth-level or reconstructed jets to generator-level quarks or final-state-radiation (FSR) candidates[6]. The parent gluino particles were required to decay into other Standard Model particles and were excluded if they "self-decayed", in which case one of the child particles had the same Particle Data Group ID (PDG ID) as the gluino. Gluinos that were not associated with any child particle were also excluded. The quark decay products were studied further to identify FSR candidates (SM particles with PDG ID below 22) with $p_T > 20$ GeV that are emitted away from the quarks (via a $\Delta R > 0.4$ requirement). The resulting collection of quarks and FSR candidates were matched to reconstructed or truth jets with $p_T > 20$ GeV within $\Delta R \leq 0.4$ of the truth particle. The matching procedure searched for the closest (in ΔR) matched truth particle, but favoured quark matches – only those jets without a quark match were considered for matching to FSR candidates.

Events were labelled as containing fully matched gluinos when there were six quark-matched jets. If this was not the case, FSR candidates associated with the quarks that were not matched to jets were considered. If multiple FSR-jet matches were

[5]The author thanks Lea Halser for providing a description of the original matching procedure and answering troubleshooting related questions. The complete matching procedure was created and optimised for the Run 2 analysis, and we apply it without significant changes. Thus, the methods were not developed by the author of this thesis, rather, the framework is adapted for the purposes of these studies.

[6]The simulated gluinos, quarks, and FSR candidates are collectively called truth particles.

found for the same quark, the highest p_{T} FSR-matched jet was taken as that which belonged to the given quark. However, reconstructed jet collections include pile-up, so the truth particles could have been matched to jets that did not originate from the hard-scatter (signal) interaction leading to an artificial increase in the efficiency for reconstructing the gluino decays. Consequently, pile-up mitigation steps were briefly considered to optimise the accuracy of the matching (i.e. reconstructing the hard-scatter interaction products).

Indeed, when the truth particles are matched to truth-level jets a slightly smaller efficiency for "full" (6-jet) matching is achieved compared to that for reconstructed jets in Table 6.3. The efficiency was calculated without any analysis selection, so we expect additional requirements imposed by the kinematic pre-selection to reduce the efficiency further. Since there is only about a 0.5% difference between the efficiencies these results may agree when one considers statistical uncertainties. Nonetheless, when pile-up mitigation techniques (a JVT selection; see Section 4.8.1) are applied, the reconstructed jet matching efficiency in Table 6.3 falls below the truth jet matching efficiency as might be expected when detector effects and resolutions are considered. Clearly, the relative differences in the truth-matching efficiencies are predominately jet multiplicity related – reconstructed jets (above a suitable 20 GeV p_{T} threshold) have a higher per-event multiplicity than truth jets due to the inclusion of pile-up jets. The JVT selection consisted of a JVT > 0.59 and JVT > 0.11 cut for jets with $20 < p_{\mathrm{T}}$ (GeV) < 120 within $|\eta| < 2.4$ and $2.4 < |\eta| < 2.5$, respectively, based on the *Medium* working point recommendation for `EMTopo` jets in Run 2.

The JVT selections in addition to jet cleaning cuts at the *LooseBad* working point were applied to both the background and signal samples. The jet cleaning procedure aims to reduce the impact of non-collision backgrounds and calorimeter noise on jet reconstruction [127]. Only jets that did not pass the cleaning cuts were removed, not entire events (e.g. with an event-level cleaning cut), in these studies. The application of JVT and event- or jet-level cleaning constitutes a baseline selection for the analysis of real data. However, neither the JVT nor jet cleaning recommendations applied to the signal are tuned for use in HL-LHC simulation, so their performance for the background needs to be considered in future work, and they should likely be removed for consistency in the final set of projections.

The final stage in the truth-matching procedure for the signal samples occured at the same time as triplets and triplet pairs are constructed. We required *fully-matched* triplets to contain three quark/FSR matched jets where the truth particles originated from the same gluino. Fully-matched triplet pairs were required to contain two *fully-matched* triplets.

The truth-matching efficiencies in Table 6.3 are only on the order of 50% for the $m_{\tilde{g}} = 400$ GeV signal point. The $m_{\tilde{g}} = 200$ GeV and $m_{\tilde{g}} = 400$ GeV signal points were studied further to determine if the efficiency loss was caused by the merging of decay products (quarks) associated with *boosted* gluinos. The fraction of gluino

Table 6.3: Efficiencies for matching truth particles to reconstructed jets with different selections compared to the matching efficiency for truth-level jets. Results are shown for both the $m_{\tilde{g}} = 400$ GeV and $m_{\tilde{g}} = 200$ GeV UDS signal points. The matching efficiencies are included outside parentheses, while the values in parentheses represent the fraction of the 10000 event sample made up of events containing partially (< 6) matched jets. The truth jet matching efficiencies remain the same in *all* of these Tables because reconstructed jet selections do not affect the truth-level jets. The efficiency is calculated without any kinematic selections on the jets other than the JVT and cleaning selections, where they are specified.

(a) Efficiencies calculated with no jet cleaning or JVT selection for `EMTopo` jets.

Signal ($m_{\tilde{g}}$ [GeV])	Truth jet matching efficiency (%)	Reconstructed jet matching efficiency (%)
200 (UDS)	19.49 (80.50)	21.10 (78.90)
400 (UDS)	47.10 (52.90)	47.64 (52.36)

(b) Efficiencies calculated after a JVT Medium selection on EMTopo jets.

Signal ($m_{\tilde{g}}$ [GeV])	Truth jet matching efficiency (%)	Reconstructed jet matching efficiency (%)
200 (UDS)	19.49 (80.50)	16.14 (83.85)
400 (UDS)	47.10 (52.90)	42.42 (57.58)

(c) Efficiencies calculated after a JVT Medium and LooseBad cleaning selection on EMTopo jets.

Signal ($m_{\tilde{g}}$ [GeV])	Truth jet matching efficiency (%)	Reconstructed jet matching efficiency (%)
200 (UDS)	19.49 (80.50)	16.11 (83.88)
400 (UDS)	47.10 (52.90)	42.33 (57.67)

decays where the minimum ΔR separation of a pair of quarks from the decay was less than 0.4 was calculated in bins of the gluino p_{T}. Profiles of this fraction of *merged* gluino decays – where a pair of signal quarks merge into a single jet – are shown in Figure 6.11 alongside the gluino p_{T} distributions. Increases in this measure of boosting at high-p_{T} should not be trusted because the number of entries in the tail of the p_{T} distribution is significantly lower than around the peak of the distribution. Around the gluino p_{T} peak less than 20% of gluino decays result in a merged quark pair for both signal points tested. Thus, boosted decays do not appear to completely explain the truth-matching efficiencies smaller than 50%, and further work is needed to consider ways to increase the matching efficiency.

The invariant mass distribution for fully-matched triplets peaks slightly below 400 GeV for the $m_{\tilde{g}} = 400$ GeV signal as shown in Figure 6.12a with similar trends for the 200 GeV signal in Figure 6.12b. This behaviour is likely a consequence of the truth-matching procedure and the implementation of the truth labelling scheme so could be studied further as this work progresses. For now, we proceed with the truth-matching procedure *as-is* because the results presented so far seem acceptable and the exact location of the resonance in invariant mass is not actually of utmost importance for these exploratory studies (e.g. to explore generic multi-jet resonances).

6.4.2 Analysis selection optimisation

A simple grid-search optimisation procedure was considered for these studies as an alternative to multivariate methods. We focused only on the $m_{\tilde{g}} = 400$ GeV signal, but for further studies and the consideration of a wider range of signal masses (i.e. $m_{\tilde{g}} = 200$ GeV), the analysis selections need to be re-optimised for each resonance mass. The optimal selections were found by evaluating event- and triplet-level figures of merit. The triplet-level figure of merit was defined using yields calculated from integrals around the signal peak of the triplet invariant mass distribution as in Ref. [109]. The total background[7] considered the combinatorial background from the signal and the QCD background, for the triplet-level calculations, and only the QCD background for event-level calculations. Since the QCD and combinatorial backgrounds are expected to behave similarly (with similar shapes) we expect the triplet-level optimisation to also reduce the contribution of incorrectly identified triplets [109]. The $t\bar{t}$ background was not considered for these optimisation studies since it behaves like the signal and the analysis selections are aimed at differentiating between the QCD background and the signal only. Event-level significance (figure of merit) calculations identified signal and background events as those that have at least two jet triplets passing all selections to mimic the six jet signal topology. Requiring that the signal jets are matched to truth particles from gluino decays

[7] In this case, the `JZOWithSW` sample was excluded from the optimisation because very few events pass the pile-up overlay cleaning procedure and the p_{T} of jets in the sample is sufficiently low that few (if any) events would contribute.

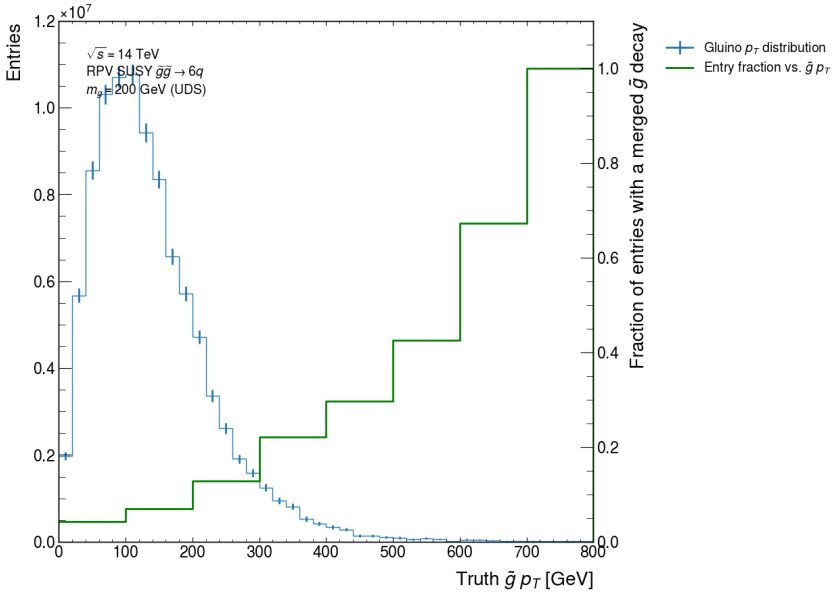

(a) $m_{\tilde{g}} = 200$ GeV (UDS)

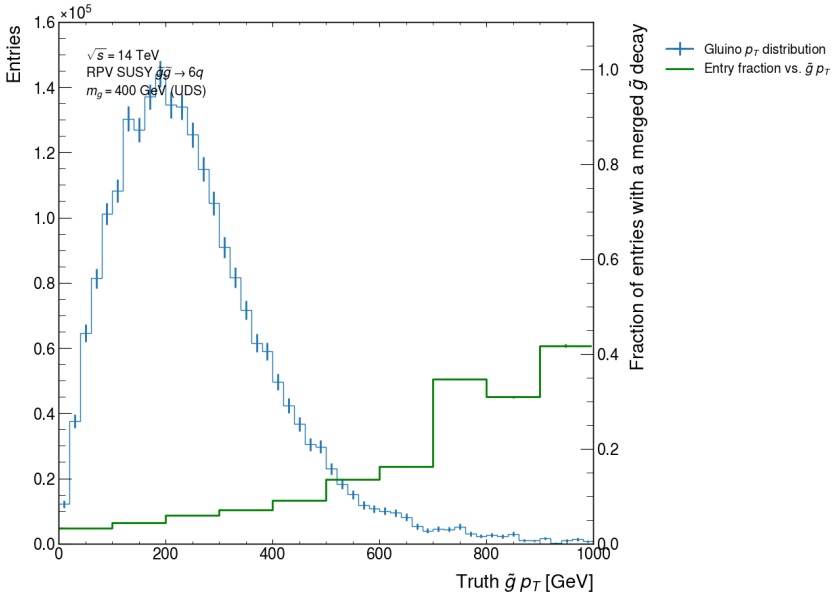

(b) $m_{\tilde{g}} = 400$ GeV (UDS)

Figure 6.11: Overlaid gluino p_{T} distribution and profile of the fraction of events where at least one gluino decay results in a quark pair separated by $\Delta R < 0.4$. The latter metric is referred to as the fraction of events with at least one merged gluino decay (i.e. referring to the merging of quarks). No JVT or jet cleaning selections were made here since the results are only for truth-level particles.

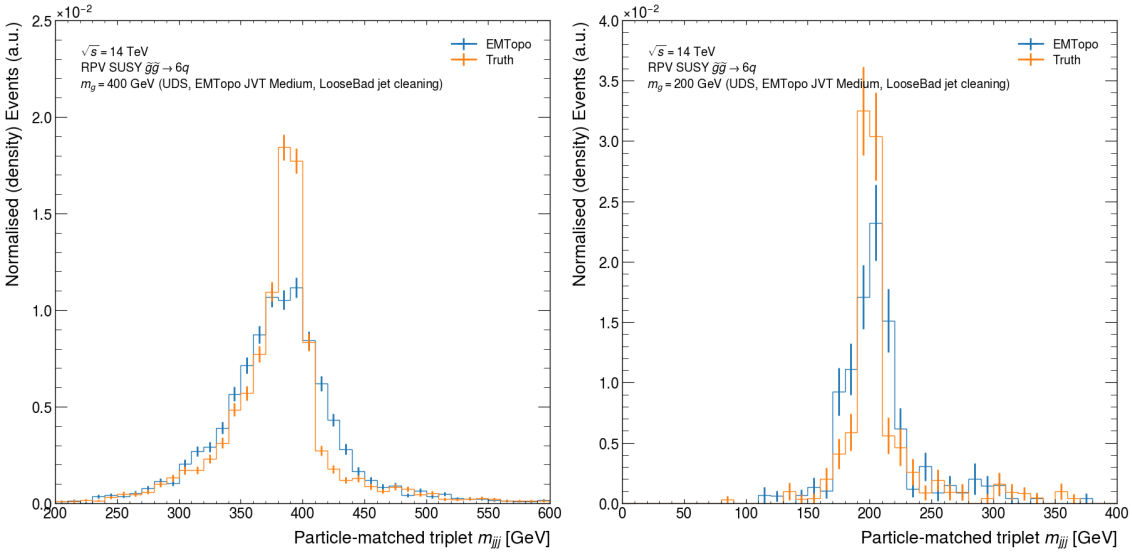

(a) $m_{\tilde{g}} = 400$ GeV (UDS) (b) $m_{\tilde{g}} = 200$ GeV (UDS)

Figure 6.12: Invariant mass distributions after matching truth-level particles to jets for the two major signal points studied. A comparion between reconstructed and truth jet matching is shown for the histograms. To prevent negative limits for the y-axis the plots have been limited to $y > 0$ for clarity due to fluctuating bins in the tails of these distributions.

(Section 6.4.1) ensured the calculation of the signal yield was representative of the "true" signal topology, but decreased the expected signal yield as a consequence of low truth-matching efficiencies (below 50%). The event-level significance was calculated as $Z_{\mathrm{e},1} = S/\sqrt{B}$ and $Z_{\mathrm{e},2} = S/\sqrt{S+B}$, where S is the signal event yield and B is the QCD dijet event yield.

The triplet-level m_{jjj} integral figure of merit was calculated as:

$$Z_{\mathrm{t},1} = \frac{S_{\mathrm{matched}}}{\sqrt{S_{\mathrm{unmatched}} + B_{\mathrm{QCD}}}} \tag{6.10}$$

where S_{matched}, $S_{\mathrm{unmatched}}$, and B_{QCD} are the integral yields of the truth-matched signal jet triplets, combinatorial background from the signal sample, and QCD background, respectively. Each integral was calculated in a window around the peak of the signal distribution – widths of 200 GeV and 300 GeV were considered here. Additional metrics with different forms (using the same conventions as Equation (6.10)) were calculated and included in the results, including:

$$Z_{\mathrm{t},2} = \frac{S_{\mathrm{total}}}{\sqrt{B_{\mathrm{QCD}}}} = \frac{S_{\mathrm{matched}}+S_{\mathrm{unmatched}}}{\sqrt{B_{\mathrm{QCD}}}}, \tag{6.11}$$

$$Z_{\mathrm{t},3} = \frac{S_{\mathrm{total}}}{\sqrt{S_{\mathrm{total}}+B_{\mathrm{QCD}}}} = \frac{S_{\mathrm{matched}}+S_{\mathrm{unmatched}}}{\sqrt{S_{\mathrm{matched}}+S_{\mathrm{unmatched}}+B_{\mathrm{QCD}}}}. \tag{6.12}$$

The triplet- and event-level yields were both normalised to a 3000 fb^{-1} integrated luminosity. Further modifications to the triplet-level yield normalisation included scaling the sum of event weights of each sample[8] by 20 (the total number of triplets possible in a 6-jet event) to correct for the fact that m_{jjj} is a triplet- rather than event-level variable. Thus, the entries in each bin of the m_{jjj} histogram were representative of a fraction of the total number of triplets if every event were to contribute six leading jets and exactly 20 triplets. The effect of this modification *decreased* the triplet-level metrics by a factor of $\sqrt{20}/20 = 1/\sqrt{20}$ relative to the case where the extra factor of 20 was not included. While the normalisation of the signal and background was important for projecting expected yields for each process, the relative magnitudes of the figures of merit after different selections were most important for the optimisation procedure. The results of the analysis optimisation were limited by the size of the event samples, evident in the large statistical uncertainties for different signal and background components of the m_{jjj} distributions in Figure 6.13 after complete analysis selections. Therefore, excesses from the signal could be lost in the statistical fluctuations of the background in a "real-world" analysis. Additional work is needed to better model the background sources for these projections compared to previous analyses with larger event samples and data-driven background estimates.

As discussed in Section 6.3, the initial kinematic pre-selection applied in Ref. [109] emulated a trigger selection applied during data-taking in these studies. For the optimisation procedure, we varied only the jet p_{T} selections, not the $|\eta|$, H_{T}, or jet multiplicity selections. The jet $|\eta|$ selection was kept constant at 2.4, since the tracking acceptance of the detector for the signal and background samples is different. The jet p_{T} selections were modified to ensure the sixth jet p_{T} threshold is never below the threshold of the primary jet p_{T} selection applied to all six jets and used in the H_{T} calculation. We allowed cases where the jet p_{T} and sixth jet p_{T} thresholds were identical to emulate the effect of removing the sixth jet selection. The primary p_{T} selection on each jet was varied between 20 GeV and 40 GeV in steps of 10 GeV. A similar procedure was used for the sixth-leading (passing the jet p_{T} and $|\eta|$ cuts) jet p_{T} cut, which was allowed to take values of 20 GeV, 40 GeV, or 50 GeV. This provides a proof-of-concept for further optimisation studies that consider a wider variety of trigger selections where the jet p_{T} selection thresholds are set by the trigger signature performance from the trigger efficiency turn-on curve.

The jet-ensemble analysis observables were considered in more detail, and we tested different thresholds including:

- the "nominal" CMS selection proposed for the low-mass (SR1) signal region,
- values ±10% above and below the CMS optimised selection,
- looser/tighter selections relative to the nominal CMS selection to capture any variation in significances not apparent with the ±10% variation.

[8] Used in the denominator of the luminosity normalisation scale-factor.

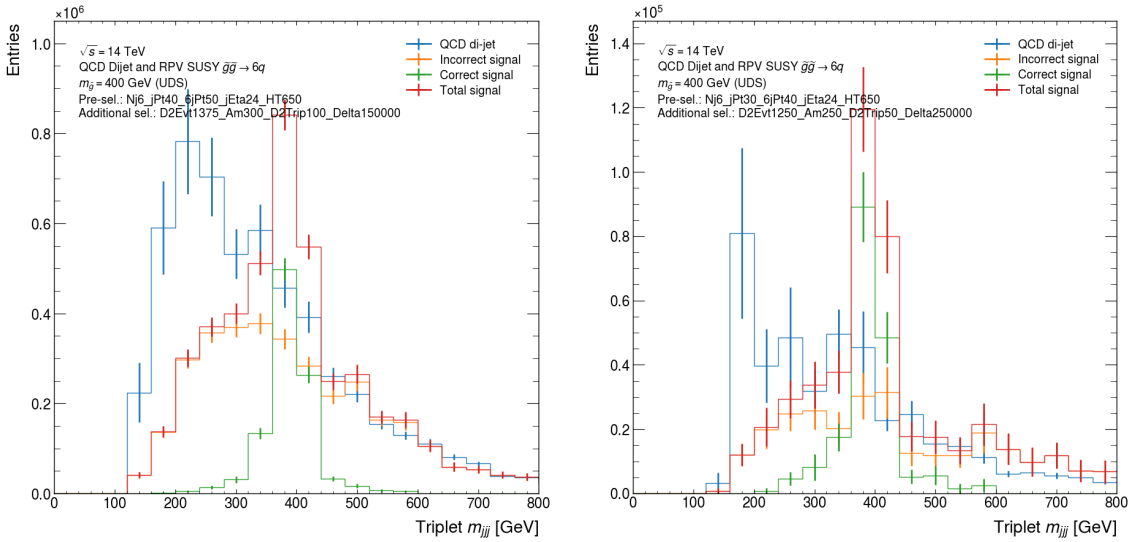

(a) Triplet m_{jjj} histogram with tight jet p_{T} selections and optimal jet-ensemble variable selections based on results in this Section.

(b) Triplet m_{jjj} histogram with CMS-like [109] selections for the low-mass signal region.

Figure 6.13: Triplet invariant mass distribution for different background and signal components with complete analysis selections. Note the large bin fluctuations for the QCD background (particularly in the plot on the right) and the relative size of the signal peak in comparison to the background. The pre-selection is described by an abbreviation where: `NjX` is the jet multiplicity cut, `jPtX` is the jet p_{T} cut, `6jPtX` is the sixth jet p_{T} cut, `jEtaX` is the jet $|\eta|$ cut (multiplied by 10), and `HTX` is the H_{T} selection. The jet-ensemble observable selections are described similarly: `D2Evt` and `D2Trip` refers to the event- and triplet-level mass-distance selections, respectively, the mass-asymmetry selection follows `Am`, and the "Delta cut" selection follows `Delta`. All selections for those variables are multiplied by 1000 in the identifier string.

These selections are overlaid on distributions of the background and signal ($m_{\tilde{g}} = 400$ GeV) analysis observables after the "nominal" (CMS) pre-selection in Figure 6.14. The looser/tighter selections beyond the ±10% variation were validated based on these plots. Further studies should consider a more complete optimisation procedure where the correlations between the analysis variables and multivariate methods for optimisation (e.g. using TMVA [128]) could be considered.

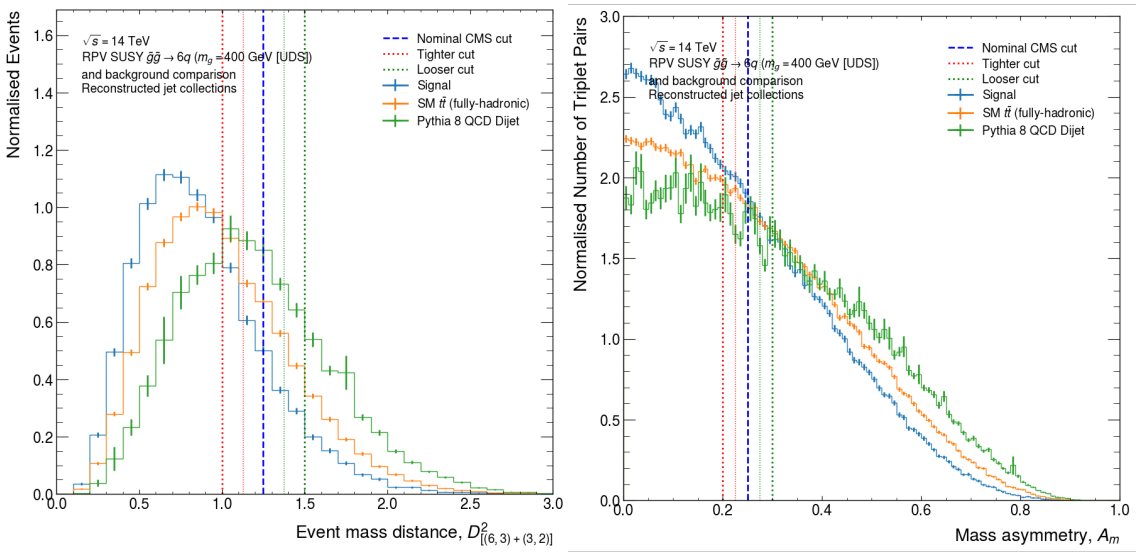

(a) Event-level mass distance.

(b) Mass asymmetry.

(c) Triplet-level mass distance.

(d) Triplet Δ cut.

Figure 6.14: Jet-ensemble analysis variables for the $m_{\tilde{g}} = 400$ GeV (UDS) mass point with overlaid selections used to consider the optimal analysis selections.

The triplet-level optimisation results are shown in Tables 6.5 and 6.6 for the 200 GeV and 300 GeV m_{jjj} integral mass windows, respectively. Event-level significance estimates are shown in Tables 6.7 to 6.9 for three different pre-selection variations:

tight jet p_{T}, loose jet p_{T}, and CMS-like jet p_{T} thresholds. The optimal selections from triplet-level results agree with event-level results where no particle-jet matching is required. The introduction of particle-jet matching requirements causes the event-level significance to fall and leads to better performance for much tighter jet-ensemble observable selections in comparison to the results without particle-jet matching. These changes are likely a consequence of the combinatorial background not being included in the signal yield[9]. The small efficiency for obtaining signal events with two particle-jet matched triplets directly impacts these conclusions since the actual (correct triplet) signal yield is likely larger.

The application of identical sixth jet p_{T} thresholds and different primary jet p_{T} thresholds leads to similar optimal selections and figures of merit for both the event- and triplet-level results. Since the jets in an event were ordered in descending order by p_{T}, a tight sixth jet p_{T} threshold produces an event that is on average harder (with higher H_{T} as in Figure 6.16). We see that the signal event yield is larger relative to the background event yield with these tighter selections in Table 6.4. The source of this behaviour could be related to the high pile-up levels and therefore enhanced contributions from the dijet samples where jets have relatively low-p_{T}. This is evident from the order of magnitude increase in the background yield in Table 6.4 when only 20 GeV p_{T} thresholds are used. For both event- and triplet-level optimisation results the tightest p_{T} selections perform optimally. However, these high thresholds decrease the sensitivity to lower mass resonances (e.g. $m_{\tilde{g}} = 200$ GeV or $m_{\tilde{g}} = 100$ GeV), which produce lower p_{T} jets compared to an $m_{\tilde{g}} = 400$ GeV signal. Consequently, further optimisation with the lower mass signals is needed to ensure that they can be evaluated in the final set of projections. Avenues with which to reject pile-up and allow lower jet p_{T} thresholds without decimating the signal acceptance or the analysis significance for lower mass signals should also be considered.

Despite the increase in p_{T} thresholds, the optimal jet-ensemble observable ($D^2_{[(6,3)+(3,2)]}$, A_m, Δ, $D^2_{[3,2]}$) selections evaluated with both triplet- and event-level[10] metrics are much looser[11]. This is the case for both m_{jjj} integral windows tested, albeit the wider window produces smaller values of the figure of merit due to a larger QCD triplet contribution. The optimal selections correspond to: $D^2_{[(6,3)+(3,2)]} < 1.375$, $A_m < 0.3$, $\Delta > 150$ GeV, and $D^2_{[3,2]} < 0.1$. These selections produce the invariant mass distributions for the signal and QCD background shown in Figure 6.15, where reasonable distribution shapes are seen but the statistical uncertainty remains large. When the truth-matching efficiency is improved to recover the full signal yield or a

[9] If the combinatorial background is included, then we effectively obtain a total $S/\sqrt{B}$ significance that is the sum of the significance for jet triplets originating from the gluino decays and those where the jets are incorrectly combined. This effect complicates the optimisation procedure resulting in looser selections because we include part of the signal component that looks similar to the QCD background in the complete signal yield.

[10] Without particle-jet matching requirements.

[11] Some of the variation with respect to Ref. [109] could be explained by different signal resonance masses being used for the optimisation.

different definition of a "signal event" is used, the optimal selections could become tighter as for the event-level results with particle-jet matching. The premise of this analysis is to maximise the signal sensitivity by removing as much of the QCD background as possible, at the cost of some signal events. Thus, tighter selections might be reasonable, but higher statistics event samples are needed to validate their performance. Little variation in the jet-ensemble variable selections is seen when the top-ten most performant selections are considered, particularly for event-level results without any form of particle-jet matching. Such behaviour is expected near the optimal set of selections since a change in one of the cuts likely only produces a small change in the analysis significance.

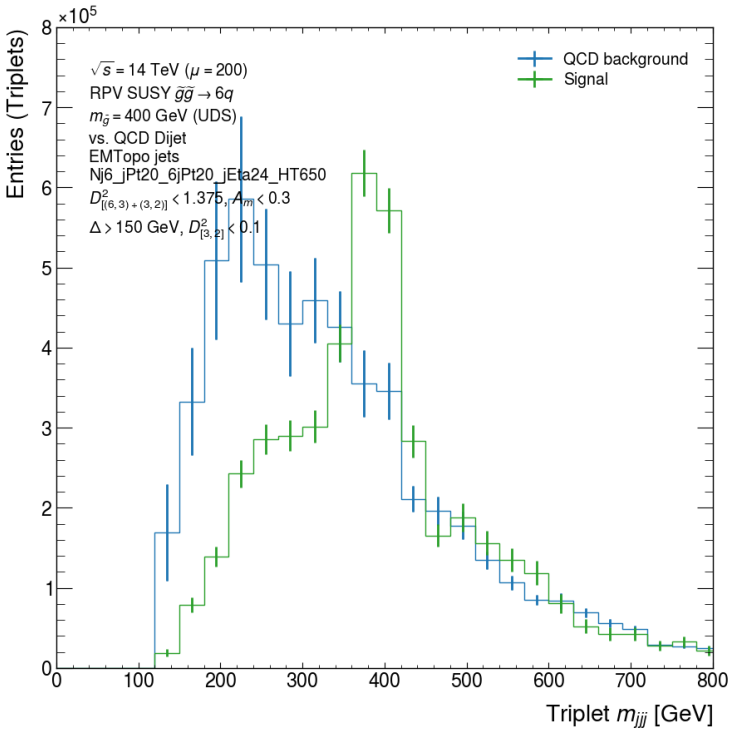

Figure 6.15: Triplet invariant mass distribution after the application of looser analysis selections optimised with the triplet-level figure of merit and the event-level significance without particle-jet matching. The same nomenclature from Figure 6.13 describes the pre-selection. The other analysis observable selections are summarised on the plot.

The m_{jjj} integral figure of merit and the event-level analysis significances we calculate are very large for the $\tilde{g}\tilde{g}$ signal. The luminosity scaling might contribute to this because for a simple $S/\sqrt{B}$ calculation the difference between 1 fb^{-1} and 3000 fb^{-1} of integrated luminosity leads to a factor of $3000/\sqrt{3000} = \sqrt{3000}$ increase in $S/\sqrt{B}$. This is evident if we consider the results from a Run 1 ATLAS search [95] where a cut-and-count procedure was used to measure event yields with 4.6 fb^{-1} of data collected at $\sqrt{s} = 7$ TeV. The expected yields for the (QCD) background and

$m_{\tilde{g}} = 400$ GeV signal[12] with a $p_{\mathrm{T}} > 160$ GeV selection on the sixth-leading jet were 62 ± 13 and 110 ± 13, respectively [95]. If we extrapolate these yields to a 3000 fb^{-1} integrated luminosity and account for the increased CM frame collision energy (at $\sqrt{s} = 14$ TeV) by inflating the cross-sections by a factor of 10 (an assumption), the expected event-level analysis significance becomes:

$$Z_{\mathrm{e},1} = \frac{S}{\sqrt{B}} = \frac{110 \times 10 \times (3000/4.6)}{\sqrt{62 \times 10 \times (3000/4.6)}} \approx 1128, \tag{6.13}$$

which agrees with the results presented in this Section to within an order of magnitude. It is also possible that large significances/figures of merit are related to the fact that these lower mass signals might already be excluded – dependent on the configuration of the signal event generation. Alternately, they could be a consequence of the signal extrapolation procedure or the relatively low statistics of the event samples considered.

Ultimately, large significances mean that the integrated luminosity needed to reach a 5σ discovery-level significance is small. The necessity for higher luminosities is instead highlighted by briefly considering a lower cross-section signal, electroweakino production. Low-mass electroweakino pair-production ($\tilde{\chi}\tilde{\chi}$) typically has a cross-section that is a factor 10^{-3} smaller than for gluino pair-production[13] [8, 89]. These results are summarised only for the event-level significance metrics in Table 6.10 with a tight jet p_{T} selection. The maximum significance (using $Z_{\mathrm{e},1} = S/\sqrt{B}$) level of $\sim 4.36\sigma$ achieved by scaling the signal cross-section indicates that even with the 3000 fb^{-1} integrated luminosity expected at the HL-LHC, it is difficult to claim discovery of very low cross-section signals without rigorous optimisation of analysis frameworks and a well configured pile-up rejection scheme. Even so, a $\sim 4.36\sigma$ significance provides evidence for the existence of new particles and is a promising result. To achieve the full 5σ discovery significance requires an integrated luminosity[14]:

$$\mathcal{L}_{5\sigma} = \left(\frac{5}{4.36858}\right)^2 \times 3000 \text{ fb}^{-1} \approx 3930 \text{ fb}^{-1}, \tag{6.14}$$

which is only 930 fb^{-1} larger than the expected HL-LHC dataset integrated luminosity. Further studies that consider more complete analysis optimisation procedures could find that electroweakino production is indeed discoverable at the HL-LHC. The

[12] The signal model in Ref. [95] was slightly different to that considered here: the gluino decay occurs with the production of an intermediate squark ($\tilde{g} \to q\tilde{q} \to qqq$), which has a significantly larger mass (5 TeV) compared to the gluino.

[13] The cross-sections in Ref. [8, 89] are for 13 TeV and 14 TeV CM energy pp collisions for $\tilde{g}$ and $\tilde{\chi}$, respectively. However, the difference in cross-section for both processes at 14 TeV CM energy collisions would be similar had both cross-sections been evaluated at the same $\sqrt{s}$.

[14] For $Z = S/\sqrt{B}$ significance/figure of merit estimates derived with luminosity $\mathcal{L}_0$, an extrapolation to a different luminosity can be achieved by scaling the significance appropriately: $Z(\mathcal{L}_1) = \sqrt{\frac{\mathcal{L}_1}{\mathcal{L}_0}} \times Z(\mathcal{L}_0)$. Where $Z(\mathcal{L}_i)$ is the significance at a given integrated luminosity and $\mathcal{L}_1$ is the new luminosity.

continuation of these studies by addressing the areas of further work discussed in detail throughout Section 6.5 and more briefly throughout this Section are necessary to obtain more accurate projections for the sensitivity of ATLAS to these processes.

Table 6.4: Event yields calculated immediately after the pre-selection is applied for signal ($m_{\tilde{g}} = 400$ GeV) and background. The yields are calculated from integrals of the H_{T} distributions in Figure 6.16. The pre-selection is described by the following nomenclature: `NjX` is the jet multiplicity cut, `jPtX` is the jet p_{T} cut, `6jPtX` is the sixth jet p_{T} cut, `jEtaX` is the jet $|\eta|$ cut (multiplied by 10), and `HTX` is the H_{T} selection.

Pre-selection	Signal events passing pre-selection	Background events passing pre-selection	S/B yield ratio	$S/\sqrt{B}$ yield ratio
Nj6_jPt20_6jPt20_jEta24_HT650	802281680	11103232648	0.0723	7614
Nj6_jPt20_6jPt40_jEta24_HT650	568804559	3402686018	0.1672	9751
Nj6_jPt30_6jPt40_jEta24_HT650	557390060	3240987411	0.172	9791
Nj6_jPt40_6jPt40_jEta24_HT650	544461923	3081579253	0.1767	9808
Nj6_jPt20_6jPt50_jEta24_HT650	431881389	1684920093	0.2563	10521
Nj6_jPt30_6jPt50_jEta24_HT650	425924560	1616370578	0.2635	10594
Nj6_jPt40_6jPt50_jEta24_HT650	419347629	1574473096	0.2663	10568

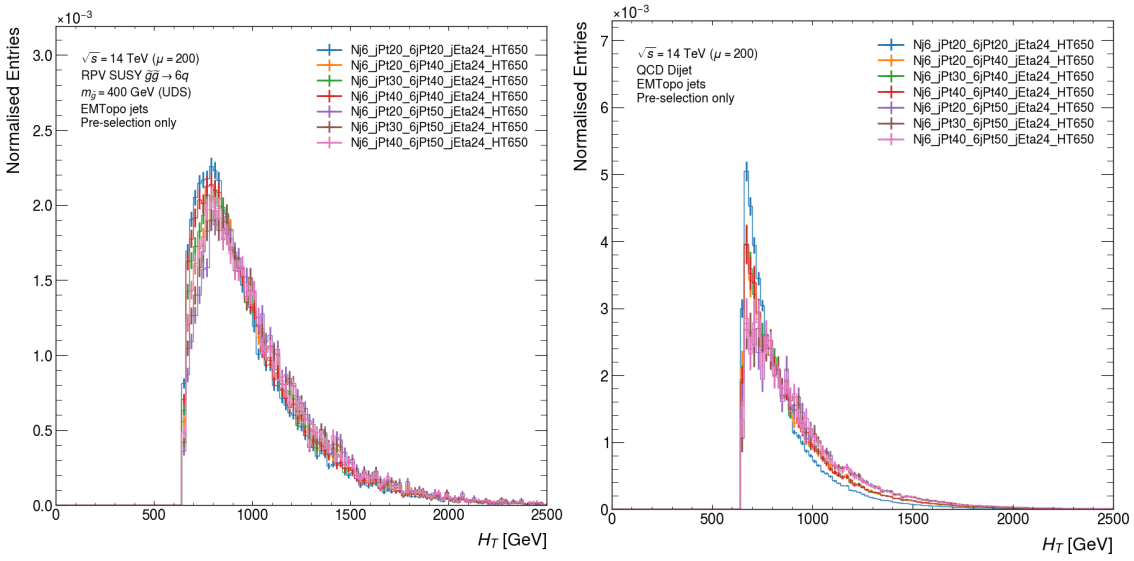

(a) $m_{\tilde{g}} = 400$ GeV signal.

(b) QCD background.

Figure 6.16: H_{T} distributions for the signal (left) and background (right) jets passing different pre-selection cuts. The pre-selection variation is included in the legend – `NjX` is the jet multiplicity cut, `jPtX` is the jet p_{T} cut, `6jPtX` is the sixth jet p_{T} cut, `jEtaX` is the jet $|\eta|$ cut (multiplied by 10), and `HTX` is the H_{T} selection.

Table 6.5: Analysis optimisation results for the $m_{\tilde{g}} = 400$ GeV signal using the triplet-level m_{jjj} integral figure of merit. The integrals for these calculations were calculated with a total mass window width of 200 GeV centred on the signal peak. Only the 10 best performing selections according to the metric denoted with ** are shown for each version of the pre-selection. The first, second, and third column display $Z_{\text{t},1}$, $Z_{\text{t},3}$, and $Z_{\text{t},2}$, respectively.

Pre-selection	Analysis selection	$Z = S/\sqrt{\sum B_{\text{QCD,sig}}}$**	$Z = S/\sqrt{S + B_{\text{QCD,sig}}}$	$Z = S_{\text{total}}/\sqrt{B_{\text{QCD}}}$
$N_{\text{jets}} \geq 6$ $p_{\text{T}}^{\text{jet}} > 20.0$ GeV, $p_{\text{T}}^{\text{jet}}(6) > 20.0$ GeV $\lvert\eta_{\text{jet}}\rvert < 2.4$, $H_{\text{T}} > 650.0$ GeV	$D^2_{[(6,3)+(3,2)]} < 1.25$ $A_m < 0.3$ $\Delta > 150$ GeV $D^2_{[3,2]} < 0.1$	467.44	1112.63	1459.2
$N_{\text{jets}} \geq 6$ $p_{\text{T}}^{\text{jet}} > 20.0$ GeV, $p_{\text{T}}^{\text{jet}}(6) > 20.0$ GeV $\lvert\eta_{\text{jet}}\rvert < 2.4$, $H_{\text{T}} > 650.0$ GeV	$D^2_{[(6,3)+(3,2)]} < 1.25$ $A_m < 0.275$ $\Delta > 150$ GeV $D^2_{[3,2]} < 0.1$	466.72	1092.2	1441.92
$N_{\text{jets}} \geq 6$ $p_{\text{T}}^{\text{jet}} > 20.0$ GeV, $p_{\text{T}}^{\text{jet}}(6) > 20.0$ GeV $\lvert\eta_{\text{jet}}\rvert < 2.4$, $H_{\text{T}} > 650.0$ GeV	$D^2_{[(6,3)+(3,2)]} < 1.375$ $A_m < 0.3$ $\Delta > 150$ GeV $D^2_{[3,2]} < 0.1$	465.52	1133.59	1442.12
$N_{\text{jets}} \geq 6$ $p_{\text{T}}^{\text{jet}} > 20.0$ GeV, $p_{\text{T}}^{\text{jet}}(6) > 20.0$ GeV $\lvert\eta_{\text{jet}}\rvert < 2.4$, $H_{\text{T}} > 650.0$ GeV	$D^2_{[(6,3)+(3,2)]} < 1.375$ $A_m < 0.275$ $\Delta > 150$ GeV $D^2_{[3,2]} < 0.1$	465.16	1114.04	1425.44
$N_{\text{jets}} \geq 6$ $p_{\text{T}}^{\text{jet}} > 20.0$ GeV, $p_{\text{T}}^{\text{jet}}(6) > 20.0$ GeV $\lvert\eta_{\text{jet}}\rvert < 2.4$, $H_{\text{T}} > 650.0$ GeV	$D^2_{[(6,3)+(3,2)]} < 1.25$ $A_m < 0.225$ $\Delta > 150$ GeV $D^2_{[3,2]} < 0.1$	463.63	1039.49	1383.72
$N_{\text{jets}} \geq 6$ $p_{\text{T}}^{\text{jet}} > 20.0$ GeV, $p_{\text{T}}^{\text{jet}}(6) > 20.0$ GeV $\lvert\eta_{\text{jet}}\rvert < 2.4$, $H_{\text{T}} > 650.0$ GeV	$D^2_{[(6,3)+(3,2)]} < 1.375$ $A_m < 0.225$ $\Delta > 150$ GeV $D^2_{[3,2]} < 0.1$	462.9	1067	1379.38
$N_{\text{jets}} \geq 6$ $p_{\text{T}}^{\text{jet}} > 20.0$ GeV, $p_{\text{T}}^{\text{jet}}(6) > 20.0$ GeV $\lvert\eta_{\text{jet}}\rvert < 2.4$, $H_{\text{T}} > 650.0$ GeV	$D^2_{[(6,3)+(3,2)]} < 1.375$ $A_m < 0.25$ $\Delta > 150$ GeV $D^2_{[3,2]} < 0.1$	462.46	1090.45	1401.08
$N_{\text{jets}} \geq 6$ $p_{\text{T}}^{\text{jet}} > 20.0$ GeV, $p_{\text{T}}^{\text{jet}}(6) > 20.0$ GeV $\lvert\eta_{\text{jet}}\rvert < 2.4$, $H_{\text{T}} > 650.0$ GeV	$D^2_{[(6,3)+(3,2)]} < 1.25$ $A_m < 0.25$ $\Delta > 150$ GeV $D^2_{[3,2]} < 0.1$	462.39	1068.36	1416.58
$N_{\text{jets}} \geq 6$ $p_{\text{T}}^{\text{jet}} > 20.0$ GeV, $p_{\text{T}}^{\text{jet}}(6) > 20.0$ GeV $\lvert\eta_{\text{jet}}\rvert < 2.4$, $H_{\text{T}} > 650.0$ GeV	$D^2_{[(6,3)+(3,2)]} < 1.5$ $A_m < 0.3$ $\Delta > 150$ GeV $D^2_{[3,2]} < 0.1$	461.25	1156.76	1440.19
$N_{\text{jets}} \geq 6$ $p_{\text{T}}^{\text{jet}} > 20.0$ GeV, $p_{\text{T}}^{\text{jet}}(6) > 20.0$ GeV $\lvert\eta_{\text{jet}}\rvert < 2.4$, $H_{\text{T}} > 650.0$ GeV	$D^2_{[(6,3)+(3,2)]} < 1.5$ $A_m < 0.275$ $\Delta > 150$ GeV $D^2_{[3,2]} < 0.1$	461.04	1138.18	1425.15

(a) Loose jet p_{T} and sixth jet p_{T} selection.

Table 6.5 (cont.): Analysis optimisation results for the $m_{\tilde{g}} = 400$ GeV signal using the triplet-level m_{jjj} integral figure of merit. The integrals for these calculations were calculated with a total mass window width of 200 GeV centred on the signal peak. Only the 10 best performing selections according to the metric denoted with ** are shown for each version of the pre-selection. The first, second, and third column display $Z_{\text{t},1}$, $Z_{\text{t},3}$, and $Z_{\text{t},2}$, respectively.

Pre-selection	Analysis selection	$Z = S/\sqrt{\sum B_{\text{QCD,sig}}}$**	$Z = S/\sqrt{S + B_{\text{QCD,sig}}}$	$Z = S_{\text{total}}/\sqrt{B_{\text{QCD}}}$
$N_{\text{jets}} \geq 6$ $p_{\text{T}}^{\text{jet}} > 30.0$ GeV, $p_{\text{T}}^{\text{jet}}(6) > 40.0$ GeV $\lvert\eta_{\text{jet}}\rvert < 2.4$, $H_{\text{T}} > 650.0$ GeV	$D^2_{[(6,3)+(3,2)]} < 1.5$ $A_m < 0.3$ $\Delta > 150$ GeV $D^2_{[3,2]} < 0.1$	501.28	1202.12	1629.66
$N_{\text{jets}} \geq 6$ $p_{\text{T}}^{\text{jet}} > 30.0$ GeV, $p_{\text{T}}^{\text{jet}}(6) > 40.0$ GeV $\lvert\eta_{\text{jet}}\rvert < 2.4$, $H_{\text{T}} > 650.0$ GeV	$D^2_{[(6,3)+(3,2)]} < 1.5$ $A_m < 0.275$ $\Delta > 150$ GeV $D^2_{[3,2]} < 0.1$	500.21	1178.01	1608.63
$N_{\text{jets}} \geq 6$ $p_{\text{T}}^{\text{jet}} > 30.0$ GeV, $p_{\text{T}}^{\text{jet}}(6) > 40.0$ GeV $\lvert\eta_{\text{jet}}\rvert < 2.4$, $H_{\text{T}} > 650.0$ GeV	$D^2_{[(6,3)+(3,2)]} < 1.375$ $A_m < 0.3$ $\Delta > 150$ GeV $D^2_{[3,2]} < 0.1$	499.96	1176.52	1625.35
$N_{\text{jets}} \geq 6$ $p_{\text{T}}^{\text{jet}} > 30.0$ GeV, $p_{\text{T}}^{\text{jet}}(6) > 40.0$ GeV $\lvert\eta_{\text{jet}}\rvert < 2.4$, $H_{\text{T}} > 650.0$ GeV	$D^2_{[(6,3)+(3,2)]} < 1.375$ $A_m < 0.275$ $\Delta > 150$ GeV $D^2_{[3,2]} < 0.1$	498.92	1151.63	1601.55
$N_{\text{jets}} \geq 6$ $p_{\text{T}}^{\text{jet}} > 30.0$ GeV, $p_{\text{T}}^{\text{jet}}(6) > 40.0$ GeV $\lvert\eta_{\text{jet}}\rvert < 2.4$, $H_{\text{T}} > 650.0$ GeV	$D^2_{[(6,3)+(3,2)]} < 1.25$ $A_m < 0.3$ $\Delta > 150$ GeV $D^2_{[3,2]} < 0.1$	498.25	1155.01	1644.29
$N_{\text{jets}} \geq 6$ $p_{\text{T}}^{\text{jet}} > 30.0$ GeV, $p_{\text{T}}^{\text{jet}}(6) > 40.0$ GeV $\lvert\eta_{\text{jet}}\rvert < 2.4$, $H_{\text{T}} > 650.0$ GeV	$D^2_{[(6,3)+(3,2)]} < 1.25$ $A_m < 0.275$ $\Delta > 150$ GeV $D^2_{[3,2]} < 0.1$	496.41	1128.23	1616.98
$N_{\text{jets}} \geq 6$ $p_{\text{T}}^{\text{jet}} > 30.0$ GeV, $p_{\text{T}}^{\text{jet}}(6) > 40.0$ GeV $\lvert\eta_{\text{jet}}\rvert < 2.4$, $H_{\text{T}} > 650.0$ GeV	$D^2_{[(6,3)+(3,2)]} < 1.5$ $A_m < 0.25$ $\Delta > 150$ GeV $D^2_{[3,2]} < 0.1$	496.2	1146.43	1570.41
$N_{\text{jets}} \geq 6$ $p_{\text{T}}^{\text{jet}} > 30.0$ GeV, $p_{\text{T}}^{\text{jet}}(6) > 40.0$ GeV $\lvert\eta_{\text{jet}}\rvert < 2.4$, $H_{\text{T}} > 650.0$ GeV	$D^2_{[(6,3)+(3,2)]} < 1.5$ $A_m < 0.225$ $\Delta > 150$ GeV $D^2_{[3,2]} < 0.1$	495.46	1118.69	1543.37
$N_{\text{jets}} \geq 6$ $p_{\text{T}}^{\text{jet}} > 30.0$ GeV, $p_{\text{T}}^{\text{jet}}(6) > 40.0$ GeV $\lvert\eta_{\text{jet}}\rvert < 2.4$, $H_{\text{T}} > 650.0$ GeV	$D^2_{[(6,3)+(3,2)]} < 1.375$ $A_m < 0.25$ $\Delta > 150$ GeV $D^2_{[3,2]} < 0.1$	494.44	1121.37	1564.73
$N_{\text{jets}} \geq 6$ $p_{\text{T}}^{\text{jet}} > 30.0$ GeV, $p_{\text{T}}^{\text{jet}}(6) > 40.0$ GeV $\lvert\eta_{\text{jet}}\rvert < 2.4$, $H_{\text{T}} > 650.0$ GeV	$D^2_{[(6,3)+(3,2)]} < 1.375$ $A_m < 0.225$ $\Delta > 150$ GeV $D^2_{[3,2]} < 0.1$	494.27	1092.67	1534.58

(b) CMS-like p_{T} and sixth jet p_{T} selection from Ref. [109].

Table 6.5 (cont.): Analysis optimisation results for the $m_{\tilde{g}} = 400$ GeV signal using the triplet-level m_{jjj} integral figure of merit. The integrals for these calculations were calculated with a total mass window width of 200 GeV centred on the signal peak. Only the 10 best performing selections according to the metric denoted with ** are shown for each version of the pre-selection. The first, second, and third column display $Z_{\text{t},1}$, $Z_{\text{t},3}$, and $Z_{\text{t},2}$, respectively.

Pre-selection	Analysis selection	$Z = S/\sqrt{\sum B_{\text{QCD,sig}}}$**	$Z = S/\sqrt{S + B_{\text{QCD,sig}}}$	$Z = S_{\text{total}}/\sqrt{B_{\text{QCD}}}$
$N_{\text{jets}} \geq 6$ $p_{\text{T}}^{\text{jet}} > 40.0$ GeV, $p_{\text{T}}^{\text{jet}}(6) > 50.0$ GeV $\lvert\eta_{\text{jet}}\rvert < 2.4$, $H_{\text{T}} > 650.0$ GeV	$D^2_{[(6,3)+(3,2)]} < 1.375$ $A_m < 0.3$ $\Delta > 150$ GeV $D^2_{[3,2]} < 0.1$	502.38	1163.28	1715.01
$N_{\text{jets}} \geq 6$ $p_{\text{T}}^{\text{jet}} > 40.0$ GeV, $p_{\text{T}}^{\text{jet}}(6) > 50.0$ GeV $\lvert\eta_{\text{jet}}\rvert < 2.4$, $H_{\text{T}} > 650.0$ GeV	$D^2_{[(6,3)+(3,2)]} < 1.5$ $A_m < 0.3$ $\Delta > 150$ GeV $D^2_{[3,2]} < 0.1$	501.98	1175.51	1702.97
$N_{\text{jets}} \geq 6$ $p_{\text{T}}^{\text{jet}} > 40.0$ GeV, $p_{\text{T}}^{\text{jet}}(6) > 50.0$ GeV $\lvert\eta_{\text{jet}}\rvert < 2.4$, $H_{\text{T}} > 650.0$ GeV	$D^2_{[(6,3)+(3,2)]} < 1.25$ $A_m < 0.3$ $\Delta > 150$ GeV $D^2_{[3,2]} < 0.1$	501.73	1142.89	1733.4
$N_{\text{jets}} \geq 6$ $p_{\text{T}}^{\text{jet}} > 40.0$ GeV, $p_{\text{T}}^{\text{jet}}(6) > 50.0$ GeV $\lvert\eta_{\text{jet}}\rvert < 2.4$, $H_{\text{T}} > 650.0$ GeV	$D^2_{[(6,3)+(3,2)]} < 1.375$ $A_m < 0.275$ $\Delta > 150$ GeV $D^2_{[3,2]} < 0.1$	498.37	1136.87	1689.2
$N_{\text{jets}} \geq 6$ $p_{\text{T}}^{\text{jet}} > 40.0$ GeV, $p_{\text{T}}^{\text{jet}}(6) > 50.0$ GeV $\lvert\eta_{\text{jet}}\rvert < 2.4$, $H_{\text{T}} > 650.0$ GeV	$D^2_{[(6,3)+(3,2)]} < 1.5$ $A_m < 0.275$ $\Delta > 150$ GeV $D^2_{[3,2]} < 0.1$	497.9	1149.48	1678.93
$N_{\text{jets}} \geq 6$ $p_{\text{T}}^{\text{jet}} > 40.0$ GeV, $p_{\text{T}}^{\text{jet}}(6) > 50.0$ GeV $\lvert\eta_{\text{jet}}\rvert < 2.4$, $H_{\text{T}} > 650.0$ GeV	$D^2_{[(6,3)+(3,2)]} < 1.25$ $A_m < 0.275$ $\Delta > 150$ GeV $D^2_{[3,2]} < 0.1$	496.44	1113.85	1700.08
$N_{\text{jets}} \geq 6$ $p_{\text{T}}^{\text{jet}} > 40.0$ GeV, $p_{\text{T}}^{\text{jet}}(6) > 50.0$ GeV $\lvert\eta_{\text{jet}}\rvert < 2.4$, $H_{\text{T}} > 650.0$ GeV	$D^2_{[(6,3)+(3,2)]} < 1.5$ $A_m < 0.225$ $\Delta > 150$ GeV $D^2_{[3,2]} < 0.1$	494.2	1091.49	1614.53
$N_{\text{jets}} \geq 6$ $p_{\text{T}}^{\text{jet}} > 40.0$ GeV, $p_{\text{T}}^{\text{jet}}(6) > 50.0$ GeV $\lvert\eta_{\text{jet}}\rvert < 2.4$, $H_{\text{T}} > 650.0$ GeV	$D^2_{[(6,3)+(3,2)]} < 1.375$ $A_m < 0.25$ $\Delta > 150$ GeV $D^2_{[3,2]} < 0.1$	493.12	1108.95	1659
$N_{\text{jets}} \geq 6$ $p_{\text{T}}^{\text{jet}} > 40.0$ GeV, $p_{\text{T}}^{\text{jet}}(6) > 50.0$ GeV $\lvert\eta_{\text{jet}}\rvert < 2.4$, $H_{\text{T}} > 650.0$ GeV	$D^2_{[(6,3)+(3,2)]} < 1.375$ $A_m < 0.225$ $\Delta > 150$ GeV $D^2_{[3,2]} < 0.1$	492.97	1078.17	1620.91
$N_{\text{jets}} \geq 6$ $p_{\text{T}}^{\text{jet}} > 40.0$ GeV, $p_{\text{T}}^{\text{jet}}(6) > 50.0$ GeV $\lvert\eta_{\text{jet}}\rvert < 2.4$, $H_{\text{T}} > 650.0$ GeV	$D^2_{[(6,3)+(3,2)]} < 1.5$ $A_m < 0.25$ $\Delta > 150$ GeV $D^2_{[3,2]} < 0.1$	492.92	1120.92	1648.13

(c) Tight p_{T} and sixth jet p_{T} selection.

Table 6.6: Analysis optimisation results for the $m_{\tilde{g}} = 400$ GeV signal using the triplet-level m_{jjj} integral figure of merit. The integrals for these calculations were calculated with a total mass window width of 300 GeV centred on the signal peak. Only the 10 best performing selections according to the metric denoted with ** are shown for each version of the pre-selection. The first, second, and third column display $Z_{\mathrm{t},1}$, $Z_{\mathrm{t},3}$, and $Z_{\mathrm{t},2}$, respectively.

Pre-selection	Analysis selection	$Z = S/\sqrt{\sum B_{\mathrm{QCD,sig}}}$**	$Z = S/\sqrt{S + B_{\mathrm{QCD,sig}}}$	$Z = S_{\mathrm{total}}/\sqrt{B_{\mathrm{QCD}}}$
$N_{\mathrm{jets}} \geq 6$ $p_{\mathrm{T}}^{\mathrm{jet}} > 20.0$ GeV, $p_{\mathrm{T}}^{\mathrm{jet}}(6) > 20.0$ GeV $\lvert\eta_{\mathrm{jet}}\rvert < 2.4$, $H_{\mathrm{T}} > 650.0$ GeV	$D^2_{[(6,3)+(3,2)]} < 1.25$ $A_m < 0.225$ $\Delta > 150$ GeV $D^2_{[3,2]} < 0.1$	383.03	1115.44	1421.03
$N_{\mathrm{jets}} \geq 6$ $p_{\mathrm{T}}^{\mathrm{jet}} > 20.0$ GeV, $p_{\mathrm{T}}^{\mathrm{jet}}(6) > 20.0$ GeV $\lvert\eta_{\mathrm{jet}}\rvert < 2.4$, $H_{\mathrm{T}} > 650.0$ GeV	$D^2_{[(6,3)+(3,2)]} < 1.25$ $A_m < 0.275$ $\Delta > 150$ GeV $D^2_{[3,2]} < 0.1$	382.55	1178.55	1490.03
$N_{\mathrm{jets}} \geq 6$ $p_{\mathrm{T}}^{\mathrm{jet}} > 20.0$ GeV, $p_{\mathrm{T}}^{\mathrm{jet}}(6) > 20.0$ GeV $\lvert\eta_{\mathrm{jet}}\rvert < 2.4$, $H_{\mathrm{T}} > 650.0$ GeV	$D^2_{[(6,3)+(3,2)]} < 1.25$ $A_m < 0.25$ $\Delta > 150$ GeV $D^2_{[3,2]} < 0.1$	382.24	1149.47	1460.46
$N_{\mathrm{jets}} \geq 6$ $p_{\mathrm{T}}^{\mathrm{jet}} > 20.0$ GeV, $p_{\mathrm{T}}^{\mathrm{jet}}(6) > 20.0$ GeV $\lvert\eta_{\mathrm{jet}}\rvert < 2.4$, $H_{\mathrm{T}} > 650.0$ GeV	$D^2_{[(6,3)+(3,2)]} < 1.25$ $A_m < 0.3$ $\Delta > 150$ GeV $D^2_{[3,2]} < 0.1$	382.12	1200.08	1507.71
$N_{\mathrm{jets}} \geq 6$ $p_{\mathrm{T}}^{\mathrm{jet}} > 20.0$ GeV, $p_{\mathrm{T}}^{\mathrm{jet}}(6) > 20.0$ GeV $\lvert\eta_{\mathrm{jet}}\rvert < 2.4$, $H_{\mathrm{T}} > 650.0$ GeV	$D^2_{[(6,3)+(3,2)]} < 1.25$ $A_m < 0.2$ $\Delta > 150$ GeV $D^2_{[3,2]} < 0.1$	381.11	1062.51	1355.57
$N_{\mathrm{jets}} \geq 6$ $p_{\mathrm{T}}^{\mathrm{jet}} > 20.0$ GeV, $p_{\mathrm{T}}^{\mathrm{jet}}(6) > 20.0$ GeV $\lvert\eta_{\mathrm{jet}}\rvert < 2.4$, $H_{\mathrm{T}} > 650.0$ GeV	$D^2_{[(6,3)+(3,2)]} < 1.375$ $A_m < 0.25$ $\Delta > 150$ GeV $D^2_{[3,2]} < 0.1$	380.74	1165.59	1438.07
$N_{\mathrm{jets}} \geq 6$ $p_{\mathrm{T}}^{\mathrm{jet}} > 20.0$ GeV, $p_{\mathrm{T}}^{\mathrm{jet}}(6) > 20.0$ GeV $\lvert\eta_{\mathrm{jet}}\rvert < 2.4$, $H_{\mathrm{T}} > 650.0$ GeV	$D^2_{[(6,3)+(3,2)]} < 1.375$ $A_m < 0.275$ $\Delta > 150$ GeV $D^2_{[3,2]} < 0.1$	380.68	1196.89	1471.38
$N_{\mathrm{jets}} \geq 6$ $p_{\mathrm{T}}^{\mathrm{jet}} > 20.0$ GeV, $p_{\mathrm{T}}^{\mathrm{jet}}(6) > 20.0$ GeV $\lvert\eta_{\mathrm{jet}}\rvert < 2.4$, $H_{\mathrm{T}} > 650.0$ GeV	$D^2_{[(6,3)+(3,2)]} < 1.375$ $A_m < 0.3$ $\Delta > 150$ GeV $D^2_{[3,2]} < 0.1$	380.19	1218.91	1491.04
$N_{\mathrm{jets}} \geq 6$ $p_{\mathrm{T}}^{\mathrm{jet}} > 20.0$ GeV, $p_{\mathrm{T}}^{\mathrm{jet}}(6) > 20.0$ GeV $\lvert\eta_{\mathrm{jet}}\rvert < 2.4$, $H_{\mathrm{T}} > 650.0$ GeV	$D^2_{[(6,3)+(3,2)]} < 1.375$ $A_m < 0.225$ $\Delta > 150$ GeV $D^2_{[3,2]} < 0.1$	380.05	1134.77	1405.46
$N_{\mathrm{jets}} \geq 6$ $p_{\mathrm{T}}^{\mathrm{jet}} > 20.0$ GeV, $p_{\mathrm{T}}^{\mathrm{jet}}(6) > 20.0$ GeV $\lvert\eta_{\mathrm{jet}}\rvert < 2.4$, $H_{\mathrm{T}} > 650.0$ GeV	$D^2_{[(6,3)+(3,2)]} < 1.125$ $A_m < 0.275$ $\Delta > 150$ GeV $D^2_{[3,2]} < 0.1$	379.03	1150.9	1513.01

(a) Loose jet p_{T} and sixth jet p_{T} selection.

Table 6.6 (cont.): Analysis optimisation results for the $m_{\tilde{g}} = 400$ GeV signal using the triplet-level m_{jjj} integral figure of merit. The integrals for these calculations were calculated with a total mass window width of 300 GeV centred on the signal peak. Only the 10 best performing selections according to the metric denoted with ** are shown for each version of the pre-selection. The first, second, and third column display $Z_{\text{t},1}$, $Z_{\text{t},3}$, and $Z_{\text{t},2}$, respectively.

Pre-selection	Analysis selection	$Z = S/\sqrt{\sum B_{\text{QCD,sig}}}$**	$Z = S/\sqrt{S + B_{\text{QCD,sig}}}$	$Z = S_{\text{total}}/\sqrt{B_{\text{QCD}}}$
$N_{\text{jets}} \geq 6$ $p_{\text{T}}^{\text{jet}} > 30.0$ GeV, $p_{\text{T}}^{\text{jet}}(6) > 40.0$ GeV $\lvert\eta_{\text{jet}}\rvert < 2.4$, $H_{\text{T}} > 650.0$ GeV	$D^2_{[(6,3)+(3,2)]} < 1.5$ $A_m < 0.25$ $\Delta > 150$ GeV $D^2_{[3,2]} < 0.1$	420.16	1250.01	1651.66
$N_{\text{jets}} \geq 6$ $p_{\text{T}}^{\text{jet}} > 30.0$ GeV, $p_{\text{T}}^{\text{jet}}(6) > 40.0$ GeV $\lvert\eta_{\text{jet}}\rvert < 2.4$, $H_{\text{T}} > 650.0$ GeV	$D^2_{[(6,3)+(3,2)]} < 1.5$ $A_m < 0.3$ $\Delta > 150$ GeV $D^2_{[3,2]} < 0.1$	419.69	1313.18	1715.05
$N_{\text{jets}} \geq 6$ $p_{\text{T}}^{\text{jet}} > 30.0$ GeV, $p_{\text{T}}^{\text{jet}}(6) > 40.0$ GeV $\lvert\eta_{\text{jet}}\rvert < 2.4$, $H_{\text{T}} > 650.0$ GeV	$D^2_{[(6,3)+(3,2)]} < 1.5$ $A_m < 0.275$ $\Delta > 150$ GeV $D^2_{[3,2]} < 0.1$	419.39	1286.67	1691.53
$N_{\text{jets}} \geq 6$ $p_{\text{T}}^{\text{jet}} > 30.0$ GeV, $p_{\text{T}}^{\text{jet}}(6) > 40.0$ GeV $\lvert\eta_{\text{jet}}\rvert < 2.4$, $H_{\text{T}} > 650.0$ GeV	$D^2_{[(6,3)+(3,2)]} < 1.5$ $A_m < 0.225$ $\Delta > 150$ GeV $D^2_{[3,2]} < 0.1$	419.04	1214.88	1613.88
$N_{\text{jets}} \geq 6$ $p_{\text{T}}^{\text{jet}} > 30.0$ GeV, $p_{\text{T}}^{\text{jet}}(6) > 40.0$ GeV $\lvert\eta_{\text{jet}}\rvert < 2.4$, $H_{\text{T}} > 650.0$ GeV	$D^2_{[(6,3)+(3,2)]} < 1.5$ $A_m < 0.2$ $\Delta > 150$ GeV $D^2_{[3,2]} < 0.1$	417.75	1164.7	1556
$N_{\text{jets}} \geq 6$ $p_{\text{T}}^{\text{jet}} > 30.0$ GeV, $p_{\text{T}}^{\text{jet}}(6) > 40.0$ GeV $\lvert\eta_{\text{jet}}\rvert < 2.4$, $H_{\text{T}} > 650.0$ GeV	$D^2_{[(6,3)+(3,2)]} < 1.375$ $A_m < 0.25$ $\Delta > 150$ GeV $D^2_{[3,2]} < 0.1$	417.08	1223.65	1643.56
$N_{\text{jets}} \geq 6$ $p_{\text{T}}^{\text{jet}} > 30.0$ GeV, $p_{\text{T}}^{\text{jet}}(6) > 40.0$ GeV $\lvert\eta_{\text{jet}}\rvert < 2.4$, $H_{\text{T}} > 650.0$ GeV	$D^2_{[(6,3)+(3,2)]} < 1.375$ $A_m < 0.3$ $\Delta > 150$ GeV $D^2_{[3,2]} < 0.1$	416.56	1285.88	1706.89
$N_{\text{jets}} \geq 6$ $p_{\text{T}}^{\text{jet}} > 30.0$ GeV, $p_{\text{T}}^{\text{jet}}(6) > 40.0$ GeV $\lvert\eta_{\text{jet}}\rvert < 2.4$, $H_{\text{T}} > 650.0$ GeV	$D^2_{[(6,3)+(3,2)]} < 1.375$ $A_m < 0.275$ $\Delta > 150$ GeV $D^2_{[3,2]} < 0.1$	416.39	1258.28	1680.11
$N_{\text{jets}} \geq 6$ $p_{\text{T}}^{\text{jet}} > 30.0$ GeV, $p_{\text{T}}^{\text{jet}}(6) > 40.0$ GeV $\lvert\eta_{\text{jet}}\rvert < 2.4$, $H_{\text{T}} > 650.0$ GeV	$D^2_{[(6,3)+(3,2)]} < 1.375$ $A_m < 0.225$ $\Delta > 150$ GeV $D^2_{[3,2]} < 0.1$	416.29	1190.25	1607.93
$N_{\text{jets}} \geq 6$ $p_{\text{T}}^{\text{jet}} > 30.0$ GeV, $p_{\text{T}}^{\text{jet}}(6) > 40.0$ GeV $\lvert\eta_{\text{jet}}\rvert < 2.4$, $H_{\text{T}} > 650.0$ GeV	$D^2_{[(6,3)+(3,2)]} < 1.375$ $A_m < 0.2$ $\Delta > 150$ GeV $D^2_{[3,2]} < 0.1$	414.52	1139.22	1547.34

(b) CMS-like p_{T} and sixth jet p_{T} selection from Ref. [109].

Table 6.6 (cont.): Analysis optimisation results for the $m_{\tilde{g}} = 400$ GeV signal using the triplet-level m_{jjj} integral figure of merit. The integrals for these calculations were calculated with a total mass window width of 300 GeV centred on the signal peak. Only the 10 best performing selections according to the metric denoted with ** are shown for each version of the pre-selection. The first, second, and third column display $Z_{\mathrm{t},1}$, $Z_{\mathrm{t},3}$, and $Z_{\mathrm{t},2}$, respectively.

Pre-selection	Analysis selection	$Z = S/\sqrt{\sum B_{\mathrm{QCD,sig}}}$**	$Z = S/\sqrt{S + B_{\mathrm{QCD,sig}}}$	$Z = S_{\mathrm{total}}/\sqrt{B_{\mathrm{QCD}}}$
$N_{\mathrm{jets}} \geq 6$ $p_{\mathrm{T}}^{\mathrm{jet}} > 40.0$ GeV, $p_{\mathrm{T}}^{\mathrm{jet}}(6) > 50.0$ GeV $\lvert\eta_{\mathrm{jet}}\rvert < 2.4$, $H_{\mathrm{T}} > 650.0$ GeV	$D^2_{[(6,3)+(3,2)]} < 1.375$ $A_m < 0.3$ $\Delta > 150$ GeV $D^2_{[3,2]} < 0.1$	425.46	1279.08	1816.76
$N_{\mathrm{jets}} \geq 6$ $p_{\mathrm{T}}^{\mathrm{jet}} > 40.0$ GeV, $p_{\mathrm{T}}^{\mathrm{jet}}(6) > 50.0$ GeV $\lvert\eta_{\mathrm{jet}}\rvert < 2.4$, $H_{\mathrm{T}} > 650.0$ GeV	$D^2_{[(6,3)+(3,2)]} < 1.5$ $A_m < 0.3$ $\Delta > 150$ GeV $D^2_{[3,2]} < 0.1$	425.05	1293.51	1805.82
$N_{\mathrm{jets}} \geq 6$ $p_{\mathrm{T}}^{\mathrm{jet}} > 40.0$ GeV, $p_{\mathrm{T}}^{\mathrm{jet}}(6) > 50.0$ GeV $\lvert\eta_{\mathrm{jet}}\rvert < 2.4$, $H_{\mathrm{T}} > 650.0$ GeV	$D^2_{[(6,3)+(3,2)]} < 1.375$ $A_m < 0.275$ $\Delta > 150$ GeV $D^2_{[3,2]} < 0.1$	423.26	1252.99	1795.78
$N_{\mathrm{jets}} \geq 6$ $p_{\mathrm{T}}^{\mathrm{jet}} > 40.0$ GeV, $p_{\mathrm{T}}^{\mathrm{jet}}(6) > 50.0$ GeV $\lvert\eta_{\mathrm{jet}}\rvert < 2.4$, $H_{\mathrm{T}} > 650.0$ GeV	$D^2_{[(6,3)+(3,2)]} < 1.5$ $A_m < 0.275$ $\Delta > 150$ GeV $D^2_{[3,2]} < 0.1$	422.71	1266.91	1783.99
$N_{\mathrm{jets}} \geq 6$ $p_{\mathrm{T}}^{\mathrm{jet}} > 40.0$ GeV, $p_{\mathrm{T}}^{\mathrm{jet}}(6) > 50.0$ GeV $\lvert\eta_{\mathrm{jet}}\rvert < 2.4$, $H_{\mathrm{T}} > 650.0$ GeV	$D^2_{[(6,3)+(3,2)]} < 1.25$ $A_m < 0.3$ $\Delta > 150$ GeV $D^2_{[3,2]} < 0.1$	422.01	1255.73	1824.18
$N_{\mathrm{jets}} \geq 6$ $p_{\mathrm{T}}^{\mathrm{jet}} > 40.0$ GeV, $p_{\mathrm{T}}^{\mathrm{jet}}(6) > 50.0$ GeV $\lvert\eta_{\mathrm{jet}}\rvert < 2.4$, $H_{\mathrm{T}} > 650.0$ GeV	$D^2_{[(6,3)+(3,2)]} < 1.5$ $A_m < 0.225$ $\Delta > 150$ GeV $D^2_{[3,2]} < 0.1$	421.47	1194.43	1701.22
$N_{\mathrm{jets}} \geq 6$ $p_{\mathrm{T}}^{\mathrm{jet}} > 40.0$ GeV, $p_{\mathrm{T}}^{\mathrm{jet}}(6) > 50.0$ GeV $\lvert\eta_{\mathrm{jet}}\rvert < 2.4$, $H_{\mathrm{T}} > 650.0$ GeV	$D^2_{[(6,3)+(3,2)]} < 1.375$ $A_m < 0.25$ $\Delta > 150$ GeV $D^2_{[3,2]} < 0.1$	421.41	1217.16	1755.87
$N_{\mathrm{jets}} \geq 6$ $p_{\mathrm{T}}^{\mathrm{jet}} > 40.0$ GeV, $p_{\mathrm{T}}^{\mathrm{jet}}(6) > 50.0$ GeV $\lvert\eta_{\mathrm{jet}}\rvert < 2.4$, $H_{\mathrm{T}} > 650.0$ GeV	$D^2_{[(6,3)+(3,2)]} < 1.5$ $A_m < 0.25$ $\Delta > 150$ GeV $D^2_{[3,2]} < 0.1$	420.81	1229.34	1740.68
$N_{\mathrm{jets}} \geq 6$ $p_{\mathrm{T}}^{\mathrm{jet}} > 40.0$ GeV, $p_{\mathrm{T}}^{\mathrm{jet}}(6) > 50.0$ GeV $\lvert\eta_{\mathrm{jet}}\rvert < 2.4$, $H_{\mathrm{T}} > 650.0$ GeV	$D^2_{[(6,3)+(3,2)]} < 1.375$ $A_m < 0.225$ $\Delta > 150$ GeV $D^2_{[3,2]} < 0.1$	420.77	1183.21	1717.53
$N_{\mathrm{jets}} \geq 6$ $p_{\mathrm{T}}^{\mathrm{jet}} > 40.0$ GeV, $p_{\mathrm{T}}^{\mathrm{jet}}(6) > 50.0$ GeV $\lvert\eta_{\mathrm{jet}}\rvert < 2.4$, $H_{\mathrm{T}} > 650.0$ GeV	$D^2_{[(6,3)+(3,2)]} < 1.25$ $A_m < 0.275$ $\Delta > 150$ GeV $D^2_{[3,2]} < 0.1$	419.15	1227.35	1798.29

(c) Tight p_{T} and sixth jet p_{T} selection.

Table 6.7: Analysis optimisation results for the $m_{\tilde{g}} = 400$ GeV signal using the event-level significance measure and the CMS-like pre-selection. A double asterisk (**) is used to indicate the metric considered for the optimisation in the header. Only the 10 best performing selections are shown for each version of the pre-selection. The first and second column display $Z_{\mathrm{e},2}$ and $Z_{\mathrm{e},1}$, respectively.

Pre-selection	Analysis selection	$Z = S/\sqrt{S + B_{\mathrm{QCD}}}$	$Z = S/\sqrt{B_{\mathrm{QCD}}}^{**}$
$N_{\mathrm{jets}} \geq 6$ $p_{\mathrm{T}}^{\mathrm{jet}} > 30.0$ GeV, $p_{\mathrm{T}}^{\mathrm{jet}}(6) > 40.0$ GeV $\lvert\eta_{\mathrm{jet}}\rvert < 2.4$, $H_{\mathrm{T}} > 650.0$ GeV	$D^2_{[(6,3)+(3,2)]} < 1.25$ $A_m < 0.3$ $\Delta > 150$ GeV $D^2_{[3,2]} < 0.1$	3037.62	4165.32
$N_{\mathrm{jets}} \geq 6$ $p_{\mathrm{T}}^{\mathrm{jet}} > 30.0$ GeV, $p_{\mathrm{T}}^{\mathrm{jet}}(6) > 40.0$ GeV $\lvert\eta_{\mathrm{jet}}\rvert < 2.4$, $H_{\mathrm{T}} > 650.0$ GeV	$D^2_{[(6,3)+(3,2)]} < 1.375$ $A_m < 0.3$ $\Delta > 150$ GeV $D^2_{[3,2]} < 0.1$	3103.71	4123.52
$N_{\mathrm{jets}} \geq 6$ $p_{\mathrm{T}}^{\mathrm{jet}} > 30.0$ GeV, $p_{\mathrm{T}}^{\mathrm{jet}}(6) > 40.0$ GeV $\lvert\eta_{\mathrm{jet}}\rvert < 2.4$, $H_{\mathrm{T}} > 650.0$ GeV	$D^2_{[(6,3)+(3,2)]} < 1$ $A_m < 0.3$ $\Delta > 150$ GeV $D^2_{[3,2]} < 0.1$	2685.11	4116.72
$N_{\mathrm{jets}} \geq 6$ $p_{\mathrm{T}}^{\mathrm{jet}} > 30.0$ GeV, $p_{\mathrm{T}}^{\mathrm{jet}}(6) > 40.0$ GeV $\lvert\eta_{\mathrm{jet}}\rvert < 2.4$, $H_{\mathrm{T}} > 650.0$ GeV	$D^2_{[(6,3)+(3,2)]} < 1.5$ $A_m < 0.3$ $\Delta > 150$ GeV $D^2_{[3,2]} < 0.1$	3145.1	4069.8
$N_{\mathrm{jets}} \geq 6$ $p_{\mathrm{T}}^{\mathrm{jet}} > 30.0$ GeV, $p_{\mathrm{T}}^{\mathrm{jet}}(6) > 40.0$ GeV $\lvert\eta_{\mathrm{jet}}\rvert < 2.4$, $H_{\mathrm{T}} > 650.0$ GeV	$D^2_{[(6,3)+(3,2)]} < 1.125$ $A_m < 0.3$ $\Delta > 150$ GeV $D^2_{[3,2]} < 0.1$	2853.2	4063.23
$N_{\mathrm{jets}} \geq 6$ $p_{\mathrm{T}}^{\mathrm{jet}} > 30.0$ GeV, $p_{\mathrm{T}}^{\mathrm{jet}}(6) > 40.0$ GeV $\lvert\eta_{\mathrm{jet}}\rvert < 2.4$, $H_{\mathrm{T}} > 650.0$ GeV	$D^2_{[(6,3)+(3,2)]} < 1.375$ $A_m < 0.275$ $\Delta > 150$ GeV $D^2_{[3,2]} < 0.1$	2985.09	3964.37
$N_{\mathrm{jets}} \geq 6$ $p_{\mathrm{T}}^{\mathrm{jet}} > 30.0$ GeV, $p_{\mathrm{T}}^{\mathrm{jet}}(6) > 40.0$ GeV $\lvert\eta_{\mathrm{jet}}\rvert < 2.4$, $H_{\mathrm{T}} > 650.0$ GeV	$D^2_{[(6,3)+(3,2)]} < 1.25$ $A_m < 0.275$ $\Delta > 150$ GeV $D^2_{[3,2]} < 0.1$	2897.73	3946.84
$N_{\mathrm{jets}} \geq 6$ $p_{\mathrm{T}}^{\mathrm{jet}} > 30.0$ GeV, $p_{\mathrm{T}}^{\mathrm{jet}}(6) > 40.0$ GeV $\lvert\eta_{\mathrm{jet}}\rvert < 2.4$, $H_{\mathrm{T}} > 650.0$ GeV	$D^2_{[(6,3)+(3,2)]} < 1.5$ $A_m < 0.275$ $\Delta > 150$ GeV $D^2_{[3,2]} < 0.1$	3018.82	3904.03
$N_{\mathrm{jets}} \geq 6$ $p_{\mathrm{T}}^{\mathrm{jet}} > 30.0$ GeV, $p_{\mathrm{T}}^{\mathrm{jet}}(6) > 40.0$ GeV $\lvert\eta_{\mathrm{jet}}\rvert < 2.4$, $H_{\mathrm{T}} > 650.0$ GeV	$D^2_{[(6,3)+(3,2)]} < 1$ $A_m < 0.275$ $\Delta > 150$ GeV $D^2_{[3,2]} < 0.1$	2566.14	3897.55
$N_{\mathrm{jets}} \geq 6$ $p_{\mathrm{T}}^{\mathrm{jet}} > 30.0$ GeV, $p_{\mathrm{T}}^{\mathrm{jet}}(6) > 40.0$ GeV $\lvert\eta_{\mathrm{jet}}\rvert < 2.4$, $H_{\mathrm{T}} > 650.0$ GeV	$D^2_{[(6,3)+(3,2)]} < 1.125$ $A_m < 0.275$ $\Delta > 150$ GeV $D^2_{[3,2]} < 0.1$	2724.49	3847.16

(a) CMS pre-selection with no particle-jet matching.

Table 6.7 (cont.): Analysis optimisation results for the $m_{\tilde{g}} = 400$ GeV signal using the event-level significance measure and the CMS-like pre-selection. A double asterisk (**) is used to indicate the metric considered for the optimisation in the header. Only the 10 best performing selections are shown for each version of the pre-selection. The first and second column display $Z_{\mathrm{e},2}$ and $Z_{\mathrm{e},1}$, respectively.

Pre-selection	Analysis selection	$Z = S/\sqrt{S+B_{\mathrm{QCD}}}$	$Z = S/\sqrt{B_{\mathrm{QCD}}}$**
$N_{\mathrm{jets}} \geq 6$ $p_{\mathrm{T}}^{\mathrm{jet}} > 30.0$ GeV, $p_{\mathrm{T}}^{\mathrm{jet}}(6) > 40.0$ GeV $\lvert\eta_{\mathrm{jet}}\rvert < 2.4$, $H_{\mathrm{T}} > 650.0$ GeV	$D^2_{[(6,3)+(3,2)]} < 1$ $A_m < 0.2$ $\Delta > 300$ GeV $D^2_{[3,2]} < 0.05$	298.01	793.77
$N_{\mathrm{jets}} \geq 6$ $p_{\mathrm{T}}^{\mathrm{jet}} > 30.0$ GeV, $p_{\mathrm{T}}^{\mathrm{jet}}(6) > 40.0$ GeV $\lvert\eta_{\mathrm{jet}}\rvert < 2.4$, $H_{\mathrm{T}} > 650.0$ GeV	$D^2_{[(6,3)+(3,2)]} < 1$ $A_m < 0.2$ $\Delta > 275$ GeV $D^2_{[3,2]} < 0.05$	335.72	777.82
$N_{\mathrm{jets}} \geq 6$ $p_{\mathrm{T}}^{\mathrm{jet}} > 30.0$ GeV, $p_{\mathrm{T}}^{\mathrm{jet}}(6) > 40.0$ GeV $\lvert\eta_{\mathrm{jet}}\rvert < 2.4$, $H_{\mathrm{T}} > 650.0$ GeV	$D^2_{[(6,3)+(3,2)]} < 1$ $A_m < 0.2$ $\Delta > 300$ GeV $D^2_{[3,2]} < 0.055$	293.89	724.46
$N_{\mathrm{jets}} \geq 6$ $p_{\mathrm{T}}^{\mathrm{jet}} > 30.0$ GeV, $p_{\mathrm{T}}^{\mathrm{jet}}(6) > 40.0$ GeV $\lvert\eta_{\mathrm{jet}}\rvert < 2.4$, $H_{\mathrm{T}} > 650.0$ GeV	$D^2_{[(6,3)+(3,2)]} < 1.25$ $A_m < 0.2$ $\Delta > 250$ GeV $D^2_{[3,2]} < 0.1$	552.94	721.35
$N_{\mathrm{jets}} \geq 6$ $p_{\mathrm{T}}^{\mathrm{jet}} > 30.0$ GeV, $p_{\mathrm{T}}^{\mathrm{jet}}(6) > 40.0$ GeV $\lvert\eta_{\mathrm{jet}}\rvert < 2.4$, $H_{\mathrm{T}} > 650.0$ GeV	$D^2_{[(6,3)+(3,2)]} < 1$ $A_m < 0.225$ $\Delta > 275$ GeV $D^2_{[3,2]} < 0.05$	329.97	713.36
$N_{\mathrm{jets}} \geq 6$ $p_{\mathrm{T}}^{\mathrm{jet}} > 30.0$ GeV, $p_{\mathrm{T}}^{\mathrm{jet}}(6) > 40.0$ GeV $\lvert\eta_{\mathrm{jet}}\rvert < 2.4$, $H_{\mathrm{T}} > 650.0$ GeV	$D^2_{[(6,3)+(3,2)]} < 1.25$ $A_m < 0.2$ $\Delta > 225$ GeV $D^2_{[3,2]} < 0.025$	421.19	712.67
$N_{\mathrm{jets}} \geq 6$ $p_{\mathrm{T}}^{\mathrm{jet}} > 30.0$ GeV, $p_{\mathrm{T}}^{\mathrm{jet}}(6) > 40.0$ GeV $\lvert\eta_{\mathrm{jet}}\rvert < 2.4$, $H_{\mathrm{T}} > 650.0$ GeV	$D^2_{[(6,3)+(3,2)]} < 1.25$ $A_m < 0.2$ $\Delta > 275$ GeV $D^2_{[3,2]} < 0.025$	346.32	710.92
$N_{\mathrm{jets}} \geq 6$ $p_{\mathrm{T}}^{\mathrm{jet}} > 30.0$ GeV, $p_{\mathrm{T}}^{\mathrm{jet}}(6) > 40.0$ GeV $\lvert\eta_{\mathrm{jet}}\rvert < 2.4$, $H_{\mathrm{T}} > 650.0$ GeV	$D^2_{[(6,3)+(3,2)]} < 1.25$ $A_m < 0.2$ $\Delta > 250$ GeV $D^2_{[3,2]} < 0.025$	393.81	703.55
$N_{\mathrm{jets}} \geq 6$ $p_{\mathrm{T}}^{\mathrm{jet}} > 30.0$ GeV, $p_{\mathrm{T}}^{\mathrm{jet}}(6) > 40.0$ GeV $\lvert\eta_{\mathrm{jet}}\rvert < 2.4$, $H_{\mathrm{T}} > 650.0$ GeV	$D^2_{[(6,3)+(3,2)]} < 1$ $A_m < 0.2$ $\Delta > 250$ GeV $D^2_{[3,2]} < 0.05$	356.78	700.98
$N_{\mathrm{jets}} \geq 6$ $p_{\mathrm{T}}^{\mathrm{jet}} > 30.0$ GeV, $p_{\mathrm{T}}^{\mathrm{jet}}(6) > 40.0$ GeV $\lvert\eta_{\mathrm{jet}}\rvert < 2.4$, $H_{\mathrm{T}} > 650.0$ GeV	$D^2_{[(6,3)+(3,2)]} < 1.375$ $A_m < 0.2$ $\Delta > 250$ GeV $D^2_{[3,2]} < 0.1$	559.57	695.8

(b) CMS pre-selection with particle-jet matching.

Table 6.8: Analysis optimisation results for the $m_{\tilde{g}} = 400$ GeV signal using the event-level significance measure and tight jet p_{T} selections. A double asterisk (**) is used to indicate the metric considered for the optimisation in the header. Only the 10 best performing selections are shown for each version of the pre-selection. The first and second column display $Z_{\mathrm{e},2}$ and $Z_{\mathrm{e},1}$, respectively.

Pre-selection	Analysis selection	$Z = S/\sqrt{S + B_{\mathrm{QCD}}}$	$Z = S/\sqrt{B_{\mathrm{QCD}}}$**
$N_{\mathrm{jets}} \geq 6$ $p_{\mathrm{T}}^{\mathrm{jet}} > 40.0$ GeV, $p_{\mathrm{T}}^{\mathrm{jet}}(6) > 50.0$ GeV $\lvert\eta_{\mathrm{jet}}\rvert < 2.4$, $H_{\mathrm{T}} > 650.0$ GeV	$D^2_{[(6,3)+(3,2)]} < 1.375$ $A_m < 0.3$ $\Delta > 150$ GeV $D^2_{[3,2]} < 0.1$	3084.78	4368.58
$N_{\mathrm{jets}} \geq 6$ $p_{\mathrm{T}}^{\mathrm{jet}} > 40.0$ GeV, $p_{\mathrm{T}}^{\mathrm{jet}}(6) > 50.0$ GeV $\lvert\eta_{\mathrm{jet}}\rvert < 2.4$, $H_{\mathrm{T}} > 650.0$ GeV	$D^2_{[(6,3)+(3,2)]} < 1.25$ $A_m < 0.3$ $\Delta > 150$ GeV $D^2_{[3,2]} < 0.1$	2984.01	4314.88
$N_{\mathrm{jets}} \geq 6$ $p_{\mathrm{T}}^{\mathrm{jet}} > 40.0$ GeV, $p_{\mathrm{T}}^{\mathrm{jet}}(6) > 50.0$ GeV $\lvert\eta_{\mathrm{jet}}\rvert < 2.4$, $H_{\mathrm{T}} > 650.0$ GeV	$D^2_{[(6,3)+(3,2)]} < 1$ $A_m < 0.3$ $\Delta > 150$ GeV $D^2_{[3,2]} < 0.1$	2671	4305.95
$N_{\mathrm{jets}} \geq 6$ $p_{\mathrm{T}}^{\mathrm{jet}} > 40.0$ GeV, $p_{\mathrm{T}}^{\mathrm{jet}}(6) > 50.0$ GeV $\lvert\eta_{\mathrm{jet}}\rvert < 2.4$, $H_{\mathrm{T}} > 650.0$ GeV	$D^2_{[(6,3)+(3,2)]} < 1.5$ $A_m < 0.3$ $\Delta > 150$ GeV $D^2_{[3,2]} < 0.1$	3098.28	4266.61
$N_{\mathrm{jets}} \geq 6$ $p_{\mathrm{T}}^{\mathrm{jet}} > 40.0$ GeV, $p_{\mathrm{T}}^{\mathrm{jet}}(6) > 50.0$ GeV $\lvert\eta_{\mathrm{jet}}\rvert < 2.4$, $H_{\mathrm{T}} > 650.0$ GeV	$D^2_{[(6,3)+(3,2)]} < 1.375$ $A_m < 0.275$ $\Delta > 150$ GeV $D^2_{[3,2]} < 0.1$	2968.97	4197.69
$N_{\mathrm{jets}} \geq 6$ $p_{\mathrm{T}}^{\mathrm{jet}} > 40.0$ GeV, $p_{\mathrm{T}}^{\mathrm{jet}}(6) > 50.0$ GeV $\lvert\eta_{\mathrm{jet}}\rvert < 2.4$, $H_{\mathrm{T}} > 650.0$ GeV	$D^2_{[(6,3)+(3,2)]} < 1.125$ $A_m < 0.3$ $\Delta > 150$ GeV $D^2_{[3,2]} < 0.1$	2789.59	4136.95
$N_{\mathrm{jets}} \geq 6$ $p_{\mathrm{T}}^{\mathrm{jet}} > 40.0$ GeV, $p_{\mathrm{T}}^{\mathrm{jet}}(6) > 50.0$ GeV $\lvert\eta_{\mathrm{jet}}\rvert < 2.4$, $H_{\mathrm{T}} > 650.0$ GeV	$D^2_{[(6,3)+(3,2)]} < 1.25$ $A_m < 0.275$ $\Delta > 150$ GeV $D^2_{[3,2]} < 0.1$	2855.85	4103.76
$N_{\mathrm{jets}} \geq 6$ $p_{\mathrm{T}}^{\mathrm{jet}} > 40.0$ GeV, $p_{\mathrm{T}}^{\mathrm{jet}}(6) > 50.0$ GeV $\lvert\eta_{\mathrm{jet}}\rvert < 2.4$, $H_{\mathrm{T}} > 650.0$ GeV	$D^2_{[(6,3)+(3,2)]} < 1.5$ $A_m < 0.275$ $\Delta > 150$ GeV $D^2_{[3,2]} < 0.1$	2981.99	4103.03
$N_{\mathrm{jets}} \geq 6$ $p_{\mathrm{T}}^{\mathrm{jet}} > 40.0$ GeV, $p_{\mathrm{T}}^{\mathrm{jet}}(6) > 50.0$ GeV $\lvert\eta_{\mathrm{jet}}\rvert < 2.4$, $H_{\mathrm{T}} > 650.0$ GeV	$D^2_{[(6,3)+(3,2)]} < 1$ $A_m < 0.275$ $\Delta > 150$ GeV $D^2_{[3,2]} < 0.1$	2557.26	4089.64
$N_{\mathrm{jets}} \geq 6$ $p_{\mathrm{T}}^{\mathrm{jet}} > 40.0$ GeV, $p_{\mathrm{T}}^{\mathrm{jet}}(6) > 50.0$ GeV $\lvert\eta_{\mathrm{jet}}\rvert < 2.4$, $H_{\mathrm{T}} > 650.0$ GeV	$D^2_{[(6,3)+(3,2)]} < 1.375$ $A_m < 0.25$ $\Delta > 150$ GeV $D^2_{[3,2]} < 0.1$	2834.32	3991.49

(a) Tight jet p_{T} and sixth jet p_{T} selection with no particle-jet matching.

Table 6.8 (cont.): Analysis optimisation results for the $m_{\tilde{g}} = 400$ GeV signal using the event-level significance measure and tight jet p_{T} selections. A double asterisk (**) is used to indicate the metric considered for the optimisation in the header. Only the 10 best performing selections are shown for each version of the pre-selection. The first and second column display $Z_{\mathrm{e},2}$ and $Z_{\mathrm{e},1}$, respectively.

Pre-selection	Analysis selection	$Z = S/\sqrt{S + B_{\mathrm{QCD}}}$	$Z = S/\sqrt{B_{\mathrm{QCD}}}$**
$N_{\mathrm{jets}} \geq 6$ $p_{\mathrm{T}}^{\mathrm{jet}} > 40.0$ GeV, $p_{\mathrm{T}}^{\mathrm{jet}}(6) > 50.0$ GeV $\lvert\eta_{\mathrm{jet}}\rvert < 2.4$, $H_{\mathrm{T}} > 650.0$ GeV	$D^2_{[(6,3)+(3,2)]} < 1$ $A_m < 0.2$ $\Delta > 300$ GeV $D^2_{[3,2]} < 0.05$	299.33	819.61
$N_{\mathrm{jets}} \geq 6$ $p_{\mathrm{T}}^{\mathrm{jet}} > 40.0$ GeV, $p_{\mathrm{T}}^{\mathrm{jet}}(6) > 50.0$ GeV $\lvert\eta_{\mathrm{jet}}\rvert < 2.4$, $H_{\mathrm{T}} > 650.0$ GeV	$D^2_{[(6,3)+(3,2)]} < 1.25$ $A_m < 0.2$ $\Delta > 250$ GeV $D^2_{[3,2]} < 0.1$	590.67	811.85
$N_{\mathrm{jets}} \geq 6$ $p_{\mathrm{T}}^{\mathrm{jet}} > 40.0$ GeV, $p_{\mathrm{T}}^{\mathrm{jet}}(6) > 50.0$ GeV $\lvert\eta_{\mathrm{jet}}\rvert < 2.4$, $H_{\mathrm{T}} > 650.0$ GeV	$D^2_{[(6,3)+(3,2)]} < 1$ $A_m < 0.2$ $\Delta > 275$ GeV $D^2_{[3,2]} < 0.05$	336.77	791.06
$N_{\mathrm{jets}} \geq 6$ $p_{\mathrm{T}}^{\mathrm{jet}} > 40.0$ GeV, $p_{\mathrm{T}}^{\mathrm{jet}}(6) > 50.0$ GeV $\lvert\eta_{\mathrm{jet}}\rvert < 2.4$, $H_{\mathrm{T}} > 650.0$ GeV	$D^2_{[(6,3)+(3,2)]} < 1$ $A_m < 0.2$ $\Delta > 225$ GeV $D^2_{[3,2]} < 0.025$	312.09	771.38
$N_{\mathrm{jets}} \geq 6$ $p_{\mathrm{T}}^{\mathrm{jet}} > 40.0$ GeV, $p_{\mathrm{T}}^{\mathrm{jet}}(6) > 50.0$ GeV $\lvert\eta_{\mathrm{jet}}\rvert < 2.4$, $H_{\mathrm{T}} > 650.0$ GeV	$D^2_{[(6,3)+(3,2)]} < 1.25$ $A_m < 0.225$ $\Delta > 250$ GeV $D^2_{[3,2]} < 0.1$	573.54	769
$N_{\mathrm{jets}} \geq 6$ $p_{\mathrm{T}}^{\mathrm{jet}} > 40.0$ GeV, $p_{\mathrm{T}}^{\mathrm{jet}}(6) > 50.0$ GeV $\lvert\eta_{\mathrm{jet}}\rvert < 2.4$, $H_{\mathrm{T}} > 650.0$ GeV	$D^2_{[(6,3)+(3,2)]} < 1.375$ $A_m < 0.2$ $\Delta > 250$ GeV $D^2_{[3,2]} < 0.1$	590.35	764.42
$N_{\mathrm{jets}} \geq 6$ $p_{\mathrm{T}}^{\mathrm{jet}} > 40.0$ GeV, $p_{\mathrm{T}}^{\mathrm{jet}}(6) > 50.0$ GeV $\lvert\eta_{\mathrm{jet}}\rvert < 2.4$, $H_{\mathrm{T}} > 650.0$ GeV	$D^2_{[(6,3)+(3,2)]} < 1.25$ $A_m < 0.2$ $\Delta > 225$ GeV $D^2_{[3,2]} < 0.025$	430.36	760
$N_{\mathrm{jets}} \geq 6$ $p_{\mathrm{T}}^{\mathrm{jet}} > 40.0$ GeV, $p_{\mathrm{T}}^{\mathrm{jet}}(6) > 50.0$ GeV $\lvert\eta_{\mathrm{jet}}\rvert < 2.4$, $H_{\mathrm{T}} > 650.0$ GeV	$D^2_{[(6,3)+(3,2)]} < 1.25$ $A_m < 0.2$ $\Delta > 275$ GeV $D^2_{[3,2]} < 0.025$	351.42	758.52
$N_{\mathrm{jets}} \geq 6$ $p_{\mathrm{T}}^{\mathrm{jet}} > 40.0$ GeV, $p_{\mathrm{T}}^{\mathrm{jet}}(6) > 50.0$ GeV $\lvert\eta_{\mathrm{jet}}\rvert < 2.4$, $H_{\mathrm{T}} > 650.0$ GeV	$D^2_{[(6,3)+(3,2)]} < 1.25$ $A_m < 0.2$ $\Delta > 275$ GeV $D^2_{[3,2]} < 0.1$	519.3	744.19
$N_{\mathrm{jets}} \geq 6$ $p_{\mathrm{T}}^{\mathrm{jet}} > 40.0$ GeV, $p_{\mathrm{T}}^{\mathrm{jet}}(6) > 50.0$ GeV $\lvert\eta_{\mathrm{jet}}\rvert < 2.4$, $H_{\mathrm{T}} > 650.0$ GeV	$D^2_{[(6,3)+(3,2)]} < 1$ $A_m < 0.2$ $\Delta > 300$ GeV $D^2_{[3,2]} < 0.055$	295.15	743.94

(b) Tight jet p_{T} and sixth jet p_{T} selection with particle-jet matching.

Table 6.9: Analysis optimisation results for the $m_{\tilde{g}} = 400$ GeV signal using the event-level significance measure and loose jet p_{T} selections (with no sixth jet p_{T} requirement). A double asterisk (**) is used to indicate the metric considered for the optimisation in the header. Only the 10 best performing selections are shown for each version of the pre-selection. The first and second column display $Z_{\mathrm{e},2}$ and $Z_{\mathrm{e},1}$, respectively.

Pre-selection	Analysis selection	$Z = S/\sqrt{S + B_{\mathrm{QCD}}}$	$Z = S/\sqrt{B_{\mathrm{QCD}}}$**
$N_{\mathrm{jets}} \geq 6$ $p_{\mathrm{T}}^{\mathrm{jet}} > 20.0$ GeV, $p_{\mathrm{T}}^{\mathrm{jet}}(6) > 20.0$ GeV $\lvert\eta_{\mathrm{jet}}\rvert < 2.4$, $H_{\mathrm{T}} > 650.0$ GeV	$D^2_{[(6,3)+(3,2)]} < 1.25$ $A_m < 0.3$ $\Delta > 150$ GeV $D^2_{[3,2]} < 0.1$	2830.5	3525.81
$N_{\mathrm{jets}} \geq 6$ $p_{\mathrm{T}}^{\mathrm{jet}} > 20.0$ GeV, $p_{\mathrm{T}}^{\mathrm{jet}}(6) > 20.0$ GeV $\lvert\eta_{\mathrm{jet}}\rvert < 2.4$, $H_{\mathrm{T}} > 650.0$ GeV	$D^2_{[(6,3)+(3,2)]} < 1.125$ $A_m < 0.3$ $\Delta > 150$ GeV $D^2_{[3,2]} < 0.1$	2677.88	3465.59
$N_{\mathrm{jets}} \geq 6$ $p_{\mathrm{T}}^{\mathrm{jet}} > 20.0$ GeV, $p_{\mathrm{T}}^{\mathrm{jet}}(6) > 20.0$ GeV $\lvert\eta_{\mathrm{jet}}\rvert < 2.4$, $H_{\mathrm{T}} > 650.0$ GeV	$D^2_{[(6,3)+(3,2)]} < 1.375$ $A_m < 0.3$ $\Delta > 150$ GeV $D^2_{[3,2]} < 0.1$	2855.49	3439.16
$N_{\mathrm{jets}} \geq 6$ $p_{\mathrm{T}}^{\mathrm{jet}} > 20.0$ GeV, $p_{\mathrm{T}}^{\mathrm{jet}}(6) > 20.0$ GeV $\lvert\eta_{\mathrm{jet}}\rvert < 2.4$, $H_{\mathrm{T}} > 650.0$ GeV	$D^2_{[(6,3)+(3,2)]} < 1.25$ $A_m < 0.275$ $\Delta > 150$ GeV $D^2_{[3,2]} < 0.1$	2740.52	3424.01
$N_{\mathrm{jets}} \geq 6$ $p_{\mathrm{T}}^{\mathrm{jet}} > 20.0$ GeV, $p_{\mathrm{T}}^{\mathrm{jet}}(6) > 20.0$ GeV $\lvert\eta_{\mathrm{jet}}\rvert < 2.4$, $H_{\mathrm{T}} > 650.0$ GeV	$D^2_{[(6,3)+(3,2)]} < 1.5$ $A_m < 0.3$ $\Delta > 150$ GeV $D^2_{[3,2]} < 0.1$	2891.3	3401.32
$N_{\mathrm{jets}} \geq 6$ $p_{\mathrm{T}}^{\mathrm{jet}} > 20.0$ GeV, $p_{\mathrm{T}}^{\mathrm{jet}}(6) > 20.0$ GeV $\lvert\eta_{\mathrm{jet}}\rvert < 2.4$, $H_{\mathrm{T}} > 650.0$ GeV	$D^2_{[(6,3)+(3,2)]} < 1.125$ $A_m < 0.275$ $\Delta > 150$ GeV $D^2_{[3,2]} < 0.1$	2608.87	3398.08
$N_{\mathrm{jets}} \geq 6$ $p_{\mathrm{T}}^{\mathrm{jet}} > 20.0$ GeV, $p_{\mathrm{T}}^{\mathrm{jet}}(6) > 20.0$ GeV $\lvert\eta_{\mathrm{jet}}\rvert < 2.4$, $H_{\mathrm{T}} > 650.0$ GeV	$D^2_{[(6,3)+(3,2)]} < 1$ $A_m < 0.275$ $\Delta > 150$ GeV $D^2_{[3,2]} < 0.1$	2444.92	3372.13
$N_{\mathrm{jets}} \geq 6$ $p_{\mathrm{T}}^{\mathrm{jet}} > 20.0$ GeV, $p_{\mathrm{T}}^{\mathrm{jet}}(6) > 20.0$ GeV $\lvert\eta_{\mathrm{jet}}\rvert < 2.4$, $H_{\mathrm{T}} > 650.0$ GeV	$D^2_{[(6,3)+(3,2)]} < 1$ $A_m < 0.3$ $\Delta > 150$ GeV $D^2_{[3,2]} < 0.1$	2484.59	3364.5
$N_{\mathrm{jets}} \geq 6$ $p_{\mathrm{T}}^{\mathrm{jet}} > 20.0$ GeV, $p_{\mathrm{T}}^{\mathrm{jet}}(6) > 20.0$ GeV $\lvert\eta_{\mathrm{jet}}\rvert < 2.4$, $H_{\mathrm{T}} > 650.0$ GeV	$D^2_{[(6,3)+(3,2)]} < 1.375$ $A_m < 0.275$ $\Delta > 150$ GeV $D^2_{[3,2]} < 0.1$	2771.8	3348.06
$N_{\mathrm{jets}} \geq 6$ $p_{\mathrm{T}}^{\mathrm{jet}} > 20.0$ GeV, $p_{\mathrm{T}}^{\mathrm{jet}}(6) > 20.0$ GeV $\lvert\eta_{\mathrm{jet}}\rvert < 2.4$, $H_{\mathrm{T}} > 650.0$ GeV	$D^2_{[(6,3)+(3,2)]} < 1.5$ $A_m < 0.275$ $\Delta > 150$ GeV $D^2_{[3,2]} < 0.1$	2798.46	3299.52

(a) Loose jet p_{T} selections with no particle-jet matching.

Table 6.9 (cont.): Analysis optimisation results for the $m_{\tilde{g}} = 400$ GeV signal using the event-level significance measure and loose jet p_{T} selections (with no sixth jet p_{T} requirement). A double asterisk (**) is used to indicate the metric considered for the optimisation in the header. Only the 10 best performing selections are shown for each version of the pre-selection. The first and second column display $Z_{\mathrm{e},2}$ and $Z_{\mathrm{e},1}$, respectively.

Pre-selection	Analysis selection	$Z = S/\sqrt{S + B_{\mathrm{QCD}}}$	$Z = S/\sqrt{B_{\mathrm{QCD}}}$**
$N_{\mathrm{jets}} \geq 6$ $p_{\mathrm{T}}^{\mathrm{jet}} > 20.0$ GeV, $p_{\mathrm{T}}^{\mathrm{jet}}(6) > 20.0$ GeV $\lvert\eta_{\mathrm{jet}}\rvert < 2.4$, $H_{\mathrm{T}} > 650.0$ GeV	$D^2_{[(6,3)+(3,2)]} < 1$ $A_m < 0.2$ $\Delta > 300$ GeV $D^2_{[3,2]} < 0.05$	298.01	793.77
$N_{\mathrm{jets}} \geq 6$ $p_{\mathrm{T}}^{\mathrm{jet}} > 20.0$ GeV, $p_{\mathrm{T}}^{\mathrm{jet}}(6) > 20.0$ GeV $\lvert\eta_{\mathrm{jet}}\rvert < 2.4$, $H_{\mathrm{T}} > 650.0$ GeV	$D^2_{[(6,3)+(3,2)]} < 1$ $A_m < 0.2$ $\Delta > 275$ GeV $D^2_{[3,2]} < 0.05$	331.89	733.4
$N_{\mathrm{jets}} \geq 6$ $p_{\mathrm{T}}^{\mathrm{jet}} > 20.0$ GeV, $p_{\mathrm{T}}^{\mathrm{jet}}(6) > 20.0$ GeV $\lvert\eta_{\mathrm{jet}}\rvert < 2.4$, $H_{\mathrm{T}} > 650.0$ GeV	$D^2_{[(6,3)+(3,2)]} < 1$ $A_m < 0.2$ $\Delta > 300$ GeV $D^2_{[3,2]} < 0.055$	292.31	701.65
$N_{\mathrm{jets}} \geq 6$ $p_{\mathrm{T}}^{\mathrm{jet}} > 20.0$ GeV, $p_{\mathrm{T}}^{\mathrm{jet}}(6) > 20.0$ GeV $\lvert\eta_{\mathrm{jet}}\rvert < 2.4$, $H_{\mathrm{T}} > 650.0$ GeV	$D^2_{[(6,3)+(3,2)]} < 1$ $A_m < 0.225$ $\Delta > 300$ GeV $D^2_{[3,2]} < 0.05$	291.53	691.06
$N_{\mathrm{jets}} \geq 6$ $p_{\mathrm{T}}^{\mathrm{jet}} > 20.0$ GeV, $p_{\mathrm{T}}^{\mathrm{jet}}(6) > 20.0$ GeV $\lvert\eta_{\mathrm{jet}}\rvert < 2.4$, $H_{\mathrm{T}} > 650.0$ GeV	$D^2_{[(6,3)+(3,2)]} < 1$ $A_m < 0.225$ $\Delta > 275$ GeV $D^2_{[3,2]} < 0.05$	326.32	678.64
$N_{\mathrm{jets}} \geq 6$ $p_{\mathrm{T}}^{\mathrm{jet}} > 20.0$ GeV, $p_{\mathrm{T}}^{\mathrm{jet}}(6) > 20.0$ GeV $\lvert\eta_{\mathrm{jet}}\rvert < 2.4$, $H_{\mathrm{T}} > 650.0$ GeV	$D^2_{[(6,3)+(3,2)]} < 1.25$ $A_m < 0.2$ $\Delta > 275$ GeV $D^2_{[3,2]} < 0.1$	486.32	647.58
$N_{\mathrm{jets}} \geq 6$ $p_{\mathrm{T}}^{\mathrm{jet}} > 20.0$ GeV, $p_{\mathrm{T}}^{\mathrm{jet}}(6) > 20.0$ GeV $\lvert\eta_{\mathrm{jet}}\rvert < 2.4$, $H_{\mathrm{T}} > 650.0$ GeV	$D^2_{[(6,3)+(3,2)]} < 1$ $A_m < 0.2$ $\Delta > 275$ GeV $D^2_{[3,2]} < 0.055$	321.86	641
$N_{\mathrm{jets}} \geq 6$ $p_{\mathrm{T}}^{\mathrm{jet}} > 20.0$ GeV, $p_{\mathrm{T}}^{\mathrm{jet}}(6) > 20.0$ GeV $\lvert\eta_{\mathrm{jet}}\rvert < 2.4$, $H_{\mathrm{T}} > 650.0$ GeV	$D^2_{[(6,3)+(3,2)]} < 1.25$ $A_m < 0.2$ $\Delta > 250$ GeV $D^2_{[3,2]} < 0.1$	514.64	638.02
$N_{\mathrm{jets}} \geq 6$ $p_{\mathrm{T}}^{\mathrm{jet}} > 20.0$ GeV, $p_{\mathrm{T}}^{\mathrm{jet}}(6) > 20.0$ GeV $\lvert\eta_{\mathrm{jet}}\rvert < 2.4$, $H_{\mathrm{T}} > 650.0$ GeV	$D^2_{[(6,3)+(3,2)]} < 1.375$ $A_m < 0.2$ $\Delta > 275$ GeV $D^2_{[3,2]} < 0.1$	499.4	625.6
$N_{\mathrm{jets}} \geq 6$ $p_{\mathrm{T}}^{\mathrm{jet}} > 20.0$ GeV, $p_{\mathrm{T}}^{\mathrm{jet}}(6) > 20.0$ GeV $\lvert\eta_{\mathrm{jet}}\rvert < 2.4$, $H_{\mathrm{T}} > 650.0$ GeV	$D^2_{[(6,3)+(3,2)]} < 1.25$ $A_m < 0.2$ $\Delta > 275$ GeV $D^2_{[3,2]} < 0.055$	422.33	622.73

(b) Loose jet p_{T} selections with particle-jet matching.

Table 6.10: Analysis optimisation results for the $m_{\tilde{g}} = 400$ GeV signal using the event-level significance measure and tight jet p_{T} selections. *To emulate EWK SUSY signals, the signal cross-section is multiplied by a factor of* 10^{-3}. A double asterisk (**) is used to indicate the metric considered for the optimisation in the header. Only the 10 best performing selections are shown for each version of the pre-selection. The first and second column display $Z_{\mathrm{e},2}$ and $Z_{\mathrm{e},1}$, respectively.

Pre-selection	Analysis selection	$Z = S/\sqrt{S + B_{\mathrm{QCD}}}$	$Z = S/\sqrt{B_{\mathrm{QCD}}}$**
$N_{\mathrm{jets}} \geq 6$ $p_{\mathrm{T}}^{\mathrm{jet}} > 40.0$ GeV, $p_{\mathrm{T}}^{\mathrm{jet}}(6) > 50.0$ GeV $\lvert\eta_{\mathrm{jet}}\rvert < 2.4$, $H_{\mathrm{T}} > 650.0$ GeV	$D^2_{[(6,3)+(3,2)]} < 1.375$ $A_m < 0.3$ $\Delta > 150$ GeV $D^2_{[3,2]} < 0.1$	4.37	4.37
$N_{\mathrm{jets}} \geq 6$ $p_{\mathrm{T}}^{\mathrm{jet}} > 40.0$ GeV, $p_{\mathrm{T}}^{\mathrm{jet}}(6) > 50.0$ GeV $\lvert\eta_{\mathrm{jet}}\rvert < 2.4$, $H_{\mathrm{T}} > 650.0$ GeV	$D^2_{[(6,3)+(3,2)]} < 1.25$ $A_m < 0.3$ $\Delta > 150$ GeV $D^2_{[3,2]} < 0.1$	4.31	4.31
$N_{\mathrm{jets}} \geq 6$ $p_{\mathrm{T}}^{\mathrm{jet}} > 40.0$ GeV, $p_{\mathrm{T}}^{\mathrm{jet}}(6) > 50.0$ GeV $\lvert\eta_{\mathrm{jet}}\rvert < 2.4$, $H_{\mathrm{T}} > 650.0$ GeV	$D^2_{[(6,3)+(3,2)]} < 1$ $A_m < 0.3$ $\Delta > 150$ GeV $D^2_{[3,2]} < 0.1$	4.3	4.31
$N_{\mathrm{jets}} \geq 6$ $p_{\mathrm{T}}^{\mathrm{jet}} > 40.0$ GeV, $p_{\mathrm{T}}^{\mathrm{jet}}(6) > 50.0$ GeV $\lvert\eta_{\mathrm{jet}}\rvert < 2.4$, $H_{\mathrm{T}} > 650.0$ GeV	$D^2_{[(6,3)+(3,2)]} < 1.5$ $A_m < 0.3$ $\Delta > 150$ GeV $D^2_{[3,2]} < 0.1$	4.26	4.27
$N_{\mathrm{jets}} \geq 6$ $p_{\mathrm{T}}^{\mathrm{jet}} > 40.0$ GeV, $p_{\mathrm{T}}^{\mathrm{jet}}(6) > 50.0$ GeV $\lvert\eta_{\mathrm{jet}}\rvert < 2.4$, $H_{\mathrm{T}} > 650.0$ GeV	$D^2_{[(6,3)+(3,2)]} < 1.375$ $A_m < 0.275$ $\Delta > 150$ GeV $D^2_{[3,2]} < 0.1$	4.2	4.2
$N_{\mathrm{jets}} \geq 6$ $p_{\mathrm{T}}^{\mathrm{jet}} > 40.0$ GeV, $p_{\mathrm{T}}^{\mathrm{jet}}(6) > 50.0$ GeV $\lvert\eta_{\mathrm{jet}}\rvert < 2.4$, $H_{\mathrm{T}} > 650.0$ GeV	$D^2_{[(6,3)+(3,2)]} < 1.125$ $A_m < 0.3$ $\Delta > 150$ GeV $D^2_{[3,2]} < 0.1$	4.13	4.14
$N_{\mathrm{jets}} \geq 6$ $p_{\mathrm{T}}^{\mathrm{jet}} > 40.0$ GeV, $p_{\mathrm{T}}^{\mathrm{jet}}(6) > 50.0$ GeV $\lvert\eta_{\mathrm{jet}}\rvert < 2.4$, $H_{\mathrm{T}} > 650.0$ GeV	$D^2_{[(6,3)+(3,2)]} < 1.25$ $A_m < 0.275$ $\Delta > 150$ GeV $D^2_{[3,2]} < 0.1$	4.1	4.1
$N_{\mathrm{jets}} \geq 6$ $p_{\mathrm{T}}^{\mathrm{jet}} > 40.0$ GeV, $p_{\mathrm{T}}^{\mathrm{jet}}(6) > 50.0$ GeV $\lvert\eta_{\mathrm{jet}}\rvert < 2.4$, $H_{\mathrm{T}} > 650.0$ GeV	$D^2_{[(6,3)+(3,2)]} < 1.5$ $A_m < 0.275$ $\Delta > 150$ GeV $D^2_{[3,2]} < 0.1$	4.1	4.1
$N_{\mathrm{jets}} \geq 6$ $p_{\mathrm{T}}^{\mathrm{jet}} > 40.0$ GeV, $p_{\mathrm{T}}^{\mathrm{jet}}(6) > 50.0$ GeV $\lvert\eta_{\mathrm{jet}}\rvert < 2.4$, $H_{\mathrm{T}} > 650.0$ GeV	$D^2_{[(6,3)+(3,2)]} < 1$ $A_m < 0.275$ $\Delta > 150$ GeV $D^2_{[3,2]} < 0.1$	4.09	4.09
$N_{\mathrm{jets}} \geq 6$ $p_{\mathrm{T}}^{\mathrm{jet}} > 40.0$ GeV, $p_{\mathrm{T}}^{\mathrm{jet}}(6) > 50.0$ GeV $\lvert\eta_{\mathrm{jet}}\rvert < 2.4$, $H_{\mathrm{T}} > 650.0$ GeV	$D^2_{[(6,3)+(3,2)]} < 1.375$ $A_m < 0.25$ $\Delta > 150$ GeV $D^2_{[3,2]} < 0.1$	3.99	3.99

(a) Tight jet p_{T} and sixth jet p_{T} selection with no particle-jet matching.

Table 6.10 (cont.): Analysis optimisation results for the $m_{\tilde{g}} = 400$ GeV signal using the event-level significance measure and tight jet p_{T} selections. *To emulate EWK SUSY signals, the signal cross-section is multiplied by a factor of* 10^{-3}. A double asterisk (**) is used to indicate the metric considered for the optimisation in the header. Only the 10 best performing selections are shown for each version of the pre-selection. The first and second column display $Z_{\mathrm{e},2}$ and $Z_{\mathrm{e},1}$, respectively.

Pre-selection	Analysis selection	$Z = S/\sqrt{S+B_{\mathrm{QCD}}}$	$Z = S/\sqrt{B_{\mathrm{QCD}}}$**
$N_{\mathrm{jets}} \geq 6$ $p_{\mathrm{T}}^{\mathrm{jet}} > 40.0$ GeV, $p_{\mathrm{T}}^{\mathrm{jet}}(6) > 50.0$ GeV $\lvert\eta_{\mathrm{jet}}\rvert < 2.4$, $H_{\mathrm{T}} > 650.0$ GeV	$D^2_{[(6,3)+(3,2)]} < 1$ $A_m < 0.2$ $\Delta > 300$ GeV $D^2_{[3,2]} < 0.05$	0.82	0.82
$N_{\mathrm{jets}} \geq 6$ $p_{\mathrm{T}}^{\mathrm{jet}} > 40.0$ GeV, $p_{\mathrm{T}}^{\mathrm{jet}}(6) > 50.0$ GeV $\lvert\eta_{\mathrm{jet}}\rvert < 2.4$, $H_{\mathrm{T}} > 650.0$ GeV	$D^2_{[(6,3)+(3,2)]} < 1.25$ $A_m < 0.2$ $\Delta > 250$ GeV $D^2_{[3,2]} < 0.1$	0.81	0.81
$N_{\mathrm{jets}} \geq 6$ $p_{\mathrm{T}}^{\mathrm{jet}} > 40.0$ GeV, $p_{\mathrm{T}}^{\mathrm{jet}}(6) > 50.0$ GeV $\lvert\eta_{\mathrm{jet}}\rvert < 2.4$, $H_{\mathrm{T}} > 650.0$ GeV	$D^2_{[(6,3)+(3,2)]} < 1$ $A_m < 0.2$ $\Delta > 275$ GeV $D^2_{[3,2]} < 0.05$	0.79	0.79
$N_{\mathrm{jets}} \geq 6$ $p_{\mathrm{T}}^{\mathrm{jet}} > 40.0$ GeV, $p_{\mathrm{T}}^{\mathrm{jet}}(6) > 50.0$ GeV $\lvert\eta_{\mathrm{jet}}\rvert < 2.4$, $H_{\mathrm{T}} > 650.0$ GeV	$D^2_{[(6,3)+(3,2)]} < 1$ $A_m < 0.2$ $\Delta > 225$ GeV $D^2_{[3,2]} < 0.025$	0.77	0.77
$N_{\mathrm{jets}} \geq 6$ $p_{\mathrm{T}}^{\mathrm{jet}} > 40.0$ GeV, $p_{\mathrm{T}}^{\mathrm{jet}}(6) > 50.0$ GeV $\lvert\eta_{\mathrm{jet}}\rvert < 2.4$, $H_{\mathrm{T}} > 650.0$ GeV	$D^2_{[(6,3)+(3,2)]} < 1.25$ $A_m < 0.225$ $\Delta > 250$ GeV $D^2_{[3,2]} < 0.1$	0.77	0.77
$N_{\mathrm{jets}} \geq 6$ $p_{\mathrm{T}}^{\mathrm{jet}} > 40.0$ GeV, $p_{\mathrm{T}}^{\mathrm{jet}}(6) > 50.0$ GeV $\lvert\eta_{\mathrm{jet}}\rvert < 2.4$, $H_{\mathrm{T}} > 650.0$ GeV	$D^2_{[(6,3)+(3,2)]} < 1.375$ $A_m < 0.2$ $\Delta > 250$ GeV $D^2_{[3,2]} < 0.1$	0.76	0.76
$N_{\mathrm{jets}} \geq 6$ $p_{\mathrm{T}}^{\mathrm{jet}} > 40.0$ GeV, $p_{\mathrm{T}}^{\mathrm{jet}}(6) > 50.0$ GeV $\lvert\eta_{\mathrm{jet}}\rvert < 2.4$, $H_{\mathrm{T}} > 650.0$ GeV	$D^2_{[(6,3)+(3,2)]} < 1.25$ $A_m < 0.2$ $\Delta > 225$ GeV $D^2_{[3,2]} < 0.025$	0.76	0.76
$N_{\mathrm{jets}} \geq 6$ $p_{\mathrm{T}}^{\mathrm{jet}} > 40.0$ GeV, $p_{\mathrm{T}}^{\mathrm{jet}}(6) > 50.0$ GeV $\lvert\eta_{\mathrm{jet}}\rvert < 2.4$, $H_{\mathrm{T}} > 650.0$ GeV	$D^2_{[(6,3)+(3,2)]} < 1.25$ $A_m < 0.2$ $\Delta > 275$ GeV $D^2_{[3,2]} < 0.025$	0.76	0.76
$N_{\mathrm{jets}} \geq 6$ $p_{\mathrm{T}}^{\mathrm{jet}} > 40.0$ GeV, $p_{\mathrm{T}}^{\mathrm{jet}}(6) > 50.0$ GeV $\lvert\eta_{\mathrm{jet}}\rvert < 2.4$, $H_{\mathrm{T}} > 650.0$ GeV	$D^2_{[(6,3)+(3,2)]} < 1.25$ $A_m < 0.2$ $\Delta > 275$ GeV $D^2_{[3,2]} < 0.1$	0.74	0.74
$N_{\mathrm{jets}} \geq 6$ $p_{\mathrm{T}}^{\mathrm{jet}} > 40.0$ GeV, $p_{\mathrm{T}}^{\mathrm{jet}}(6) > 50.0$ GeV $\lvert\eta_{\mathrm{jet}}\rvert < 2.4$, $H_{\mathrm{T}} > 650.0$ GeV	$D^2_{[(6,3)+(3,2)]} < 1$ $A_m < 0.2$ $\Delta > 300$ GeV $D^2_{[3,2]} < 0.055$	0.74	0.74

(b) Tight jet p_{T} and sixth jet p_{T} selection with particle-jet matching.

6.5 Future work

6.5.1 Current limitations

The studies in their current form are limited by the level of statistics in the MC samples used for both the signal and background. The background estimation procedure governs the sensitivity of these searches and is therefore an integral part of these studies. Future work should focus on ways to increase the statistical power of the background estimation and in turn these projections. One avenue under consideration is the use of particle-level (truth-level) event samples without the associated CPU costs of the $\mu = 200$ reconstruction. This provides an opportunity to explore the case of perfect pile-up rejection (i.e. using only the truth-level information) and also emulate the HL-LHC conditions with smearing functions that modify the samples to reflect the expected detector response.

For the reconstructed event samples we also need to ensure that any selections (JVT, jet cleaning, etc.) applied are valid. Since we do not yet have measurements for non-collision backgrounds in HL-LHC conditions, the jet cleaning selection should be removed as discussed in Section 6.4.1. Since the JVT selection initially applied is that tuned for $\sqrt{s} = 13$ TeV analyses, the p_{T} selections on the jets do not reflect those that may exist at the HL-LHC, so this should also be considered further. Some sample differences are unavoidable since a combination of Run 2 signal samples and HL-LHC background samples have been considered. However, since the JVT selection is only used to ensure pile-up jets are not matched to truth particles from the $\tilde{g}$ decay, it could be removed to favour an inclusive jet selection allowing other pile-up rejection methods to be studied[15]. Instead of the JVT selection, the reconstructed jets could be matched to hard-scatter truth jets with a ΔR association, and a matching truth jet required to exist before considering any reconstructed jets for particle matching. Initial testing of this procedure considered matching truth-level (hard-scatter) jets with $p_{\mathrm{T}} > 10$ GeV to reconstructed jets with a $\Delta R(\text{truth},\ \text{reco}) < 0.3$ requirement adopted from existing code configured for the `xAODAnaHelpers` package [108]. Only a 1% lower efficiency to obtain events with six gluino-matched jets was seen for reconstructed jets in a smaller 10000 (MC16a) $m_{\tilde{g}} = 400$ GeV signal sample compared to truth jets (without the jet-jet ΔR matching). Since the truth jets are the "true" hard-scatter jets we can therefore be more certain that this method approximates the "hard-scatter only" matching scenario well. These methods should be studied further as we proceed to further develop the projections[16].

[15] This is important to eventually study the performance of different trigger signatures since any trigger selection should be applied to an inclusive collection of jets.

[16] An additional consideration is the efficiency for the reconstructed to truth jet matching, which might decrease the (already small) total truth matching efficiency further.

6.5.2 Making trigger selections

These projection studies are intended to lead to an evaluation of the sensitivity of multi-jet TLA searches in HL-LHC conditions with different trigger strategies. We foresee several potential trigger scenarios for testing based on the outcomes from Run 3 TLA trigger studies (discussed in Chapter 5), including:

- A multi-jet selection with asymmetric trigger thresholds.
- A H_{T} selection (for both hardware and software triggers).
- Single-jet selections similar to the legacy `L1J100` selection from Chapter 5 to establish a baseline and conservative estimate of the analysis performance.

The emulation of these selections should consider both the Level-0 (hardware) trigger selection and the ensuing software trigger selection in the HLT/Event-Filter. The configuration of the Level-0 Global Trigger at the HL-LHC is intended to allow the use of offline-like jet algorithms and calibrations [45], so `EMTopo` jets can likely be used to emulate hardware trigger decisions. Nonetheless, further work is needed to explore the exact procedure for the trigger emulation.

6.5.3 Next steps for the background estimation

The background estimation for the original analysis in Ref. [109] proceeded by modelling the QCD background and contributions from the signal combinatorial background with a smooth template function. For the low-mass 200 GeV to 400 GeV region, a functional form motivated by the Planck Black-body function was used [109]:

$$\frac{dN}{dm_{\mathrm{jjj}}} = \frac{1}{(x+c)^{5+d\ln\left(m_{\mathrm{jjj}}/\sqrt{s}\right)}} \frac{a}{e^{b/(m_{\mathrm{jjj}}+c)}-1}. \tag{6.15}$$

The first term in Equation (6.15) acts like a power-law and the second is the black-body term that determines how the turn-on of the m_{jjj} distribution for QCD jet production is described. The behaviour of the model is controlled by the a (normalisation), b (black-body "temperature"), c (horizontal translation), and d (ln term strength) parameters [109]. For these studies $\sqrt{s}$ was set to 14 TeV to reflect HL-LHC pp collision conditions.

Fitting the models after the CMS selections, while limited by the statistics for the background samples, allowed us to gauge the performance of the templates in the ATLAS simulation. The model was fit using a χ^2 minimisation routine provided by [129] for $m_{\mathrm{jjj}} > 100$ GeV. To avoid issues with divergences in the model during the fitting, the parameters were constrained in the following ways:

- The normalisation, a, was fixed by normalising the histogram to unit area before fitting. The fitted model was then scaled by the integral of the un-normalised histogram.

- Divergences where $x + c \leq 0$ were avoided by assigning a minimum value to the c parameter equal to the product of -1 and the lowest bin-centre on the m_{jjj} axis plus 1 (acceptable if the bin width is above 1 GeV, which with low-statistics is always the case in the results here). A maximum c value equal to the highest bin-centre on the m_{jjj} axis was also assigned.
- The temperature parameter, b, was constrained to vary between $\epsilon = 1 \times 10^{-10}$ and ∞.
- The ln strength parameter, d, was allowed to vary between 0 and 10.

Initial fits of this model for the background (QCD) only hypothesis in Figure 6.17 show reasonable modelling in the high-m_{jjj} tail (with relatively high-statistics) but poorer modelling in the low-mass region. This is primarily a result of the statistical fluctuations in different low-mass bins as a result of low-statistics. We also see a cut-off in the invariant mass distribution at low-m_{jjj}, which could be a consequence of the choice of analysis selections. Similar effects are noted in Ref. [122] and attributed to trigger-level H_{T} selections. This feature is also evident in the m_{jjj} distributions shown in Figure 6.15. Thus, a looser (kinematic) pre-selection might be needed, particularly in the search for lower mass signals. The choice of this pre-selection is dependent on the trigger signatures and their performance in terms of the trigger efficiency turn-on. Additional study of the impact of the $t\bar{t}$ contribution to the background estimation is necessary since the contribution of the top quark resonance can introduce non-linearities in the background modelling. In Figure 6.18 the total background is shown with the 400 GeV signal overlaid on the distribution. The large statistical uncertainty on the background means no resonance emerges for the $t\bar{t}$ background and as noted earlier we see a low-m_{jjj} cut-off. The signal peak is very significant relative to the background in the vicinity of $m_{\text{jjj}} = 400$ GeV, which also supports the large significance metrics from previous Sections. Otherwise, these results confirm that further work is needed to reduce the statistical uncertainty on the background estimation.

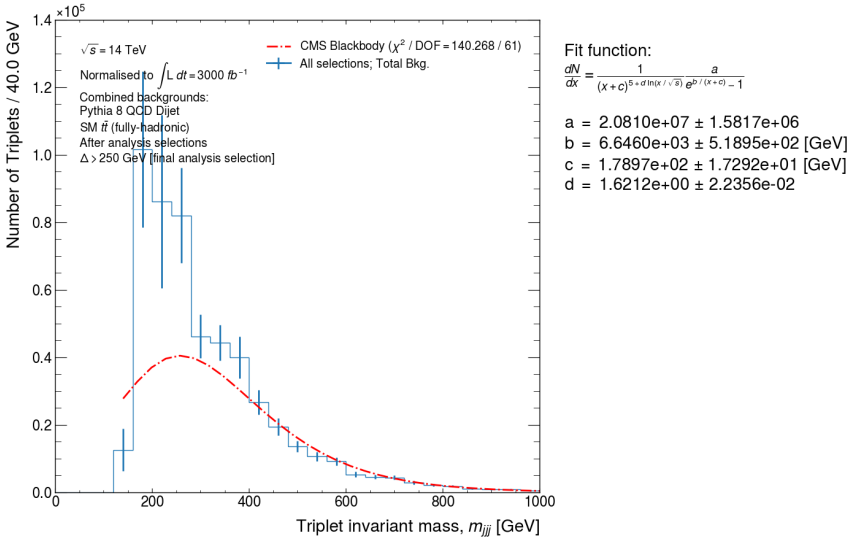

(a) Narrow m_{jjj} binning (40 GeV bin width).

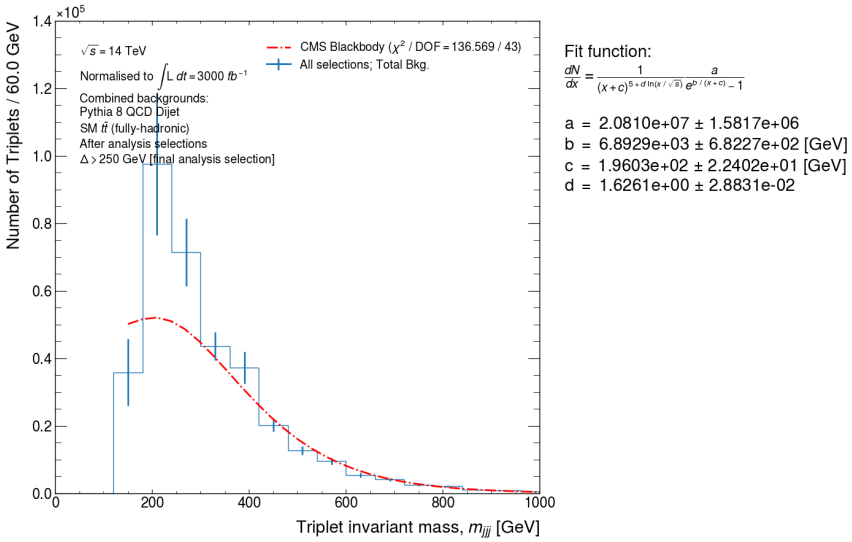

(b) Wide m_{jjj} binning (60 GeV bin width).

Figure 6.17: Fits of the low-mass region background model from Ref. [109] to the ATLAS QCD dijet samples scaled to the full HL-LHC integrated luminosity. The fits are included with two different invariant mass bin widths, but similar results are seen for the fit performance at low-m_{jjj} in both cases.

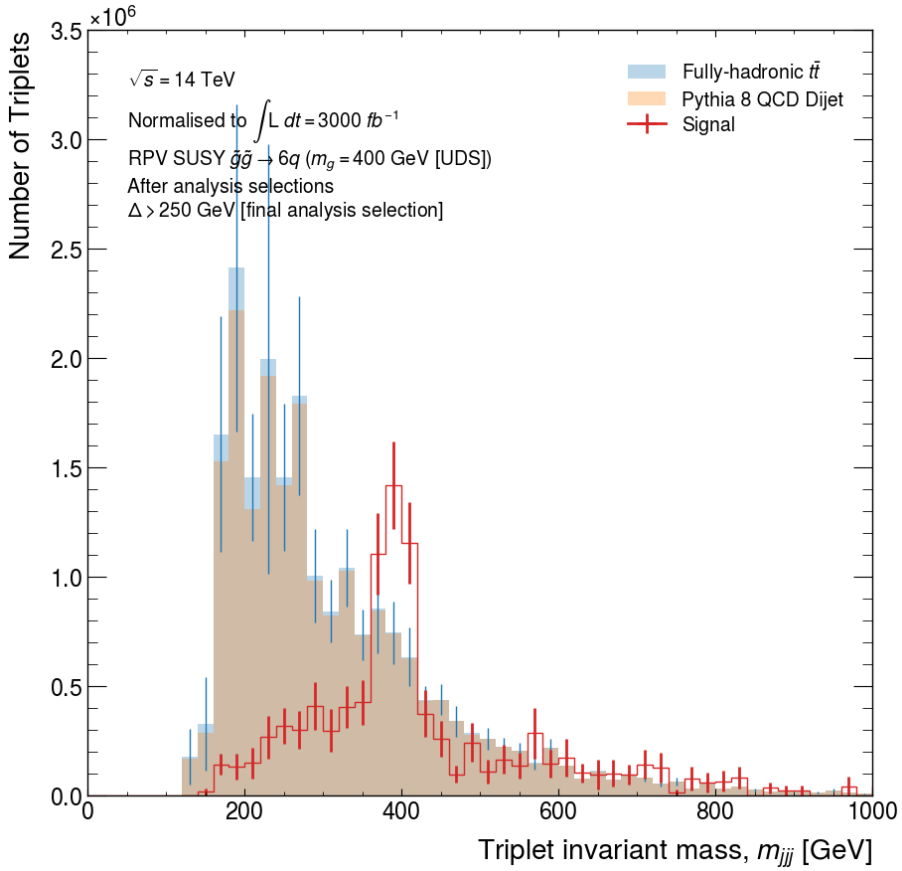

Figure 6.18: The stacked background m_{jjj} distribution with an overlaid $m_{\tilde{g}} = 400$ GeV signal distribution scaled to the appropriate $\sqrt{s} = 14$ TeV cross-section and the total integrated luminosity (3000 fb^{-1}) for the HL-LHC. The same selections as those applied in SR1 from Ref. [109] were applied.

6.6 Summary

The sensitivity of ATLAS to rare signal processes in hadronic final states will increase significantly with the higher luminosity achieved at the HL-LHC. The sheer amount of data collected during the HL-LHC lifetime will open pathways to significant advances in the exploration of challenging signatures of new physics using near real-time analysis techniques. This Chapter discussed some of the first results of studies to predict the sensitivity of ATLAS to multi-jet RPV SUSY signals using trigger-level analyses in the HL-LHC era. The results so far are limited by the relatively small size of the event samples used for the background and signal modelling. However, with basic analysis optimisation and the emulation of cross-sections anticipated for electroweakino pair-production we see that an analysis significance close to the 5σ discovery-level can be achieved with the full HL-LHC 3000 fb^{-1} integrated luminosity. These upgrade studies will be expanded to consider and evaluate different HL-LHC trigger scenarios in addition to addressing areas of further study discussed throughout the Chapter.

Chapter 7

Boosted jet tagging at the HL-LHC

When the HL-LHC begins operation in the late 2020s, a significantly greater instantaneous luminosity will be achieved in pp collisions. Consequently, the number of simultaneous interactions per bunch crossing (pile-up) will increase dramatically – there will be up to 200 interactions per bunch crossing. Since hadronic jets are a significant feature in many tests of the standard model and searches for new physics it is important to develop performant jet reconstruction and identification algorithms for these conditions.

The following Chapter details the results of studies of large-R jet top quark identification (tagging) performance in HL-LHC simulations. The substructure of large-R jets is exploited to develop *cut-based* taggers that discriminate between the signal (top quark) jets and those originating from QCD jet production (backgrounds). These taggers provide a starting point from which more complex jet identification tools can be developed and adapted for use in HL-LHC conditions.

7.1 Simulated event samples

The performance studies were undertaken using officially produced ATLAS MC event samples with the same conditions as anticipated at the HL-LHC, including high pile-up levels at $\mu = 200$ interactions per bunch crossing. The top quark signal sample models the decay of hypothetical Z' bosons to a $t\bar{t}$ pair, which decay fully hadronically with an approximately flat jet p_{T} distribution leading to high jet yields even at high-momentum. These events were simulated in Pythia 8.240 [98] and EvtGen 1.7.0 [99] using the A14 PDF tune [116] and the NNPDF23LO PDF set [117].

The primary background source considered for the tagging studies was QCD dijet production. These events were again simulated with Pythia 8 and EvtGen using the same generator versions and PDFs as for the signal sample. The QCD background samples were simulated in slices to ensure the jet p_{T} distribution was adequate sampled across a wide p_{T} range. The slices were binned in the p_{T} of truth-level

jets, and it was necessary to re-scale the event weights to obtain correct event yields across the p_{T} spectrum. The scale factor is defined:

$$\mathrm{SF} = \frac{\epsilon_f \times \sigma_{\mathrm{slice}} \times \mathcal{L}}{\sum_{\mathrm{event,\ i}} \mathcal{W}_i} \tag{7.1}$$

where SF is the event weight scale factor, ϵ_f is the filter efficiency of the MC generator, σ_{slice} is the total cross-section for the dijet slice, $\mathcal{L}$ is the equivalent integrated luminosity for the event sample, and the denominator represents the sum of the (unmodified) event weights for the complete dijet slice (only those events processed). The luminosity factor was not used for these studies (set to 1 fb^{-1}) because it cancels in ratios of event (or jet) yields used to estimate selection efficiencies.

For these studies, only the dijet slices from `JZ3WithSW` onwards were used. The other lower p_{T} slices are outside the $p_{\mathrm{T}} > 350$ GeV range in which top quark decays are considered to be fully contained within an $R = 1.0$ jet – see the start of Section 4.7 for more discussion.

Several of the background samples used a different primary-vertex reconstruction configuration to that used for the signal sample, causing distributions of the number of primary vertices per event (N_{PV}), shown in Figure 7.1, to be separated for signal and background. This effect is purely associated with the reconstruction methods and therefore N_{PV} is a biased variable for these studies. It was not anticipated that these differences have significant impacts on the tagging studies of `LCTopo` jets that are reconstructed from only calorimeter-based detector information (without origin[1] corrections).

7.2 Event reconstruction

7.2.1 Jet reconstruction

Large-R anti-k_t jets with a size parameter, $R = 1.0$, were reconstructed from LCW-scale topoclusters without origin correction. No additional calibrations were applied to the jets so that the tagging performance of the ungroomed and groomed `LCTopo` jet definitions could be established. Additionally, no jet input level pile-up mitigation algorithms were applied. Truth jets were reconstructed from generator-level particles with the same jet algorithm. These jets were used for two purposes: to identify whether the simulated top quark decay products were completely contained within the jets, and to define kinematic ranges considered for studies of the tagging performance.

To prevent biases in the results of tagging studies the background jet p_{T} distribution was re-weighted (by scaling the event weights) to have the same shape as the flat

[1] Correcting the 4-momentum of jet constituents to point from the primary-vertex rather than the geometric centre of the detector.

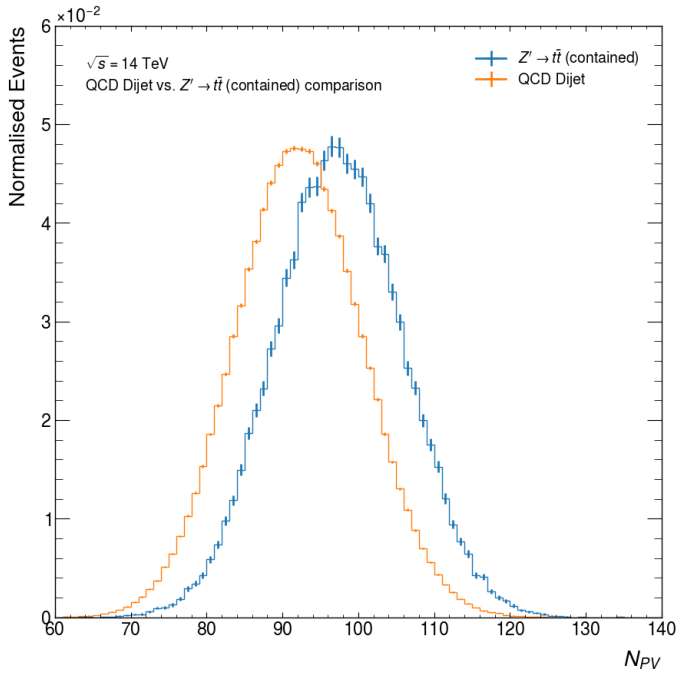

Figure 7.1: An N_{PV} distribution comparison for the signal and background samples.

signal jet p_{T} distribution. Scale-factors for the event-weights were derived using finely binned p_{T} distributions for the leading ungroomed truth jet. Thus, the leading truth (and reconstructed) jet p_{T} distributions for the signal and background have better agreement than the sub-leading (second) jet. Example jet p_{T} distributions after the re-weighting procedure are shown in Figure 7.3. Reasonable closure (without significant shape differences) between the signal and background jet p_{T} distributions is seen allowing the tagging performance studies to proceed. As a result of these changes, the ungroomed jet mass distributions for the signal and background have much smaller separation (Figure 7.2), which impacts the performance of the ungroomed jet mass in later tagging studies. However, much better separation is seen for groomed jet collections, which are most important for the development of pile-up stable taggers.

Two different large-R jet grooming algorithms (introduced in Section 4.7.1) were studied to compare their performance. These algorithms and their parameters include:

- Trimming: sub-jet size parameter $R_{\mathrm{sub}} = 0.2$, with a minimum sub-jet p_{T} fraction (relative to the ungroomed jet) of $f_{\mathrm{cut}} = 0.05$.
- SoftDrop: $z_{\mathrm{cut}} = 0.1$, $\beta = 1.0$.

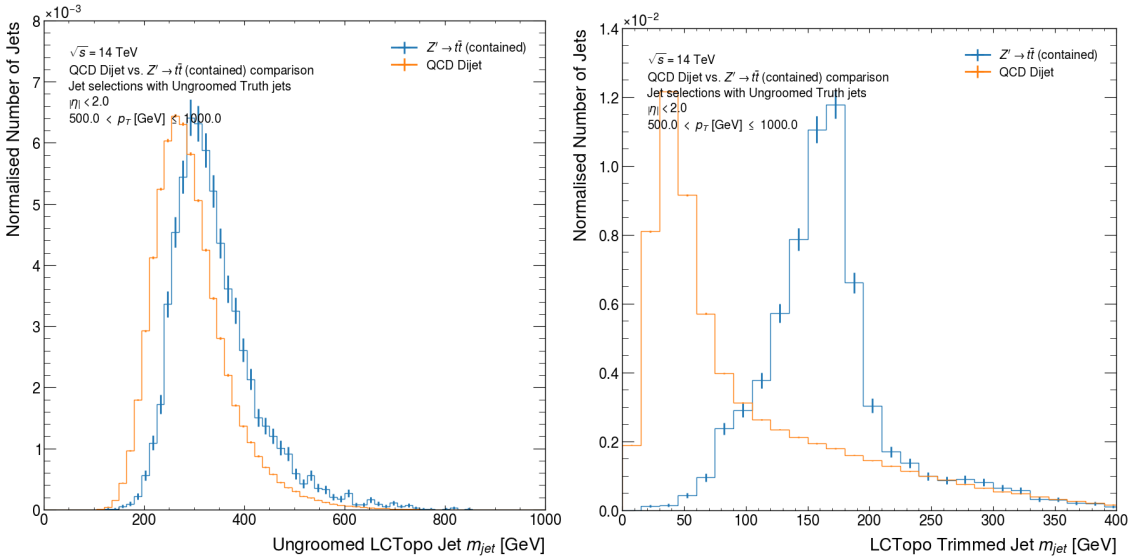

(a) `LCTopo` jet mass after re-weighting. (b) `LCTopoTrimmed` jet mass after re-weighting.

Figure 7.2: A comparison of ungroomed and trimmed `LCTopo` jet mass distributions for signal and background after re-weighting the p_{T} distribution of the QCD jet background.

7.2.2 Jet labelling procedure

Hadronic top quark decays occur most commonly through the process $t \to bW \to bq\bar{q}'$. A truth labelling procedure was applied only to the signal sample to identify jets that contained all decay products of the top quark [80, 130]. First, ungroomed truth-level jets (j_{truth}) were matched to generator-level top partons (t) with a $\Delta R(j_{\mathrm{truth}},\ t) < 0.75$ requirement. The ungroomed (`LCTopo`) reconstructed jets were then matched to the parton-matched truth jets with a $\Delta R(j_{\mathrm{truth}},\ j_{\mathrm{reco}}) < 0.75$ requirement. Since top quarks are massive and therefore the large-R jet does not have a negligible mass we used the jet rapidity to define $\Delta R = \sqrt{\Delta y^2 + \Delta\phi^2}$. This definition is used for the remainder of this Chapter.

Recent studies of top quark tagging with Unified Flow Object jet inputs (Section 4.2.2) applied additional selections to the ungroomed truth jets to ensure the top quark decay was fully contained [130]. These selections include [130]:

- There being at least one ghost-associated B-hadron (truth-level particle).
- A jet mass selection, $m_{\mathrm{jet}} > 140$ GeV.
- A selection on the k_t splitting scale variable, $\sqrt{d_{23}}$, calculated for the ungroomed truth jet requiring: $\sqrt{d_{23}}$ (GeV) $> \exp(3.3 - 6.98 \times 10^{-4} \times (p_{\mathrm{T}}\ /\ \mathrm{GeV}))$.

For `LCTopo` jet tagging we adopted all but the final $\sqrt{d_{23}}$ selection for the contained top quark label. This ensured greater consistency with Run 2 `LCTopo` jet tagging

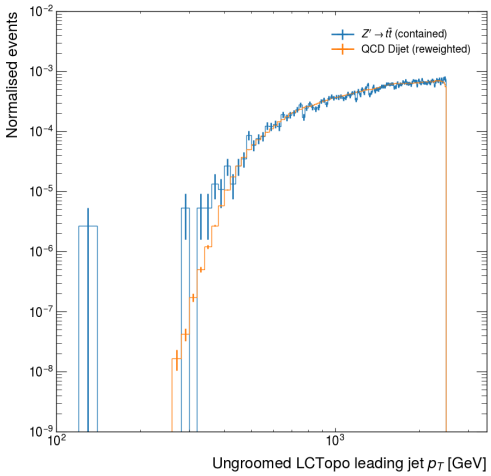

(a) Leading `LCTopo` jet

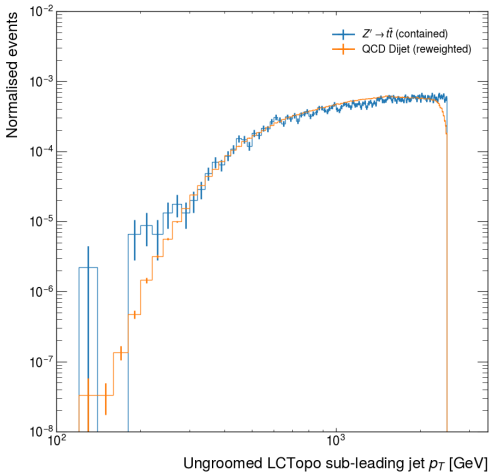

(b) Sub-leading `LCTopo` jet

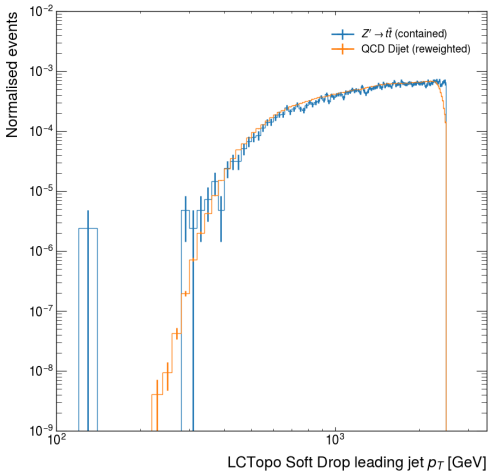

(c) Leading `LCTopoSoftDrop` jet

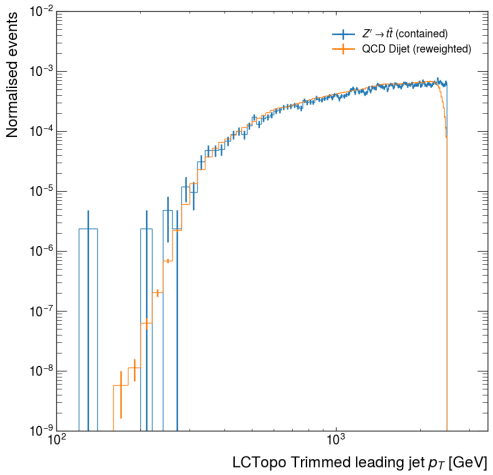

(d) Leading `LCTopoTrimmed` jet

Figure 7.3: Comparison of reconstructed jet p_{T} distributions after applying the re-weighting procedure to the QCD background. Reasonable closure is seen for the leading jet, but this deteriorates for sub-leading jets.

results that used different labelling schemes [80]. It is important to note that other `LCTopo` jet tagging studies typically matched the groomed truth jets to the reconstructed groomed jets. However, for the development of the cut-based tagging recommendations we maintained the relationships between groomed jets and their parent ungroomed jets by only matching the ungroomed jets as in Ref. [66]. The groomed truth jets were simply required to have a matched truth top parton. Similarly, the groomed reconstructed jets were associated with their parent ungroomed jet and no additional ΔR criteria were imposed. This allowed comparisons of the performance of different jet collections (with varying grooming algorithms) similar to Ref. [66].

For the study of Run 2 (`LCTopoTrimmed`) jet DNN taggers, an alternate truth labelling scheme was applied to ensure consistency between the definitions of contained top quark jets between the HL-LHC cut-based taggers (for comparison) and the existing Run 2 tagger definitions. The truth labelling scheme was similar to that mentioned above with the exception that no matching was performed for the ungroomed jets, only the trimmed jets. Thus, the particle-level trimmed (truth) jets were subjected to the *contained-ness* criteria: $m > 140$ GeV, at least 1 ghost-associated[2] B-hadron, and association with a truth top quark ($\Delta R < 0.75$). The trimmed `LCTopo` jets were matched to the truth trimmed jets using a $\Delta R < 0.75$ association.

Based on results from Ref. [130] a larger truth labelling efficiency is expected when selections are made on the ungroomed truth jets instead of groomed truth jets. The labelling efficiencies in HL-LHC simulation were briefly estimated for (truth) jets matched to a truth top-parton. The results for both labelling schemes discussed above are shown in Table 7.1. For the ungroomed labelling scheme, the efficiency is above 95% for all jet p_{T} bins. However, the efficiency for the trimmed jet truth label only reaches about 86% for truth jets with $p_{\mathrm{T}} > 1000$ GeV. The increase in efficiency as the jets are required to have higher p_{T} for both labelling methods results from the increased containment of the top quark decay products at high truth jet p_{T} (i.e. they are more boosted).

7.2.3 Event and jet selections

The large-R jets and events used in the tagging studies were subjected to basic event/jet selections to ensure the events contained valid truth matched jets in a particular kinematic range. Events were required to have exactly two truth matched jets for the $t\bar{t}$ signal sample and exactly two saved jets for the QCD background sample (without matching). Only two jets were originally saved per event, so this selection ensured we removed events where one of the truth jets did not satisfy the truth label in the signal sample.

[2]The ghost association of a particle to a jet involves assigning an infinitesimal energy to the particle and determining its association by including it in the consitituent particles/objects provided to the jet clustering algorithm.

Table 7.1: Truth labelling efficiencies for the ungroomed and trimmed jet labelling schemes with different selections on the truth jet p_{T}. The efficiencies were calculated only considering the particle-level jets that were matched to a generator-level top quark.

Ungroomed jet labelling scheme	
Selection	Labelling Efficiency (%)
No selection	95.1
Jet $p_{\mathrm{T}} > 350$ GeV	97.5
Jet $p_{\mathrm{T}} > 500$ GeV	98.2
Jet $p_{\mathrm{T}} > 1000$ GeV	99.1
Trimmed jet (DNN) labelling scheme	
Selection	Labelling Efficiency (%)
No selection	80.8
Jet $p_{\mathrm{T}} > 350$ GeV	83.1
Jet $p_{\mathrm{T}} > 500$ GeV	83.8
Jet $p_{\mathrm{T}} > 1000$ GeV	85.6

Additional jet selections were applied to either truth jets or reconstructed jets. Both the leading and second-leading (sub-leading) jets passing selections in events were used throughout the studies. For comparisons of jet collections, results were binned in the p_{T} of the ungroomed truth jet with an additional $|\eta| < 2$ selection on the jets. Reconstructed jets were required to have $350 < p_{\mathrm{T}}$ (GeV) < 2500 and $|\eta| < 2$. This was imposed since particle-level (truth) jets have a different energy scale to reconstructed jets, and we therefore wanted to ensure that the reconstructed jet kinematics were valid for the taggers. The motivation for the $|\eta| < 2$ selections was to consider well-reconstructed jets without the pile-up contamination associated with higher calorimeter occupancy in the forward region. However, this also allows the results to be compared with other Run 2/3 studies (that tag central jets) in the future. For these studies we focused purely on central jets and further exploration of the tagging of high-η jets was left for future work. The final tagging recommendation results were *only* binned in the p_{T} of the reconstructed (groomed) jet to provide tagger definitions suitable for implementation in ATLAS software.

7.3 Important definitions and notes

For the remainder of this Chapter a range of tagger metrics will be discussed including the:

- Signal(background) efficiency: the proportion of signal(background) jets passing a tagger selection calculated by integrating over finely-binned histograms of observables. The signal and background efficiency are denoted with ϵ_{sig} and ϵ_{bkg}, respectively.
- Background rejection: used to represent a (dimensionless) metric of the tagger performance calculated as the inverse of the background efficiency – $1/\epsilon_{\mathrm{bkg}}$.

Uncertainties in ϵ_{sig} and ϵ_{bkg} were estimated as one standard deviation intervals from a normal distribution using the `ROOT TEfficiency` implementation documented at https://root.cern.ch/doc/master/classTEfficiency.html. The normal distribution methods were used to ensure event weights could be considered in the `TEfficiency` calculations. However, this approximation breaks down when the efficiency is 0 or 1, at which point the estimated standard deviation of the distribution vanishes. The calculation of the uncertainty in the background efficiency was propagated to obtain the background rejection uncertainty:

$$\sigma^2_{\mathrm{rej}} = \left(\frac{1}{\epsilon^2_{\mathrm{bkg}}}\right)^2 \times \sigma^2_{\epsilon_{\mathrm{bkg}}} \tag{7.2}$$

where σ_{rej} and $\sigma_{\epsilon_{\mathrm{bkg}}}$ are the background rejection and efficiency uncertainties, respectively. The upper and lower bounds for the efficiency uncertainty were flipped in the calculation of the background rejection uncertainty – the lower limit of the efficiency leads to a larger background rejection. Since the normal uncertainty interval is

symmetric, the upper and lower bounds of the efficiency uncertainties are identical except where the bounds are cut-off to prevent efficiencies exceeding 100% or falling below 0% after the addition or subtraction of the uncertainty. This procedure is used in the plots of the tagger performance results involving efficiencies throughout this Chapter.

7.4 Jet substructure moments for top quark tagging

Previous studies considered all possible combinations of observables for top quark tagging leading to a jet mass and τ_{32}^{wta} selection recommendation [80]. There are several ways to calculate the jet mass with a combination of calorimeter and track based methods, but we focused explicitly on calorimeter jets and therefore a calorimeter-only mass definition. The combination of the jet mass selection with an additional selection is necessary to increase the background rejection of taggers as illustrated for some single- and two-variable HL-LHC taggers in Figure 7.4. We considered a range of variables outlined further in Appendix B:

- Kinematic variables – the jet mass (m_{jet}).
- Jet shape variables: N-subjettiness ratios (τ_{32}^{wta}), sphericity, aplanarity.
- (Generalised) Energy Correlation Function ratios: D_2, C_2.
- k_t splitting scales: $\sqrt{d_{12}}$, $\sqrt{d_{23}}$, and associated z-variables (z_{12}, z_{23}) where $z_{ij} = d_{ij}/(d_{ij} + m^2)$ (m is the invariant mass of the last sub-jet split in the exclusive k_t clustering sequence [131]).

Some of these variables are actually intended for 2-prong decay discrimination (e.g. D_2, C_2, $\sqrt{d_{12}}$, z_{12}) and likely will not provide better performance than other 3-prong sensitive variables[3].

We restricted the focus of these studies to $m_{\text{jet}}+X$ taggers where X is any other tagger observable used in the studies. The first jet mass selection is well motivated by the differences in shape between the QCD and top quark groomed jet mass distributions[4] The jet mass selection can be used to isolate the three-prong kinematics characteristic of a top quark decay, increasing the sensitivity of other suitable variables to the differences between signal and background topologies as discussed in Ref. [132]. Nonetheless, the study of alternative pairs of variables is still warranted and should be considered in the future for further cut-based tagger development.

[3] However, the consideration of an inclusive top quark selection where decays do not need to be fully contained could lead to better performance for these observables when only the W decay but not the additional b-quark from the t-quark decay is reconstructed in the jet. This is left for future work.

[4] The top quark resonance produces a prominent peak close to 173 GeV and the QCD distribution is generally smoothly falling in that region.

7.5 Tagger observable comparisons

The performance of cut-based taggers is governed by both the correlation and separation (between signal and background) of observables used in tagger definitions. Thus, an understanding of the correlations between the jet mass and other substructure observables is important. A selection on one variable cuts into the distribution of another correlated variable, reducing its potential to have good background rejection performance. Thus, variables with minimal correlation were considered for two-variable top quark taggers. The correlation coefficients calculated from two-dimensional histograms of the observables are shown with correlation matrices in Figures 7.5 and 7.6 for trimmed jets and soft-drop groomed jets, respectively.

The key finding from these results is that the jet mass is best combined with the τ_{32}^{wta}, τ_{21}^{wta}, aplanarity, and sphericity observables. The τ_{32}^{wta} and jet mass correlation coefficients for the trimmed signal jets increase with p_{T} but are smaller in magnitude than the soft-drop jet correlation coefficients. The background and signal correlation coefficients for trimmed jets show opposite behaviour for A (aplanarity) and S (sphericity) as a function of p_{T} – the background jet coefficients become more positive, while the signal jet coefficients become more negative. The performance of combinations involving the jet mass and $\sqrt{d_{ij}}$ variables are impacted by their significant correlation. Some negative correlations are seen for the trimmed jet z_{ij} variables in the signal sample compared to larger positive correlations for the background. The soft-drop jet z_{12} variables have negative correlation coefficients that become more positive as the truth jet p_{T} increases for signal jets, and increasing positive coefficients for the background jets. Alternative combinations of variables, including those involving $\sqrt{d_{ij}}$, with low correlation coefficients could also yield reasonable tagger performance exist, but that is left for further study. This includes the $\sqrt{d_{23}}$ and τ_{32}^{wta} combination for trimmed jets (similar to taggers evaluated in Ref. [133]) – albeit the performance of those taggers would be determined by the separation of the signal and background distributions for each observable.

The separation between the top quark and QCD groomed jet masses in Figure 7.7 motivates the consideration of $m_{\text{jet}} + X$ taggers as discussed in Section 7.4. This is the case for both the soft-drop and trimmed jet collections, but more extensive tails are seen in the low-p_{T} jet mass distributions for soft-drop jets. In high-p_{T} bins the jet mass distributions become "cleaner" and are visibly peaked around the top quark mass – the top quark decay products are more boosted and therefore better contained within the jet at high p_{T}. We expect three-prong sensitive variables (e.g. τ_{32}^{wta} and $\sqrt{d_{23}}$) to provide significant separation but also see significant separation between jet shape variables that encapsulate the uniformity of a distribution of jet constituents in the jet rest frame (aplanarity and sphericity) [83, 86]. Indeed, the variables that have significant separation for top quark and QCD jets include the aplanarity (Figure 7.10), sphericity, τ_{32}^{wta} (Figure 7.8), τ_{21}^{wta} (Figure 7.11), and k_t splitting scale observables ($\sqrt{d_{ij}}$) (Figures 7.12 and 7.13). The separation of some of these variables varies between the grooming algorithm applied to the jets, which is

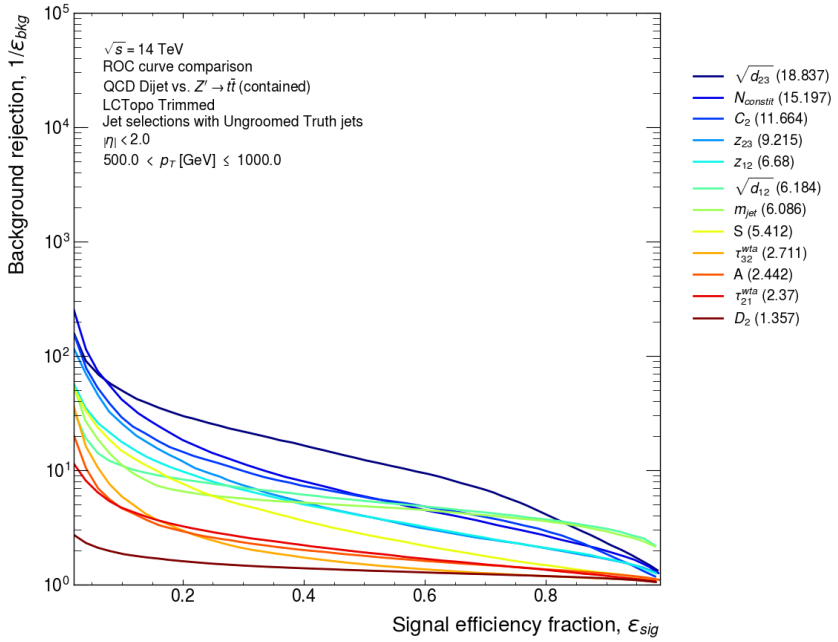

(a) Single variable selections.

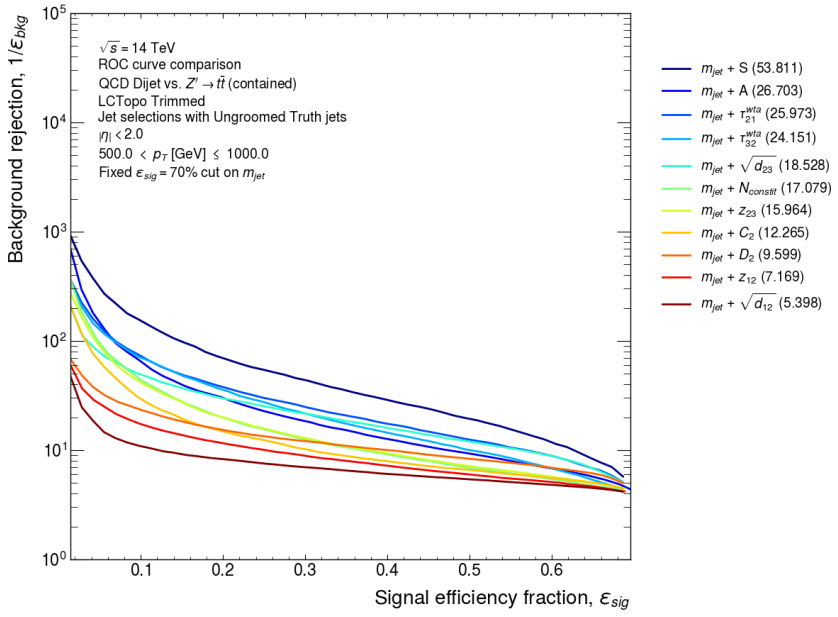

(b) Two-variable $m_{\text{jet}} + X$ taggers with a first 70% signal efficiency jet mass selection.

Figure 7.4: A comparison of single-variable (top) and two-variable (bottom) tagger performance. The legend entries for both plots are ordered by the area under the ROC curve. The ROC curve is plotted with the background rejection on the y-axis and signal efficiency on the x-axis in a similar convention to Ref. [66, 80]. The limits of the signal efficiency axis are chosen to minimise the effect of rapid variations in the background efficiency that cause the background rejection to blow up at low-ϵ_{sig}.

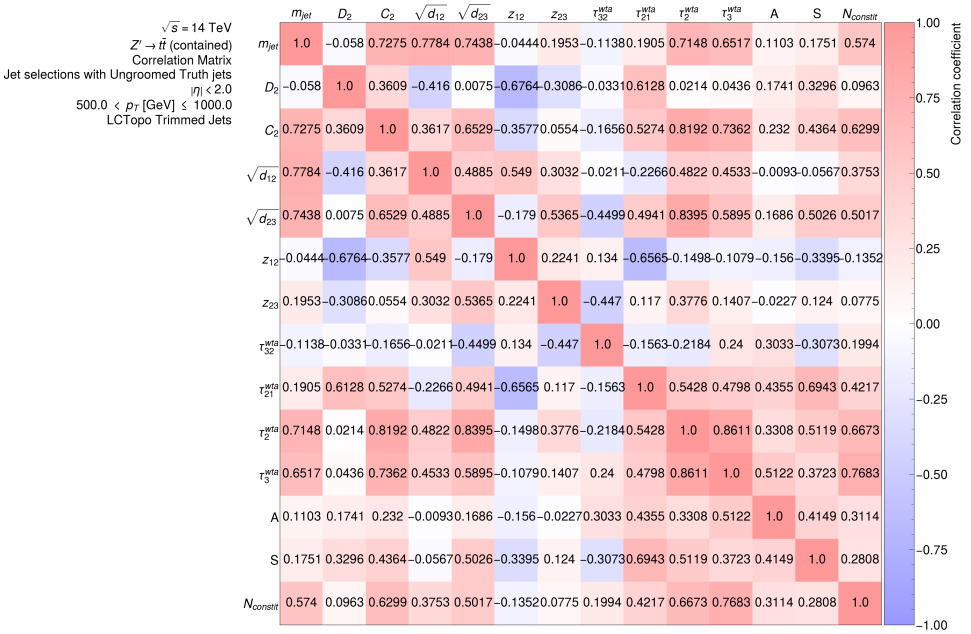

(a) Trimmed signal jets $500 < p_{\mathrm{T}}^{\mathrm{truth}}$ (GeV) ≤ 1000

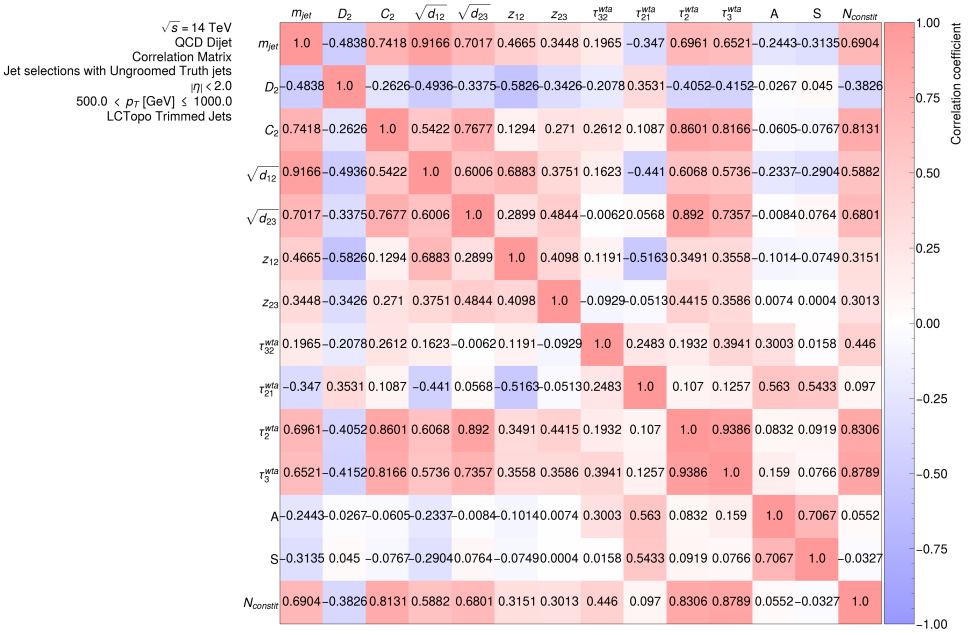

(b) Trimmed QCD jets $500 < p_{\mathrm{T}}^{\mathrm{truth}}$ (GeV) ≤ 1000

Figure 7.5: Tagger observable correlation matrices calculated for the contained top quark ($Z' \to t\bar{t}$) signal jets and the QCD background jets in different ungroomed truth jet p_{T} bins (with an additional $|\eta| < 2.0$ selection) for trimmed `LCTopo` jets.

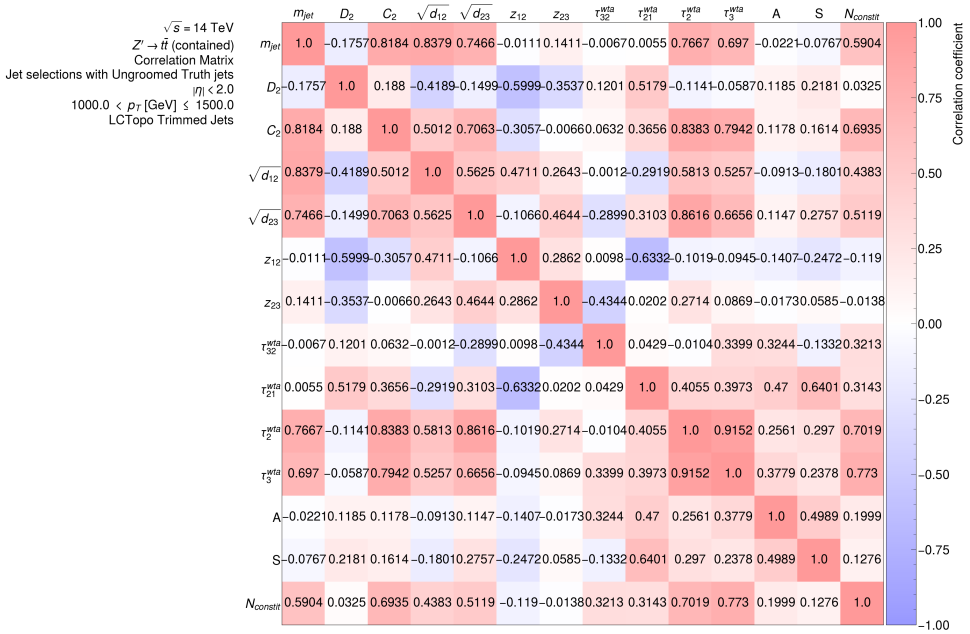

(c) Trimmed signal jets $1000 < p_{\mathrm{T}}^{\mathrm{truth}}$ (GeV) ≤ 1500

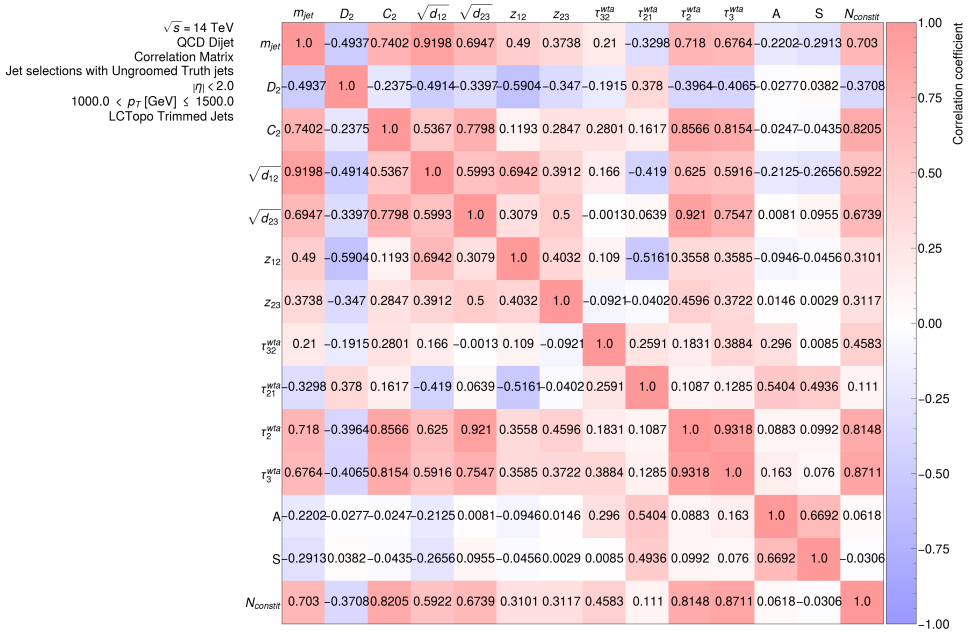

(d) Trimmed QCD jets $1000 < p_{\mathrm{T}}^{\mathrm{truth}}$ (GeV) ≤ 1500

Figure 7.5 (cont.): Tagger observable correlation matrices calculated for the contained top quark ($Z' \to t\bar{t}$) signal jets and the QCD background jets in different ungroomed truth jet p_{T} bins (with an additional $|\eta| < 2.0$ selection) for trimmed `LCTopo` jets.

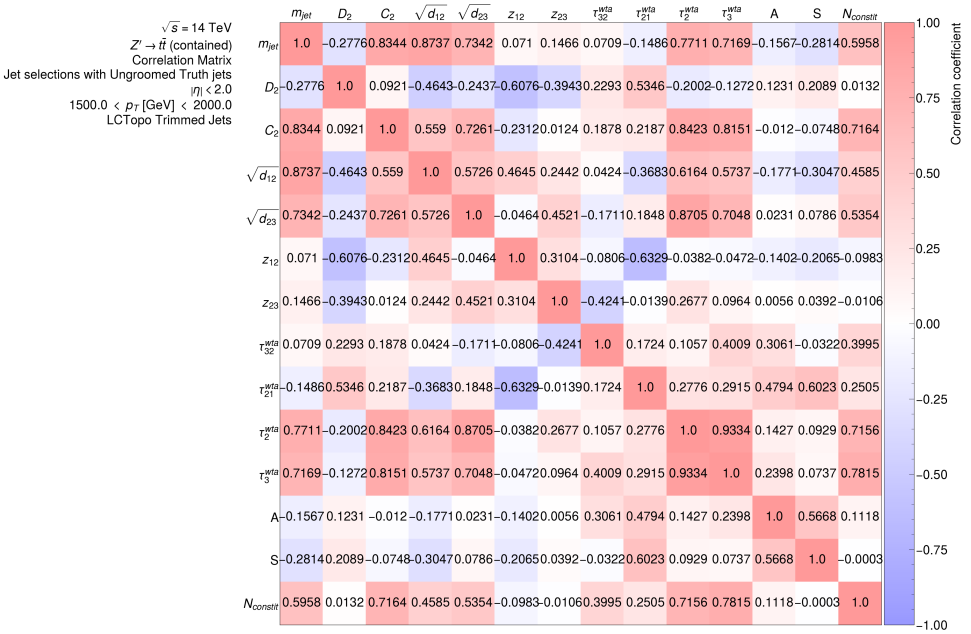

(e) Trimmed signal jets $1500 < p_{\mathrm{T}}^{\mathrm{truth}}$ (GeV) < 2000

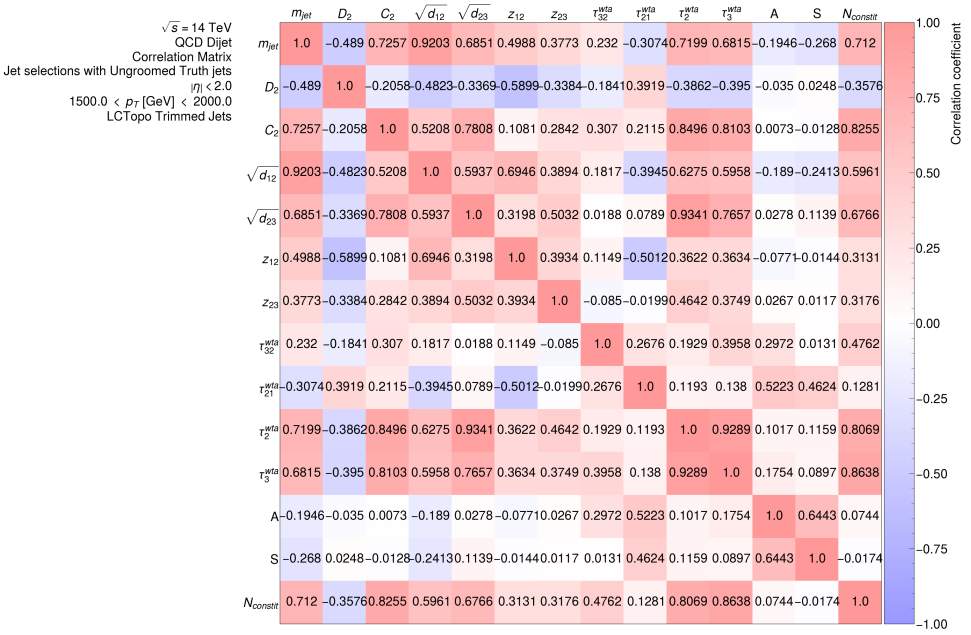

(f) Trimmed QCD jets $1500 < p_{\mathrm{T}}^{\mathrm{truth}}$ (GeV) < 2000

Figure 7.5 (cont.): Tagger observable correlation matrices calculated for the contained top quark ($Z' \to t\bar{t}$) signal jets and the QCD background jets in different ungroomed truth jet p_{T} bins (with an additional $|\eta| < 2.0$ selection) for trimmed `LCTopo` jets.

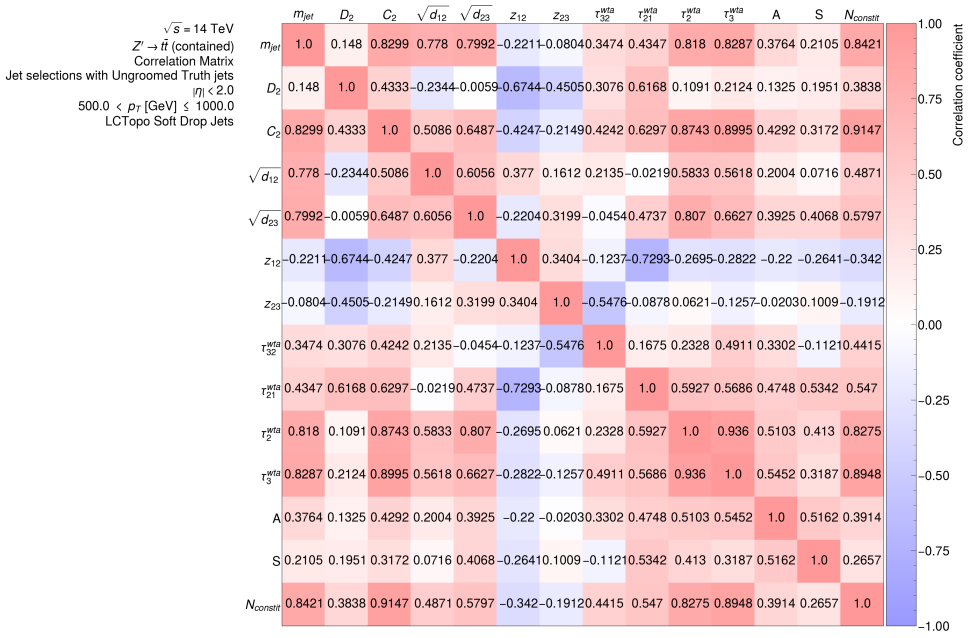

(a) Soft-drop signal jets $500 < p_{\mathrm{T}}^{\mathrm{truth}}$ (GeV) ≤ 1000

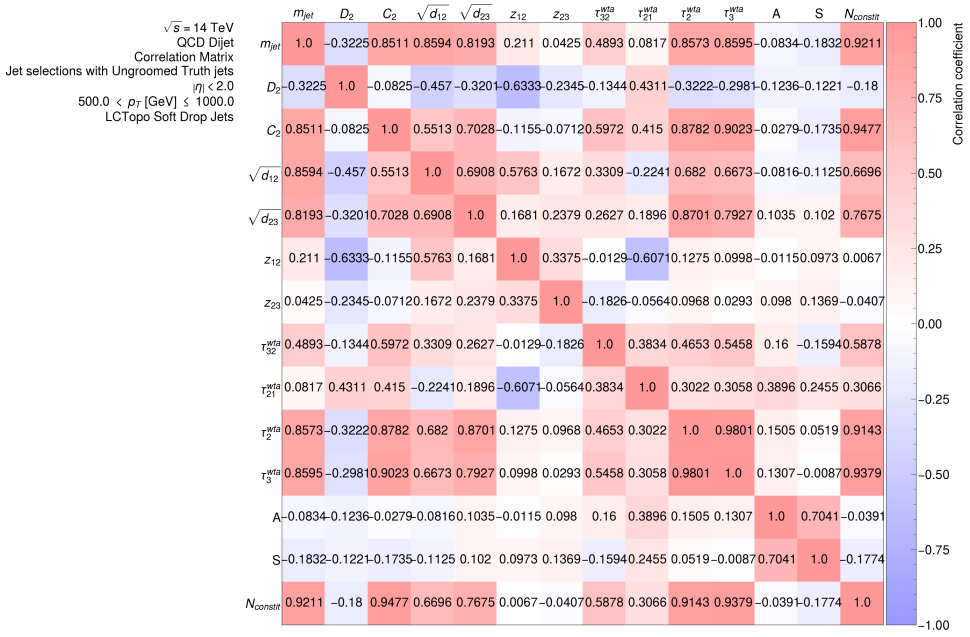

(b) Soft-drop QCD jets $500 < p_{\mathrm{T}}^{\mathrm{truth}}$ (GeV) ≤ 1000

Figure 7.6: Tagger observable correlation matrices calculated for the contained top quark ($Z' \to t\bar{t}$) signal jets and the QCD background jets in different ungroomed truth jet p_{T} bins (with an additional $|\eta| < 2.0$ selection) for soft-drop groomed `LCTopo` jets.

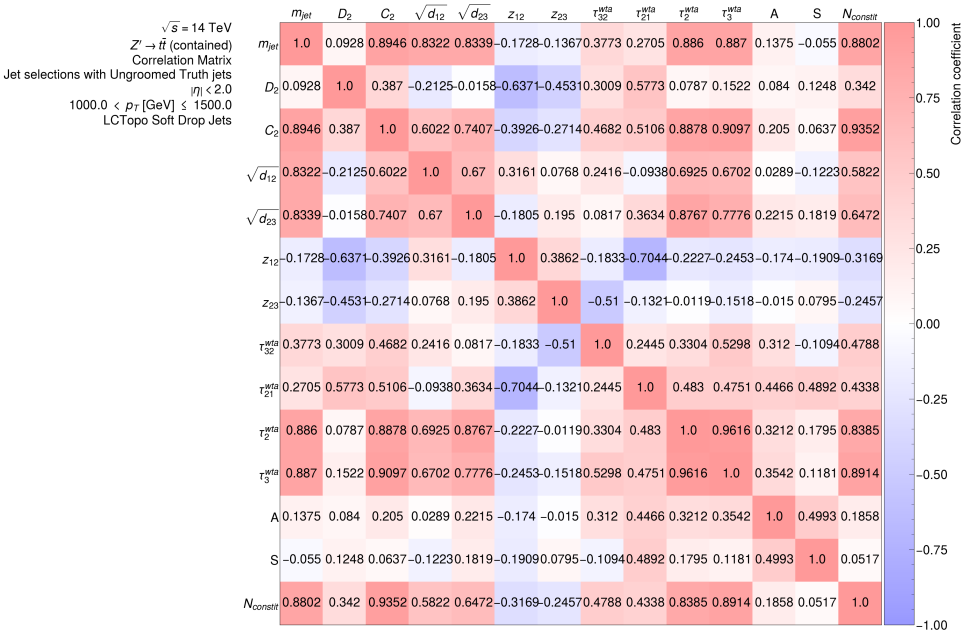

(c) Soft-drop signal jets $1000 < p_{\mathrm{T}}^{\mathrm{truth}}$ (GeV) ≤ 1500

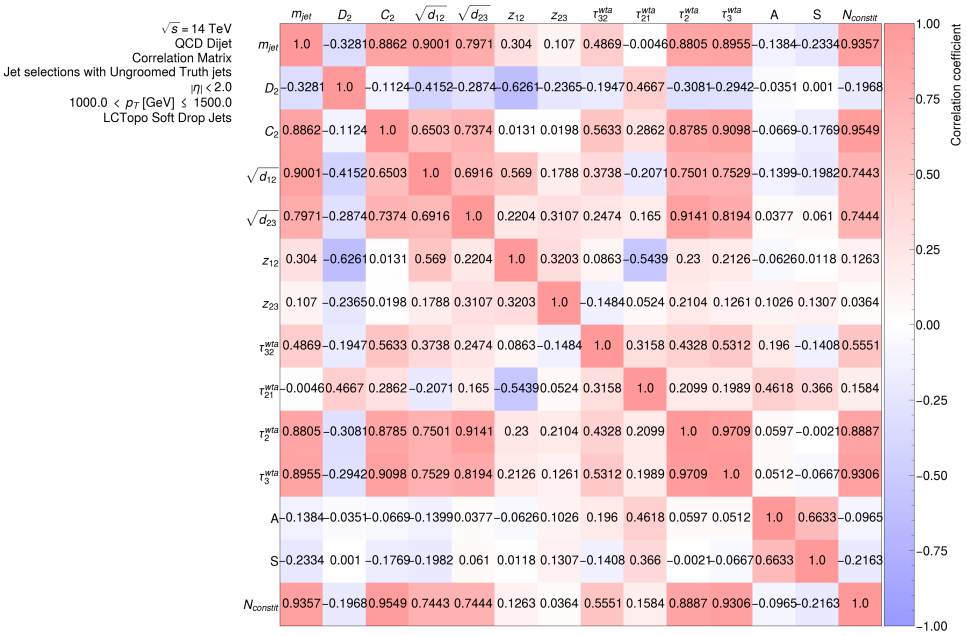

(d) Soft-drop QCD jets $1000 < p_{\mathrm{T}}^{\mathrm{truth}}$ (GeV) ≤ 1500

Figure 7.6 (cont.): Tagger observable correlation matrices calculated for the contained top quark ($Z' \to t\bar{t}$) signal jets and the QCD background jets in different ungroomed truth jet p_{T} bins (with an additional $|\eta| < 2.0$ selection) for soft-drop groomed `LCTopo` jets.

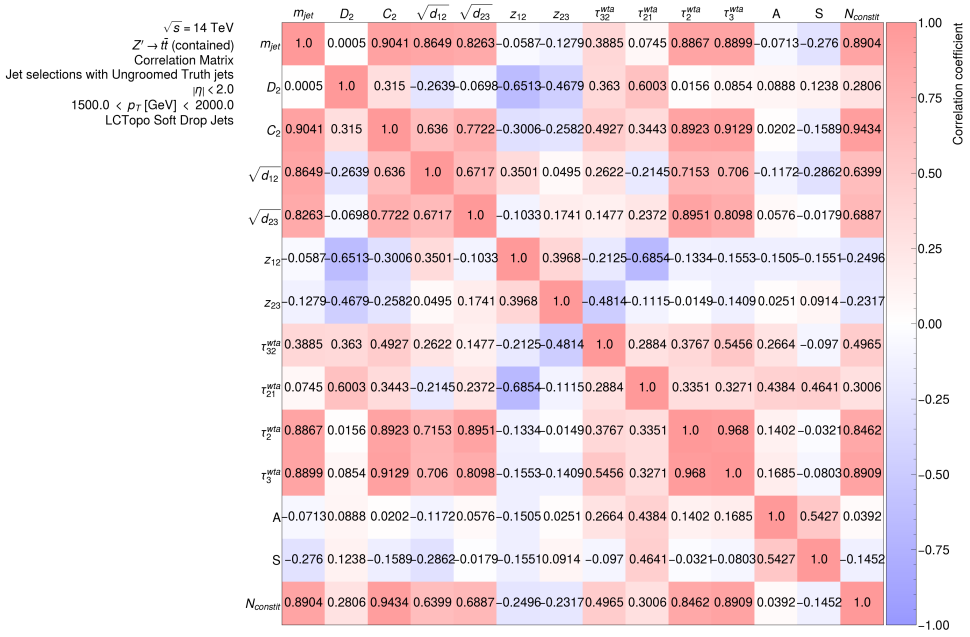

(e) Soft-drop signal jets $1500 < p_{\mathrm{T}}^{\mathrm{truth}}$ (GeV) < 2000

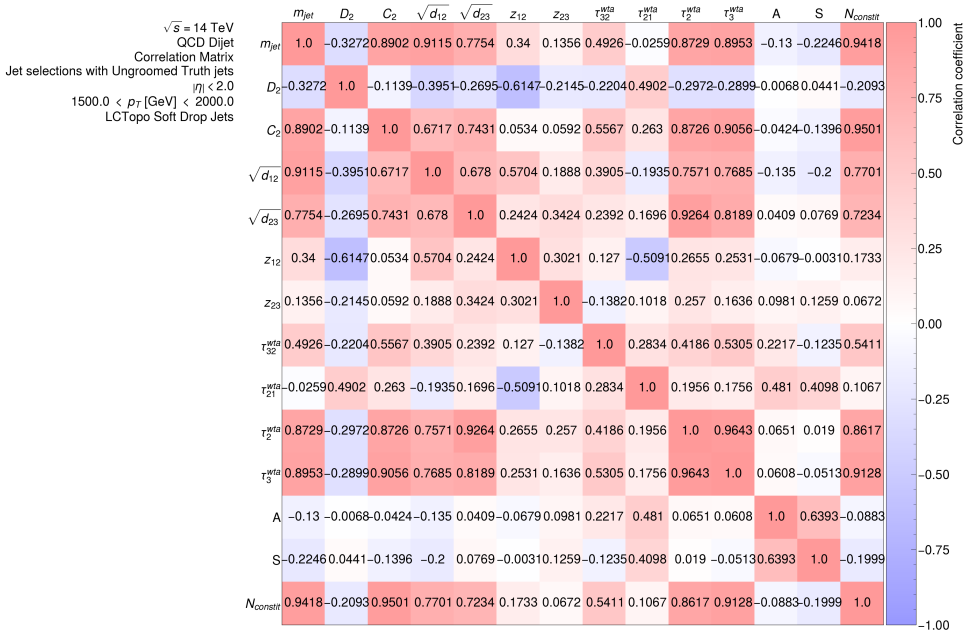

(f) Soft-drop QCD jets $1500 < p_{\mathrm{T}}^{\mathrm{truth}}$ (GeV) < 2000

Figure 7.6 (cont.): Tagger observable correlation matrices calculated for the contained top quark ($Z' \to t\bar{t}$) signal jets and the QCD background jets in different ungroomed truth jet p_{T} bins (with an additional $|\eta| < 2.0$ selection) for soft-drop groomed `LCTopo` jets.

to be expected since different grooming algorithms remove different amounts of soft and wide-angle radiation from the jets. The observables with the greatest amount of separation between the signal and background distributions are more likely to produce better background rejection in a two-variable tagger.

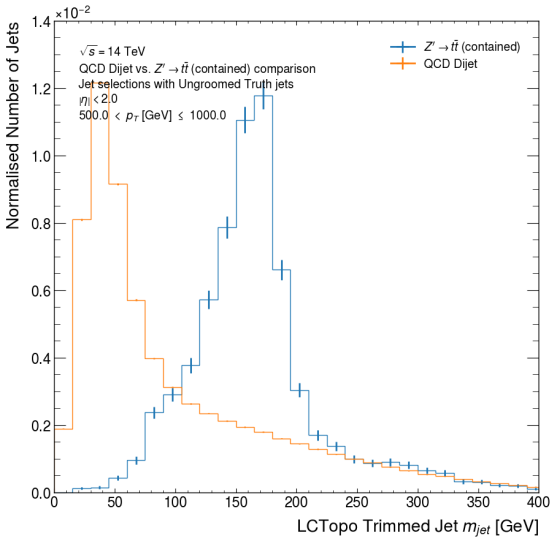

(a) Trimmed jets ($500 < p_{\mathrm{T}}^{\mathrm{truth}}$ [GeV] ≤ 1000)

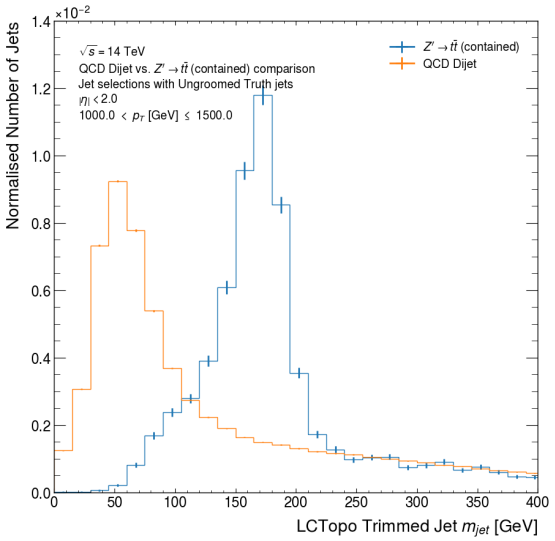

(b) Trimmed jets ($1000 < p_{\mathrm{T}}^{\mathrm{truth}}$ [GeV] ≤ 1500)

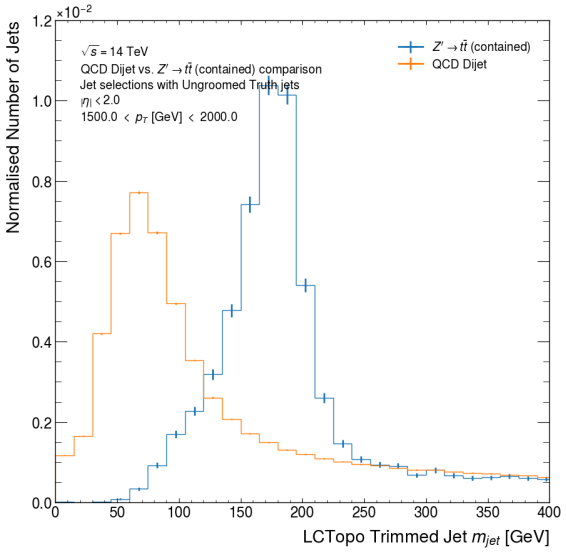

(c) Trimmed jets ($1500 < p_{\mathrm{T}}^{\mathrm{truth}}$ [GeV] < 2000)

Figure 7.7: Jet mass comparisons for signal and background jets in bins of the ungroomed truth jet p_{T}. Results are included for both the trimmed and soft-drop groomed jets.

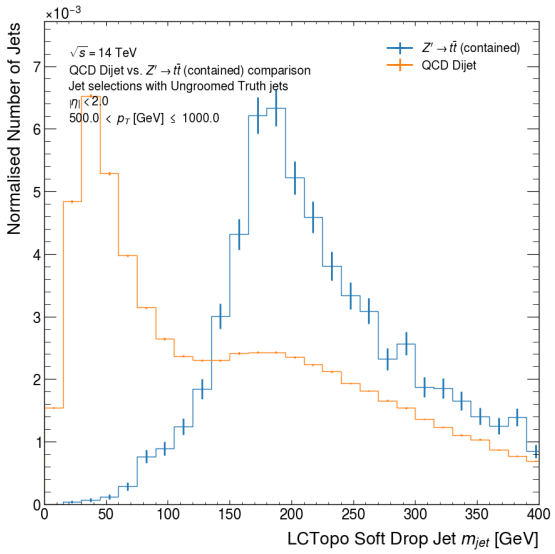

(d) Soft-drop jets ($500 < p_{\mathrm{T}}^{\mathrm{truth}}$ [GeV] ≤ 1000)

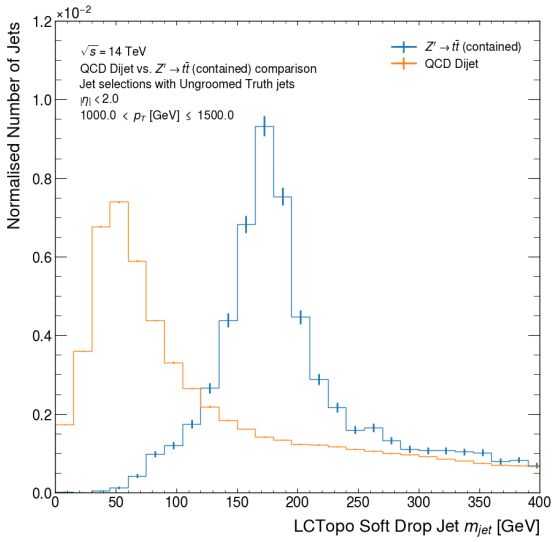

(e) Soft-drop jets ($1000 < p_{\mathrm{T}}^{\mathrm{truth}}$ [GeV] ≤ 1500)

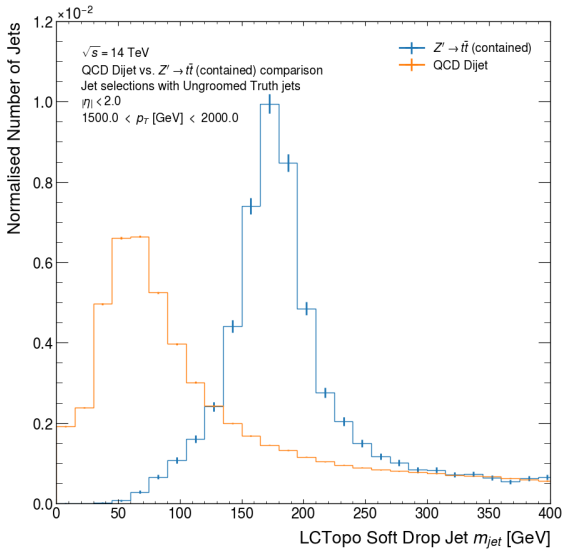

(f) Soft-drop jets ($1500 < p_{\mathrm{T}}^{\mathrm{truth}}$ [GeV] < 2000)

Figure 7.7 (cont.): Jet mass comparisons for signal and background jets in bins of the ungroomed truth jet p_{T}. Results are included for both the trimmed and soft-drop groomed jets.

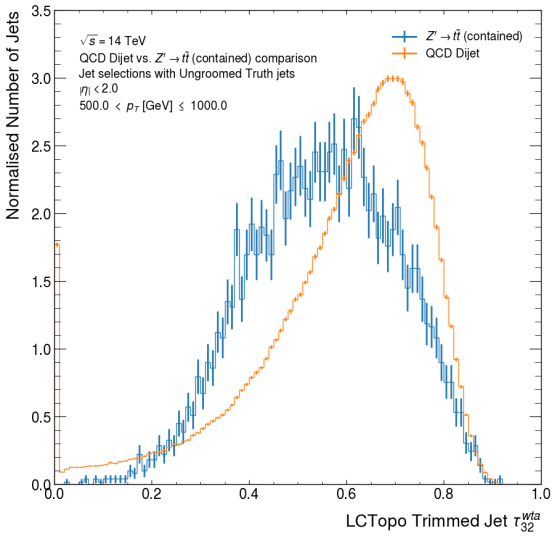

(a) Trimmed jet τ_{32}^{wta} ($500 < p_{\text{T}}^{\text{truth}}$ [GeV] ≤ 1000)

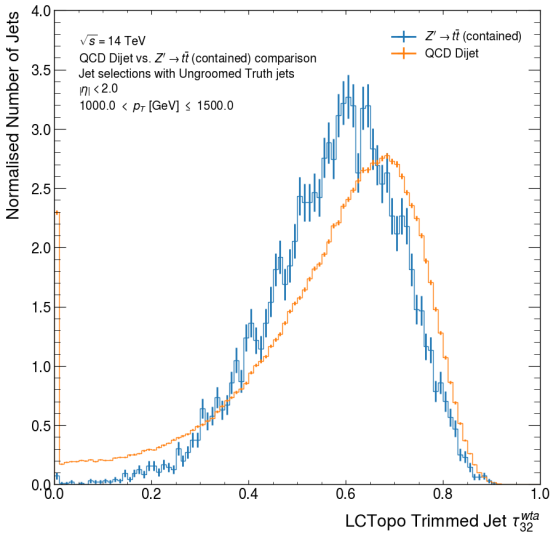

(b) Trimmed jet τ_{32}^{wta} ($1000 < p_{\text{T}}^{\text{truth}}$ [GeV] ≤ 1500)

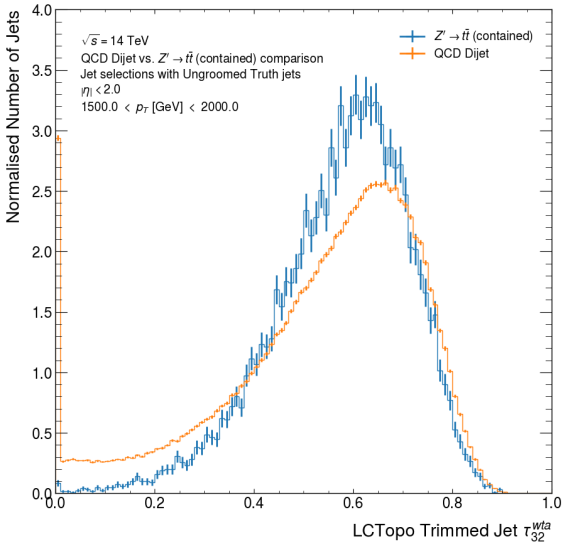

(c) Trimmed jet τ_{32}^{wta} ($1500 < p_{\text{T}}^{\text{truth}}$ [GeV] < 2000)

Figure 7.8: Comparisons of the τ_{32}^{wta} tagging observable for the trimmed and soft-drop collections in both the top quark signal and QCD background sample. Each plot is binned in the p_{T} of the ungroomed truth jet with a central η selection ($|\eta| < 2$).

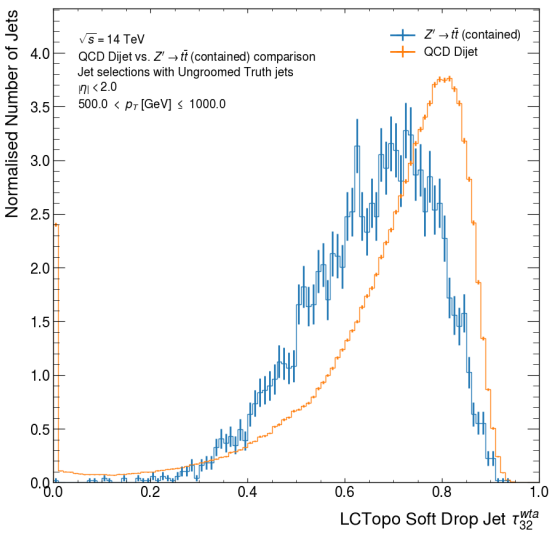

(d) Soft-drop jet τ_{32}^{wta} ($500 < p_{\text{T}}^{\text{truth}}$ [GeV] ≤ 1000)

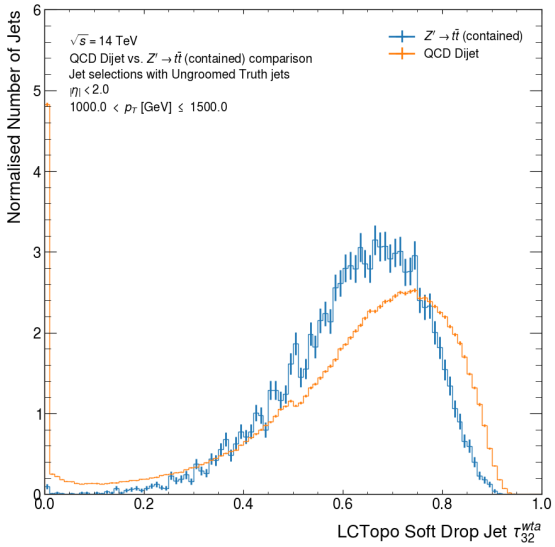

(e) Soft-drop jet τ_{32}^{wta} ($1000 < p_{\text{T}}^{\text{truth}}$ [GeV] ≤ 1500)

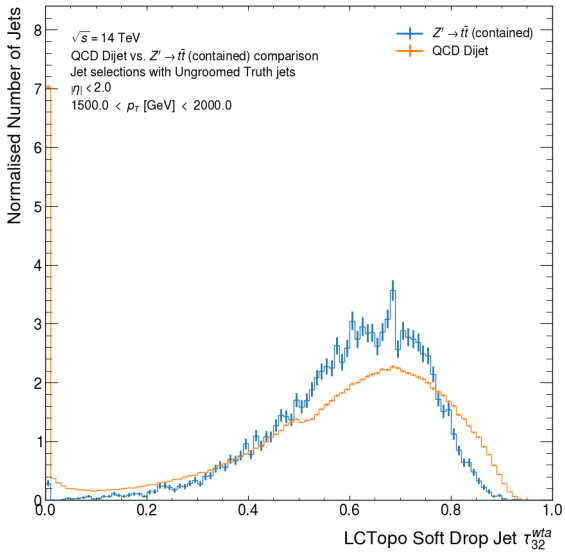

(f) Soft-drop jet τ_{32}^{wta} ($1500 < p_{\text{T}}^{\text{truth}}$ [GeV] < 2000)

Figure 7.8 (cont.): Comparisons of the τ_{32}^{wta} tagging observable for the trimmed and soft-drop collections in both the top quark signal and QCD background sample. Each plot is binned in the p_{T} of the ungroomed truth jet with a central η selection ($|\eta| < 2$).

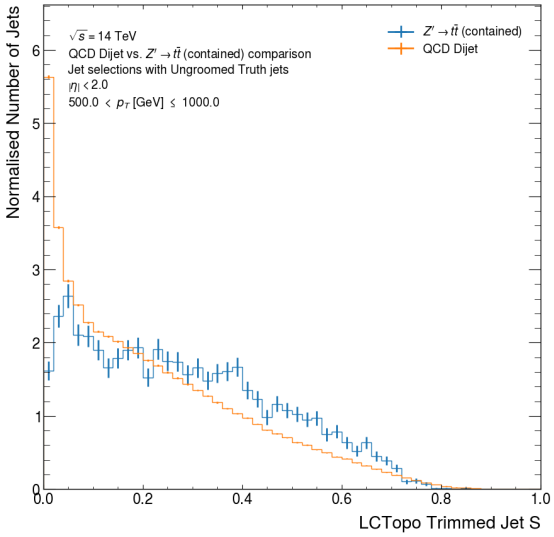

(a) Trimmed jet S ($500 < p_{\mathrm{T}}^{\mathrm{truth}}$ [GeV] ≤ 1000)

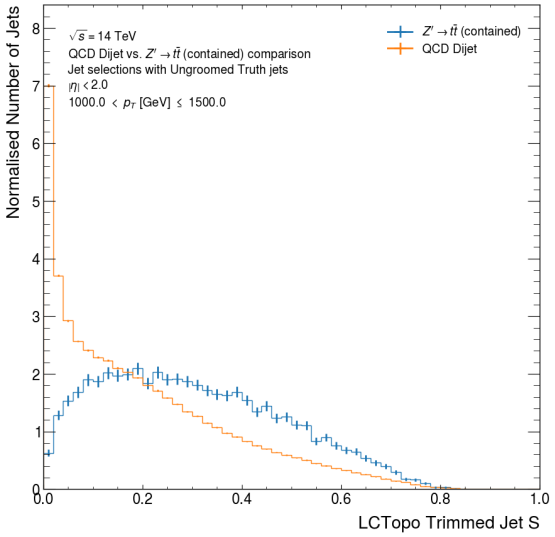

(b) Trimmed jet S ($1000 < p_{\mathrm{T}}^{\mathrm{truth}}$ [GeV] ≤ 1500)

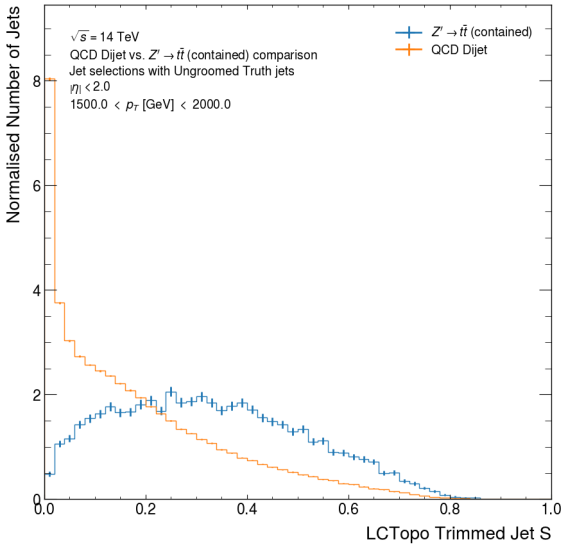

(c) Trimmed jet S ($1500 < p_{\mathrm{T}}^{\mathrm{truth}}$ [GeV] < 2000)

Figure 7.9: Comparisons of the sphericity tagging observable for the trimmed and soft-drop collections in both the top quark signal and QCD background sample. Each plot is binned in the p_{T} of the ungroomed truth jet with a central η selection ($|\eta| < 2$).

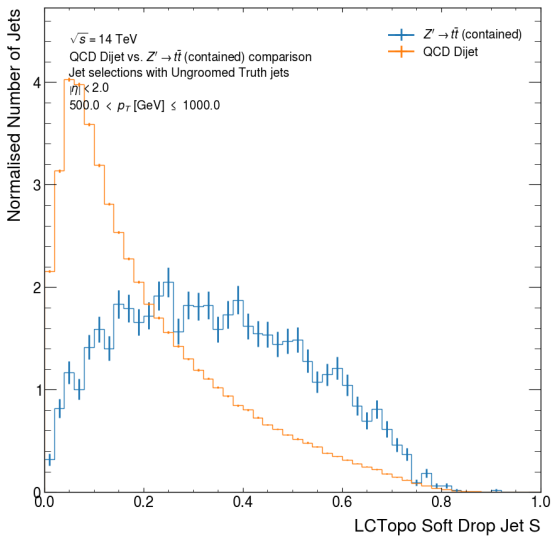

(d) Soft-drop jet S ($500 < p_{\mathrm{T}}^{\mathrm{truth}}$ [GeV] ≤ 1000)

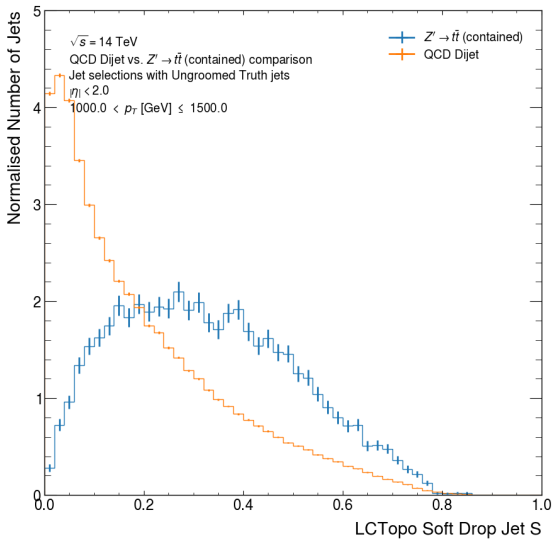

(e) Soft-drop jet S ($1000 < p_{\mathrm{T}}^{\mathrm{truth}}$ [GeV] ≤ 1500)

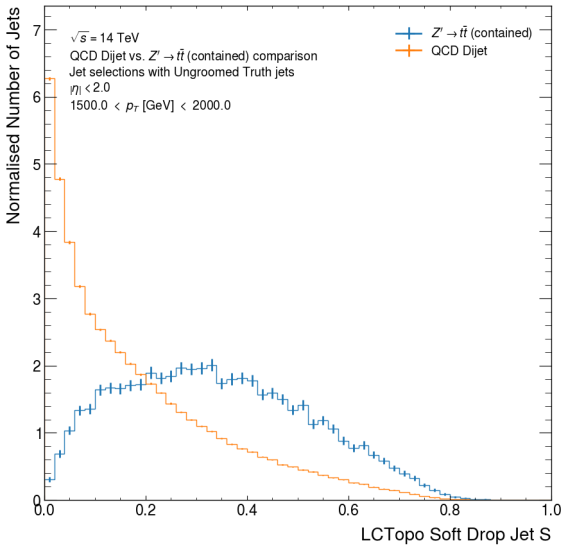

(f) Soft-drop jet S ($1500 < p_{\mathrm{T}}^{\mathrm{truth}}$ [GeV] < 2000)

Figure 7.9 (cont.): Comparisons of the sphericity tagging observable for the trimmed and soft-drop collections in both the top quark signal and QCD background sample. Each plot is binned in the p_{T} of the ungroomed truth jet with a central η selection ($|\eta| < 2$).

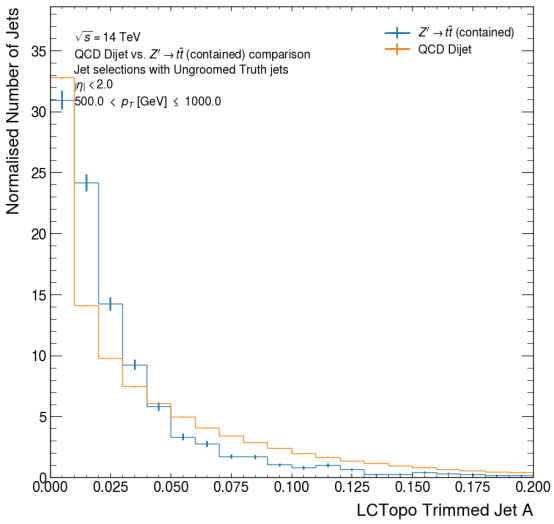

(a) Trimmed jet A ($500 < p_{\mathrm{T}}^{\mathrm{truth}}$ [GeV] ≤ 1000)

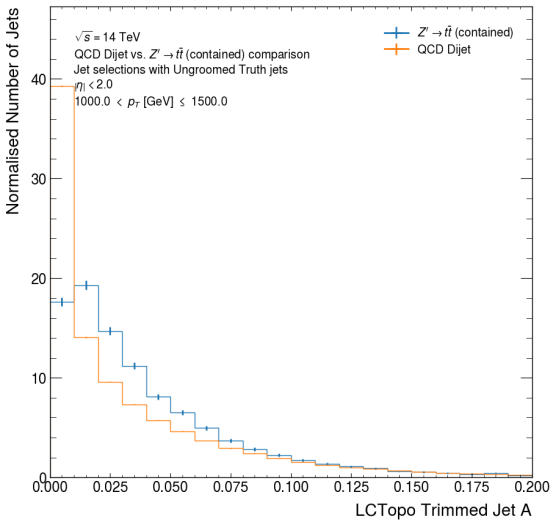

(b) Trimmed jet A ($1000 < p_{\mathrm{T}}^{\mathrm{truth}}$ [GeV] ≤ 1500)

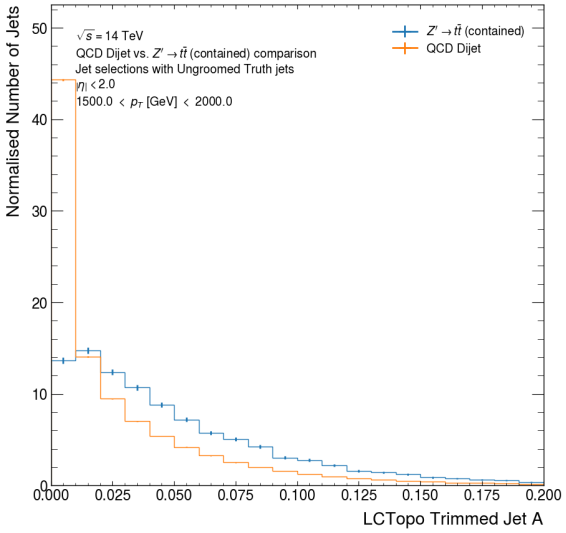

(c) Trimmed jet A ($1500 < p_{\mathrm{T}}^{\mathrm{truth}}$ [GeV] < 2000)

Figure 7.10: Comparisons of the aplanarity tagging observable for the trimmed and soft-drop collections in both the top quark signal and QCD background sample. Each plot is binned in the p_{T} of the ungroomed truth jet with a central η selection ($|\eta| < 2$).

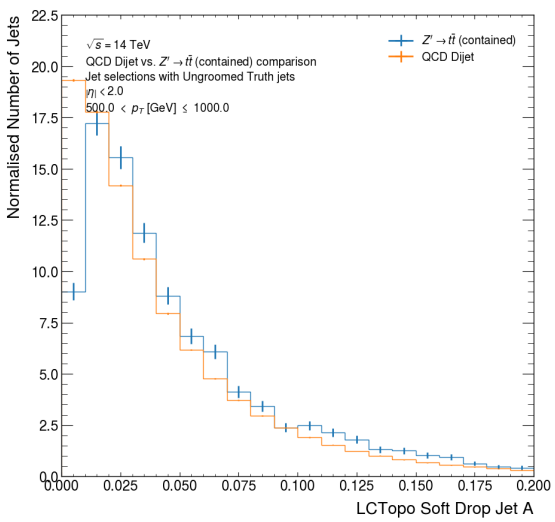

(d) Soft-drop jet A ($500 < p_{\mathrm{T}}^{\mathrm{truth}}$ [GeV] ≤ 1000)

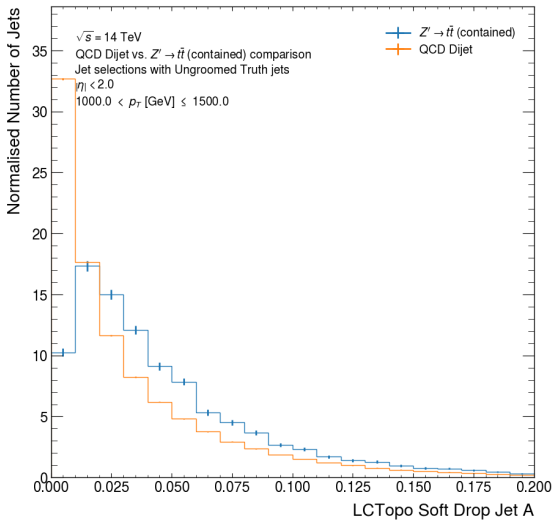

(e) Soft-drop jet A ($1000 < p_{\mathrm{T}}^{\mathrm{truth}}$ [GeV] ≤ 1500)

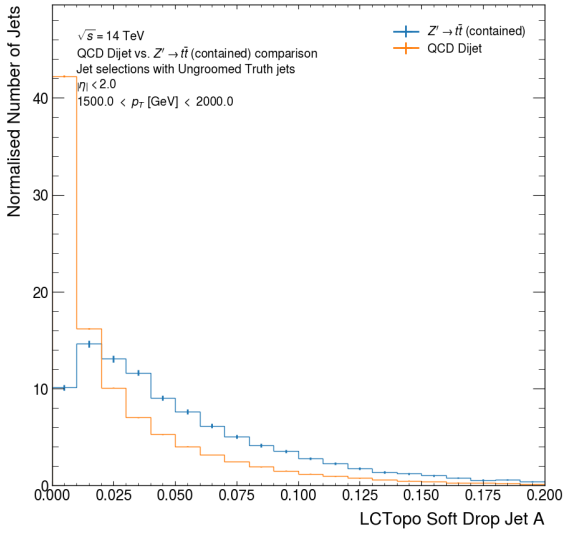

(f) Soft-drop jet A ($1500 < p_{\mathrm{T}}^{\mathrm{truth}}$ [GeV] < 2000)

Figure 7.10 (cont.): Comparisons of the aplanarity tagging observable for the trimmed and soft-drop collections in both the top quark signal and QCD background sample. Each plot is binned in the p_{T} of the ungroomed truth jet with a central η selection ($|\eta| < 2$).

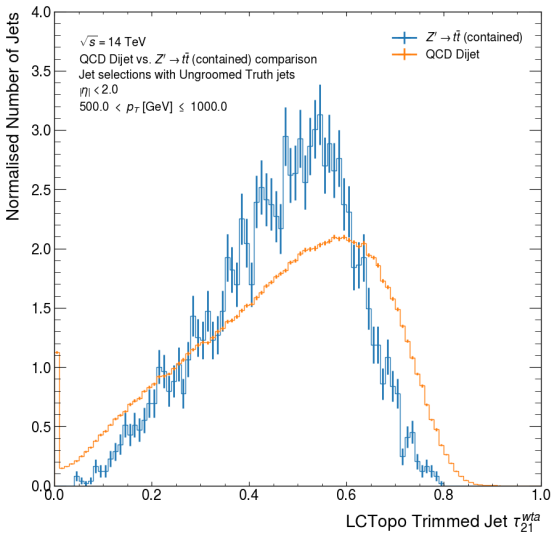

(a) Trimmed jet τ_{21}^{wta} ($500 < p_{\text{T}}^{\text{truth}}$ [GeV] $\leq$ 1000)

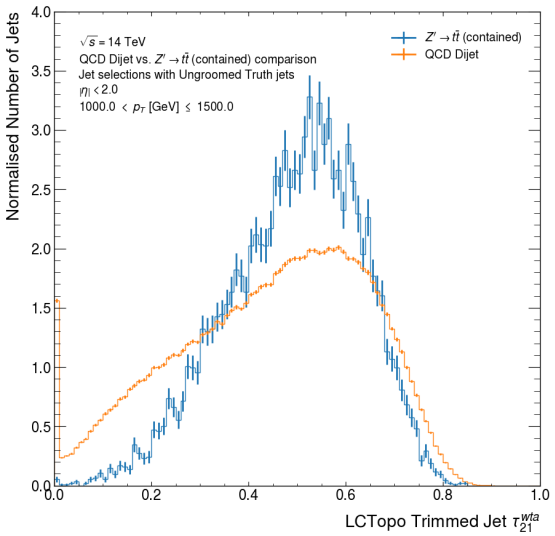

(b) Trimmed jet τ_{21}^{wta} ($1000 < p_{\text{T}}^{\text{truth}}$ [GeV] $\leq$ 1500)

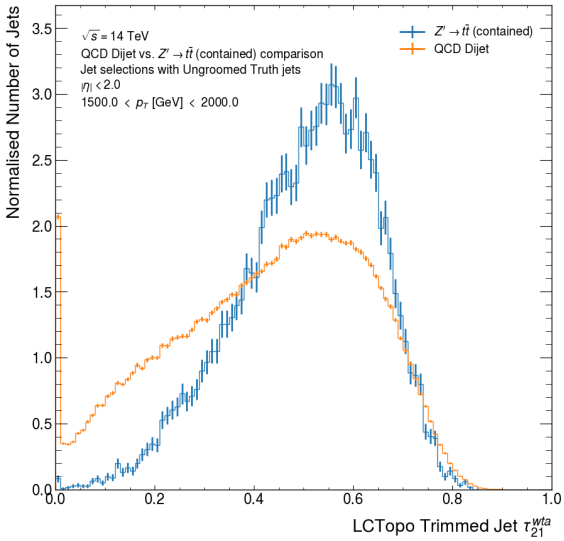

(c) Trimmed jet τ_{21}^{wta} ($1500 < p_{\text{T}}^{\text{truth}}$ [GeV] $<$ 2000)

Figure 7.11: Comparisons of the τ_{21}^{wta} tagging observable for the trimmed and soft-drop collections in both the top quark signal and QCD background sample. Each plot is binned in the p_{T} of the ungroomed truth jet with a central η selection ($|\eta| < 2$).

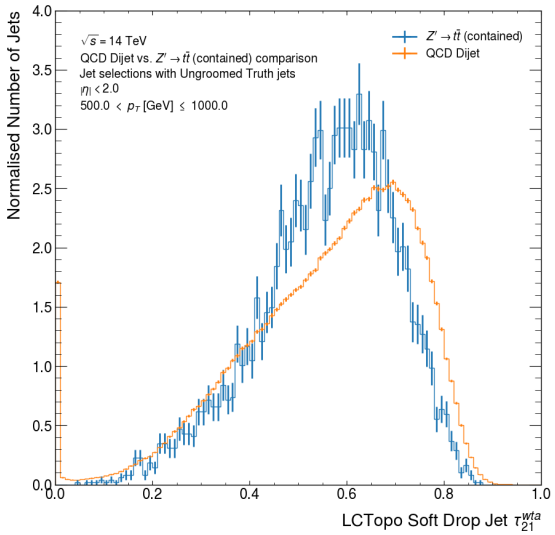

(d) Soft-drop jet τ_{21}^{wta} ($500 < p_{\text{T}}^{\text{truth}}$ [GeV] $\leq$ 1000)

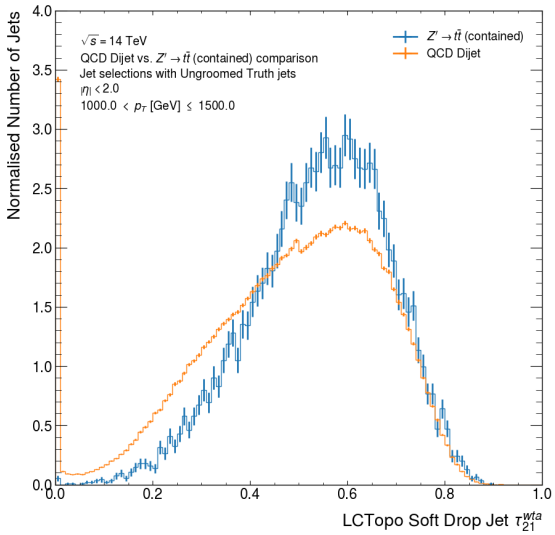

(e) Soft-drop jet τ_{21}^{wta} ($1000 < p_{\text{T}}^{\text{truth}}$ [GeV] $\leq$ 1500)

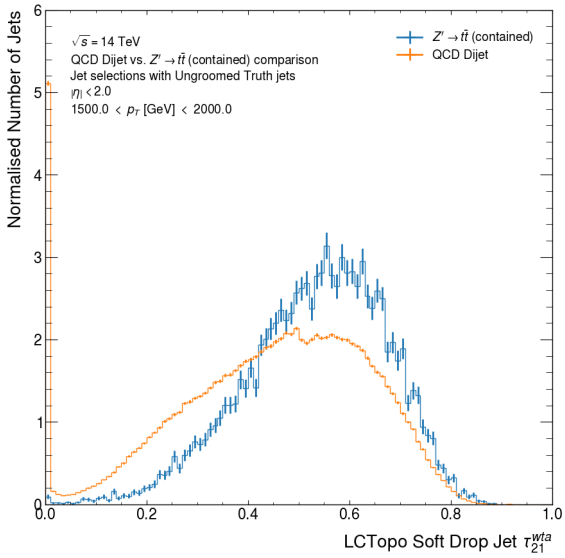

(f) Soft-drop jet τ_{21}^{wta} ($1500 < p_{\text{T}}^{\text{truth}}$ [GeV] < 2000)

Figure 7.11 (cont.): Comparisons of the τ_{21}^{wta} tagging observable for the trimmed and soft-drop collections in both the top quark signal and QCD background sample. Each plot is binned in the p_{T} of the ungroomed truth jet with a central η selection ($|\eta| < 2$).

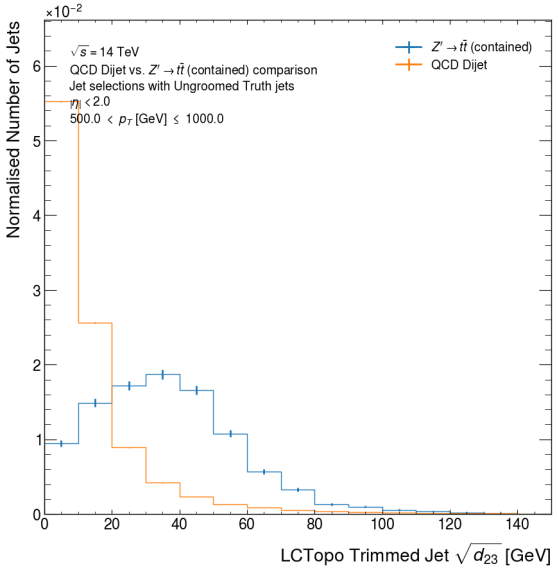

(a) Trimmed jet $\sqrt{d_{23}}$ ($500 < p_{\mathrm{T}}^{\mathrm{truth}}$ [GeV] ≤ 1000)

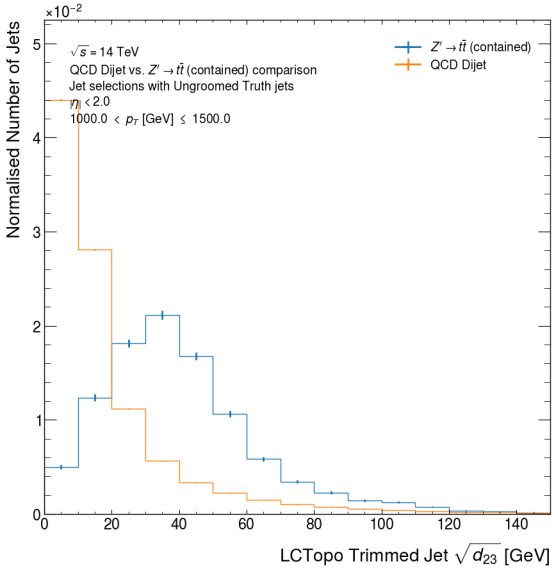

(b) Trimmed jet $\sqrt{d_{23}}$ ($1000 < p_{\mathrm{T}}^{\mathrm{truth}}$ [GeV] ≤ 1500)

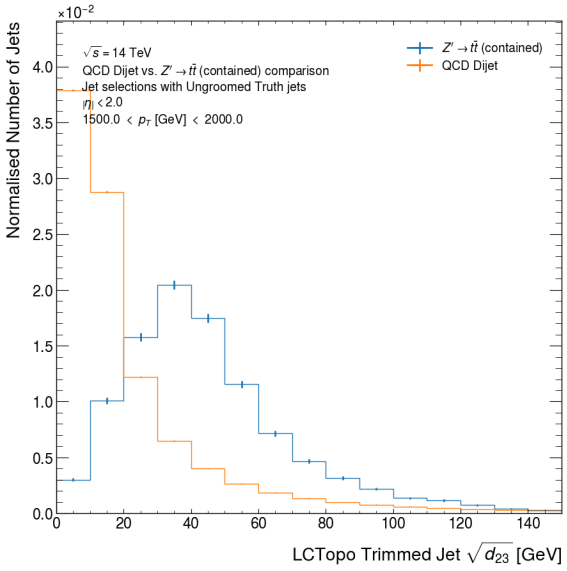

(c) Trimmed jet $\sqrt{d_{23}}$ ($1500 < p_{\mathrm{T}}^{\mathrm{truth}}$ [GeV] < 2000)

Figure 7.12: Comparisons of the $\sqrt{d_{23}}$ tagging observable for the trimmed and soft-drop collections in both the top quark signal and QCD background sample. Each plot is binned in the p_{T} of the ungroomed truth jet with a central η selection ($|\eta| < 2$).

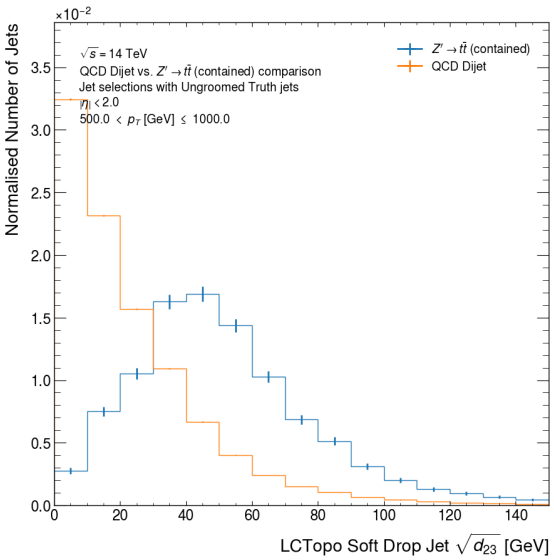

(d) Soft-drop jet $\sqrt{d_{23}}$ ($500 < p_{\mathrm{T}}^{\mathrm{truth}}$ [GeV] ≤ 1000)

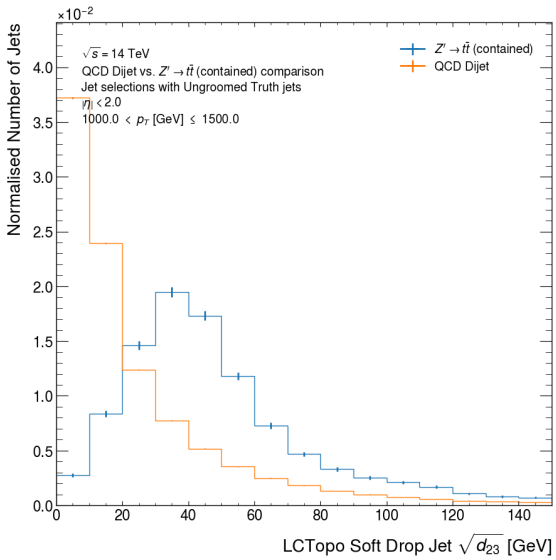

(e) Soft-drop jet $\sqrt{d_{23}}$ ($1000 < p_{\mathrm{T}}^{\mathrm{truth}}$ [GeV] ≤ 1500)

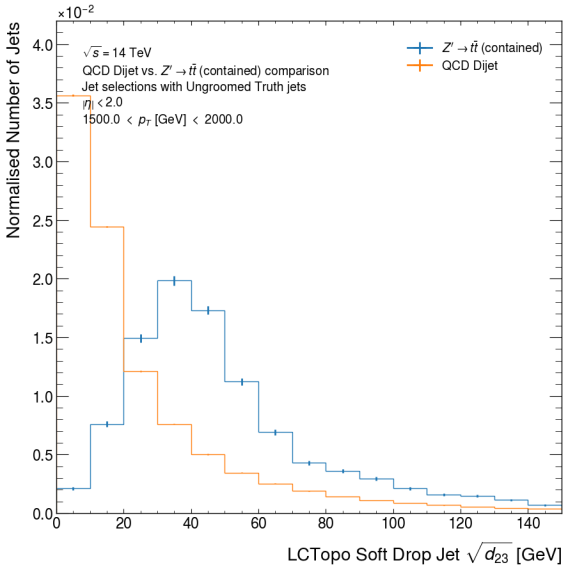

(f) Soft-drop jet $\sqrt{d_{23}}$ ($1500 < p_{\mathrm{T}}^{\mathrm{truth}}$ [GeV] < 2000)

Figure 7.12 (cont.): Comparisons of the $\sqrt{d_{23}}$ tagging observable for the trimmed and soft-drop collections in both the top quark signal and QCD background sample. Each plot is binned in the p_{T} of the ungroomed truth jet with a central η selection ($|\eta| < 2$).

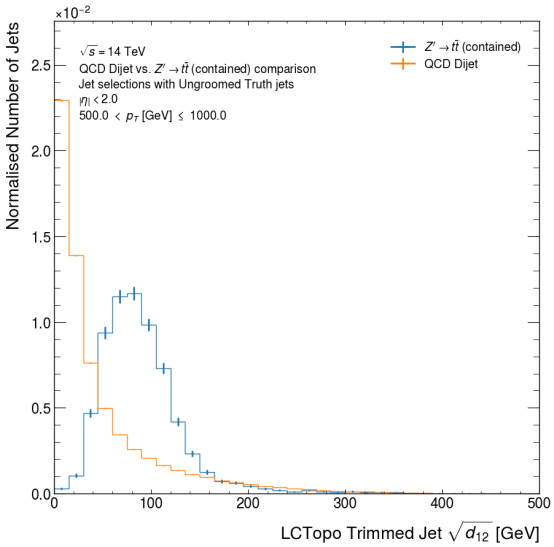

(a) Trimmed jet $\sqrt{d_{12}}$ ($500 < p_{\mathrm{T}}^{\mathrm{truth}}$ [GeV] ≤ 1000)

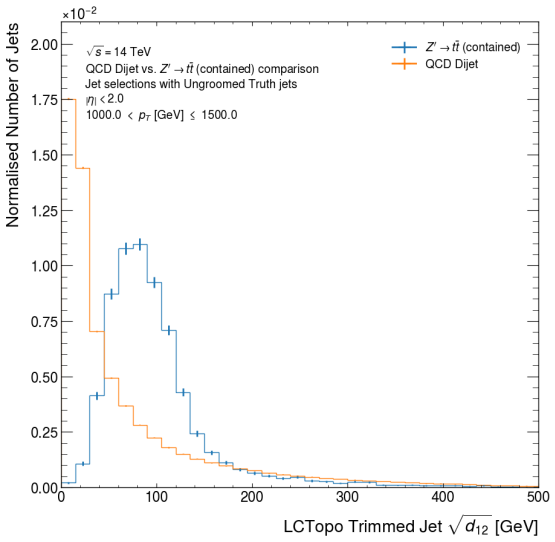

(b) Trimmed jet $\sqrt{d_{12}}$ ($1000 < p_{\mathrm{T}}^{\mathrm{truth}}$ [GeV] ≤ 1500)

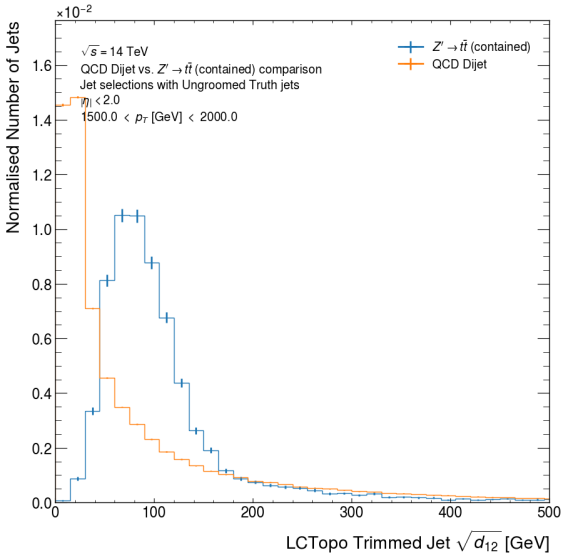

(c) Trimmed jet $\sqrt{d_{12}}$ ($1500 < p_{\mathrm{T}}^{\mathrm{truth}}$ [GeV] < 2000)

Figure 7.13: Comparisons of the $\sqrt{d_{12}}$ tagging observable for the trimmed and soft-drop collections in both the top quark signal and QCD background sample. Each plot is binned in the p_{T} of the ungroomed truth jet with a central η selection ($|\eta| < 2$).

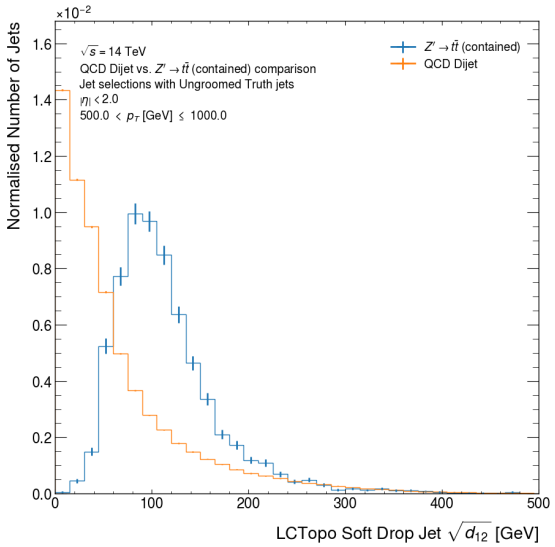

(d) Soft-drop jet $\sqrt{d_{12}}$ ($500 < p_{\mathrm{T}}^{\mathrm{truth}}$ [GeV] ≤ 1000)

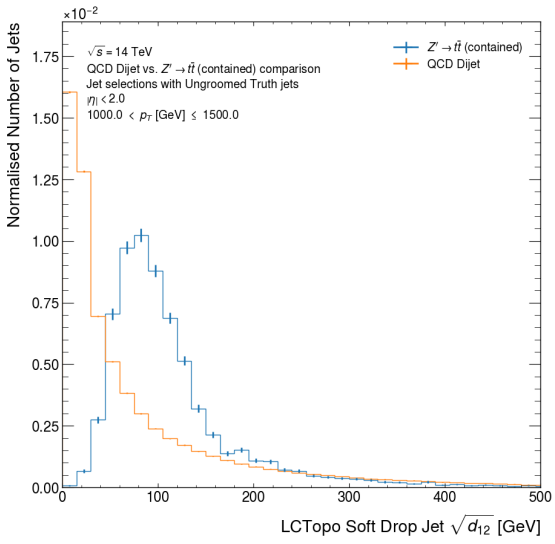

(e) Soft-drop jet $\sqrt{d_{12}}$ ($1000 < p_{\mathrm{T}}^{\mathrm{truth}}$ [GeV] ≤ 1500)

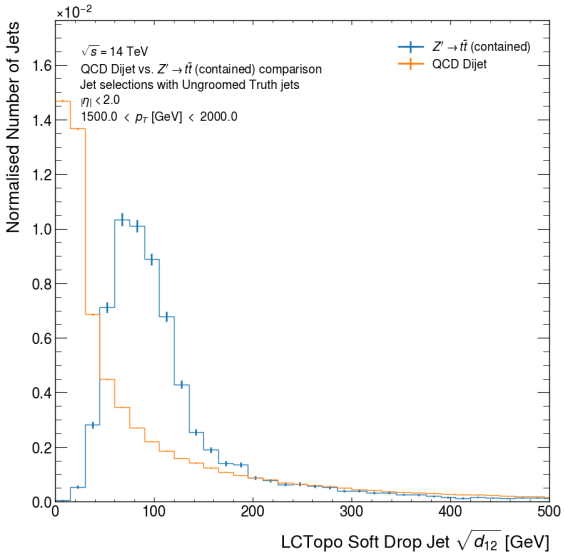

(f) Soft-drop jet $\sqrt{d_{12}}$ ($1500 < p_{\mathrm{T}}^{\mathrm{truth}}$ [GeV] < 2000)

Figure 7.13 (cont.): Comparisons of the $\sqrt{d_{12}}$ tagging observable for the trimmed and soft-drop collections in both the top quark signal and QCD background sample. Each plot is binned in the p_{T} of the ungroomed truth jet with a central η selection ($|\eta| < 2$).

7.6 Tagger construction and optimisation

Two-variable taggers were constructed by making a first fixed signal efficiency selection on m_{jet}. These studies considered signal efficiencies (ϵ_f) of 60%, 70%, 80%, and 90% for the jet mass selections. A selection on the second variable (X) for the tagger was then made with signal efficiency:

$$\epsilon_X = \frac{\epsilon_{\text{total}}}{\epsilon_f} \tag{7.3}$$

accounting for the efficiency of the initial selection. In Equation (7.3), ϵ_{total} is the total signal efficiency of the tagger, chosen to be either 80% or 50%. To identify the appropriate direction for selections on the tagger variables, the signal and background histogram modes were considered. For instance, if the signal histogram mode is above the background histogram mode then the cut direction for the variable was taken as ">". Thus, the jet mass selections for the taggers discussed in this Chapter are single sided and no jet mass window selections were applied similar to Ref. [80].

For the tagger performance studies and derivation of the tagger cuts as a function of p_{T} (to achieve a flat total signal efficiency) the tagger background rejection and signal efficiency was derived in different jet p_{T} bins. In each bin, the tagger cuts (on the first *and* second variable) were recalculated to achieve the efficiencies required for the tagger and the first selection. This method ensured we achieved an approximately constant total signal efficiency for the taggers as a function of the jet momentum. The optimisation of the tagger definitions proceeded by considering the performance of different mass selections and combinations of the jet mass with the second tagger observable in wide (inclusive) jet p_{T} bins. The most performant tagger definition was taken as that which achieved the largest background rejection in the inclusive jet p_{T} bins and a stable signal efficiency as a function of the jet p_{T} (using a finer binning). For the 50% (total) signal efficiency tagger, all possible selection efficiencies for the jet mass were considered. However, for the 80% signal efficiency tagger working point, only the 90% signal efficiency jet mass selection was used.

7.7 Two-variable tagger ROC curves

The ROC (signal efficiency vs. background rejection) curves for $m_{\text{jet}} + X$ two-variable taggers were studied in a wide kinematic regime and across a broad range of signal efficiencies to determine optimal tagger definitions for further study. The taggers were ranked quantitatively based on the area under these curves allowing performance comparisons between p_{T} bins and jet collections. The ROC curves for ungroomed (`LCTopo`) jets are excluded since they have no pile-up mitigations in place and would therefore have poor pile-up stability. All ROC curves were derived in three broad ungroomed truth jet p_{T} bins (with an additional $|\eta| < 2.0$ selection). The low-p_{T} bin ranges from 500 GeV to 1000 GeV, an intermediate bin ranges from 1000 GeV to 1500 GeV, and the final high-p_{T} bin ranges from 1500 GeV to 2000 GeV. The p_{T} bin

selections were made to ensure continuity between bin edges in later studies with a finer binning: the lower cut is "$<$" and upper cut is "$\leq$", except in the final bin where a "$<$" cut is made for the upper bin edge. This approach is taken for all performance studies presented in this Chapter whether binning in jet- or event-level quantities, unless otherwise stated. Since the lowest p_{T} bin begins at $p_{\mathrm{T}} = 500$ GeV we expect that the top quark decays are quite well contained in the jets due to the large boost of the jets relative to the $p_{\mathrm{T}} \gtrapprox 350$ GeV expectation for complete containment. Only the tagger performance plots for jet mass selections with 80% (suitable for 50% signal efficiency taggers) and 90% (suitable for 80% or 50% signal efficiency taggers) signal efficiency are included here – they are seen to perform optimally in Section 7.8. Trimmed jet taggers with an 80% and 90% signal efficiency m_{jet} selection are shown in Figures 7.14 and 7.15, respectively. Soft-drop groomed jet taggers are shown only for the 90% signal efficiency m_{jet} selection in Figure 7.15.

The sphericity tagger is most performant (it has the largest area under the ROC curves) for trimmed jet taggers in both Figures 7.14 and 7.15 across the entire p_{T} range from 500 GeV to 2500 GeV. The aplanarity tagger performance is worse at low-p_{T} but improves in the higher jet p_{T} bins. In comparison, the τ_{32}^{wta} tagger ROC curve area is smaller and falls significiantly with the truth jet p_{T}. These differences might be explained by the definition of sphericity and aplanarity as jet shape observables in terms of the 4-momenta of jet constituents in the jet rest-frame [86] and the τ_{32}^{wta} definition using lab-frame sub-jets [82] (see Appendix B for more detail). Similar results are seen for aplanarity and sphericity soft-drop jet taggers in Figure 7.15. However, at low-p_{T} the τ_{32}^{wta} observable is most performant – unlike for the trimmed jet taggers. Nonetheless, like for trimmed jet taggers, the τ_{32} soft-drop jet tagger performance falls rapidly with p_{T}. This is consistent with the definition of τ_{32} as a p_{T} weighted sum of the angular separation of sub-jets. The constituents of higher p_{T} jets are more collimated, which degrades the performance of any tagging observable that intrinsically relies on re-clustered jet/constituent based calculations. The same is true for almost all other tagger definitions, except for the aplanarity tagger for which the ROC curve area increases with p_{T} up to 2500 GeV.

7.8 Optimisation of the two-variable taggers

The background rejection for different tagger definitions was considered as a function of the mass selection as discussed in Section 7.6 to obtain the results shown in Figures 7.16 and 7.17 for the soft-drop and trimmed jet taggers with 50% and 80% signal efficiency, respectively. The same p_{T} bins as for the ROC curves in the previous section are used. A significant level of variation in the tagger performance is seen for the 50% (total) signal efficiency taggers using different mass selection signal efficiencies. The single mass selection considered for 80% signal efficiency taggers leads to similar conclusions regarding tagger performance. Lower background rejection is seen for the higher efficiency working point, but the same combination of tagger observables for both trimmed and soft-drop jets performs optimally.

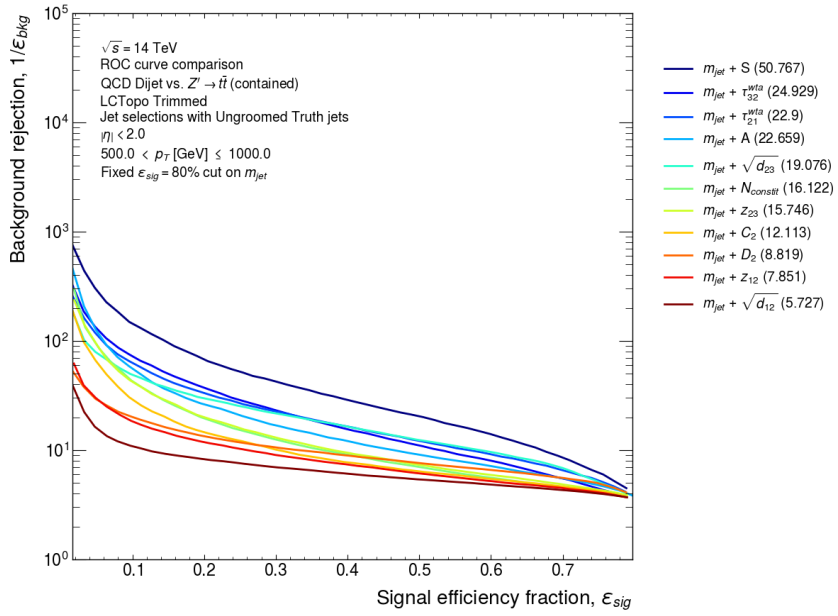

(a) Trimmed jets $500 < p_{\mathrm{T}}^{\mathrm{truth}}$ (GeV) ≤ 1000

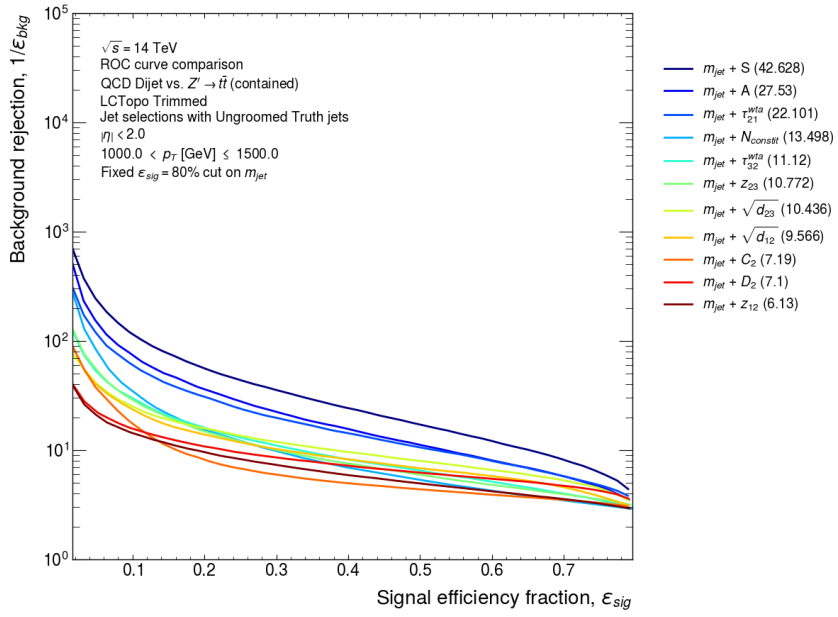

(b) Trimmed jets $1000 < p_{\mathrm{T}}^{\mathrm{truth}}$ (GeV) ≤ 1500

Figure 7.14: ROC curves for trimmed jet taggers in ungroomed truth jet p_{T} bins. Results are shown for taggers with an initial 80% signal efficiency selection on the jet mass. The legend of each plot is ordered by the area under the ROC curve (in brackets), so different taggers have different line colours on each plot.

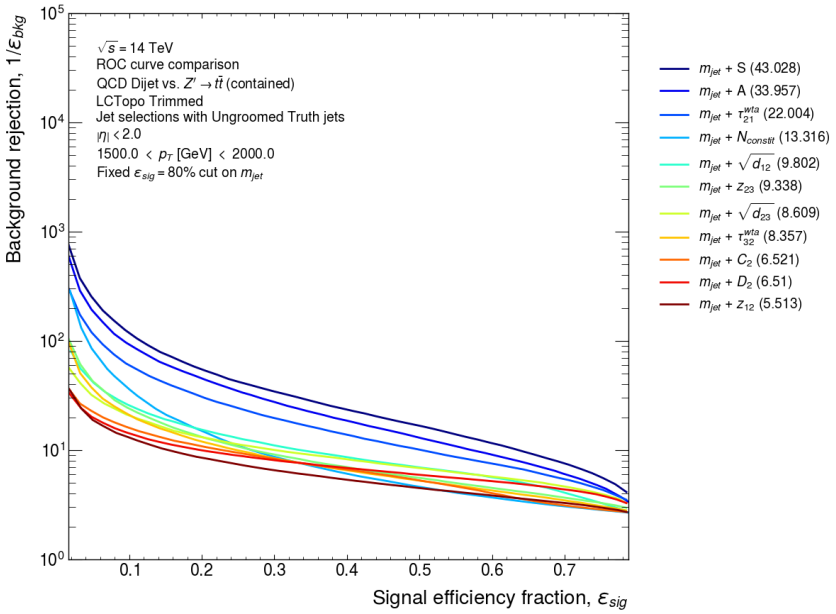

(c) Trimmed jets $1500 < p_{\mathrm{T}}^{\mathrm{truth}}$ (GeV) < 2000

Figure 7.14 (cont.): ROC curves for trimmed jet taggers in ungroomed truth jet p_{T} bins. Results are shown for taggers with an initial 80% signal efficiency selection on the jet mass. The legend of each plot is ordered by the area under the ROC curve (in brackets), so different taggers have different line colours on each plot.

A sphericity selection following the jet mass selection is optimal for both grooming algorithms in all p_{T} bins and the jet mass selection to achieve maximum background rejection changes between jet collections. Complementary to Section 7.5, the background rejection performance is impacted most by the qualitative separation of different tagger observables as a function of p_{T} after different mass selections. This is illustrated for the trimmed and soft-drop jet collections in Figures 7.20 to 7.23 and Figures 7.24 to 7.27, respectively. More separation is seen between the signal and background distributions for aplanarity and sphericity compared to τ_{32}^{wta} after different mass selections. Interestingly, much better separation is seen between the τ_{21}^{wta} distributions compared to the τ_{32}^{wta} distributions across the complete p_{T} range. Indeed, for trimmed jets, the τ_{21}^{wta} tagger background rejection is higher than that for the τ_{32}^{wta} tagger even though the τ_{21}^{wta} variable is intended for 2-prong decay tagging, not 3-prong tagging as for τ_{32}^{wta}.

For the soft-drop jet taggers in Figure 7.16, the τ_{32}^{wta} tagger performance rivals that of the trimmed jet taggers at low-p_{T}, but only for the 50% signal efficiency working point. As the jet p_{T} increases, the τ_{32}^{wta} tagger performance falls but maintains a higher background rejection than for trimmed jets. Nonetheless, the $m_{\mathrm{jet}} + \tau_{32}^{\mathrm{wta}}$ soft-drop jet tagger performance in the low-p_{T} bin is comparable to the trimmed jet $m_{\mathrm{jet}} + S$ performance. There is no substantial performance benefit from the use of soft-drop jet taggers relative to the trimmed jet taggers.

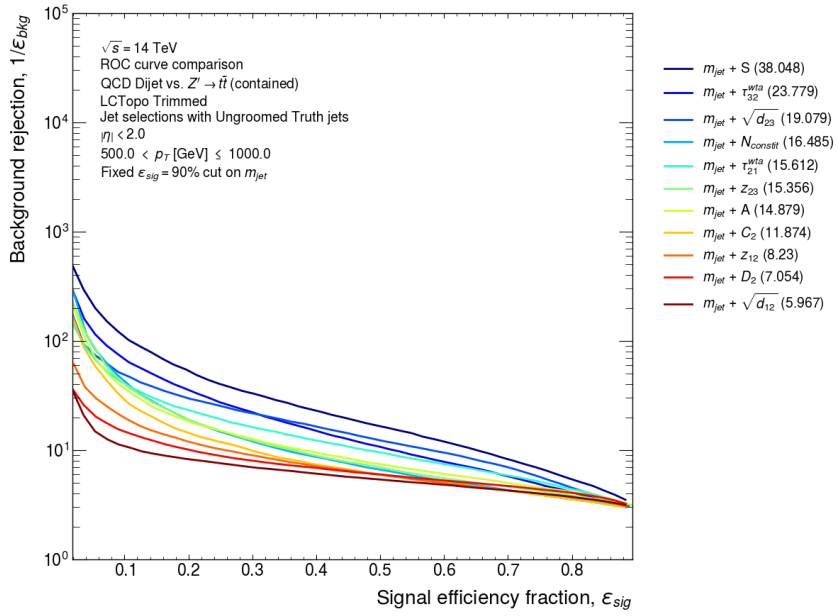

(a) Trimmed jets $500 < p_{\mathrm{T}}^{\mathrm{truth}}$ (GeV) ≤ 1000

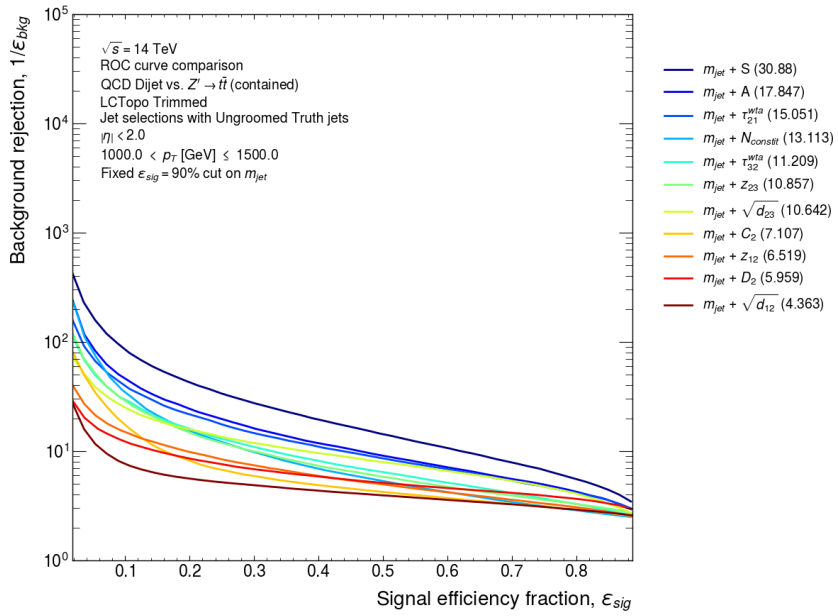

(b) Trimmed jets $1000 < p_{\mathrm{T}}^{\mathrm{truth}}$ (GeV) ≤ 1500

Figure 7.15: ROC curves for trimmed jet and soft-drop jet taggers in ungroomed truth jet p_{T} bins. Results are shown for taggers with an initial 90% signal efficiency selection on the jet mass. The legend of each plot is ordered by the area under the ROC curve (in brackets), so different taggers have different line colours on each plot.

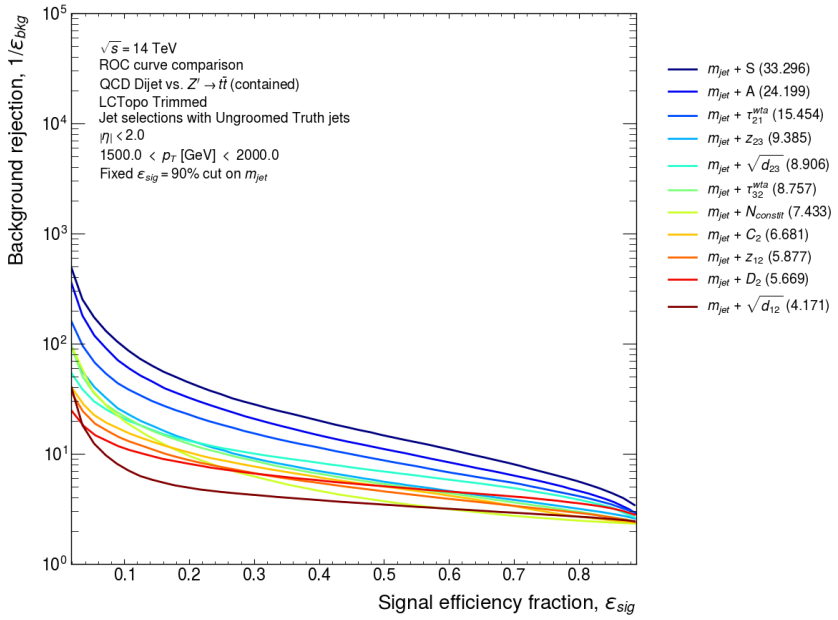

(c) Trimmed jets $1500 < p_{\mathrm{T}}^{\mathrm{truth}}$ (GeV) < 2000

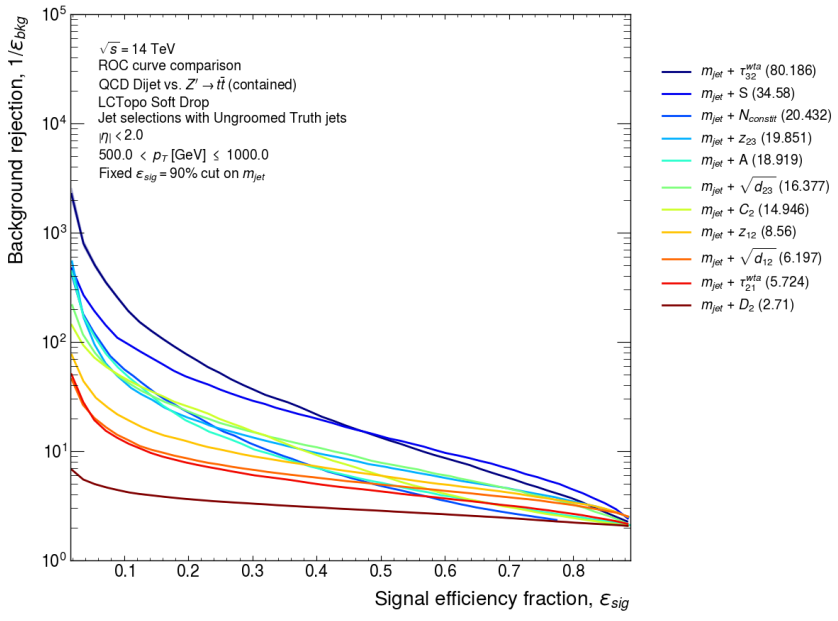

(d) Soft-drop jets $500 < p_{\mathrm{T}}^{\mathrm{truth}}$ (GeV) ≤ 1000

Figure 7.15 (cont.): ROC curves for trimmed jet and soft-drop jet taggers in ungroomed truth jet p_{T} bins. Results are shown for taggers with an initial 90% signal efficiency selection on the jet mass. The legend of each plot is ordered by the area under the ROC curve (in brackets), so different taggers have different line colours on each plot.

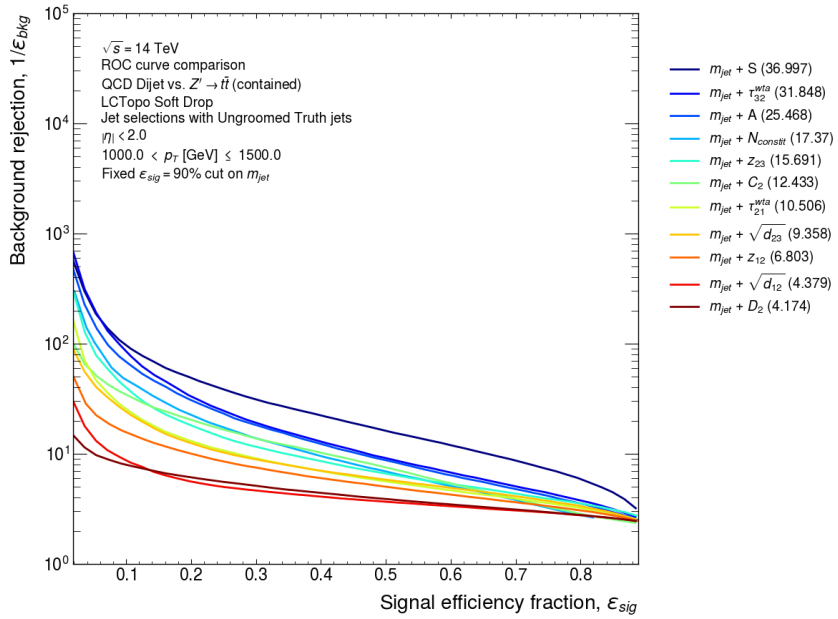

(e) Soft-drop jets $1000 < p_{\mathrm{T}}^{\mathrm{truth}}$ (GeV) ≤ 1500

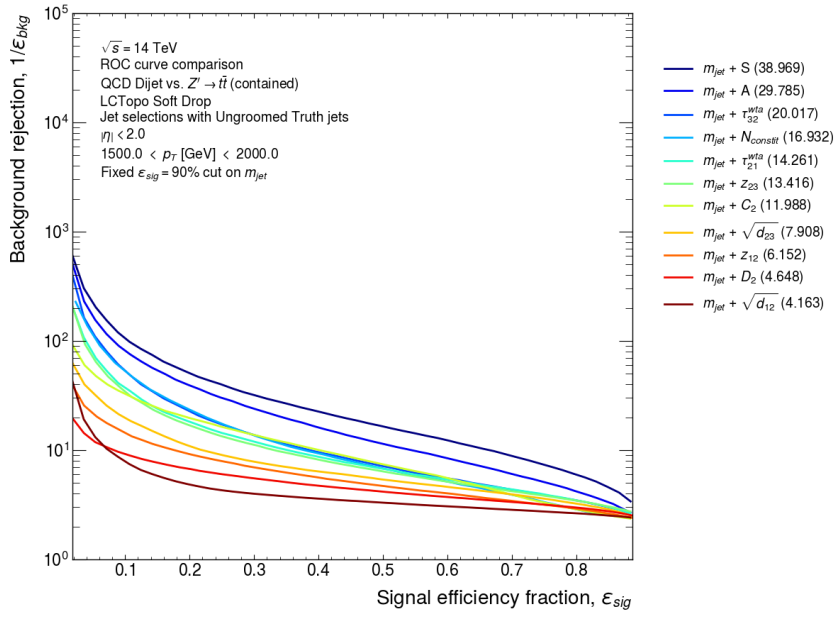

(f) Soft-drop jets $1500 < p_{\mathrm{T}}^{\mathrm{truth}}$ (GeV) < 2000

Figure 7.15 (cont.): ROC curves for trimmed jet and soft-drop jet taggers in ungroomed truth jet p_{T} bins. Results are shown for taggers with an initial 90% signal efficiency selection on the jet mass. The legend of each plot is ordered by the area under the ROC curve (in brackets), so different taggers have different line colours on each plot.

Taggers with 50% signal efficiency perform best[5] with an 80% and 90% signal efficiency mass selection for trimmed and soft-drop jets, respectively. At the 80% tagger efficiency working point only the 90% signal efficiency mass selection was tested producing a smaller background rejection from the looser tagger selections as noted earlier. The difference between the trimmed and soft-drop jet mass selection for the 50% signal efficiency working point originates from differences in the shape of the mass distributions as a function of the truth jet p_{T}. The soft-drop distributions in Figure 7.7 have a much larger population in the high-mass tail at low-p_{T} resulting in tighter mass selections (above the top quark mass!) shown at the top of each plot in Figure 7.18. Looser mass selections are seen for the trimmed jets in Figure 7.19 except at high-p_{T} where the tightest selection is above the 172-173 GeV top quark mass. The looser optimal mass selection for soft-drop jets must therefore be a consequence of the separation power of each observable after a jet mass selection. A decrease in separation between signal and background distributions for the second tagger observables is seen for tighter jet mass selections in Figure 7.22 and Figure 7.26 for trimmed and soft-drop jets, respectively.

Clearly, the most performant taggers for further studies consist of the $m_{\mathrm{jet}} + \tau_{32}^{\mathrm{wta}}$[6] (soft-drop jets only), $m_{\mathrm{jet}} + A$, and $m_{\mathrm{jet}} + S$ taggers. Soft-drop and trimmed m_{jet} selections with 90% and 80% efficiency, respectively, are optimal for the 50% signal efficiency working point, and 90% signal efficiency m_{jet} selections work well for both jet collections when an 80% signal efficiency tagger is considered. To reach the final recommendation discussed in Section 7.13 the p_{T} and pile-up stability of the tagger definitions was considered. Additional results for the tagger optimisation binned in the reconstructed jet p_{T} are included in Appendix E, but the optimal tagger definitions do not change.

7.9 Tagger performance as a function of jet p_{T}

The tagger performance (background rejection and signal efficiency) was studied as a function of the truth jet p_{T}. These results show how the performance of the taggers varies as the top quark becomes more boosted such that the separation between the decay products (in the lab frame) decreases. Figure 7.28 shows the variation of the background rejection for trimmed and soft-drop jets. The background rejection falls for trimmed jet taggers constructed from observables that rely on the jet constituents (including sub-jets) or the (re-)clustering sequence of a jet as the p_{T} increases and the jet constituents become more collimated. Notable exceptions include the aplanarity tagger, which has increasing background rejection as the truth jet p_{T} increases in

[5] These conclusions are primarily for the taggers that produce the highest background rejection (i.e. $m_{\mathrm{jet}} + S$). In some cases, worse performing taggers (e.g. $m_{\mathrm{jet}} + \tau_{21}^{\mathrm{wta}}$ or $m_{\mathrm{jet}} + \sqrt{d_{23}}$ in Figure 7.16a) have different optimal selections.

[6] Some other taggers (for trimmed jets: $m_{\mathrm{jet}} + \tau_{21}^{\mathrm{wta}}$, $m_{\mathrm{jet}} + z_{23}$, $m_{\mathrm{jet}} + D_2$) have larger background rejection but are intended for tagging 2-prong decays or in some p_{T} bins have significant correlation with the jet mass compared to τ_{32}^{wta}.

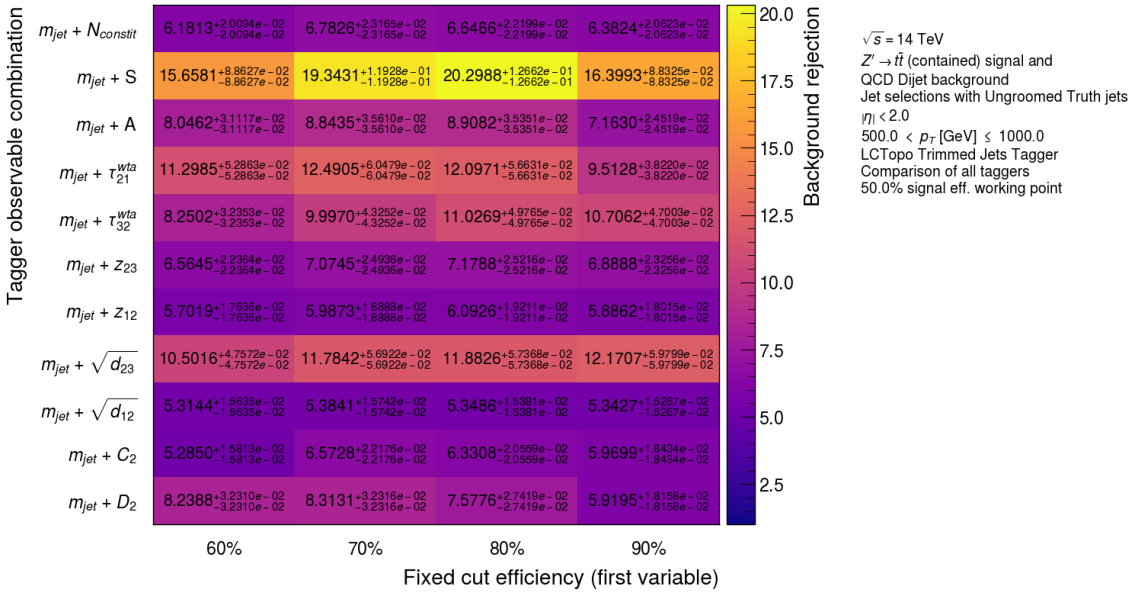

(a) Trimmed jets

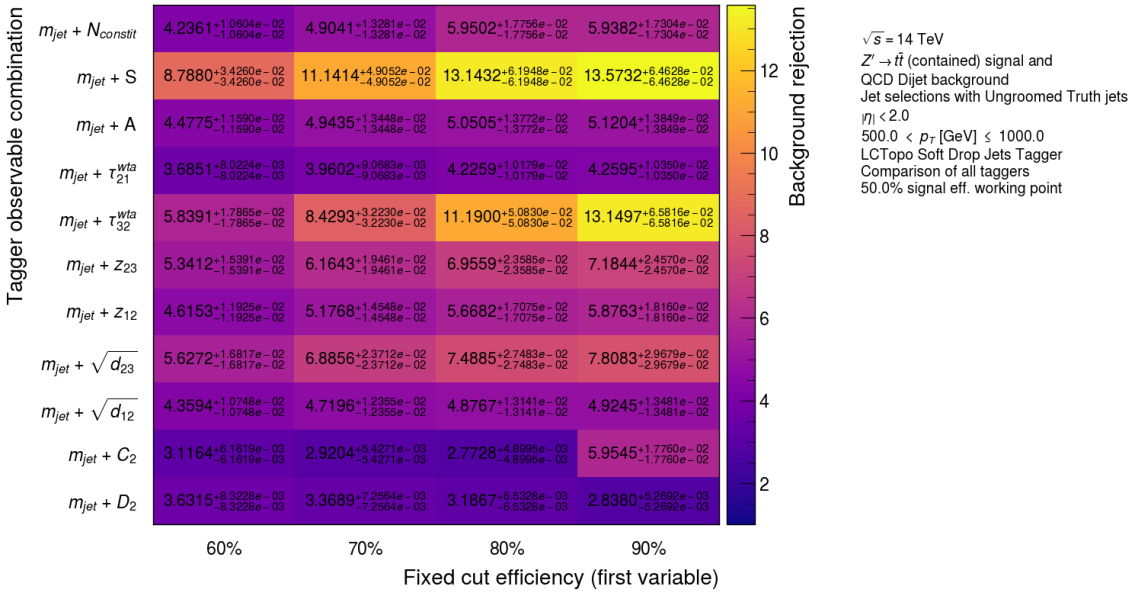

(b) Soft-drop jets

Figure 7.16: Heat-maps illustrating the background rejection for each 50% signal efficiency tagger definition with different mass selections. These results are for both the trimmed and soft-drop jets in a $500 < p_{\mathrm{T}}^{\mathrm{truth}}$ (GeV) ≤ 1000 bin. The x-axis displays the signal efficiency of the mass selection.

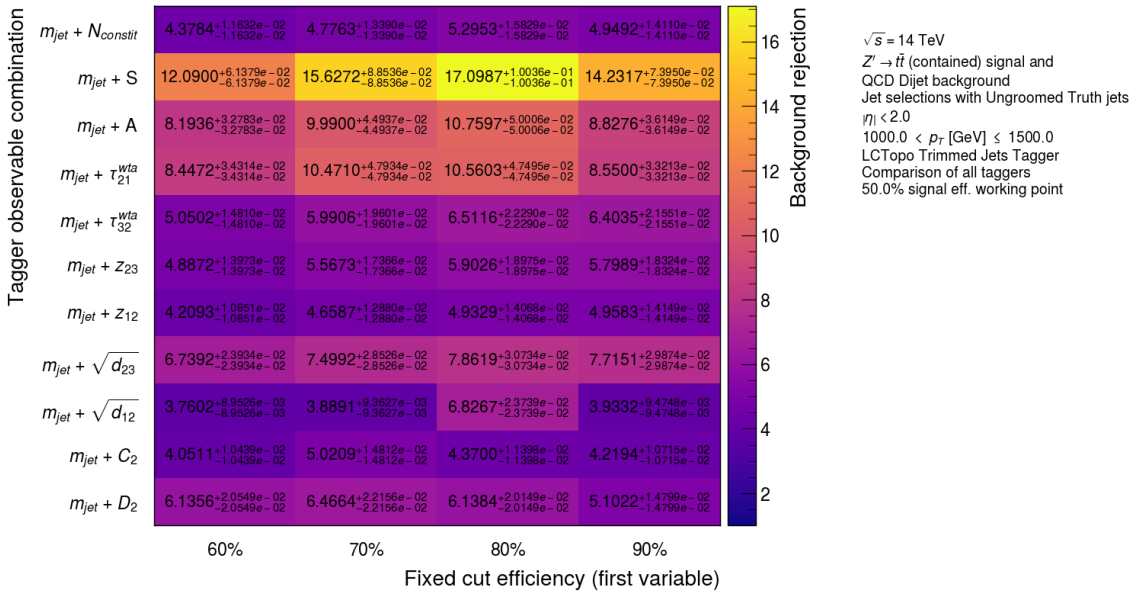

(c) Trimmed jets

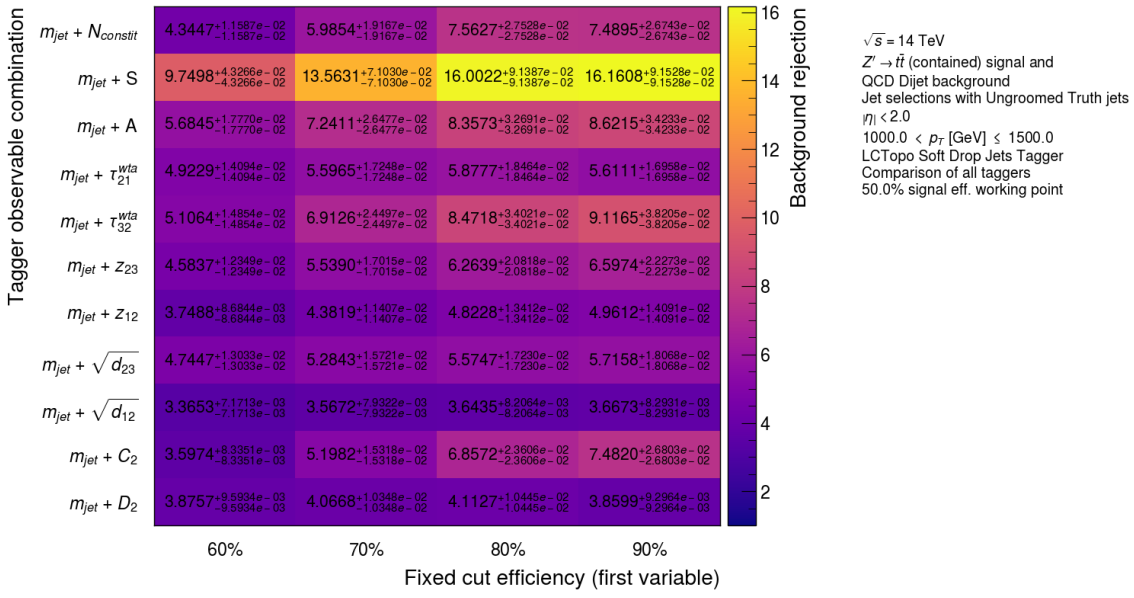

(d) Soft-drop jets

Figure 7.16 (cont.): Heat-maps illustrating the background rejection for each 50% signal efficiency tagger definition with different mass selections. These results are for both the trimmed and soft-drop jets in a $1000 < p_{\mathrm{T}}^{\mathrm{truth}}$ (GeV) ≤ 1500 bin. The x-axis displays the signal efficiency of the mass selection.

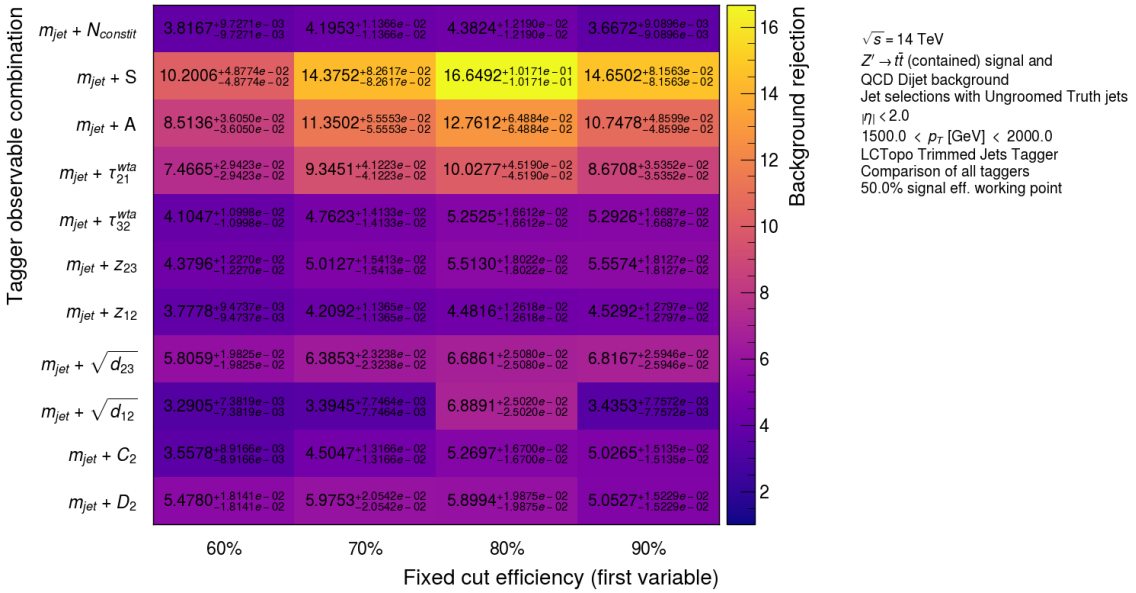

(e) Trimmed jets

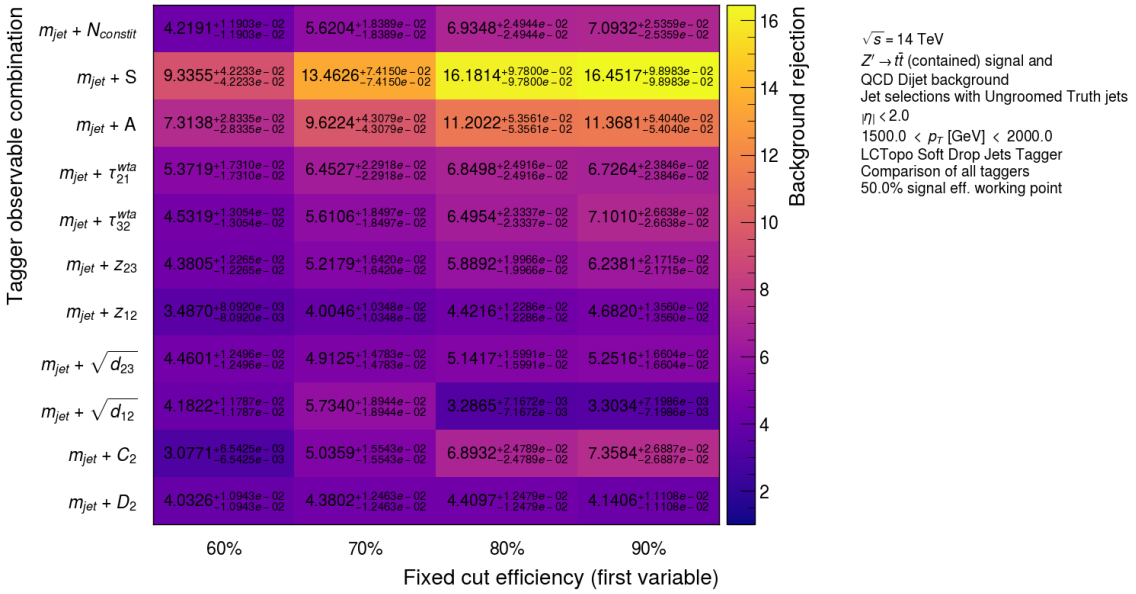

(f) Soft-drop jets

Figure 7.16 (cont.): Heat-maps illustrating the background rejection for 50% signal efficiency tagger definition with different mass selections. These results are for both the trimmed and soft-drop jets in a $1500 < p_{\mathrm{T}}^{\mathrm{truth}}$ (GeV) < 2000 bin. The x-axis displays the signal efficiency of the mass selection.

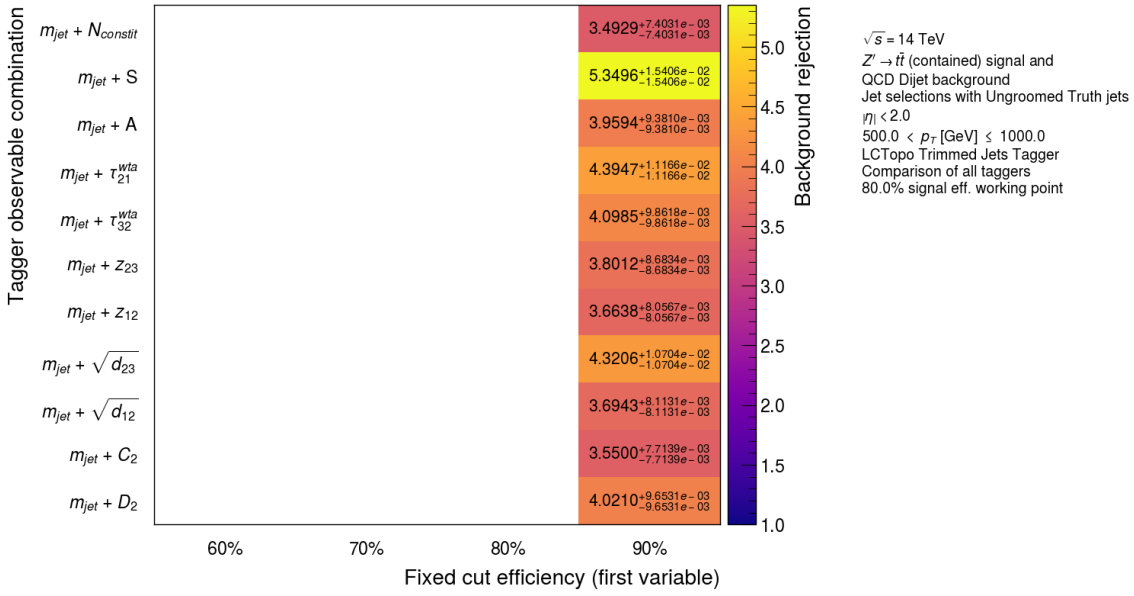

(a) Trimmed jets

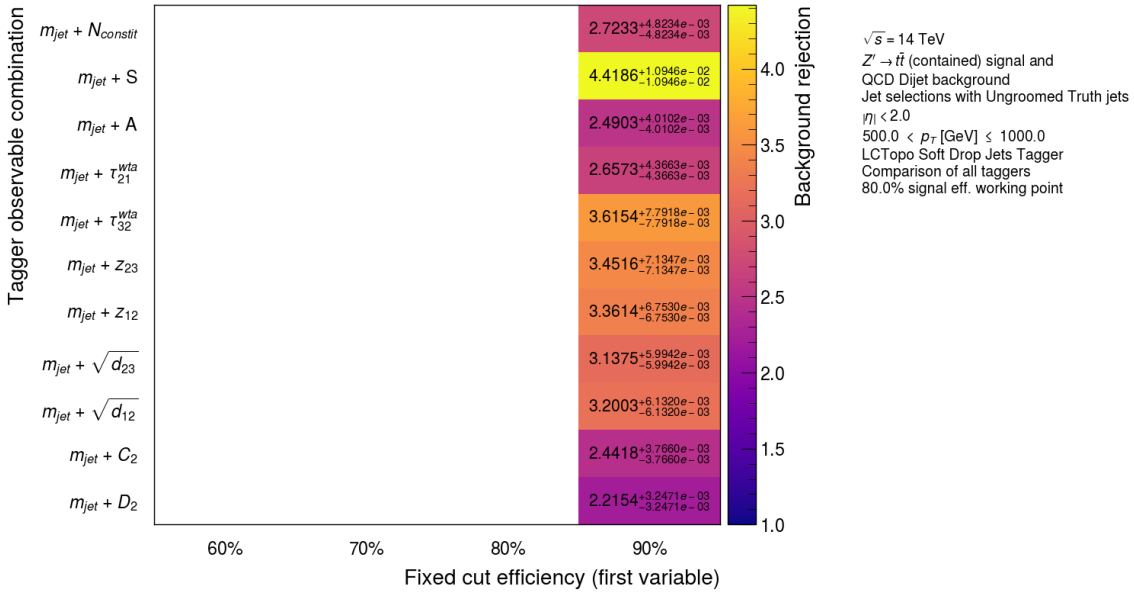

(b) Soft-drop jets

Figure 7.17: Heat-maps illustrating the background rejection for each 80% signal efficiency tagger definition with different mass selections. These results are for both the trimmed and soft-drop jets in a $500 < p_{\mathrm{T}}^{\mathrm{truth}}$ (GeV) ≤ 1000 bin. The x-axis displays the signal efficiency of the mass selection.

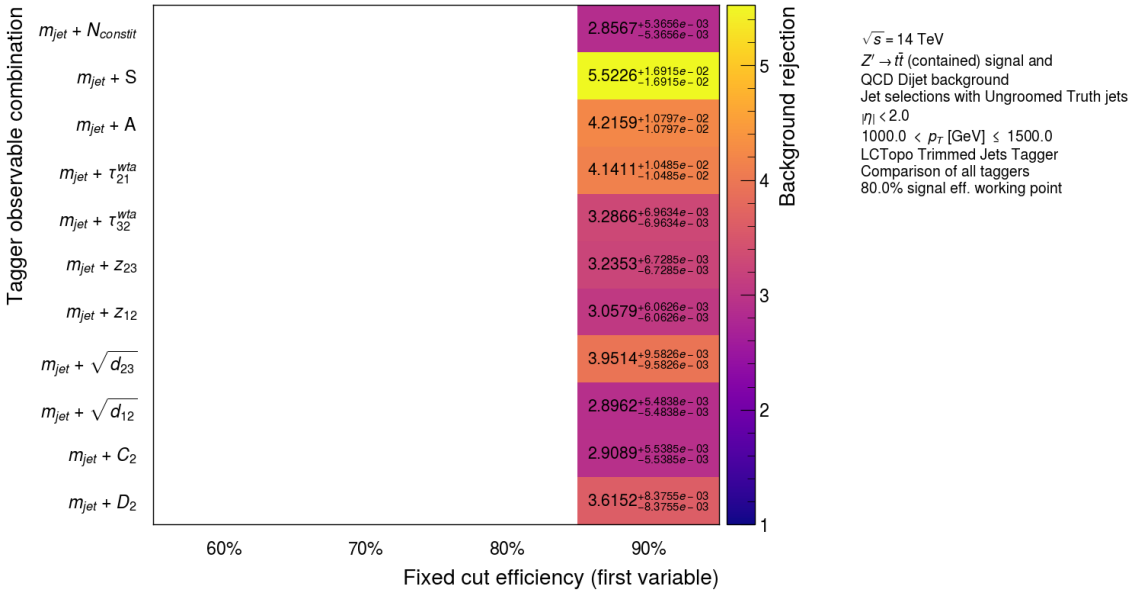

(c) Trimmed jets

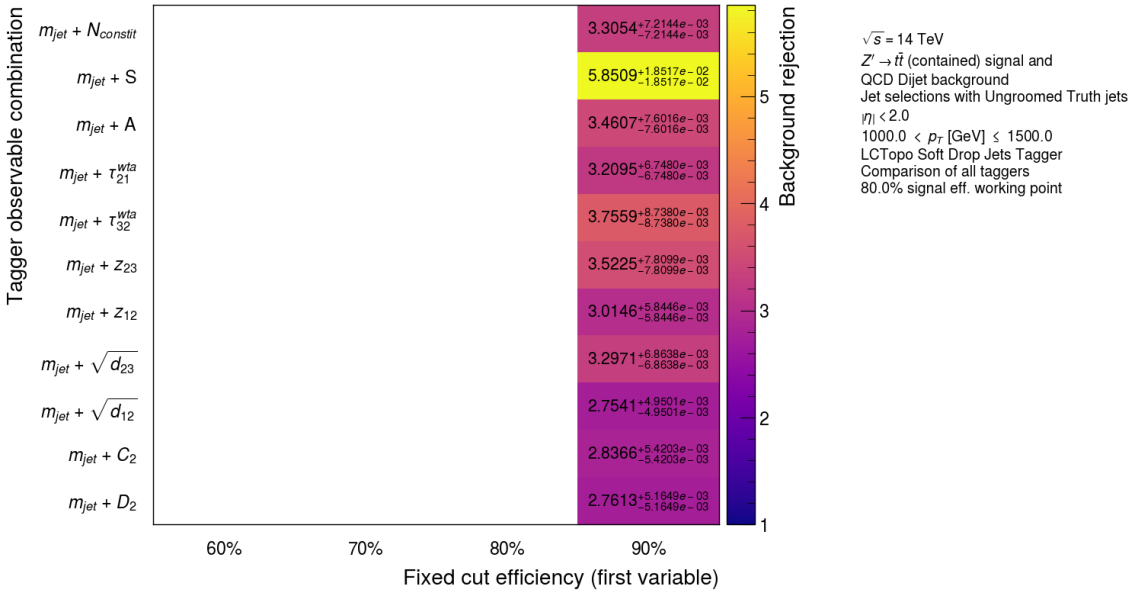

(d) Soft-drop jets

Figure 7.17 (cont.): Heat-maps illustrating the background rejection for each 80% signal efficiency tagger definition with different mass selections. These results are for both the trimmed and soft-drop jets in a $1000 < p_{\mathrm{T}}^{\mathrm{truth}}$ (GeV) ≤ 1500 bin. The x-axis displays the signal efficiency of the mass selection.

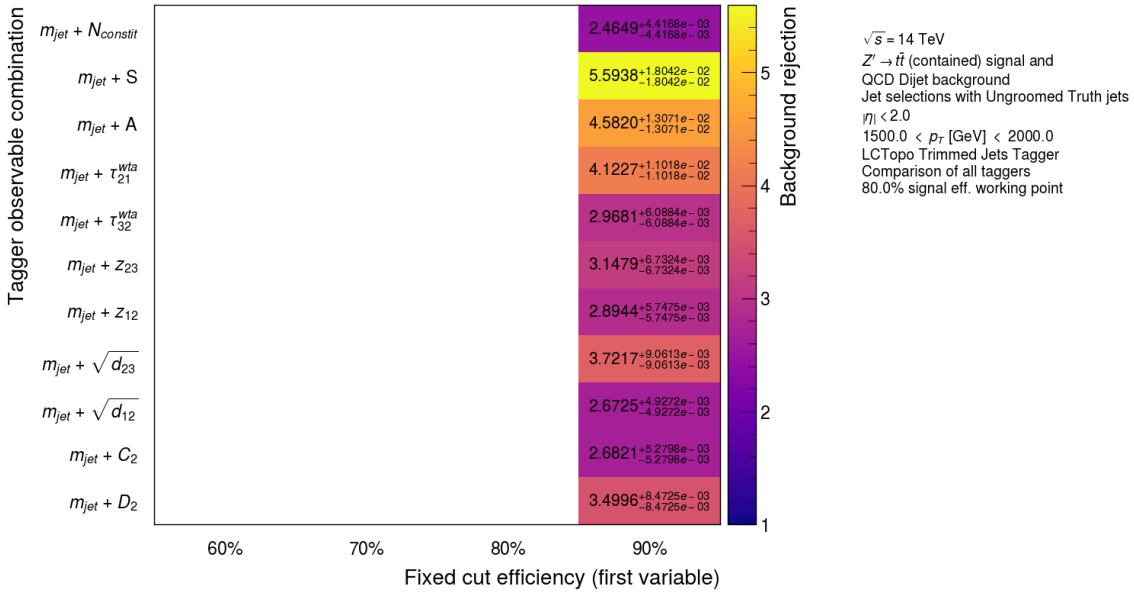

(e) Trimmed jets

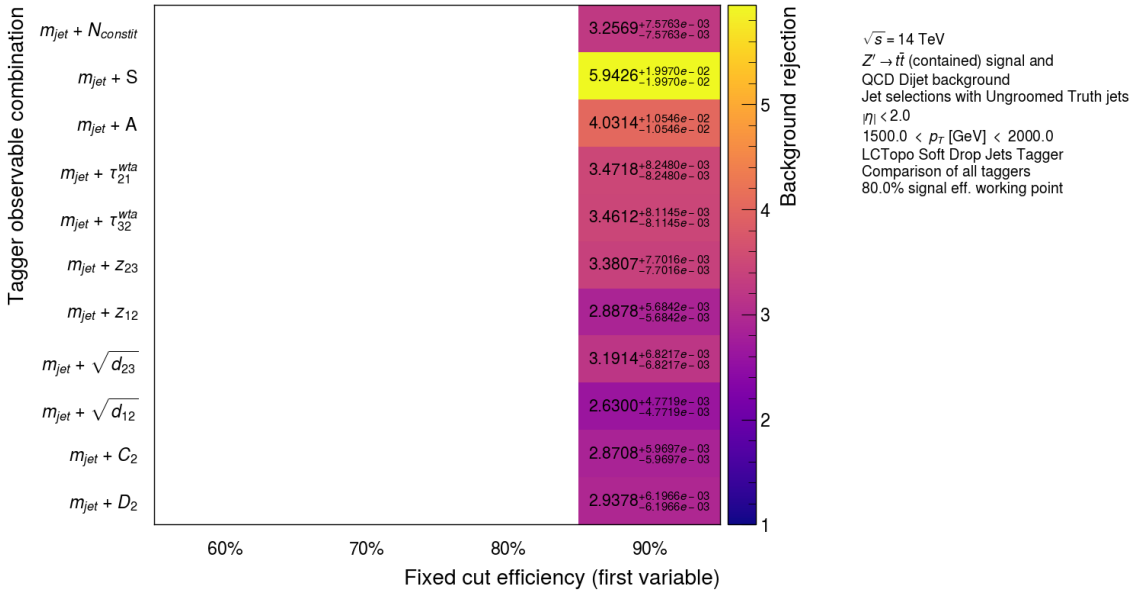

(f) Soft-drop jets

Figure 7.17 (cont.): Heat-maps illustrating the background rejection for 80% signal efficiency tagger definition with different mass selections. These results are for both the trimmed and soft-drop jets in a $1500 < p_{\mathrm{T}}^{\mathrm{truth}}$ (GeV) < 2000 bin. The x-axis displays the signal efficiency of the mass selection.

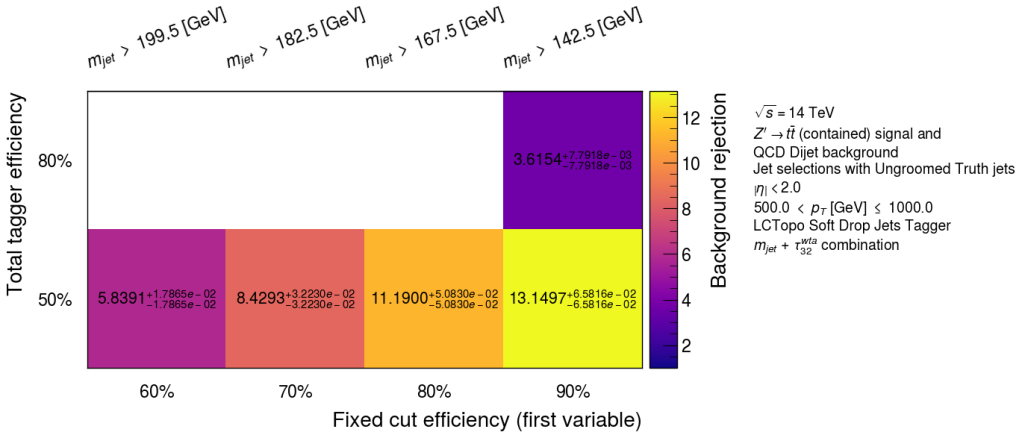

(a) $500 < p_{\mathrm{T}}^{\mathrm{truth}}$ (GeV) ≤ 1000

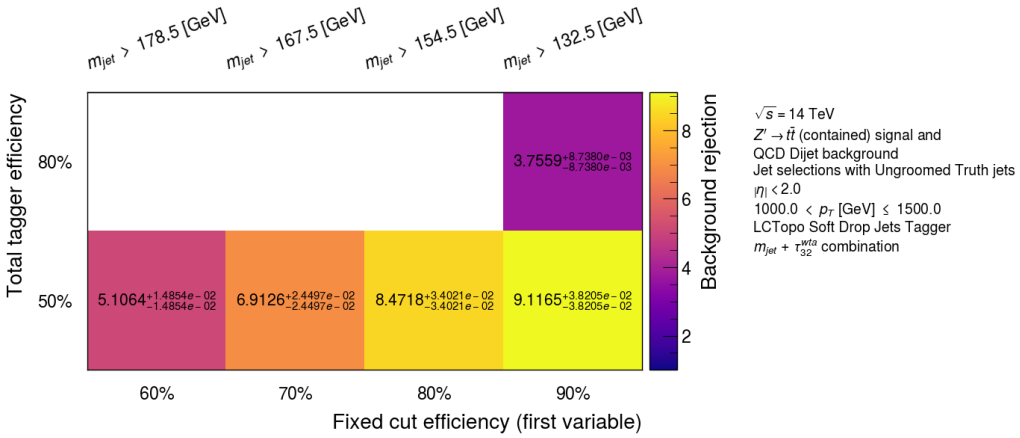

(b) $1000 < p_{\mathrm{T}}^{\mathrm{truth}}$ (GeV) ≤ 1500

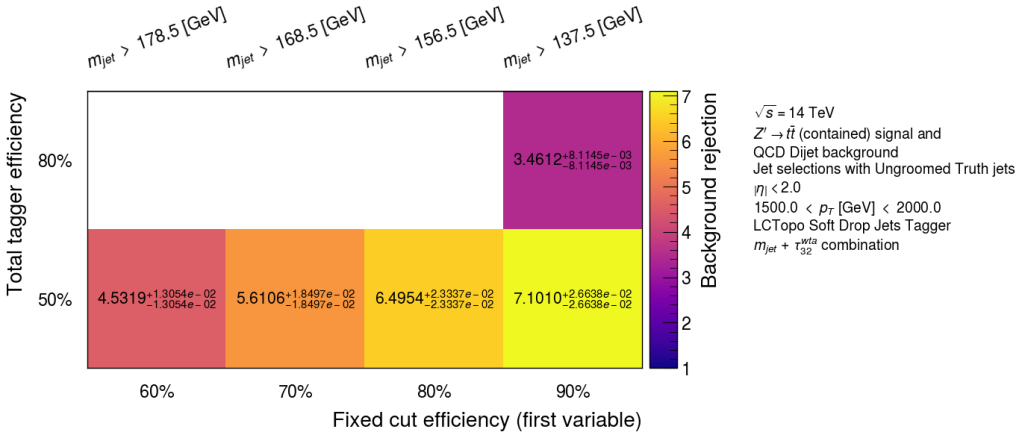

(c) $1500 < p_{\mathrm{T}}^{\mathrm{truth}}$ (GeV) < 2000

Figure 7.18: Tagger background rejection heat-map for the $m_{\mathrm{jet}} + \tau_{32}^{\mathrm{wta}}$ soft-drop jet tagger. The jet mass selections are highlighted at the top of the plot.

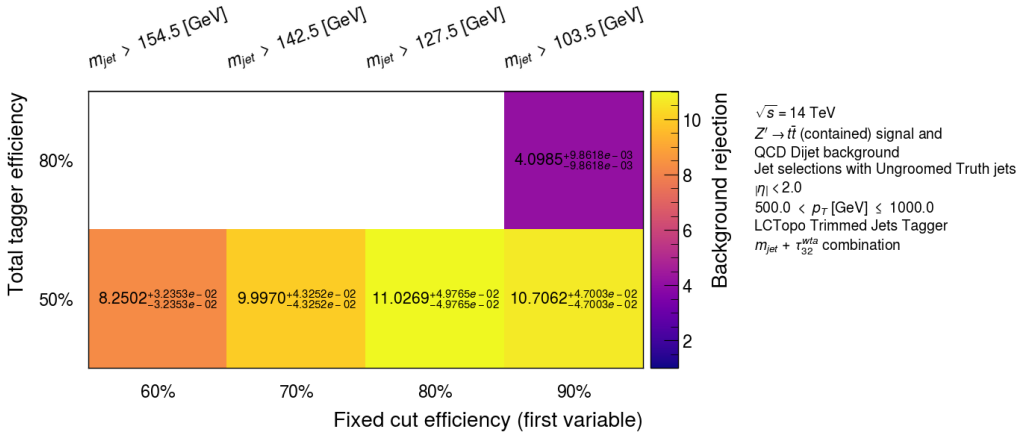

(a) $500 < p_{\mathrm{T}}^{\mathrm{truth}}$ (GeV) ≤ 1000

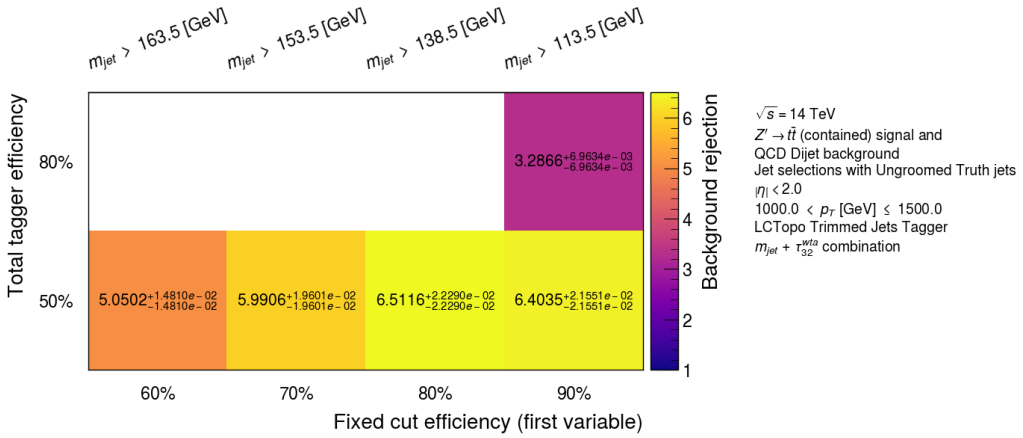

(b) $1000 < p_{\mathrm{T}}^{\mathrm{truth}}$ (GeV) ≤ 1500

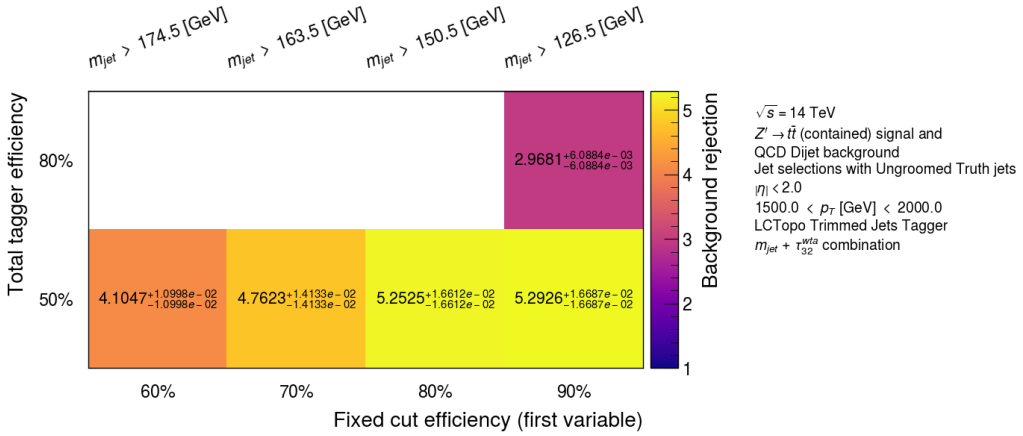

(c) $1500 < p_{\mathrm{T}}^{\mathrm{truth}}$ (GeV) < 2000

Figure 7.19: Tagger background rejection heat-map for the $m_{\mathrm{jet}} + \tau_{32}^{\mathrm{wta}}$ trimmed jet tagger. The jet mass selections are highlighted at the top of the plot.

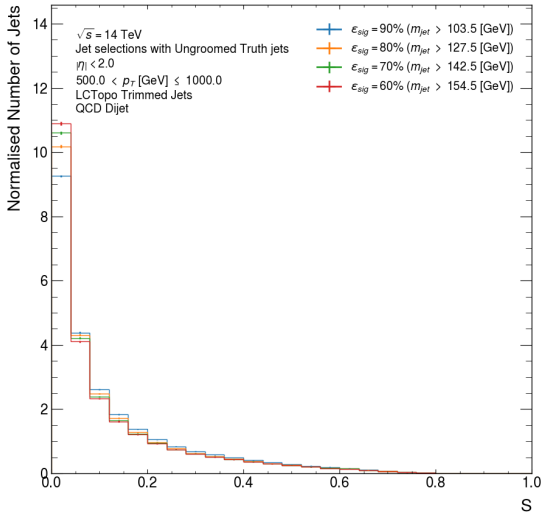

(a) QCD jets $500 < p_{\mathrm{T}}^{\mathrm{truth}}$ (GeV) ≤ 1000

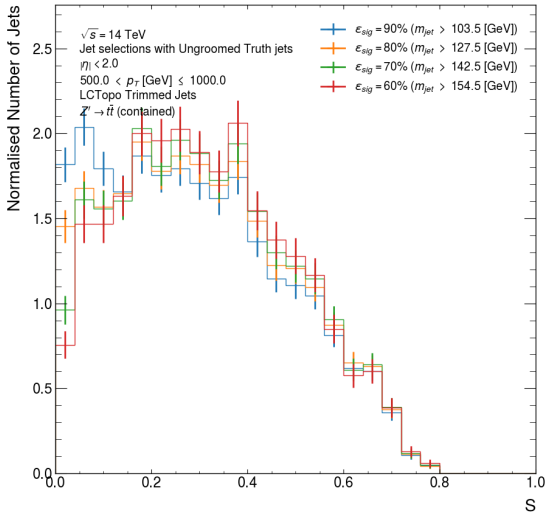

(b) Top quark jets $500 < p_{\mathrm{T}}^{\mathrm{truth}}$ (GeV) ≤ 1000

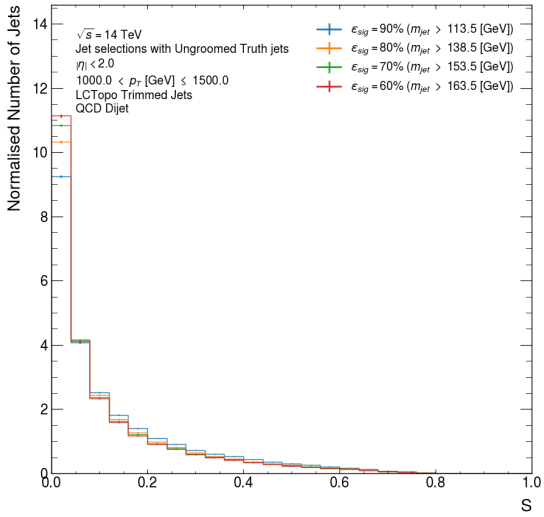

(c) QCD jets $1000 < p_{\mathrm{T}}^{\mathrm{truth}}$ (GeV) ≤ 1500

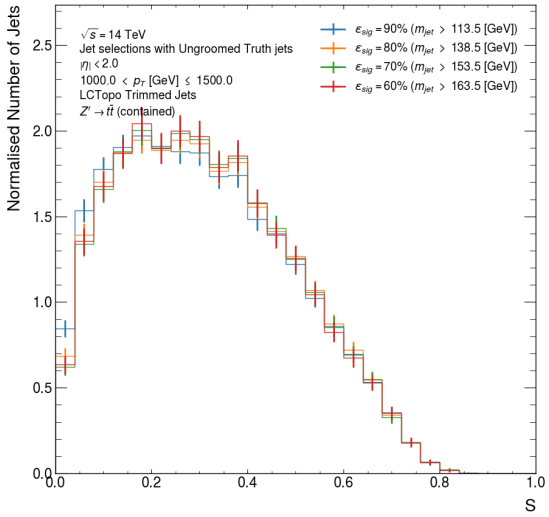

(d) Top quark jets $1000 < p_{\mathrm{T}}^{\mathrm{truth}}$ (GeV) ≤ 1500

Figure 7.20: Trimmed jet sphericity distributions after different mass selections (on reconstructed jets) binned in the p_{T} of the ungroomed truth jet. The QCD jet distributions are shown on the left and the signal top quark jet distributions are shown on the right.

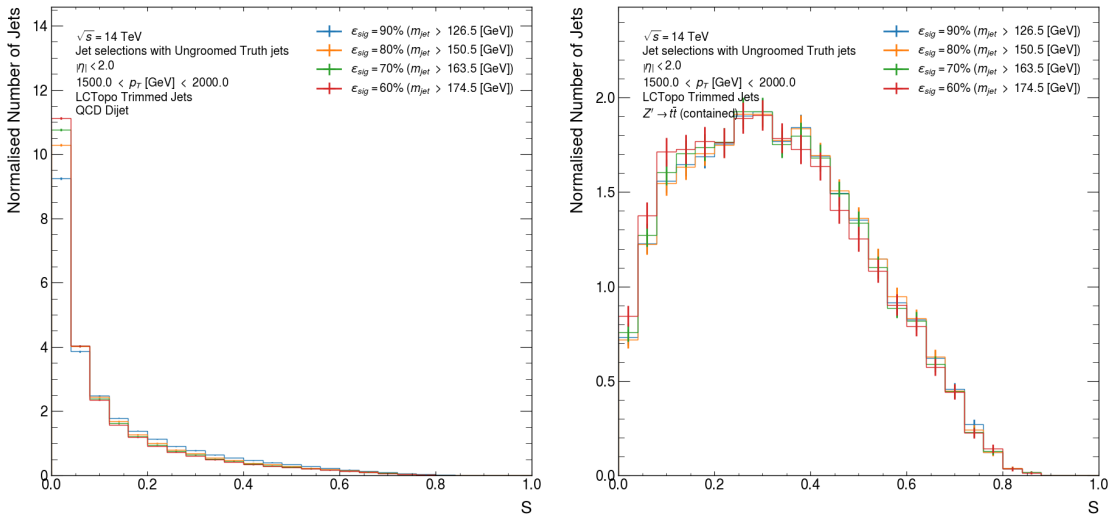

(e) QCD jets $1500 < p_{\mathrm{T}}^{\mathrm{truth}}$ (GeV) < 2000 (f) Top quark jets $1500 < p_{\mathrm{T}}^{\mathrm{truth}}$ (GeV) < 2000

Figure 7.20 (cont.): Trimmed jet sphericity distributions after different mass selections (on reconstructed jets) binned in the p_{T} of the ungroomed truth jet. The QCD jet distributions are shown on the left and the signal top quark jet distributions are shown on the right.

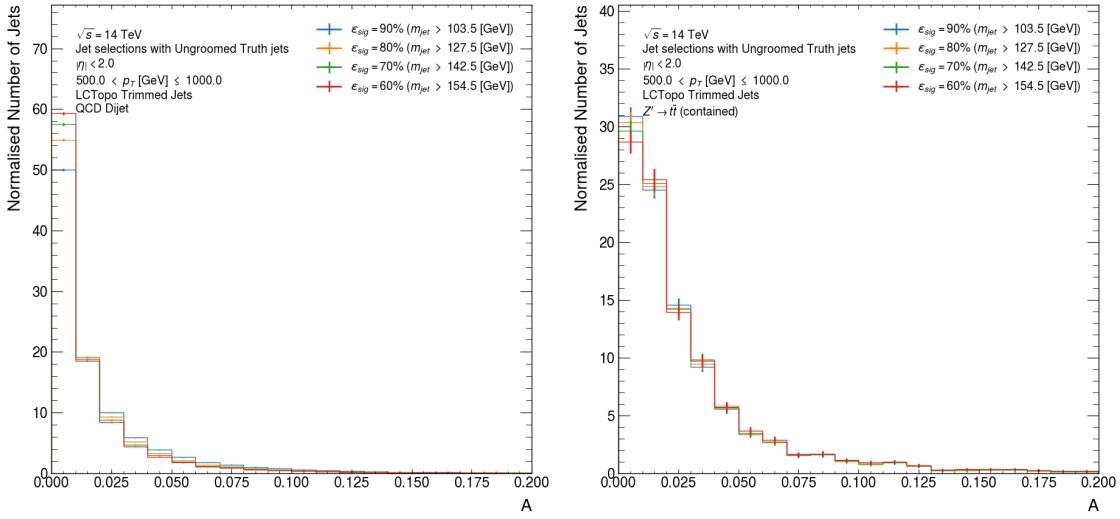

(a) QCD jets $500 < p_{\mathrm{T}}^{\mathrm{truth}}$ (GeV) ≤ 1000 (b) Top quark jets $500 < p_{\mathrm{T}}^{\mathrm{truth}}$ (GeV) ≤ 1000

Figure 7.21: Trimmed jet aplanarity distributions after different mass selections (on reconstructed jets) binned in the p_{T} of the ungroomed truth jet. The QCD jet distributions are shown on the left and the signal top quark jet distributions are shown on the right.

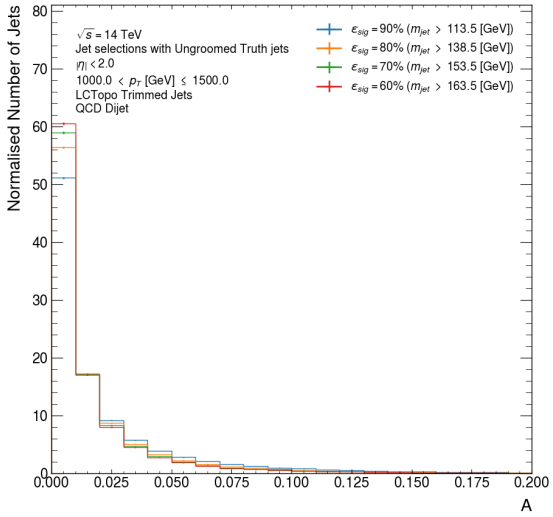

(c) QCD jets $1000 < p_{\mathrm{T}}^{\mathrm{truth}}$ (GeV) ≤ 1500

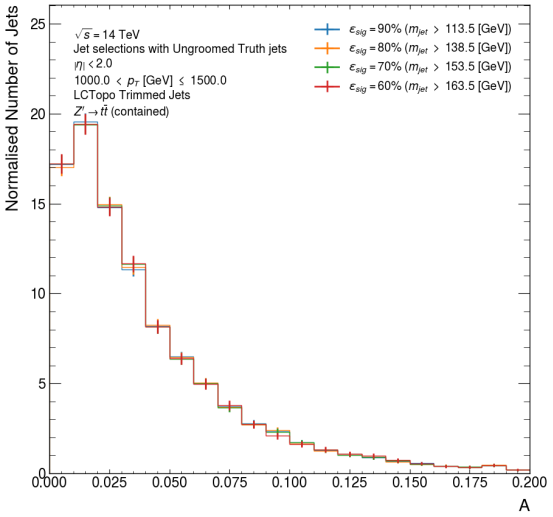

(d) Top quark jets $1000 < p_{\mathrm{T}}^{\mathrm{truth}}$ (GeV) ≤ 1500

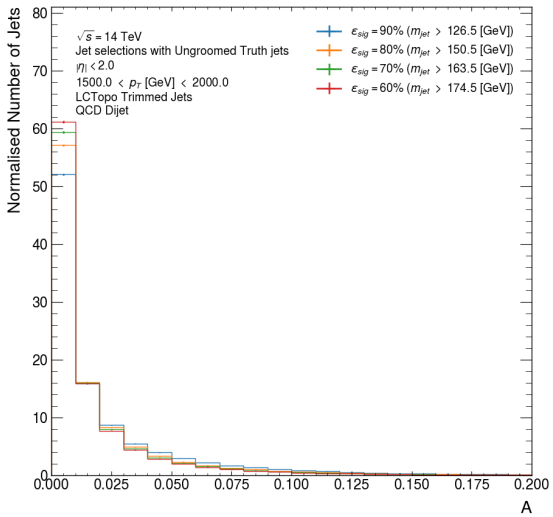

(e) QCD jets $1500 < p_{\mathrm{T}}^{\mathrm{truth}}$ (GeV) < 2000

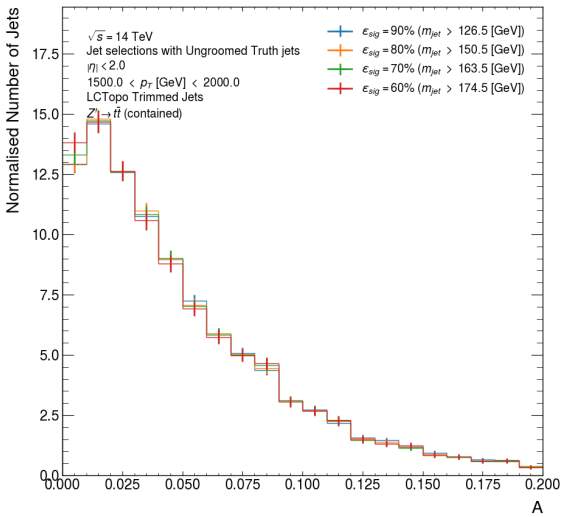

(f) Top quark jets $1500 < p_{\mathrm{T}}^{\mathrm{truth}}$ (GeV) < 2000

Figure 7.21 (cont.): Trimmed jet aplanarity distributions after different mass selections (on reconstructed jets) binned in the p_{T} of the ungroomed truth jet. The QCD jet distributions are shown on the left and the signal top quark jet distributions are shown on the right.

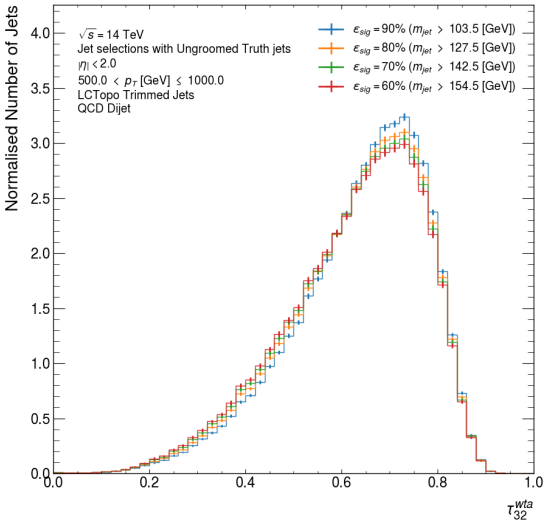

(a) QCD jets $500 < p_{\mathrm{T}}^{\mathrm{truth}}$ (GeV) ≤ 1000

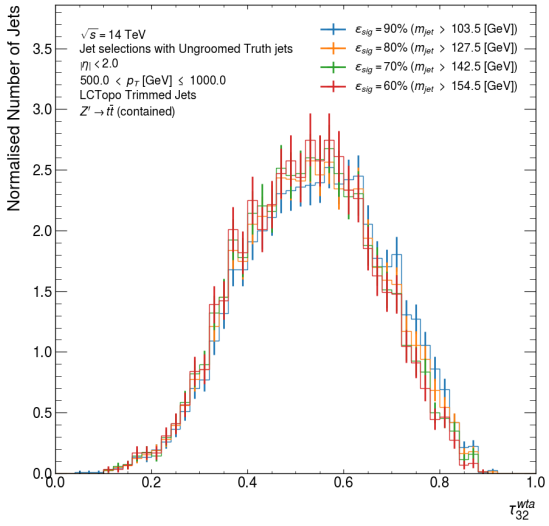

(b) Top quark jets $500 < p_{\mathrm{T}}^{\mathrm{truth}}$ (GeV) ≤ 1000

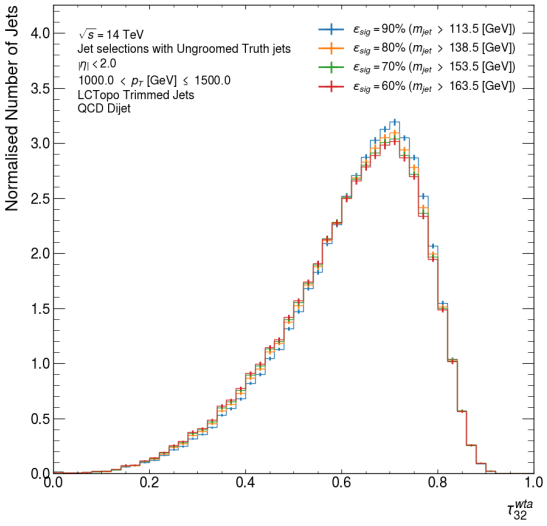

(c) QCD jets $1000 < p_{\mathrm{T}}^{\mathrm{truth}}$ (GeV) ≤ 1500

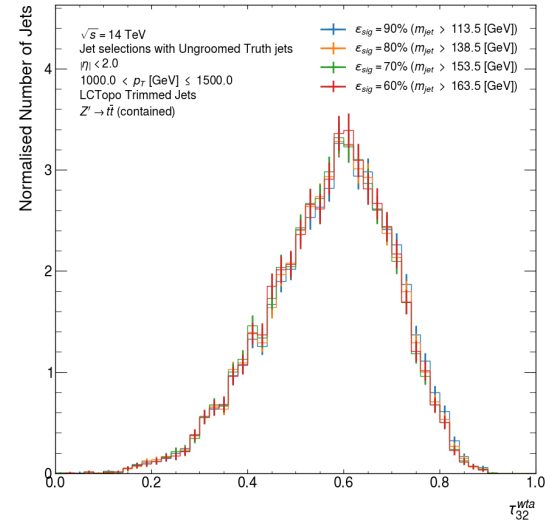

(d) Top quark jets $1000 < p_{\mathrm{T}}^{\mathrm{truth}}$ (GeV) ≤ 1500

Figure 7.22: Trimmed jet τ_{32}^{wta} distributions after different mass selections (on reconstructed jets) binned in the p_{T} of the ungroomed truth jet. The QCD jet distributions are shown on the left and the signal top quark jet distributions are shown on the right.

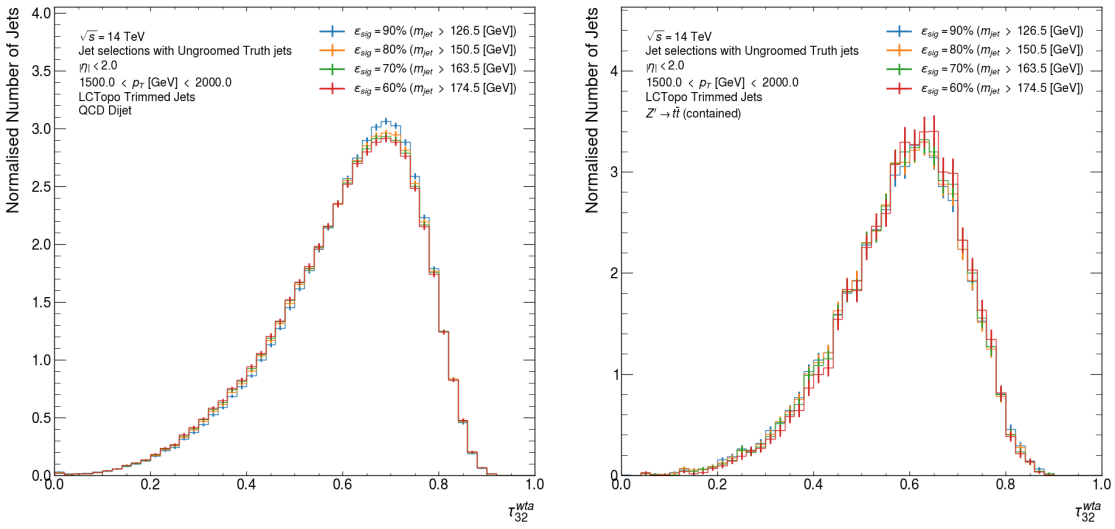

(e) QCD jets $1500 < p_{\mathrm{T}}^{\mathrm{truth}}$ (GeV) < 2000 (f) Top quark jets $1500 < p_{\mathrm{T}}^{\mathrm{truth}}$ (GeV) < 2000

Figure 7.22 (cont.): Trimmed jet τ_{32}^{wta} distributions after different mass selections (on reconstructed jets) binned in the p_{T} of the ungroomed truth jet. The QCD jet distributions are shown on the left and the signal top quark jet distributions are shown on the right.

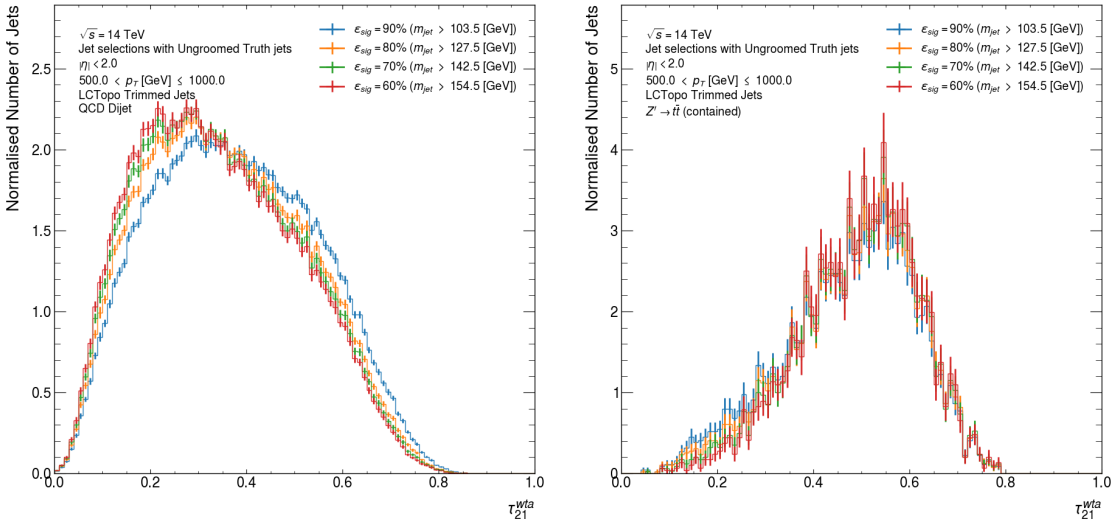

(a) QCD jets $500 < p_{\mathrm{T}}^{\mathrm{truth}}$ (GeV) ≤ 1000 (b) Top quark jets $500 < p_{\mathrm{T}}^{\mathrm{truth}}$ (GeV) ≤ 1000

Figure 7.23: Trimmed jet τ_{21}^{wta} distributions after different mass selections (on reconstructed jets) binned in the p_{T} of the ungroomed truth jet. The QCD jet distributions are shown on the left and the signal top quark jet distributions are shown on the right.

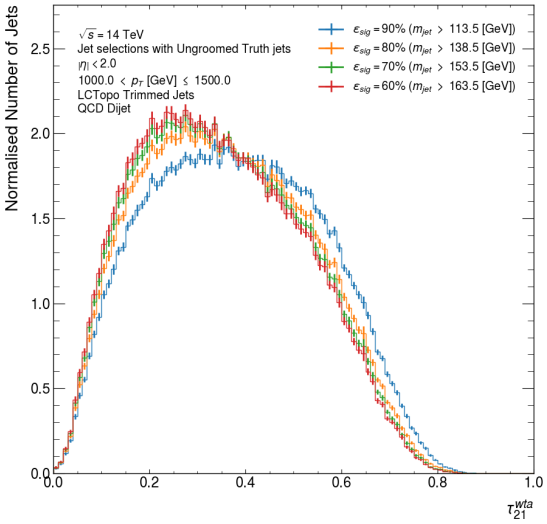

(c) QCD jets $1000 < p_{\mathrm{T}}^{\mathrm{truth}}$ (GeV) ≤ 1500

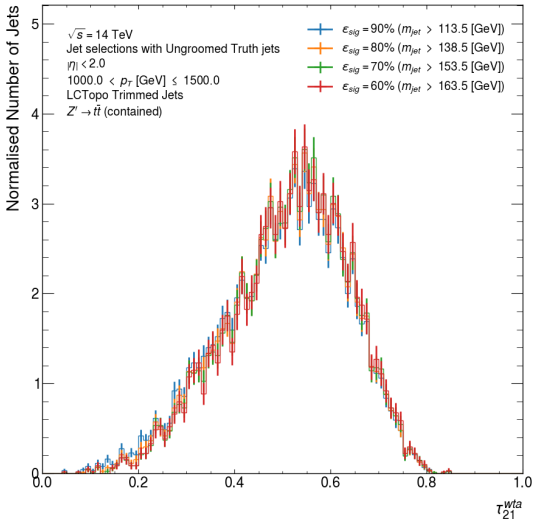

(d) Top quark jets $1000 < p_{\mathrm{T}}^{\mathrm{truth}}$ (GeV) ≤ 1500

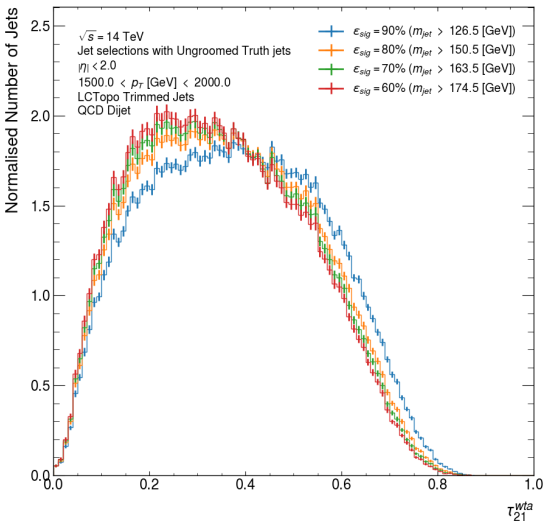

(e) QCD jets $1500 < p_{\mathrm{T}}^{\mathrm{truth}}$ (GeV) < 2000

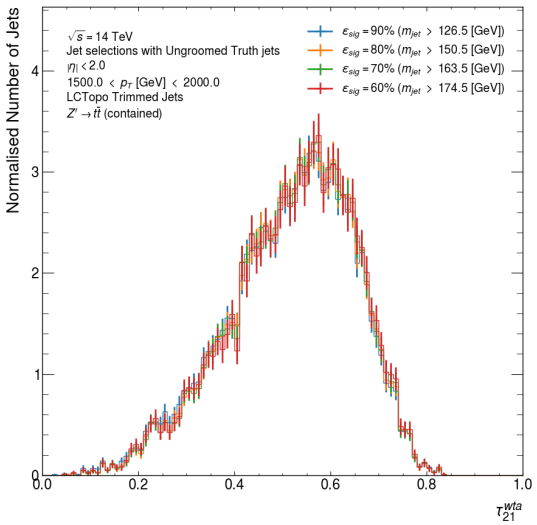

(f) Top quark jets $1500 < p_{\mathrm{T}}^{\mathrm{truth}}$ (GeV) < 2000

Figure 7.23 (cont.): Trimmed jet τ_{21}^{wta} distributions after different mass selections (on reconstructed jets) binned in the p_{T} of the ungroomed truth jet. The QCD jet distributions are shown on the left and the signal top quark jet distributions are shown on the right.

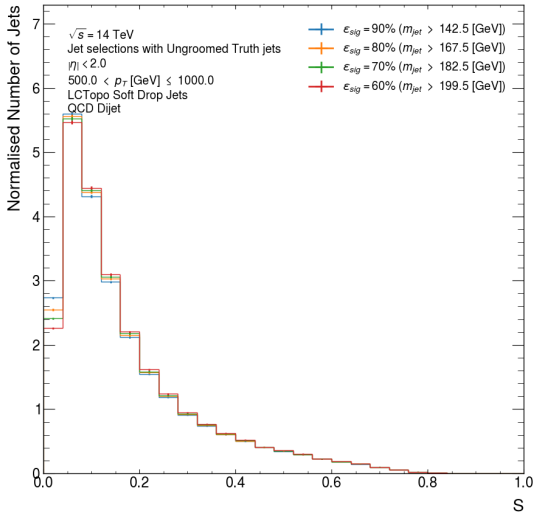

(a) QCD jets $500 < p_{\mathrm{T}}^{\mathrm{truth}}$ (GeV) ≤ 1000

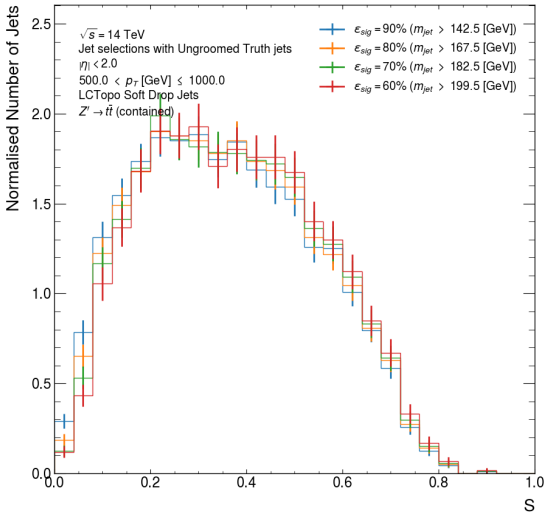

(b) Top quark jets $500 < p_{\mathrm{T}}^{\mathrm{truth}}$ (GeV) ≤ 1000

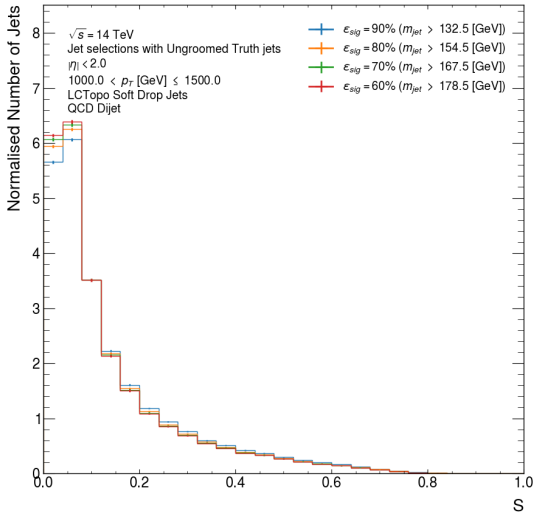

(c) QCD jets $1000 < p_{\mathrm{T}}^{\mathrm{truth}}$ (GeV) ≤ 1500

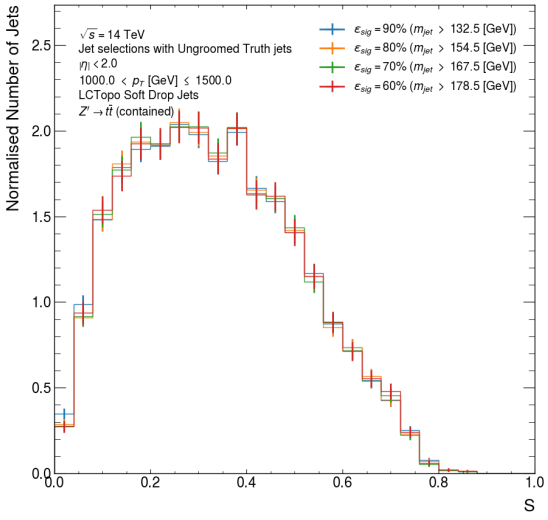

(d) Top quark jets $1000 < p_{\mathrm{T}}^{\mathrm{truth}}$ (GeV) ≤ 1500

Figure 7.24: Soft-drop jet sphericity distributions after different mass selections (on reconstructed jets) binned in the p_{T} of the ungroomed truth jet. The QCD jet distributions are shown on the left and the signal top quark jet distributions are shown on the right.

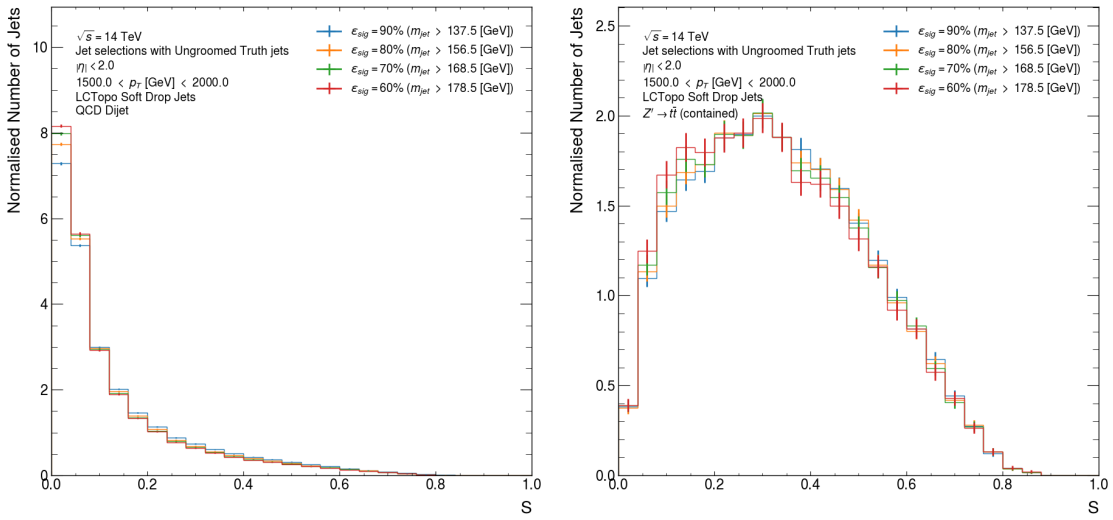

(e) QCD jets $1500 < p_{\mathrm{T}}^{\mathrm{truth}}$ (GeV) < 2000 (f) Top quark jets $1500 < p_{\mathrm{T}}^{\mathrm{truth}}$ (GeV) < 2000

Figure 7.24 (cont.): Soft-drop jet sphericity distributions after different mass selections (on reconstructed jets) binned in the p_{T} of the ungroomed truth jet. The QCD jet distributions are shown on the left and the signal top quark jet distributions are shown on the right.

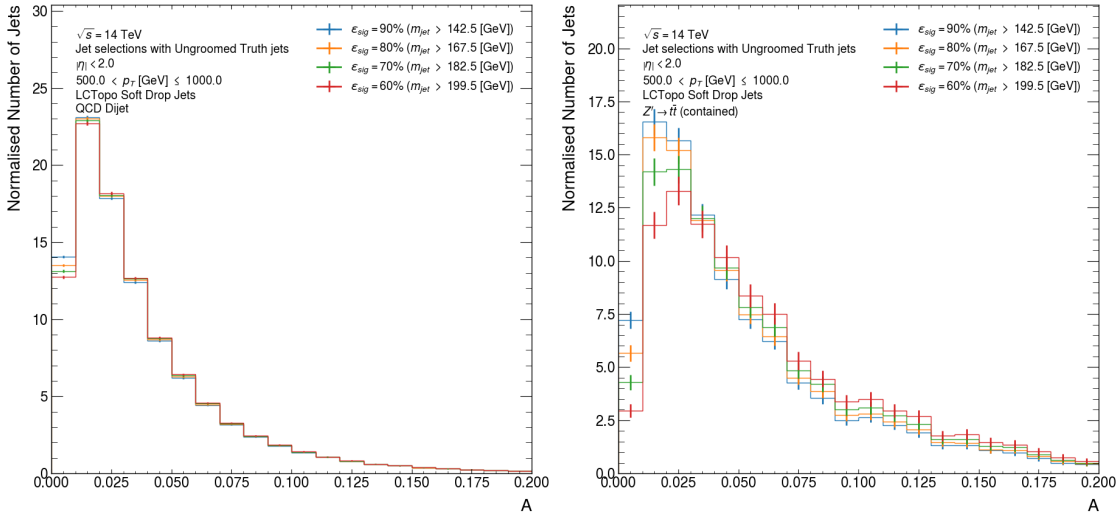

(a) QCD jets $500 < p_{\mathrm{T}}^{\mathrm{truth}}$ (GeV) ≤ 1000 (b) Top quark jets $500 < p_{\mathrm{T}}^{\mathrm{truth}}$ (GeV) ≤ 1000

Figure 7.25: Soft-drop jet aplanarity distributions after different mass selections (on reconstructed jets) binned in the p_{T} of the ungroomed truth jet. The QCD jet distributions are shown on the left and the signal top quark jet distributions are shown on the right.

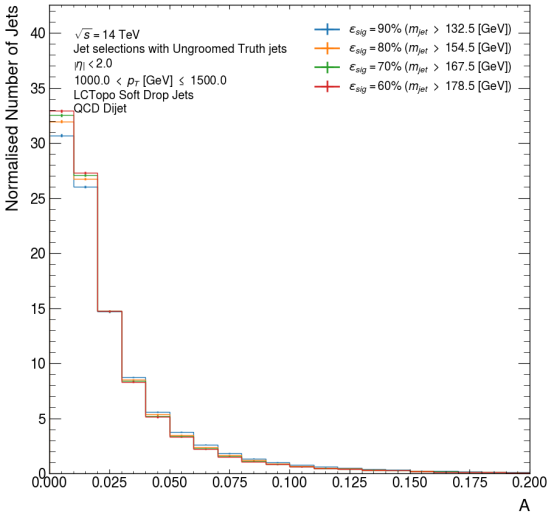

(c) QCD jets $1000 < p_{\mathrm{T}}^{\mathrm{truth}}$ (GeV) ≤ 1500

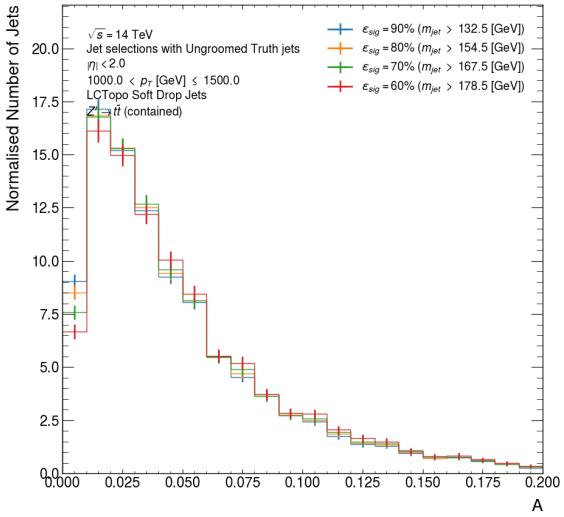

(d) Top quark jets $1000 < p_{\mathrm{T}}^{\mathrm{truth}}$ (GeV) ≤ 1500

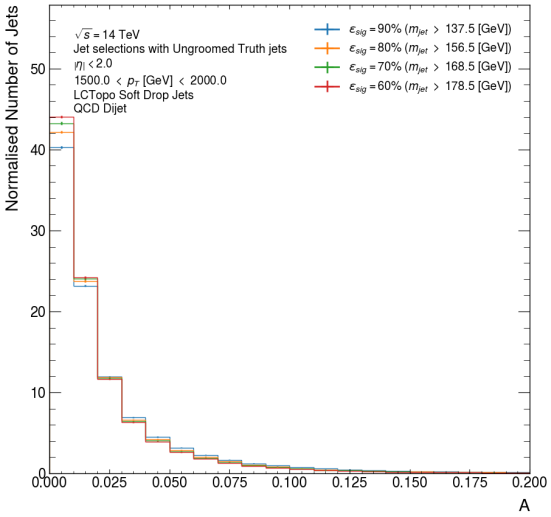

(e) QCD jets $1500 < p_{\mathrm{T}}^{\mathrm{truth}}$ (GeV) < 2000

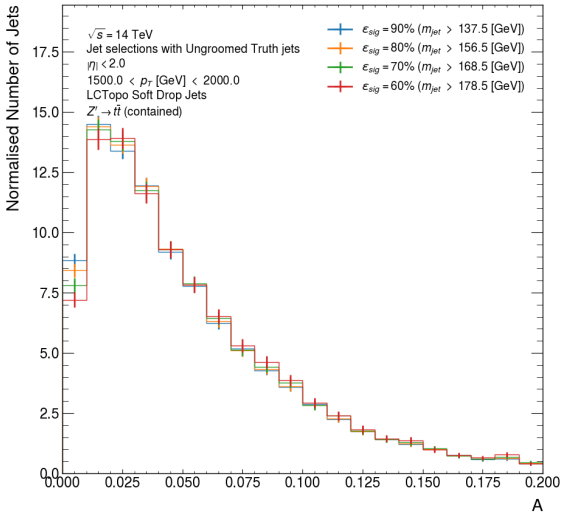

(f) Top quark jets $1500 < p_{\mathrm{T}}^{\mathrm{truth}}$ (GeV) < 2000

Figure 7.25 (cont.): Soft-drop jet aplanarity distributions after different mass selections (on reconstructed jets) binned in the p_{T} of the ungroomed truth jet. The QCD jet distributions are shown on the left and the signal top quark jet distributions are shown on the right.

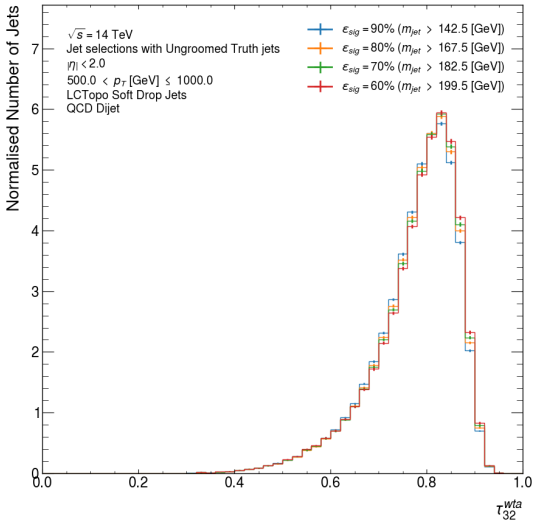

(a) QCD jets $500 < p_{\mathrm{T}}^{\mathrm{truth}}$ (GeV) ≤ 1000

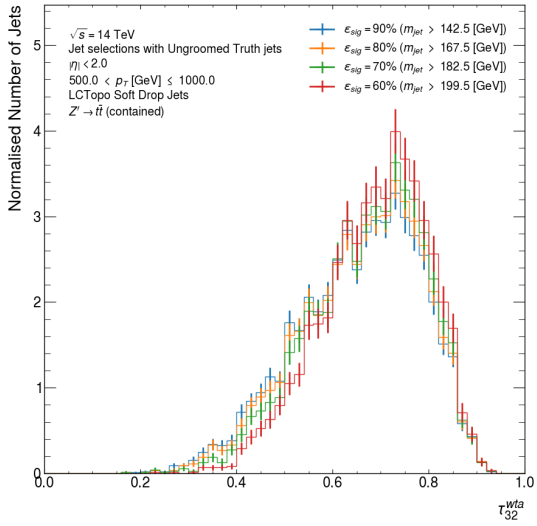

(b) Top quark jets $500 < p_{\mathrm{T}}^{\mathrm{truth}}$ (GeV) ≤ 1000

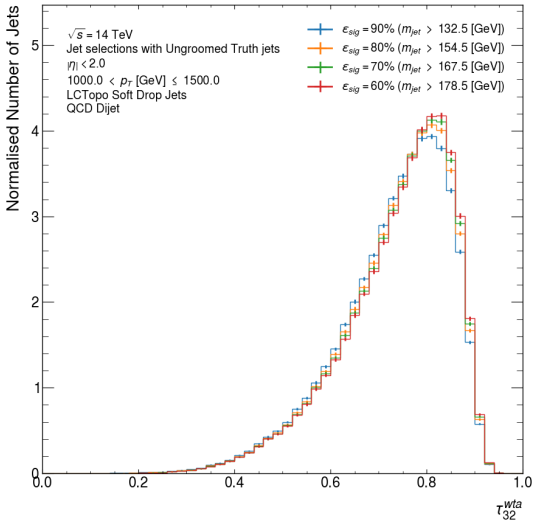

(c) QCD jets $1000 < p_{\mathrm{T}}^{\mathrm{truth}}$ (GeV) ≤ 1500

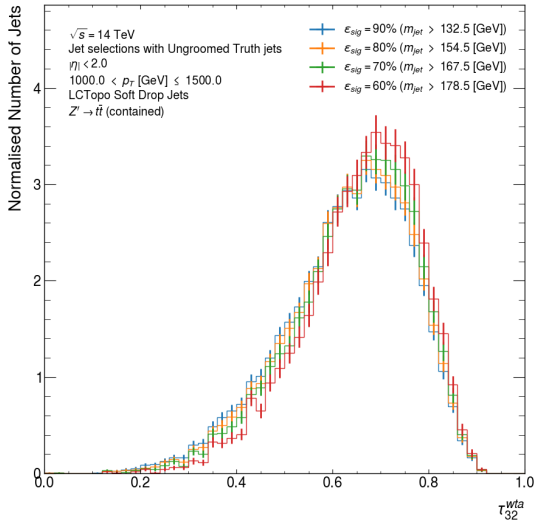

(d) Top quark jets $1000 < p_{\mathrm{T}}^{\mathrm{truth}}$ (GeV) ≤ 1500

Figure 7.26: Soft-drop jet τ_{32}^{wta} distributions after different mass selections (on reconstructed jets) binned in the p_{T} of the ungroomed truth jet. The QCD jet distributions are shown on the left and the signal top quark jet distributions are shown on the right.

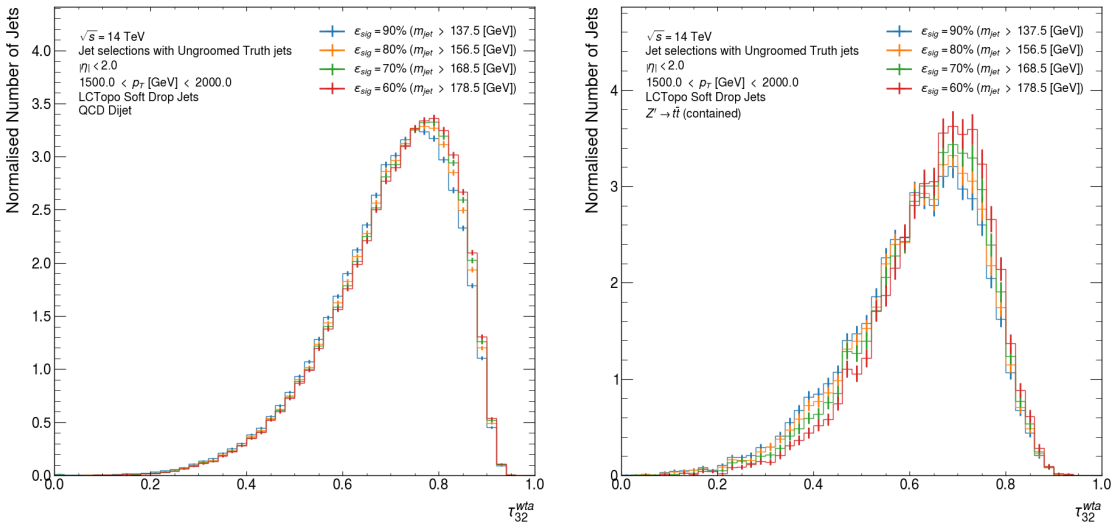

(e) QCD jets $1500 < p_{\mathrm{T}}^{\mathrm{truth}}$ (GeV) < 2000 (f) Top quark jets $1500 < p_{\mathrm{T}}^{\mathrm{truth}}$ (GeV) < 2000

Figure 7.26 (cont.): Soft-drop jet τ_{32}^{wta} distributions after different mass selections (on reconstructed jets) binned in the p_{T} of the ungroomed truth jet. The QCD jet distributions are shown on the left and the signal top quark jet distributions are shown on the right.

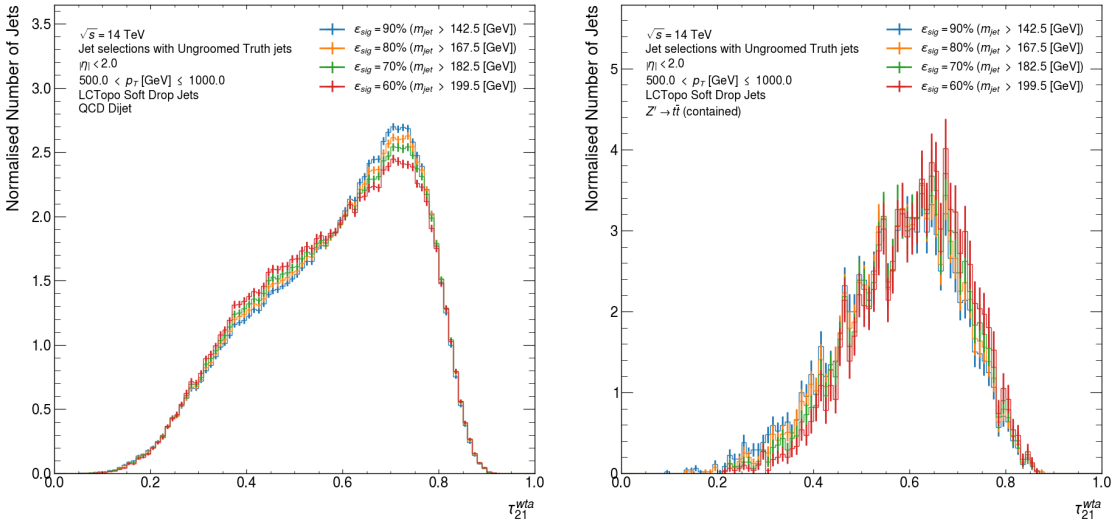

(a) QCD jets $500 < p_{\mathrm{T}}^{\mathrm{truth}}$ (GeV) ≤ 1000 (b) Top quark jets $500 < p_{\mathrm{T}}^{\mathrm{truth}}$ (GeV) ≤ 1000

Figure 7.27: Soft-drop jet τ_{21}^{wta} distributions after different mass selections (on reconstructed jets) binned in the p_{T} of the ungroomed truth jet. The QCD jet distributions are shown on the left and the signal top quark jet distributions are shown on the right.

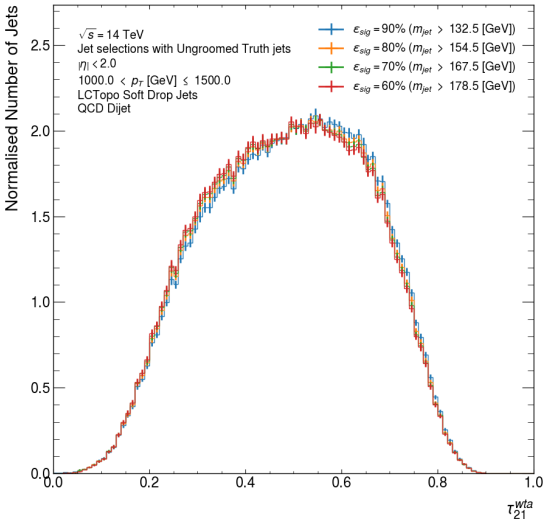

(c) QCD jets $1000 < p_{\mathrm{T}}^{\mathrm{truth}}$ (GeV) ≤ 1500

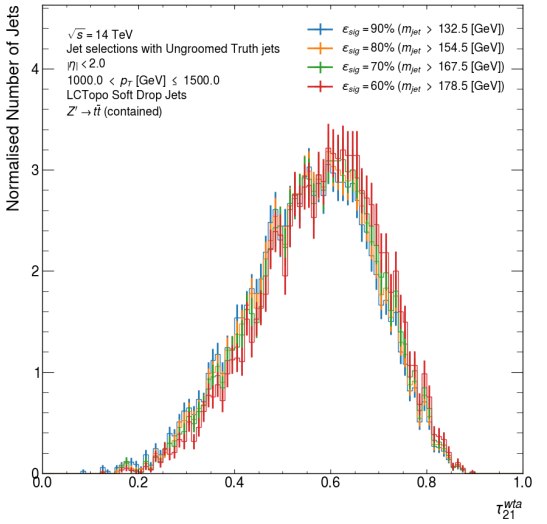

(d) Top quark jets $1000 < p_{\mathrm{T}}^{\mathrm{truth}}$ (GeV) ≤ 1500

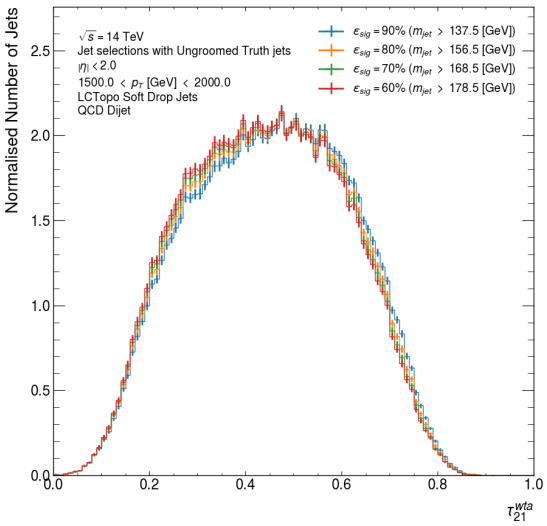

(e) QCD jets $1500 < p_{\mathrm{T}}^{\mathrm{truth}}$ (GeV) < 2000

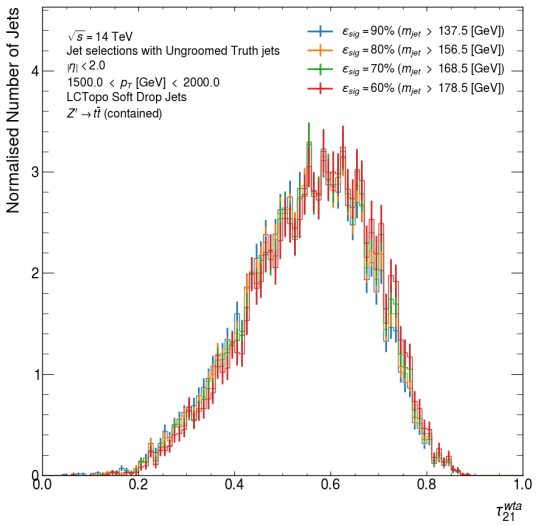

(f) Top quark jets $1500 < p_{\mathrm{T}}^{\mathrm{truth}}$ (GeV) < 2000

Figure 7.27 (cont.): Soft-drop jet τ_{21}^{wta} distributions after different mass selections (on reconstructed jets) binned in the p_{T} of the ungroomed truth jet. The QCD jet distributions are shown on the left and the signal top quark jet distributions are shown on the right.

Figures 7.28a and 7.28b. The sphericity and aplanarity soft-drop jet taggers show similar features in Figures 7.28c and 7.28d.

Such behaviour is most evident when the results are binned in the p_{T} of the reconstructed jets in Figures 7.30 and 7.31 for the trimmed and soft-drop groomed collections, respectively. The looser mass selection provided by the 80% signal efficiency trimmed jet tagger working point (Figure 7.30b) leads to an optimal aplanarity and sphericity tagger background rejection between 1600 GeV and 2000 GeV. One explanation for this is that the increased jet p_{T} leads to better containment of the top decay products but eventually the performance falls as the angular separation of the jet constituents falls towards the limit of the finite detector granularity[7]. Similar results are seen for the soft-drop jets where an optimal jet p_{T} range for maximum background rejection is apparent for both tagger working points (Figures 7.31a and 7.31b). Conversely, the 50% efficiency trimmed jet sphericity tagger background rejection (Figure 7.30a) falls monotonically with increasing p_{T}, potentially a consequence of the tighter selections. Like in Section 7.8, the background rejection of the soft-drop jet τ_{32}^{wta} tagger outperforms other tagger definitions in the lowest p_{T} bin, except for the 80% signal efficiency tagger working point.

The signal efficiency (Figure 7.29) of all taggers is relatively stable with the truth jet p_{T} since the tagger selections are re-derived in each p_{T} bin. In Figure 7.29, the most significant variation in signal efficiency is observed for soft-drop jets where the taggers that rely on the number of jet constituents, N_{constit}, have lower signal efficiency at low-p_{T} and converge to the expected tagger efficiency at high-p_{T}. This could be an effect of the binning and shape of the N_{constit} observable for soft-drop jets but since the number of jet constituents is significantly p_{T} (merging of constituents) and pile-up dependent, the N_{constit} taggers will not be pursued for the recommendations.

7.10 Pile-up dependence of tagger performance

The pile-up stability performance of the taggers was studied in two different ways. The first considered the application of complete tagger selections in different bins of the median (event-level) LCW-scale momentum-density, ρ_{LCW}[8], calculated with $R = 0.4$ k_t jets with $|y| < 2$[9]. The ρ_{LCW} observable is particularly pile-up sensitive since its calculation from k_t jets means soft radiation is clustered first, and favoured over hard radiation, which is clustered last. The second pile-up stability study considered jet response distributions for different observables used in tagger definitions, only for the QCD jet sample. The jet response was also parameterised as a function of

[7] The author thanks Maximilian Swiatlowski for discussions and suggestions that helped explain this behaviour.

[8] The ρ_{LCW} observable has the same definition (albeit with a different energy scale) to that used for the pile-up subtraction stage of the small-R jet calibration discussed in Section 4.5 and Appendix A.3.

[9] The author thanks Dag Gillberg for suggesting this observable for the pile-up stability studies as an alternative to $\langle\mu\rangle$ and N_{PV}.

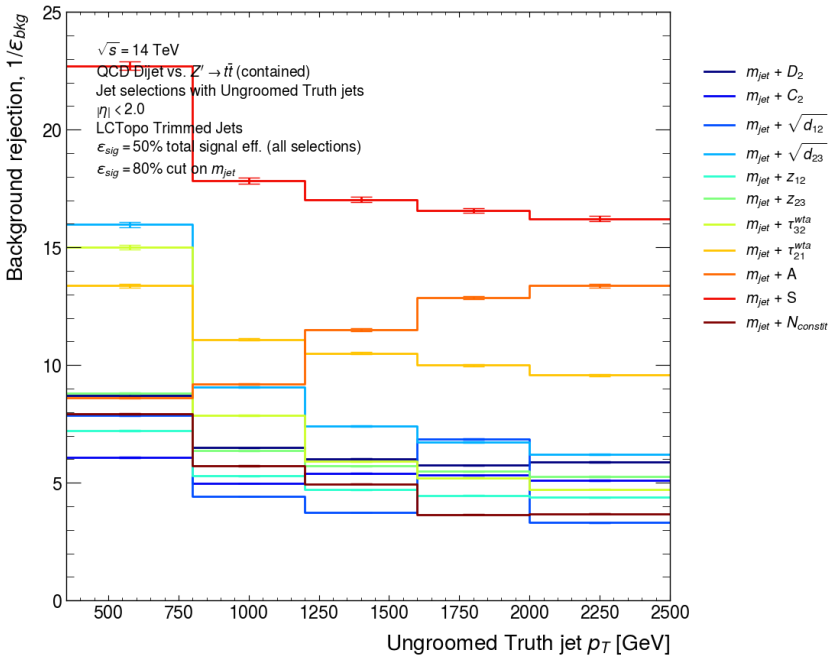

(a) Trimmed jets 50% efficiency working point

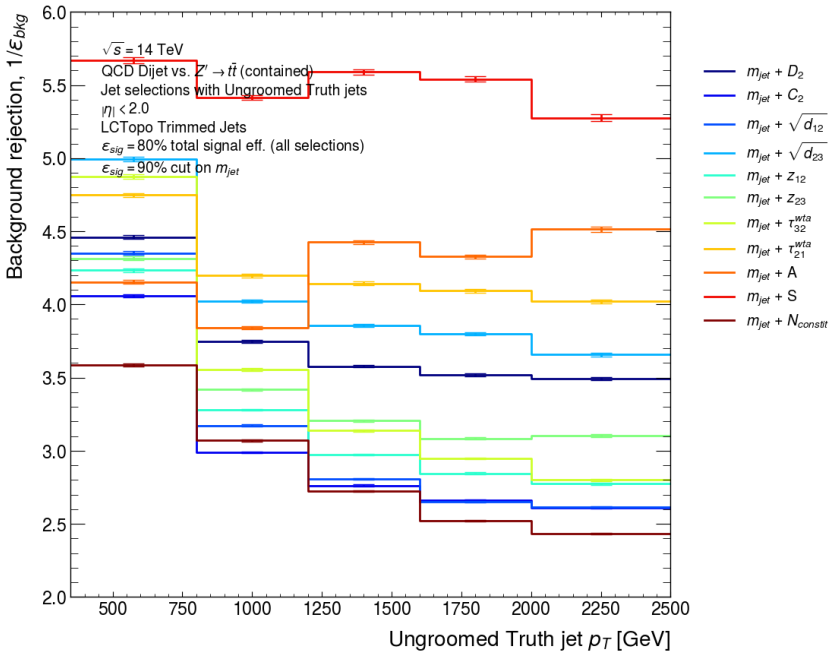

(b) Trimmed jets 80% efficiency working point

Figure 7.28: Background rejection for selected tagger working points as a function of the ungroomed truth jet p_{T}.

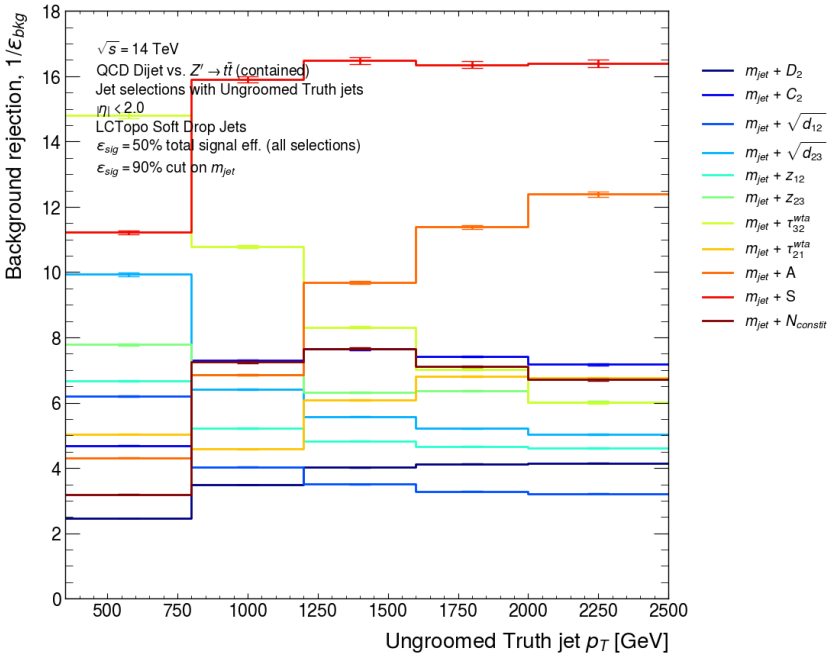

(c) Soft-drop jets 50% efficiency working point

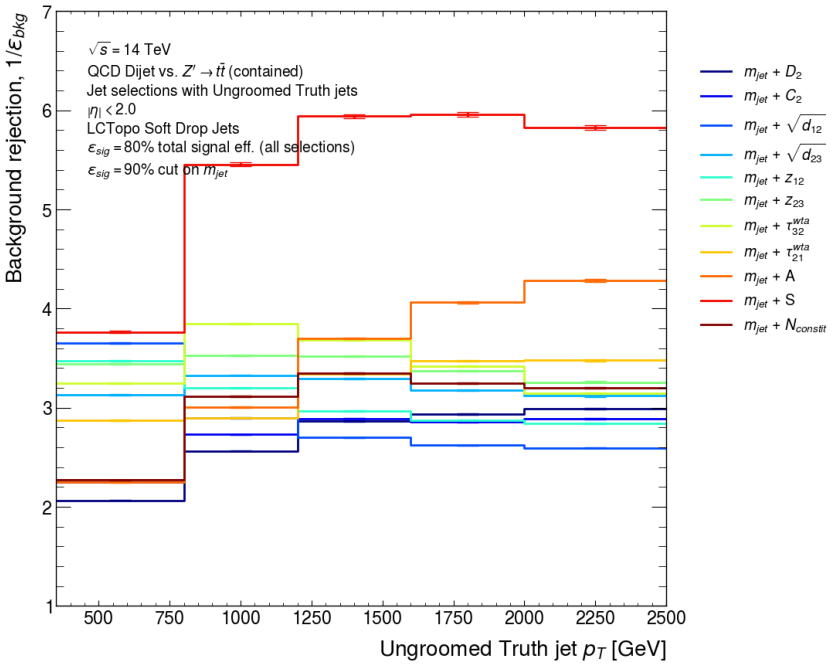

(d) Soft-drop jets 80% efficiency working point

Figure 7.28 (cont.): Background rejection for selected tagger working points as a function of the ungroomed truth jet p_{T}.

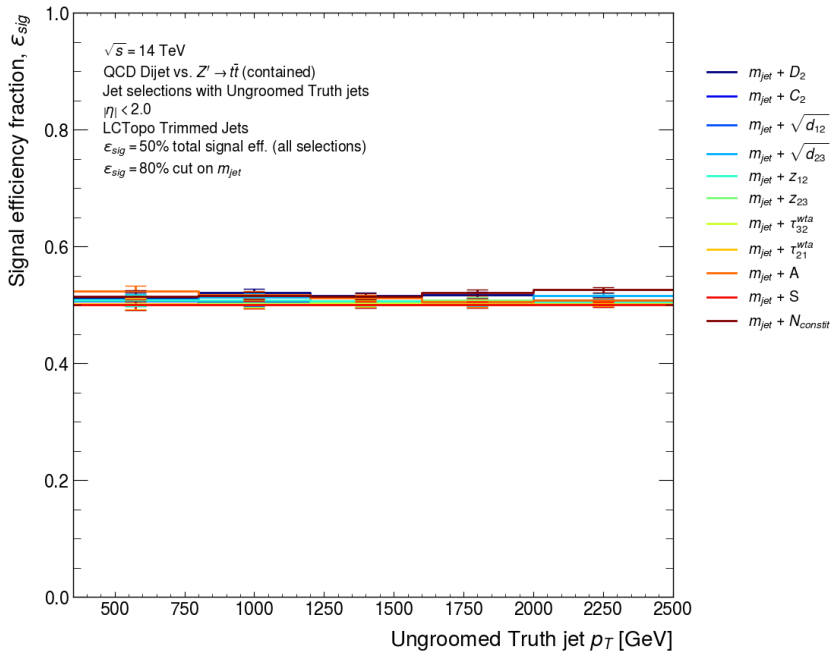

(a) Trimmed jets 50% efficiency working point

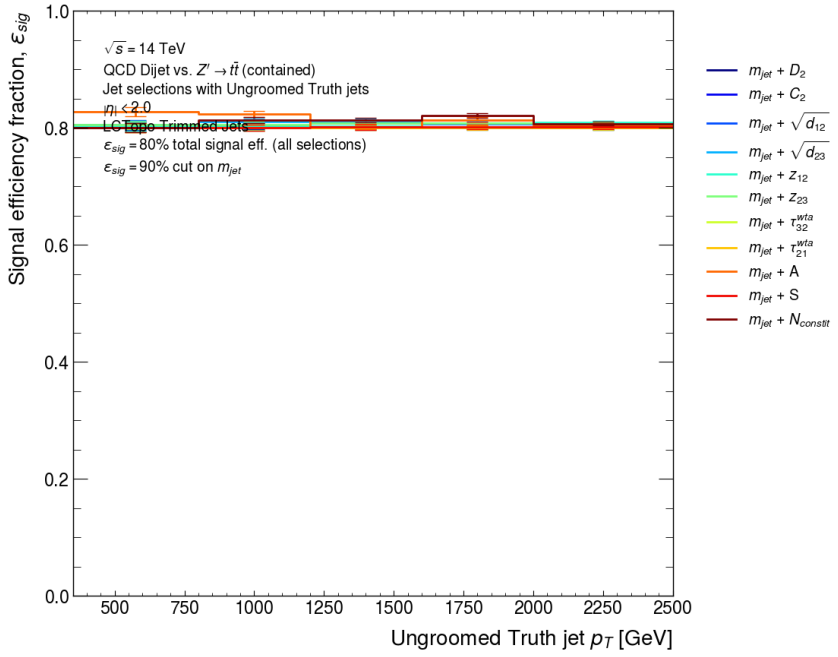

(b) Trimmed jets 80% efficiency working point

Figure 7.29: Signal efficiency for selected tagger working points as a function of the ungroomed truth jet p_{T}.

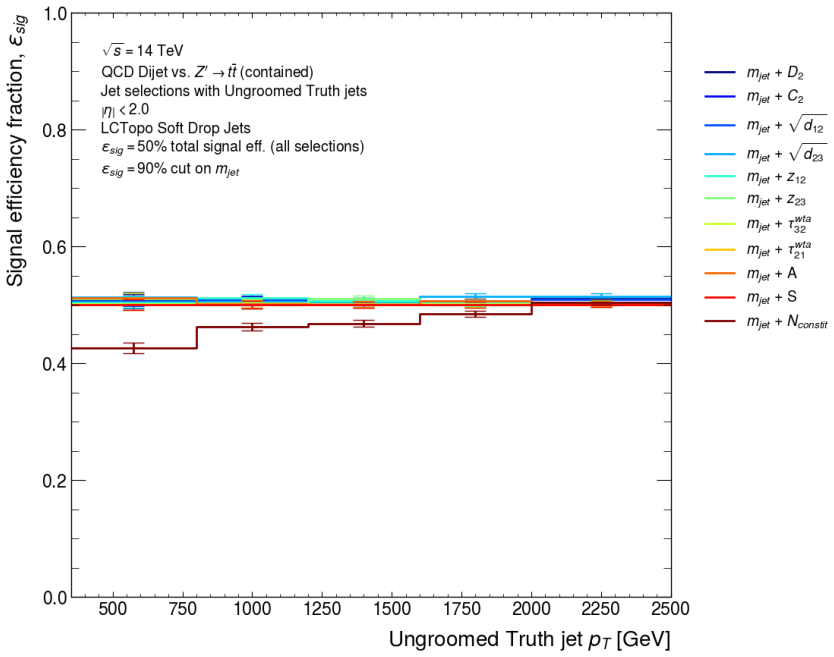

(c) Soft-drop jets 50% efficiency working point

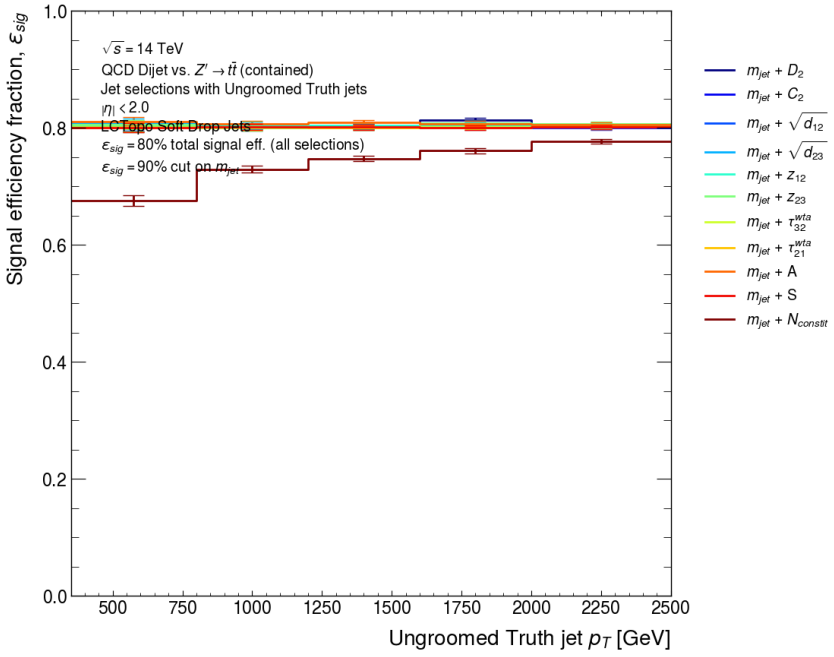

(d) Soft-drop jets 80% efficiency working point

Figure 7.29 (cont.): Signal efficiency for selected tagger working points as a function of the ungroomed truth jet p_{T}.

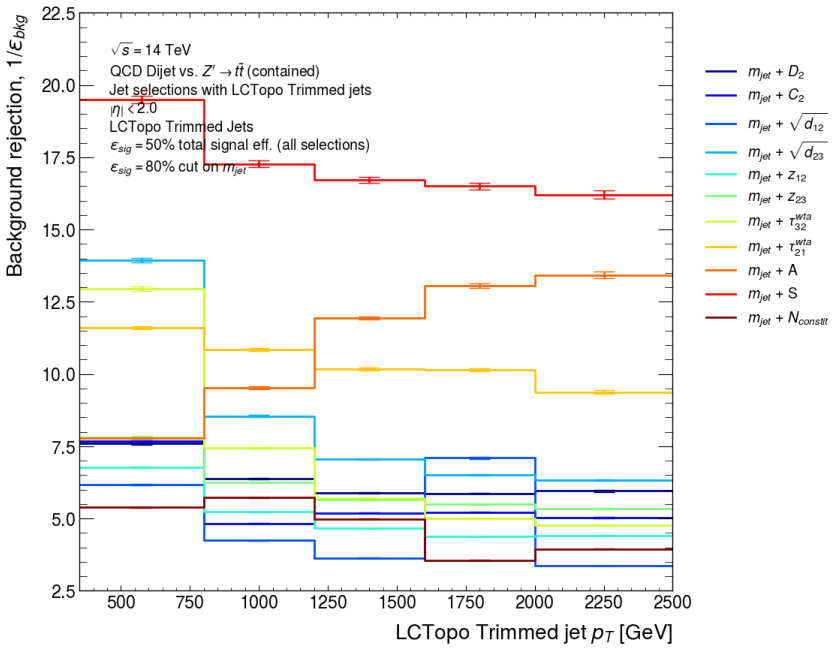

(a) 50% efficiency working point

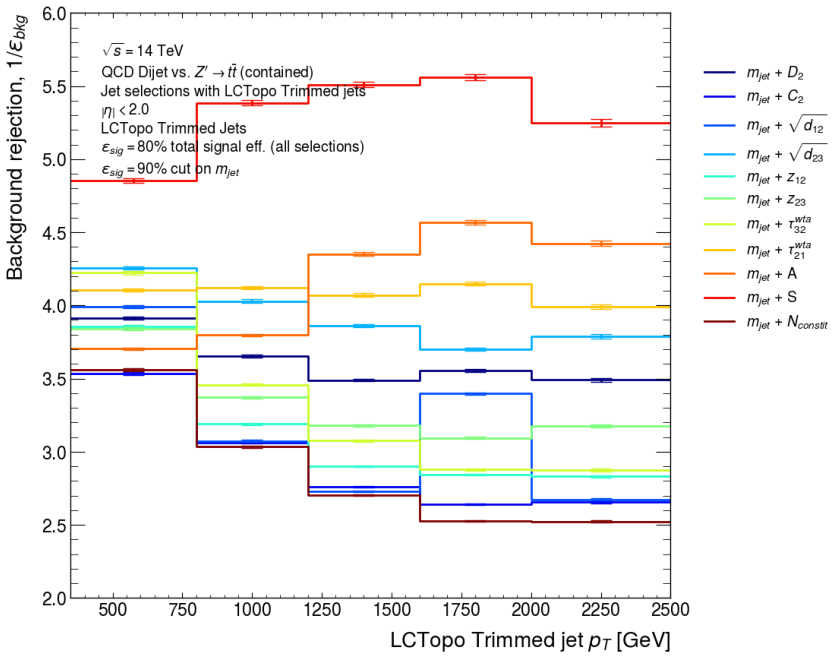

(b) 80% efficiency working point

Figure 7.30: Background rejection of trimmed jet taggers binned in the p_{T} of the `LCTopoTrimmed` jet.

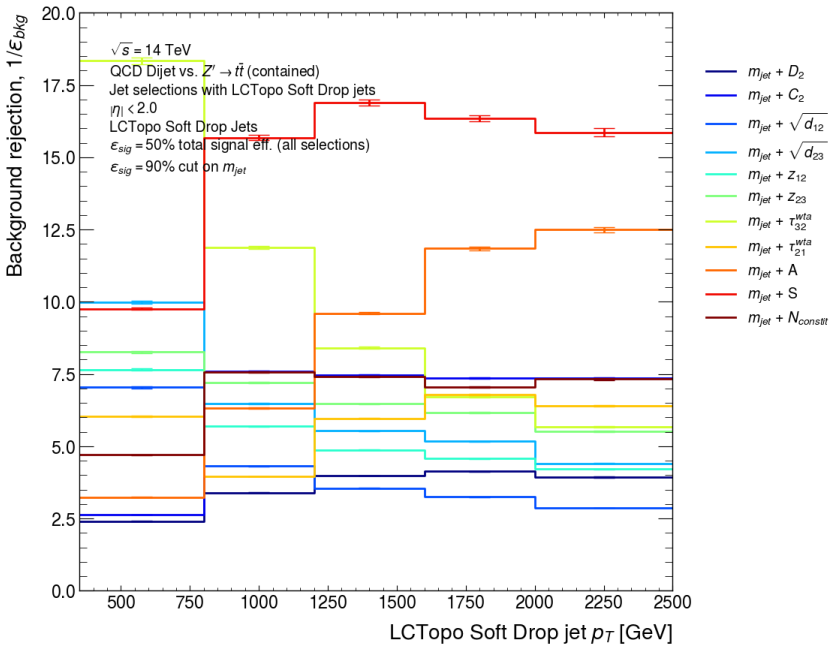

(a) 50% efficiency working point

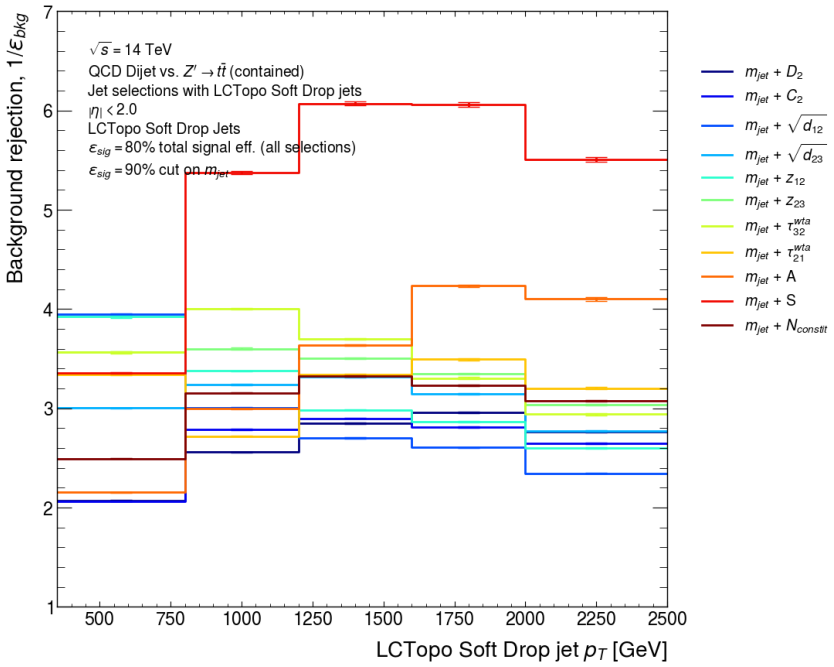

(b) 80% efficiency working point

Figure 7.31: Background rejection of soft-drop jet taggers binned in the p_{T} of the `LCTopoSoftDrop` jet.

ρ_{LCW}. The tagger stability and jet response studies are discussed in Sections 7.10.1 and 7.10.2, respectively.

For both studies, four ρ_{LCW} bins were used. The initial and final bin were made slightly wider to accommodate a sufficient number of events and reduce statistical uncertainties in the efficiency estimates. The results are presented in the same ungroomed truth jet p_{T} bins as for previous sections. Additionally, the final ρ_{LCW} bin is contaminated by radiation from the hard-scatter interaction, evident from the varying tail behaviour of ρ_{LCW} for the signal and background in Figure 7.32. Nonetheless, the observable is sensitive to the *total* activity in any event and is therefore still a good measure of the pile-up activity. An alternative study considered the tagger performance as the average number of interactions per bunch crossing ($\langle\mu\rangle$) increased. However, for these studies, the MC event samples only have $\langle\mu\rangle$ in a narrow range from 190 to 210, which leads to little variation in the tagger performance. Therefore, the tagger performance was primarily considered as a function of ρ_{LCW}, and the $\langle\mu\rangle$ binned results are included in Appendix G for completeness. Additional jet response studies with the $\langle\mu\rangle$ binning were not completed.

7.10.1 Two-variable tagger pile-up stability

This section documents the signal efficiency and background rejection variation with ρ_{LCW} for two-variable tagger definitions. The tagger selection was derived in inclusive ungroomed truth jet p_{T} bins and applied in each ρ_{LCW} bin. Only three tagger definitions are included in the results of this section (jet mass selections combined with an aplanarity, sphericity, or τ_{32}^{wta} selection) for clarity. Detailed plots with all tagger definitions are shown in Appendix F.

The signal efficiency of the trimmed jet shape variable (aplanarity [A] and sphericity [S]) taggers in Figures 7.35a, 7.35c, and 7.35e (50% signal efficiency) and Figures 7.36a, 7.36c, and 7.36e (80% signal efficiency) has an upwards trend as a function of ρ_{LCW} compared to the approximate downwards trend of the τ_{32}^{wta} tagger signal efficiency. Despite the large statistical uncertainties on the signal efficiency, the performance of the sphericity ($m_{\text{jet}} + S$) tagger is more stable than the aplanarity ($m_{\text{jet}} + A$) tagger. This is apparent in the low- and high-ρ_{LCW} bins for the $500 < p_{\text{T}}^{\text{truth}}$ (GeV) ≤ 1000 and $1000 < p_{\text{T}}^{\text{truth}}$ (GeV) ≤ 1500 bins where a statistically significant difference is seen between their signal efficiencies. At high-p_{T} ($1500 < p_{\text{T}}^{\text{truth}}$ [GeV] < 2000), the signal efficiency of both taggers agrees to within statistical uncertainty in all ρ_{LCW} bins, indicating reduced pile-up stability. Comparatively, the soft-drop jet taggers in Figures 7.34b, 7.34d, and 7.34f and Figures 7.33b, 7.33d, and 7.33f show much more variation in their signal efficiency. They are therefore less pile-up stable than the trimmed jet taggers. One explanation for this behaviour results from the difference in the soft-drop and trimming grooming algorithms. Trimming removes $R = 0.2$ k_t subjets from the large-R jet, whilst soft-drop grooming operates on the C/A branching sequence. Thus, trimming is likely a more aggressive grooming algorithm for the removal of soft radiation compared to the current soft-drop grooming configuration.

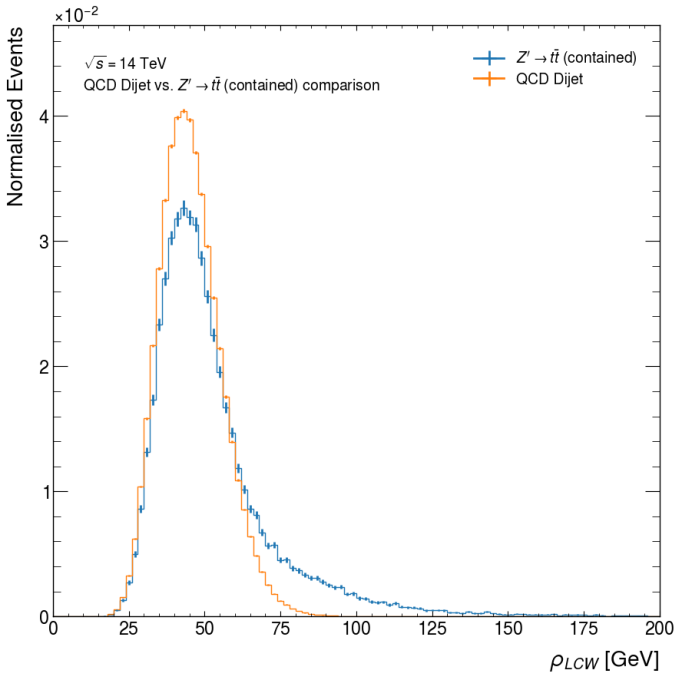

Figure 7.32: Comparison of signal ($Z' \to t\bar{t}$) and background (QCD dijet) ρ_{LCW} distribution. Since ρ_{LCW} is an event-level variable, no jet selections were applied to make this comparison.

The signal efficiency trends for the soft-drop jet taggers are otherwise similar to the trimmed jet taggers.

The background rejection variation for trimmed and soft-drop jet taggers is shown for the 50% and 80% signal efficiency working points in Figures 7.33 and 7.34, respectively. For very trimmed jet tagger, the background rejection falls with increasing ρ_{LCW} in each p_{T} bin. The same is true for the soft-drop jet taggers excluding the 50% signal efficiency τ_{32}^{wta} variant, which has increasing background rejection (with ρ_{LCW}) in each p_{T} bin. The origin of this behaviour could be explained by changes in the jet response (relative to truth jets) for τ_{32}^{wta}, but indicates that the combination of the individual τ_{3}^{wta} and τ_{2}^{wta} pile-up dependence in τ_{32}^{wta} leads to more complicated (and seemingly contradictory) pile-up dependence. Since the soft-drop jets are ultimately less pile-up stable (evident in the signal efficiency results), this warrants removing the "oddly" performing soft-drop tagger definitions from consideration. Further investigation would be needed to determine the exact cause of differences between the 50% and 80% signal efficiency soft-drop jet τ_{32}^{wta} tagger background rejection as a function of ρ_{LCW}.

For both trimmed and soft-drop groomed jets the sphericity tagger background rejection falls by a larger amount than for the aplanarity tagger and this effect is most significant at low-p_{T} where we expect to see a larger fraction of pile-up radiation. Despite this, the sphericity tagger is clearly the most performant in terms of its background rejection, and it has a relatively stable signal efficiency compared to

the aplanarity tagger. Thus, we conclude that the sphericity tagger is more pile-up stable and focus solely on its development in Section 7.13.

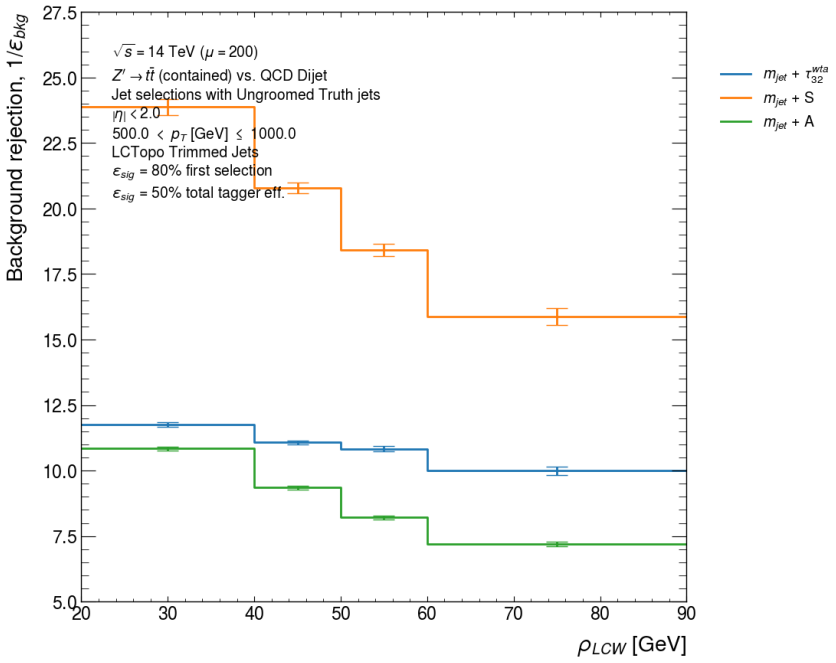

(a) Trimmed jets with $500 < p_{\mathrm{T}}^{\mathrm{truth}}$ (GeV) ≤ 1000

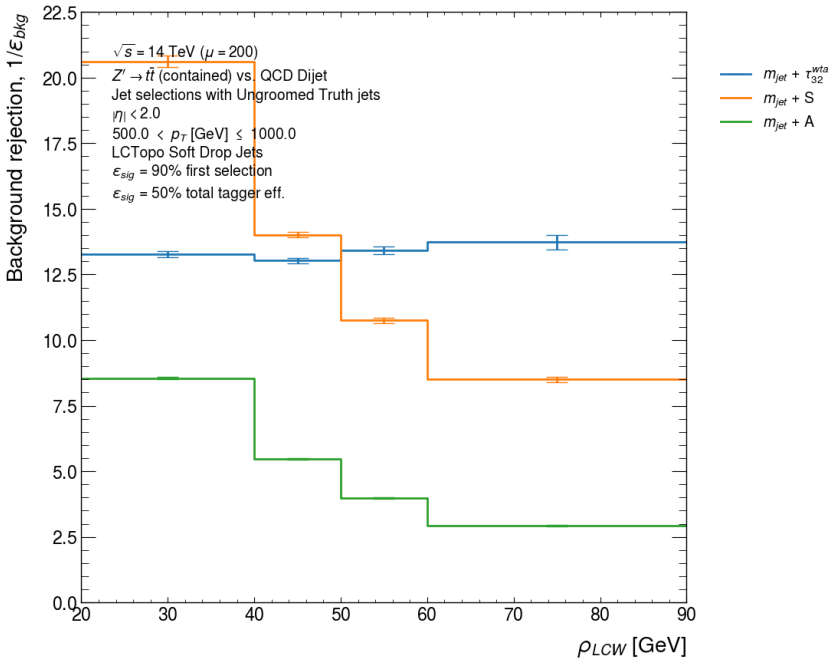

(b) Soft-drop jets with $500 < p_{\mathrm{T}}^{\mathrm{truth}}$ (GeV) ≤ 1000

Figure 7.33: Pile-up stability profiles for the tagger background rejection as a function of the momentum density ρ_{LCW} for 50% signal efficiency trimmed and soft-drop jet taggers.

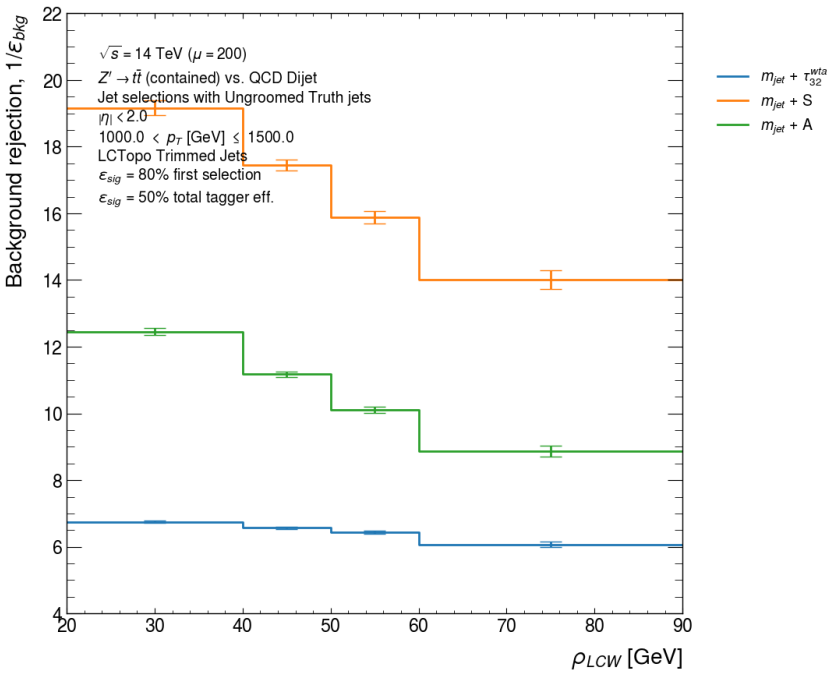

(c) Trimmed jets with $1000 < p_{\mathrm{T}}^{\mathrm{truth}}$ (GeV) ≤ 1500

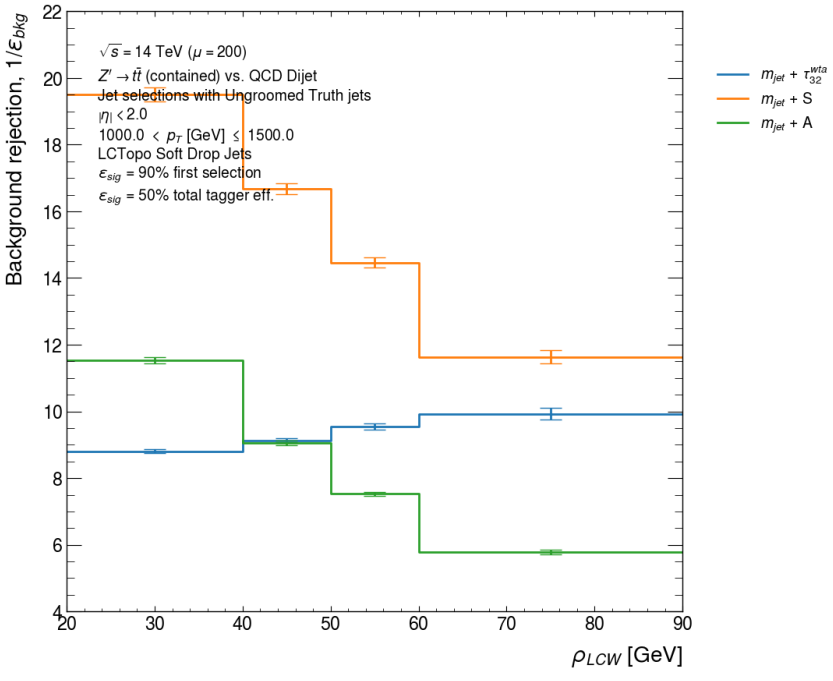

(d) Soft-drop jets with $1000 < p_{\mathrm{T}}^{\mathrm{truth}}$ (GeV) ≤ 1500

Figure 7.33 (cont.): Pile-up stability profiles for the tagger background rejection as a function of the momentum density ρ_{LCW} for 50% signal efficiency trimmed and soft-drop jet taggers.

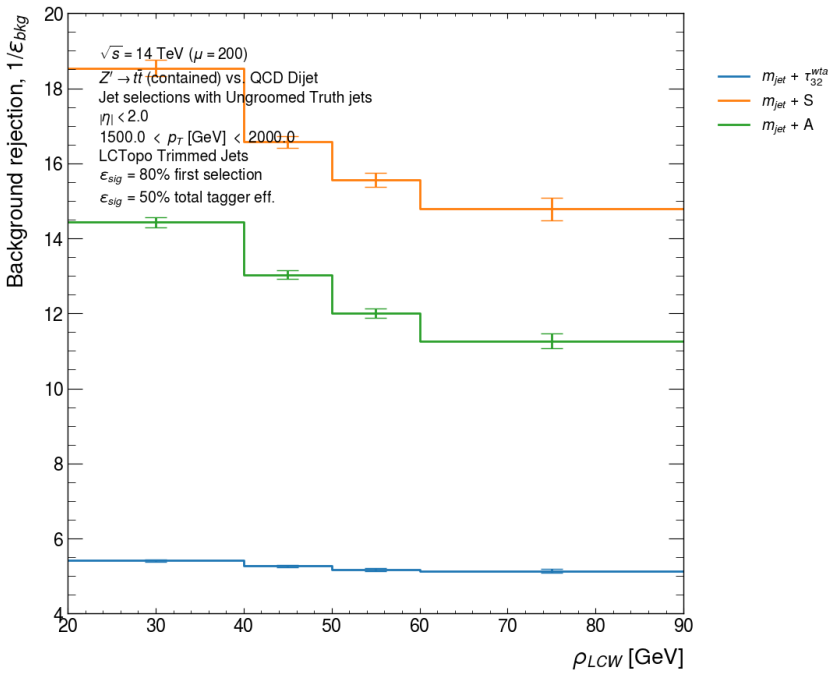

(e) Trimmed jets with $1500 < p_{\mathrm{T}}^{\mathrm{truth}}$ (GeV) < 2000

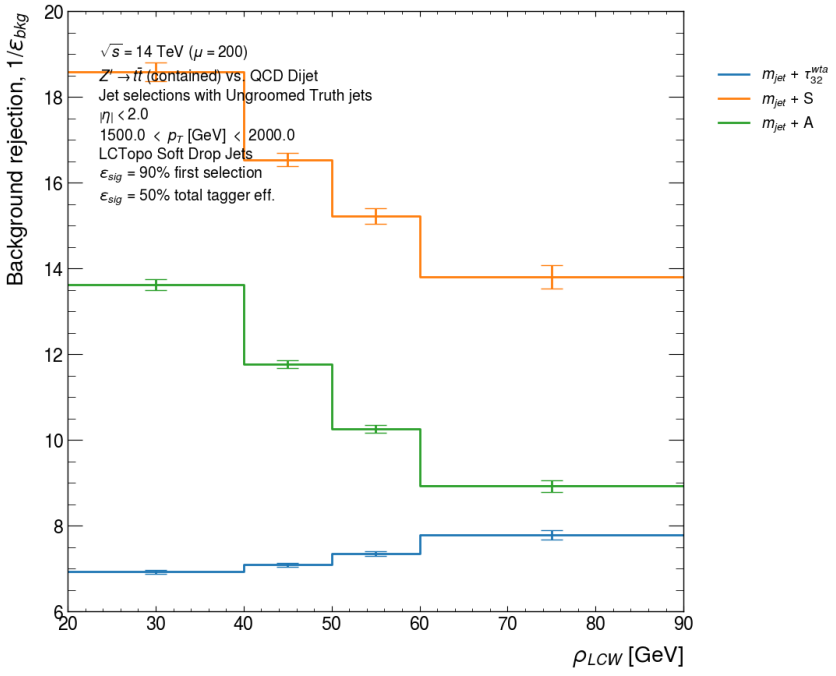

(f) Soft-drop jets with $1500 < p_{\mathrm{T}}^{\mathrm{truth}}$ (GeV) < 2000

Figure 7.33 (cont.): Pile-up stability profiles for the tagger background rejection as a function of the momentum density ρ_{LCW} for 50% signal efficiency trimmed and soft-drop jet taggers.

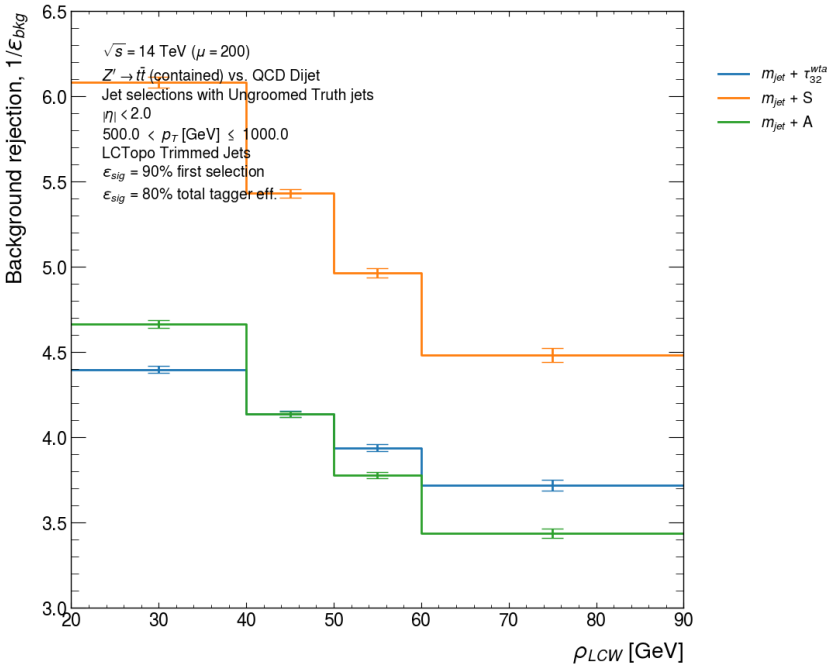

(a) Trimmed jets with $500 < p_{\mathrm{T}}^{\mathrm{truth}}$ (GeV) ≤ 1000

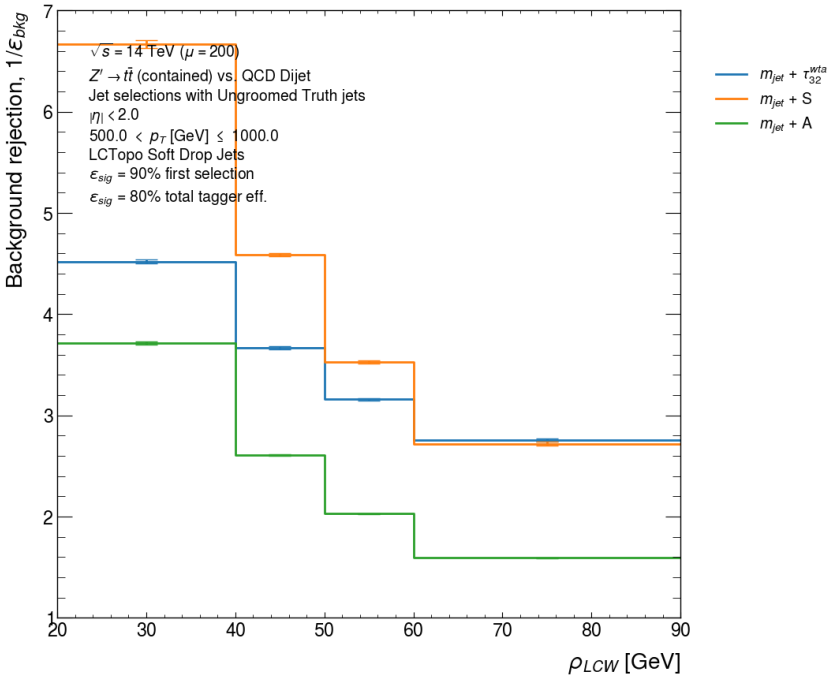

(b) Soft-drop jets with $500 < p_{\mathrm{T}}^{\mathrm{truth}}$ (GeV) ≤ 1000

Figure 7.34: Pile-up stability profiles for the tagger background rejection as a function of the momentum density ρ_{LCW} for 80% signal efficiency trimmed and soft-drop jet taggers.

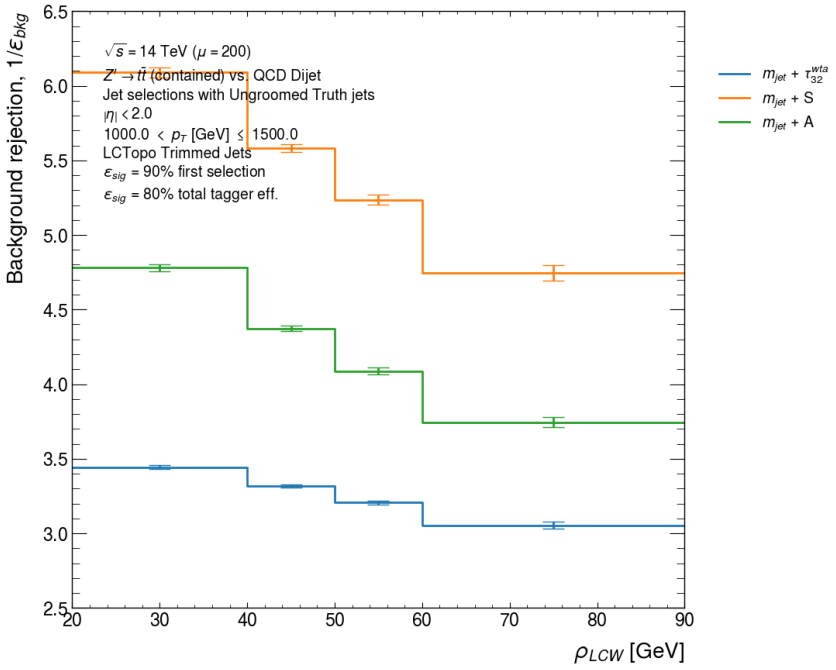

(c) Trimmed jets with $1000 < p_{\mathrm{T}}^{\mathrm{truth}}$ (GeV) ≤ 1500

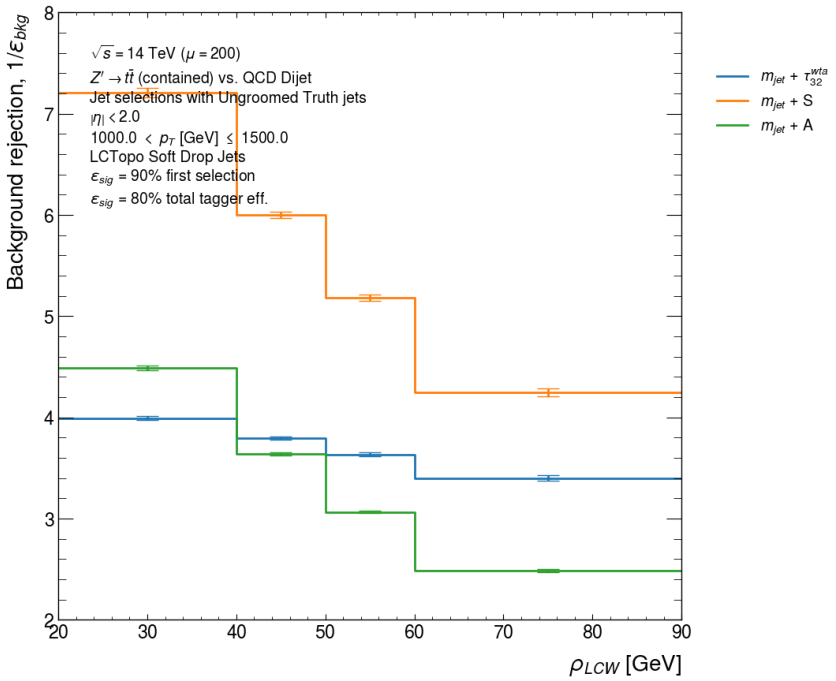

(d) Soft-drop jets with $1000 < p_{\mathrm{T}}^{\mathrm{truth}}$ (GeV) ≤ 1500

Figure 7.34 (cont.): Pile-up stability profiles for the tagger background rejection as a function of the momentum density ρ_{LCW} for 80% signal efficiency trimmed and soft-drop jet taggers.

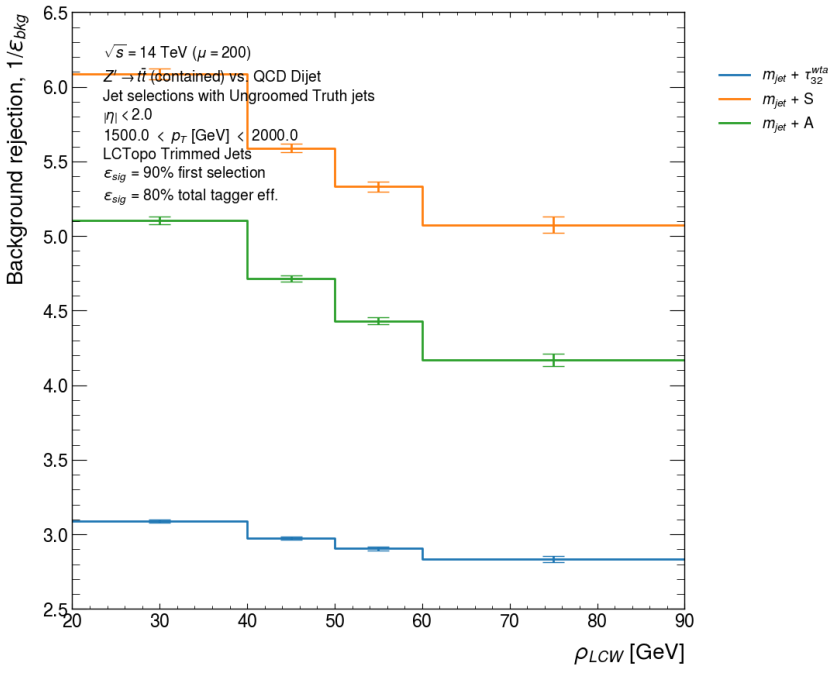

(e) Trimmed jets with $1500 < p_{\mathrm{T}}^{\mathrm{truth}}$ (GeV) < 2000

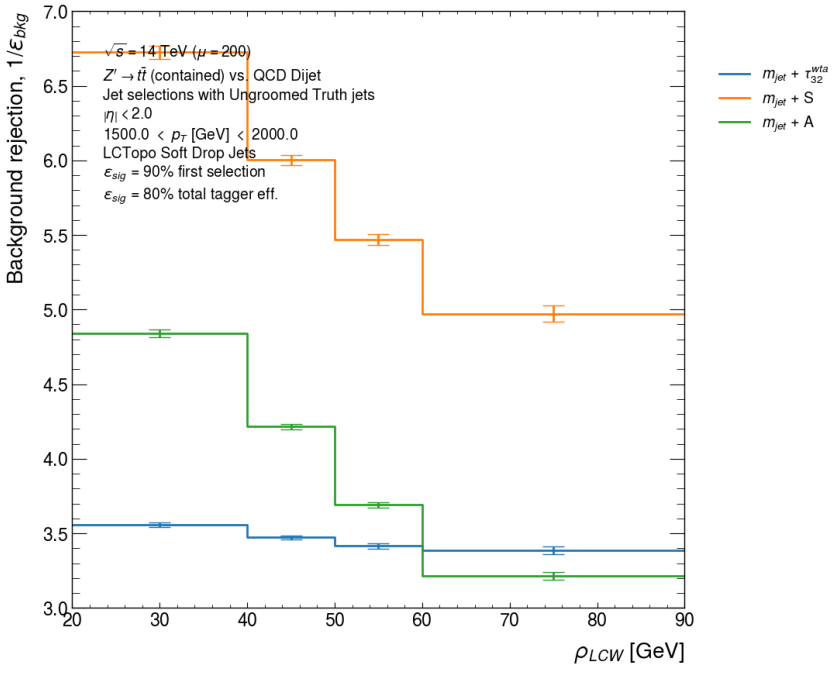

(f) Soft-drop jets with $1500 < p_{\mathrm{T}}^{\mathrm{truth}}$ (GeV) < 2000

Figure 7.34 (cont.): Pile-up stability profiles for the tagger background rejection as a function of the momentum density ρ_{LCW} for 80% signal efficiency trimmed and soft-drop jet taggers.

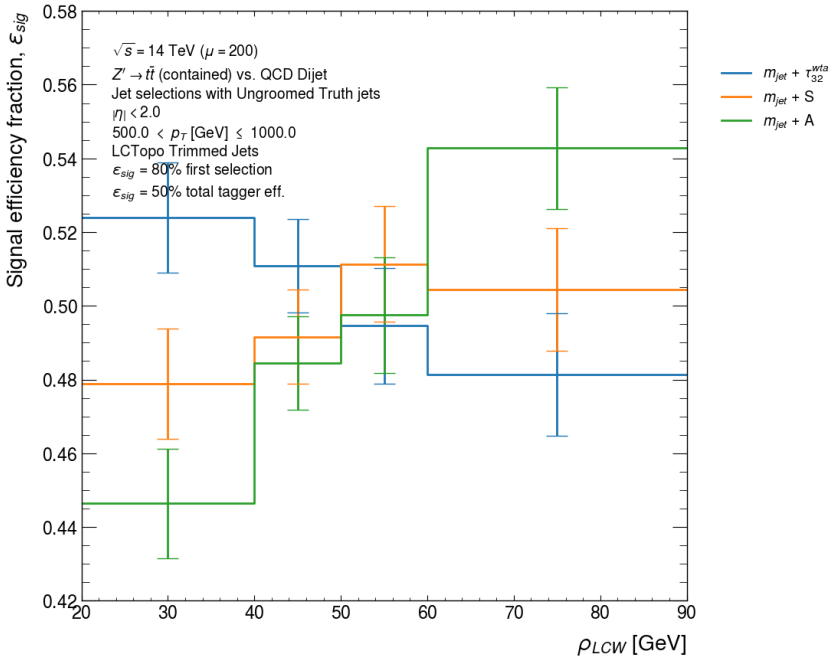

(a) Trimmed jets with $500 < p_{\mathrm{T}}^{\mathrm{truth}}$ (GeV) ≤ 1000

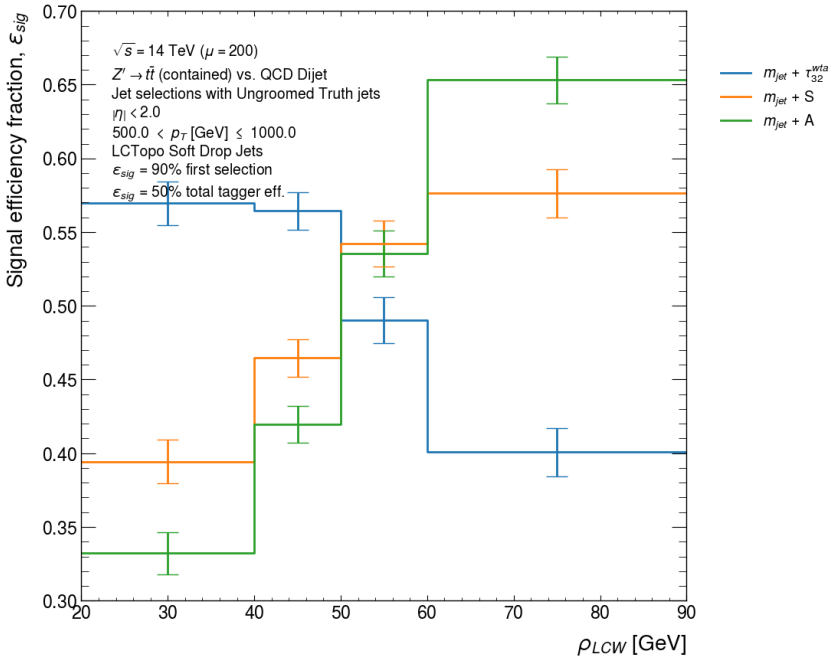

(b) Soft-drop jets with $500 < p_{\mathrm{T}}^{\mathrm{truth}}$ (GeV) ≤ 1000

Figure 7.35: Pile-up stability profiles for the tagger signal efficiency as a function of the momentum density ρ_{LCW} for 50% signal efficiency trimmed and soft-drop jet taggers.

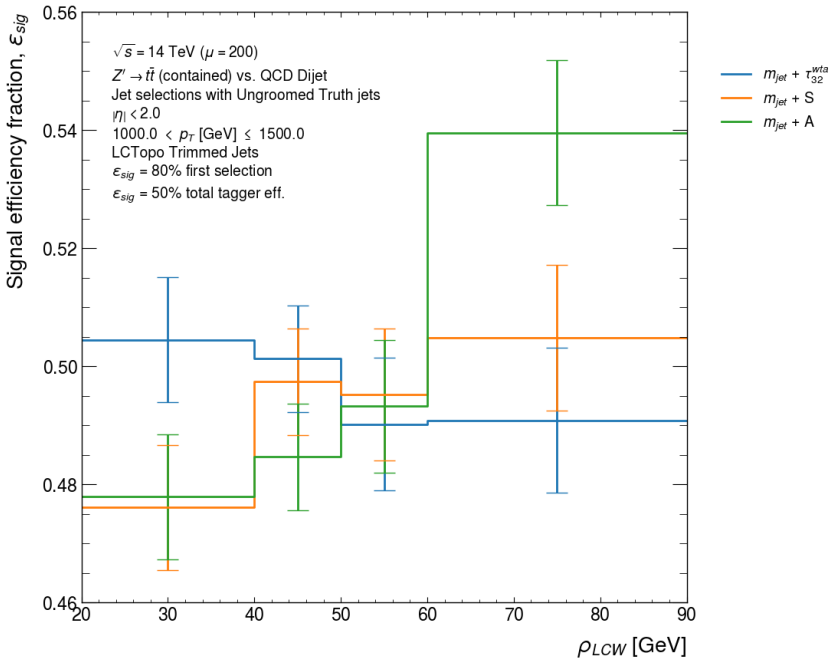

(c) Trimmed jets with $1000 < p_{\mathrm{T}}^{\mathrm{truth}}$ (GeV) ≤ 1500

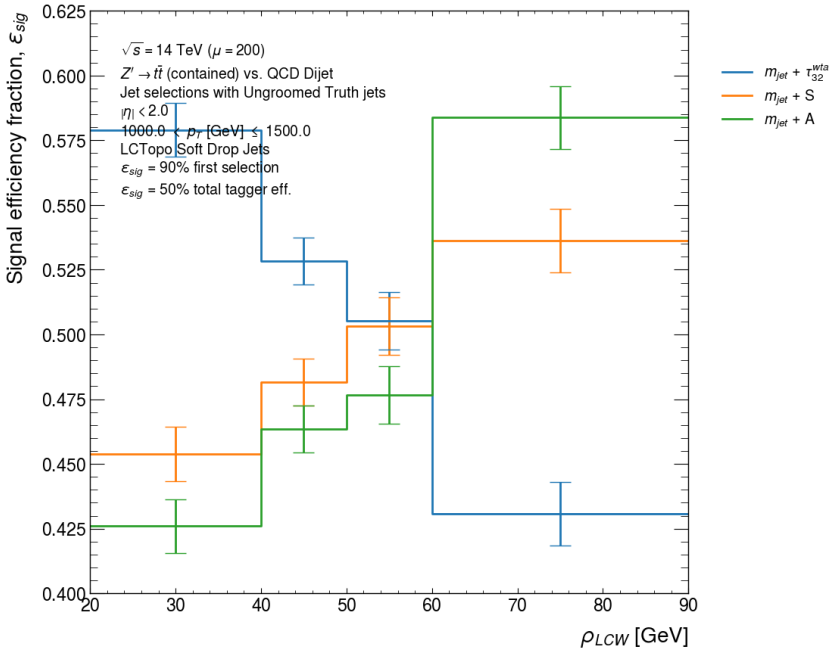

(d) Soft-drop jets with $1000 < p_{\mathrm{T}}^{\mathrm{truth}}$ (GeV) ≤ 1500

Figure 7.35 (cont.): Pile-up stability profiles for the tagger signal efficiency as a function of the momentum density ρ_{LCW} for 50% signal efficiency trimmed and soft-drop jet taggers.

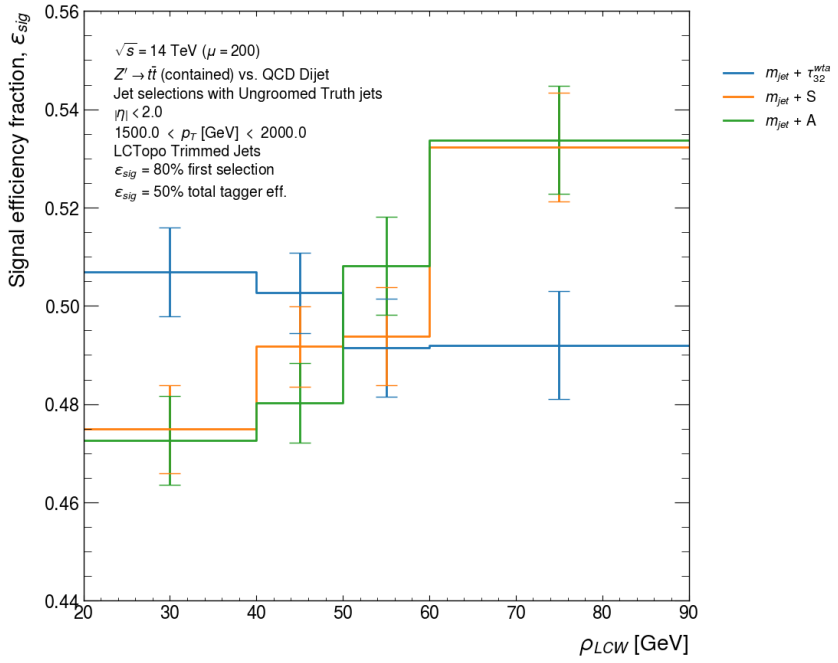

(e) Trimmed jets with $1500 < p_{\mathrm{T}}^{\mathrm{truth}}$ (GeV) < 2000

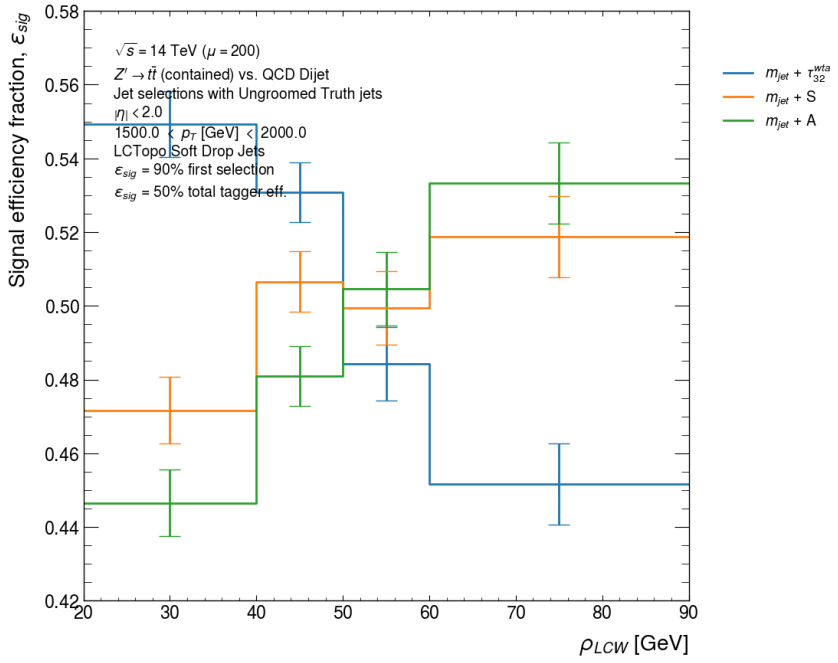

(f) Soft-drop jets with $1500 < p_{\mathrm{T}}^{\mathrm{truth}}$ (GeV) < 2000

Figure 7.35 (cont.): Pile-up stability profiles for the tagger signal efficiency as a function of the momentum density ρ_{LCW} for 50% signal efficiency trimmed and soft-drop jet taggers.

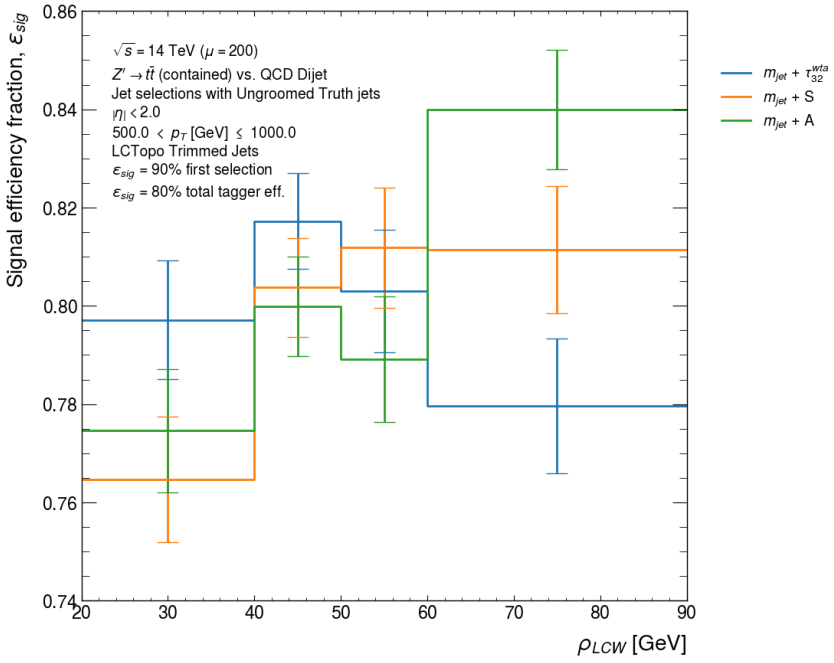

(a) Trimmed jets with $500 < p_{\mathrm{T}}^{\mathrm{truth}}$ (GeV) ≤ 1000

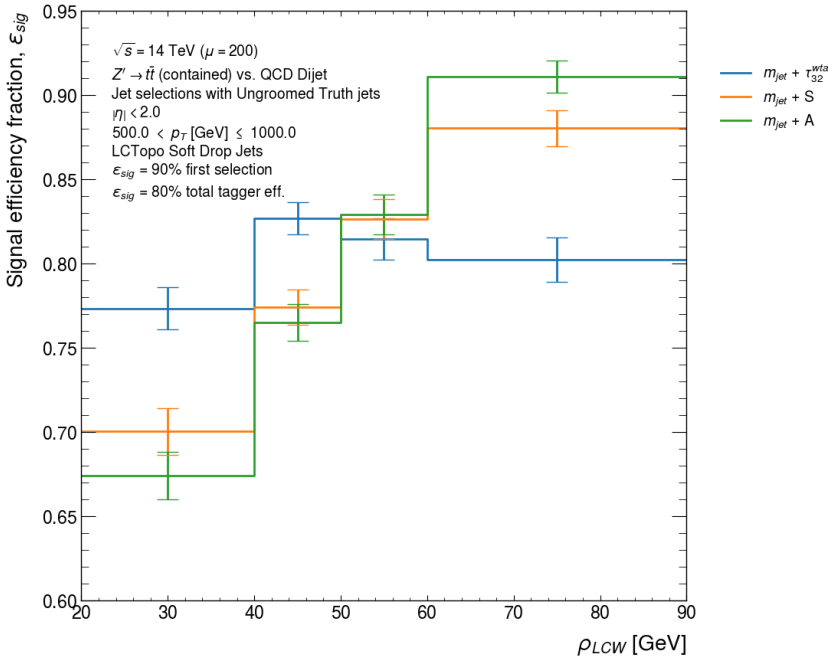

(b) Soft-drop jets with $500 < p_{\mathrm{T}}^{\mathrm{truth}}$ (GeV) ≤ 1000

Figure 7.36: Pile-up stability profiles for the tagger signal efficiency as a function of the momentum density ρ_{LCW} for 80% signal efficiency trimmed and soft-drop jet taggers.

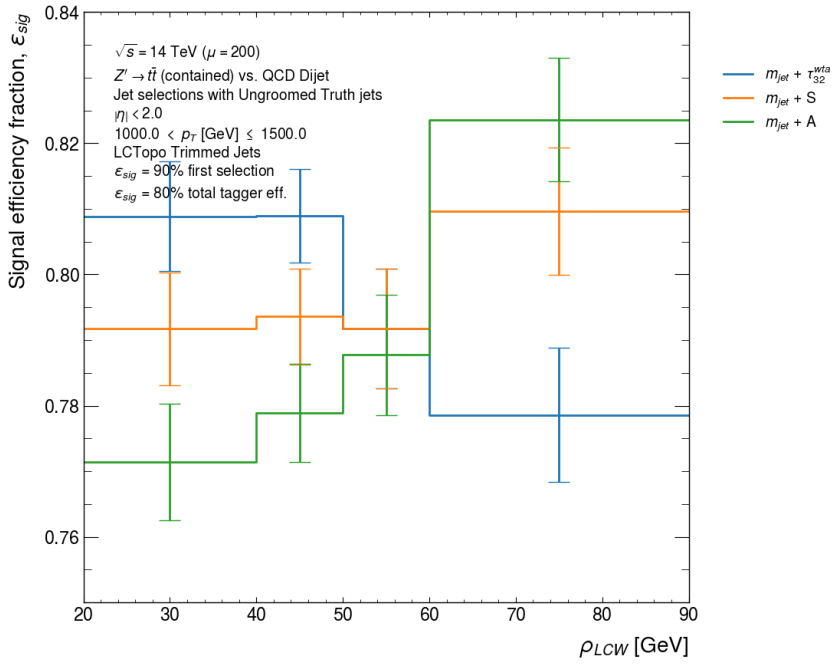

(c) Trimmed jets with $1000 < p_{\mathrm{T}}^{\mathrm{truth}}$ (GeV) ≤ 1500

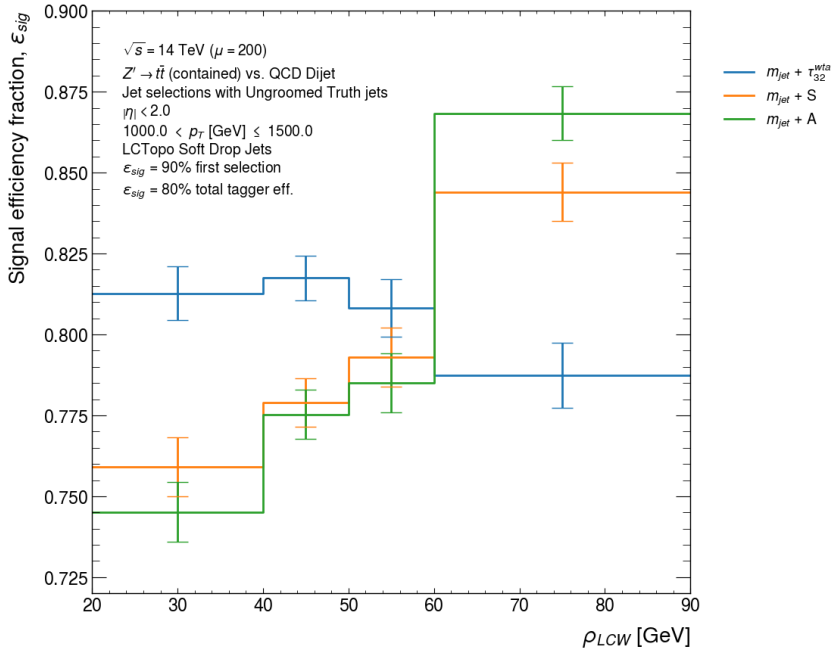

(d) Soft-drop jets with $1000 < p_{\mathrm{T}}^{\mathrm{truth}}$ (GeV) ≤ 1500

Figure 7.36 (cont.): Pile-up stability profiles for the tagger signal efficiency as a function of the momentum density ρ_{LCW} for 80% signal efficiency trimmed and soft-drop jet taggers.

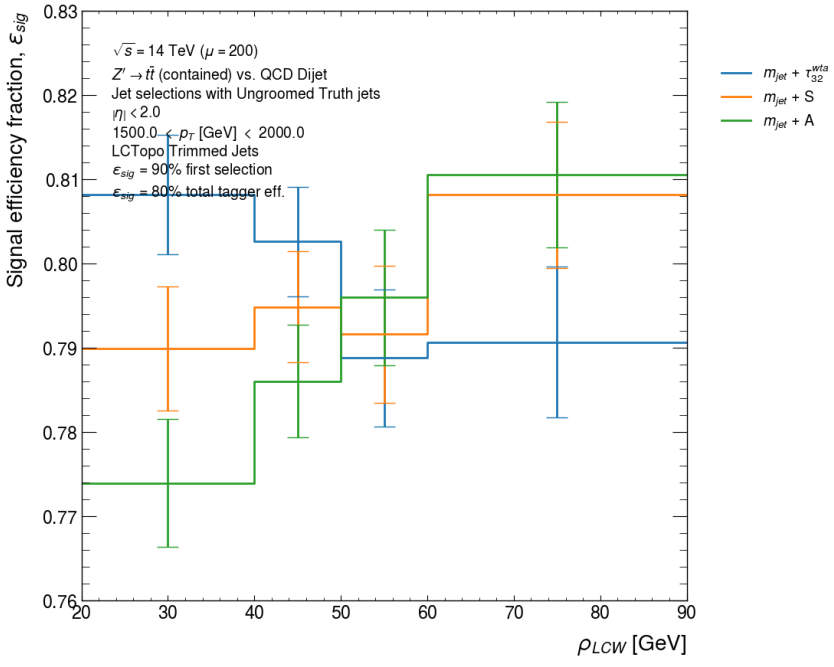

(e) Trimmed jets with $1500 < p_{\mathrm{T}}^{\mathrm{truth}}$ (GeV) < 2000

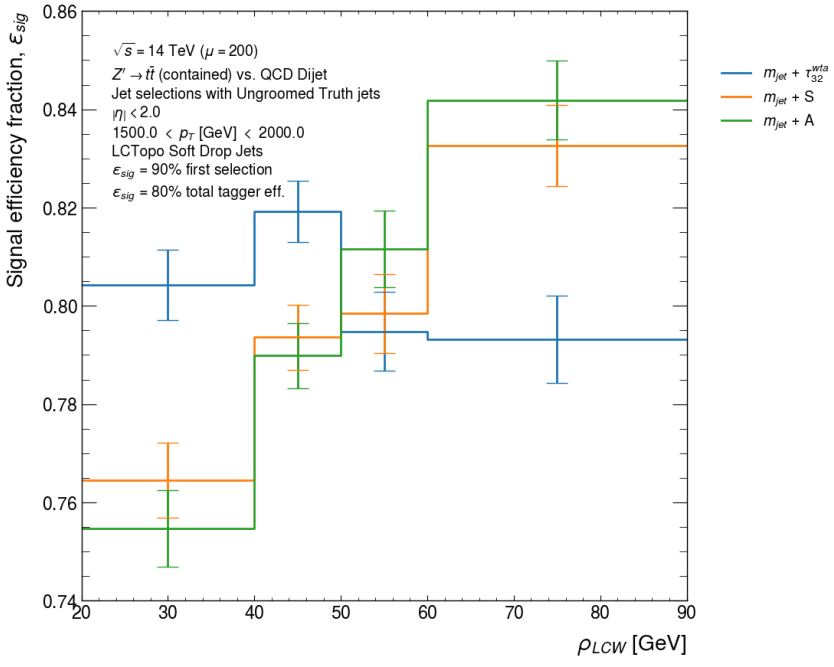

(f) Soft-drop jets with $1500 < p_{\mathrm{T}}^{\mathrm{truth}}$ (GeV) < 2000

Figure 7.36 (cont.): Pile-up stability profiles for the tagger signal efficiency as a function of the momentum density ρ_{LCW} for 80% signal efficiency trimmed and soft-drop jet taggers.

7.10.2 Jet response stability

The jet response calculated as the ratio of the reconstructed jet to truth jet observable was considered for individual observables to estimate their pile-up stability. We only considered the QCD background sample due to its high level of statistics and implemented the same jet matching procedure as for the signal sample, but without any truth particle matching. The jet response was derived in bins of the (groomed) truth jet p_{T} with the same $|\eta|$ selection ($|\eta| < 2$) applied for previous results[10]. The same ρ_{LCW} bins as in Section 7.10 were used. Normally the jet response is derived after applying a jet isolation requirement that requires truth and reconstructed jets to be well separated [134] – no such requirements were considered here since we only saved 2 jets per event in the datasets used for the tagging studies. Thus, the application of isolation requirements may alter the results presented in this Section.

Since the response distributions are typically non-Gaussian, they were parameterised in terms of the *scale* (median), *resolution* (half the 68.27% central[11] inter-quantile range [IQnR]), and *fractional resolution* (resolution divided by scale) [134] for each distribution. Additional selections were imposed on the reconstructed and truth jets, including[12]:

- A $m_{\mathrm{jet}} > 40$ GeV selection for both reconstructed and truth jets – this brought the jet mass above the minimum mass threshold typically used for calibrated large-R jets.
- A requirement that reconstructed jets had at least 3 constituents (i.e. for top quark tagging) to prevent unexpected features resulting from the merging of jet constituents at high-p_{T}.

The jet response for only a select few observables of interest is discussed here including m_{jet}, aplanarity, sphericity, τ_{32}^{wta}, τ_{3}^{wta}, and τ_{2}^{wta}. The median response (scale) and IQnR resolution metric are shown in Figures 7.41 and 7.42, respectively, for trimmed jet observables as a function of both the truth jet p_{T} and ρ_{LCW}. The same plots are shown for soft-drop jets in Figures 7.43 and 7.44, respectively. Profiles of the scale, resolution, and fractional resolution as a function of ρ_{LCW} are shown in Figures 7.39 and 7.40 for trimmed and soft-drop jets in a low-p_{T} ($350 < p_{\mathrm{T}}$ [GeV] ≤ 800) and high-p_{T} ($2000 < p_{\mathrm{T}}$ [GeV] < 2500) bin, respectively. Additional jet response histograms for m_{jet}, aplanarity, sphericity, and τ_{32}^{wta} are included in Appendix H.

The complete variation of the jet response metrics combines the effect of the increasing jet p_{T} and increasing ρ_{LCW}. The former change leads to further collimation of the

[10] This is different to the ungroomed truth p_{T} binning of the initial tagger performance studies since we rely on the (groomed) truth jets in the response calculation. Thus, the trimmed jet response is binned in the p_{T} of the truth trimmed jet (and vice versa).

[11] That is, the difference between the $\sim 16\%$ and $\sim 84\%$ quantiles.

[12] The author thanks Josu Cantero Garcia for his input regarding troubleshooting the jet response with these jet selections.

jet constituents (decreased angular separation), and impacts the ability to resolve constituents of high-p_{T} jets due to the finite calorimeter granularity. This is evident for m_{jet} where the resolution (half the IQnR) increases[13] with jet p_{T} for trimmed jets in Figure 7.41f. Different behaviour is seen for the soft-drop jets in Figure 7.43f where the resolution decreases as the truth jet p_{T} increases – some of this variation could be related to the extensive tails of the soft-drop jet mass distribution at low-p_{T}. When ρ_{LCW} increases, different effects are seen depending on the observable considered. The interpretation of an increase in ρ_{LCW} as an increase in pile-up activity means that more (typically) soft radiation is added to the jets. For m_{jet}, this leads to an overall increase in the reconstructed m_{jet} and the distribution broadens. Hence, the mass resolution metrics and the median response (the jet mass scale) increase as a function of ρ_{LCW} for the trimmed and soft-drop jets. But, for other observables (e.g. τ_{32}^{wta}) certain metrics (i.e. the resolution and fractional resolution) decrease with increasing ρ_{LCW}, primarily in the high-p_{T} bin.

Different behaviour is seen at low-p_{T} where the τ_{32}^{wta} resolution increases with ρ_{LCW} as expected for distributions that broaden with the addition of soft radiation. Some of this behaviour could arise from the combined change in τ_3^{wta} and τ_2^{wta}. If τ_3^{wta} and τ_2^{wta} have similar pile-up dependence, some variation might partially cancel in the $\tau_3^{\mathrm{wta}}/\tau_2^{\mathrm{wta}}$ ratio. Alternatively, the different trends at low- and high-p_{T} might result from differences in the amount of hard-scatter radiation that contaminates ρ_{LCW} – since the calculation of ρ_{LCW} favours soft radiation this effect is less likely to explain the trends. The potential impact of hard-scatter contributions to ρ_{LCW} is motivated by Figure 7.37 where a departure from the smoothly falling p_{T} distributions of truth-level trimmed and soft-drop jets is seen just before the upper edge of the final $2000 < p_{\mathrm{T}}\ [\mathrm{GeV}] < 2500$ bin. When the ρ_{LCW} selection is removed, the distributions fall smoothly in Figure 7.38, lending credibility to an explanation that involves some extent of hard-scatter contamination[14]. This behaviour suggests that low-p_{T} performance, where we expect to see a greater fraction of pile-up radiation, is most important for the pile-up stability considerations. Nonetheless, the complete p_{T} and ρ_{LCW} variation is needed to fully describe the observed jet response changes.

The low-p_{T} ($350 < p_{\mathrm{T}}^{\mathrm{truth}}\ [\mathrm{GeV}] \leq 800$) behaviour of the trimmed jet response resolution metric in Figures 7.39c and 7.39e indicates that the aplanarity response distributions are wider than the sphericity response distributions. In the same p_{T} bin, the scale (median response) of the QCD jet aplanarity in Figure 7.39a is larger than that for sphericity. Thus, the sphericity observable appears less pile-up affected since the reconstructed observable is more comparable to the truth-level observable. Whereas the fractional resolution of the trimmed jet aplanarity increases by a smaller amount than for sphericity as a function of ρ_{LCW}, which indicates that aplanarity is more stable at low-p_{T} if the relative magnitude of the resolution metrics are not taken into account. The low-p_{T} soft-drop jet response metrics in Figures 7.39b,

[13] A small decrease is evident in the second p_{T} bin, but the increasing trend continues at higher p_{T}.
[14] As noted in the caption of Figure 7.37, further consideration of these features, which are not completely understood, is left to future work.

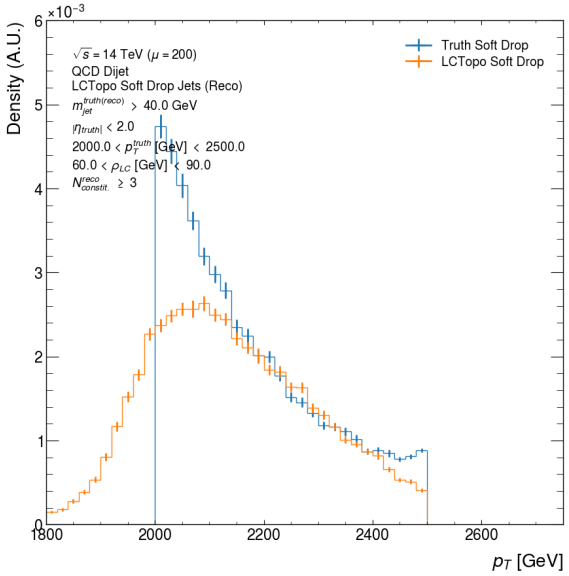

(a) Soft-drop groomed jets.

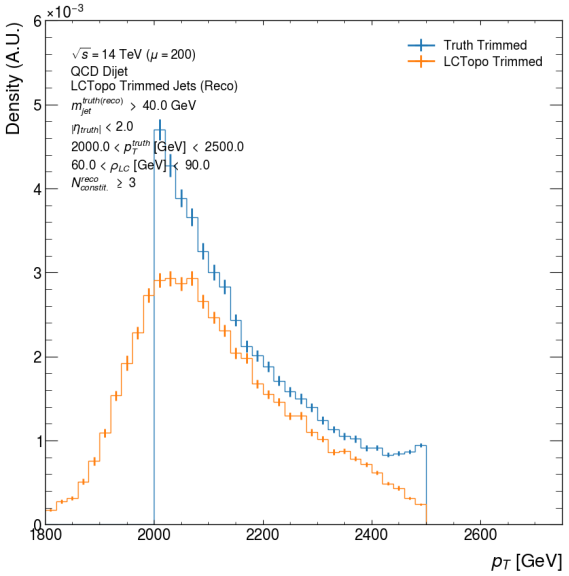

(b) Trimmed jets.

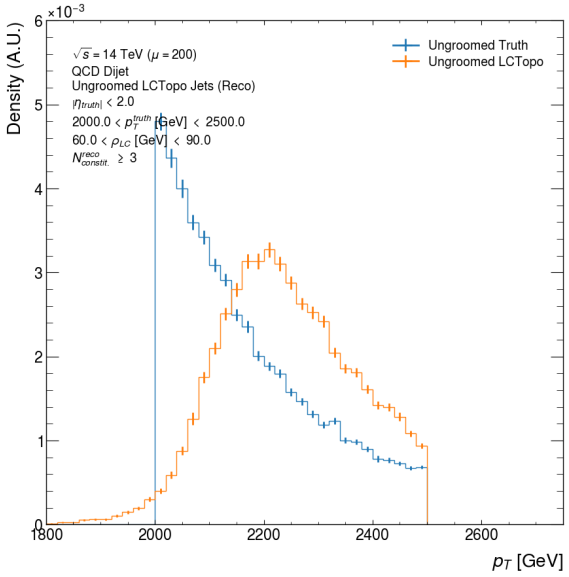

(c) Ungroomed jets.

Figure 7.37: A jet p_{T} distribution comparison for the reconstructed and truth jets in the $2000 < p_{\mathrm{T}}^{\mathrm{truth}}$ (GeV) < 2500 and $60 < \rho_{\mathrm{LCW}}$ (GeV) < 90 bin. The jet selections here were modified such that the reconstructed jets had all truth-level selections except the truth jet mass selection. The truth-level jets only had the truth-level selections (i.e. no selection on the number of jet constituents or the mass of the reconstructed jets). Note the departure from the smoothly falling truth-jet p_{T} distribution in the high-p_{T} tails. This could be related to contamination from hard-scatter jets, which would occupy the high-ρ_{LCW} tail in Figure 7.32. However, more work is needed to completely understand these features.

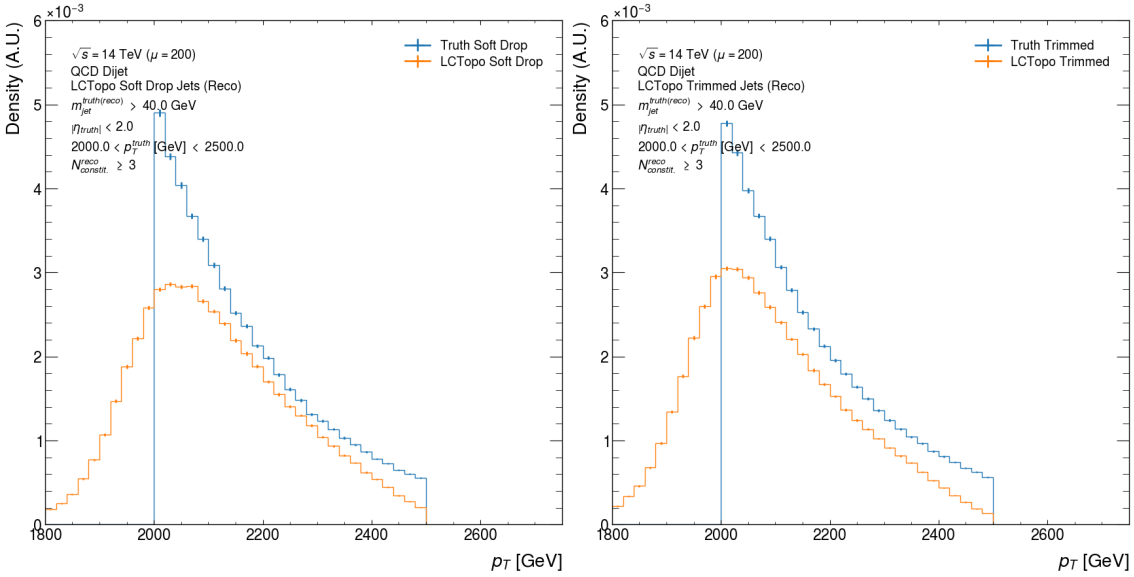

(a) Soft-drop groomed jets.

(b) Trimmed jets.

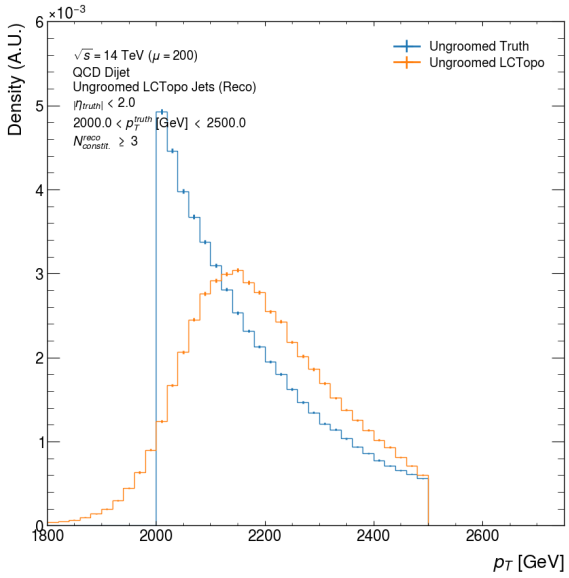

(c) Ungroomed jets.

Figure 7.38: Jet p_{T} distribution comparison for the reconstructed and truth jets in the $2000 < p_{\mathrm{T}}^{\mathrm{truth}}$ (GeV) < 2500 bin *without* ρ_{LCW} selections. The jet selections here were modified such that the reconstructed jets had all truth-level selections except the truth jet mass selection. The truth-level jets only had the truth-level selections (i.e. no selection on the number of jet constituents or the mass of the reconstructed jets). A smoothly falling distribution for the truth trimmed jet p_{T} results from the removal of the high-ρ_{LCW} selection.

7.39d, and 7.39f show similar relative variation for aplanarity and sphericity, but the fractional resolution of the sphericity observable is larger than for the aplanarity observable in each ρ_{LCW} bin. Thus, sphericity appears to be less succeptible to pile-up than aplanarity *primarily* for trimmed jets, which is consistent with the tagger stability conclusions from Section 7.10.1. However, it is difficult to relate the response of individual observables to the tagger performance without the same jet mass selections.

A note on the jet response distributions

Unexpected spikes are seen in the first bin of certain jet response distributions. These features appear in several p_{T} bins and could be a consequence of:

- Cases where the observables are shifted towards zero for the QCD background (a continuous "spike" in the first bin of the distributions for reconstructed observables).
- Cases where the reconstructed observable is zero (e.g. for the reconstructed jet τ_{32}^{wta} evident in Figure 7.8 from Section 7.5).

These features are highlighted for the trimmed jet aplanarity and sphericity response in Figure 7.45 with a spike seen in the first bin of the $2000 < p_{\text{T}}^{\text{truth}}$ (GeV) < 2500 histograms. This behaviour is *not* isolated to the high-ρ_{LCW} bins where we expect any hard-scatter contributions to be most significant. However, the absence of these features in the distributions for low-p_{T} jets seems to suggest that they are in some way linked to the jet p_{T} and potentially the selections applied to jets. The comparison of jet response distributions where the reconstructed jets have both vanishing and non-vanishing observables leads to the conclusion that the behaviour is not solely explained by the second option listed above. In Figure 7.46 the contribution in the first bin from the histogram, where the reconstructed observable is zero, is negligible. These features were further understood by considering the correlation between the reconstructed and truth observables (Figures 7.47a and 7.47b for aplanarity and sphericity, respectively), and the number of jet constituents and the jet response (Figures 7.48a and 7.48b for aplanarity and sphericity, respectively)[15]. The values of both reconstructed and truth-level observables are close to zero given the clustering of the distributions in Figures 7.47a and 7.47b near the origin. However, the correlation of the number of (reconstructed) jet constituents with the jet response indicates an apparent reduction in the number of jet constituents in the first response bin shown in Figures 7.48a and 7.48b. Therefore, the features we see in the jet response *could be linked* to the number of constituents of the reconstructed jets (especially at high-p_{T} where calorimeter energy deposits can merge) combined with the shapes of the reconstructed distributions relative to their truth-level counterparts. Since the distribution of the QCD jet constituents in p_{T} is likely asymmetric, small values

[15]The author thanks Josu Cantero Garcia for his suggestions for troubleshooting these jet response distributions and his comments regarding their interpretation.

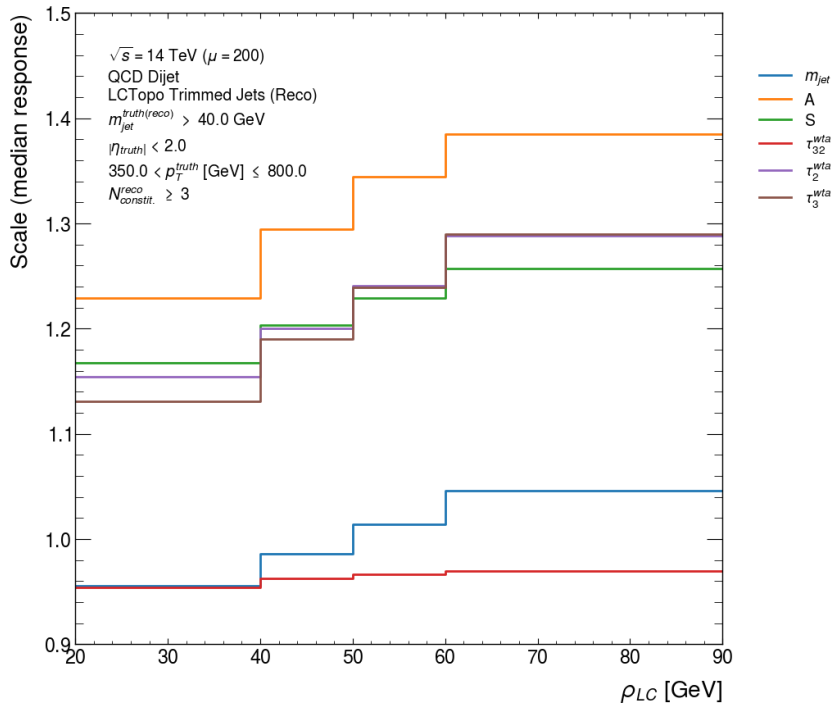

(a) Trimmed jet observable scale.

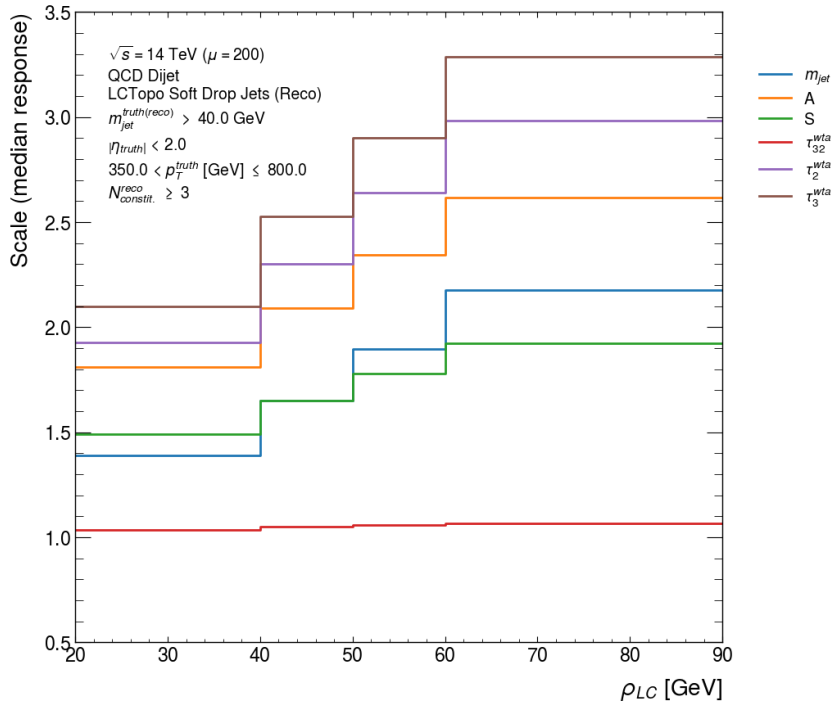

(b) Soft-drop jet observable scale.

Figure 7.39: Jet response metrics (scale, resolution, fractional resolution) as a function of ρ_{LCW} in a low-p_{T} $350 < p_{\mathrm{T}}$ (GeV) ≤ 800 bin. Plots are included for the trimmed and soft-drop jet observables.

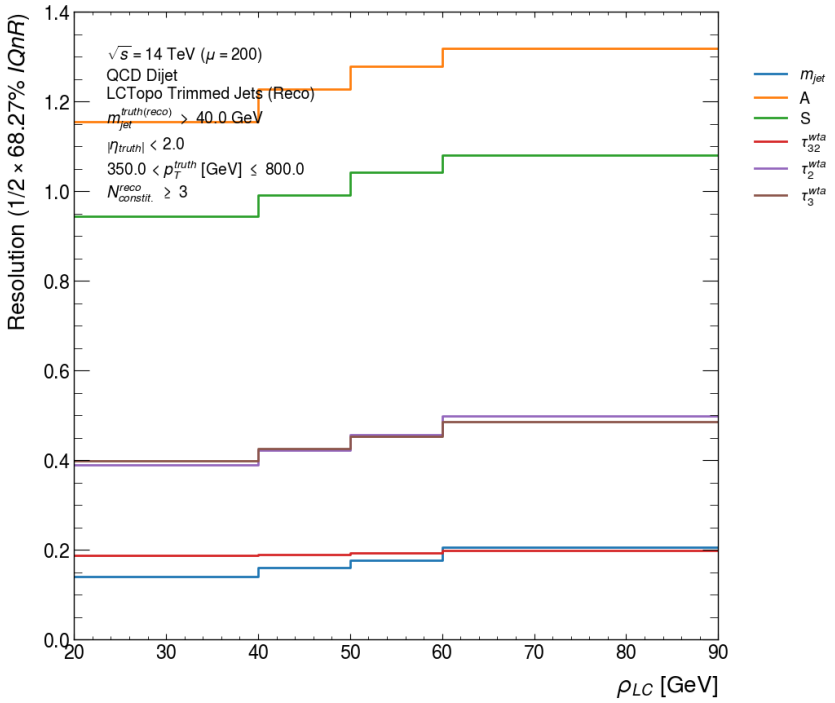

(c) Trimmed jet observable resolution.

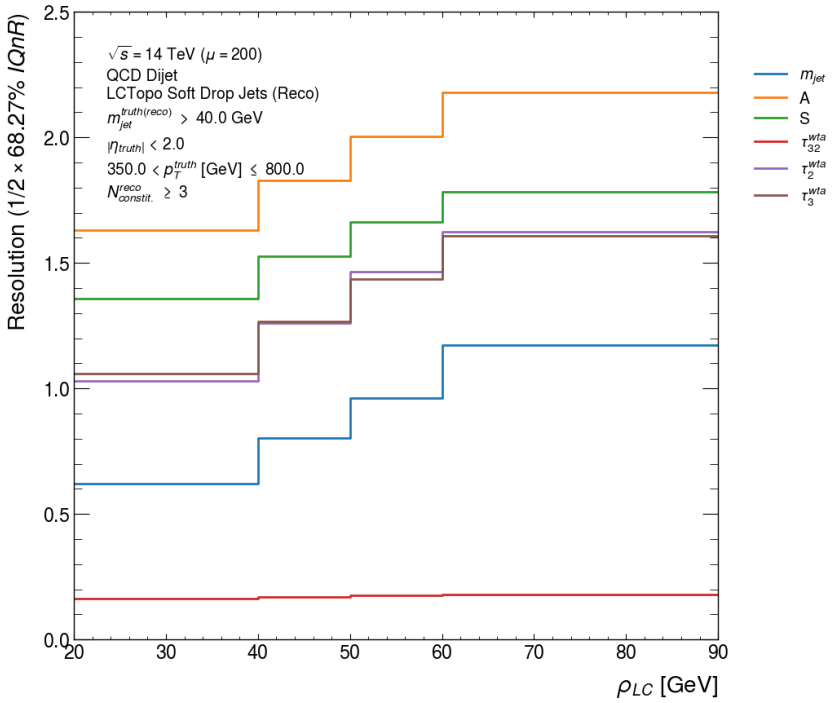

(d) Soft-drop jet observable resolution.

Figure 7.39 (cont.): Jet response metrics (scale, resolution, fractional resolution) as a function of ρ_{LCW} in a low-p_{T} $350 < p_{\mathrm{T}}$ (GeV) ≤ 800 bin. Plots are included for the trimmed and soft-drop jet observables.

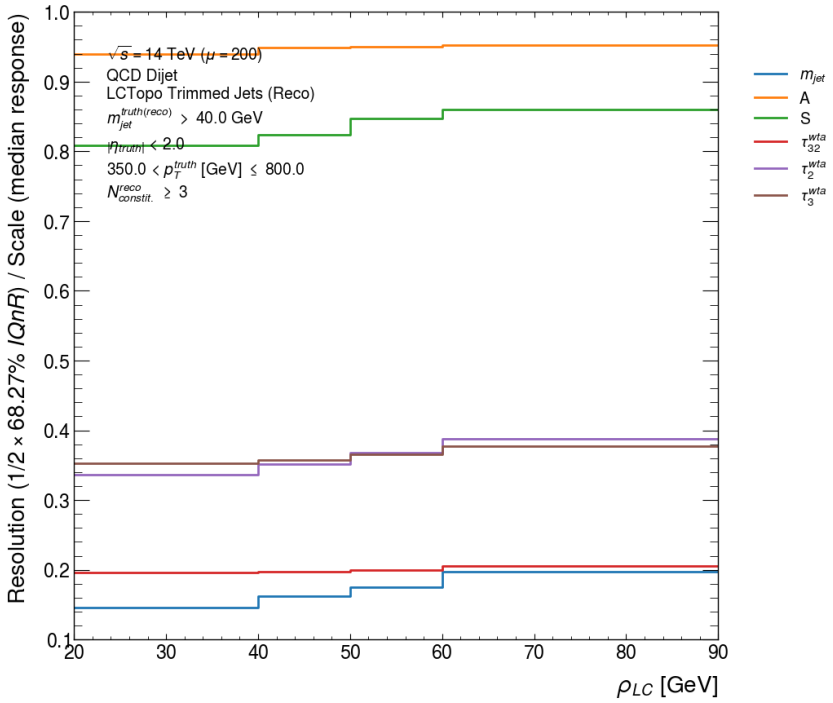

(e) Trimmed jet observable fractional resolution.

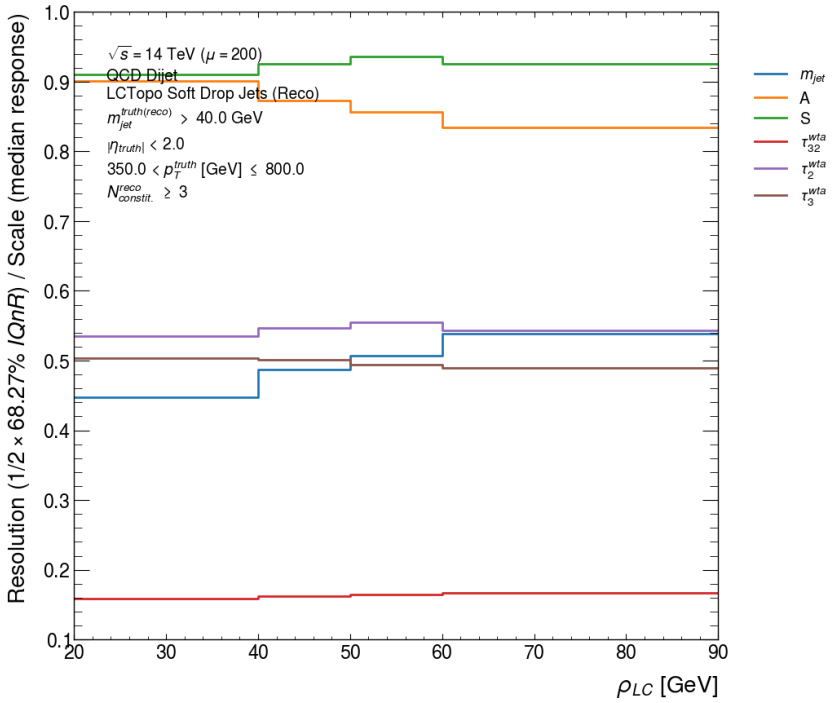

(f) Soft-drop jet observable fractional resolution.

Figure 7.39 (cont.): Jet response metrics (scale, resolution, fractional resolution) as a function of ρ_{LCW} in a low-p_{T} $350 < p_{\mathrm{T}}$ (GeV) ≤ 800 bin. Plots are included for the trimmed and soft-drop jet observables.

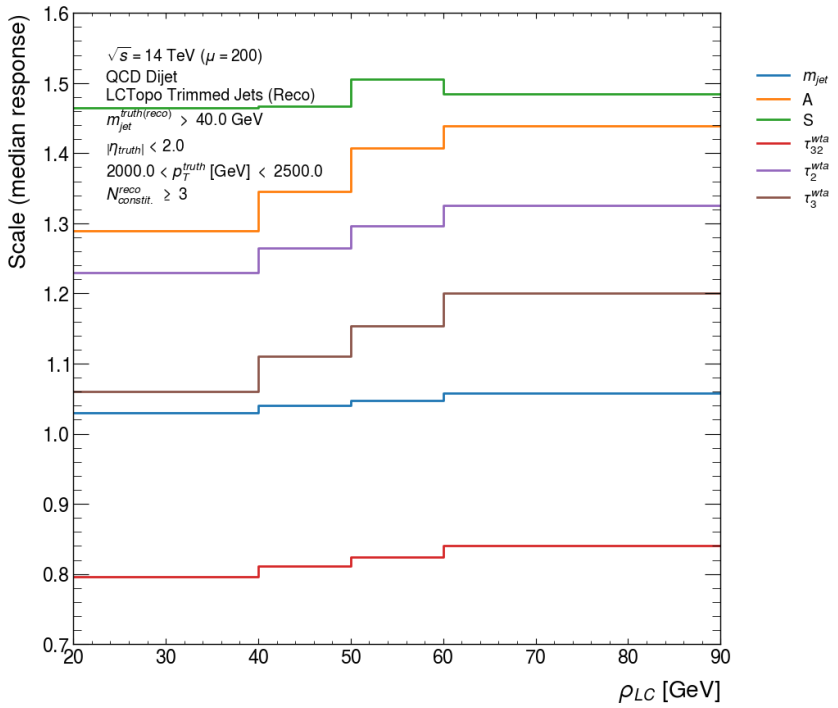

(a) Trimmed jet observable scale.

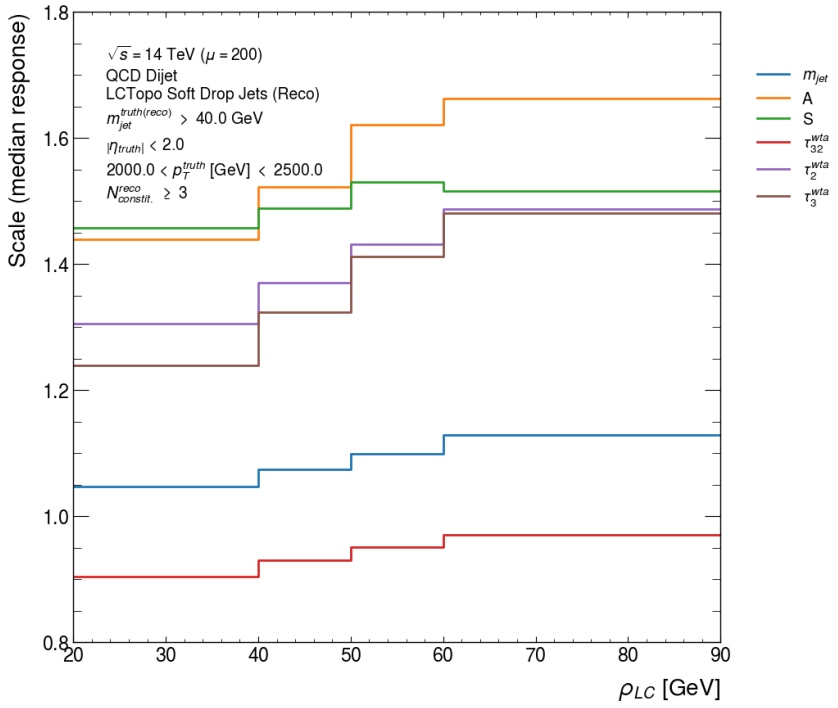

(b) Soft-drop jet observable scale.

Figure 7.40: Jet response metrics (scale, resolution, fractional resolution) as a function of ρ_{LCW} in a high-p_{T} $2000 < p_{\mathrm{T}}$ (GeV) < 2500 bin. Plots are included for the trimmed and soft-drop jet observables.

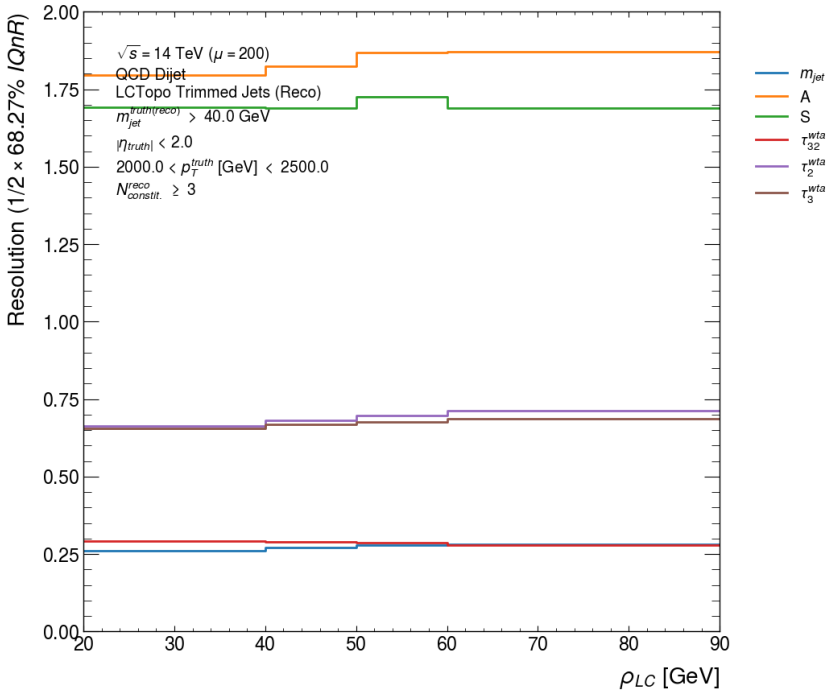

(c) Trimmed jet observable resolution.

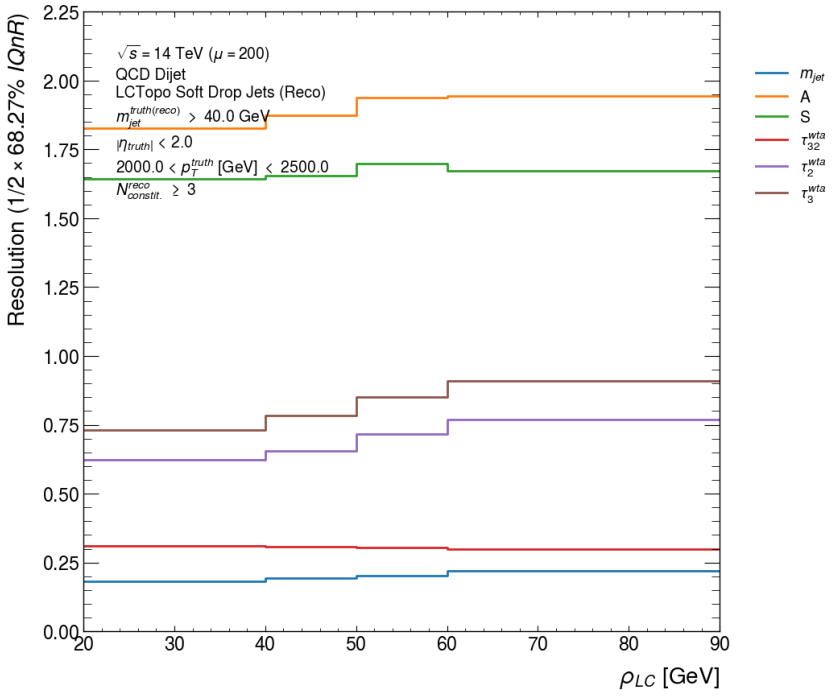

(d) Soft-drop jet observable resolution.

Figure 7.40 (cont.): Jet response metrics (scale, resolution, fractional resolution) as a function of ρ_{LCW} in a high-p_{T} $2000 < p_{\mathrm{T}}$ (GeV) < 2500 bin. Plots are included for the trimmed and soft-drop jet observables.

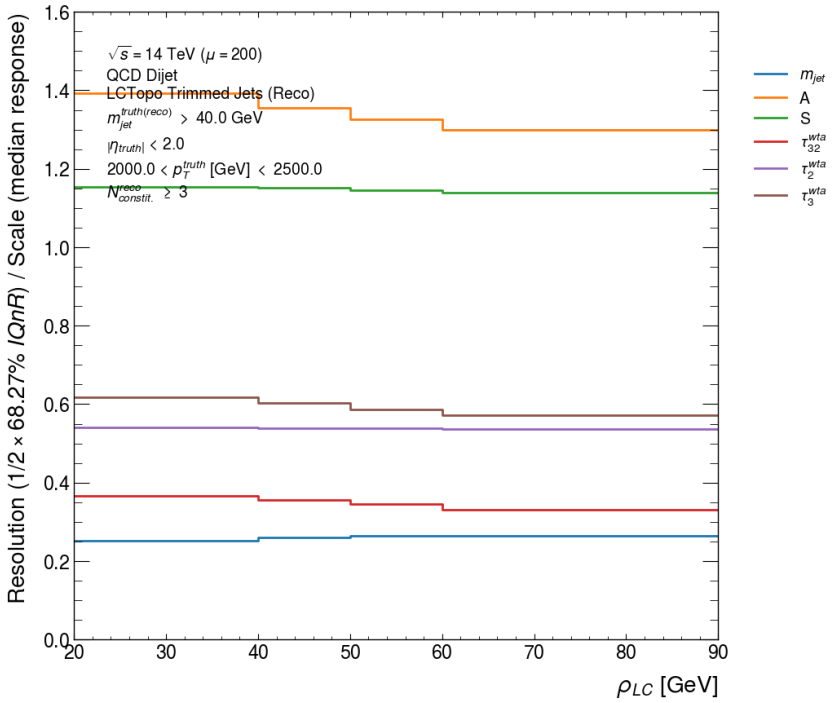

(e) Trimmed jet observable fractional resolution.

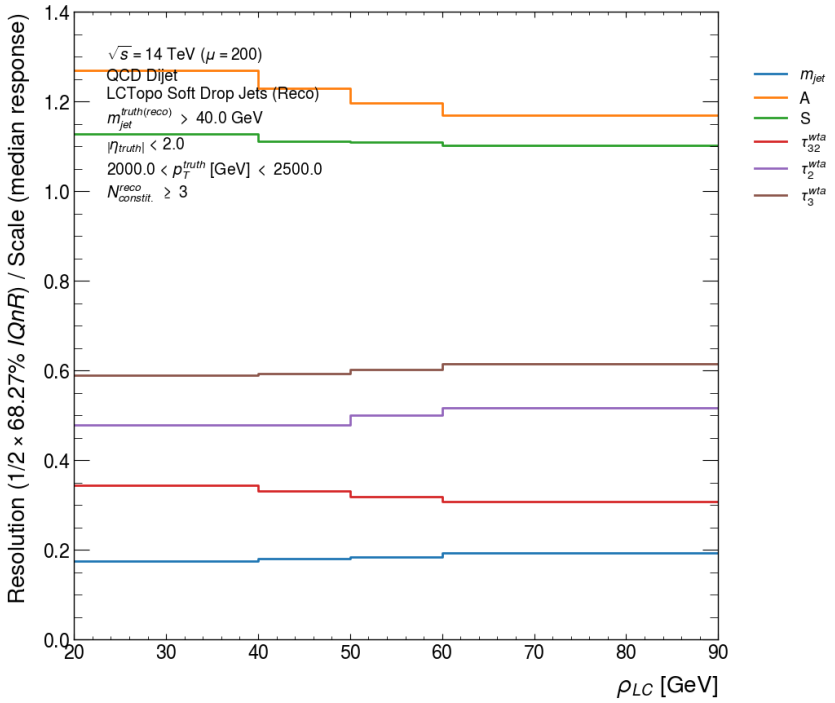

(f) Soft-drop jet observable fractional resolution.

Figure 7.40 (cont.): Jet response metrics (scale, resolution, fractional resolution) as a function of ρ_{LCW} in a high-p_{T} $2000 < p_{\mathrm{T}}$ (GeV) < 2500 bin. Plots are included for the trimmed and soft-drop jet observables.

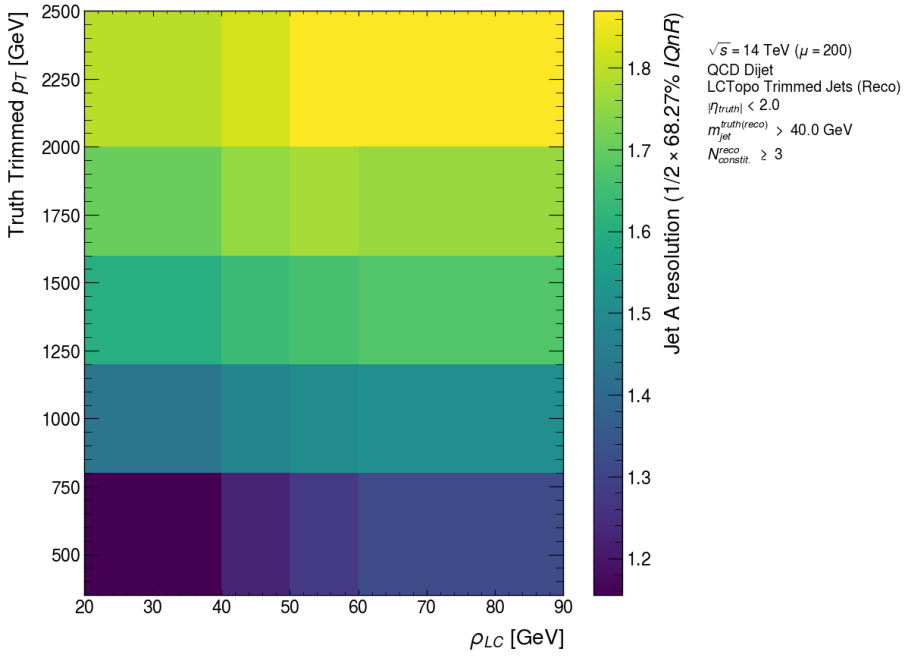

(a) Aplanarity

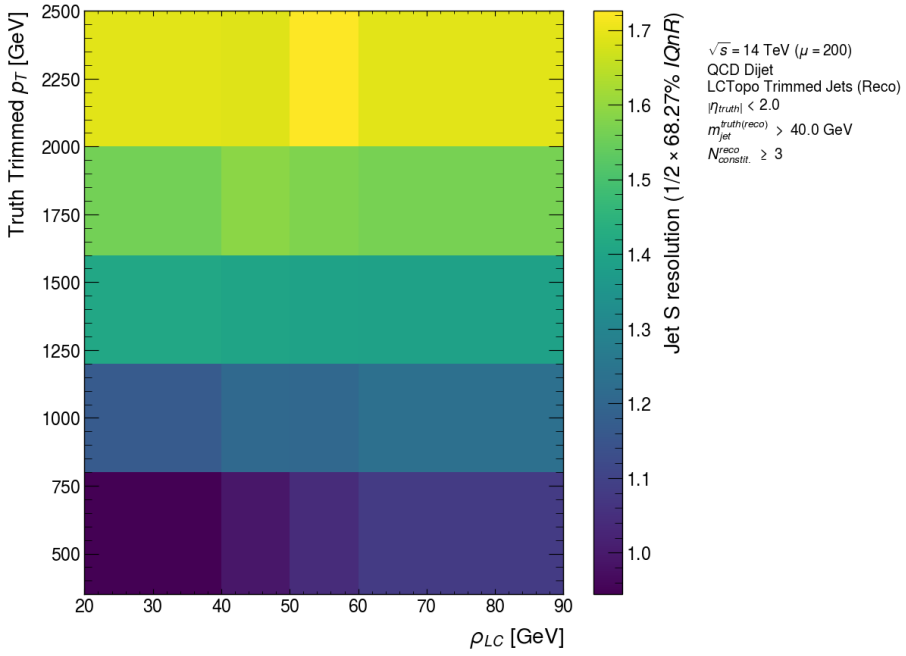

(b) Sphericity

Figure 7.41: Variation of observable response resolution (trimmed jets only) with the truth trimmed jet p_{T} and ρ_{LCW}. Plots are included for the aplanarity, sphericity, and jet mass in addition to the τ_2^{wta}, τ_2^{wta}, and τ_{32}^{wta} observables.

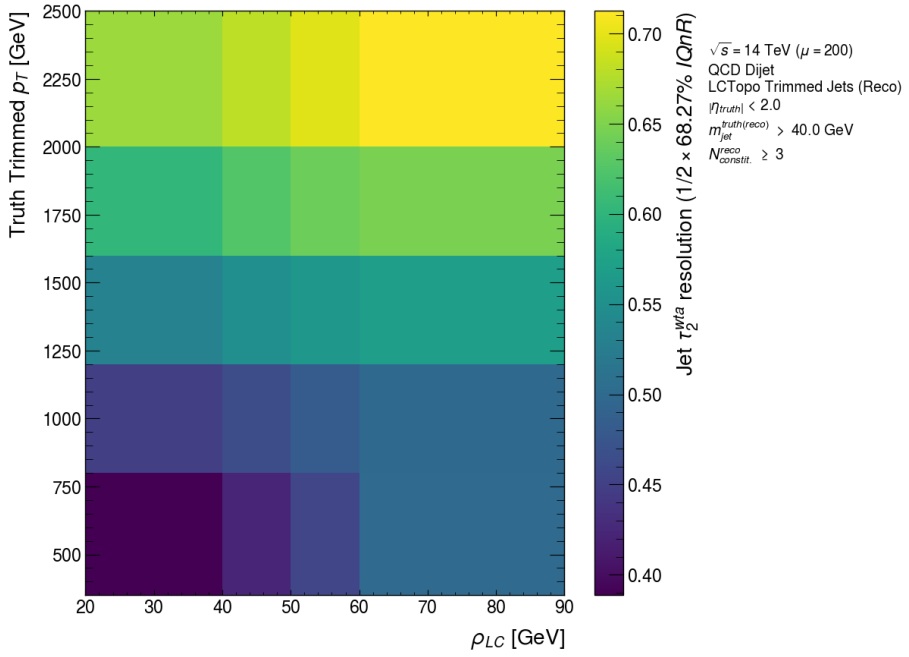

(c) τ_2^{wta}

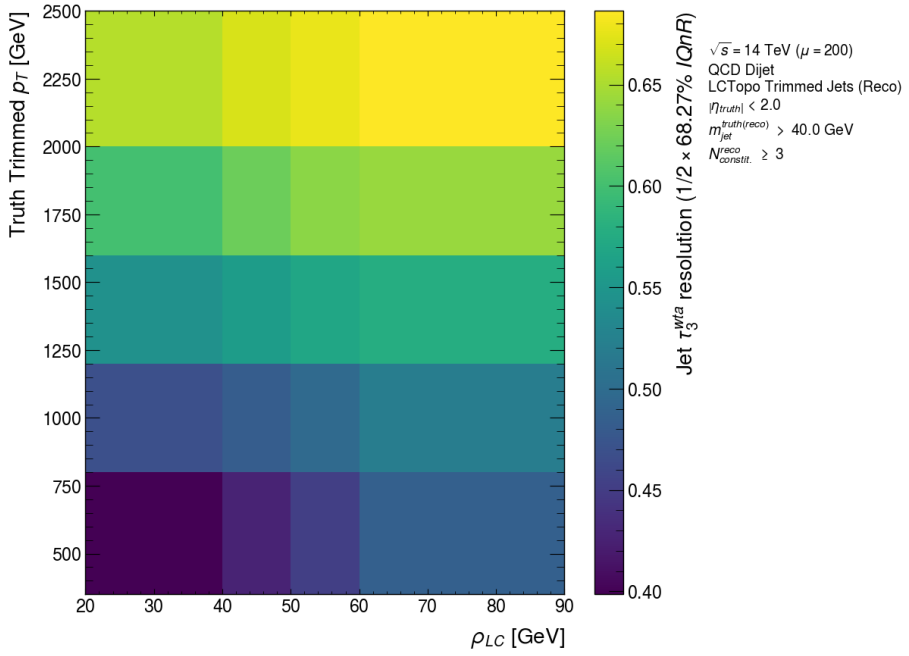

(d) τ_3^{wta}

Figure 7.41 (cont.): Variation of observable response resolution (trimmed jets only) with the truth trimmed jet p_{T} and ρ_{LCW}. Plots are included for the aplanarity, sphericity, and jet mass in addition to the τ_2^{wta}, τ_2^{wta}, and τ_{32}^{wta} observables.

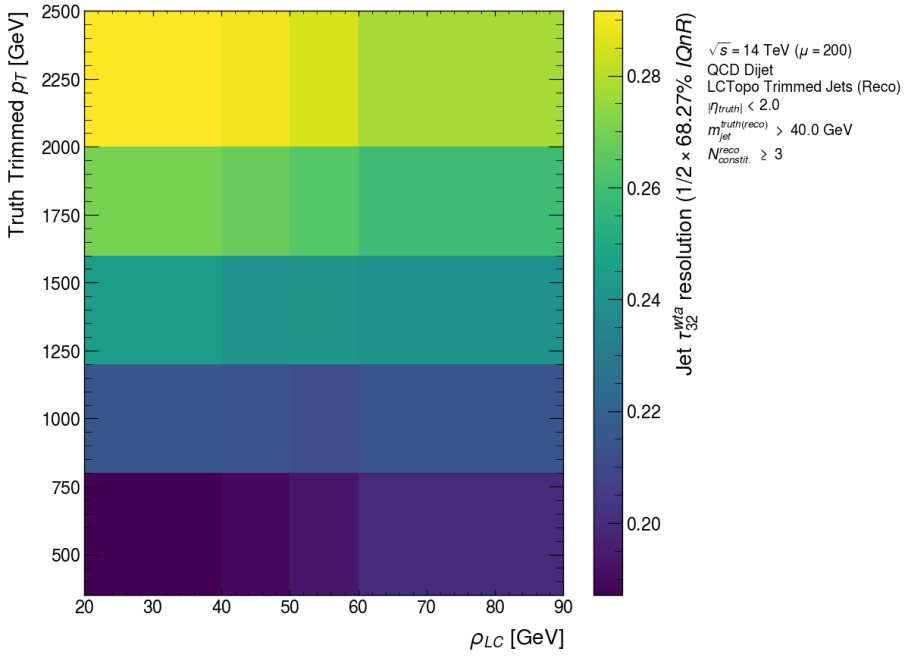

(e) τ_{32}^{wta}

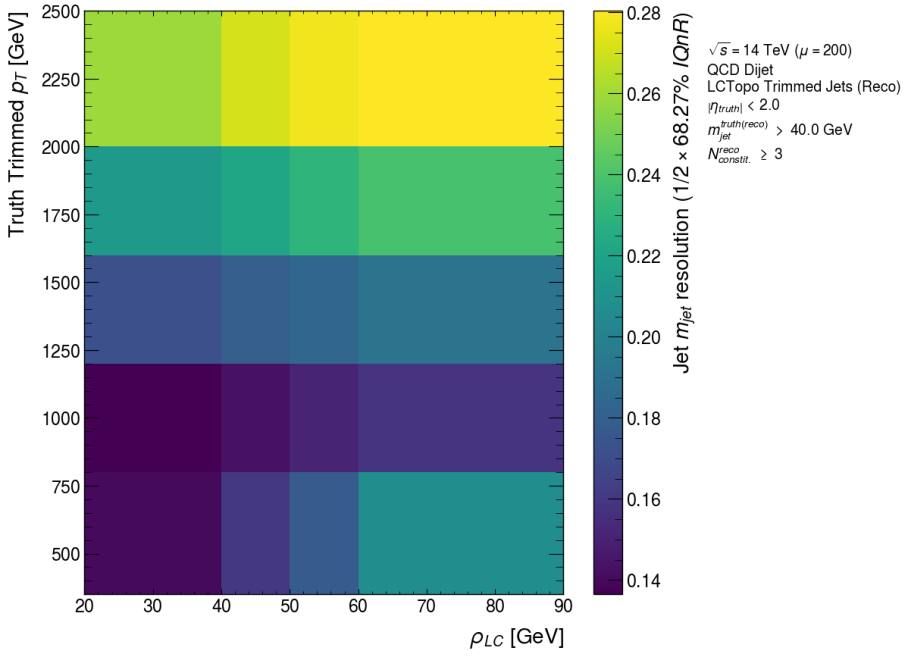

(f) m_{jet}

Figure 7.41 (cont.): Variation of observable response resolution (trimmed jets only) with the truth trimmed jet p_{T} and ρ_{LCW}. Plots are included for the aplanarity, sphericity, and jet mass in addition to the τ_2^{wta}, τ_2^{wta}, and τ_{32}^{wta} observables.

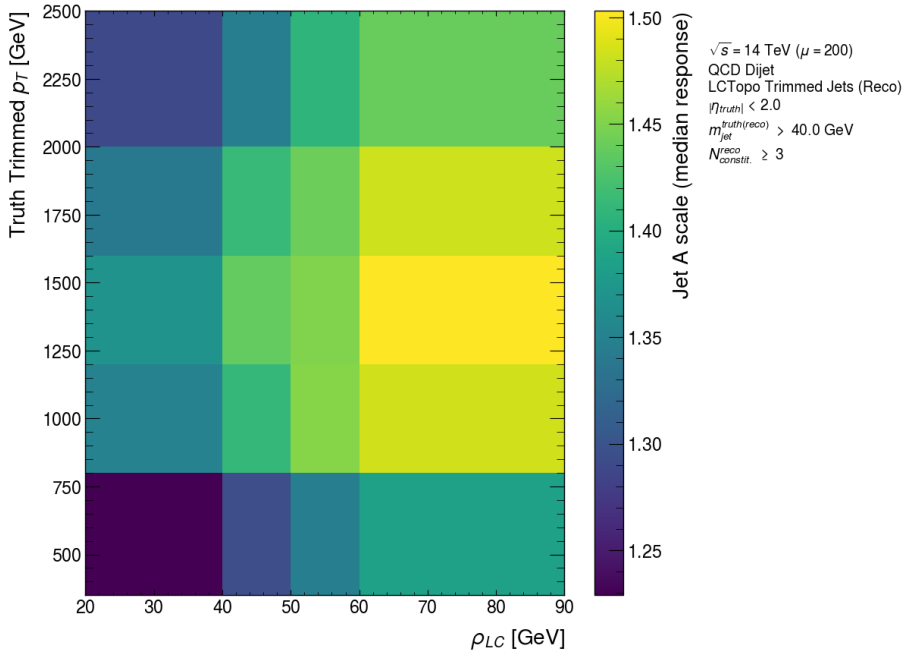

(a) Aplanarity

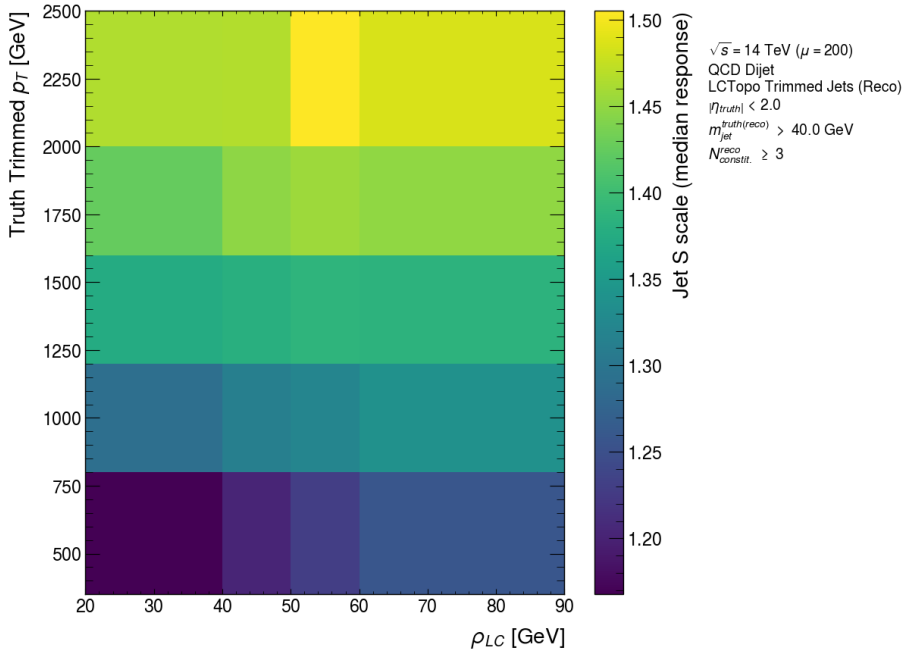

(b) Sphericity

Figure 7.42: Variation of observable response scale (trimmed jets only) with the truth trimmed jet p_{T} and ρ_{LCW}. Plots are included for the aplanarity, sphericity, and jet mass in addition to the τ_2^{wta}, τ_2^{wta}, and τ_{32}^{wta} observables.

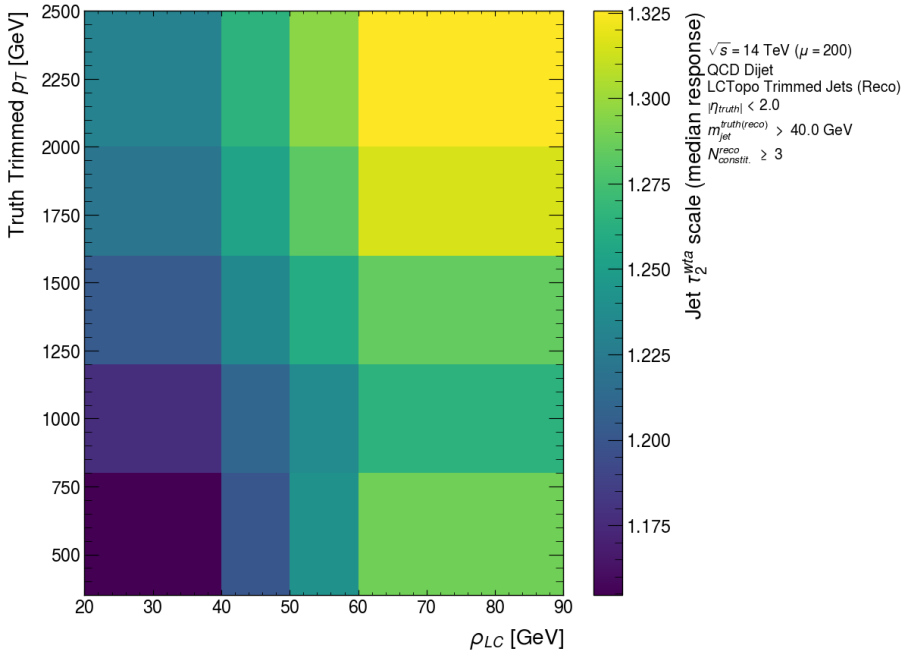

(c) τ_2^{wta}

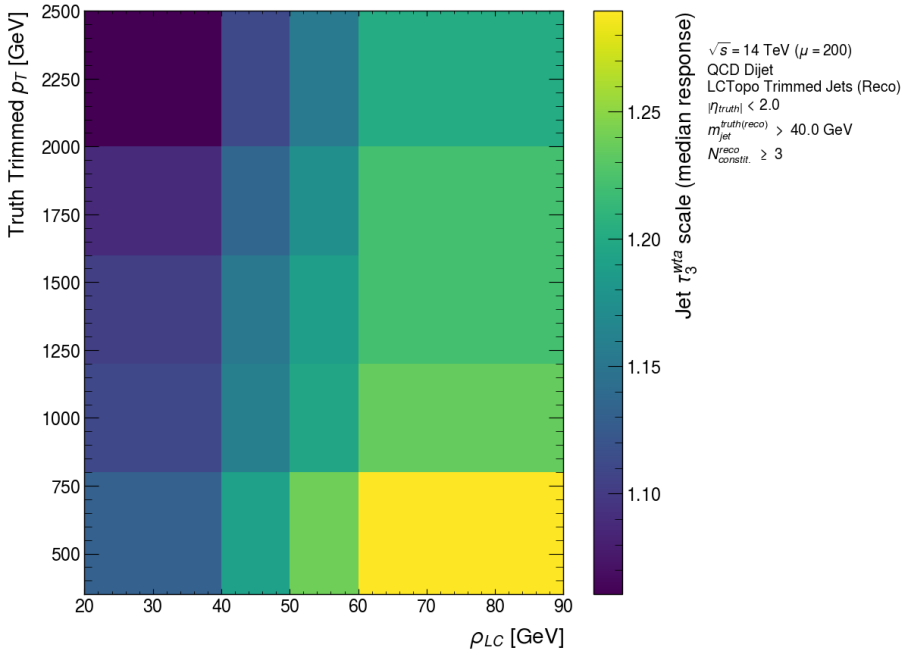

(d) τ_3^{wta}

Figure 7.42 (cont.): Variation of observable response scale (trimmed jets only) with the truth trimmed jet p_{T} and ρ_{LCW}. Plots are included for the aplanarity, sphericity, and jet mass in addition to the τ_2^{wta}, τ_2^{wta}, and τ_{32}^{wta} observables.

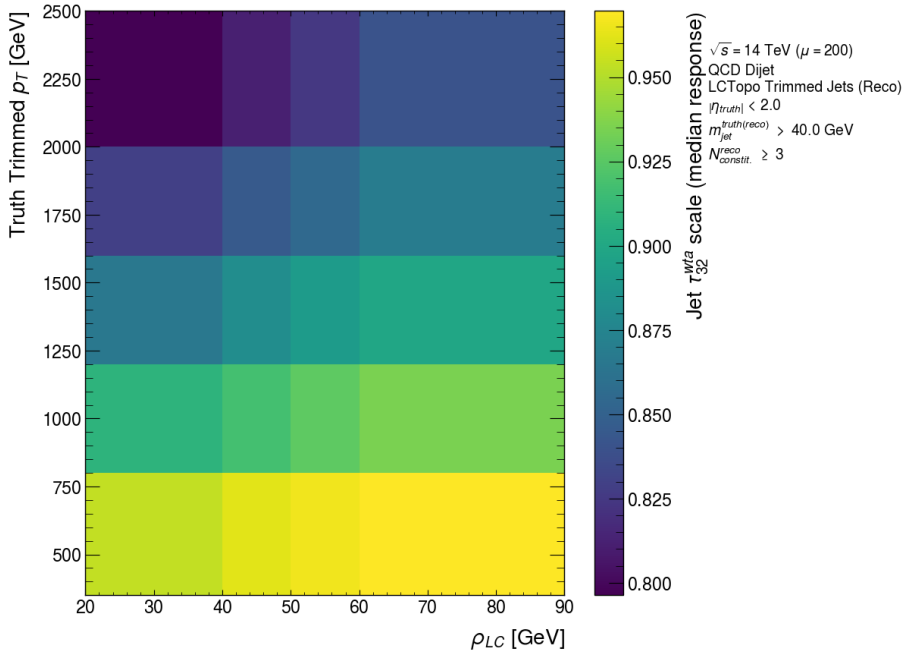

(e) τ_{32}^{wta}

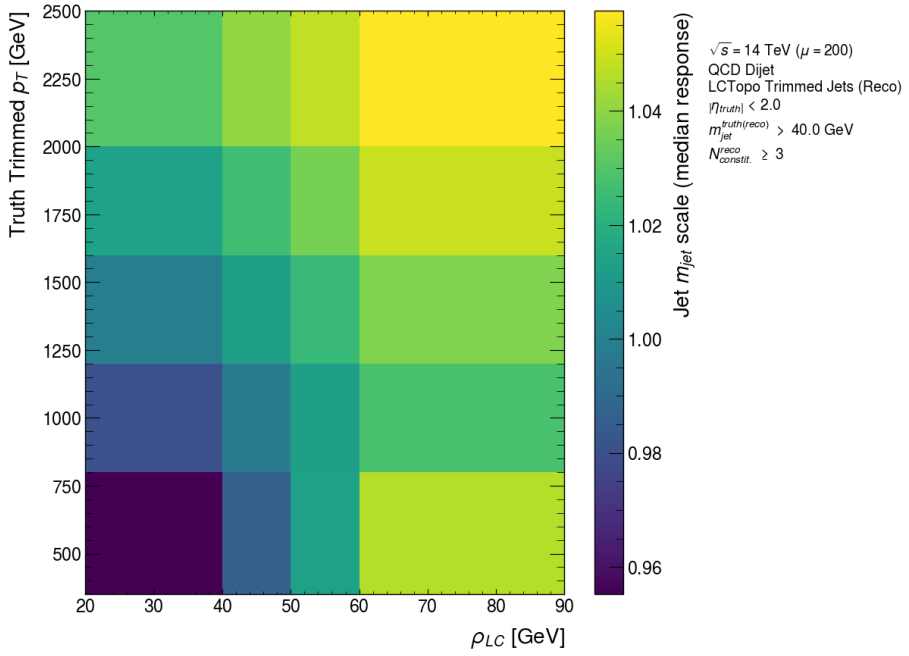

(f) m_{jet}

Figure 7.42 (cont.): Variation of observable response scale (trimmed jets only) with the truth trimmed jet p_{T} and ρ_{LCW}. Plots are included for the aplanarity, sphericity, and jet mass in addition to the τ_2^{wta}, τ_2^{wta}, and τ_{32}^{wta} observables.

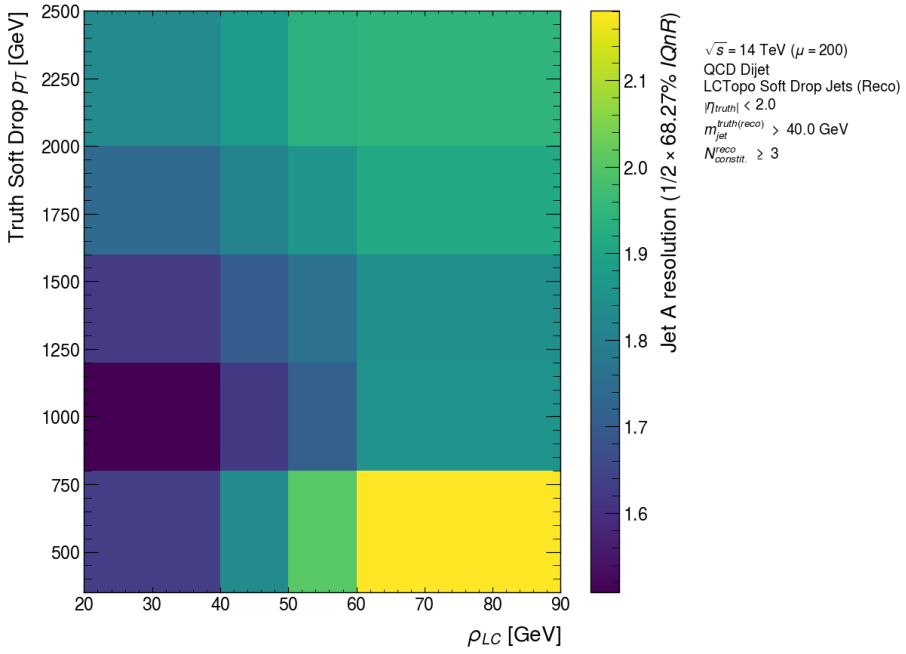

(a) Aplanarity

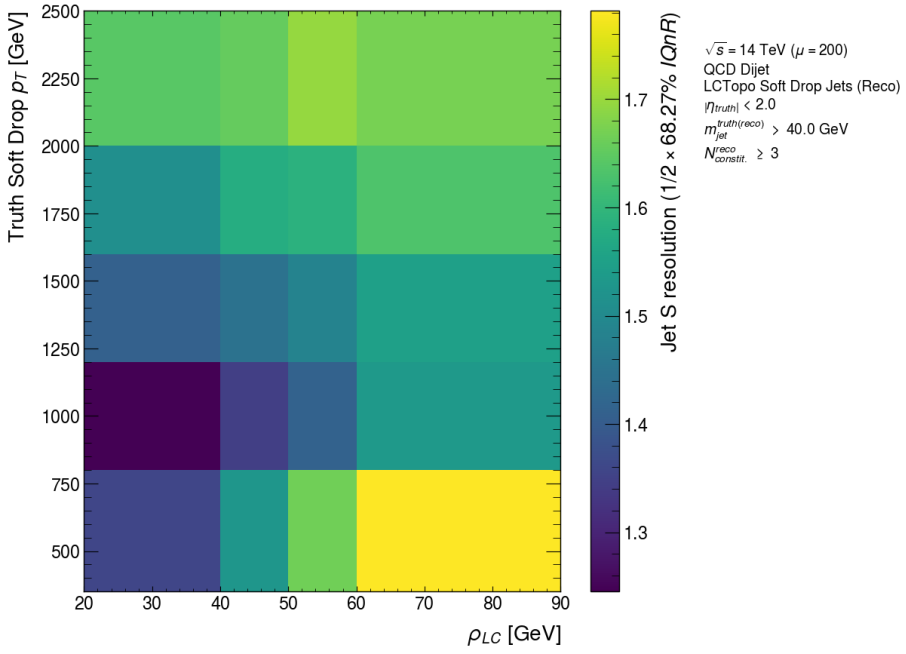

(b) Sphericity

Figure 7.43: Variation of observable response resolution (soft-drop jets only) with the truth soft-drop jet p_{T} and ρ_{LCW}. Plots are included for the aplanarity, sphericity, and jet mass in addition to the τ_2^{wta}, τ_2^{wta}, and τ_{32}^{wta} observables.

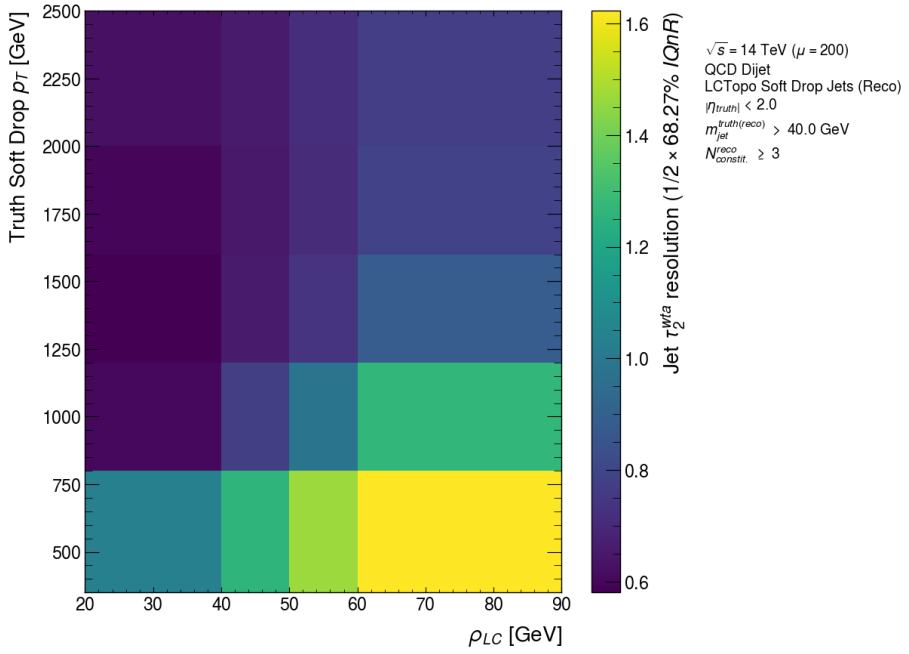

(c) τ_2^{wta}

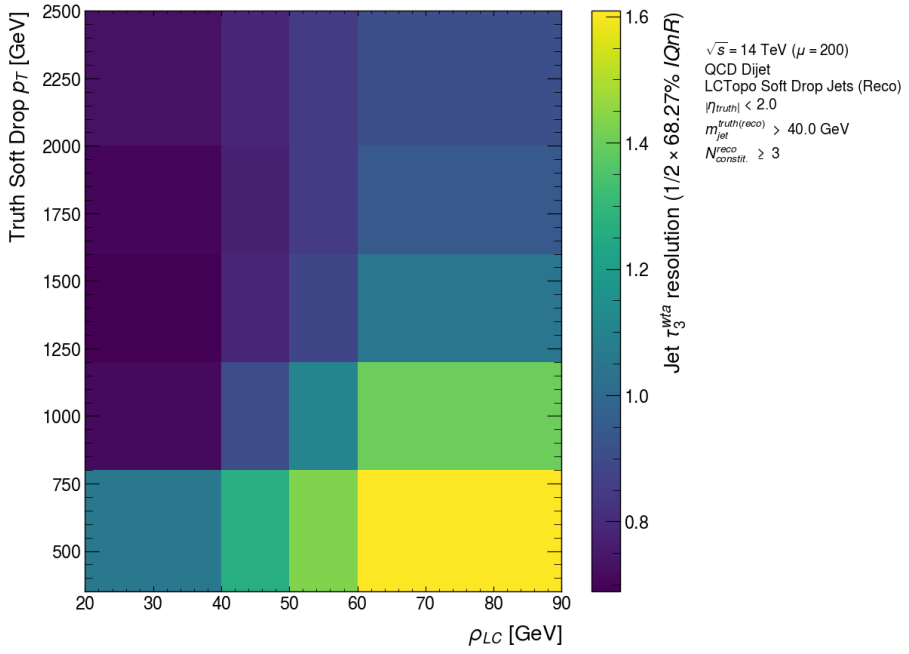

(d) τ_3^{wta}

Figure 7.43 (cont.): Variation of observable response resolution (soft-drop jets only) with the truth soft-drop jet p_{T} and ρ_{LCW}. Plots are included for the aplanarity, sphericity, and jet mass in addition to the τ_2^{wta}, τ_2^{wta}, and τ_{32}^{wta} observables.

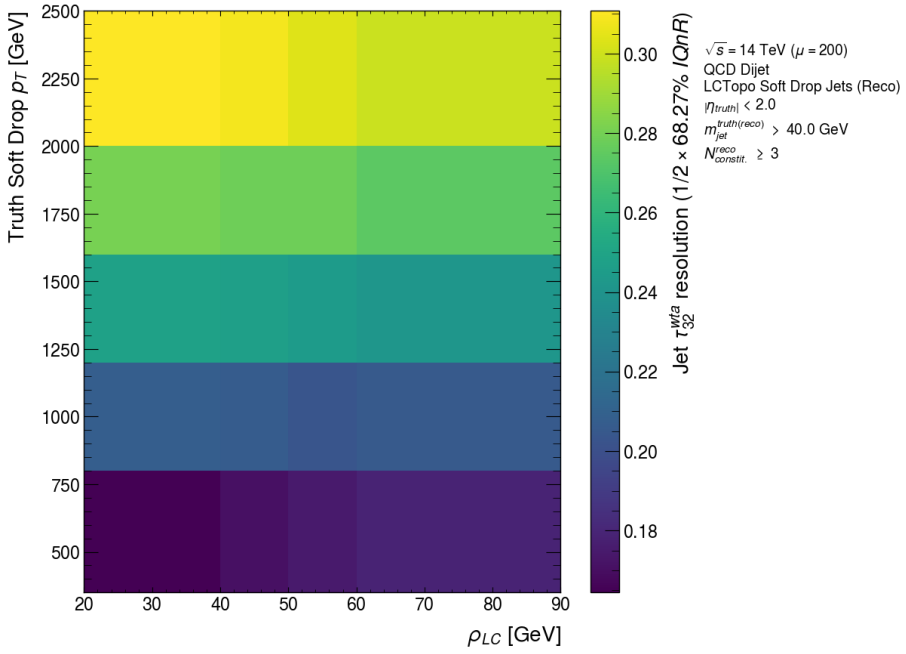

(e) τ_{32}^{wta}

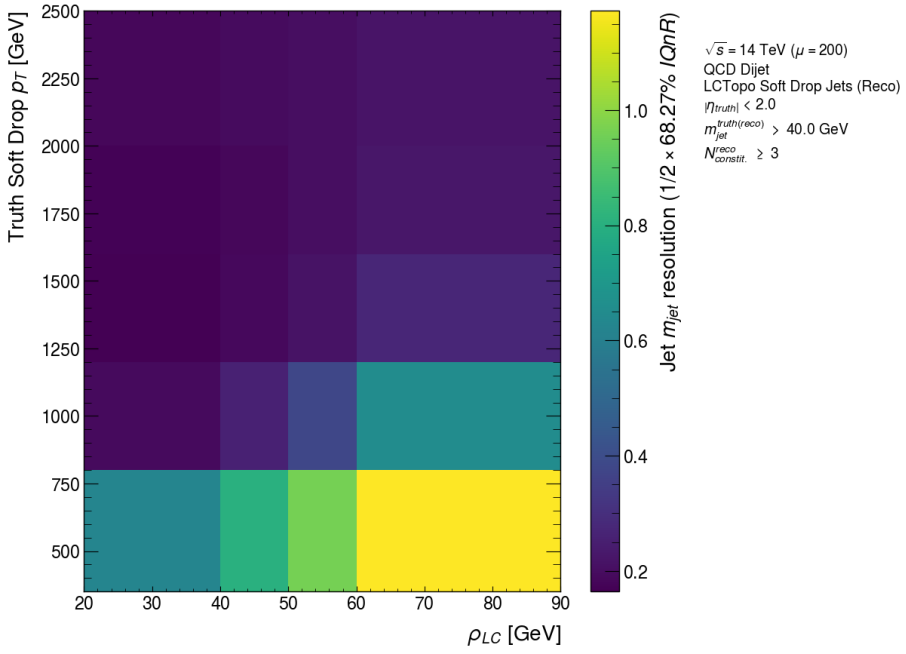

(f) m_{jet}

Figure 7.43 (cont.): Variation of observable response resolution (soft-drop jets only) with the truth soft-drop jet p_{T} and ρ_{LCW}. Plots are included for the aplanarity, sphericity, and jet mass in addition to the τ_2^{wta}, τ_2^{wta}, and τ_{32}^{wta} observables.

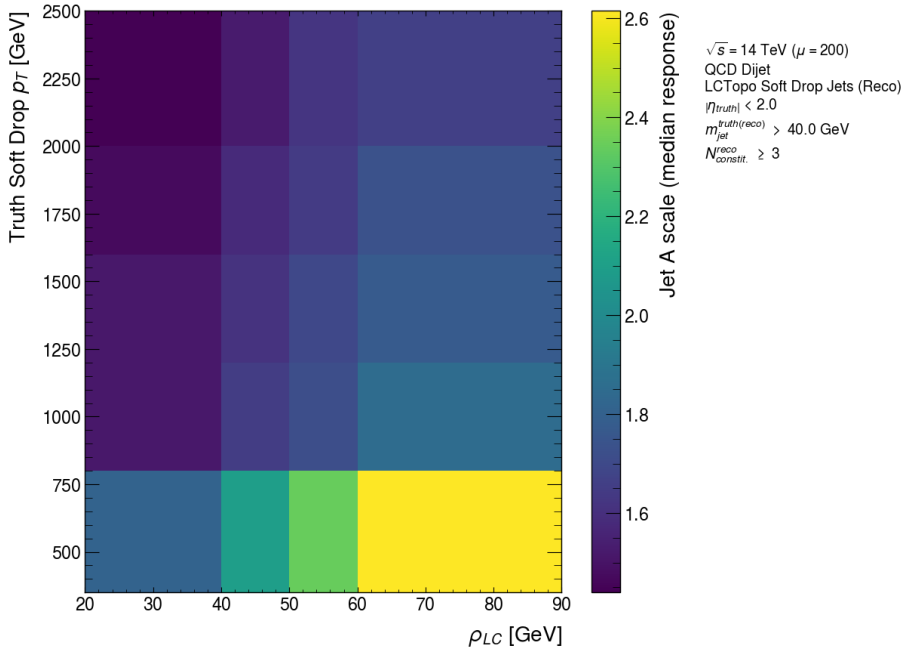

(a) Aplanarity

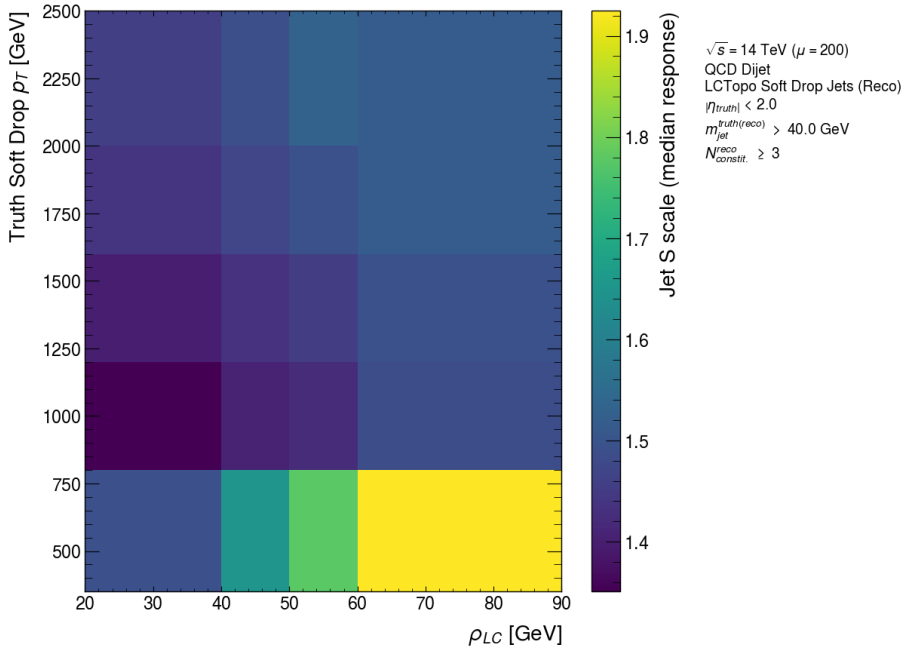

(b) Sphericity

Figure 7.44: Variation of observable response scale (soft-drop jets only) with the truth soft-drop jet p_{T} and ρ_{LCW}. Plots are included for the aplanarity, sphericity, and jet mass in addition to the τ_2^{wta}, τ_2^{wta}, and τ_{32}^{wta} observables.

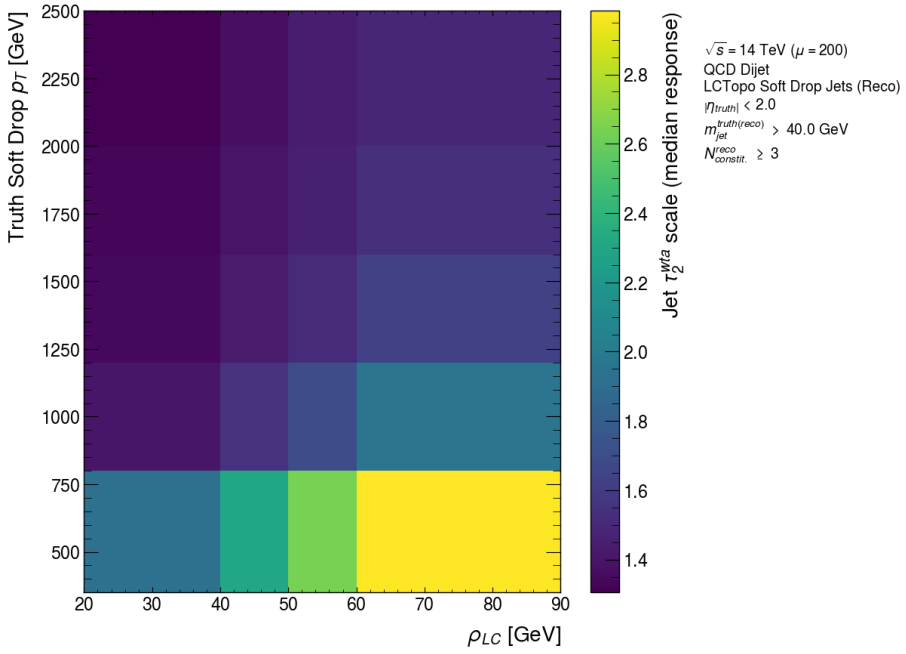

(c) τ_2^{wta}

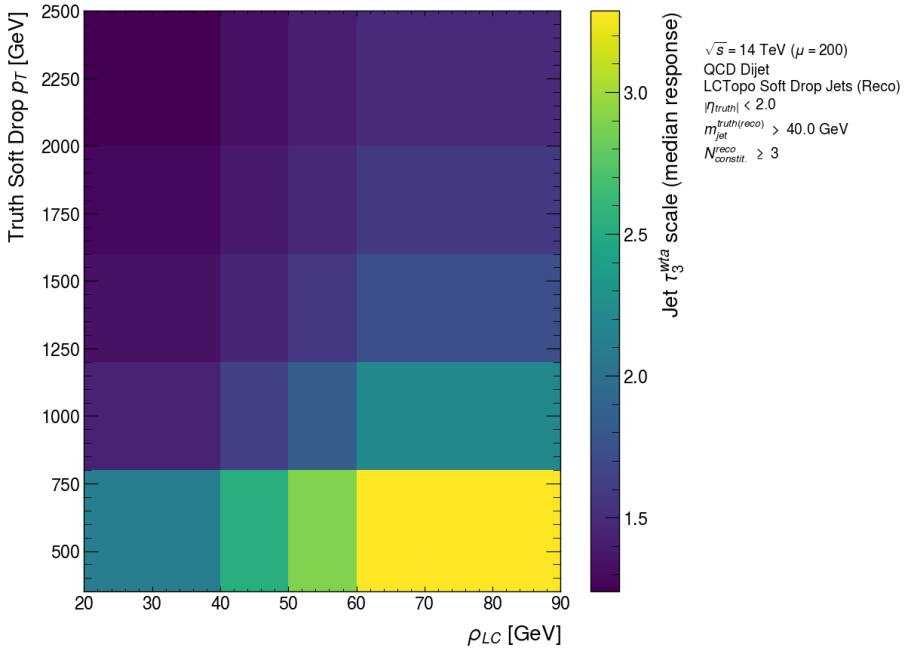

(d) τ_3^{wta}

Figure 7.44 (cont.): Variation of observable response scale (soft-drop jets only) with the truth soft-drop jet p_{T} and ρ_{LCW}. Plots are included for the aplanarity, sphericity, and jet mass in addition to the τ_2^{wta}, τ_2^{wta}, and τ_{32}^{wta} observables.

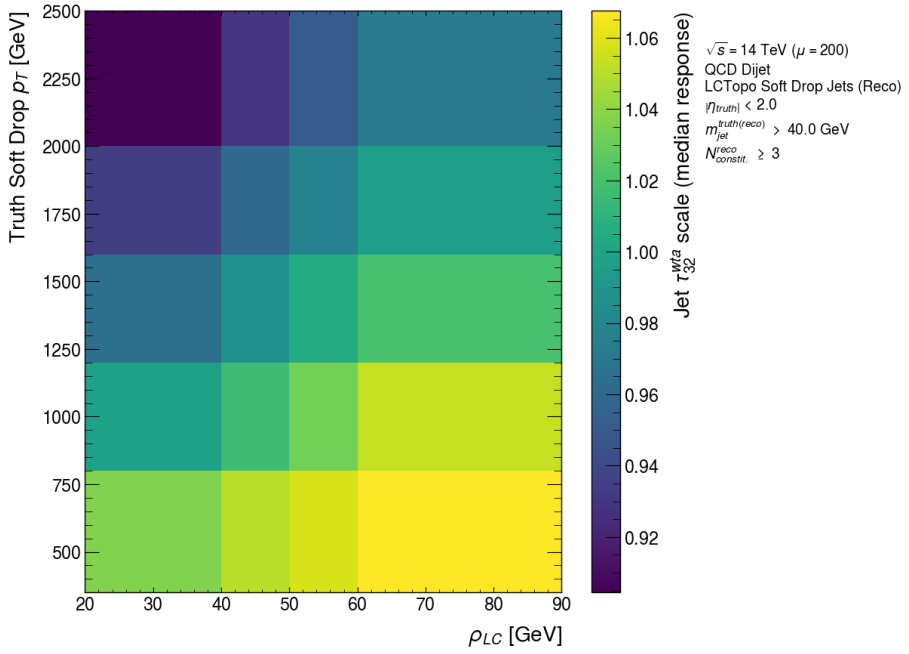

(e) τ_{32}^{wta}

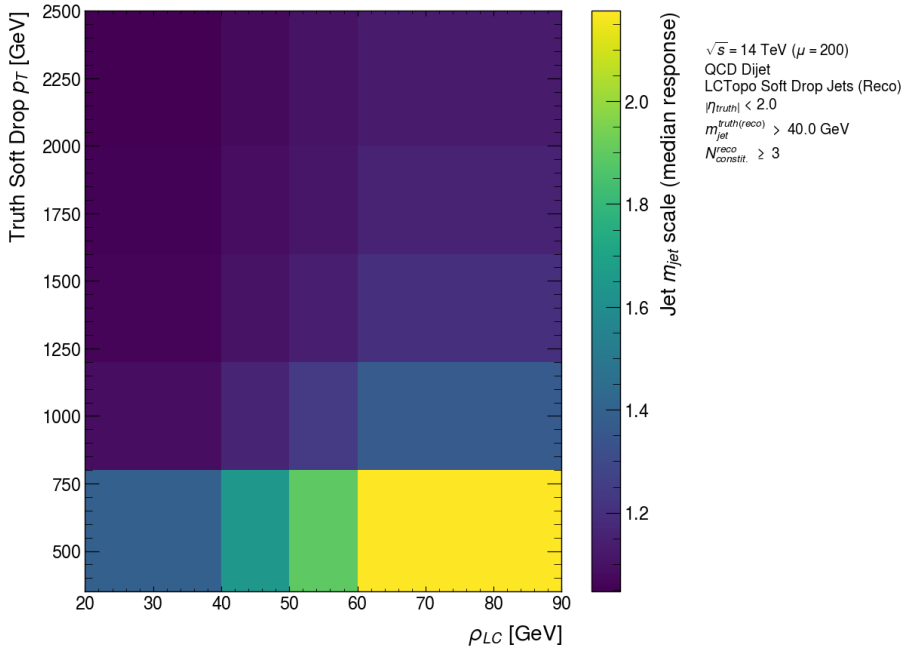

(f) m_{jet}

Figure 7.44 (cont.): Variation of observable response scale (soft-drop jets only) with the truth soft-drop jet p_{T} and ρ_{LCW}. Plots are included for the aplanarity, sphericity, and jet mass in addition to the τ_2^{wta}, τ_2^{wta}, and τ_{32}^{wta} observables.

of the reconstructed sphericity or aplanarity observable can result when there are few constituents in the jet, which causes small jet response values if the truth jet observable is larger in magnitude. Further study would be needed to determine if these explanations are indeed the case and to build a better understanding of these results.

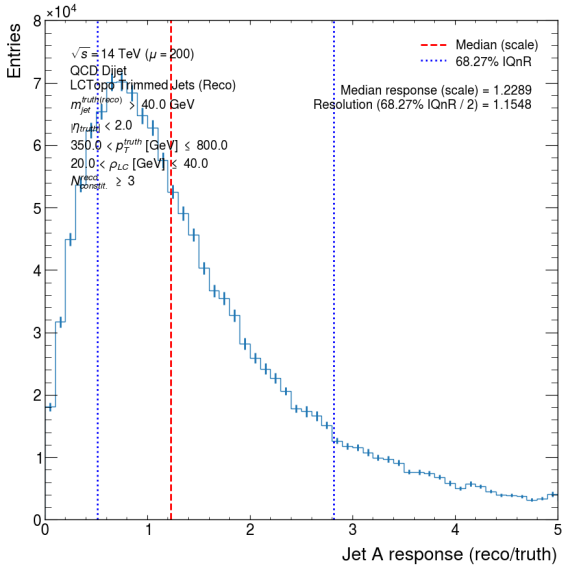

(a) Aplanarity ($350 < p_{\mathrm{T}}^{\mathrm{truth}}$ [GeV] < 800)

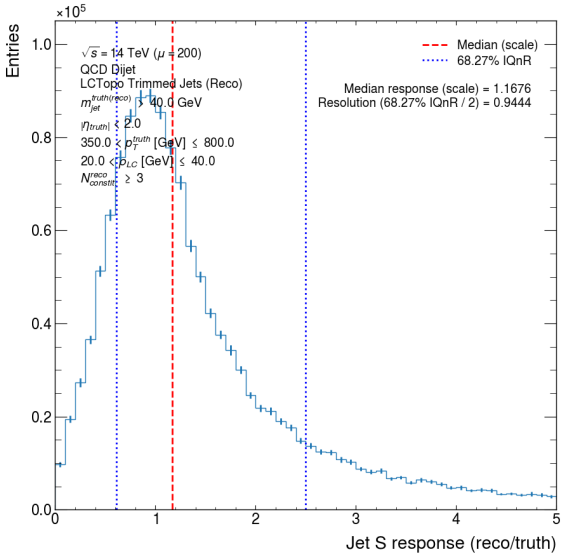

(b) Sphericity ($350 < p_{\mathrm{T}}^{\mathrm{truth}}$ [GeV] < 800)

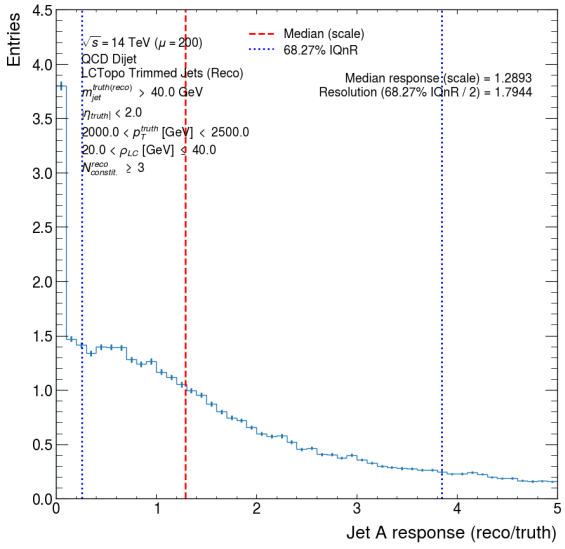

(c) Aplanarity ($2000 < p_{\mathrm{T}}^{\mathrm{truth}}$ [GeV] < 2500)

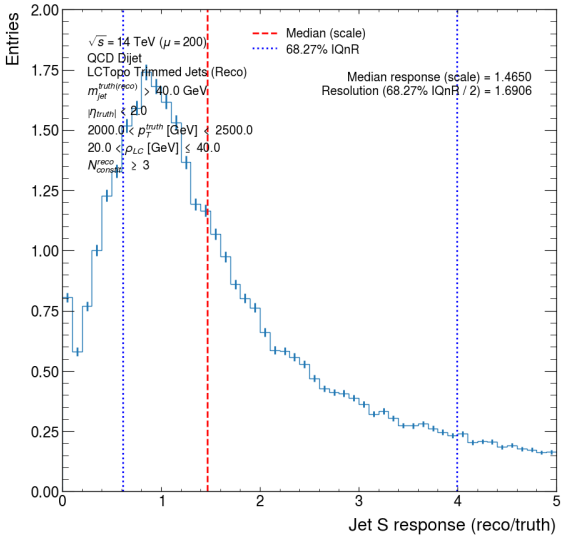

(d) Sphericity ($2000 < p_{\mathrm{T}}^{\mathrm{truth}}$ [GeV] < 2500)

Figure 7.45: Aplanarity (left) and sphericity (right) trimmed jet response distributions in low- and high-p_{T} bins to highlight apparent spikes in the first bin of the response distributions when a low-ρ_{LCW} selection is applied.

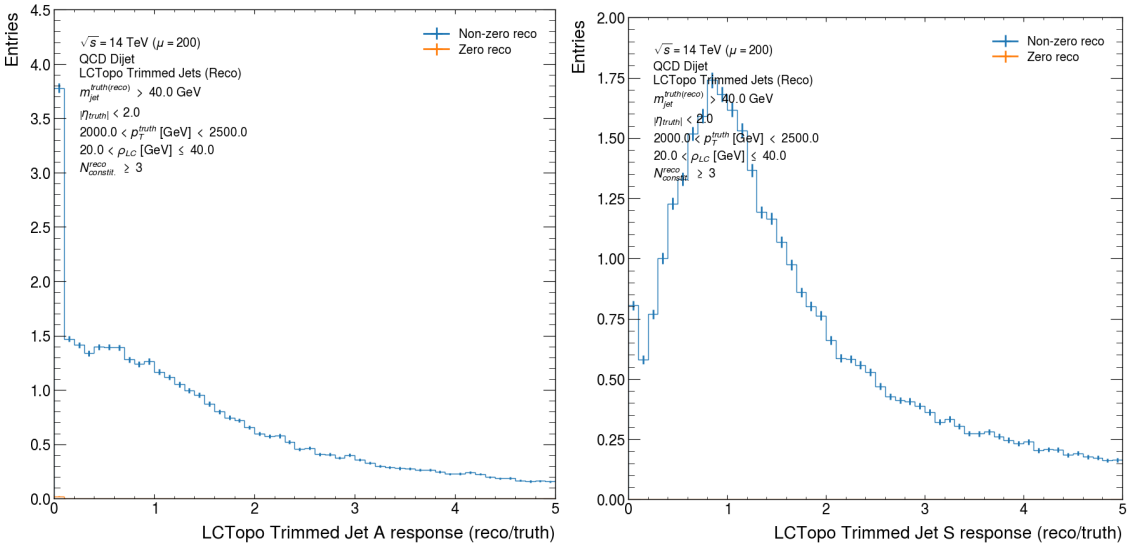

(a) Aplanarity (b) Sphericity

Figure 7.46: Jet response distributions for trimmed jet aplanarity and sphericity observables affected by spikes in the first bin of the response distribution. The histograms in these plots are plotted according to whether the reconstructed observable is zero (*Zero reco*) or non-zero (*Non-zero reco*). The jet response distributions are derived in a high-p_{T} ($2000 < p_{\mathrm{T}}^{\mathrm{truth}}$ (GeV) < 2500) and low-ρ_{LCW} ($20 < \rho_{\mathrm{LCW}}$ (GeV) ≤ 40) bin. The *Zero reco* histogram in both of these plots has a very small contribution to the total jet response histogram. The first bin of the *Zero reco* histogram is only evident on the left-hand side plot in the bottom left corner. Whereas, on the right-hand side plot, all *Zero reco* histogram bins are empty and the histogram integral is zero.

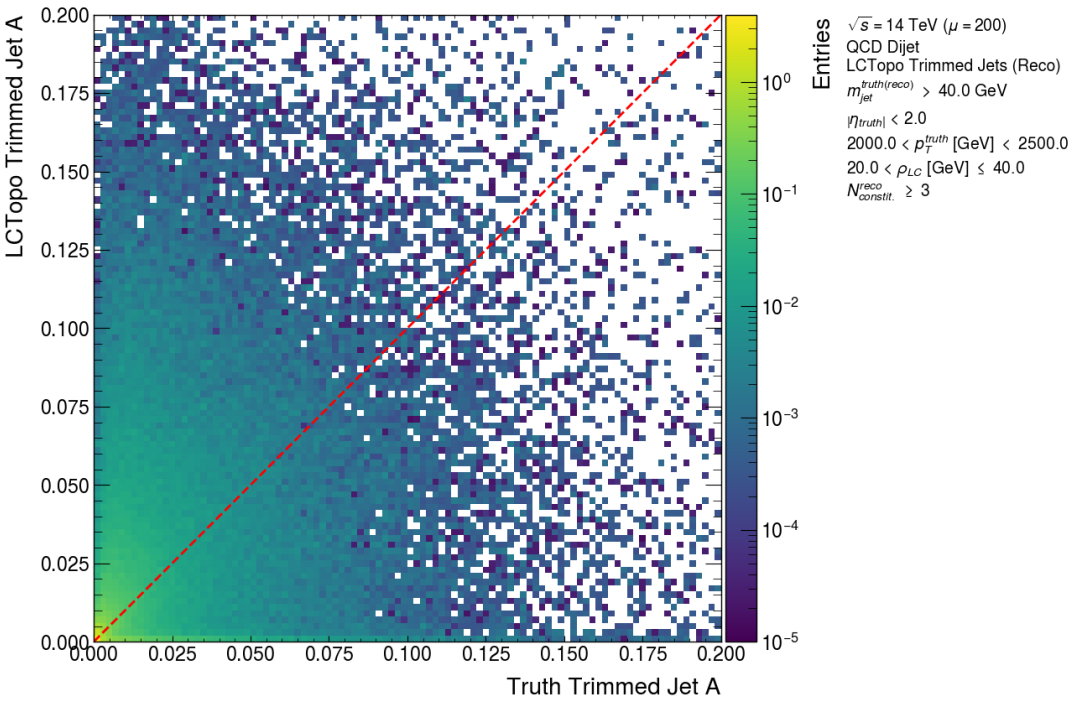

(a) Aplanarity

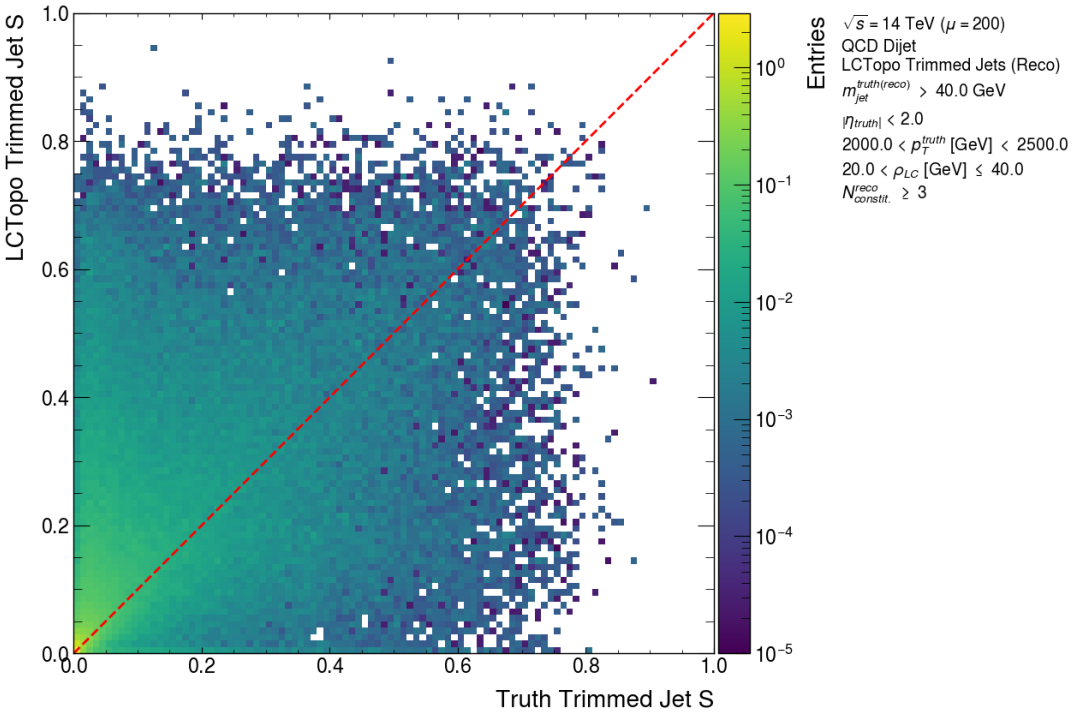

(b) Sphericity

Figure 7.47: Correlations between the truth-level and reconstructed observable for the trimmed jet aplanarity and sphericity. The plots included have a $2000 < p_{\mathrm{T}}^{\mathrm{truth}}$ (GeV) < 2500 jet selection and an additional $20 < \rho_{\mathrm{LCW}}$ (GeV) ≤ 40 event-level selection.

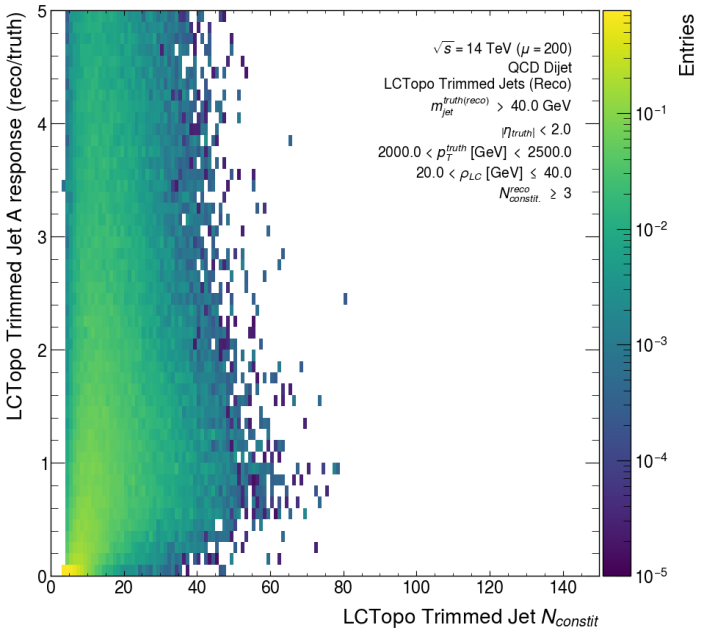

(a) Aplanarity

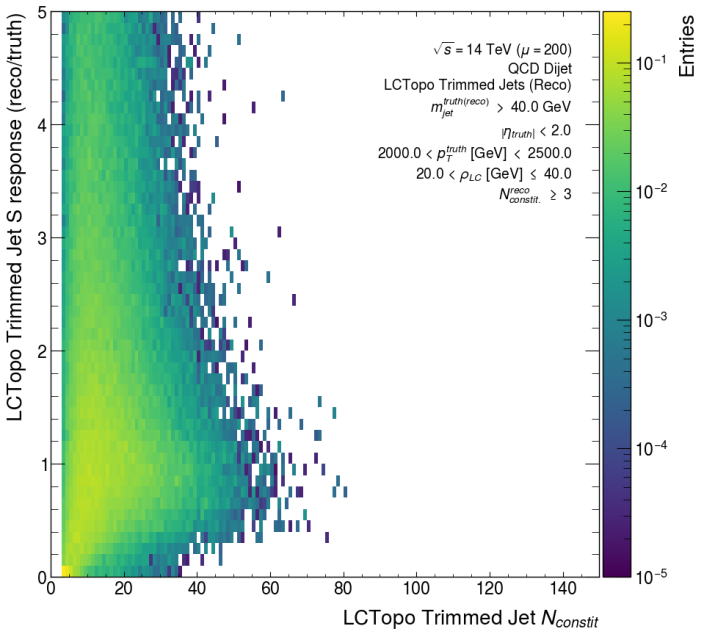

(b) Sphericity

Figure 7.48: Correlations between the number of (reconstructed) jet constituents and the jet response for the trimmed jet aplanarity and sphericity. The plots included have a $2000 < p_{\mathrm{T}}^{\mathrm{truth}}$ (GeV) < 2500 jet selection and an additional $20 < \rho_{\mathrm{LCW}}$ (GeV) ≤ 40 event-level selection.

7.11 Pile-up stability of the jet mass calibration

The stability of the jet mass "calibration" (i.e. the jet mass at the LCW scale) for the large-R `LCTopo` jets was briefly studied. A qualitative measure of the stability was achieved by considering the correlation of the ungroomed and groomed jet masses with ρ_{LCW}. Only the QCD dijet background sample (with a much greater level of statistics than the signal sample) was considered, but with the same p_{T} re-weighting scheme used for the earlier tagging studies. The results of these comparisons are shown in Figures 7.49 and 7.50 for the ungroomed and groomed `LCTopo` jets, respectively.

The ungroomed `LCTopo` m_{jet} (Figure 7.49) shows significant dependence on ρ_{LCW} regardless of the (ungroomed truth jet) p_{T} bin. This is expected since ungroomed jets have no pile-up mitigation/subtraction. The soft-drop groomed (Figures 7.50d to 7.50f) and trimmed (Figures 7.50a to 7.50c) m_{jet} is comparatively stable as a function of the pile-up activity. Qualitative comparisons of the two grooming methods indicate that the trimmed m_{jet} is in fact more stable than the soft-drop m_{jet} as a function of ρ_{LCW}. This provides further support to the argument from Section 7.10.1 that the trimmed jet taggers are more pile-up stable than the soft-drop jet taggers. The dependence of m_{jet} on the pile-up conditions means there is ultimately a "convolution" of the m_{jet} pile-up stability and that of other tagger variables, which leads to the observed tagger pile-up stability discussed in Section 7.10.

7.12 Performance benchmarks for Run 2 DNN taggers

DNN (Deep Neural Network) taggers were developed for Run 2 analyses using `LCTopoTrimmed` jets [80]. Their performance in HL-LHC simulation had not yet been established, so we briefly evaluated the tagger working points to provide a first indication of their performance. The input variables for this tagger are introduced in Section 4.8.3. The original DNN tagger relies on the *combined jet mass*[16], not the calorimeter-only jet mass considered for these studies, which could lead to differences in performance relative to the Run 2 ($\sqrt{s} = 13$ TeV) results. Four different working points were tested, including the contained and inclusive top quark taggers each with 50% or 80% signal efficiency configurations. Only jets with $350 < p_{\text{T}}$ (GeV) < 2500 and $m_{\text{jet}} > 40$ GeV[17] are valid for these taggers, and they must pass both the kinematic requirements (p_{T} and mass) and the DNN score selection to be tagged as a top quark jet. The DNN performance was evaluated in bins of the `LCTopoTrimmed` jet p_{T} for jets within $|\eta| < 2$ using the same p_{T} bin edges as for previous studies. A modified truth-labelling scheme introduced in Section 7.2.2 was applied for consistency with the original DNN tagger definitions.

[16] This requires both a track-assisted jet mass (using ghost-associated tracks in the jet mass calculation) and the calorimeter jet mass [80].
[17] The mass selections are discussed further in Ref. [80].

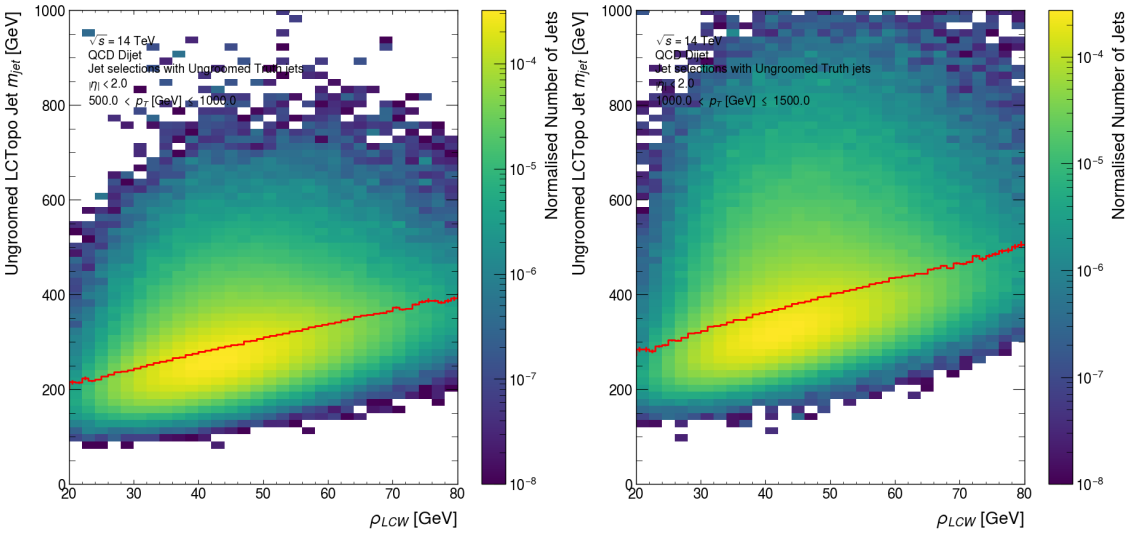

(a) $500 < p_{\mathrm{T}}^{\mathrm{truth}} \leq 1000$ (b) $1000 < p_{\mathrm{T}}^{\mathrm{truth}} \leq 1500$

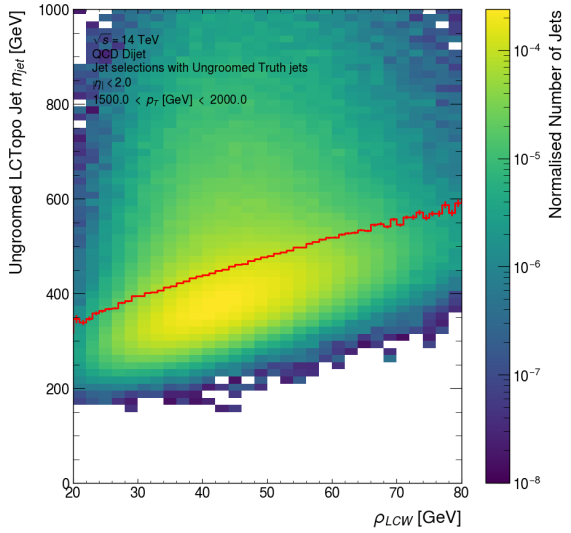

(c) $1500 < p_{\mathrm{T}}^{\mathrm{truth}} < 2000$

Figure 7.49: Variation of jet mass for ungroomed (`LCTopo`) jets as a function of ρ_{LCW} (i.e. as the pile-up activity increases). The overlaid profile (red) shows the average mass in each ρ_{LCW} bin. The colour scale is normalised using a density normalisation scheme.

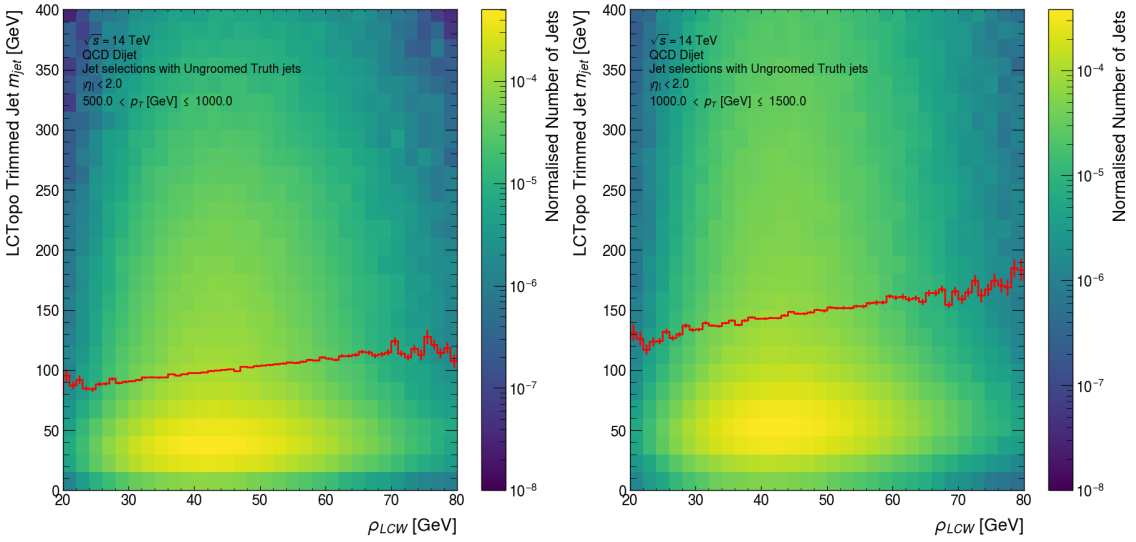

(a) Trimmed jets ($500 < p_{\mathrm{T}}^{\mathrm{truth}} \leq 1000$). (b) Trimmed jets ($1000 < p_{\mathrm{T}}^{\mathrm{truth}} \leq 1500$).

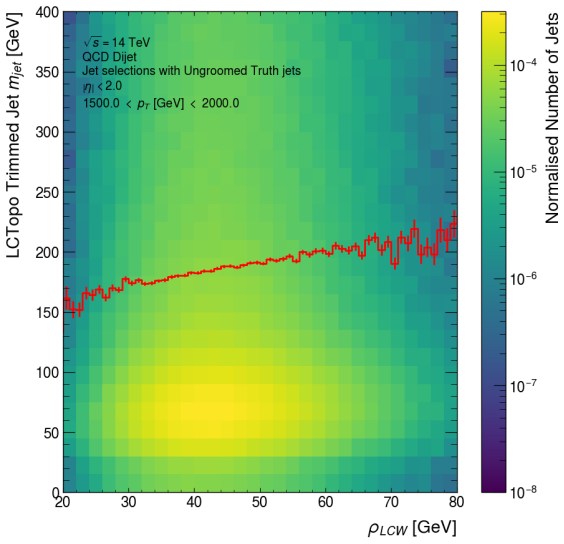

(c) Trimmed jets ($1500 < p_{\mathrm{T}}^{\mathrm{truth}} < 2000$).

Figure 7.50: Variation of jet mass for trimmed and soft-drop groomed `LCTopo` jets as a function of ρ_{LCW} (i.e. as the pile-up activity increases). The overlaid profile (red) shows the average mass in each ρ_{LCW} bin. The colour scale is normalised using a density normalisation scheme.

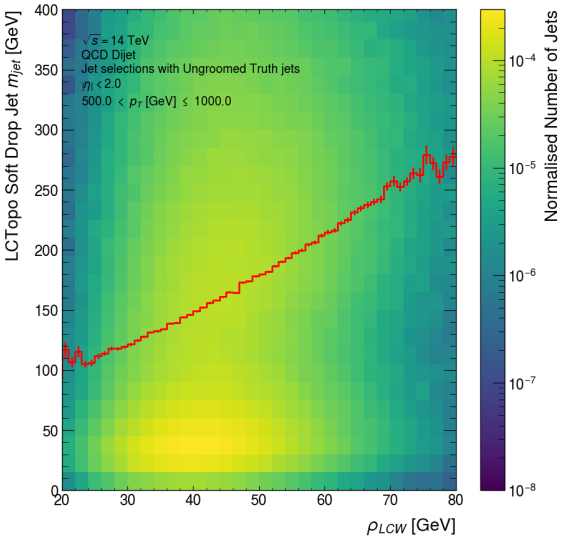

(d) Soft-drop jets ($500 < p_{\mathrm{T}}^{\mathrm{truth}} \leq 1000$).

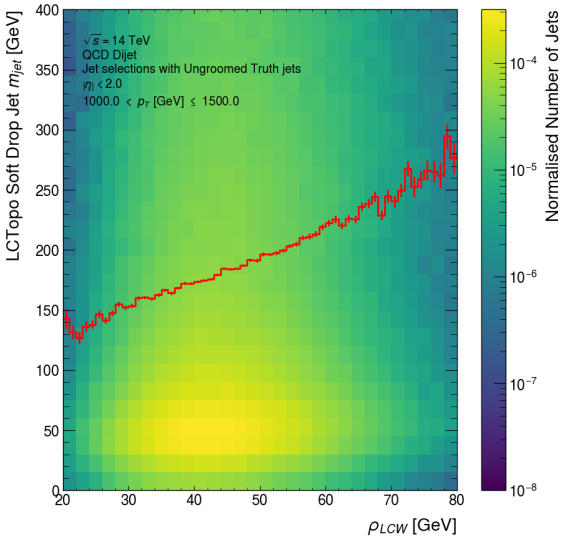

(e) Soft-drop jets ($1000 < p_{\mathrm{T}}^{\mathrm{truth}} \leq 1500$).

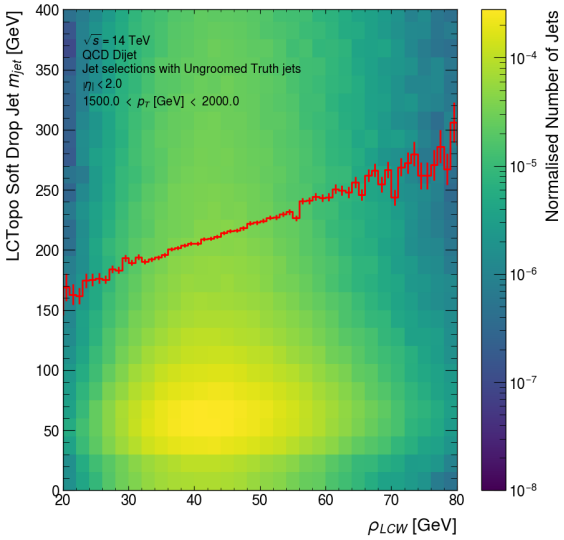

(f) Soft-drop jets ($1500 < p_{\mathrm{T}}^{\mathrm{truth}} < 2000$).

Figure 7.50 (cont.): Variation of jet mass for trimmed and soft-drop groomed `LCTopo` jets as a function of ρ_{LCW} (i.e. as the pile-up activity increases). The overlaid profile (red) shows the average mass in each ρ_{LCW} bin. The colour scale is normalised using a density normalisation scheme.

The signal and background efficiency of the DNN taggers, and the statistical uncertainty in those estimates was determined using the sum of the event weights and the sum of squared event weights, respectively. The performance results are summarised in Table 7.2. Figure 7.51 compares the performance of these DNN taggers with $m_{\text{jet}} + X$ taggers suitable for an 80% efficiency tagger. It is clear that the DNN taggers outperform the cut-based taggers from the differences in their background rejection. The same conclusions are drawn when two-variable taggers with a tighter (80% signal efficiency) jet mass selection are compared to the DNN working points in Figure 7.52.

The measured signal efficiency in HL-LHC simulation is slightly lower than expected for the corresponding 50%/80% contained top tagger working points. This is expected since the DNN is being evaluated under different conditions – pile-up especially – and a different jet mass definition is used. The signal efficiency in Table 7.2 falls with p_{T} as expected, except for the 80% signal efficiency contained top tagger at high-p_{T}, which might be a statistical effect. The background rejection for all contained top tagger working points is similar for the same signal efficiency configuration, but larger decreases for the 50% efficiency tagger are seen. As for other studies, the decreasing background rejection of taggers is consistent with the merging of jet constituents at high-p_{T} resulting in an (eventual) inability to resolve the individual calorimeter deposits as noted in [80].

The inclusive top tagger working points are included, but they do not reflect the true performance of this tagger evaluated in HL-LHC simulations. We applied the contained top quark label for these studies, which selects *only* a subset of the jets that would be labelled as inclusive top quark decays. Thus, odd results are expected and are indeed evident in the signal efficiencies for these tagger working points in Table 7.2. We will not comment further on these performance comparisons and recommend that the performance of these inclusive top quark taggers is studied further using the appropriate truth label in the future.

The performance of the DNN tagger working points was briefly evaluated as a function of ρ_{LCW} as for two-variable taggers in Section 7.10.1. The results shown in Figures 7.53 and 7.54 for the contained top taggers with 50% and 80% signal efficiency working points, respectively, suggest that the taggers are reasonably stable under different pile-up conditions. This is particularly promising seeing as no dedicated pile-up rejection method is employed for these taggers other than the trimming of the large-R jets. Like for the two-variable trimmed jet taggers, the background rejection for the tagger working points in Figures 7.55 and 7.56 falls at large ρ_{LCW}, but some fluctuations are seen in the high-p_{T} bin for the 50% signal efficiency taggers.

Overall, given the reasonable performance of the DNN taggers and their pile-up stability, it is possible that the DNN tagger definitions can be applied without re-optimisation in HL-LHC simulation to obtain higher background rejection at the cost of a small signal efficiency loss. However, further study of these taggers and their pile-

up dependence should be considered as an important future step towards developing recommendations that are more performant than simple cut-based taggers.

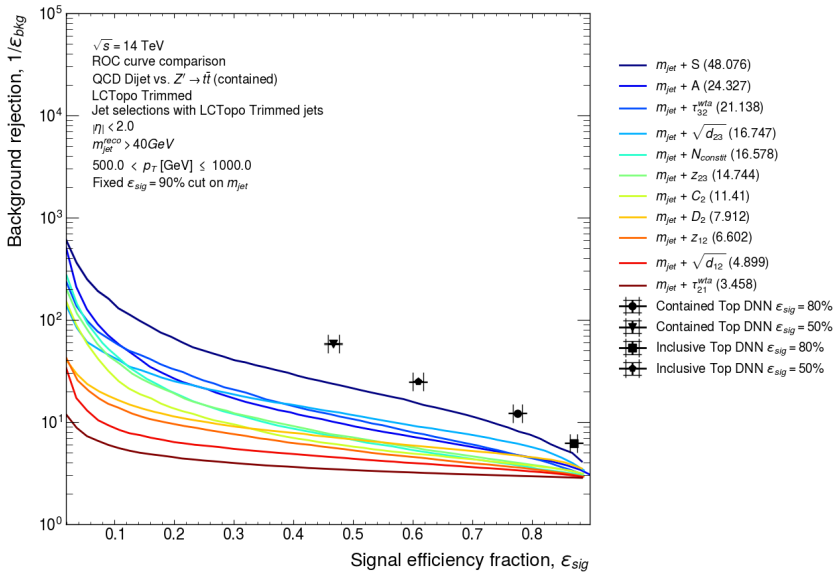

(a) $500 < p_{\mathrm{T}}$ (GeV) ≤ 1000

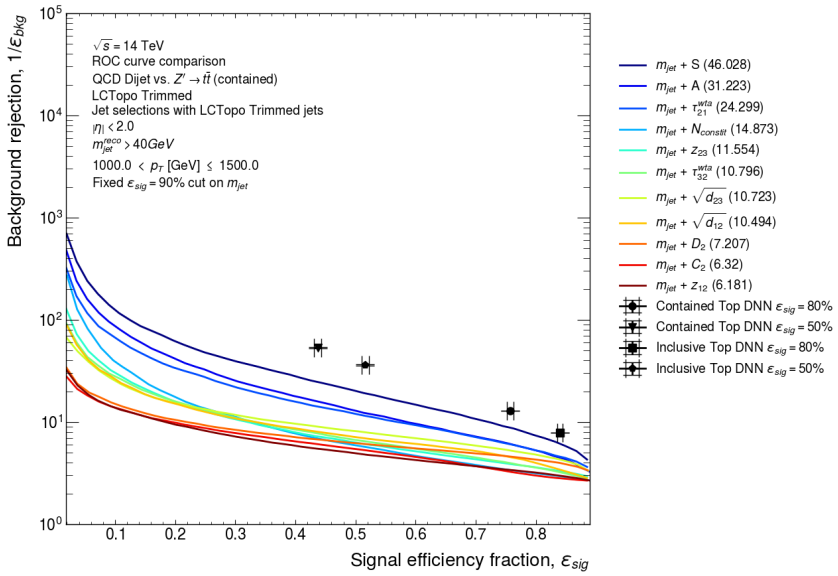

(b) $1000 < p_{\mathrm{T}}$ (GeV) ≤ 1500

Figure 7.51: Performance comparisons for Run 2 DNN taggers and the $m_{\mathrm{jet}} + X$ derived in HL-LHC simulations for different p_{T} bins. As before, the ROC curve legend for the $m_{\mathrm{jet}} + X$ taggers is sorted by the area under the ROC curve. The $m_{\mathrm{jet}} + X$ taggers have a 90% signal efficiency jet mass selection as those for the 80% signal efficiency tagger recommendations would have.

Table 7.2: Run 2 DNN tagger performance results in HL-LHC simulation for all tagger working points binned in the `LCTopoTrimmed` jet p_{T}.

$500 < p_{\mathrm{T}}$ (GeV) ≤ 1000		
Working point	Signal efficiency	Background rejection
Contained 50%	0.467 ± 0.009	58.6 ± 0.7
Contained 80%	0.776 ± 0.008	12.2 ± 0.1
Inclusive 50%	0.609 ± 0.009	24.7 ± 0.2
Inclusive 80%	0.870 ± 0.006	6.23 ± 0.02
$1000 < p_{\mathrm{T}}$ (GeV) ≤ 1500		
Working point	Signal efficiency	Background rejection
Contained 50%	0.437 ± 0.006	53.2 ± 0.7
Contained 80%	0.757 ± 0.005	12.9 ± 0.1
Inclusive 50%	0.516 ± 0.006	36.2 ± 0.4
Inclusive 80%	0.840 ± 0.005	7.88 ± 0.03
$1500 < p_{\mathrm{T}}$ (GeV) < 2000		
Working point	Signal efficiency	Background rejection
Contained 50%	0.384 ± 0.005	54.6 ± 0.6
Contained 80%	0.763 ± 0.005	11.9 ± 0.1
Inclusive 50%	0.469 ± 0.005	37.1 ± 0.3
Inclusive 80%	0.829 ± 0.004	8.13 ± 0.03

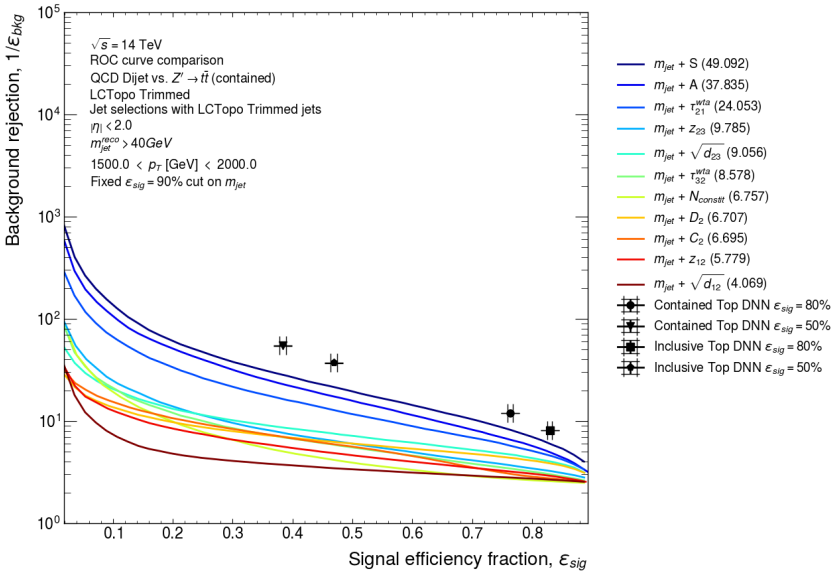

(c) $1500 < p_{\mathrm{T}}$ (GeV) < 2000

Figure 7.51 (cont.): Performance comparisons for Run 2 DNN taggers and the $m_{\mathrm{jet}} + X$ derived in HL-LHC simulations for different p_{T} bins. As before, the ROC curve legend for the $m_{\mathrm{jet}} + X$ taggers is sorted by the area under the ROC curve. The $m_{\mathrm{jet}} + X$ taggers have a 90% signal efficiency jet mass selection as those for the 80% signal efficiency tagger recommendations would have.

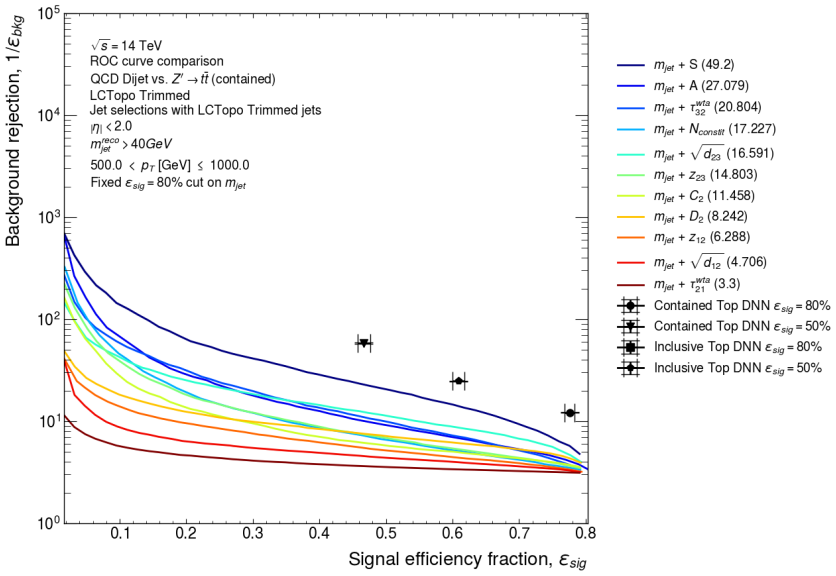

(a) $500 < p_{\mathrm{T}}$ (GeV) ≤ 1000

Figure 7.52: Performance comparisons for Run 2 DNN taggers and the $m_{\mathrm{jet}} + X$ derived in HL-LHC simulations for different p_{T} bins. As before, the ROC curve legend for the $m_{\mathrm{jet}} + X$ taggers is sorted by the area under the ROC curve. The $m_{\mathrm{jet}} + X$ taggers have an 80% signal efficiency jet mass selection as those for the 50% signal efficiency tagger recommendations would have.

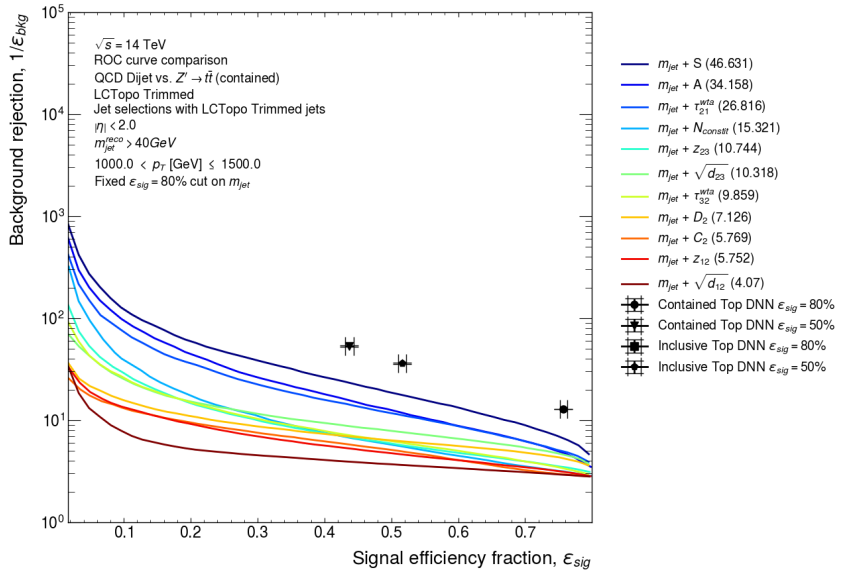

(b) $1000 < p_{\mathrm{T}}$ (GeV) ≤ 1500

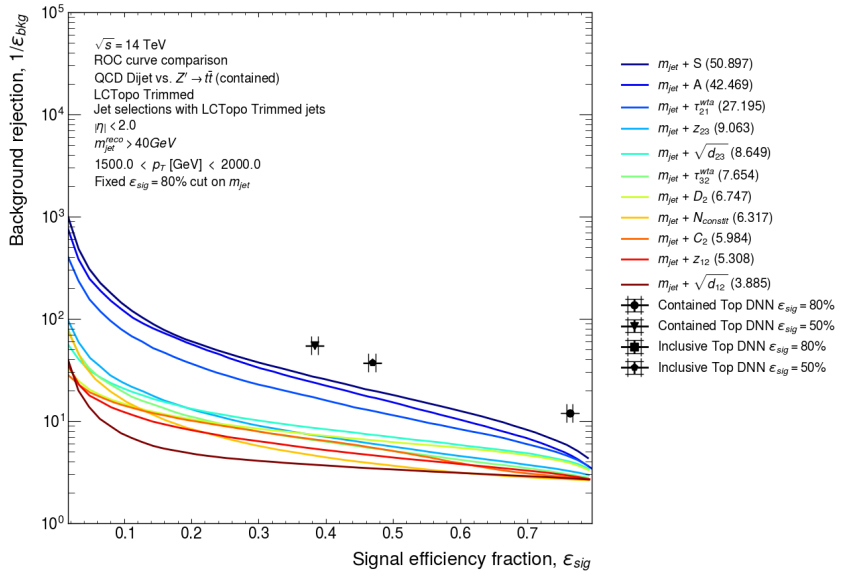

(c) $1500 < p_{\mathrm{T}}$ (GeV) < 2000

Figure 7.52 (cont.): Performance comparisons for Run 2 DNN taggers and the $m_{\mathrm{jet}} + X$ derived in HL-LHC simulations for different p_{T} bins. As before, the ROC curve legend for the $m_{\mathrm{jet}} + X$ taggers is sorted by the area under the ROC curve. The $m_{\mathrm{jet}} + X$ taggers have an 80% signal efficiency jet mass selection as those for the 50% signal efficiency tagger recommendations would have.

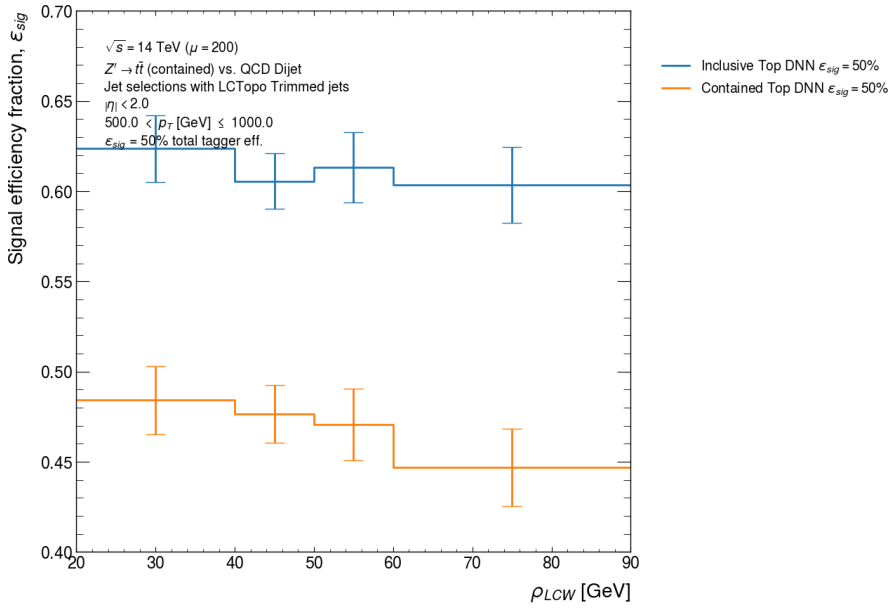

(a) $500 < p_{\mathrm{T}}$ (GeV) ≤ 1000

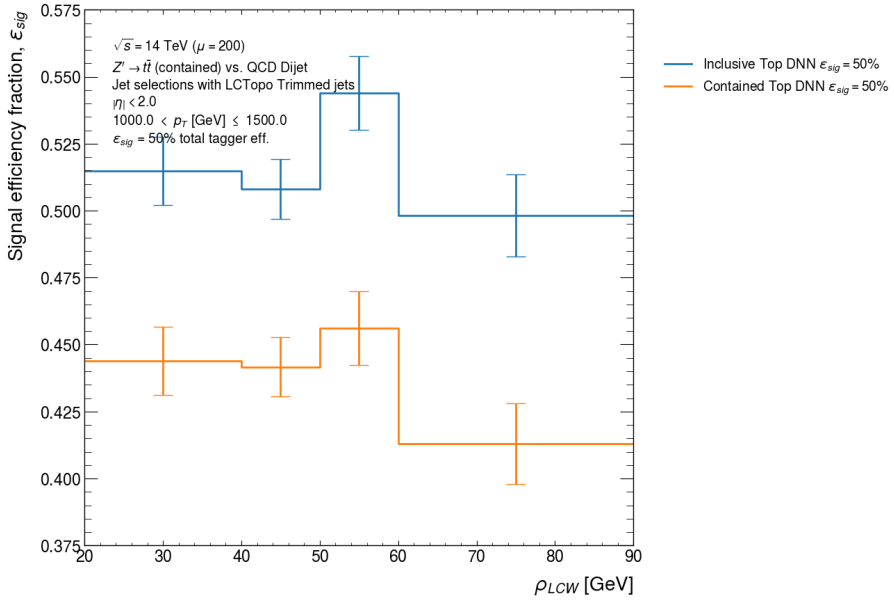

(b) $1000 < p_{\mathrm{T}}$ (GeV) ≤ 1500

Figure 7.53: Signal efficiency for 50% signal efficiency DNN tagger working points as a function of ρ_{LCW}.

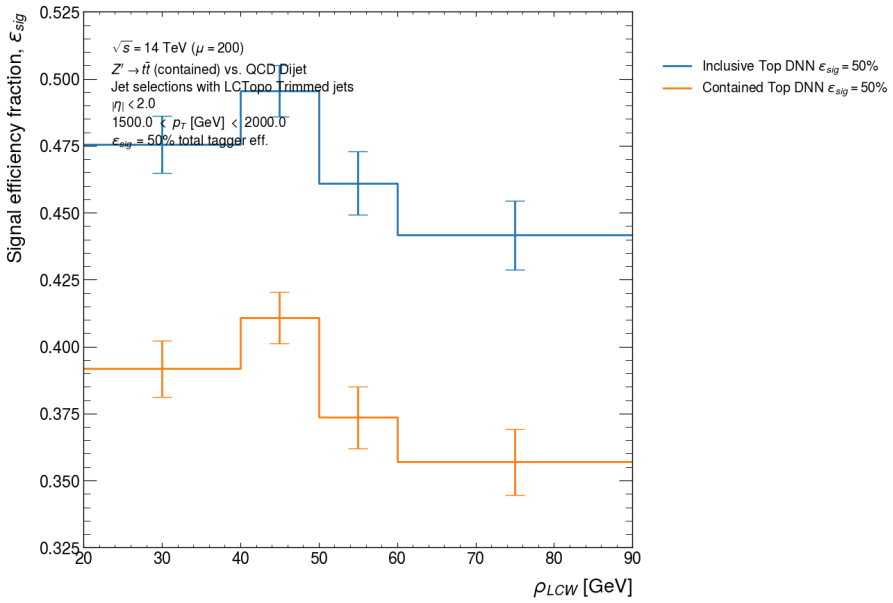

(c) $1500 < p_{\mathrm{T}}$ (GeV) < 2000

Figure 7.53 (cont.): Signal efficiency for 50% signal efficiency DNN tagger working points as a function of ρ_{LCW}.

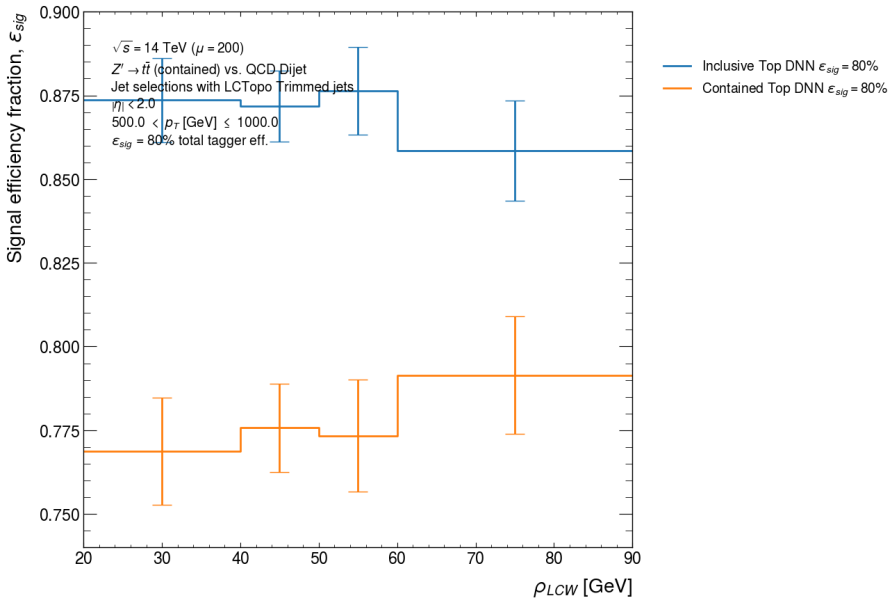

(a) $500 < p_{\mathrm{T}}$ (GeV) ≤ 1000

Figure 7.54: Signal efficiency for 80% signal efficiency DNN tagger working points as a function of ρ_{LCW}.

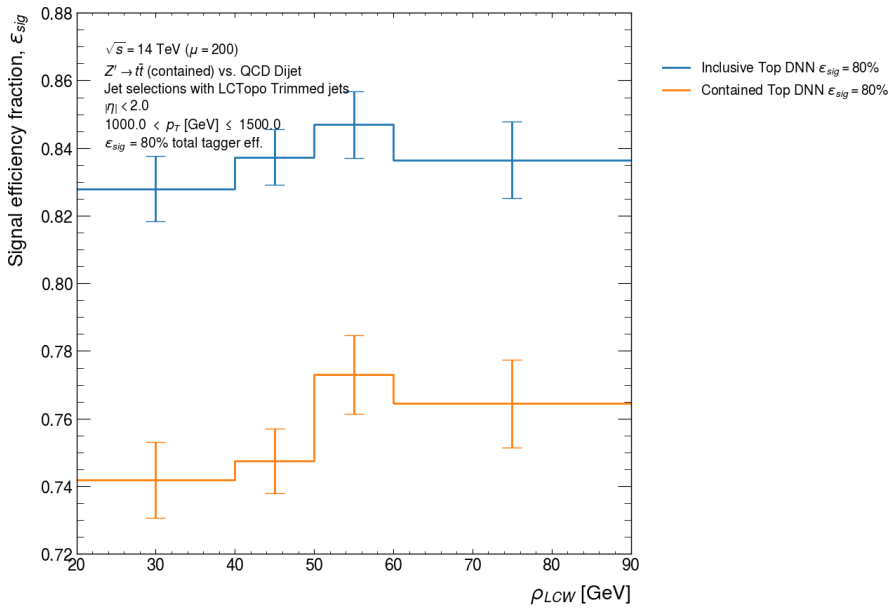

(b) $1000 < p_{\mathrm{T}}$ (GeV) ≤ 1500

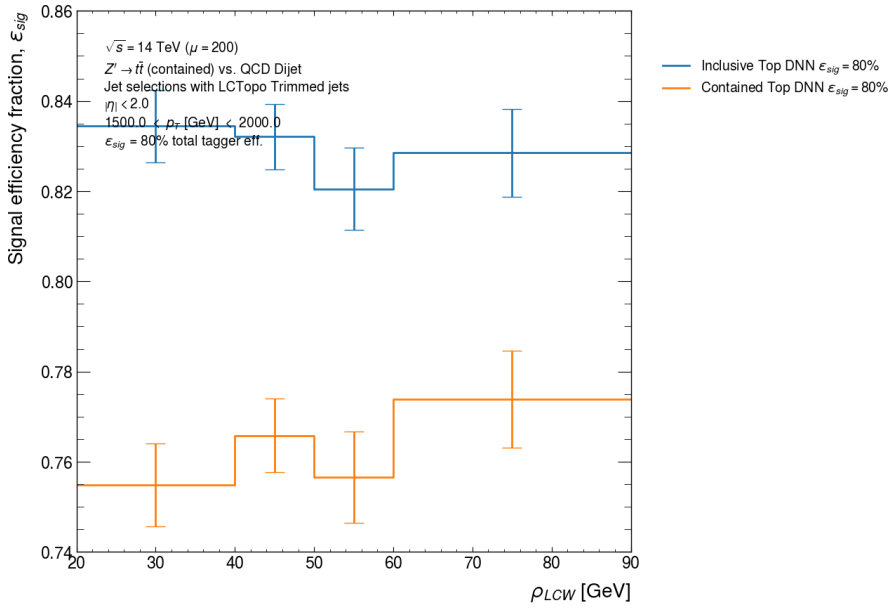

(c) $1500 < p_{\mathrm{T}}$ (GeV) < 2000

Figure 7.54 (cont.): Signal efficiency for 80% signal efficiency DNN tagger working points as a function of ρ_{LCW}.

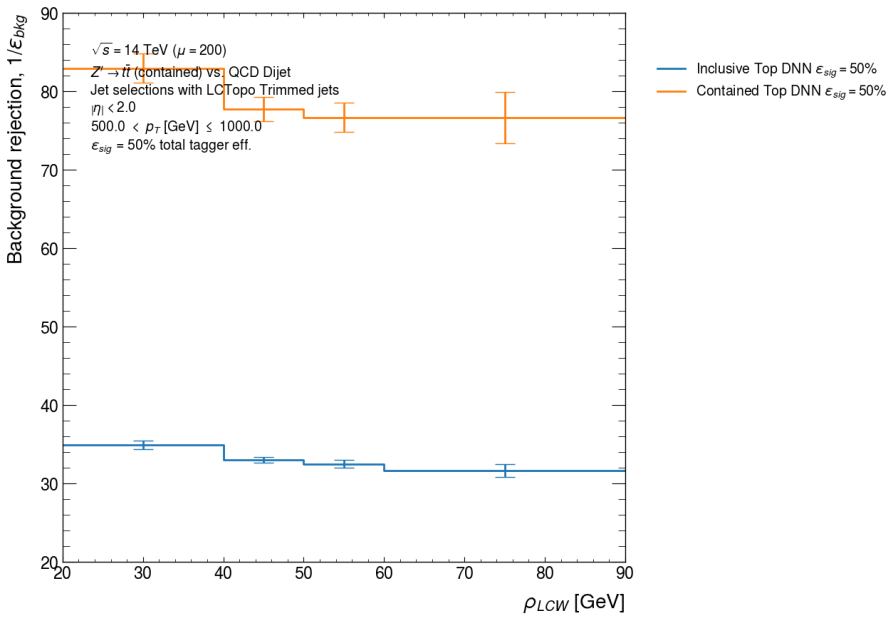

(a) $500 < p_{\mathrm{T}}$ (GeV) ≤ 1000

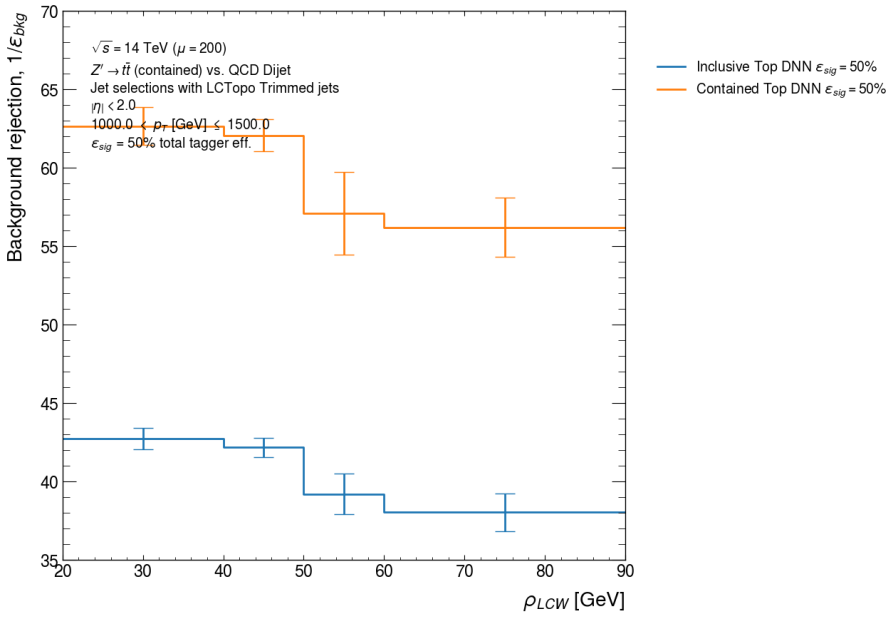

(b) $1000 < p_{\mathrm{T}}$ (GeV) ≤ 1500

Figure 7.55: Background rejection for 50% signal efficiency DNN tagger working points as a function of ρ_{LCW}.

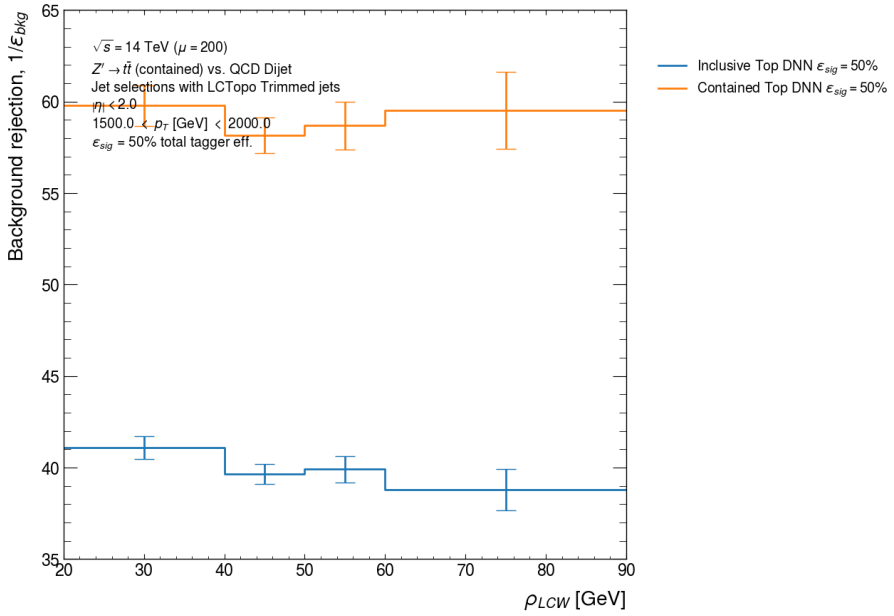

(c) $1500 < p_{\mathrm{T}}$ (GeV) < 2000

Figure 7.55 (cont.): Background rejection for 50% signal efficiency DNN tagger working points as a function of ρ_{LCW}.

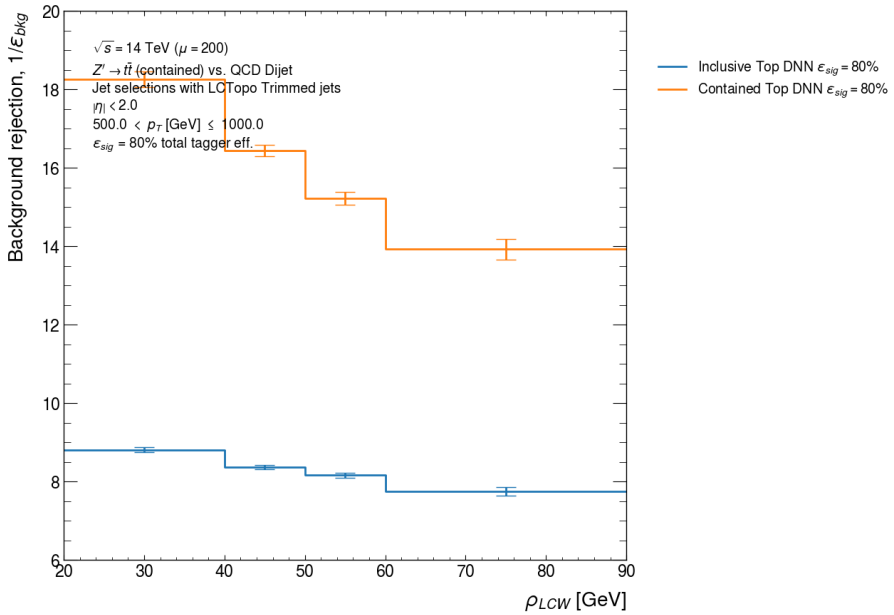

(a) $500 < p_{\mathrm{T}}$ (GeV) ≤ 1000

Figure 7.56: Background rejection for 80% signal efficiency DNN tagger working points as a function of ρ_{LCW}.

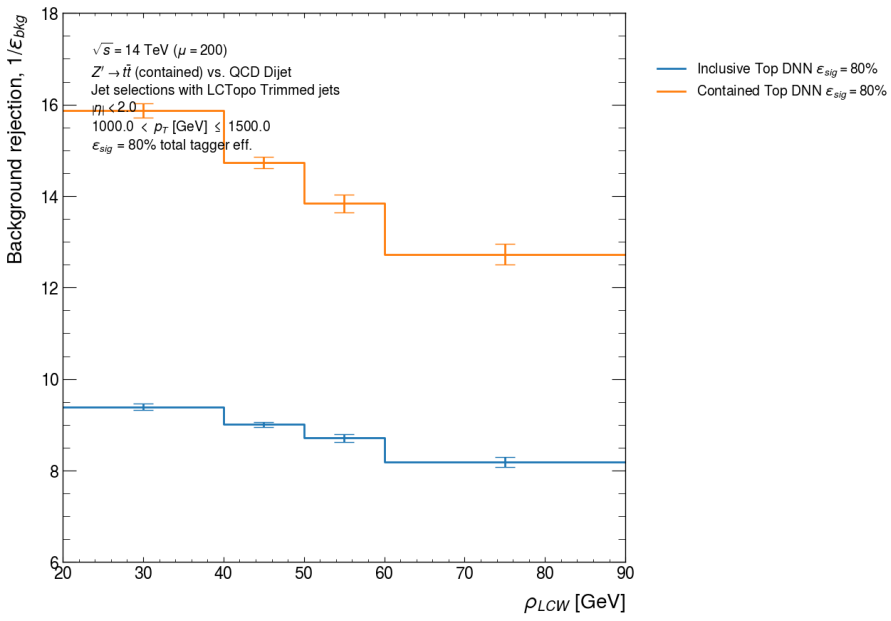

(b) $1000 < p_{\mathrm{T}}$ (GeV) ≤ 1500

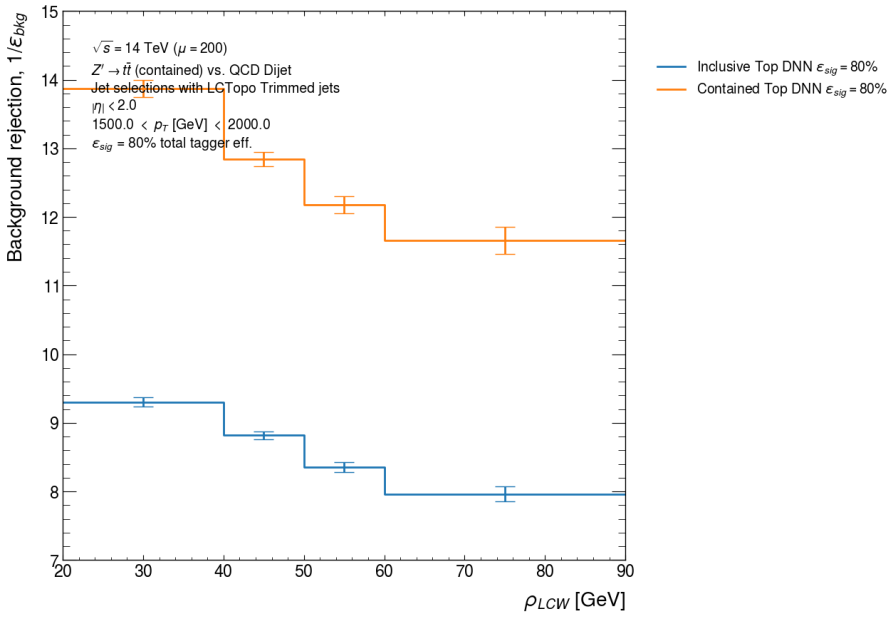

(c) $1500 < p_{\mathrm{T}}$ (GeV) < 2000

Figure 7.56 (cont.): Background rejection for 80% signal efficiency DNN tagger working points as a function of ρ_{LCW}.

7.13 Tagger recommendation development

The best performing trimmed jet $m_{\text{jet}} + S$ tagger was developed further for implementation in the ATLAS code-base, allowing its use in further HL-LHC oriented studies. Other taggers were deemed to have lower background rejection or poorer pile-up stability (e.g. soft-drop jet taggers). The selections on m_{jet} and the sphericity, S, were parameterised as a function of the `LCTopoTrimmed` jet p_{T} so that the tagger can be applied directly to reconstructed jets. We also ensured the cut direction derived for the taggers in each p_{T} bin was the same – if this was not the case it indicated an unexpected (potentially statistics related) fluctuation. The complete tagger definition consists of the optimised 80% or 90% signal efficiency m_{jet} selection from Section 7.8 and the second S cut derived to achieve the 50% or 80% total signal efficiency, respectively.

Polynomials were used to model the m_{jet} and S cuts using a χ^2 fit to the tagger cuts as a function of the p_{T} bin centres. The fits were penalised to ensure the functions passed through the initial/final bin centre point. Below and above the initial and final bin centres, respectively, we assigned these models the value of the tagger cut derived in the complete p_{T} bin. This ensures that the tagger can be applied to jets in the kinematic range of "taggable" (i.e. valid) jets from 350 GeV to 2500 GeV. This procedure leads to approximately continuous, but not necessarily smooth, models of the tagger selection. The variation in the tagger signal efficiency with the jet p_{T} after applying these models in the tagger selection is discussed further later. Five wide p_{T} bins were chosen to describe the tagger cuts due to the limited size of the top quark signal sample, reducing the impact of statistical uncertainties, which were not estimated for the tagger cuts. Thus, the models should provide a set of tagger selections that do not produce rapid (and large) signal efficiency fluctuations. While higher-order models led to a low number of degrees of freedom for the fit (and therefore overfitting), we were primarily concerned with the interpolation performance between known tagger selections. The m_{jet} cut models were evaluated with an F-test procedure to determine the polynomial order that best fit the mass cuts, but the S cut modelling used only a minimisation of the (reduced) χ^2.

The trimmed jet mass cut for both the 80% and 50% signal efficiency taggers in Figure 7.57 is single-sided (">") in all p_{T} bins and increases linearly as a function of the bin-centres. For the 80% signal efficiency tagger, the mass cut for $p_{\text{T}} < 575$ GeV (below the initial bin centre) is set to $m_{\text{jet}} > 96.5$ GeV and for $p_{\text{T}} > 2250$ GeV (above the final bin centre) the cut is set to $m_{\text{jet}} > 142.5$ GeV. The 50% signal efficiency tagger uses tighter selections of $m_{\text{jet}} > 121.5$ GeV (for $p_{\text{T}} < 575$ GeV) and $m_{\text{jet}} > 163.5$ GeV (for $p_{\text{T}} > 2250$ GeV) in those regions. The full functional form for each model is included in text on the plots along with the χ^2 and the number of degrees of freedom for the polynomial fits. Three degrees of freedom exist for the linear mass cut fits, while a single degree of freedom exists for the sphericity cut fits using cubic polynomials, making them more susceptible to overfitting. The sphericity selection for the tagger is non-linear and is well modelled by a cubic polynomial. Like

the mass cut, the sphericity cuts are single sided (“>”) in Figure 7.58. Below the initial bin centre a sphericity cut $S > 0.2115$ and $S > 0.0445$ is made for the 50% and 80% signal efficiency taggers, respectively. Above the final bin centre a sphericity cut $S > 0.2665$ and $S > 0.0965$ is made for the 50% and 80% signal efficiency taggers, respectively.

The 50% signal efficiency tagger sphericity cut model in Figure 7.58a, peaks just before the final fit point. To avoid this, a quartic model was tested, but it recovered very similar parameters to the cubic fit – a consequence of the low number (1) of degrees of freedom for the higher-order fit. The only way explored to remove this peak was to fix the coefficients of some terms (i.e. the quadratic and cubic terms) to zero during the fit. A more complete consideration of the interpolation between the tagger cuts could explore a wider range of alternate fit functions and different interpolation techniques with a finer p_{T} binning. However, for our purposes the cubic fit achieves reasonable interpolation given the limitations of the signal sample size and the wide p_{T} bins used.

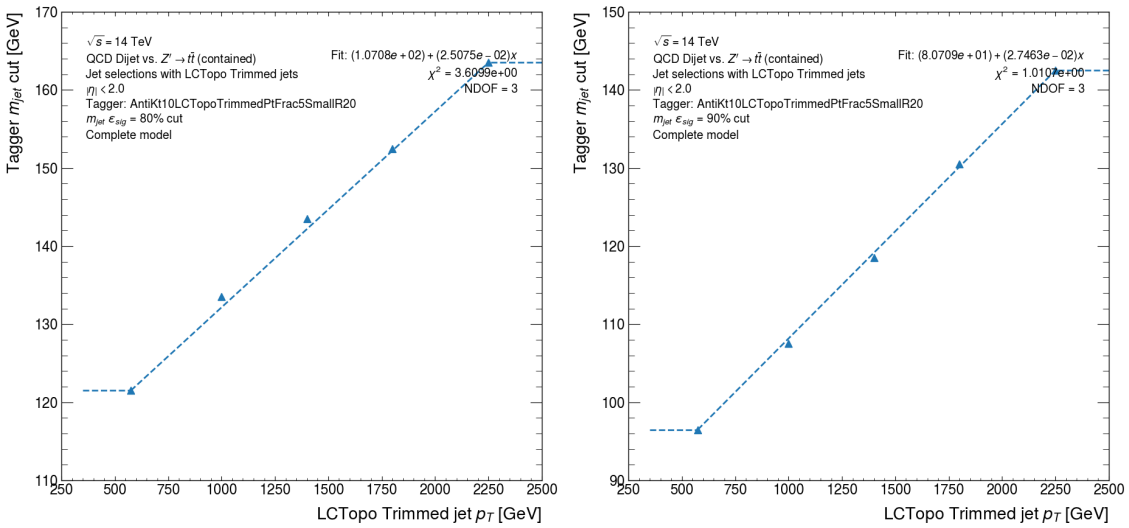

(a) 50% signal efficiency tagger (b) 80% signal efficiency tagger

Figure 7.57: Complete models for the trimmed jet mass selections used in the two-variable tagger recommendations.

Three different p_{T} binning schemes were used to evaluate the stability of the tagger signal efficiency with the complete tagger definitions after deriving the m_{jet} and S cut models. The first is the same as that used to derive the tagger selections, and we see reasonable stability for both efficiency working points in Figure 7.59. An apparent increase in the signal efficiency with p_{T} likely results from better containment of the top quark decay in the jet. Secondly, we split the initial and final bins of the first p_{T} binning scheme to determine if significant signal efficiency variation results from using models that are approximately continuous but not smooth. Similar stability to the first binning is seen in Figure 7.60 where at low-p_{T} the signal efficiencies of the

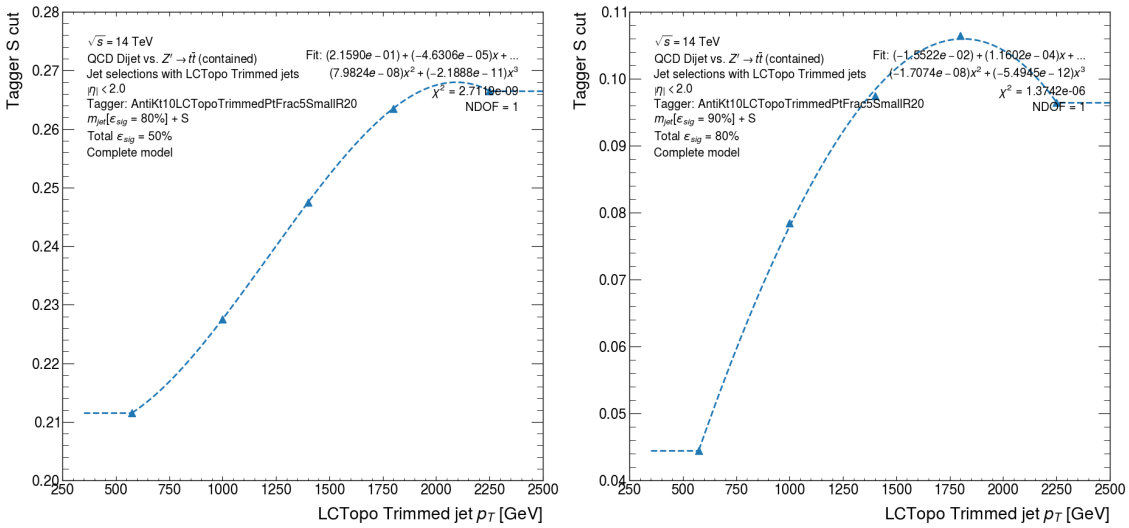

(a) 50% signal efficiency tagger (b) 80% signal efficiency tagger

Figure 7.58: Complete models for the trimmed jet sphericity selections used in the two-variable tagger recommendations.

two halves of the original bin agree to within statistical uncertainty. However, in the highest p_{T} bin a fluctuation to greater signal efficiency is seen, but it is not a significant deviation (e.g. several percent) with respect to the required total tagger signal efficiency. The third and final binning in Figure 7.61 accessed a larger p_{T} range by adding a lower bin with a width of 50 GeV to reach $p_{\mathrm{T}} = 300$ GeV and an upper bin from 2500 GeV to 3000 GeV. The addition of the narrow lower bin leads to a significant statistical uncertainty, which obscures an apparent drop in the tagger signal efficiency. However, the uppermost bin is consistent with the increasing signal efficiency trend at higher p_{T}. A larger fluctuation in signal efficiency is seen for the 50% signal efficiency tagger than for the 80% signal efficiency tagger. The stability of the signal efficiency with these different p_{T} binning schemes indicates that there is no apparent problem with the models used for the m_{jet} and S cuts.

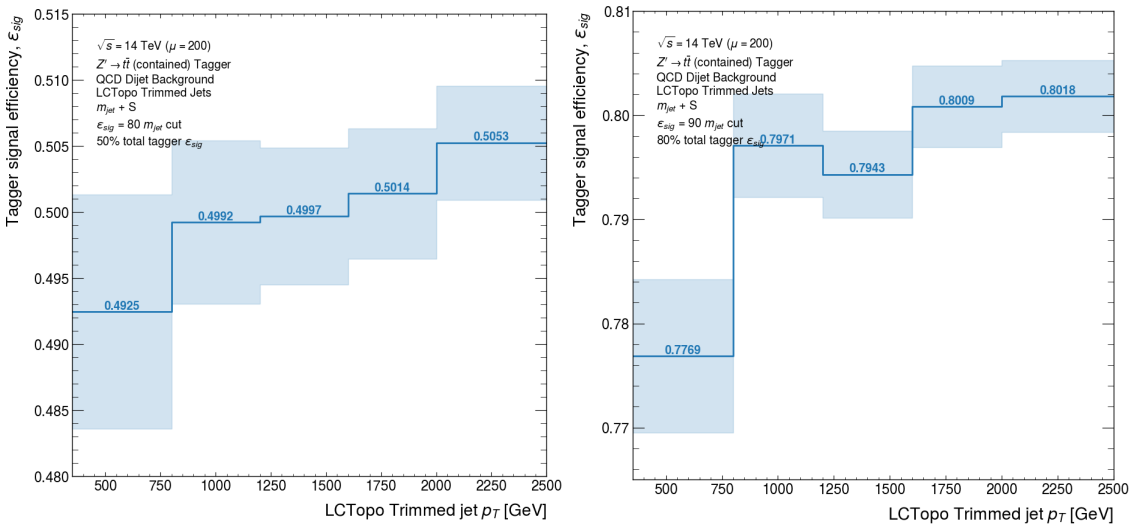

(a) 50% signal efficiency working point (b) 80% signal efficiency working point

Figure 7.59: The signal efficiency as a function of the reconstructed jet p_{T} for the trimmed jet tagger recommendation. The p_{T} binning is the same as that used for deriving the tagger cuts. The statistical uncertainty in the signal efficiency is indicated by the shaded area.

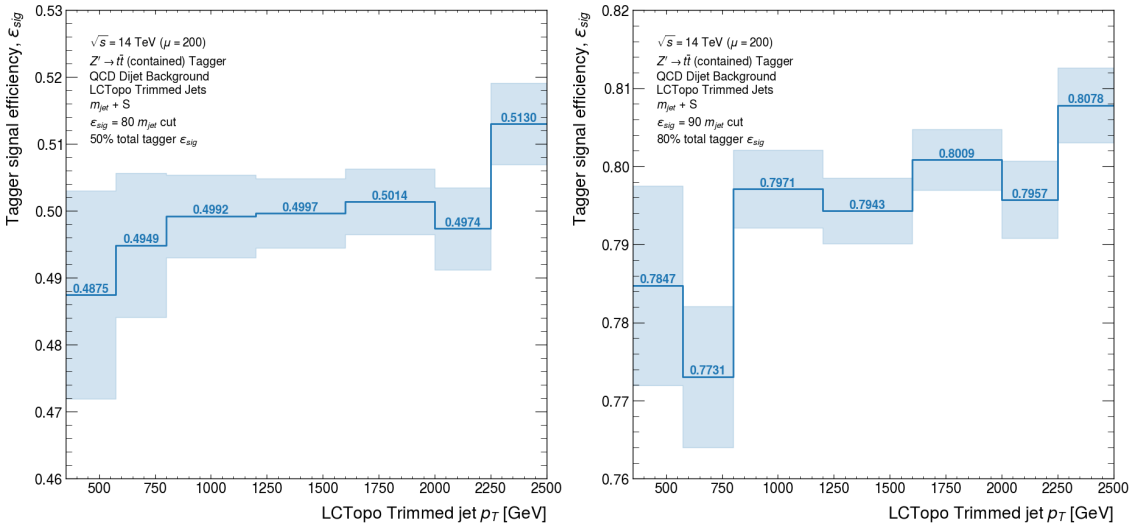

(a) 50% signal efficiency working point (b) 80% signal efficiency working point

Figure 7.60: The signal efficiency as a function of the reconstructed jet p_{T} for the trimmed jet tagger recommendation. The p_{T} binning is the same as that used for deriving the tagger cuts with the exception that the initial and final bins are split into two equal width bins. The statistical uncertainty in the signal efficiency is indicated by the shaded area.

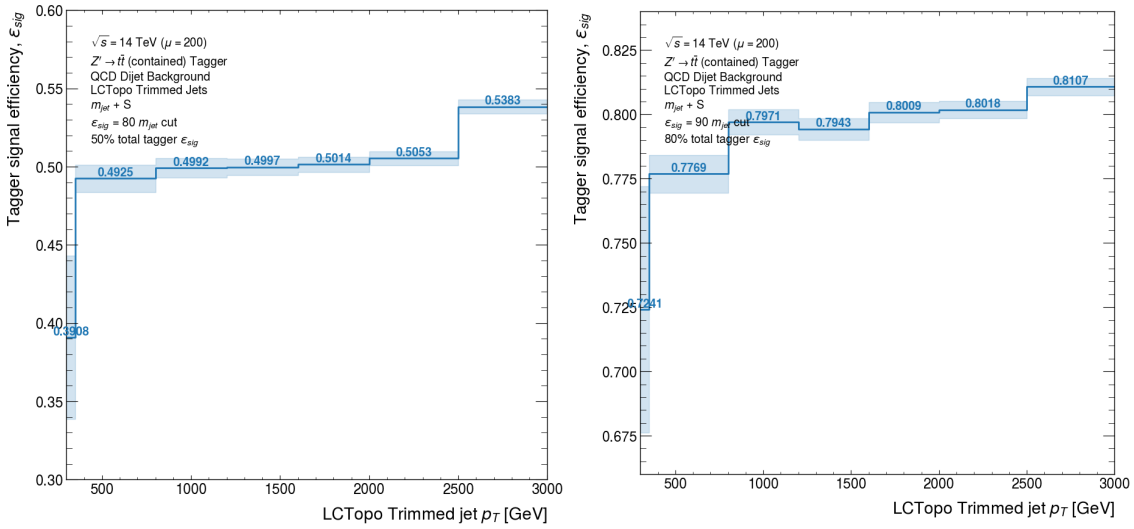

(a) 50% signal efficiency working point

(b) 80% signal efficiency working point

Figure 7.61: The signal efficiency as a function of the reconstructed jet p_{T} for the trimmed jet tagger recommendation. The p_{T} binning is the same as that used for deriving the tagger cuts with additional bins at low and high p_{T} to consider the tagger performance in a 300 GeV to 3000 GeV p_{T} range. The statistical uncertainty in the signal efficiency is indicated by the shaded area.

7.14 Summary and further work

The development of recommendations for a first set of HL-LHC top quark taggers was discussed in detail throughout this Chapter. The results indicate that a jet mass and sphericity selection are optimal for a trimmed jet tagger definition, and provide reasonable pile-up stability compared to other tagger definitions. These taggers will be implemented and used in HL-LHC physics studies in the future, but should also be studied further and extended. Run 2 neural network (DNN) taggers for contained top quark decays were also evaluated, and they outperform the two-variable tagger definitions despite a small signal efficiency loss (relative to the 50% or 80% signal efficiency expected).

Avenues for future study include:

- Adapting the truth labelling scheme discussed in Section 7.2.2 to apply the contained top quark definition to the ungroomed truth jet collection, but match the truth groomed jets to the reconstructed groomed jets as in Ref. [130]. With these changes the truth matching/labelling would be more consistent with recent jet labelling techniques.

- Validating the two-variable tagger recommendations further in simulation. Firstly, the jet mass distributions for tagged `LCTopoTrimmed` jets should be studied to ensure no unwanted effects result from any of the chosen selections.

Secondly, the performance of the top quark taggers could be measured in an independent event sample to compare their performance. Finally, the jets in this study were required to be centrally located within $|\eta| < 2$, but at the HL-LHC the tracking acceptance will be larger. It could be quite interesting to study the η dependence of the tagger performance for calorimeter jets and compare that to jets that use tracking information[18].

- Extending the optimisation of the 80% signal efficiency cut-based (two-variable) taggers by means of considering additional mass selections.

- Verifying the performance of the sphericity observable compared to τ_{32}^{wta} in Run 2 simulation to further understand changes in the tagger performance relative to previous studies where τ_{32}^{wta} is generally more performant [80].

- Extending the taggers to different jet inputs. This includes more recent jet inputs such as the Unified Flow Objects introduced in Chapter 4 (Section 4.2.2) and origin-corrected `LCTopo` inputs. The limitations of the samples[19] used for these studies meant that only the `LCTopo` jets with no origin correction could be studied.

- Considering a wider range of tagger observables for the cut-based algorithms, including taggers with up to three variables. The selection on the third variable can be used to achieve even higher background rejection.

- Developing and testing more complex tagger algorithms. Since the Run 2 DNN taggers perform so well relative to the cut-based taggers we studied, it is possible that simply re-optimising the DNN taggers in HL-LHC simulation (and using a different jet mass definition) could recover their signal efficiency loss.

There is clearly still much to study in the field of boosted jet identification in the lead up to the commissioning of the ATLAS detector for HL-LHC operations. The use of more sophisticated algorithms that include additional forms of pile-up mitigation will be essential for jet substructure analyses in the anticipated $\mu = 200$ high pile-up environment. Further innovations in jet substructure tagging and their inclusion in the ATLAS trigger systems could also provide a means to identify the

[18] We expect that the calorimeter occupancy will increase in the forward region as in previous LHC runs – there is more pile-up contamination in the forward region. Thus, the performance of calorimeter only jet taggers *should* fall, whereas, pile-up rejection methods could be applied for jet inputs with tracking information, improving the large-$|\eta|$ tagger performance.

[19] Differences in distributions between the primary reconstruction between signal and background samples.

most "interesting" hadronic events in real-time with connections to Chapters 5 and 6.

Chapter 8

Conclusion

The start of Run 3 in mid-2022 and the eventual commissioning of the HL-LHC provides an opportunity to explore Standard Model physics further and expand the limits imposed on Beyond the Standard Model physics – hopefully with more discoveries. However, increases in luminosity will lead to an increase in the level of contamination from simultaneous pp interactions necessitating additional considerations for triggering and data acquisition, as well as the reconstruction of hadronic final states. Innovations in these areas will be essential to handle the much more demanding environment of HL-LHC pp collisions. The results presented in this thesis address triggering for low-mass searches in both Run 3 and at the HL-LHC, as well as the identification of top quarks in HL-LHC conditions.

The low-mass search studies were aimed at a multi-jet R-parity violating SUSY gluino pair-production signal, but the results are also interpreted in the context of obtaining sensitivity to electroweakino production. Thus, the general findings need not be limited to a particular signal process. We considered the application of TLA – the study of trigger-level information rather than complete offline events – to alleviate limitations on data acquisition. Different Level-1 (hardware) trigger selections were tested with basic kinematic selections on multiple jets (multi-jet triggers, especially those with asymmetric thresholds) and the H_{T}, an event-level measure of the total momentum contribution from hadronic jets. Both trigger signatures produced better signal acceptances than the previous high-p_{T} threshold single-jet trigger selections. These results have informed the development of the ATLAS trigger menu for Run 3, where TLA will be used to search for multiple signatures of new physics. The outcomes of the work in this thesis indicate that the Level-1 trigger H_{T} selections warrant further study for a wider range of signal processes. These triggers do not have an explicit single-jet selection (with high thresholds) and therefore are potentially a more flexible choice for a wide range of signal topologies. Although a basic study of the effect of pile-up mitigation techniques was conducted (in the form of pile-up jet rejection selections), a broader study is also needed to more accurately emulate the conditions of the ATLAS trigger *and* consider a wider range of pile-up mitigation strategies. While the HL-LHC TLA studies were only introduced briefly, we saw that a loosening of certain selections produces better analysis performance for a higher mass $m = 400$ GeV resonance. Using the expected 3000 fb^{-1} integrated luminosity

of the complete anticipated HL-LHC dataset we extrapolated the cross-section of this signal to that expected for electroweakinos and found that it is possible to nearly achieve discovery-level significance. Nonetheless, there are numerous areas for further study based on these results. Most significantly, the low statistics of the event samples led to modelling issues for the background and could also influence the results for analysis significances. Significant further work will need to be carried out to solve these (and other) problems in addition to emulating the effect of different HL-LHC trigger selections.

In the high-mass and high-momentum regime, HL-LHC jet tagging studies led to the development of a selection-based tagger recommendation for boosted, hadronically decaying top quarks. This employs selections on both the jet mass and sphericity, a jet/event shape variable. Tagging boosted objects in the HL-LHC conditions will require significant additional work to develop more pile-up stable recommendations. However, even without re-optimisation, more complicated Run 2 taggers (the DNN tagger) showed reasonable performance despite the increase in pile-up levels and CM frame energy. Several follow-up studies and avenues for the work were addressed in the summary of Chapter 7 so they will not be replicated here. However, we will stress that this first set of studies is only the beginning of the development of the HL-LHC jet taggers. Since we only considered tagging central ($|\eta| < 2$) jets, further studies should aim to explore the η dependence of the tagging performance, particularly because the tracking acceptance increases significantly at the HL-LHC. Further to this, more pile-up robust jet inputs could be studied as an alternative to the calorimeter-only jets used to develop the existing recommendations. While these studies have focused explicitly on top quark tagging, they should be extended to consider a wider variety of event topologies including hadronic W/Z-boson decays (and potentially even Higgs boson decays).

Appendix A

Jet reconstruction procedures

This Appendix provides more detail regarding the reconstruction and calibration of hadronic jets discussed in Chapter 4.

A.1 LCW calibration for calorimeter topological clusters

The Local Hadronic Cell Weighting (LCW) calibration described for calorimeter topological clusters in Section 4.2.2 is discussed here in more detail and focuses primarily on an overview of the calibration procedure.

The LCW calibration relies on a two-dimensional likelihood to determine the EM or hadronic origin of clusters [64]. The discriminating variables for the likelihood are related to the differences between the depths of hadronic and EM showers (hadronic showers penetrate further) in the calorimeter and the fluctuations seen in those showers [64]. The threshold for hadronic/EM classification is defined as the $\mathcal{P}_{\text{clus}}^{\text{EM}} > 50\%$ contour ($\mathcal{P}_{\text{clus}}^{\text{EM}} \to 1$ for EM deposits) [64]. The classification is introduced into the calibration constant (or scale factor) for a particular cell as [64]:

$$w_{\text{cell}}^{\text{cal}} = \mathcal{P}_{\text{clus}}^{\text{EM}} \times w_{\text{cell}}^{\text{em-cal}} + (1 - \mathcal{P}_{\text{clus}}^{\text{EM}}) \times w_{\text{cell}}^{\text{had-cal}} \tag{A.1}$$

where $w_{\text{cell}}^{\text{had-cal}}$ is a hadronic calibration scale factor and $w_{\text{cell}}^{\text{em-cal}}$ an EM calibration scale factor. The scale factors are determined for each cell by the ratio of the actual deposited energy and corresponding EM scale deposited energy [64]. Both the hadronic and EM scale factors are used in the $w_{\text{cell}}^{\text{cal}}$ to limit the impact of a particular classification (hadronic vs. EM) on the total cell scale-factor [64]. The LCW (hadronic) part of the calibration above aims to unify the response of the calorimeters (after measurements) to EM (e.g. electron) deposits and hadronic (e.g. pion) deposits [64].

The dead material and out-of-cluster corrections are implemented similarly to the hadronic calibration (albeit with differences discussed in Ref. [64]) so that the total

energy of a cluster can be calculated as [64]:

$$E_{\text{clus}}^{\text{cal}} = \sum_{\text{cell},i} w_{\text{cell},i}^{\text{cal}} \times E_{\text{cell},i}^{\text{EM}} \tag{A.2}$$

where the total calibration scale factor is given by the product of the factors for each individual correction [64]:

$$w_{\text{cell}}^{\text{cal}} = \prod_{\text{calibrations (cal)}} \left[\mathcal{P}_{\text{clus}}^{\text{EM}} \times w_{\text{cell}}^{\text{em-cal}} + (1 - \mathcal{P}_{\text{clus}}^{\text{EM}}) \times w_{\text{cell}}^{\text{had-cal}} \right]. \tag{A.3}$$

Further discussion of the calibration procedures for topoclusters is given in Ref. [64].

A.2 Further jet inputs

Different inputs to jet reconstruction are discussed in Section 4.2.2. Some of the more complicated jet inputs are introduced in additional detail below.

Particle flow objects

Particle flow (`PFlow`) objects combine calorimeter and tracking information to produce more pile-up robust jet inputs with improved energy and mass resolution [63, 66]. The reconstruction of `PFlow` objects is designed to combine the track and calorimeter information without double counting their energy contributions [63, 66]. This proceeds by matching every charged particle track to a calorimeter topocluster [66]. When a particle deposits energy in several clusters, additional topoclusters are added to the `PFlow` object based on calculated probabilities of the extra energy deposits [66]. Neutral particles are associated with topoclusters with no matching track, and their clusters remain in the `PFlow` object with no further modifications [66]. The double-counting prevention consists of subtracting energy from topoclusters equal to the expected deposit from the matched track [66]. When the track fully reconstructs the particle and the topocluster signal is consistent with the noise from a single particle, the complete topocluster energy is removed [66]. At high track p_{T}, the double-counting subtraction is not performed since the performance of charged particle tracking decreases at high-p_{T}. For any track with p_{T} above 100 GeV no subtraction is applied, and tracks are no longer used in the `PFlow` objects [66, 67]. The subtraction is only applied provided the track p_{T} is below 100 GeV and the requirement below is *not* satisfied [66, 67]:

$$\frac{E^{\text{clus}} - \langle E_{\text{dep}} \rangle}{\sigma(E_{\text{dep}})} > 33.2 \times \log_{10}\left(\frac{40\ \text{GeV}}{p_{\text{T}}^{\text{trk}}}\right) \tag{A.4}$$

In Equation (A.4) E^{clus} and E_{dep} are the energy deposit in a $\Delta R = 0.15$ cone around the track and the energy deposit predicted for a charged pion, respectively.

Recent developments

Recent studies of the performance of different jet inputs in large-R jet reconstruction have shown promising performance for *Track Calo-Clusters* (TCCs) and *Unified Flow Objects* (UFOs) [66]. TCCs provide beneficial performance over `PFlow` objects at high-p_{T} where the double-counting prevention mechanism for `PFlow` inputs is disabled [66]. Unlike `PFlow` inputs, the basic premise of TCC reconstruction is that tracks determine the angular coordinates (η, ϕ) and the topocluster determines the TCC p_{T} [66]. A combination of TCCs and `PFlow` objects are used in UFOs to obtain good reconstruction performance across a wide p_{T} range [66]. For UFO reconstruction, the TCCs are built from `PFlow` objects and charged particle tracks that were not combined with topoclusters during the construction of `PFlow` objects [66].

A.3 Small-R jet calibration procedures

Further to the short description of the small-R jet calibration procedure in Section 4.5 this Section provides a more complete overview of the steps in the calibration. The corrections for each calibration step are applied directly to the jet 4-momentum vectors (or individual components in certain cases) and address detector reconstruction effects including transitions to different detector granularity and technologies. The calibration sequence displayed in Figure 4.4 (Section 4.5) shows the various stages of the *Jet Energy Scale* calibration. In principle, this sequence can be applied to jets clustered from any input object regardless of whether they are reconstructed from tracking or calorimeter information (e.g. `PFlow` objects or topoclusters). The calibrations discussed here are based on those for `EMTopo` jets in Ref. [74], but similar methods are applied for `EMPFlow` jets in Ref. [67].

A.3.1 Jet origin correction

Jet origin corrections can be applied at the level of jet inputs (topoclusters, etc.) before jet reconstruction or to the jet constituents as part of the calibration sequence (for `EMTopo` jets) and ultimately improve the η coordinate resolution [74]. The origin correction ensures that the jet 4-momentum points from the primary vertex rather than the geometrical centre of the detector [74]. Consequently, this correction only impacts the jet 4-momentum direction, not its magnitude [74]. The η coordinate derived with respect to the geometric centre of the detector is commonly referred to as the detector η (η_{det}).

A.3.2 Pile-up corrections

Soft pile-up radiation clustered into jets is a source of contamination and necessitates a pile-up subtraction procedure [74]. The pile-up activity in events is determined as the *median* momentum-density calculated by clustering $R = 0.4$ k_t jets from positive energy topoclusters and measuring [74]:

$$\rho = \left\langle \frac{p_{\mathrm{T}}}{A} \right\rangle \tag{A.5}$$

from (central) jets within $|\eta| < 2$ (avoiding the significant pile-up occupancy in the foward region) where A is the k_t jet area and p_{T} is its transverse momentum. The area of an anti-k_t (and k_t) jet is measured by ghost-association[1] such that the area is a measure of the number of ghost-associated particles [74]. The pile-up subtraction proceeds using the uncorrected anti-k_t jet p_{T} ($p_{\mathrm{T}}^{\mathrm{reco}}$) and its area A to give $p_{\mathrm{T}}^{\mathrm{sub,A}} = p_{\mathrm{T}}^{\mathrm{reco}} - \rho \times A$, the pile-up subtracted jet p_{T} [74].

A residual pile-up correction is then made in terms of [74]:

- N_{PV}, the number of primary vertices and a measure of in-time (within a bunch crossing) pile-up activity.
- μ, the average number of interactions per bunch crossing and a measure of the out-of-time (between bunch crossings) pile-up activity.

This is required since the earlier calculation of ρ does not consider the forward region, which leads to additional pile-up dependence for non-central or very energetic jets [74].

The residual correction measures the dependence of the jet p_{T} on N_{PV} and μ in bins of the p_{T} of truth jets matched (with a ΔR association) to the reconstructed jet ($p_{\mathrm{T}}^{\mathrm{true}}$) and the jet $|\eta|$ (or detector $|\eta|$ ($|\eta_{\mathrm{det}}|$) in Ref. [67] for `PFlow` jets) [74]. Linear fits of the reconstructed jet p_{T} in ($p_{\mathrm{T}}^{\mathrm{true}}$, $|\eta_{(\mathrm{det})}|$) bins are used to obtain coefficients α, β for use in the complete pile-up subtraction [74]:

$$p_{\mathrm{T}}^{\mathrm{sub}} = p_{\mathrm{T}}^{\mathrm{reco}} - \rho \times A - \alpha \times (N_{\mathrm{PV}} - 1) - \beta \times \mu \tag{A.6}$$

where α and β correspond to the fitted parameters at $p_{\mathrm{T}}^{\mathrm{true}} = 25$ GeV in each $|\eta|$ bin. After both the pile-up subtraction and residual pile-up correction, the jet p_{T} is approximately independent of N_{PV} and μ as seen in Figure A.1 [74].

The complete correction is applied using a 4-momentum scale factor [74]:

$$\mathcal{R} = \frac{\rho \text{ subtracted jet } p_{\mathrm{T}}}{\text{uncorrected jet } p_{\mathrm{T}}} \tag{A.7}$$

that only alters the magnitude of the 4-momentum (i.e. not the direction).

[1] The association (by jet clustering) of particles with infinitesimally small energies to the jet, thus drawing on only the angular components of the distance measures in the (anti-)k_t algorithm [74].

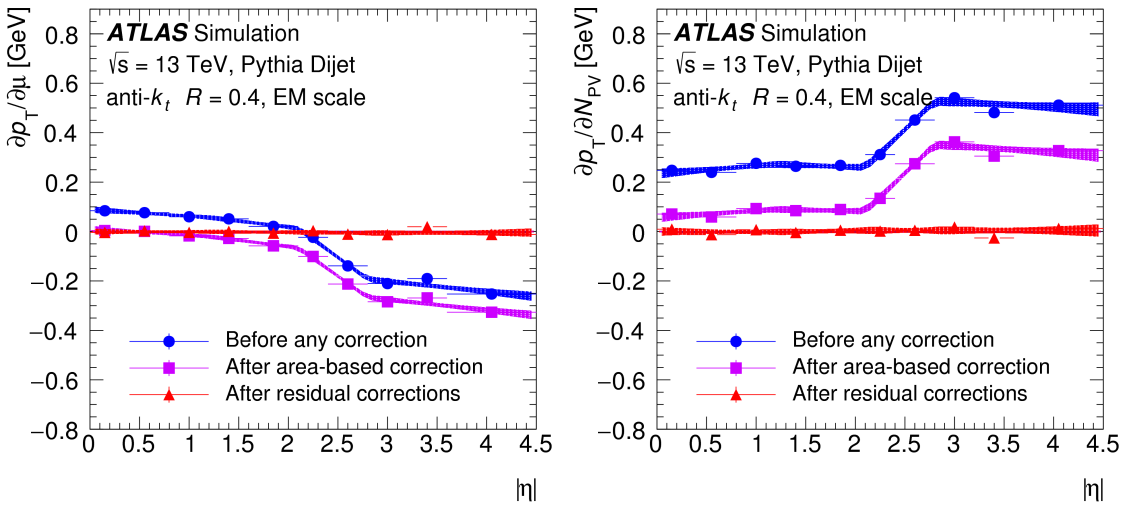

(a) (b)

Figure A.1: The pile-up dependence of the `EMTopo` jet p_{T} before and after JES pile-up corrections for $p_{\mathrm{T}}^{\mathrm{true}} = 25$ GeV [74]. This is quantified as the derivative of the jet p_{T} with respect to N_{PV} averaged over μ (right) and the average number of interactions per bunch crossing averaged over N_{PV} (left) as a function of $|\eta|$ [74]. Taken from [74].

A.3.3 Jet energy scale calibration

The next calibration step is an MC based energy scaling of reconstructed jets matched to truth-level jets to achieve an energy scale comparable to that of the truth jets. Additional isolation requirements are considered for the reconstructed jets to avoid energy contamination from overlapping objects [74]. The reconstructed and truth jets are used to define a jet energy response [74]:

$$\mathcal{R} = \frac{E^{\mathrm{reco}}}{E^{\mathrm{truth}}} \tag{A.8}$$

where E^{reco} is the reconstructed jet energy and E^{truth} is the truth jet energy. The average jet energy response, $\langle\mathcal{R}\rangle$, is determined by fitting a Gaussian function to the peak of the response distribution and is parameterised in bins of $|\eta_{\mathrm{det}}|$ and E^{truth} [74].

The calibration coefficients for the jet 4-momentum, c_{JES}, are obtained with numerical inversion [74]. First the average jet energy response ($\langle\mathcal{R}\rangle$) and the average reconstructed jet energy ($\langle E^{\mathrm{reco}}\rangle$) are calculated in every E^{truth} and η_{det} bin [75]. The ($\langle E^{\mathrm{reco}}\rangle$, $\langle\mathcal{R}\rangle$) points are then parameterised with the function [75]:

$$\mathcal{F}(E^{\mathrm{reco}}) = \sum_{i=0}^{N_{\mathrm{max}}} a_i \times (\ln E^{\mathrm{reco}})^i \tag{A.9}$$

over the complete E^{truth} binning range in each η_{det} bin. In Equation (A.9) the terminating order of the fit, N_{max}, (between 1 and 6) and fit parameters, a_i, are optimised to achieve the best fit [75]. Finally, the correction scale factors (c_{JES}) are calculated as $1/\mathcal{F}$, as in the energy correction shown in Equation (A.10), which is evaluated in terms of E^{reco} and η_{det} [75].

$$E_{\text{EM+JES}} = c_{\text{JES}} \times E^{\text{reco}} = \frac{1}{\mathcal{F}(E^{\text{reco}})\big|_{\eta_{\text{det}}}} \times E^{\text{reco}} \tag{A.10}$$

In transition regions between parts of the detector where the granularity or detector material changes significantly, the difference between the reconstructed and truth jet η can depart from zero [74, 75]. Thus, an η correction is derived using the difference between the reconstructed and truth jet η as a function of the truth jet energy and η_{det} [67, 74, 75], and numerical inversion is used for the energy correction (which affects the reconstructed jet p_{T}). These corrections *only* affect the η and p_{T} coordinates of the 4-momentum [67, 74].

A.3.4 Global sequential calibration

Quark- and gluon-initiated jets behave differently in the detector. Gluon-initiated jets typically contain softer radiation that does not penetrate as far into calorimeters [74]. Whereas the hadrons in quark-initiated jets are detected at greater depths in calorimeters since they are more energetic [74]. The *Global Sequential Calibration* (GSC) is applied to reduce the dependence of the jet calibration on the initiating particle [74]. Numerical inversion is used to sequentially derive 4-momentum correction factors in terms of five different variables [74]:

1. f_{Tile0}, the proportion of the reconstructed jet energy deposited in the first Tile calorimeter layer.
2. f_{LAr3}, the proportion of the reconstructed jet energy deposited in the third EM LAr calorimeter layer.
3. n_{trk}, the number of ghost-associated tracks matched to the jet with $p_{\text{T}} > 1$ GeV.
4. $\mathcal{W}_{\text{trk}}$, the p_{T} weighted (η, ϕ) plane distance between the jet axis and ghost-associated tracks from (3).
5. n_{segments}, the number of ghost-associated track segments reconstructed in the Muon Spectrometer, measuring the "punch through" of jet radiation not absorbed by the EM/hadronic calorimeters.

All corrections are determined in bins of the jet momentum (p_{T}), except the final n_{segments} correction where the jet energy better describes the radiation exiting the calorimeters and is used for the binning [74]. An additional observable dependent on tracking information is used at the beginning of the `PFlow` GSC correction in Ref. [67].

A.3.5 In situ calibration

The final *in situ* correction step in the jet calibration procedure is applied only to data (not simulated MC samples). Both data and MC samples are used to correct for remaining differences between the measured and simulated jet 4-momentum [74]. The *in situ* correction accounts both for any mis-modelling of physical processes in MC simulations and the response of the detector [74]. The correction factors for the jet 4-momenta are again derived using numerical inversion but from a double ratio of the form [74]:

$$c = \frac{\mathcal{R}^{\text{data}}}{\mathcal{R}^{\text{MC}}} \tag{A.11}$$

where $\mathcal{R}$ is the jet response calculated for data and MC simulations.

A range of event topologies are used to correct the jet 4-momenta in different detector regions and p_{T} ranges [74]. Each of the corrections uses a *balancing* procedure where an event selection is applied to data to identify topologies with a jet recoiling against other well measured (and calibrated) objects [74]. Thus, the jet response in data and MC is defined as the ratio of the p_{T} of these objects, but some exceptions exist to this definition depending on the physics process used for the correction.

The *in situ* corrections begin with the η intercalibration, which corrects the jet response of forward jets ($0.8 < |\eta_{\text{det}}| < 4.5$, including those outside the tracking acceptance) to that of centrally measured jets ($|\eta_{\text{det}}| < 0.8$) by balancing the forward jet with a central jet [74]. This correction is particularly important since the response measured in the central region differs to that measured in the forward region [67, 74], which might be associated with the higher pile-up levels at large $|\eta|$.

The next corrections are derived from $Z+$jet (for jets with $20 < p_{\text{T}}$ [GeV] < 500) and $\gamma+$jet (for jets with $36 < p_{\text{T}}$ [GeV] < 950) events, and exploit topologies where a leptonic Z decay and photon recoil against a jet, respectively [74]. These corrections are limited to particular ranges in jet p_{T} due to the allowable kinematics for the Z decay and the scarcity of very high momentum photons among other factors [74]. Additional event selections are used to prevent cases where extraneous hadronic (jet) radiation boosts the Z/γ further, and measurements involving surrounding tracks quantify any energy lost from the jet during hadronisation [74]. A second step exploits the $\vec{E}_{\text{T}}^{\text{miss}}$ to encapsulate all hadronic activity in the event that recoils against the Z/γ [74].

The final stage in the *in situ* correction is the multi-jet balance where jets with $p_{\text{T}} < 2$ TeV not considered in previous steps are balanced against a collection of already calibrated (i.e. in the p_{T} ranges for previous corrections) jets [74]. This is achieved with an event selection requiring at least three jets, and the highest p_{T} jet is balanced against the other jets [74]. The combined p_{T} of these recoiling jets is calculated from a 4-momentum sum and used in the jet p_{T} response measurement [74].

The total *in situ* correction to the jet 4-momentum culminates in a statistical combination of each *in situ* balance where their relative contributions depend on the jet p_{T} and the uncertainty in the response calculated with each method [74].

Further detail regarding these calibration procedures is available in Ref. [67, 74].

Appendix B

Jet substructure observables

This Appendix provides an overview of the jet substructure observables introduced briefly in 4.7 and those used for the HL-LHC jet tagging studies in Chapter 7.

(Generalised) energy correlation functions

The results provided by energy correlation functions are both IRC safe[1] and they (for generalised energy correlation functions) are independent of the re-clustering of the jet to define sub-jet axes [82]. The N-point energy correlation function is described by [82]:

$$\mathrm{ECF}(N,\beta) = \sum_{i<i_2<\cdots<i_{N_J}} \left(\prod_{a=1}^{N} p_{\mathrm{T},i_a}\right)\left(\prod_{b=1}^{N-1}\prod_{c=b+1}^{N} \Delta R_{i_b i_c}\right)^{\beta} \tag{B.1}$$

where β is a parameter controlling the impact of the angular separation of jet constituents on the ECF, N_J is the number of jet constituents, and i_a runs over the constituent indices. Ratios of the ECFs are used to define dimensionless observables that for an $(N+1)$-point correlation function provide discrimination for N-prong jet substructures [82, 84]. These include [82, 84]:

- $C_N^{(\beta)}$ variables: $C_N^{(\beta)} = \mathrm{ECF}(N+1,\beta)\ \mathrm{ECF}(N-1,\beta)\ /\ [\mathrm{ECF}(N,\beta)]^2$.
- D_N variables: defined in terms of $e_N^{(\beta)} = \mathrm{ECF}(N,\beta)\ /\ [\mathrm{ECF}(1,\beta)]^N$ (e.g. $D_2^{(\alpha,\beta)} = e_3^{(\beta)}\ /\ [e_2^{(\beta)}]^{3\alpha/\beta}$).

The $N = 2$ variables are most useful for 2-prong decay (e.g. heavy W/Z-boson) identification, and $N = 3$ variables are useful for identifying 3-prong (e.g. t-quark) decays (where the variable achieves sufficient separation performance relative to "background" jets) [82].

Generalised energy correlation functions encapsulate more information about the angular separation of jet constituents and are used to defined M-series and N-series variables [82, 85]. Like before, $M_2^{(\beta)}$ and $N_2^{(\beta)}$ are applied to 2-prong topologies, and $M_3^{(\beta)}$ and $N_3^{(\beta)}$ to 3-prong topologies [82, 85]. An exception for the M-series variable

[1] They do not change with additional collinear splittings or soft emissions within the jet.

arises from differences in the role of angular information in the generalised ECF, in which case the variables should be considered only when groomed jets (introduced in Section 4.7.1) are studied [85].

N-subjettiness variables

The N-subjettiness variable, τ_N, gives a measure of the level to which the constituents of a large-R jet correspond to an N-prong topology [82]. The first step in the calculation of these variables is to re-cluster the original jet into N sub-jets [82]. For example, using a variant of the exclusive k_t algorithm – the sub-jet axes could be chosen to minimise the value of τ_N [82]. An alternate method used by ATLAS [131, 135] is to calculate τ_N from sub-jets identified with the exclusive[2] k_t algorithm, and define the sub-jet axis to point along the axis corresponding to the 4-momentum of the hardest sub-jet constituent [81]. This is referred to as the winner-take-all scheme (denoted WTA in τ_N^{WTA}).

The τ_N[3] variable is defined as a p_{T}-weighted sum over the sub-jets [82]:

$$\tau_N = \frac{1}{d_0} \sum_k p_{\text{T},k} \min(\Delta R_{1,k}^{\beta}, \Delta R_{2,k}^{\beta}, \ldots, \Delta R_{N,k}^{\beta}) \tag{B.2}$$

where $d_0 = \sum_k p_{\text{T},k} R$, R is the size-parameter of the original jet [83]. Here, β is a parameter chosen to control the effect of the angular separations ΔR_{ij} of sub-jet axes on the τ_N observable [82]. When the sub-jet axes are at wide-angles, the ΔR_{ij} are large leading to large τ_N – the large-R jet fits an $N+1$ sub-jet hypothesis [83]. Whereas, when the sub-jets are relatively collinear with small ΔR_{ij}, τ_N is small (and close to zero) indicating agreement with a $\leq N$ sub-jet hypothesis [83].

For the purpose of discriminating between an N-prong and $(N-1)$-prong structure, ratios of N-subjettiness variables of the form [82, 130]:

$$\tau_{N(N-1)} = \frac{\tau_N}{\tau_{N-1}} \tag{B.3}$$

can be used to isolate the N-prong topology. These ratios are useful for both W/Z-boson (τ_{21}) and top quark (τ_{21}, τ_{32}) identification [80, 82, 130].

k_t splitting scales

The k_T splitting scale observable originates from the distance parameter used to define the separation of jet constituents in sequential recombination algorithms [87, 88]. The distance measure is defined for jets reclustered with the k_t algorithm

[2] Finding *exactly* N sub-jets.
[3] The "WTA" notation was dropped since this expression is independent of the choice of jet axes and only requires a collection of sub-jets to exist.

as [87, 88]:

$$d_{ij} = \min(p_{\mathrm{T},i}^2,\ p_{\mathrm{T},j}^2) \times \left(\frac{\Delta R_{ij}}{R}\right)^2 \tag{B.4}$$

and then the commonly used k_t splitting scale is denoted (using a modified calculation) [87, 88]:

$$d_{ij} = \min(p_{\mathrm{T},i}^2,\ p_{\mathrm{T},j}^2) \times \Delta R_{ij}^2 \tag{B.5}$$

where the R^2 factor has been multiplied out of the equation. Typically, $\sqrt{d_{ij}}$ will be used instead of d_{ij}.

Further "z-cut" variables can be defined in terms of d_{ij} to describe the energy-sharing of two jet constituents [87]. In Ref. [87], these variables are calculated as[4]:

$$z_{ij,\mathrm{cut}} = \frac{d_{ij}}{d_{ij} + m^2} \tag{B.6}$$

where m is the invariant mass of the large-R jet. A slightly different calculation procedure is used in the ATLAS code-base [131], where m is the invariant mass of the sub-jet last split (i.e. with the highest p_{T} constituent clustered last with the k_t algorithm). For example, to calculate z_{23}, 2 exclusive k_t sub-jets are identified and the invariant mass of the final sub-jet clustered from two (higher p_{T}) constituents would be used in the calculation.

Jet shape (and other substructure) variables

Other jet shape variables (besides τ_N) provide further information about the symmetry of the distribution of jet constituents within a large-R jet. Early variables commonly used in substructure analyses include the jet *thrust*, a variable defined in the CM frame of the large-R jet [86]. The thrust is defined in two ways with a "major" and "minor" observable. The former uses a projection onto the constituent momentum such that the thrust is calculated as [86]:

$$T_{\mathrm{maj}} = \frac{\sum_i \left|\hat{T} \cdot \vec{p}_i\right|}{\sum_i |\vec{p}_i|} \tag{B.7}$$

where the summations are over jet constituents with CM frame momenta $\vec{p}_i$ and the unit vector $\hat{T}$ (the thrust axis) is constructed to maximise the sum of the longitudinal components of the constituent momenta (i.e. perpendicular to the transverse plane in the CM frame).

[4] In this thesis $z_{ij,\mathrm{cut}}$ is denoted z_{ij}, particularly in Chapter 7.

The minor thrust is defined similarly but in terms of a vector pointing perpendicularly to $\hat{T}$ and the constituent momentum $\vec{p}_i$ [86]:

$$T_{\text{min}} = \frac{\sum_i \left| \vec{p}_i \times \hat{T} \right|}{\sum_i |\vec{p}_i|}. \tag{B.8}$$

The different thrust variables provide complementary discrimination power. When $T_{\text{min}} \to 0.5$, the jet constituents are uniformly distributed, and the opposite for small values of T_{min} [86]. Similarly, as $T_{\text{maj}} \to 0.5$, the distribution of jet constituents is uniform, and the opposite as $T_{\text{maj}} \to 1$ [86].

Additional jet shape variables are defined in terms of the momenta of jet constituents in the large-R jet rest frame – including sphericity and aplanarity. Both of these observables draw on the rank-2 sphericity tensor defined [86]:

$$S^{\alpha\beta} = \frac{\sum_i p_i^\alpha p_i^\beta}{\sum_i |\vec{p}_i|^2} \tag{B.9}$$

where the summation is again over jet constituents with rest-frame 3-momenta, $\vec{p}_i$, and α and β run over the 3-vector components. The diagonalisation of $S^{\alpha\beta}$ yields three eigenvalues denoted λ_i $(i = 1,\ 2,\ 3)$ where $\lambda_i \geq \lambda_j$ for $i < j$ and $\sum_i \lambda_i = 1$ [86]. The aplanarity observable is constructed from a single eigenvalue [86]:

$$A = \frac{3}{2}\lambda_3 \tag{B.10}$$

and lies in the range from 0 to 1/2, the latter value indicative of a uniform jet constituent distribution.

The sphericity observable is defined similarly but in terms of both λ_2 and λ_3 [86]:

$$S = \frac{3}{2}(\lambda_2 + \lambda_3), \tag{B.11}$$

and is always in the range between 0 and 1. A value of $S = 1$ indicates a uniform constituent distribution (e.g. from resonances, not QCD jets) [86]. The $S = 0$ case suggests a 2-prong like jet rest-frame structure where the constituent momentum vectors point in opposite directions [86].

Other jet shape variables include Fox-Wolfram moments defined in terms of Legendre polynomials (using the angle between jet constituents) and the planar-flow, another variable that draws on jet constituent momenta to define a tensor from which the observable is derived [86, 132]. The authors of Ref. [132] note that jet shape variables (i.e. planar-flow) provide optimal discrimination power when the kinematics of the (uniform) resonance particle are isolated with some other selection such as the application of a jet mass requirement.

Additional variables that consider the kinematic or topological distribution of jet constituents also discriminate between symmetric signal topologies and asymmetric background topologies. In the case of top quark tagging, one can consider the minimum invariant mass of pairs of jet constituents denoted Q_W [87]. The origin of this notation arises from the hadronic W-boson decay in a fully hadronic t-quark decay [87]. Thus, the variable peaks around the W-boson mass for top quark jets with appropriate kinematics [87].

Appendix C

Statistical uncertainties for trigger efficiencies

The calculation of statistical uncertainties in the trigger (signal) acceptances in Chapter 5 used a method of calculating confidence intervals in efficiencies using the F distribution. Typically, the F distribution is used to represent the ratio of two different χ^2-distributed variables, defined [136]:

$$F = \frac{V_1 \ / \ N_{\mathrm{DOF},1}}{V_2 \ / \ N_{\mathrm{DOF},2}} \tag{C.1}$$

where V_i are the χ^2-distributed variables and $N_{\mathrm{DOF},i}$ are the number of degrees of freedom for each distribution.

To estimate the statistical uncertainty in event selection efficiencies, it was assumed that the number of events passing each selection was binomially distributed [8]. The probability for the event to pass a selection (p) is given by the efficiency estimate. The statistical uncertainty can then be determined by means of a central confidence interval (confidence level CL) for which the lower bound (p_{low}) is [8]:

$$p_{\mathrm{low}} = \frac{n_{\mathrm{p}} \times F^{-1}[\gamma;\ 2n_{\mathrm{p}},\ 2(N_{\mathrm{total}} - n_{\mathrm{p}} + 1)]}{N_{\mathrm{total}} - n_{\mathrm{p}} + 1 + n_{\mathrm{p}} \times F^{-1}[\gamma;\ 2n_{\mathrm{p}},\ 2(N_{\mathrm{total}} - n_{\mathrm{p}} + 1)]} \tag{C.2}$$

where n_{p} is the number of passing events, N_{total} is the total number of events, where $\gamma = \frac{1-\mathrm{CL}}{2}$, and F^{-1} is the inverse cumulative F-distribution.

Similarly, the upper bound of the confidence interval (p_{high}) is given by [8]:

$$p_{\mathrm{high}} = \frac{(n_{\mathrm{p}} + 1) \times F^{-1}[1-\gamma;\ 2(n_{\mathrm{p}} + 1),\ 2(N_{\mathrm{total}} - n_{\mathrm{p}})]}{N_{\mathrm{total}} - n_{\mathrm{p}} + (n_{\mathrm{p}} + 1) \times F^{-1}[1-\gamma;\ 2(n_{\mathrm{p}} + 1),\ 2(N_{\mathrm{total}} - n_{\mathrm{p}})]}. \tag{C.3}$$

The calculation of these uncertainties was implemented in `Python` code using the `Scipy` library [137] to calculate the F^{-1} factors.

Appendix D

Further pile-up rejection comparisons for Run 3 TLA studies

The Figures in this Appendix illustrate the effects of JVT selections combined with a trigger selection on the UDS gluino-pair production signal points from Chapter 5. These results are for the MC16a only event sample, which is significantly smaller than the combined MC16 event sample (see definitions in Section 5.2.1). Additional plots are included for the UDB signal points that were not included in Section 5.9.

Figures D.1 to D.3 show the jet p_{T} distributions when different JVT and trigger selections are applied to the UDS decay mode MC16a event sample. Figures D.4 to D.6 show the same plots but for the UDB decay mode MC16a event sample. Finally, the jet p_{T} distributions with the same selections are shown for UDB decay mode with the combined MC16 event sample in Figures D.7 to D.9.

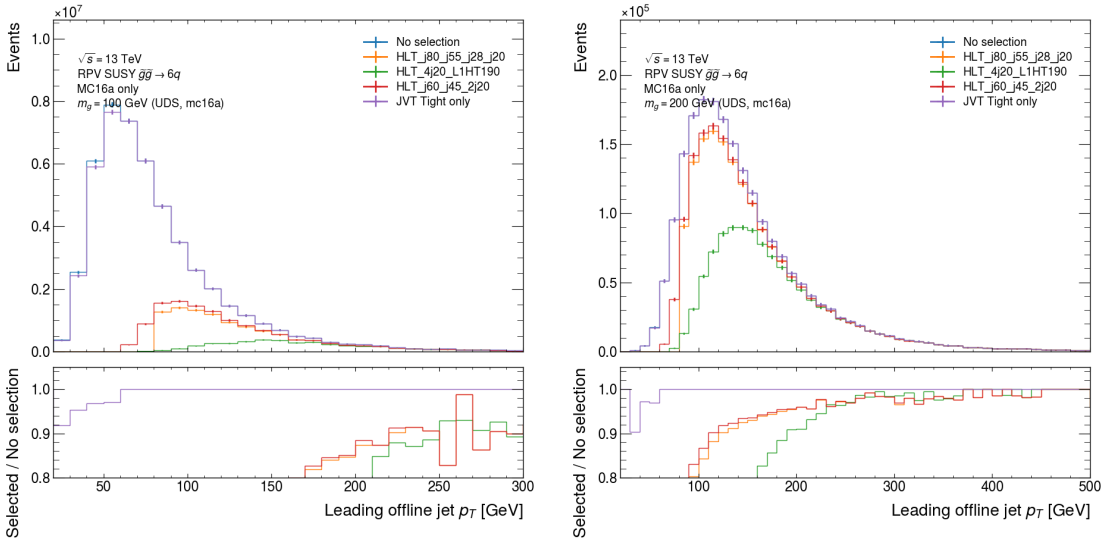

(a) $m_g = 100$ GeV

(b) $m_g = 200$ GeV

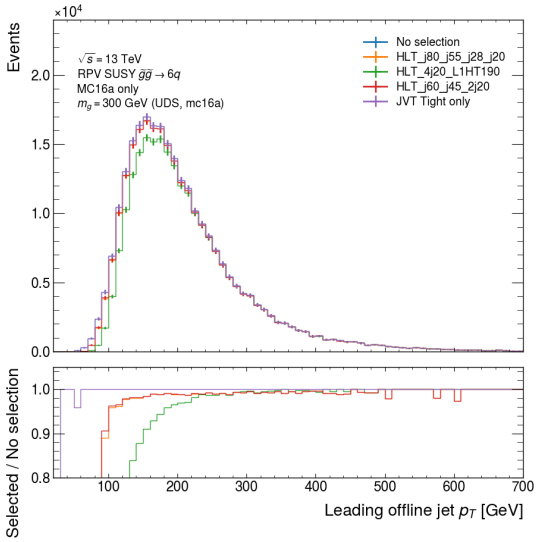

(c) $m_g = 300$ GeV

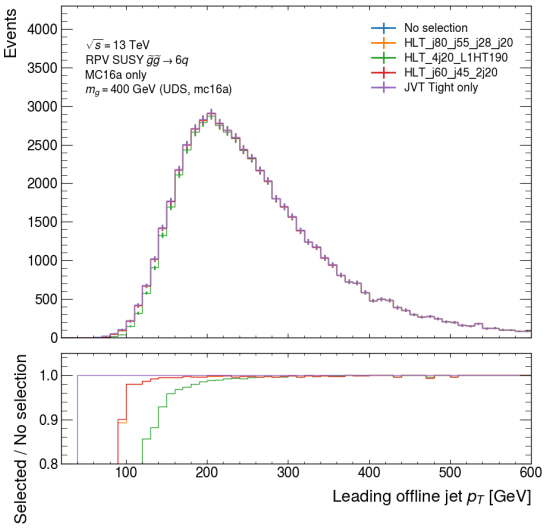

(d) $m_g = 400$ GeV

Figure D.1: Plots of the leading jet p_{T} distributions for all (MC16a only) UDS gluino pair-production signals without any selections (blue), with only JVT selections (purple), and with both JVT and trigger selections applied (orange, red, and green). The trigger selections are abbreviated such that `HLT_j80_j55_j28_j20` (orange) and `HLT_j60_j45_2j20` (red) are the two asymmetric threshold triggers with an `L1J45p0ETA21_3J15p0ETA25` seed. The final trigger selection (green) is the `HLT_4j20_L1HT190-J15s5pETA21` selection.

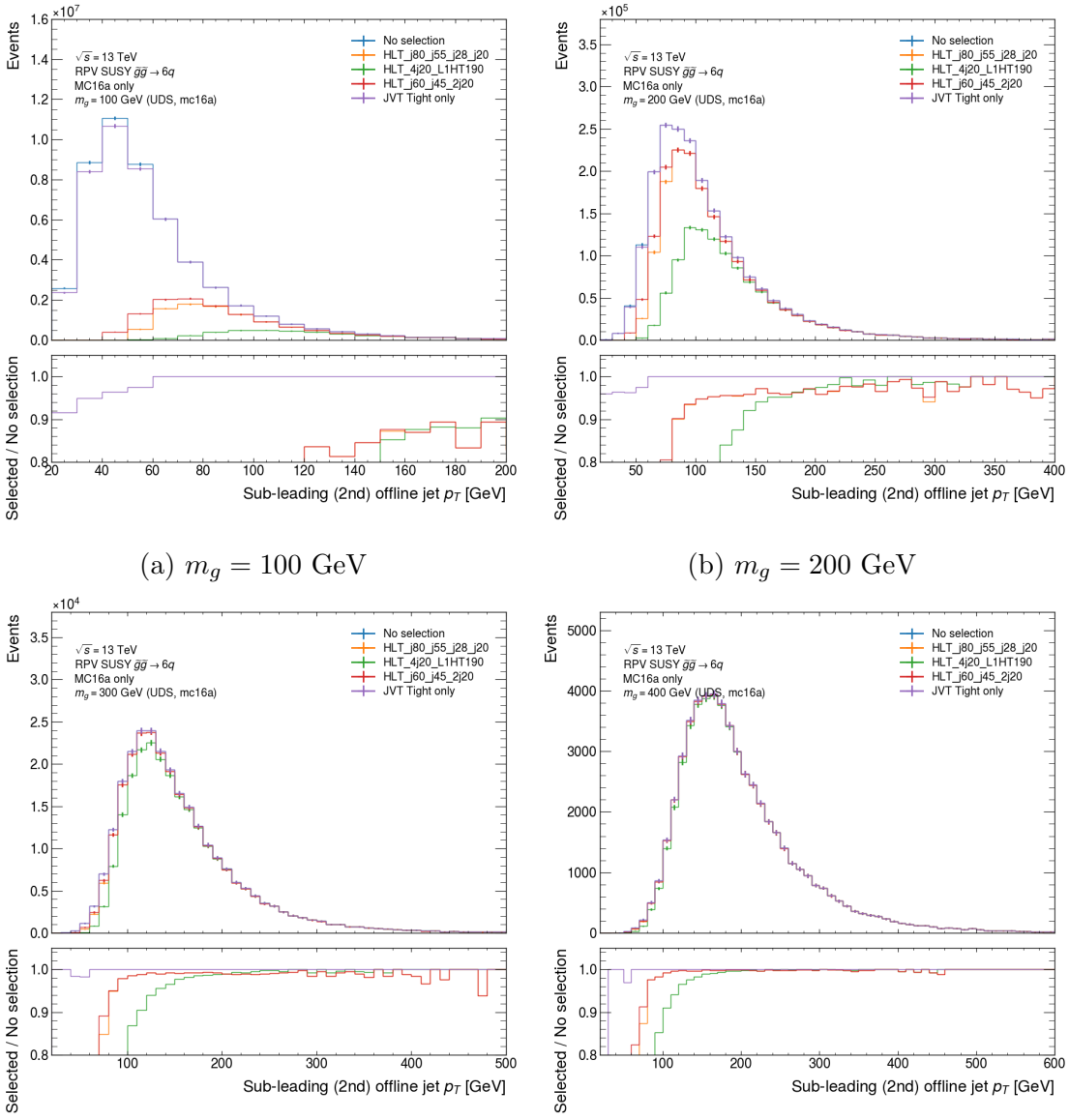

(a) $m_g = 100$ GeV

(b) $m_g = 200$ GeV

(c) $m_g = 300$ GeV

(d) $m_g = 400$ GeV

Figure D.2: Plots of the sub-leading (2nd) jet p_{T} distributions for all (MC16a only) UDS gluino pair-production signals without any selections (blue), with only JVT selections (purple), and with both JVT and trigger selections applied (orange, red, and green). The trigger selections are abbreviated such that `HLT_j80_j55_j28_j20` (orange) and `HLT_j60_j45_2j20` (red) are the two asymmetric threshold triggers with an `L1J45p0ETA21_3J15p0ETA25` seed. The final trigger selection (green) is the `HLT_4j20_L1HT190-J15s5pETA21` selection.

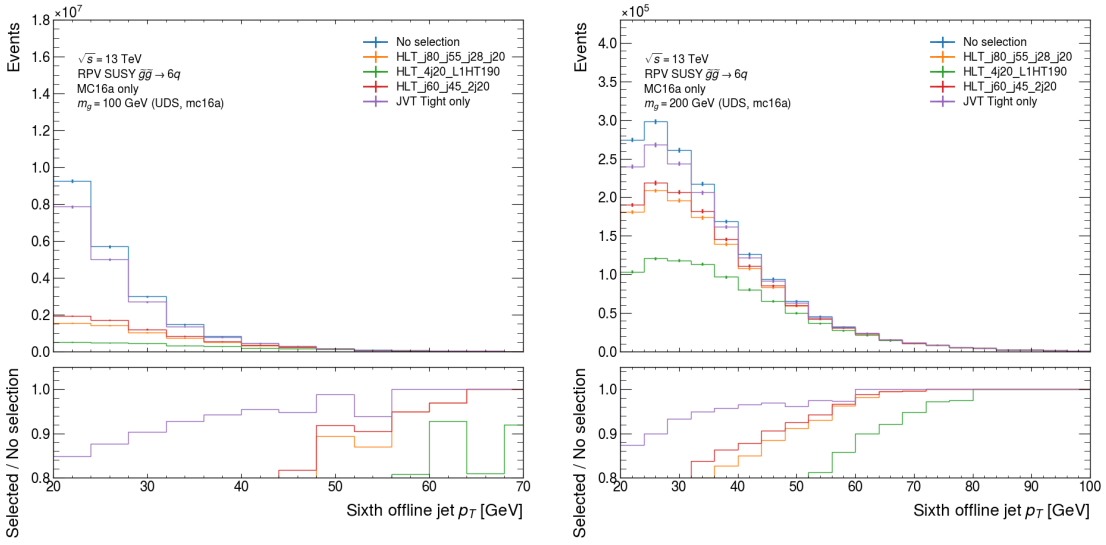

(a) $m_g = 100$ GeV (b) $m_g = 200$ GeV

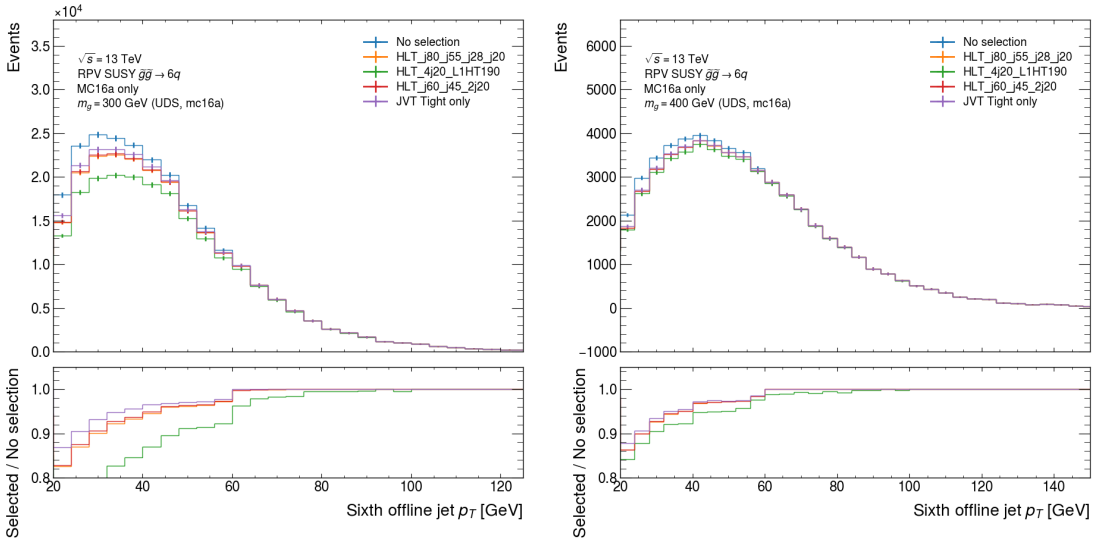

(c) $m_g = 300$ GeV (d) $m_g = 400$ GeV

Figure D.3: Plots of the sixth-leading jet p_{T} distributions for all (MC16a only) UDS gluino pair-production signals without any selections (blue), with only JVT selections (purple), and with both JVT and trigger selections applied (orange, red, and green). The trigger selections are abbreviated such that `HLT_j80_j55_j28_j20` (orange) and `HLT_j60_j45_2j20` (red) are the two asymmetric threshold triggers with an `L1J45p0ETA21_3J15p0ETA25` seed. The final trigger selection (green) is the `HLT_4j20_L1HT190-J15s5pETA21` selection.

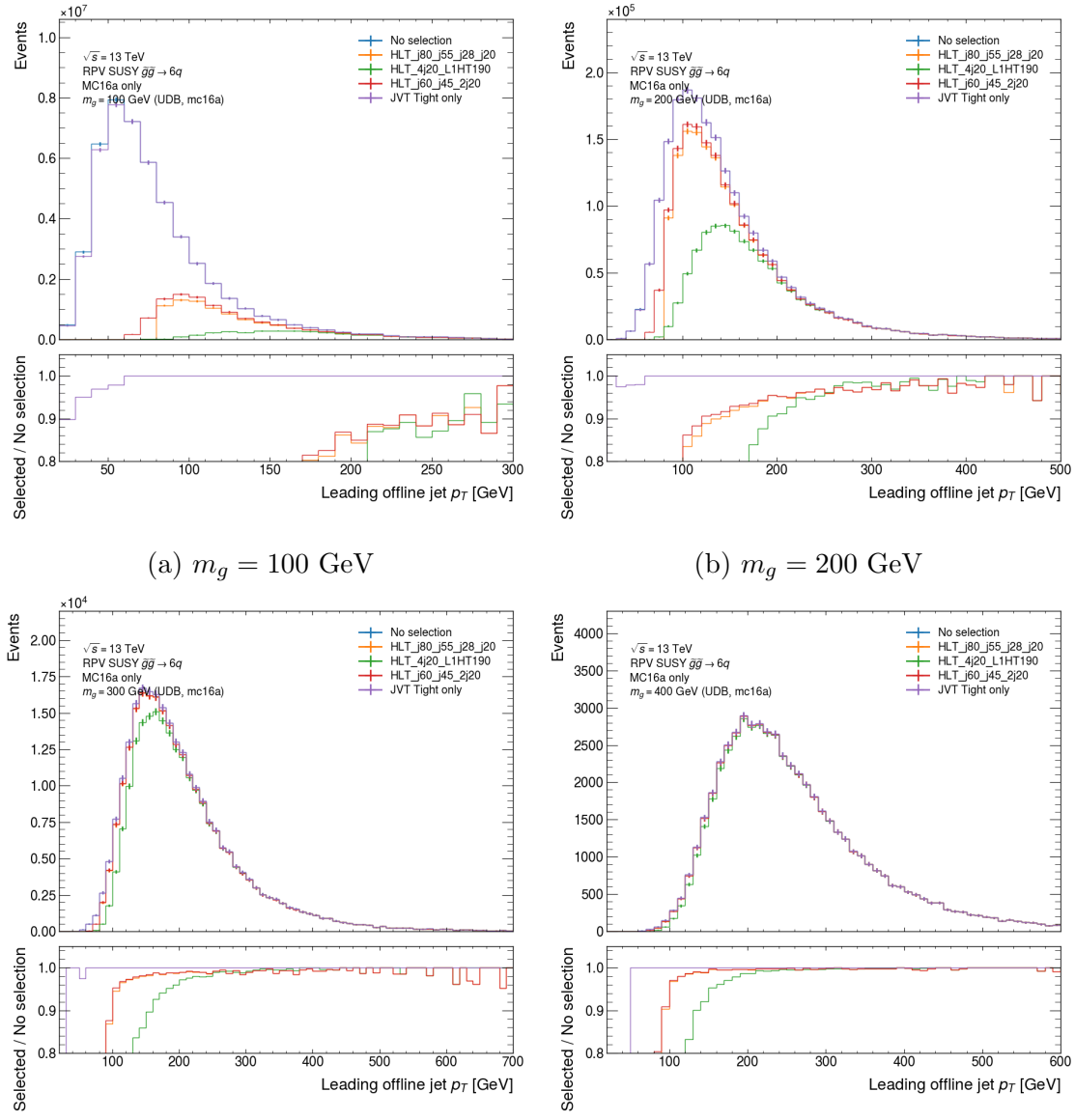

(a) $m_g = 100$ GeV

(b) $m_g = 200$ GeV

(c) $m_g = 300$ GeV

(d) $m_g = 400$ GeV

Figure D.4: Plots of the leading jet p_{T} distributions for all (MC16a only) UDB gluino pair-production signals without any selections (blue), with only JVT selections (purple), and with both JVT and trigger selections applied (orange, red, and green). The trigger selections are abbreviated such that `HLT_j80_j55_j28_j20` (orange) and `HLT_j60_j45_2j20` (red) are the two asymmetric threshold triggers with an `L1J45p0ETA21_3J15p0ETA25` seed. The final trigger selection (green) is the `HLT_4j20_L1HT190-J15s5pETA21` selection.

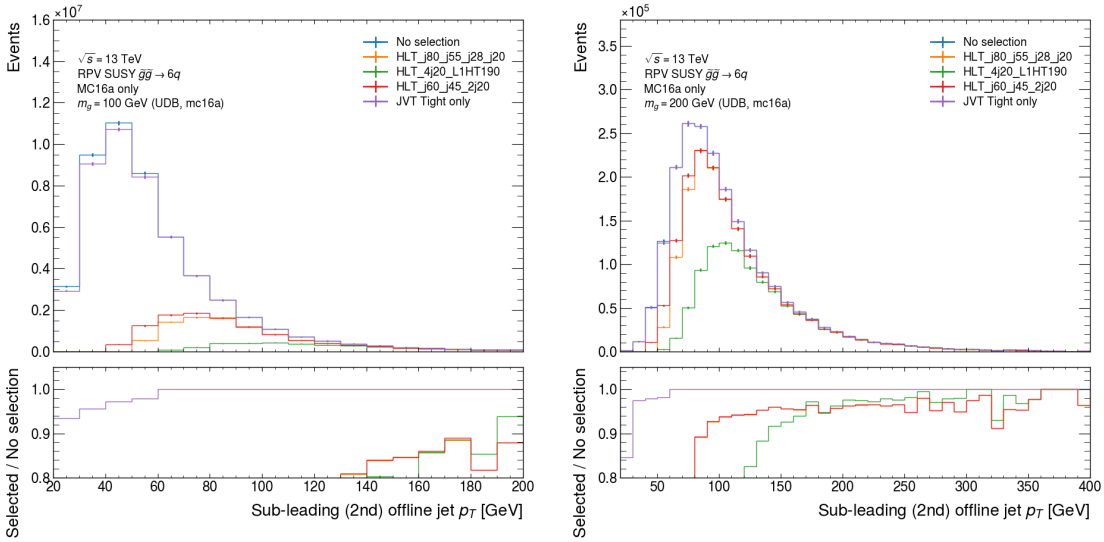

(a) $m_g = 100$ GeV (b) $m_g = 200$ GeV

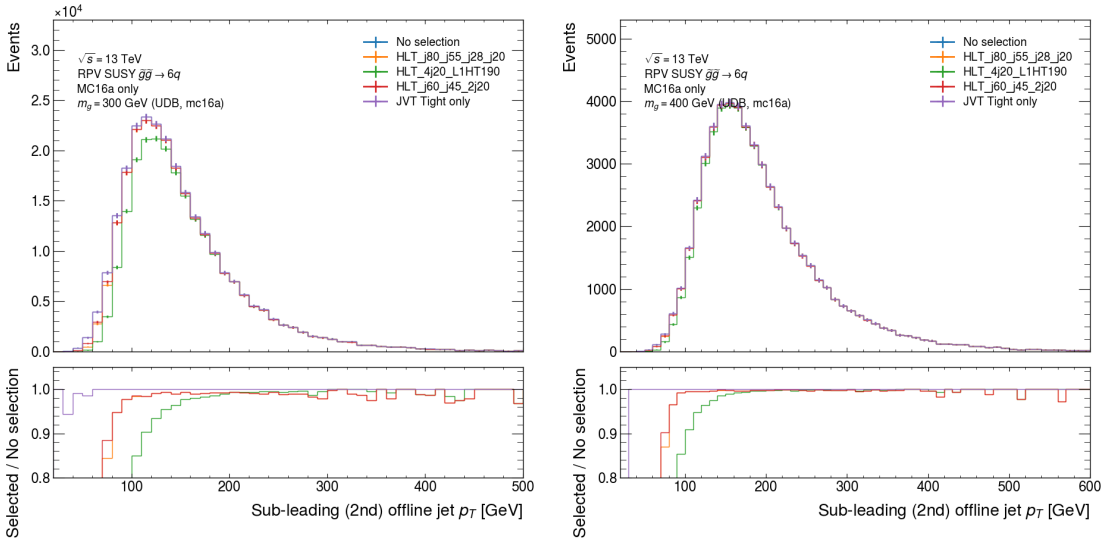

(c) $m_g = 300$ GeV (d) $m_g = 400$ GeV

Figure D.5: Plots of the sub-leading (2nd) jet p_{T} distributions for all (MC16a only) UDB gluino pair-production signals without any selections (blue), with only JVT selections (purple), and with both JVT and trigger selections applied (orange, red, and green). The trigger selections are abbreviated such that `HLT_j80_j55_j28_j20` (orange) and `HLT_j60_j45_2j20` (red) are the two asymmetric threshold triggers with an `L1J45p0ETA21_3J15p0ETA25` seed. The final trigger selection (green) is the `HLT_4j20_L1HT190-J15s5pETA21` selection.

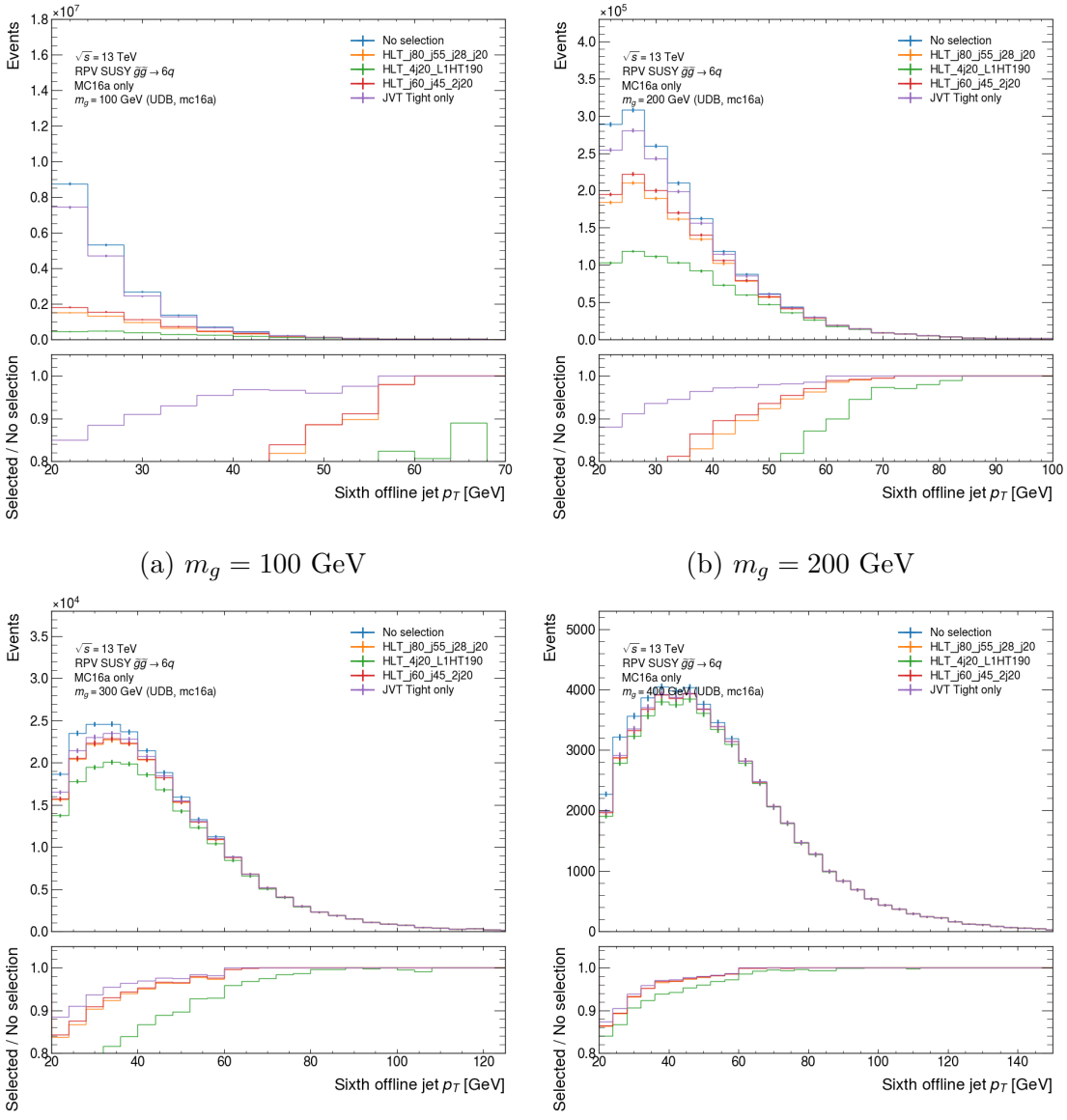

(a) $m_g = 100$ GeV

(b) $m_g = 200$ GeV

(c) $m_g = 300$ GeV

(d) $m_g = 400$ GeV

Figure D.6: Plots of the sixth-leading jet p_{T} distributions for all (MC16a only) UDB gluino pair-production signals without any selections (blue), with only JVT selections (purple), and with both JVT and trigger selections applied (orange, red, and green). The trigger selections are abbreviated such that `HLT_j80_j55_j28_j20` (orange) and `HLT_j60_j45_2j20` (red) are the two asymmetric threshold triggers with an `L1J45p0ETA21_3J15p0ETA25` seed. The final trigger selection (green) is the `HLT_4j20_L1HT190-J15s5pETA21` selection.

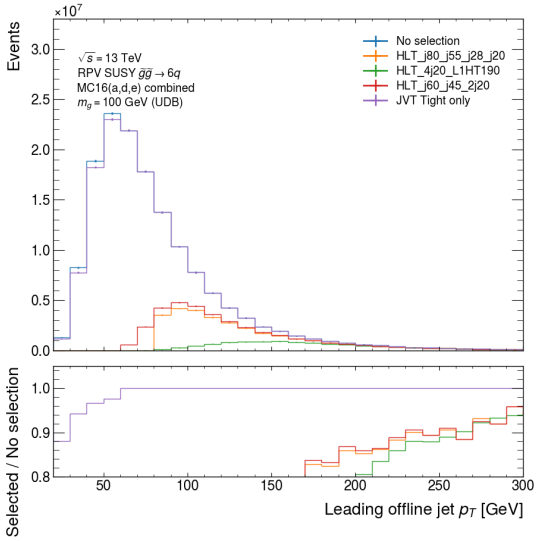

(a) $m_g = 100$ GeV

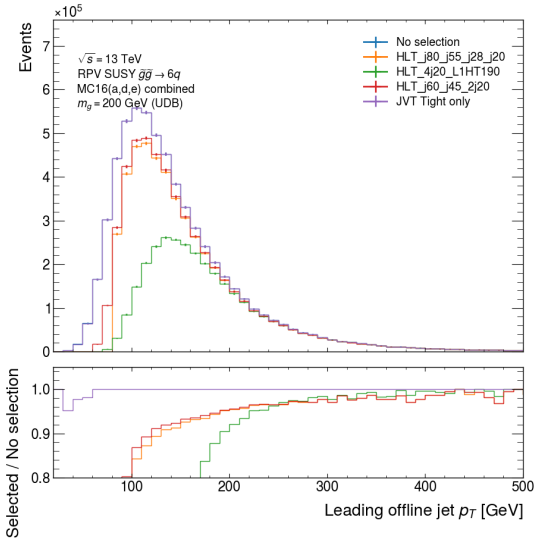

(b) $m_g = 200$ GeV

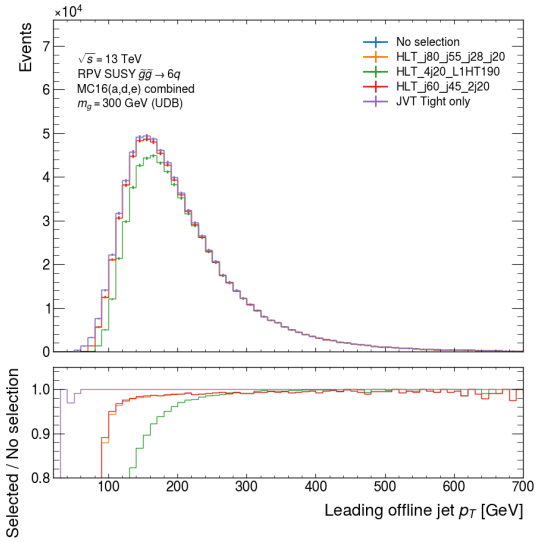

(c) $m_g = 300$ GeV

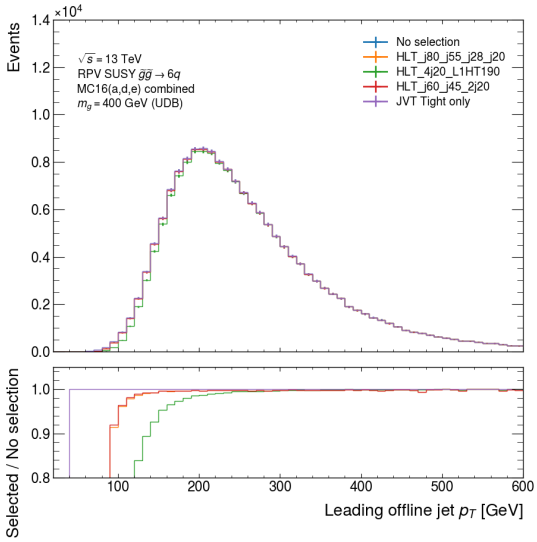

(d) $m_g = 400$ GeV

Figure D.7: Plots of the leading jet p_{T} distributions for all (combined MC16) UDB gluino pair-production signals without any selections (blue), with only JVT selections (purple), and with both JVT and trigger selections applied (orange, red, and green). The trigger selections are abbreviated such that `HLT_j80_j55_j28_j20` (orange) and `HLT_j60_j45_2j20` (red) are the two asymmetric threshold triggers with an `L1J45p0ETA21_3J15p0ETA25` seed. The final trigger selection (green) is the `HLT_4j20_L1HT190-J15s5pETA21` selection.

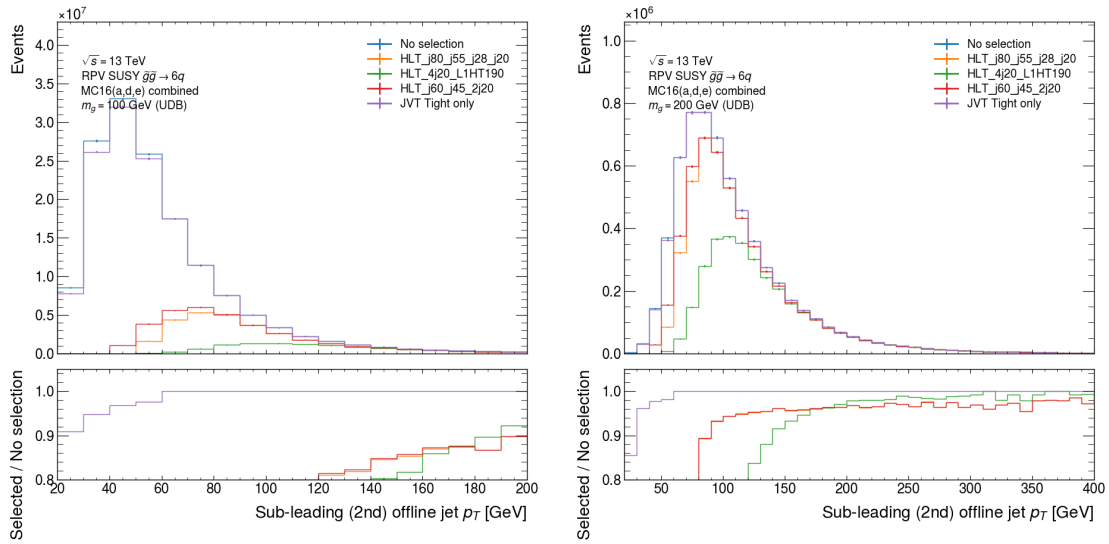

(a) $m_g = 100$ GeV

(b) $m_g = 200$ GeV

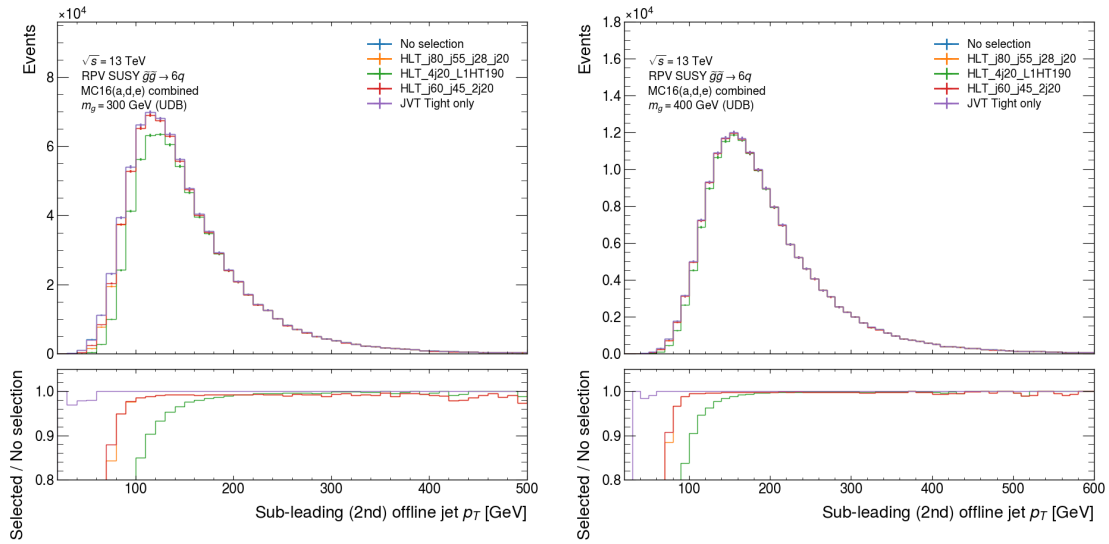

(c) $m_g = 300$ GeV

(d) $m_g = 400$ GeV

Figure D.8: Plots of the sub-leading (2nd) jet p_{T} distributions for all (combined MC16) UDB gluino pair-production signals without any selections (blue), with only JVT selections (purple), and with both JVT and trigger selections applied (orange, red, and green). The trigger selections are abbreviated such that `HLT_j80_j55_j28_j20` (orange) and `HLT_j60_j45_2j20` (red) are the two asymmetric threshold triggers with an `L1J45p0ETA21_3J15p0ETA25` seed. The final trigger selection (green) is the `HLT_4j20_L1HT190-J15s5pETA21` selection.

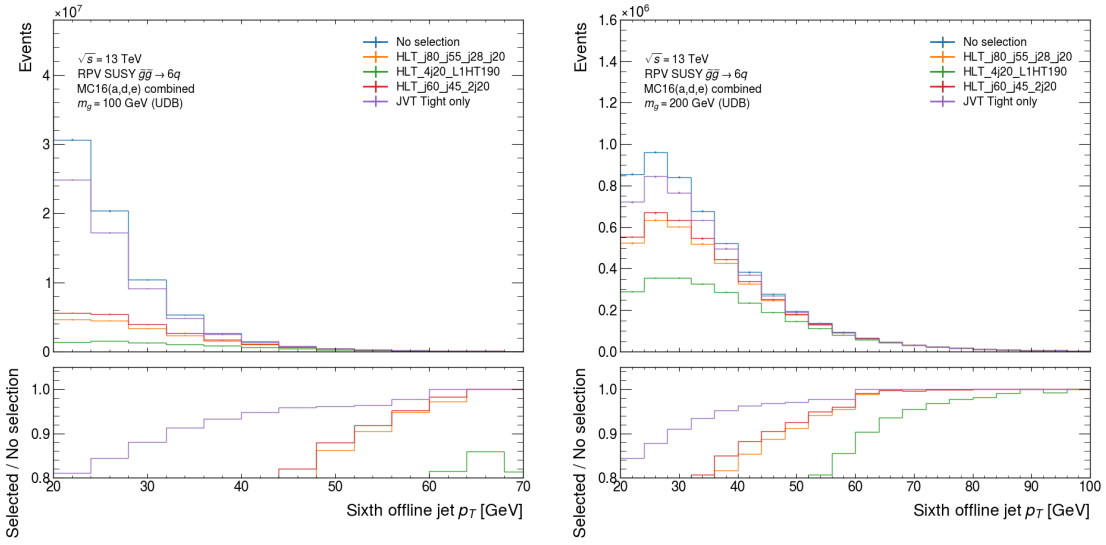

(a) $m_g = 100$ GeV

(b) $m_g = 200$ GeV

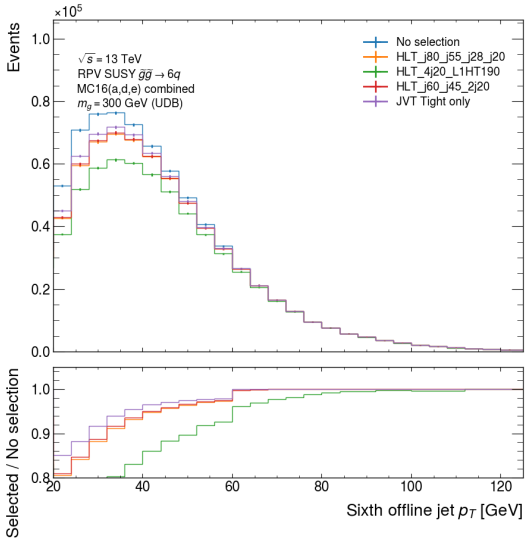

(c) $m_g = 300$ GeV

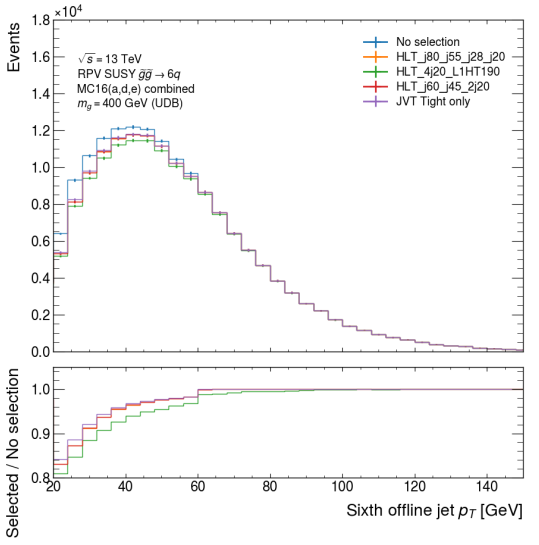

(d) $m_g = 400$ GeV

Figure D.9: Plots of the sixth-leading jet p_{T} distributions for all (combined MC16) UDB gluino pair-production signals without any selections (blue), with only JVT selections (purple), and with both JVT and trigger selections applied (orange, red, and green). The trigger selections are abbreviated such that `HLT_j80_j55_j28_j20` (orange) and `HLT_j60_j45_2j20` (red) are the two asymmetric threshold triggers with an `L1J45p0ETA21_3J15p0ETA25` seed. The final trigger selection (green) is the `HLT_4j20_L1HT190-J15s5pETA21` selection.

Appendix E

Further HL-LHC top-tagger optimisation results

This Appendix provides further tagger optimisation results to those discussed in Chapter 7 (Section 7.8). The results provided here display the background rejection for each of the tagger definitions studied with different jet mass selections, *but* the results are presented in bins of the (groomed) reconstructed jet p_{T} rather than the (ungroomed) truth jet p_{T}. All selections, including the $|\eta| < 2$ selection, are applied to the reconstructed jets.

The results for trimmed and soft-drop jet tagger definitions are shown in Figures E.1 and E.2 for 50% and 80% signal efficiency taggers, respectively. The x-axis of the plots shows the signal efficiency of the jet mass selection. The background rejection for both the trimmed and soft-drop jet taggers differs from those in Section 7.8 numerically. However, the same jet mass selections provide optimal background rejection – no modifications to the tagger recommendations are warranted due to differences associated with binning in the reconstructed jet kinematics.

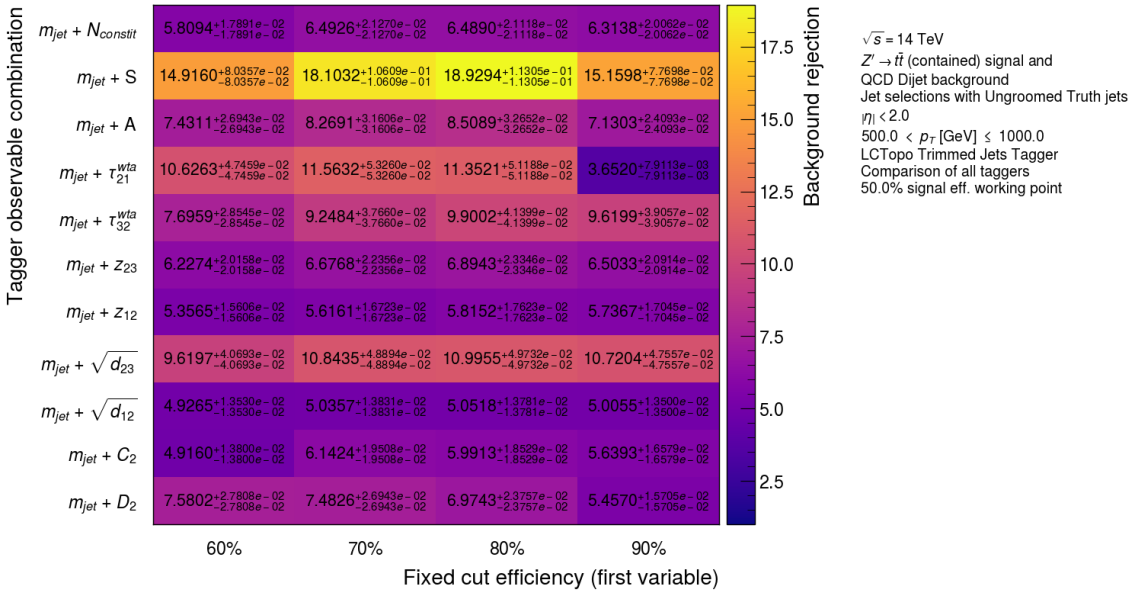

(a) Trimmed jets

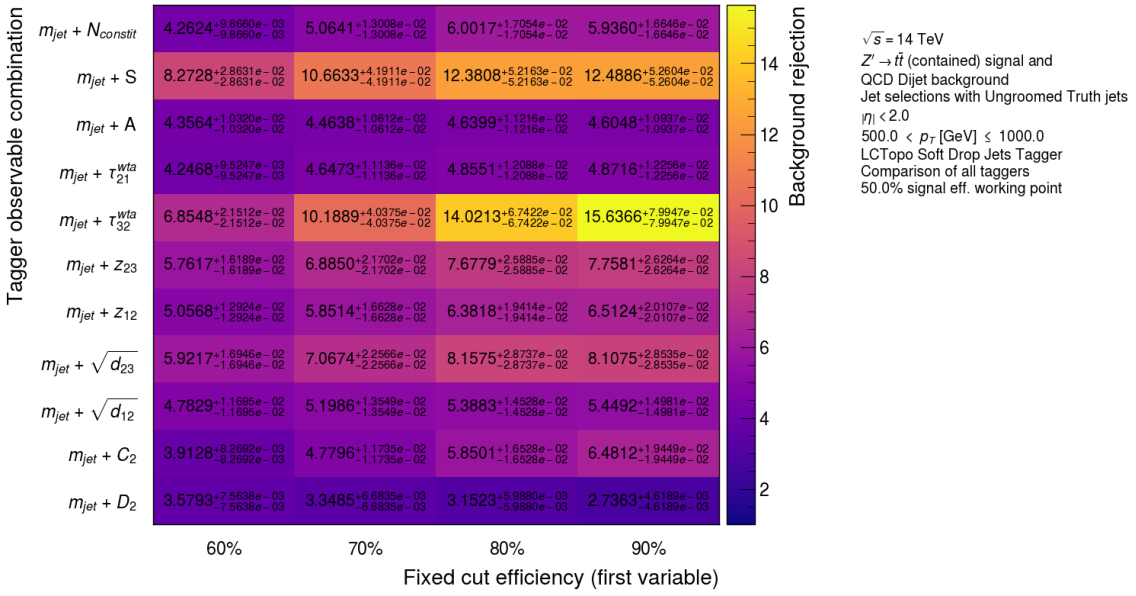

(b) Soft-drop jets

Figure E.1: Heat-maps illustrating the background rejection for each 50% signal efficiency tagger definition with different mass selections. These results are for both the trimmed and soft-drop jets in a $500 < p_{\mathrm{T}}^{\mathrm{reco}}$ (GeV) ≤ 1000 bin. The x-axis displays the signal efficiency of the mass selection.

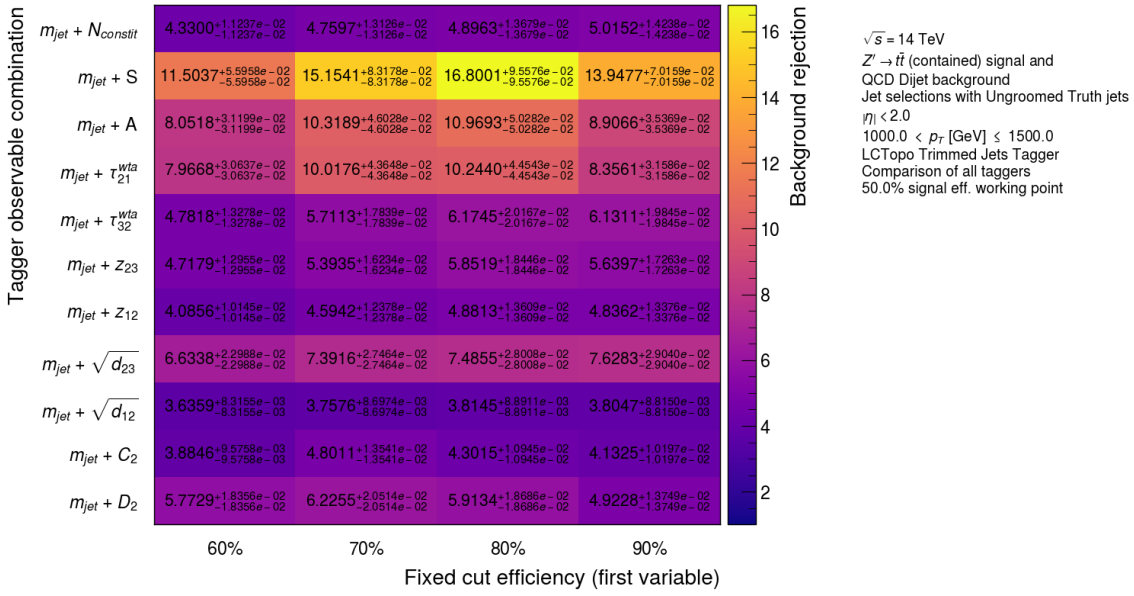

(c) Trimmed jets

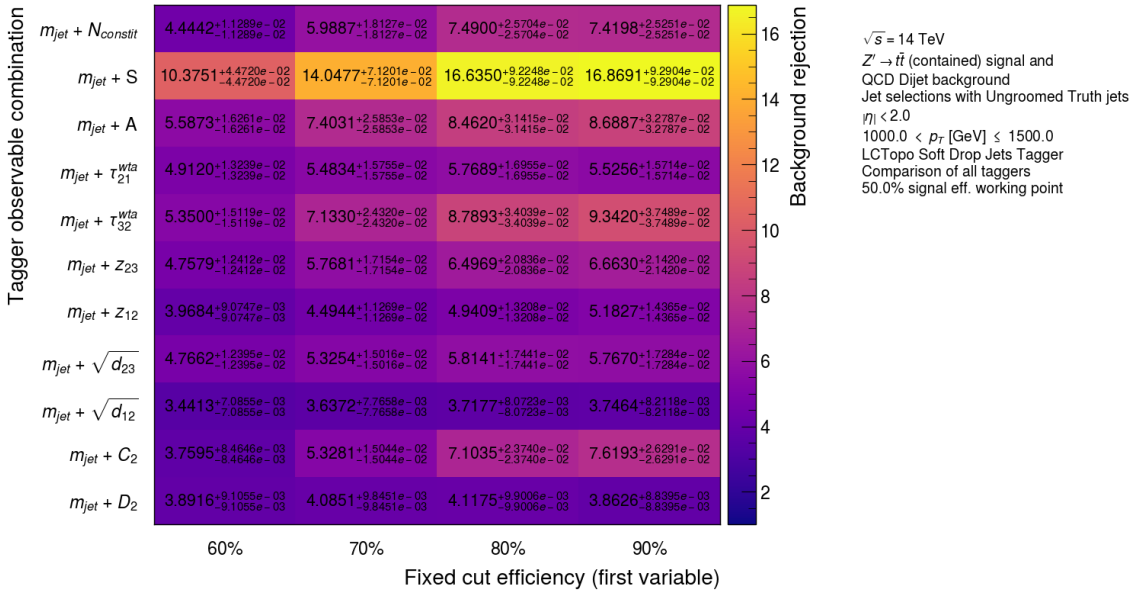

(d) Soft-drop jets

Figure E.1 (cont.): Heat-maps illustrating the background rejection for each 50% signal efficiency tagger definition with different mass selections. These results are for both the trimmed and soft-drop jets in a $1000 < p_{\mathrm{T}}^{\mathrm{reco}}$ (GeV) ≤ 1500 bin. The x-axis displays the signal efficiency of the mass selection.

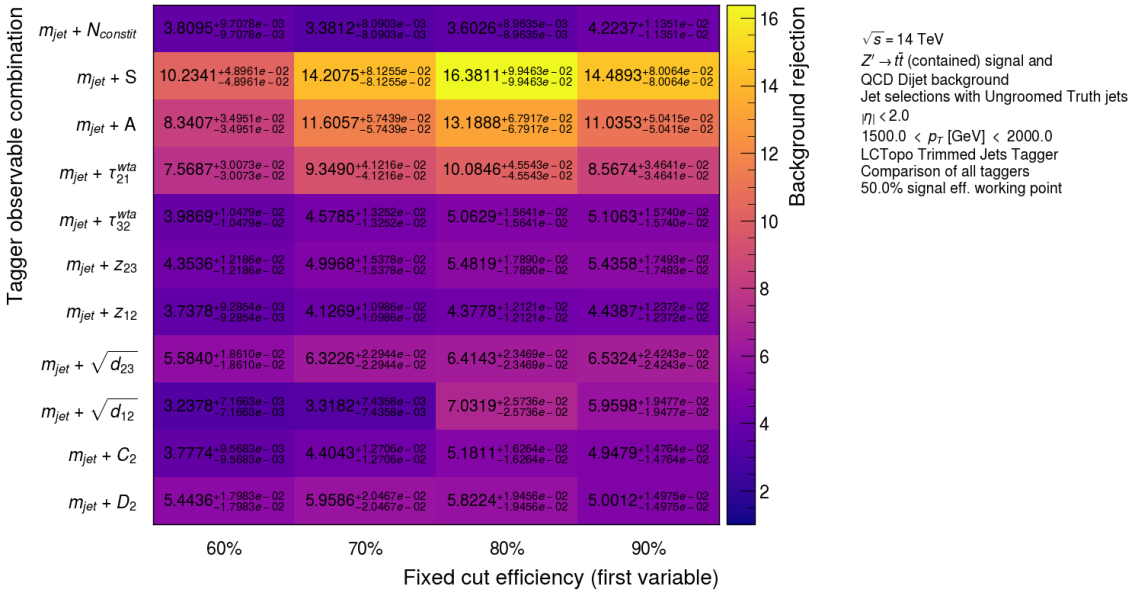

(e) Trimmed jets

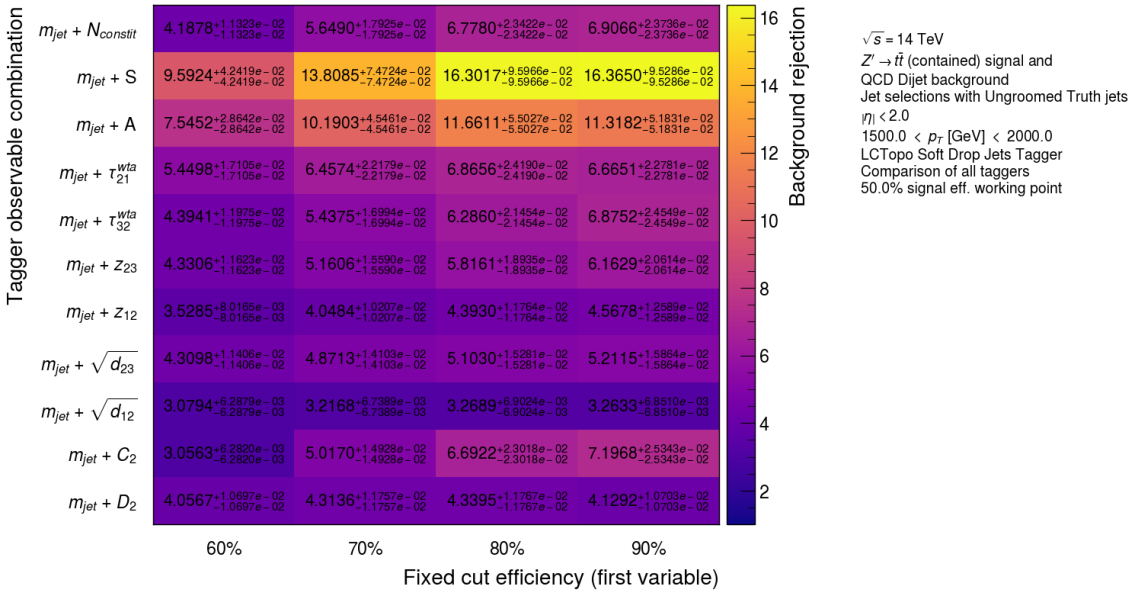

(f) Soft-drop jets

Figure E.1 (cont.): Heat-maps illustrating the background rejection for each 50% signal efficiency tagger definition with different mass selections. These results are for both the trimmed and soft-drop jets in a $1500 < p_{\mathrm{T}}^{\mathrm{reco}}$ (GeV) < 2000 bin. The x-axis displays the signal efficiency of the mass selection.

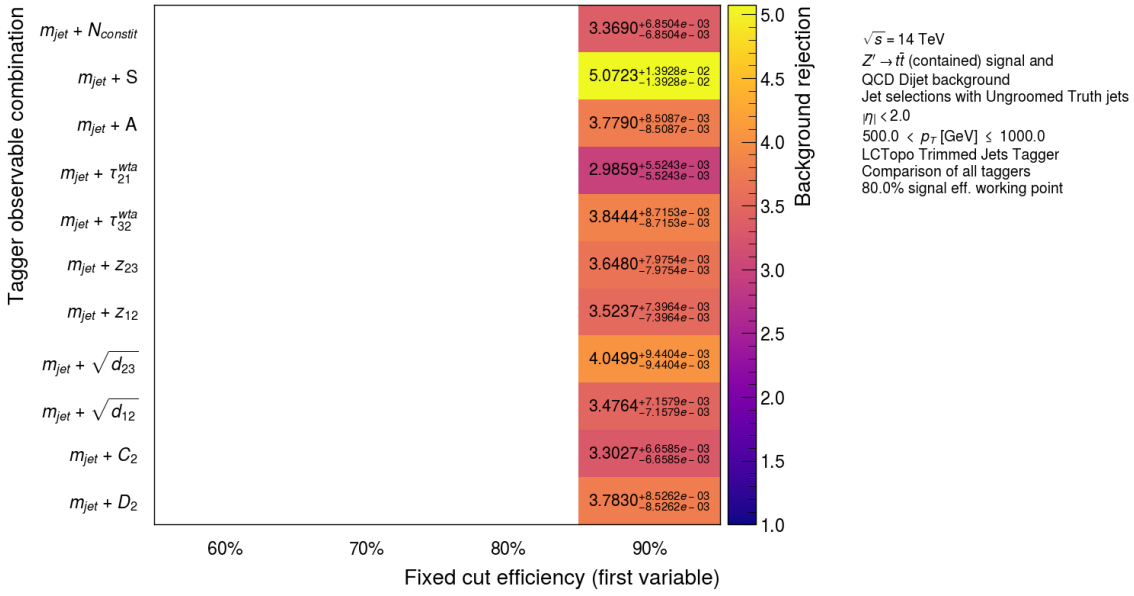

(a) Trimmed jets

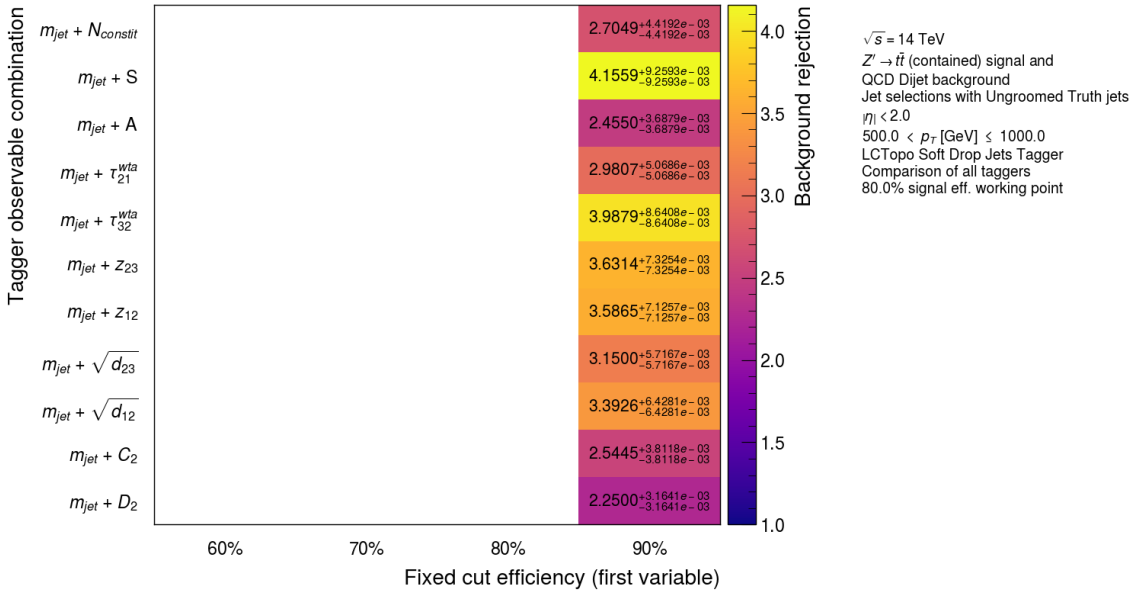

(b) Soft-drop jets

Figure E.2: Heat-maps illustrating the background rejection for each 80% signal efficiency tagger definition with different mass selections. These results are for both the trimmed and soft-drop jets in a $500 < p_{\mathrm{T}}^{\mathrm{reco}}$ (GeV) ≤ 1000 bin. The x-axis displays the signal efficiency of the mass selection.

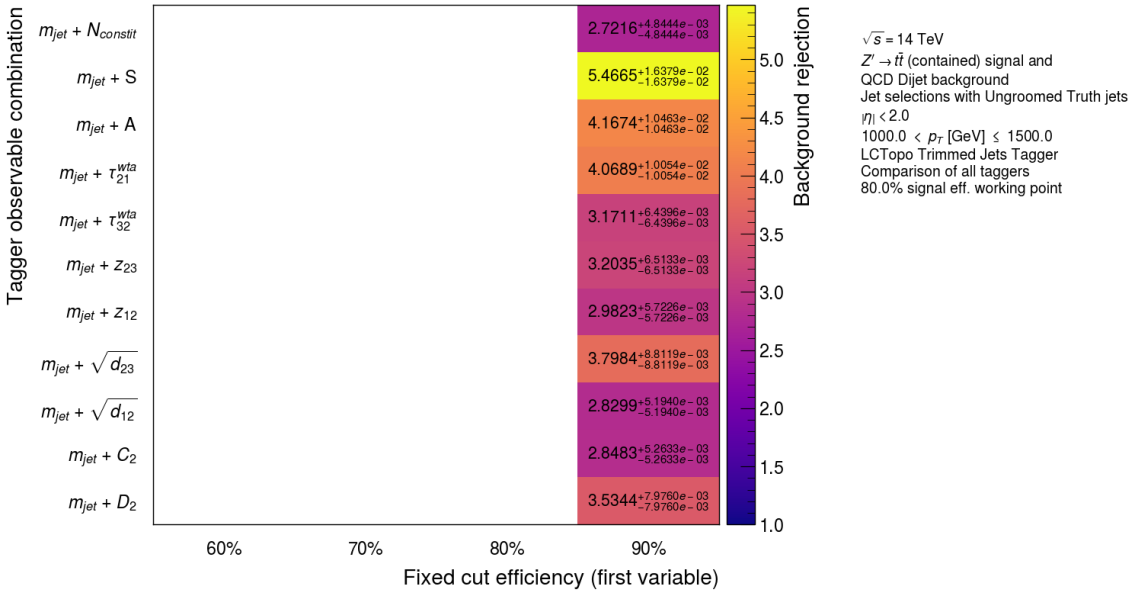

(c) Trimmed jets

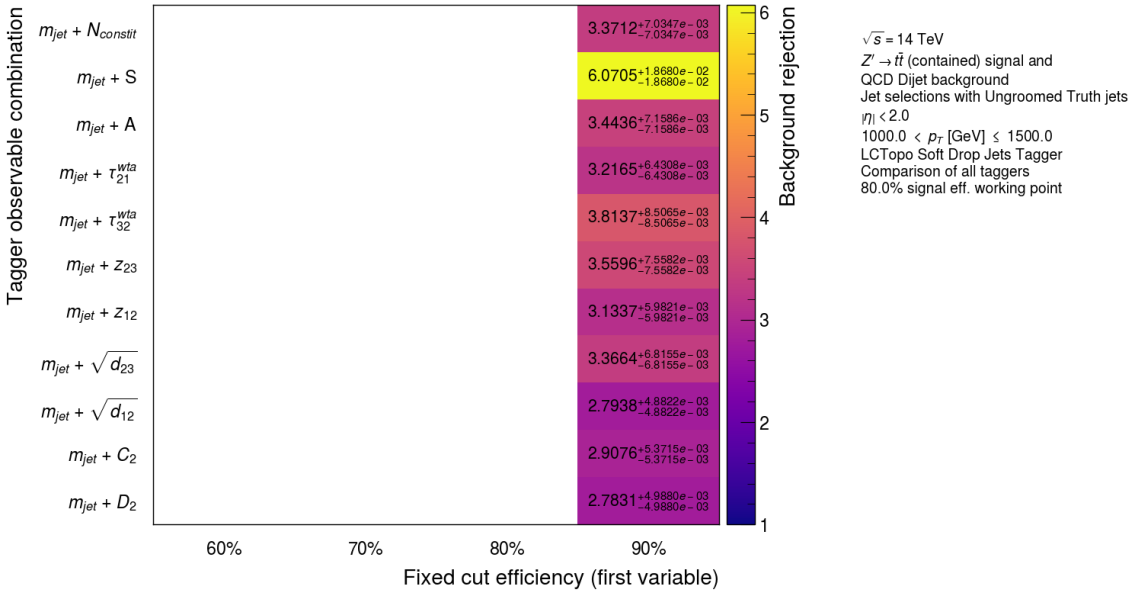

(d) Soft-drop jets

Figure E.2 (cont.): Heat-maps illustrating the background rejection for each 80% signal efficiency tagger definition with different mass selections. These results are for both the trimmed and soft-drop jets in a $1000 < p_{\mathrm{T}}^{\mathrm{reco}}$ (GeV) ≤ 1500 bin. The x-axis displays the signal efficiency of the mass selection.

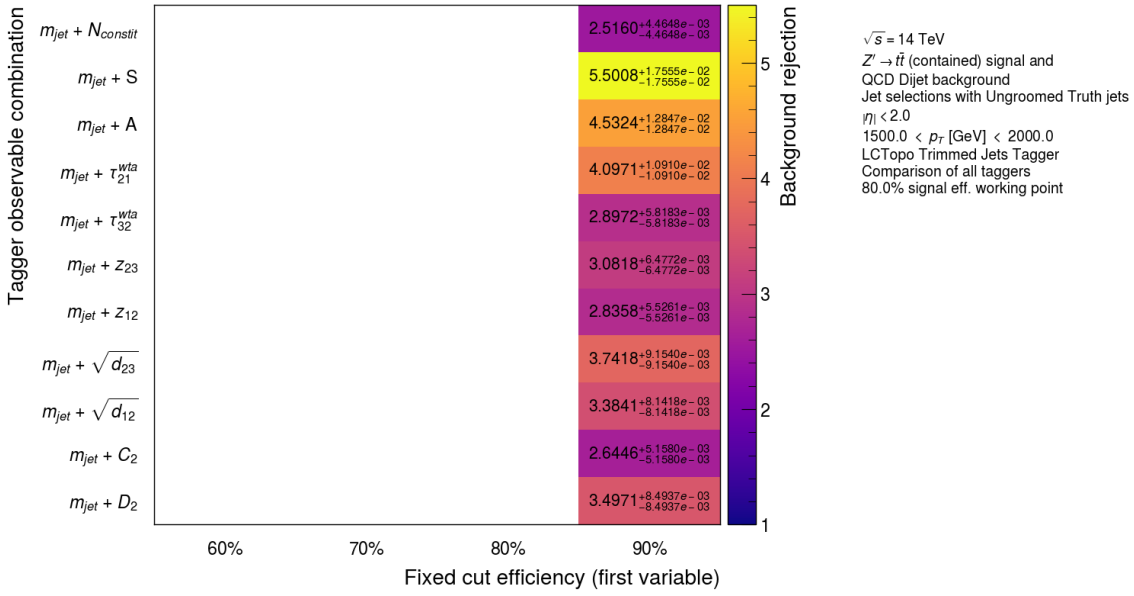

(e) Trimmed jets

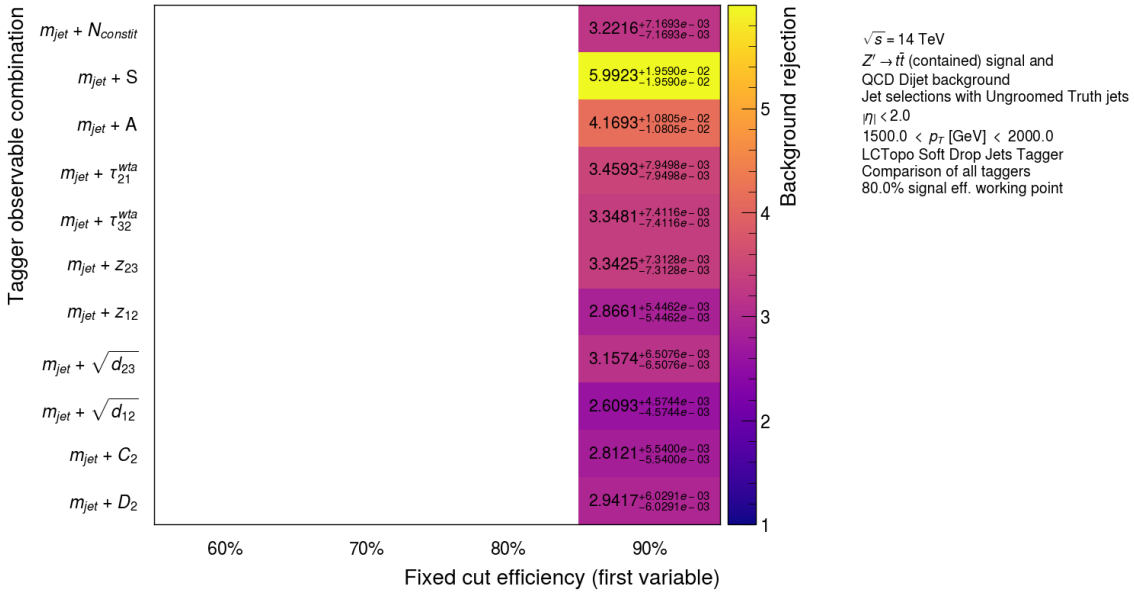

(f) Soft-drop jets

Figure E.2 (cont.): Heat-maps illustrating the background rejection for each 80% signal efficiency tagger definition with different mass selections. These results are for both the trimmed and soft-drop jets in a $1500 < p_{\mathrm{T}}^{\mathrm{reco}}$ (GeV) < 2000 bin. The x-axis displays the signal efficiency of the mass selection.

Appendix F

Detailed HL-LHC top-tagger pile-up stability

This Appendix includes additional Figures not shown in Chapter 7 (Section 7.10.1) for the complete range of two-variable top quark tagger definitions studied in HL-LHC simulation. Figure F.1 shows the signal efficiency performance of the 50% signal efficiency taggers for trimmed and soft-drop jets. Figure F.2 shows the same results but for the 80% signal efficiency working point taggers. The background rejection stability is illustrated in Figures F.3 and F.4 for the 50% and 80% signal efficiency taggers, respectively.

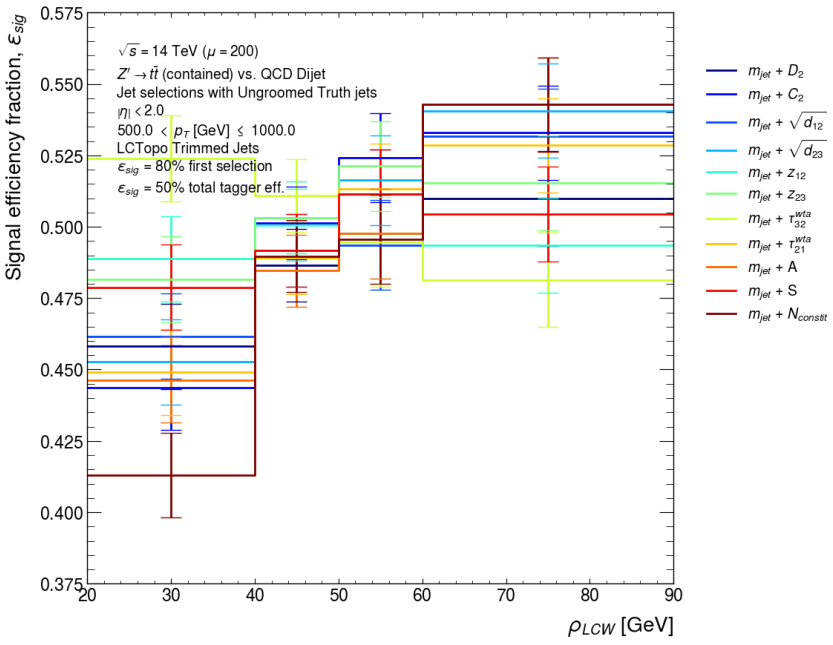

(a) Trimmed jets with $500 < p_{\mathrm{T}}^{\mathrm{truth}}$ (GeV) ≤ 1000

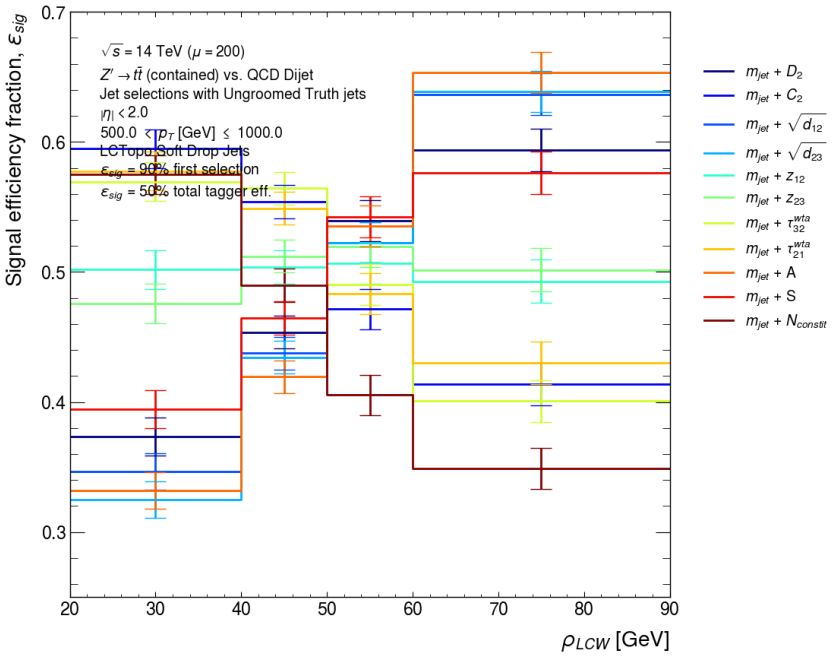

(b) Soft-drop jets with $500 < p_{\mathrm{T}}^{\mathrm{truth}}$ (GeV) ≤ 1000

Figure F.1: Pile-up stability profiles for the tagger signal efficiency as a function of the momentum density ρ_{LCW} for 50% signal efficiency trimmed and soft-drop jet taggers.

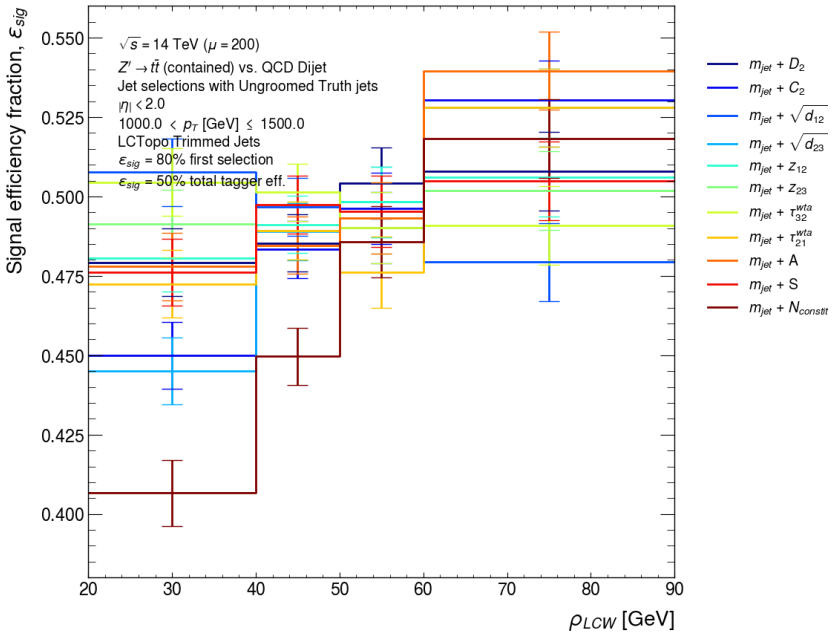

(c) Trimmed jets with $1000 < p_{\mathrm{T}}^{\mathrm{truth}}$ (GeV) ≤ 1500

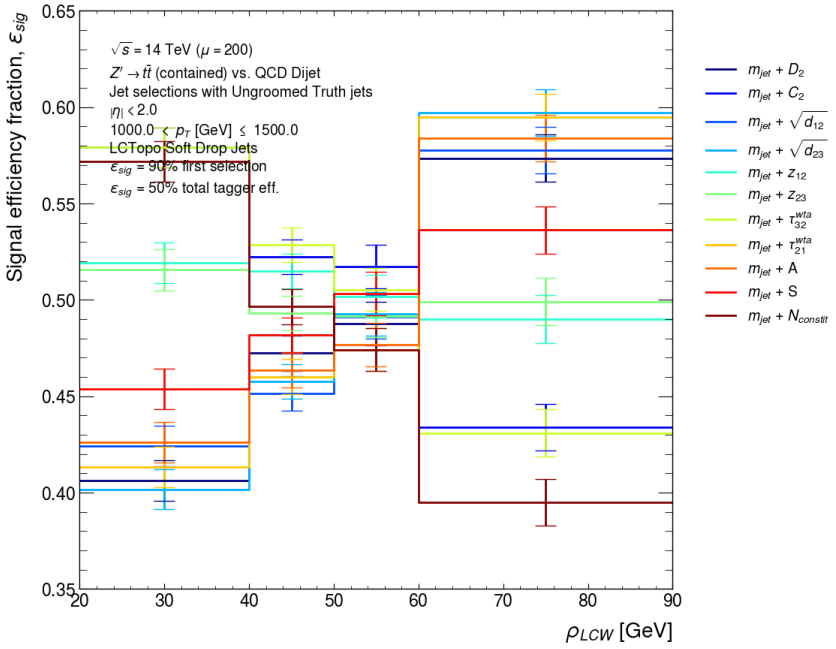

(d) Soft-drop jets with $1000 < p_{\mathrm{T}}^{\mathrm{truth}}$ (GeV) ≤ 1500

Figure F.1 (cont.): Pile-up stability profiles for the tagger signal efficiency as a function of the momentum density ρ_{LCW} for 50% signal efficiency trimmed and soft-drop jet taggers.

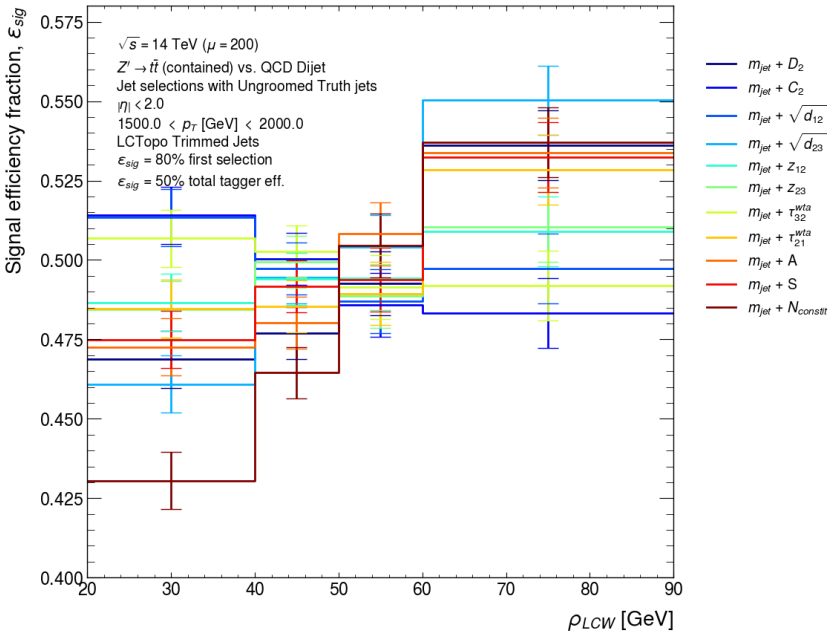

(e) Trimmed jets with $1500 < p_{\mathrm{T}}^{\mathrm{truth}}$ (GeV) < 2000

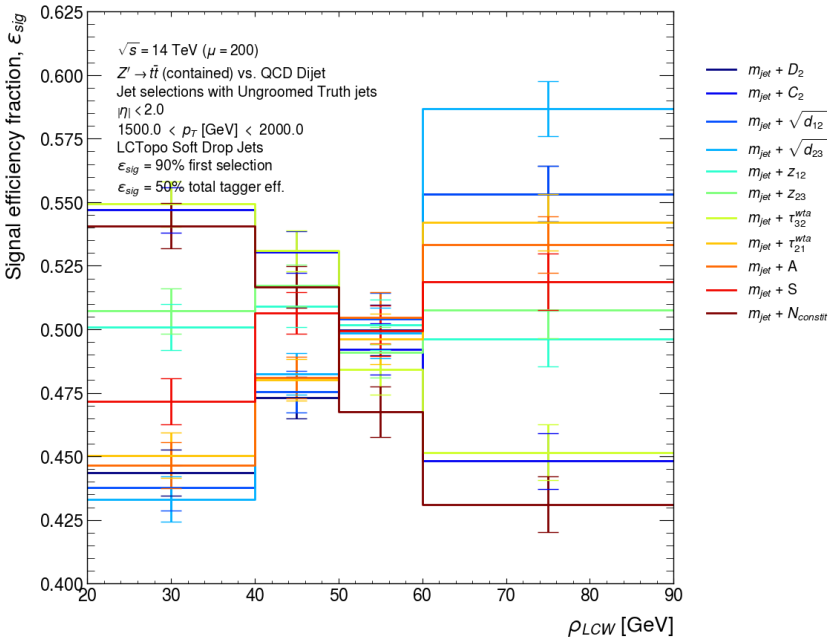

(f) Soft-drop jets with $1500 < p_{\mathrm{T}}^{\mathrm{truth}}$ (GeV) < 2000

Figure F.1 (cont.): Pile-up stability profiles for the tagger signal efficiency as a function of the momentum density ρ_{LCW} for 50% signal efficiency trimmed and soft-drop jet taggers.

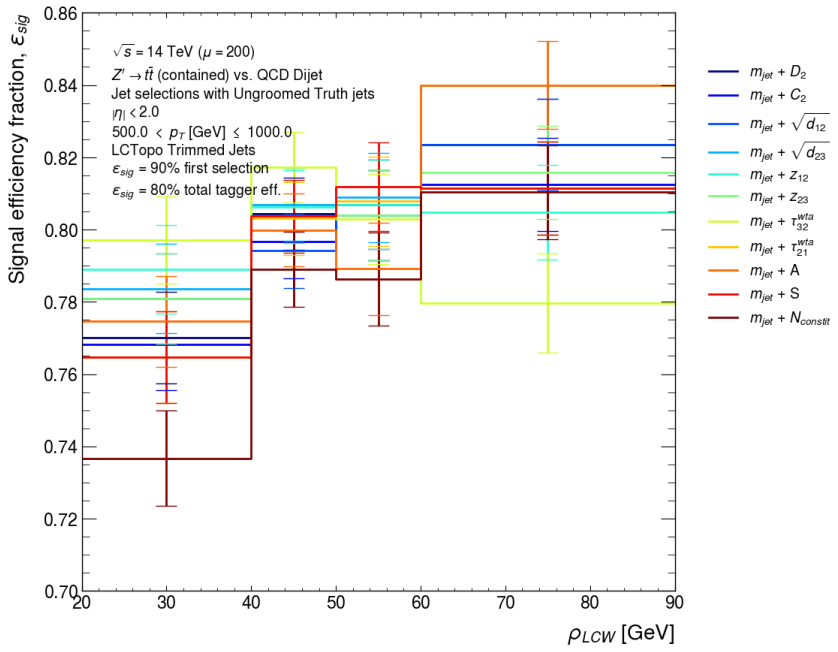

(a) Trimmed jets with $500 < p_{\mathrm{T}}^{\mathrm{truth}}$ (GeV) ≤ 1000

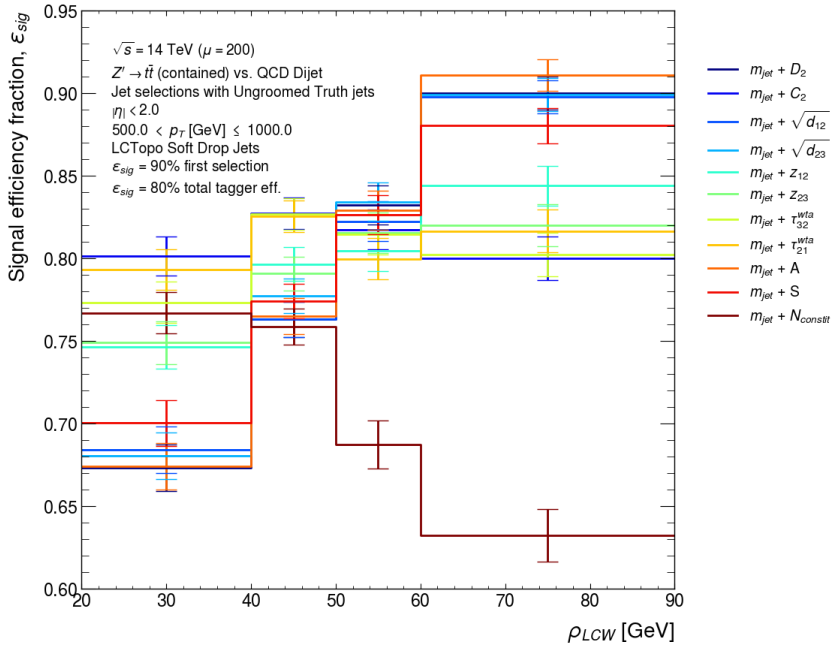

(b) Soft-drop jets with $500 < p_{\mathrm{T}}^{\mathrm{truth}}$ (GeV) ≤ 1000

Figure F.2: Pile-up stability profiles for the tagger signal efficiency as a function of the momentum density ρ_{LCW} for 80% signal efficiency trimmed and soft-drop jet taggers.

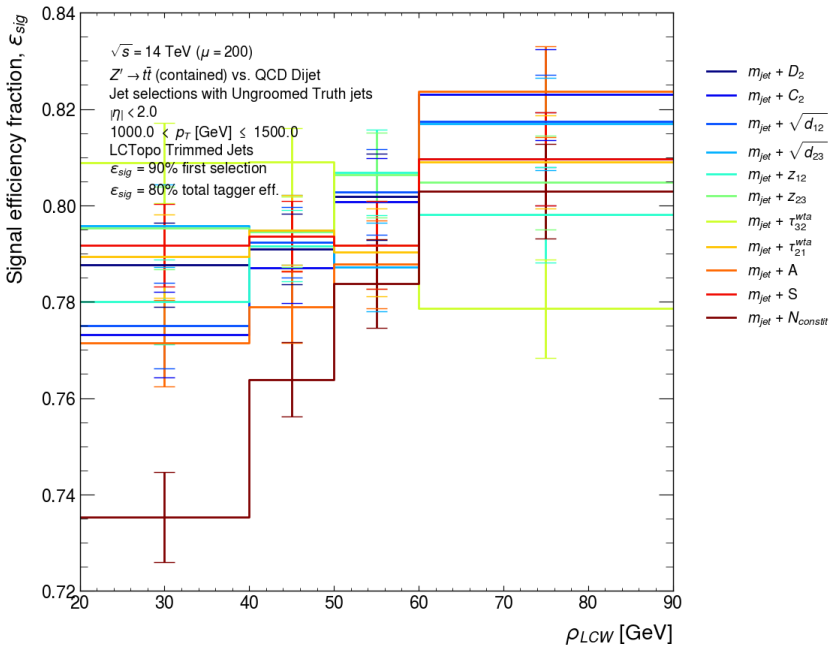

(c) Trimmed jets with $1000 < p_{\mathrm{T}}^{\mathrm{truth}}$ (GeV) ≤ 1500

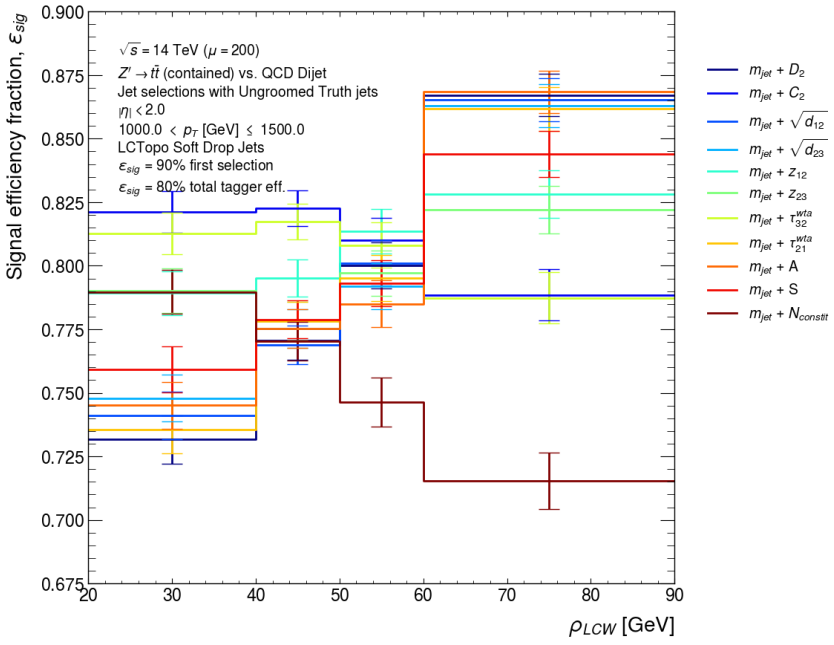

(d) Soft-drop jets with $1000 < p_{\mathrm{T}}^{\mathrm{truth}}$ (GeV) ≤ 1500

Figure F.2 (cont.): Pile-up stability profiles for the tagger signal efficiency as a function of the momentum density ρ_{LCW} for 80% signal efficiency trimmed and soft-drop jet taggers.

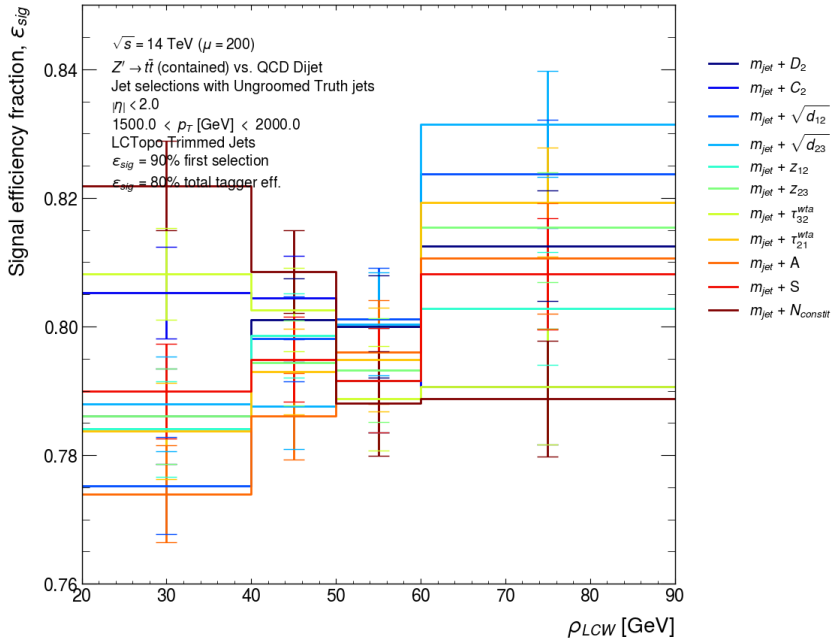

(e) Trimmed jets with $1500 < p_{\mathrm{T}}^{\mathrm{truth}}$ (GeV) < 2000

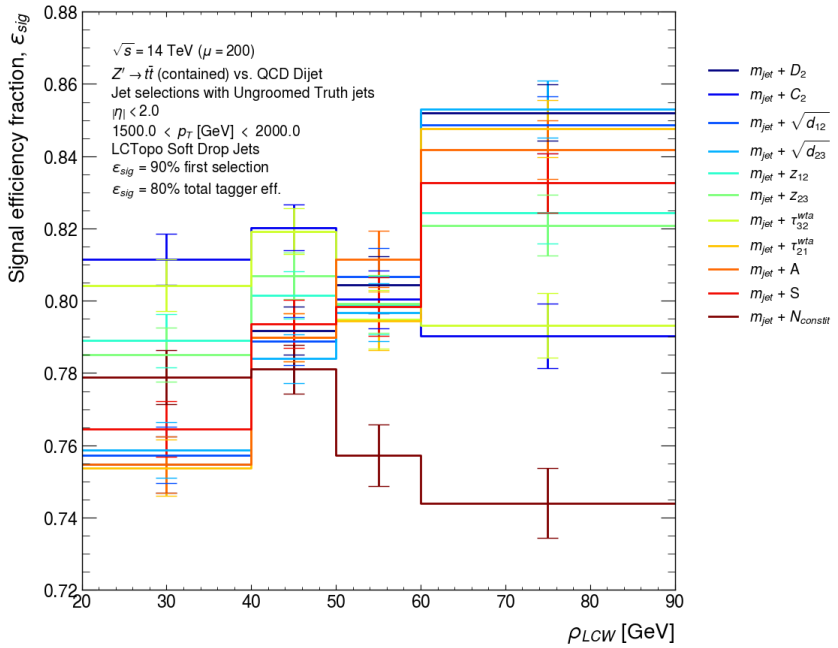

(f) Soft-drop jets with $1500 < p_{\mathrm{T}}^{\mathrm{truth}}$ (GeV) < 2000

Figure F.2 (cont.): Pile-up stability profiles for the tagger signal efficiency as a function of the momentum density ρ_{LCW} for 80% signal efficiency trimmed and soft-drop jet taggers.

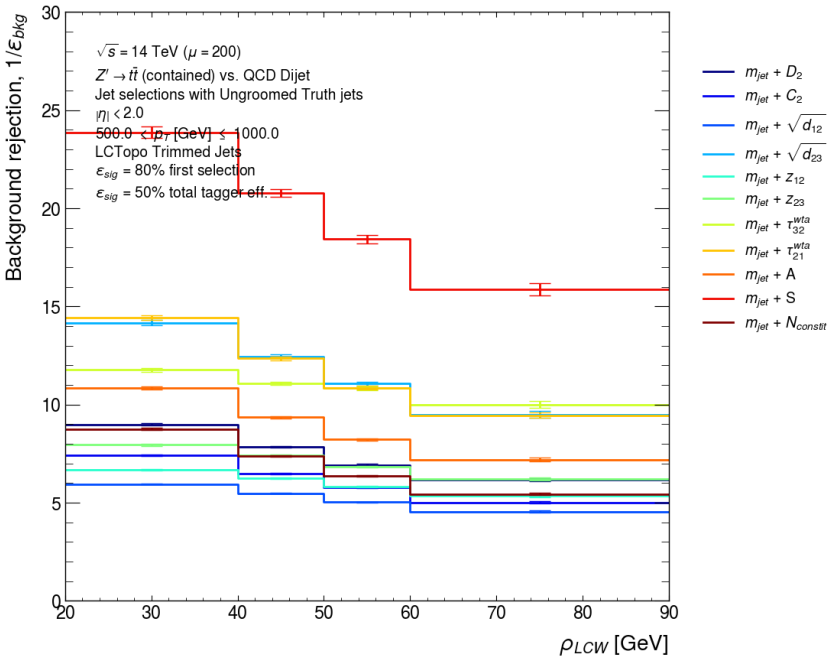

(a) Trimmed jets with $500 < p_{\mathrm{T}}^{\mathrm{truth}}$ (GeV) ≤ 1000

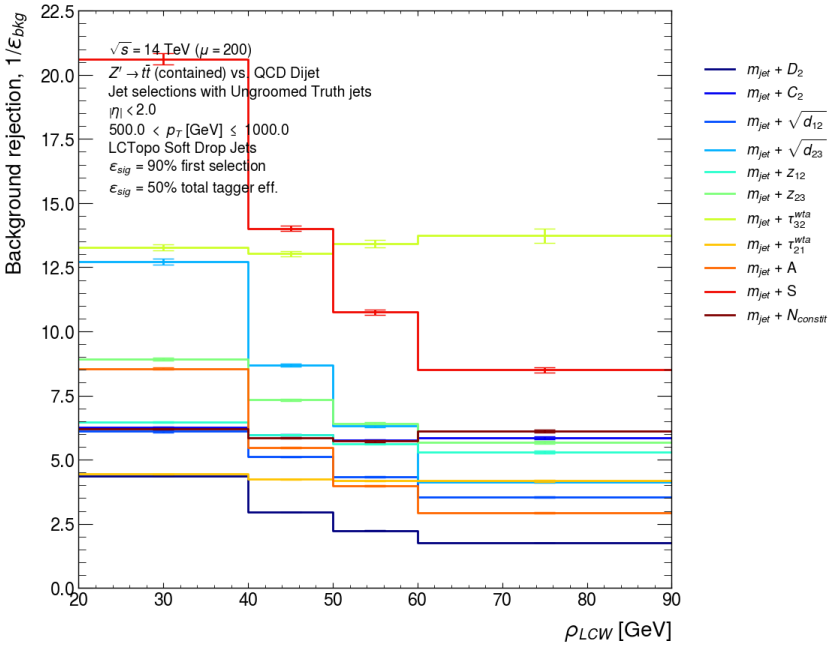

(b) Soft-drop jets with $500 < p_{\mathrm{T}}^{\mathrm{truth}}$ (GeV) ≤ 1000

Figure F.3: Pile-up stability profiles for the tagger background rejection as a function of the momentum density ρ_{LCW} for 50% signal efficiency trimmed and soft-drop jet taggers.

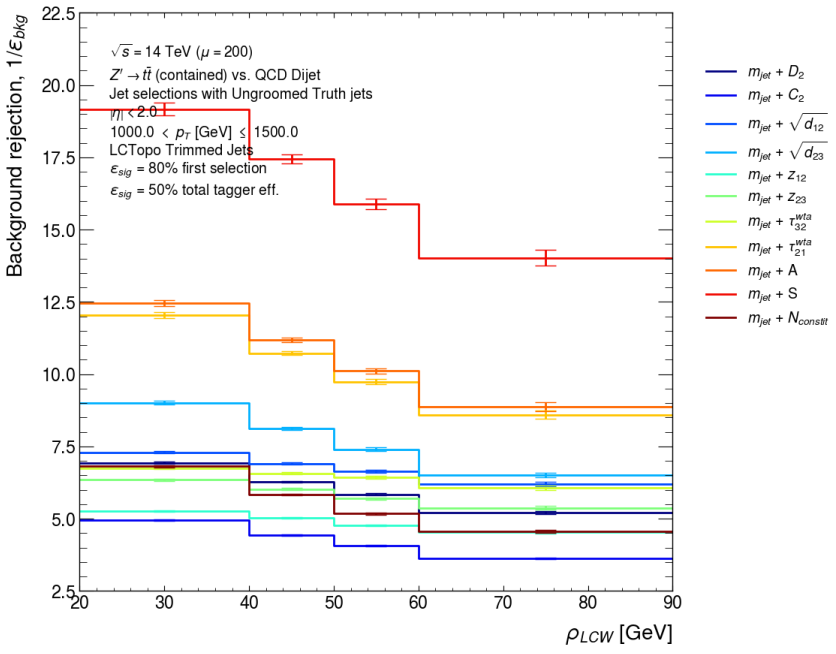

(c) Trimmed jets with $1000 < p_{\mathrm{T}}^{\mathrm{truth}}$ (GeV) ≤ 1500

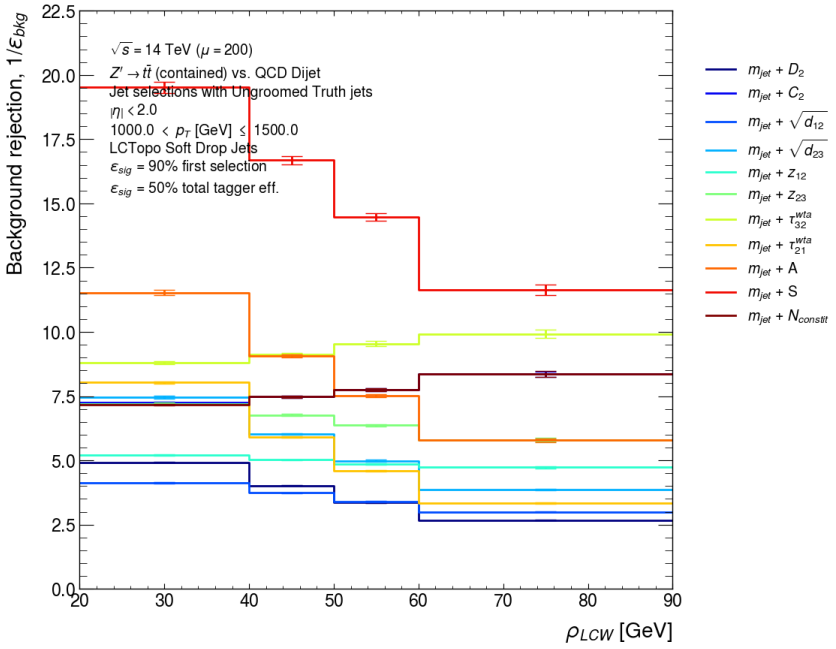

(d) Soft-drop jets with $1000 < p_{\mathrm{T}}^{\mathrm{truth}}$ (GeV) ≤ 1500

Figure F.3 (cont.): Pile-up stability profiles for the tagger background rejection as a function of the momentum density ρ_{LCW} for 50% signal efficiency trimmed and soft-drop jet taggers.

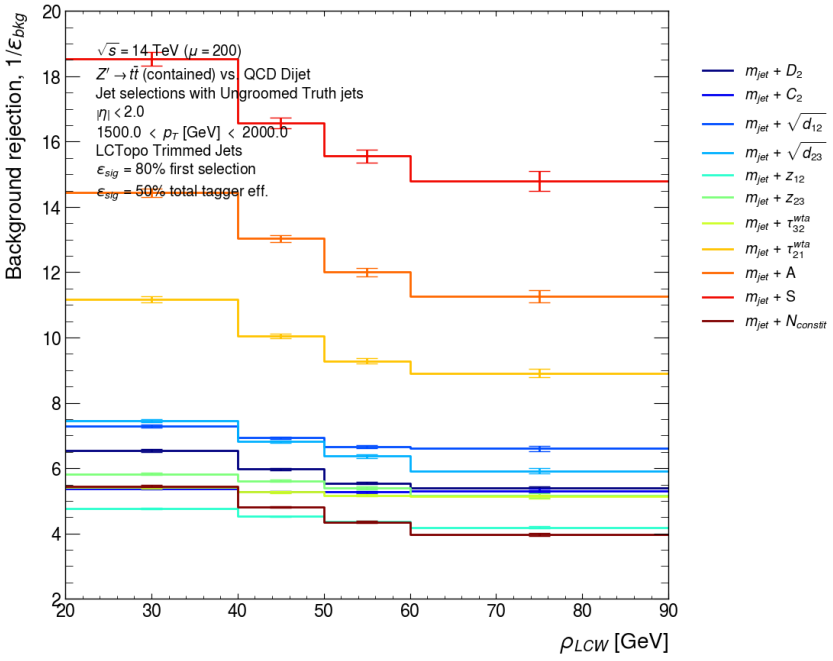

(e) Trimmed jets with $1500 < p_{\mathrm{T}}^{\mathrm{truth}}$ (GeV) < 2000

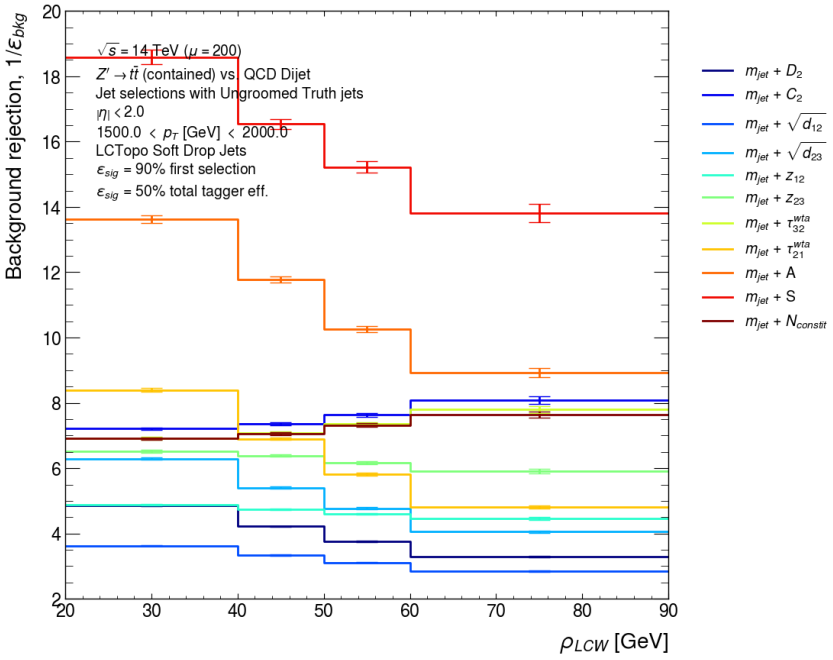

(f) Soft-drop jets with $1500 < p_{\mathrm{T}}^{\mathrm{truth}}$ (GeV) < 2000

Figure F.3 (cont.): Pile-up stability profiles for the tagger background rejection as a function of the momentum density ρ_{LCW} for 50% signal efficiency trimmed and soft-drop jet taggers.

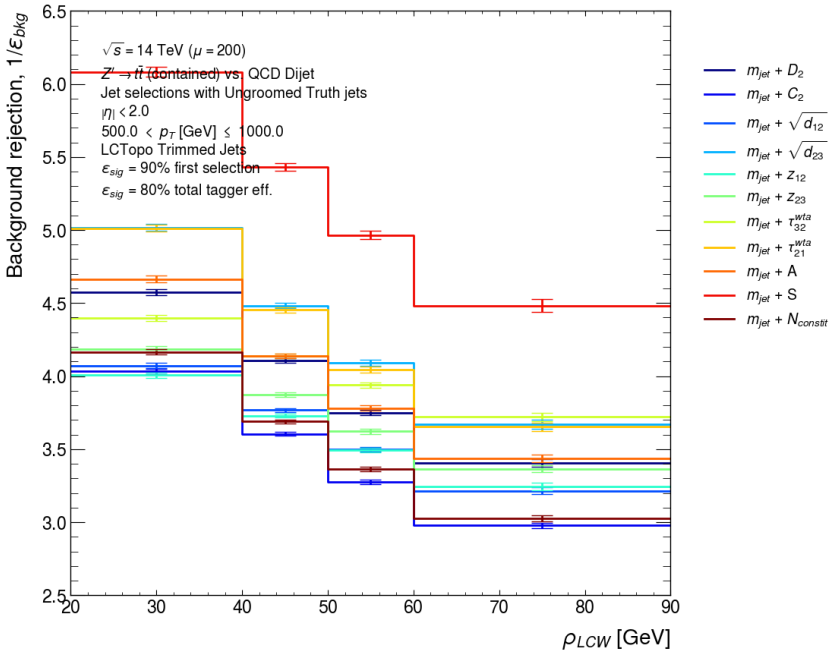

(a) Trimmed jets with $500 < p_{\mathrm{T}}^{\mathrm{truth}}$ (GeV) ≤ 1000

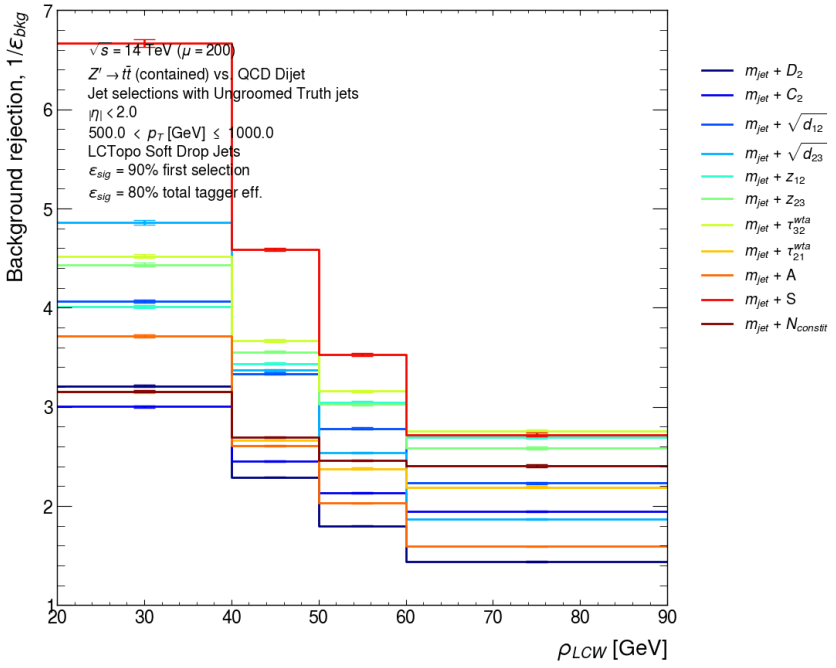

(b) Soft-drop jets with $500 < p_{\mathrm{T}}^{\mathrm{truth}}$ (GeV) ≤ 1000

Figure F.4: Pile-up stability profiles for the tagger background rejection as a function of the momentum density ρ_{LCW} for 80% signal efficiency trimmed and soft-drop jet taggers.

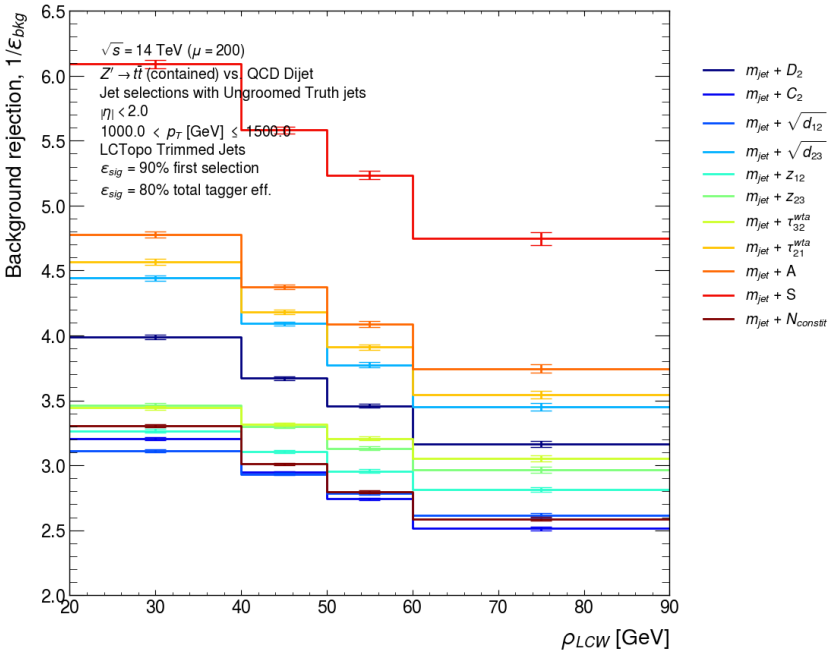

(c) Trimmed jets with $1000 < p_{\mathrm{T}}^{\mathrm{truth}}$ (GeV) ≤ 1500

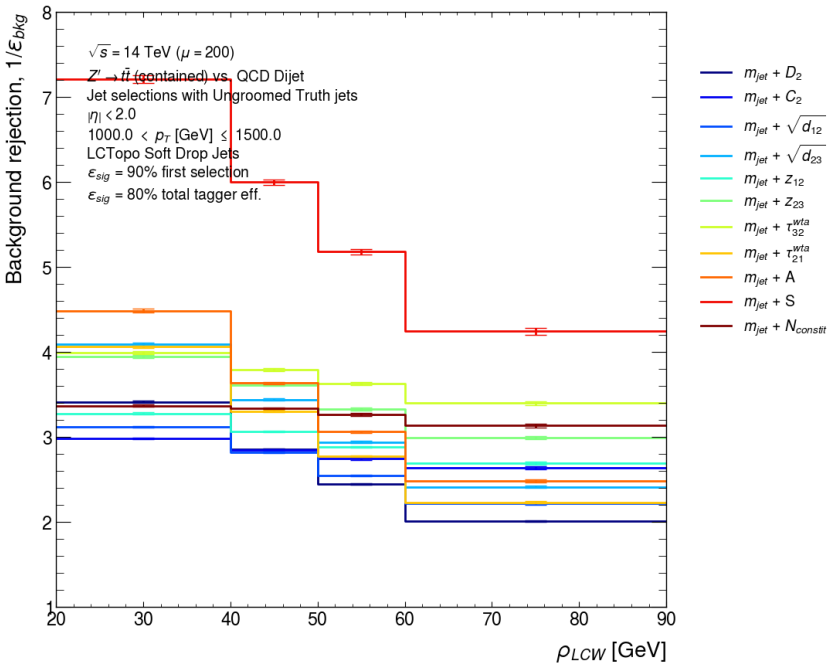

(d) Soft-drop jets with $1000 < p_{\mathrm{T}}^{\mathrm{truth}}$ (GeV) ≤ 1500

Figure F.4 (cont.): Pile-up stability profiles for the tagger background rejection as a function of the momentum density ρ_{LCW} for 80% signal efficiency trimmed and soft-drop jet taggers.

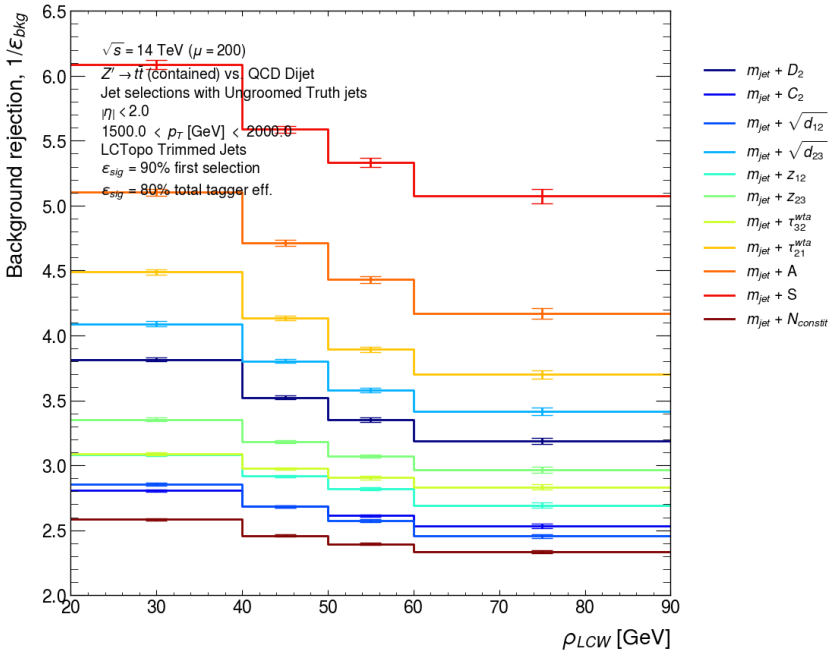

(e) Trimmed jets with $1500 < p_{\mathrm{T}}^{\mathrm{truth}}$ (GeV) < 2000

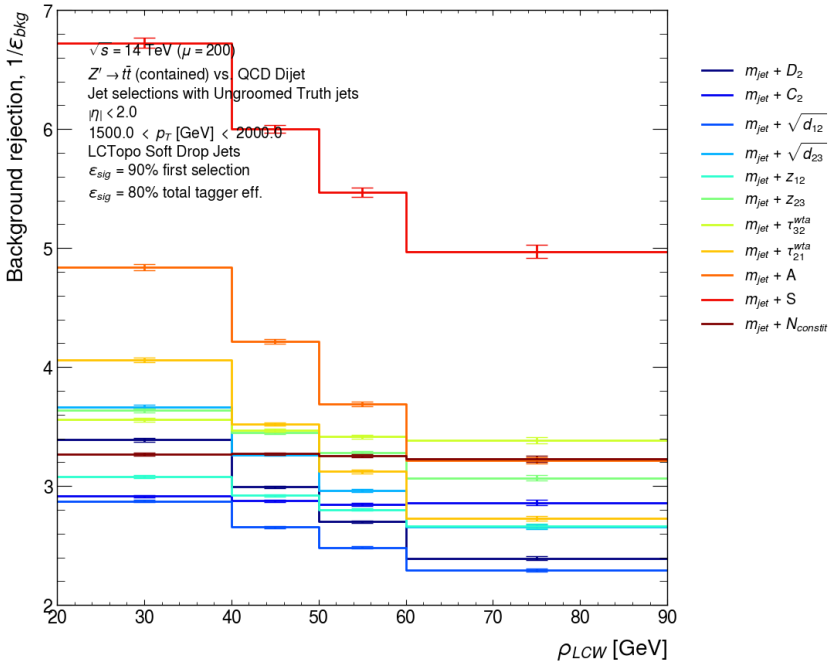

(f) Soft-drop jets with $1500 < p_{\mathrm{T}}^{\mathrm{truth}}$ (GeV) < 2000

Figure F.4 (cont.): Pile-up stability profiles for the tagger background rejection as a function of the momentum density ρ_{LCW} for 80% signal efficiency trimmed and soft-drop jet taggers.

Appendix G

Pile-up stability for HL-LHC top-taggers as a function of $\langle\mu\rangle$

Further to the tagger pile-up stability discussion in Chapter 7 (Section 7.10.1), this Appendix provides the same results, but parametrised as a function of the average number of interactions per bunch crossing ($\langle\mu\rangle$) instead of the event-level momentum-density (ρ_{LCW}). For clarity, only selected tagger definitions are included here for comparison to the ρ_{LCW} binned performance results in Section 7.10.1. The same procedure as in Section 7.10.1 was used to study the tagger performance[1]. The $\langle\mu\rangle$ binning considered is inclusive of the lower and upper bin edges to retain events that would otherwise be lost, ensuring the impact of statistical uncertainties does not significantly detract from the results. The signal efficiency of the trimmed and soft-drop jet taggers is shown as a function of $\langle\mu\rangle$ for the 50% and 80% signal efficiency taggers in Figures G.3 and G.4, respectively. The background rejection as a function of $\langle\mu\rangle$ for the 50% and 80% signal efficiency taggers is illustrated in Figures G.1 and G.2, respectively.

Significantly less variation is seen in the background rejection and signal efficiencies for the trimmed jet taggers. This is a consequence of the narrow range of $\langle\mu\rangle$ available in the MC event samples as discussed in Section 7.10.1. For the soft-drop jets, more variation is seen in the signal efficiency, and the background rejection falls for all taggers except the τ_{32}^{wta} ($m_{\text{jet}} + \tau_{32}^{\text{wta}}$) variant[2]. The soft-drop jet taggers were found to be significantly less pile-up stable than trimmed jet taggers in Section 7.10.1, which could explain why more variation in the tagger performance is seen for the soft-drop jets compared to trimmed jets here. Nonetheless, the statistical uncertainty in the tagger metrics combined with smaller variations over the $\langle\mu\rangle$ binning compared to the ρ_{LCW} binning impacts the extent to which these conclusions can be relied upon, especially for trimmed jets.

[1] Apply a tagger selection derived in an inclusive p_{T} bin in different $\langle\mu\rangle$ bins then study the signal efficiency and background rejection stability.

[2] In the lowest p_{T} bin for the 80% signal efficiency taggers a decrease in the background rejection with increasing $\langle\mu\rangle$ is seen for this tagger similar to the other tagger definitions.

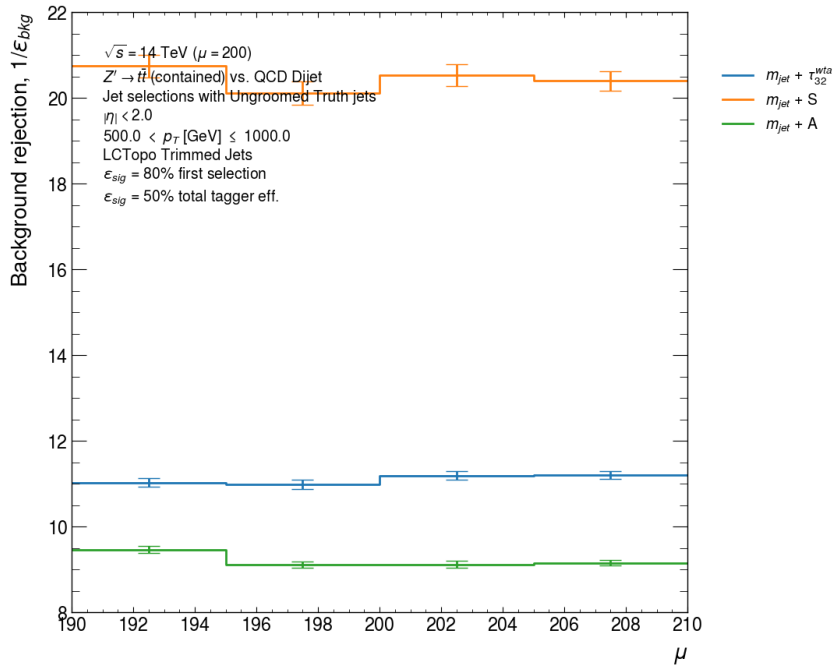

(a) Trimmed jets with $500 < p_{\mathrm{T}}^{\mathrm{truth}}$ (GeV) ≤ 1000

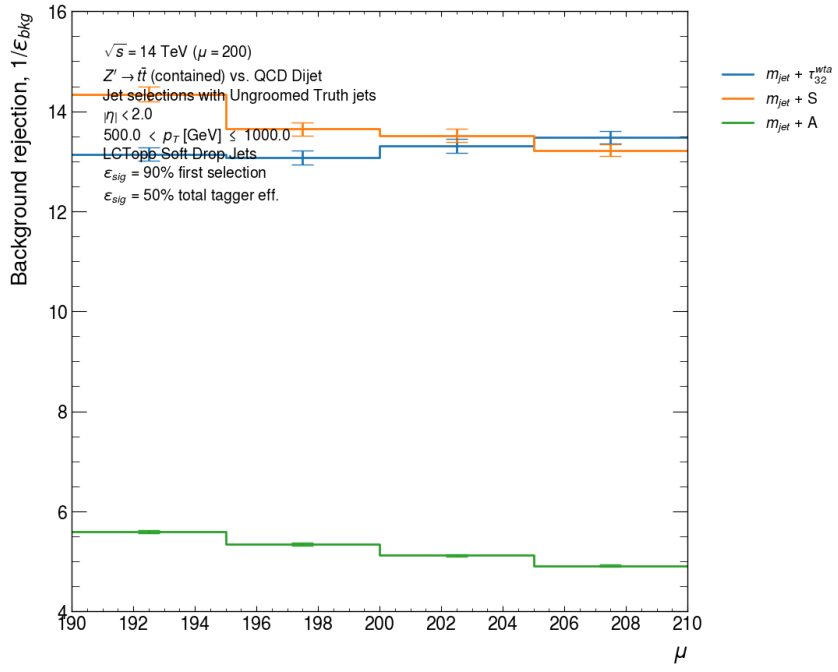

(b) Soft-drop jets with $500 < p_{\mathrm{T}}^{\mathrm{truth}}$ (GeV) ≤ 1000

Figure G.1: Pile-up stability profiles for the tagger background rejection as a function of the average number of interactions per bunch crossing $\langle\mu\rangle$ (μ in axis labels) for 50% signal efficiency trimmed and soft-drop jet taggers.

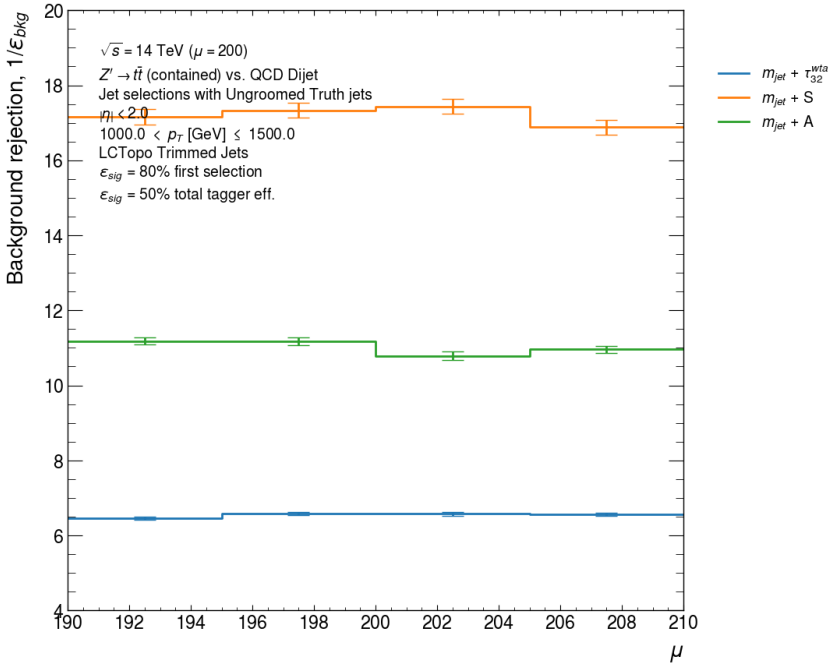

(c) Trimmed jets with $1000 < p_{\mathrm{T}}^{\mathrm{truth}}$ (GeV) ≤ 1500

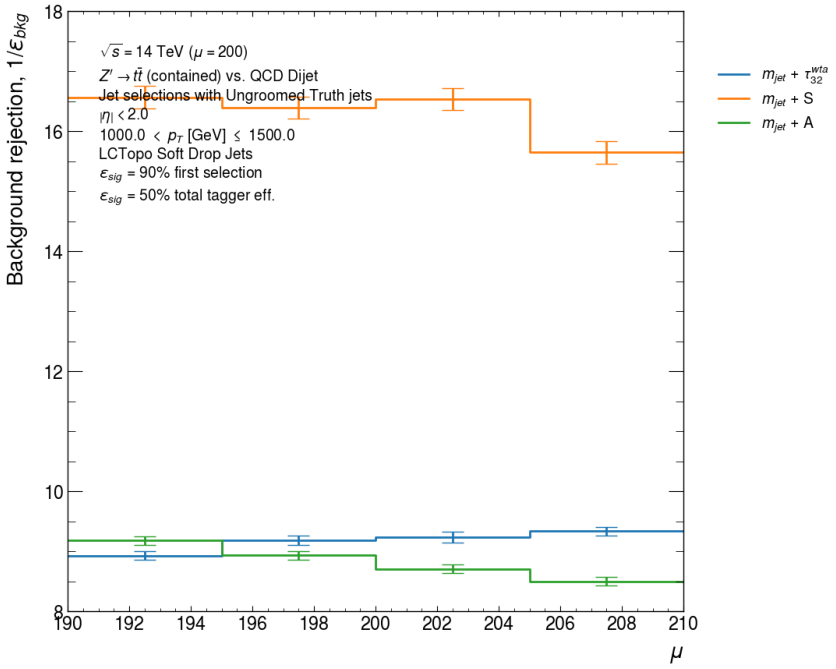

(d) Soft-drop jets with $1000 < p_{\mathrm{T}}^{\mathrm{truth}}$ (GeV) ≤ 1500

Figure G.1 (cont.): Pile-up stability profiles for the tagger background rejection as a function of the average number of interactions per bunch crossing $\langle\mu\rangle$ (μ in axis labels) for 50% signal efficiency trimmed and soft-drop jet taggers.

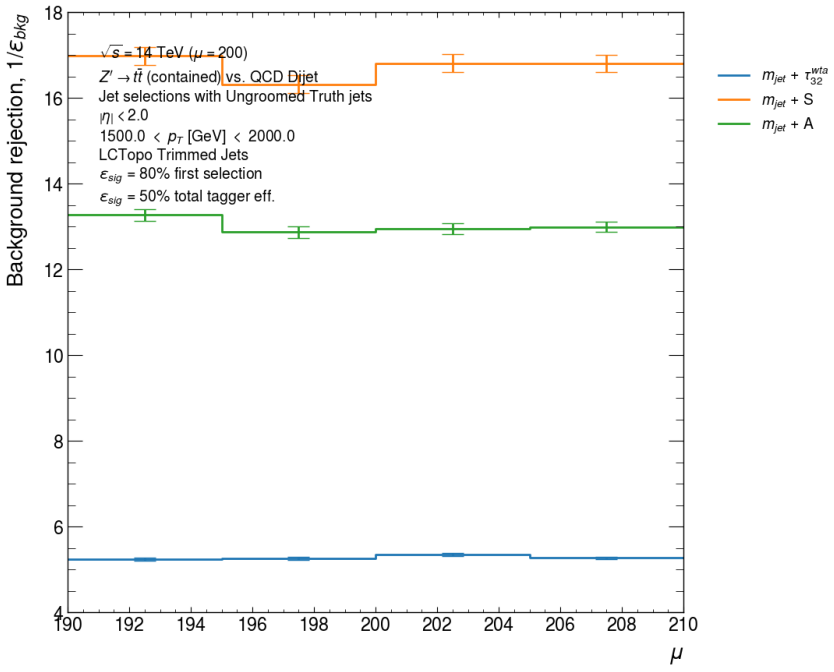

(e) Trimmed jets with $1500 < p_{\mathrm{T}}^{\mathrm{truth}}$ (GeV) < 2000

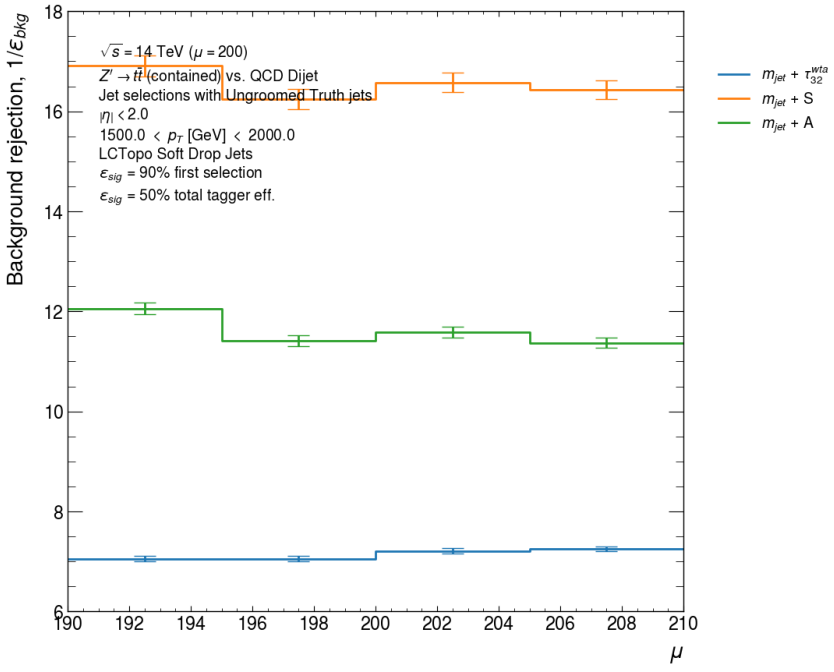

(f) Soft-drop jets with $1500 < p_{\mathrm{T}}^{\mathrm{truth}}$ (GeV) < 2000

Figure G.1 (cont.): Pile-up stability profiles for the tagger background rejection as a function of the average number of interactions per bunch crossing $\langle\mu\rangle$ (μ in axis labels) for 50% signal efficiency trimmed and soft-drop jet taggers.

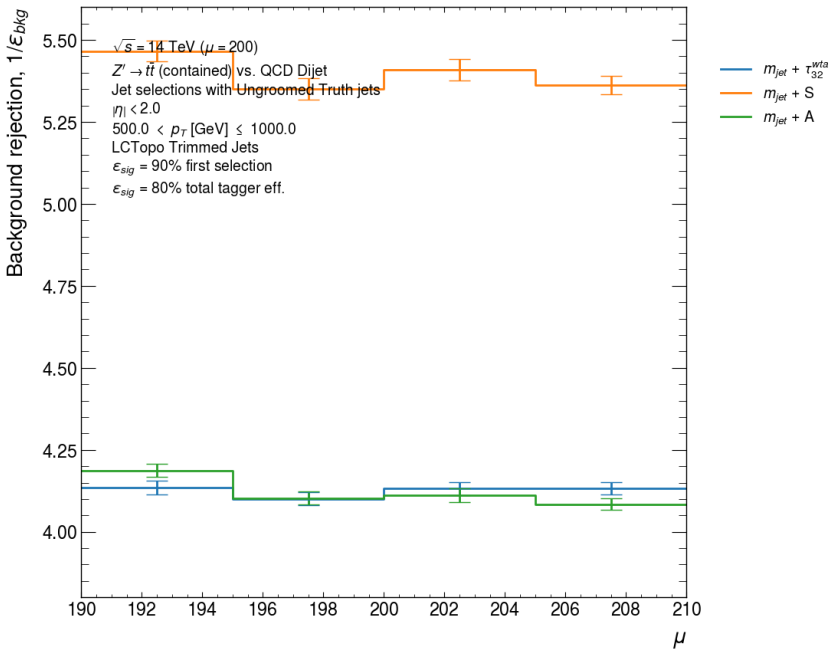

(a) Trimmed jets with $500 < p_{\mathrm{T}}^{\mathrm{truth}}$ (GeV) ≤ 1000

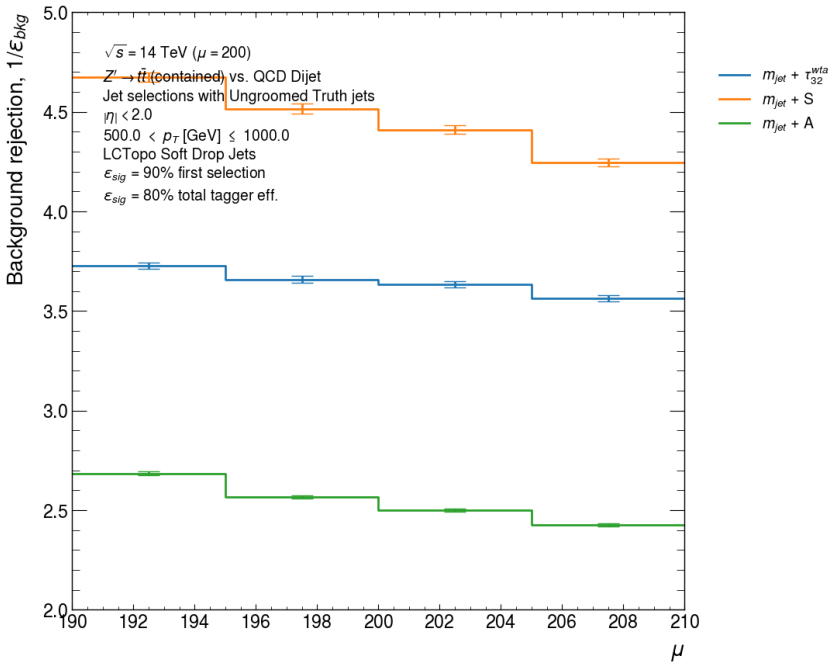

(b) Soft-drop jets with $500 < p_{\mathrm{T}}^{\mathrm{truth}}$ (GeV) ≤ 1000

Figure G.2: Pile-up stability profiles for the tagger background rejection as a function of the average number of interactions per bunch crossing $\langle\mu\rangle$ (μ in axis labels) for 80% signal efficiency trimmed and soft-drop jet taggers.

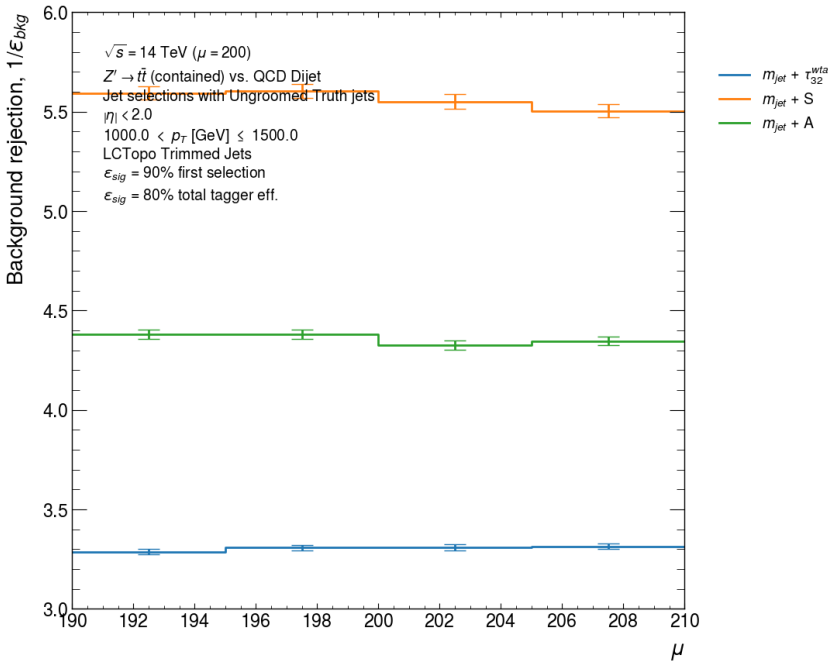

(c) Trimmed jets with $1000 < p_{\mathrm{T}}^{\mathrm{truth}}$ (GeV) ≤ 1500

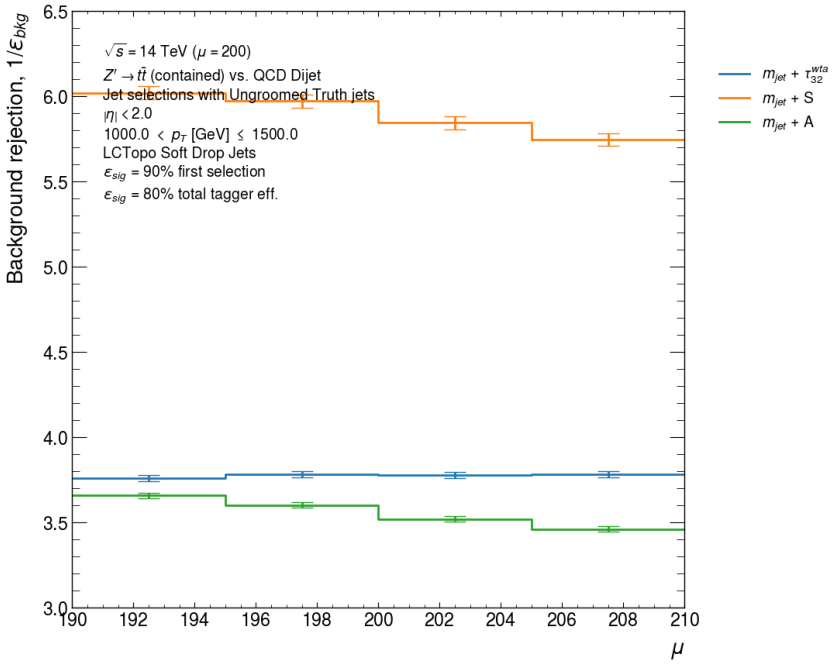

(d) Soft-drop jets with $1000 < p_{\mathrm{T}}^{\mathrm{truth}}$ (GeV) ≤ 1500

Figure G.2 (cont.): Pile-up stability profiles for the tagger background rejection as a function of the average number of interactions per bunch crossing $\langle\mu\rangle$ (μ in axis labels) for 80% signal efficiency trimmed and soft-drop jet taggers.

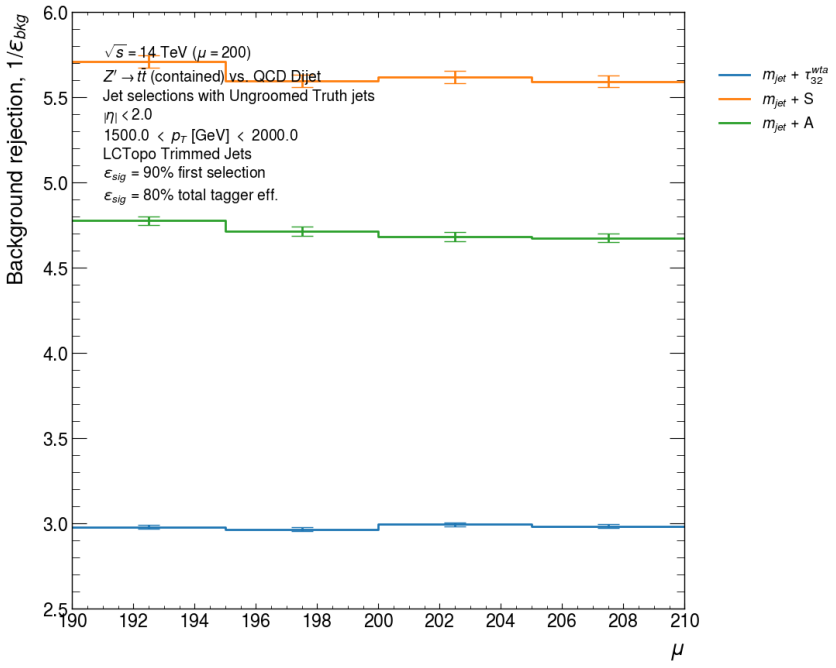

(e) Trimmed jets with $1500 < p_{\mathrm{T}}^{\mathrm{truth}}$ (GeV) < 2000

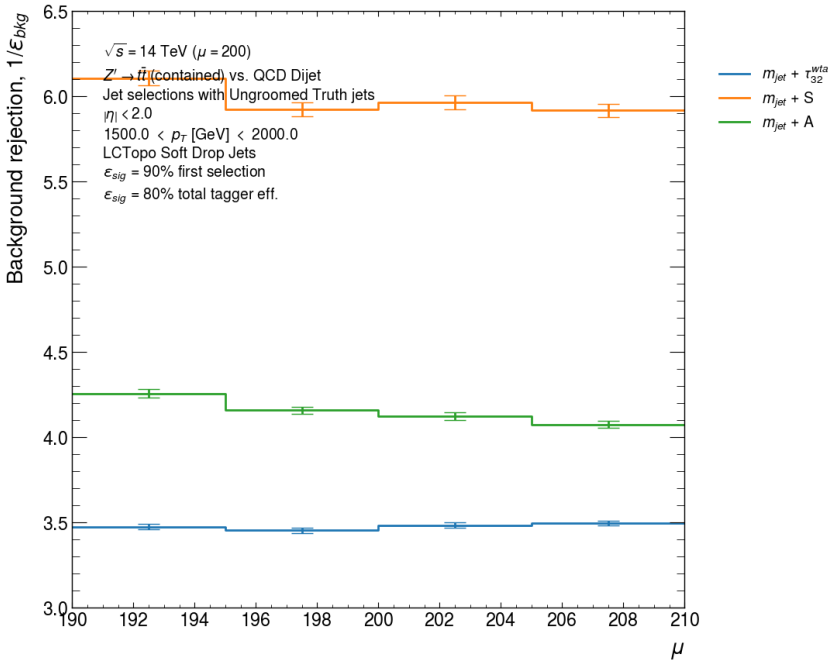

(f) Soft-drop jets with $1500 < p_{\mathrm{T}}^{\mathrm{truth}}$ (GeV) < 2000

Figure G.2 (cont.): Pile-up stability profiles for the tagger background rejection as a function of the average number of interactions per bunch crossing $\langle\mu\rangle$ (μ in axis labels) for 80% signal efficiency trimmed and soft-drop jet taggers.

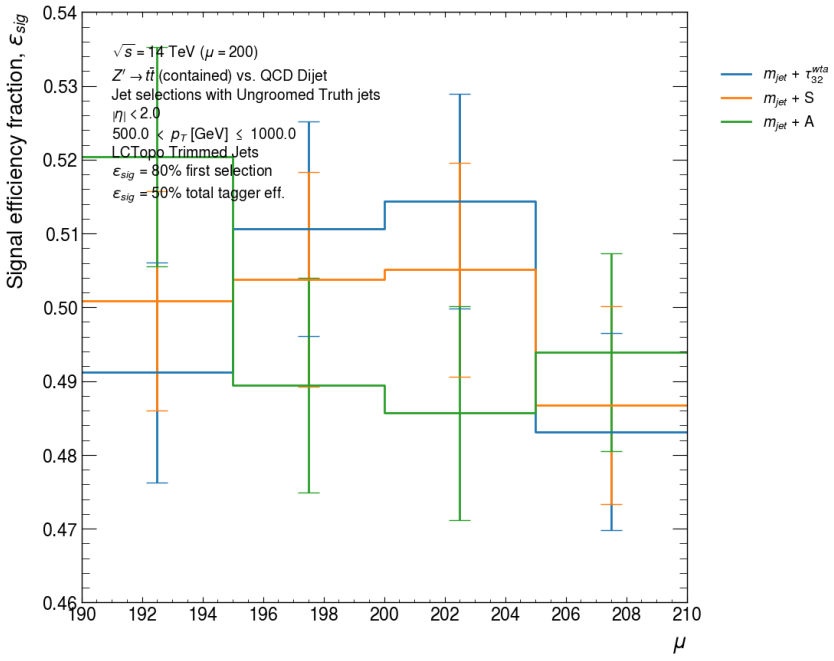

(a) Trimmed jets with $500 < p_{\mathrm{T}}^{\mathrm{truth}}$ (GeV) ≤ 1000

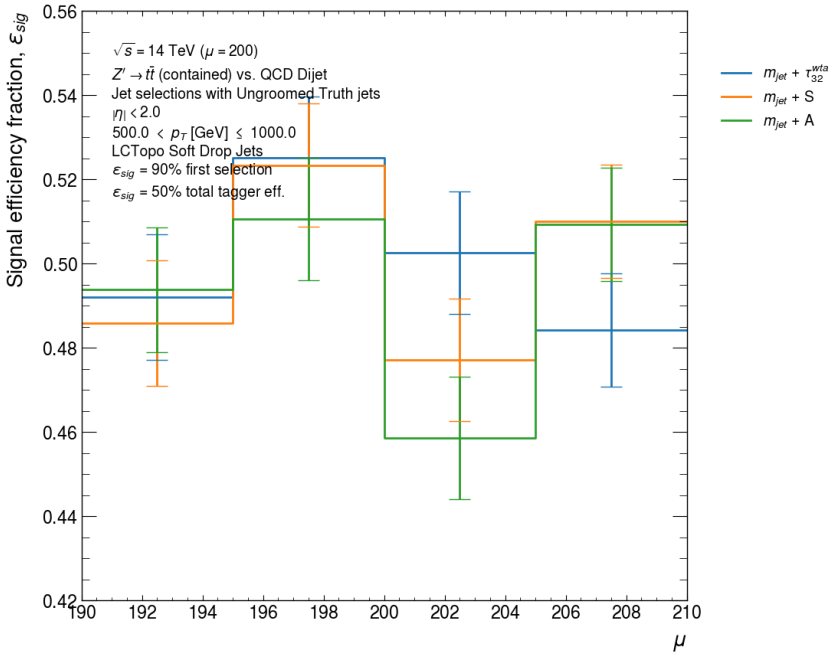

(b) Soft-drop jets with $500 < p_{\mathrm{T}}^{\mathrm{truth}}$ (GeV) ≤ 1000

Figure G.3: Pile-up stability profiles for the tagger signal efficiency as a function of the average number of interactions per bunch crossing $\langle\mu\rangle$ (μ in axis labels) for 50% signal efficiency trimmed and soft-drop jet taggers.

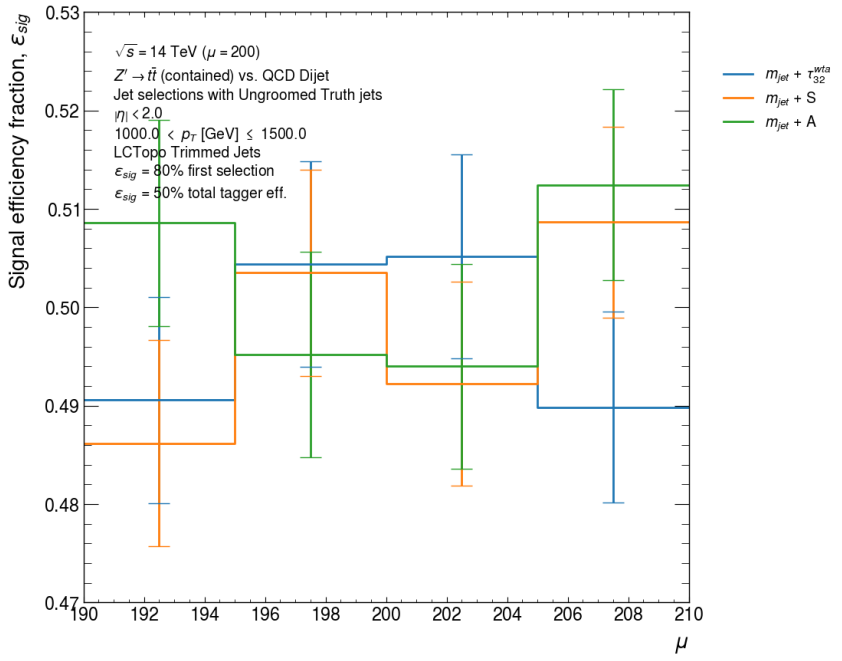

(c) Trimmed jets with $1000 < p_{\mathrm{T}}^{\mathrm{truth}}$ (GeV) ≤ 1500

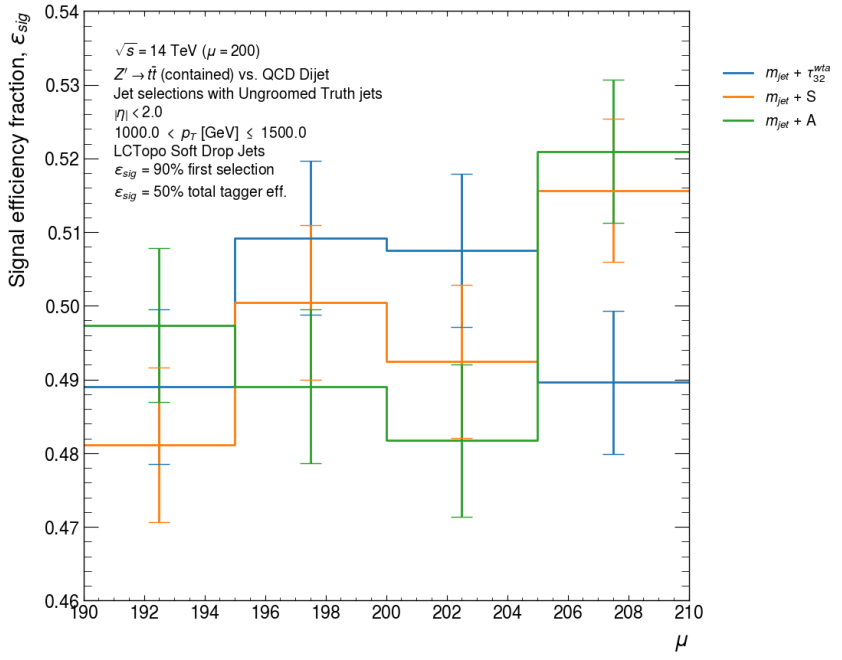

(d) Soft-drop jets with $1000 < p_{\mathrm{T}}^{\mathrm{truth}}$ (GeV) ≤ 1500

Figure G.3 (cont.): Pile-up stability profiles for the tagger signal efficiency as a function of the average number of interactions per bunch crossing $\langle\mu\rangle$ (μ in axis labels) for 50% signal efficiency trimmed and soft-drop jet taggers.

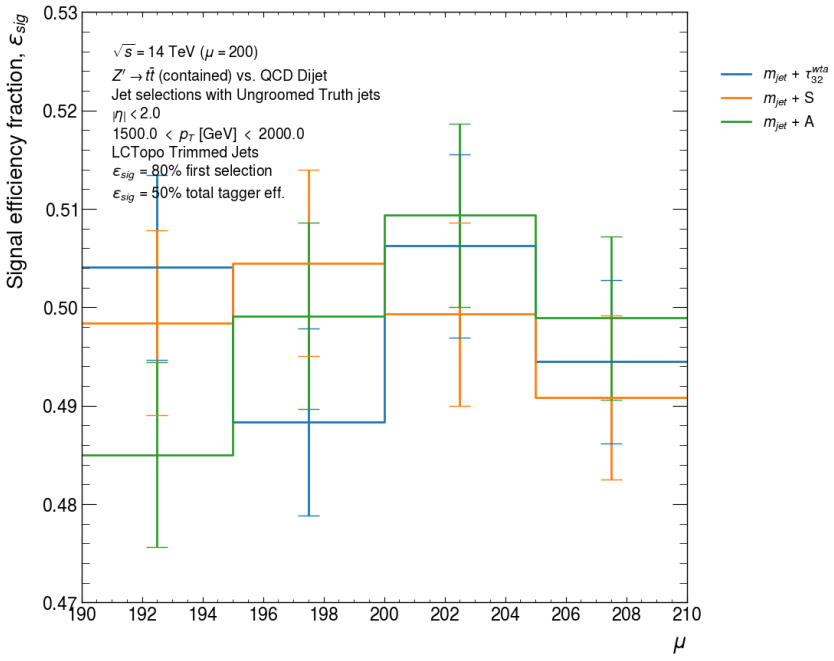

(e) Trimmed jets with $1500 < p_{\mathrm{T}}^{\mathrm{truth}}$ (GeV) < 2000

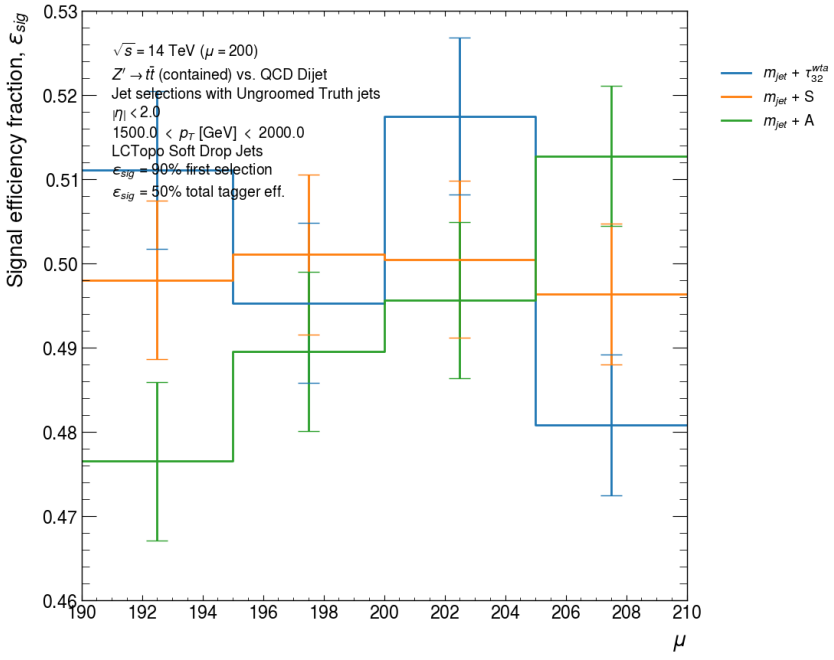

(f) Soft-drop jets with $1500 < p_{\mathrm{T}}^{\mathrm{truth}}$ (GeV) < 2000

Figure G.3 (cont.): Pile-up stability profiles for the tagger signal efficiency as a function of the average number of interactions per bunch crossing $\langle\mu\rangle$ (μ in axis labels) for 50% signal efficiency trimmed and soft-drop jet taggers.

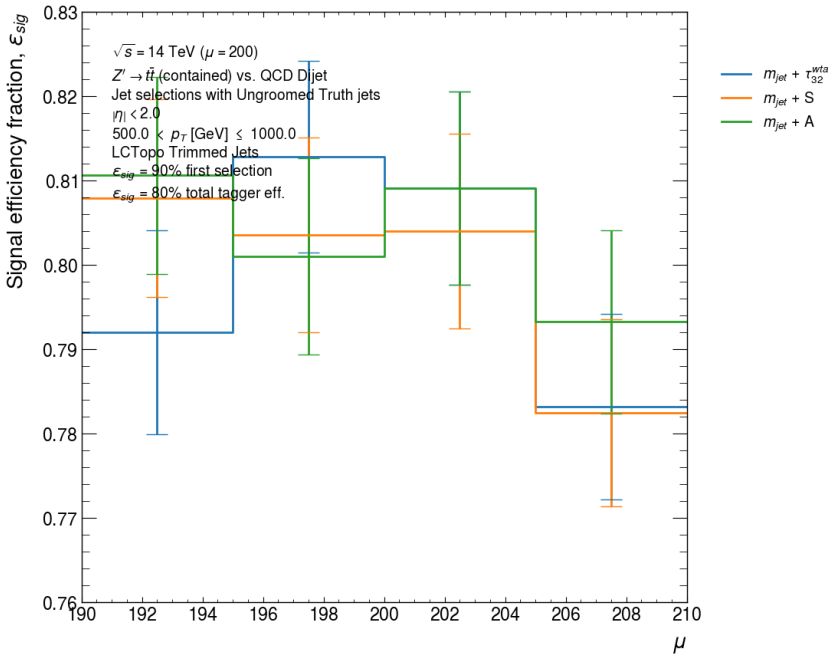

(a) Trimmed jets with $500 < p_{\mathrm{T}}^{\mathrm{truth}}$ (GeV) ≤ 1000

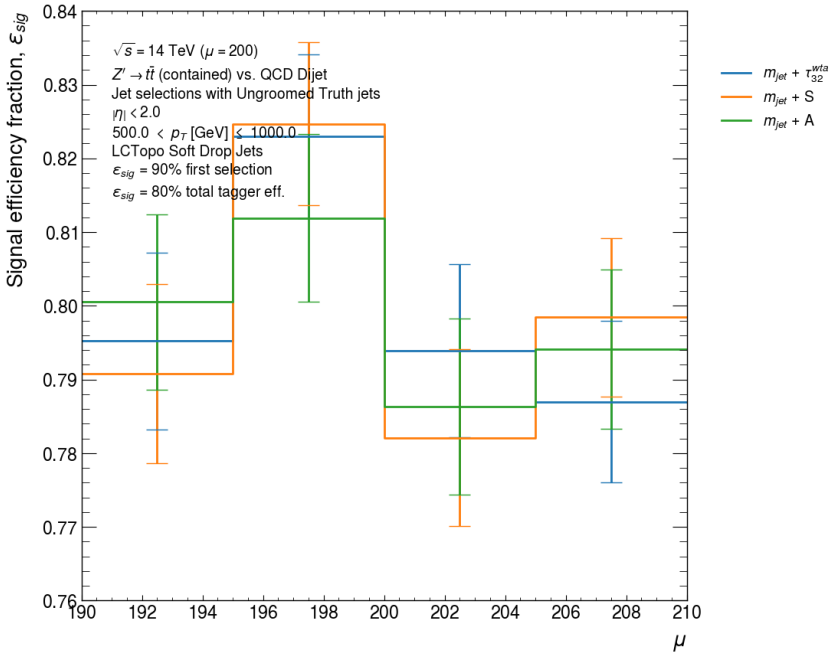

(b) Soft-drop jets with $500 < p_{\mathrm{T}}^{\mathrm{truth}}$ (GeV) ≤ 1000

Figure G.4: Pile-up stability profiles for the tagger signal efficiency as a function of the average number of interactions per bunch crossing $\langle\mu\rangle$ (μ in axis labels) for 80% signal efficiency trimmed and soft-drop jet taggers.

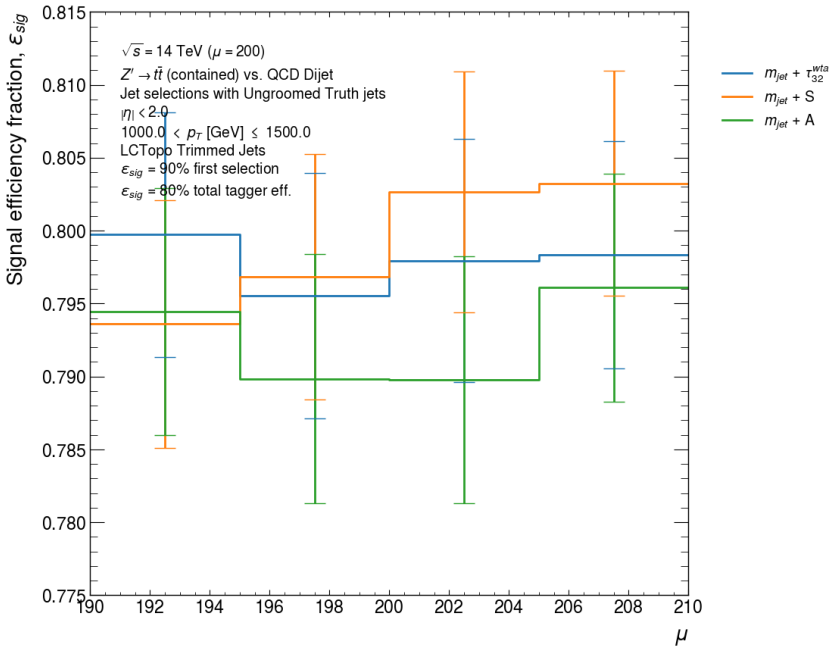

(c) Trimmed jets with $1000 < p_{\mathrm{T}}^{\mathrm{truth}}$ (GeV) ≤ 1500

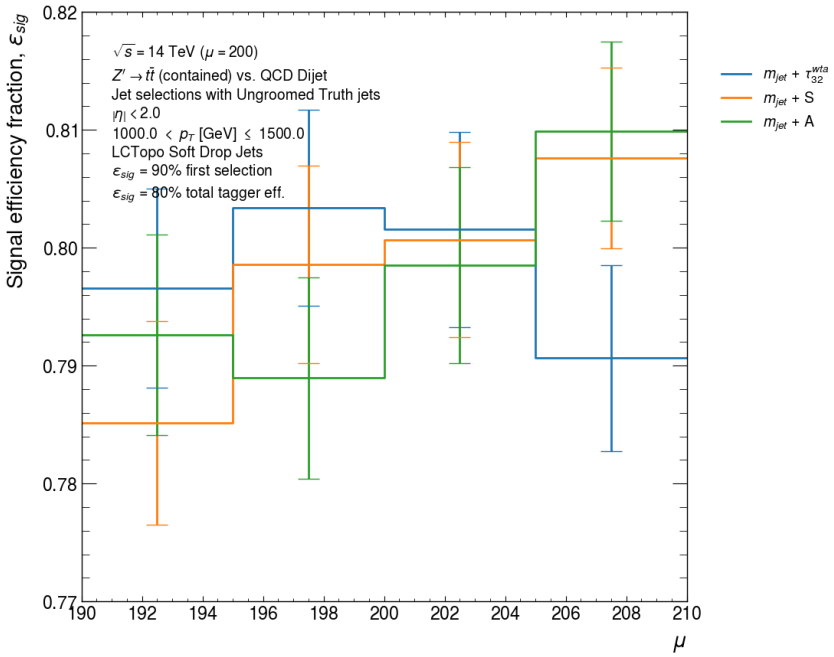

(d) Soft-drop jets with $1000 < p_{\mathrm{T}}^{\mathrm{truth}}$ (GeV) ≤ 1500

Figure G.4 (cont.): Pile-up stability profiles for the tagger signal efficiency as a function of the average number of interactions per bunch crossing $\langle\mu\rangle$ (μ in axis labels) for 80% signal efficiency trimmed and soft-drop jet taggers.

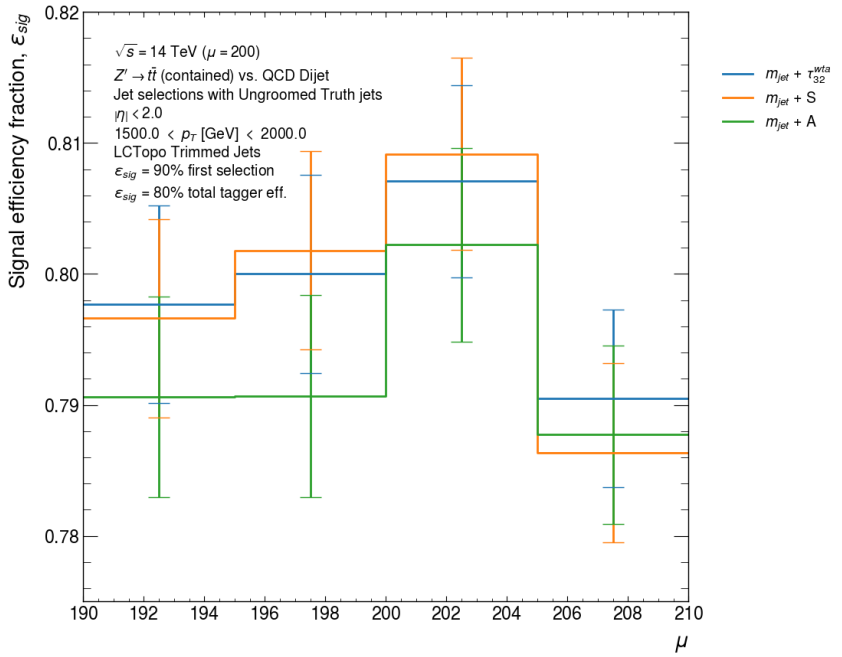

(e) Trimmed jets with $1500 < p_{\mathrm{T}}^{\mathrm{truth}}$ (GeV) < 2000

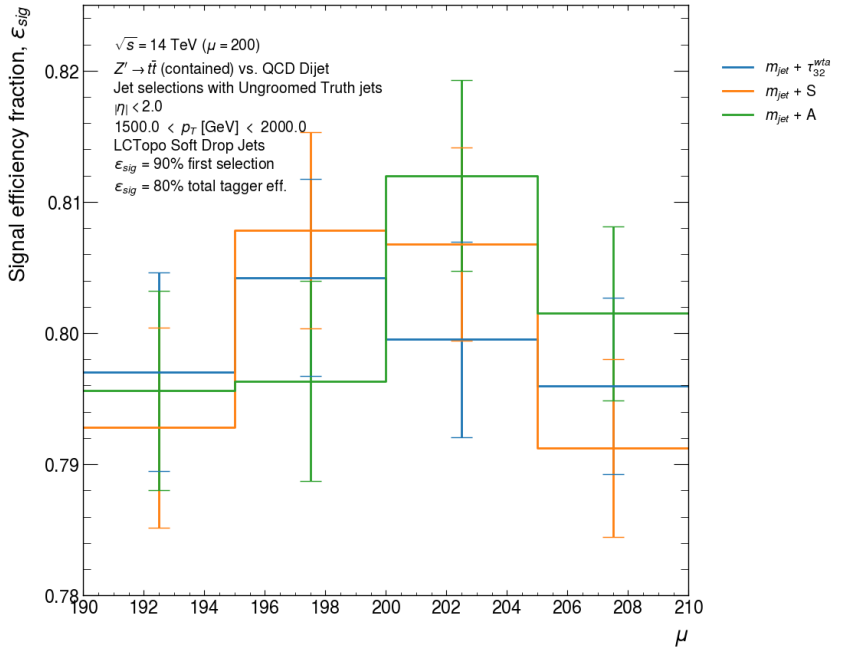

(f) Soft-drop jets with $1500 < p_{\mathrm{T}}^{\mathrm{truth}}$ (GeV) < 2000

Figure G.4 (cont.): Pile-up stability profiles for the tagger signal efficiency as a function of the average number of interactions per bunch crossing $\langle\mu\rangle$ (μ in axis labels) for 80% signal efficiency trimmed and soft-drop jet taggers.

Appendix H

Jet response distributions in HL-LHC simulation

This Appendix provides further Figures to supplement the discussion of the jet response stability in Section 7.10.2. Jet response distributions are included for selected observables: τ_{32}^{wta}, aplanarity (A), sphericity (S), and m_{jet}. Each jet response distribution corresponds to a different p_{T} bin (of the groomed truth jets) with an additional ρ_{LCW} selection. As discussed in Section 7.10, ρ_{LCW} (the median momentum-density) measures the complete hadronic activity and event. Thus, large values of ρ_{LCW} can be associated with increased pile-up activity. Additional selections on jets include a $m_{\text{jet}} > 40$ GeV cut on both truth and reconstructed jets, and a requirement that all reconstructed jets have ≥ 3 constituents ($N_{\text{constit.}}^{\text{reco}} \geq 3$). All response distributions were derived with the QCD dijet sample from Chapter 7.

The jet response distributions for trimmed and soft-drop jets are shown in Figures H.1 to H.4 and Figures H.5 to H.8, respectively. All of these plots include overlaid vertical lines to indicate:

- The "scale": the median of the response distribution.
- Limits of the "resolution": the 68.27% (central) inter-quantile range (IQnR) of the response distribution.

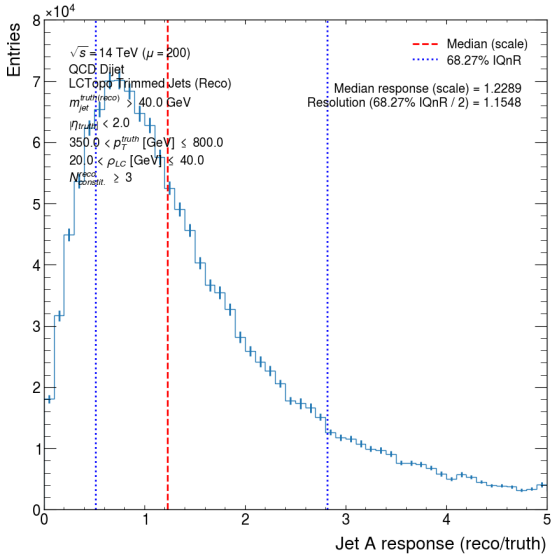

(a) $350 < p_{\mathrm{T}}^{\mathrm{truth}}$ (GeV) ≤ 800 and $20 < \rho_{\mathrm{LCW}}$ (GeV) ≤ 40

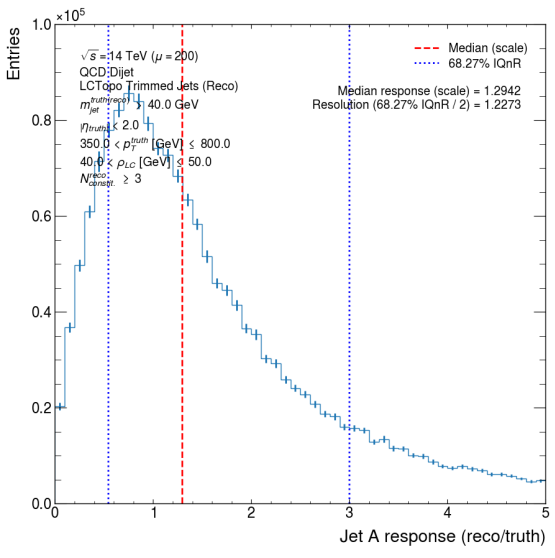

(b) $350 < p_{\mathrm{T}}^{\mathrm{truth}}$ (GeV) ≤ 800 and $40 < \rho_{\mathrm{LCW}}$ (GeV) ≤ 50

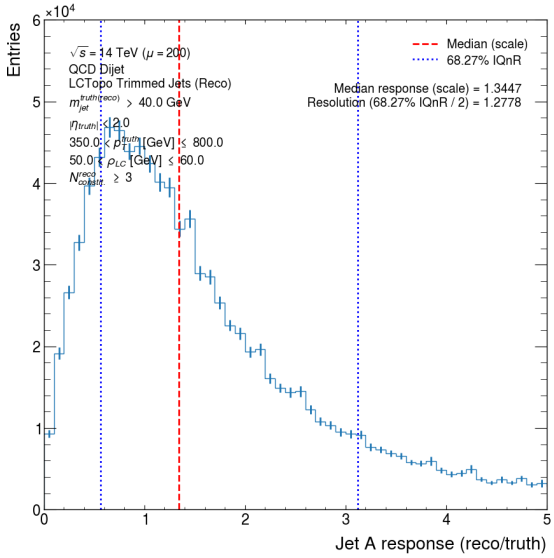

(c) $350 < p_{\mathrm{T}}^{\mathrm{truth}}$ (GeV) ≤ 800 and $50 < \rho_{\mathrm{LCW}}$ (GeV) ≤ 60

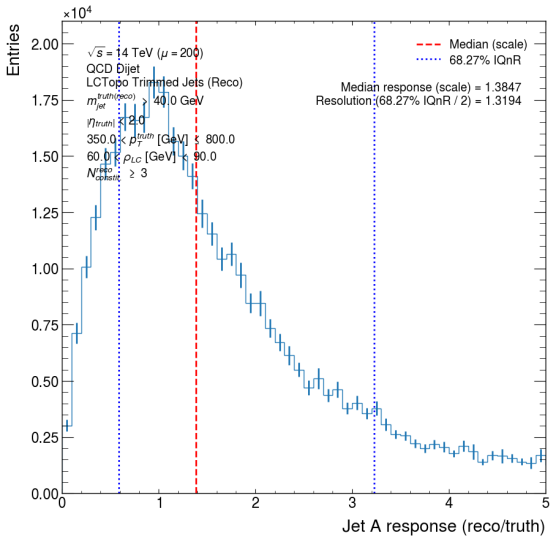

(d) $350 < p_{\mathrm{T}}^{\mathrm{truth}}$ (GeV) ≤ 800 and $60 < \rho_{\mathrm{LCW}}$ (GeV) < 90

Figure H.1: Trimmed jet A response distributions binned in the truth trimmed jet p_{T} and ρ_{LCW}.

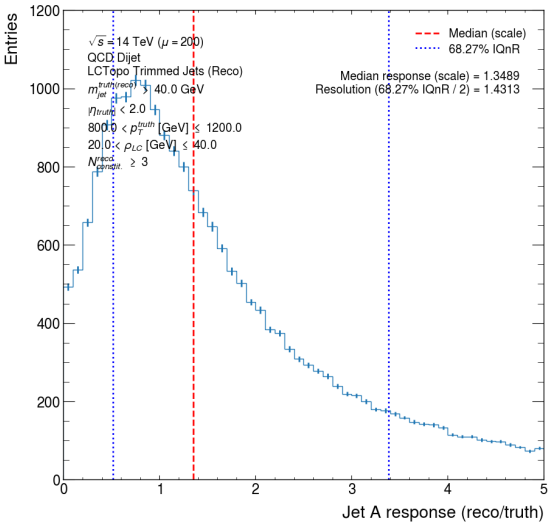

(e) $800 < p_{\mathrm{T}}^{\mathrm{truth}}$ (GeV) ≤ 1200 and $20 < \rho_{\mathrm{LCW}}$ (GeV) ≤ 40

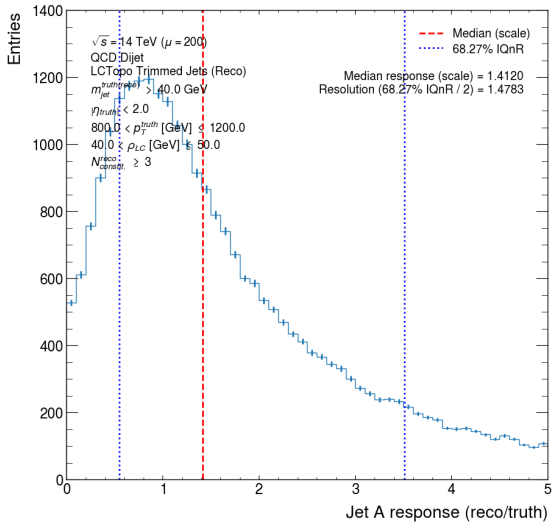

(f) $800 < p_{\mathrm{T}}^{\mathrm{truth}}$ (GeV) ≤ 1200 and $40 < \rho_{\mathrm{LCW}}$ (GeV) ≤ 50

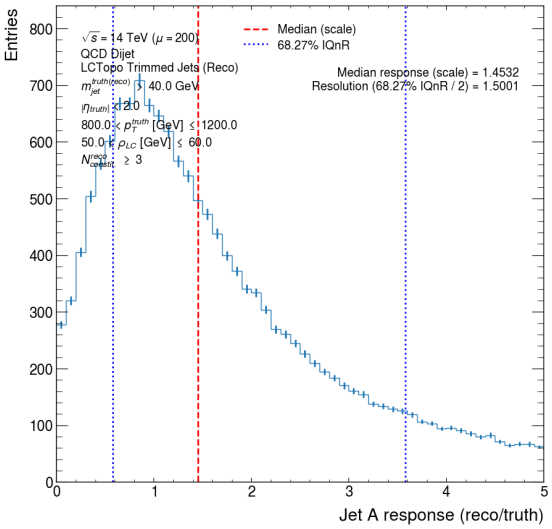

(g) $800 < p_{\mathrm{T}}^{\mathrm{truth}}$ (GeV) ≤ 1200 and $50 < \rho_{\mathrm{LCW}}$ (GeV) ≤ 60

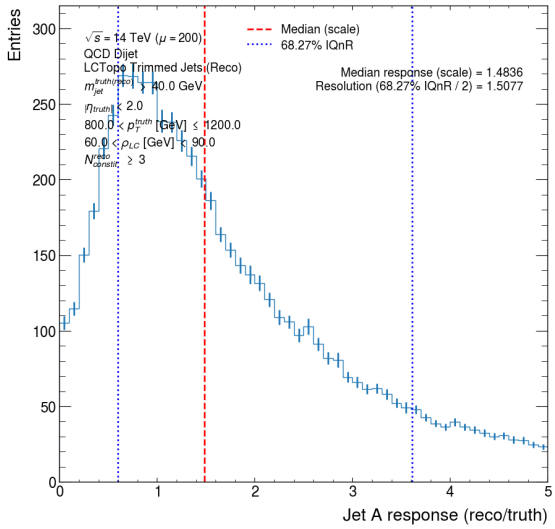

(h) $800 < p_{\mathrm{T}}^{\mathrm{truth}}$ (GeV) ≤ 1200 and $60 < \rho_{\mathrm{LCW}}$ (GeV) < 90

Figure H.1 (cont.): Trimmed jet A response distributions binned in the truth trimmed jet p_{T} and ρ_{LCW}.

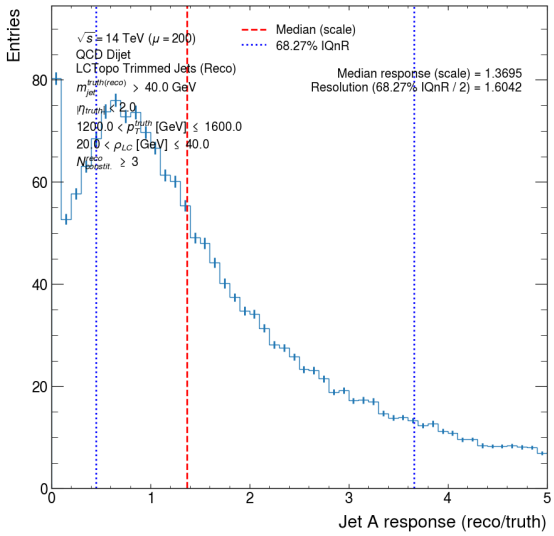

(i) $1200 < p_{\mathrm{T}}^{\mathrm{truth}}$ (GeV) ≤ 1600 and $20 < \rho_{\mathrm{LCW}}$ (GeV) ≤ 40

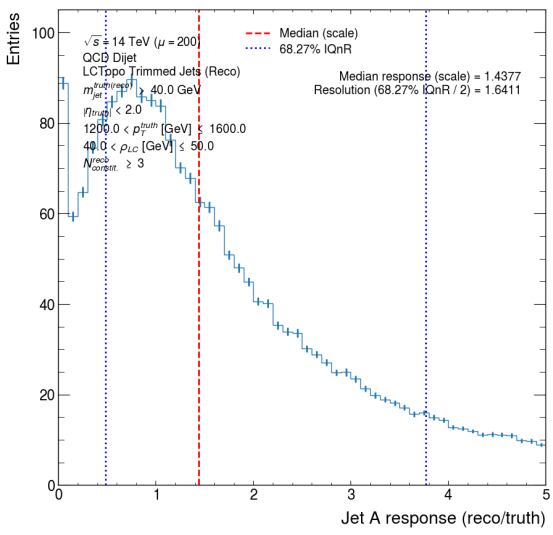

(j) $1200 < p_{\mathrm{T}}^{\mathrm{truth}}$ (GeV) ≤ 1600 and $40 < \rho_{\mathrm{LCW}}$ (GeV) ≤ 50

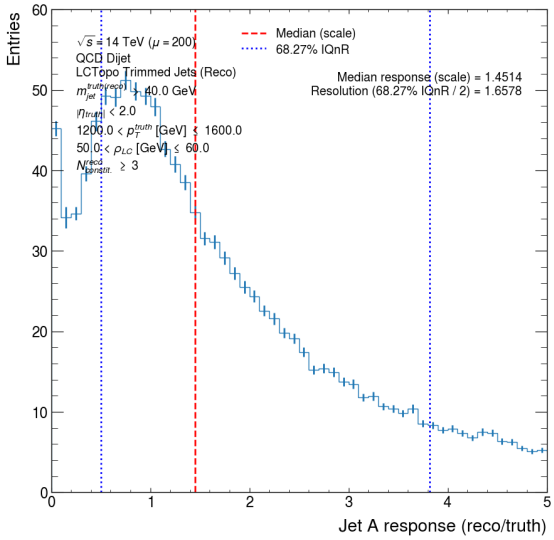

(k) $1200 < p_{\mathrm{T}}^{\mathrm{truth}}$ (GeV) ≤ 1600 and $50 < \rho_{\mathrm{LCW}}$ (GeV) ≤ 60

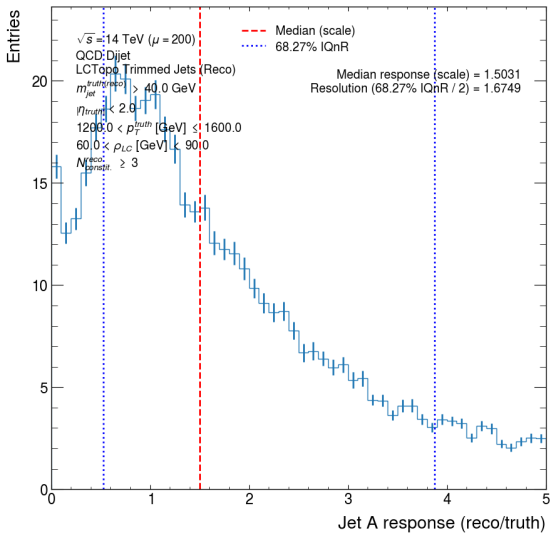

(l) $1200 < p_{\mathrm{T}}^{\mathrm{truth}}$ (GeV) ≤ 1600 and $60 < \rho_{\mathrm{LCW}}$ (GeV) < 90

Figure H.1 (cont.): Trimmed jet A response distributions binned in the truth trimmed jet p_{T} and ρ_{LCW}.

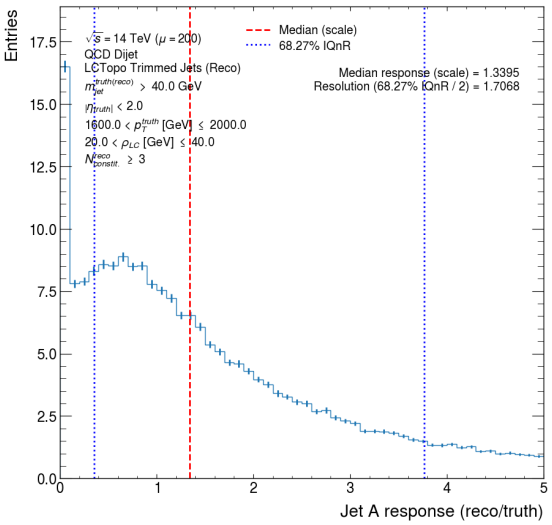

(m) $1600 < p_{\mathrm{T}}^{\mathrm{truth}}$ (GeV) ≤ 2000 and $20 < \rho_{\mathrm{LCW}}$ (GeV) ≤ 40

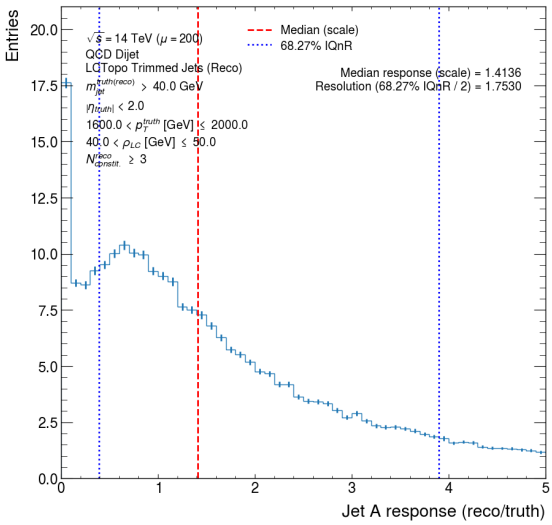

(n) $1600 < p_{\mathrm{T}}^{\mathrm{truth}}$ (GeV) ≤ 2000 and $40 < \rho_{\mathrm{LCW}}$ (GeV) ≤ 50

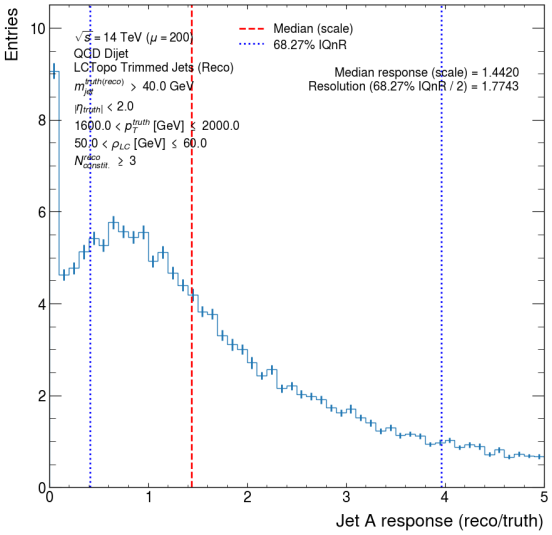

(o) $1600 < p_{\mathrm{T}}^{\mathrm{truth}}$ (GeV) ≤ 2000 and $50 < \rho_{\mathrm{LCW}}$ (GeV) ≤ 60

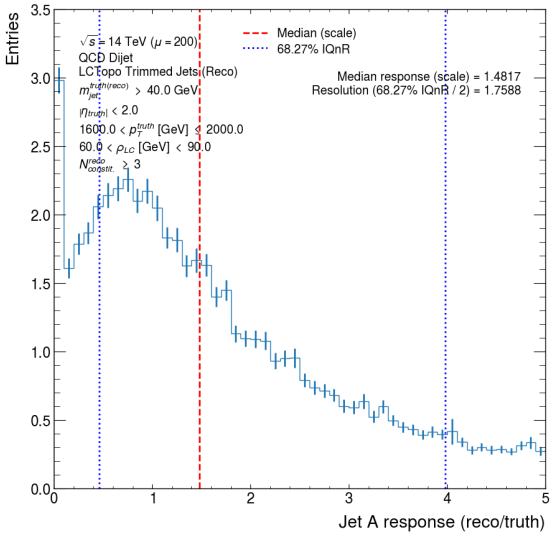

(p) $1600 < p_{\mathrm{T}}^{\mathrm{truth}}$ (GeV) ≤ 2000 and $60 < \rho_{\mathrm{LCW}}$ (GeV) < 90

Figure H.1 (cont.): Trimmed jet A response distributions binned in the truth trimmed jet p_{T} and ρ_{LCW}.

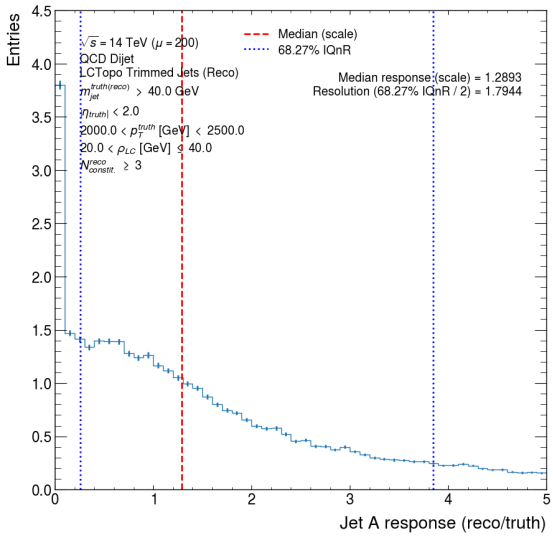

(q) $2000 < p_{\mathrm{T}}^{\mathrm{truth}}$ (GeV) < 2500 and $20 < \rho_{\mathrm{LCW}}$ (GeV) ≤ 40

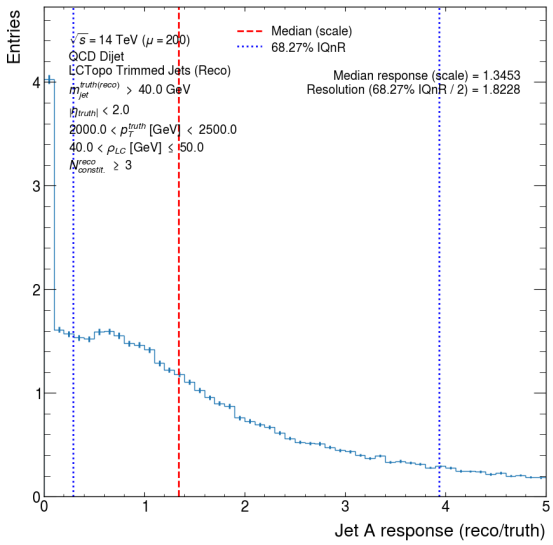

(r) $2000 < p_{\mathrm{T}}^{\mathrm{truth}}$ (GeV) < 2500 and $40 < \rho_{\mathrm{LCW}}$ (GeV) ≤ 50

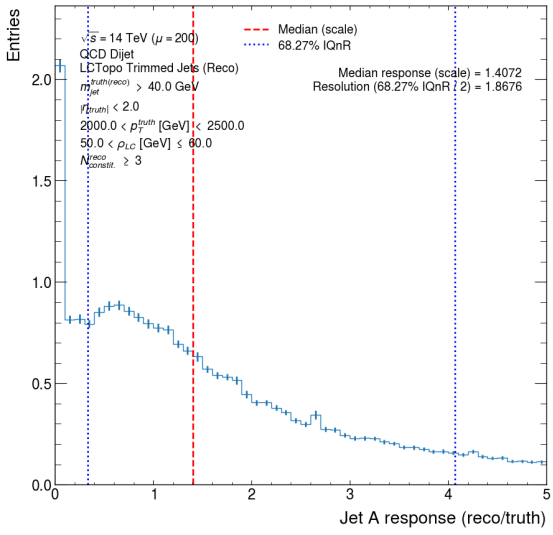

(s) $2000 < p_{\mathrm{T}}^{\mathrm{truth}}$ (GeV) < 2500 and $50 < \rho_{\mathrm{LCW}}$ (GeV) ≤ 60

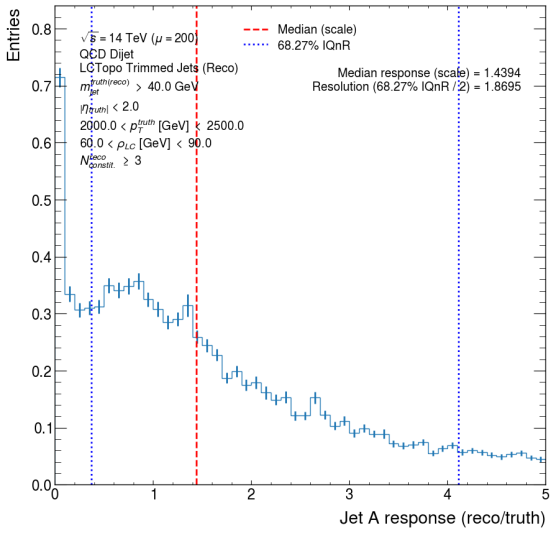

(t) $2000 < p_{\mathrm{T}}^{\mathrm{truth}}$ (GeV) < 2500 and $60 < \rho_{\mathrm{LCW}}$ (GeV) < 90

Figure H.1 (cont.): Trimmed jet A response distributions binned in the truth trimmed jet p_{T} and ρ_{LCW}.

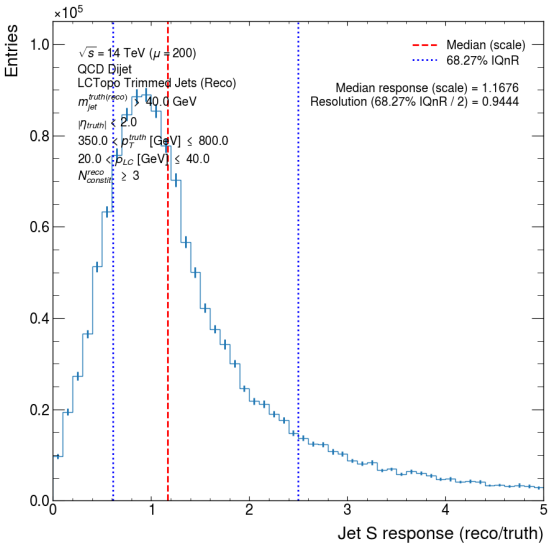

(a) $350 < p_{\mathrm{T}}^{\mathrm{truth}}$ (GeV) ≤ 800 and $20 < \rho_{\mathrm{LCW}}$ (GeV) ≤ 40

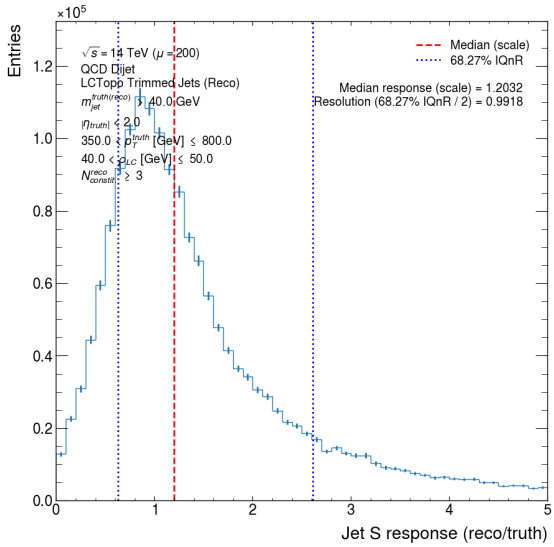

(b) $350 < p_{\mathrm{T}}^{\mathrm{truth}}$ (GeV) ≤ 800 and $40 < \rho_{\mathrm{LCW}}$ (GeV) ≤ 50

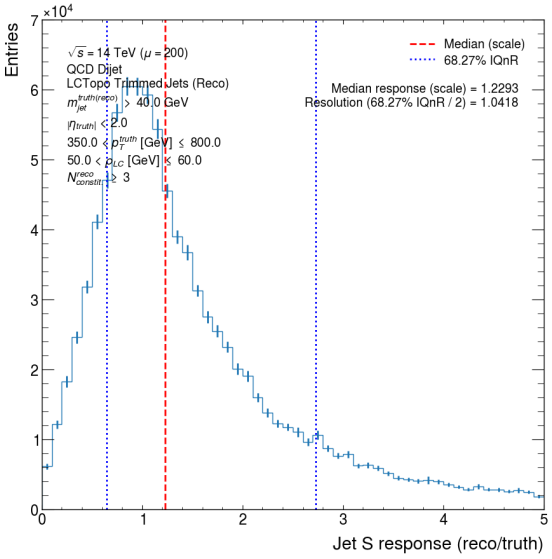

(c) $350 < p_{\mathrm{T}}^{\mathrm{truth}}$ (GeV) ≤ 800 and $50 < \rho_{\mathrm{LCW}}$ (GeV) ≤ 60

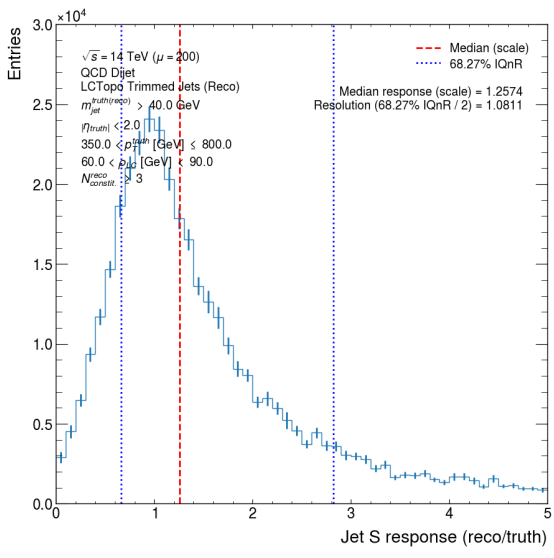

(d) $350 < p_{\mathrm{T}}^{\mathrm{truth}}$ (GeV) ≤ 800 and $60 < \rho_{\mathrm{LCW}}$ (GeV) < 90

Figure H.2: Trimmed jet S response distributions binned in the truth trimmed jet p_{T} and ρ_{LCW}.

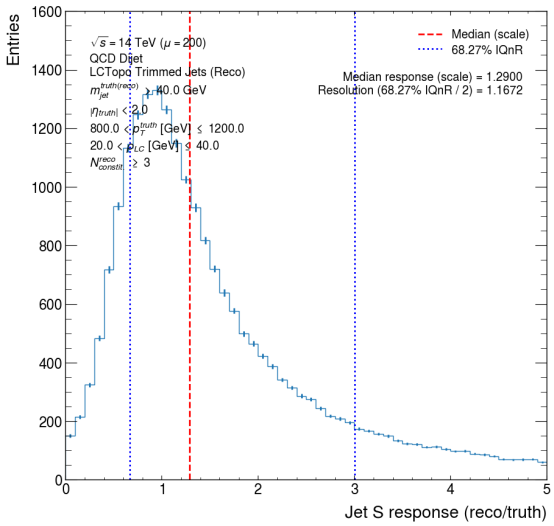

(e) $800 < p_{\mathrm{T}}^{\mathrm{truth}}$ (GeV) ≤ 1200 and $20 < \rho_{\mathrm{LCW}}$ (GeV) ≤ 40

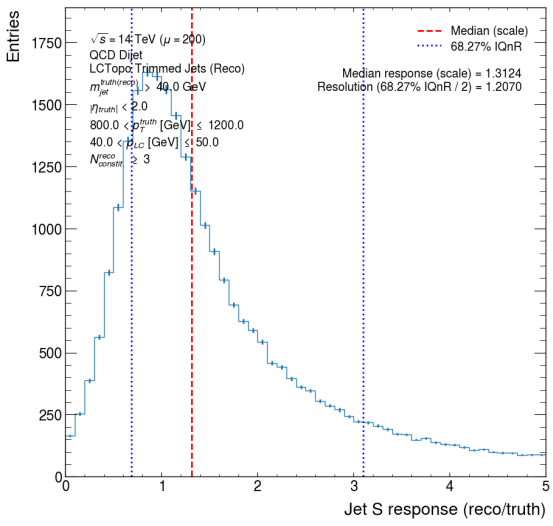

(f) $800 < p_{\mathrm{T}}^{\mathrm{truth}}$ (GeV) ≤ 1200 and $40 < \rho_{\mathrm{LCW}}$ (GeV) ≤ 50

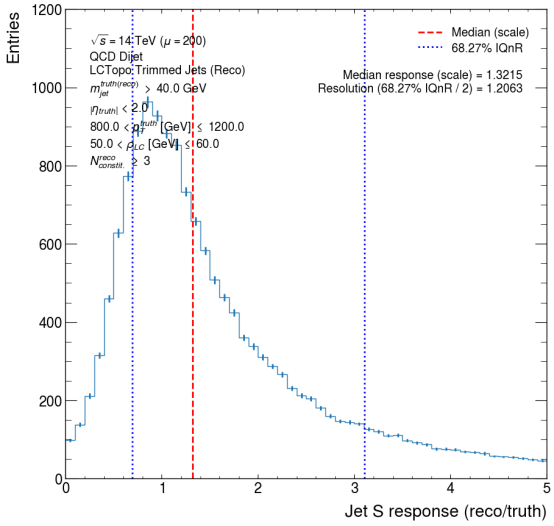

(g) $800 < p_{\mathrm{T}}^{\mathrm{truth}}$ (GeV) ≤ 1200 and $50 < \rho_{\mathrm{LCW}}$ (GeV) ≤ 60

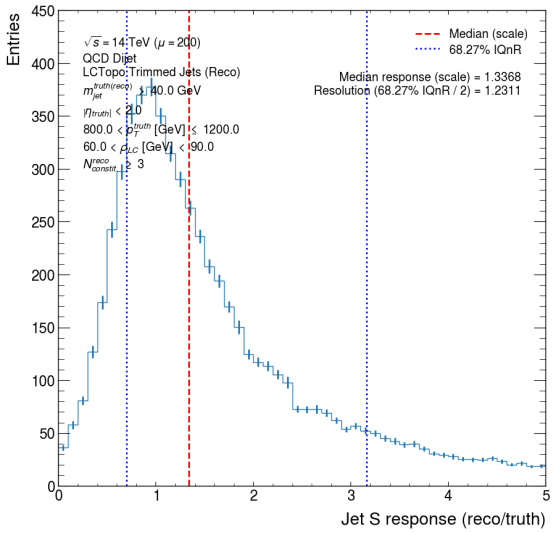

(h) $800 < p_{\mathrm{T}}^{\mathrm{truth}}$ (GeV) ≤ 1200 and $60 < \rho_{\mathrm{LCW}}$ (GeV) < 90

Figure H.2 (cont.): Trimmed jet S response distributions binned in the truth trimmed jet p_{T} and ρ_{LCW}.

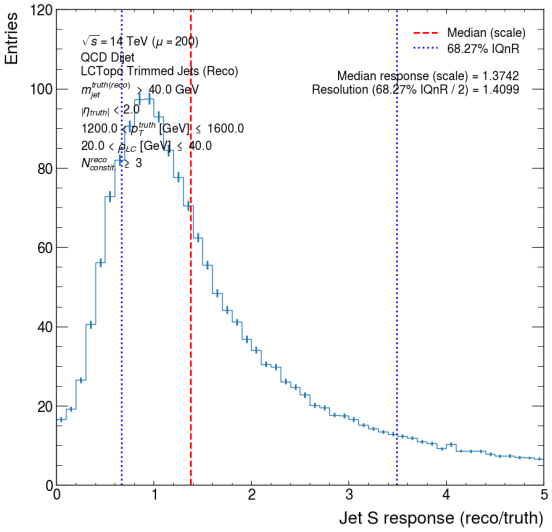

(i) $1200 < p_{\mathrm{T}}^{\mathrm{truth}}$ (GeV) ≤ 1600 and $20 < \rho_{\mathrm{LCW}}$ (GeV) ≤ 40

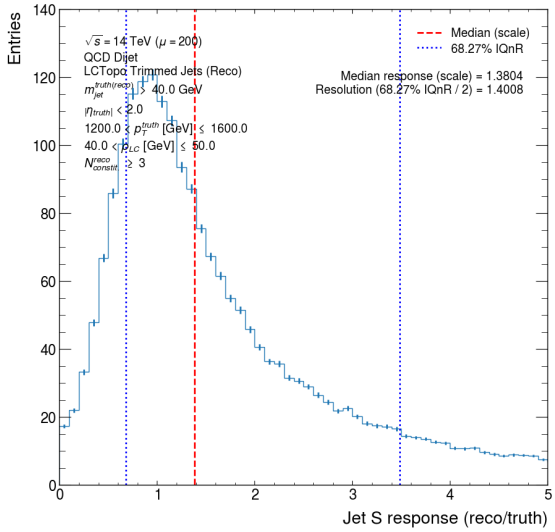

(j) $1200 < p_{\mathrm{T}}^{\mathrm{truth}}$ (GeV) ≤ 1600 and $40 < \rho_{\mathrm{LCW}}$ (GeV) ≤ 50

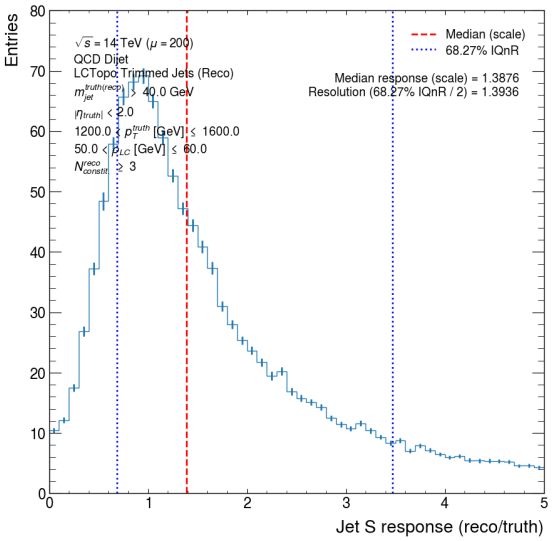

(k) $1200 < p_{\mathrm{T}}^{\mathrm{truth}}$ (GeV) ≤ 1600 and $50 < \rho_{\mathrm{LCW}}$ (GeV) ≤ 60

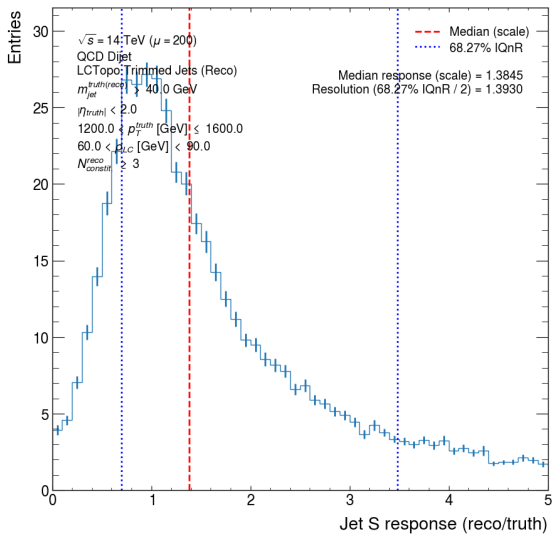

(l) $1200 < p_{\mathrm{T}}^{\mathrm{truth}}$ (GeV) ≤ 1600 and $60 < \rho_{\mathrm{LCW}}$ (GeV) < 90

Figure H.2 (cont.): Trimmed jet S response distributions binned in the truth trimmed jet p_{T} and ρ_{LCW}.

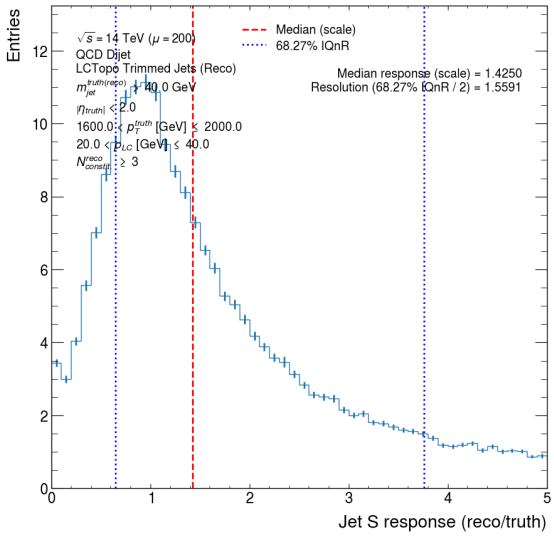

(m) $1600 < p_{\mathrm{T}}^{\mathrm{truth}}$ (GeV) ≤ 2000 and $20 < \rho_{\mathrm{LCW}}$ (GeV) ≤ 40

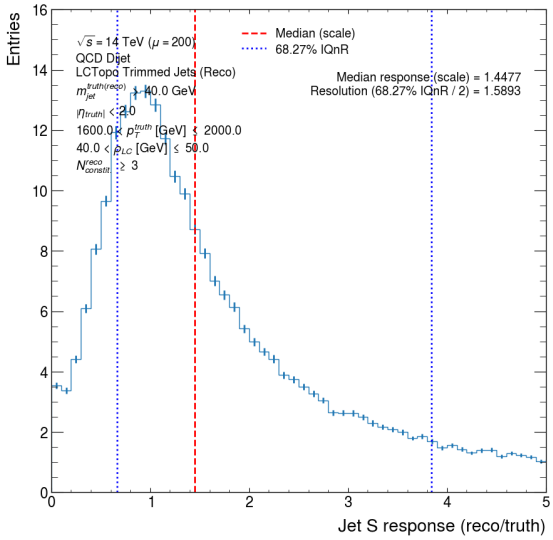

(n) $1600 < p_{\mathrm{T}}^{\mathrm{truth}}$ (GeV) ≤ 2000 and $40 < \rho_{\mathrm{LCW}}$ (GeV) ≤ 50

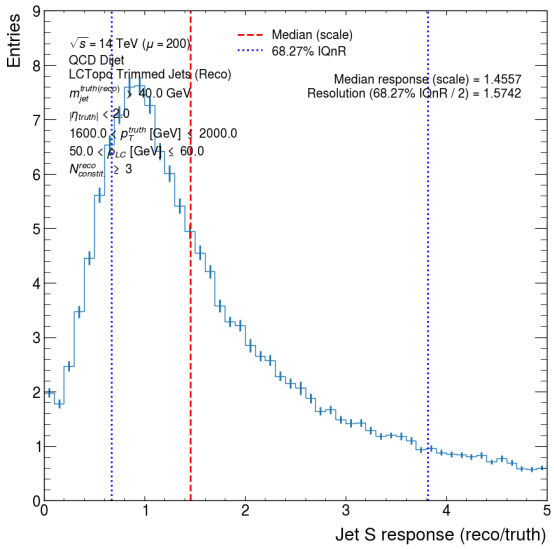

(o) $1600 < p_{\mathrm{T}}^{\mathrm{truth}}$ (GeV) ≤ 2000 and $50 < \rho_{\mathrm{LCW}}$ (GeV) ≤ 60

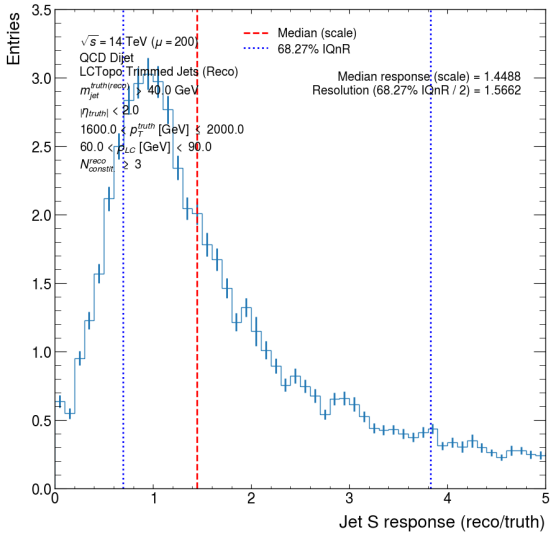

(p) $1600 < p_{\mathrm{T}}^{\mathrm{truth}}$ (GeV) ≤ 2000 and $60 < \rho_{\mathrm{LCW}}$ (GeV) < 90

Figure H.2 (cont.): Trimmed jet S response distributions binned in the truth trimmed jet p_{T} and ρ_{LCW}.

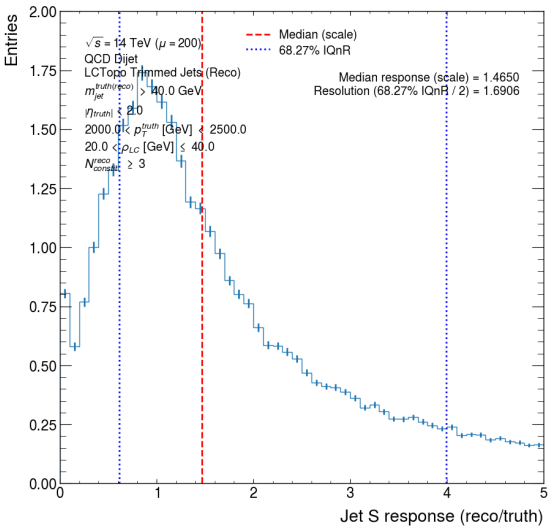

(q) $2000 < p_{\mathrm{T}}^{\mathrm{truth}}$ (GeV) < 2500 and $20 < \rho_{\mathrm{LCW}}$ (GeV) ≤ 40

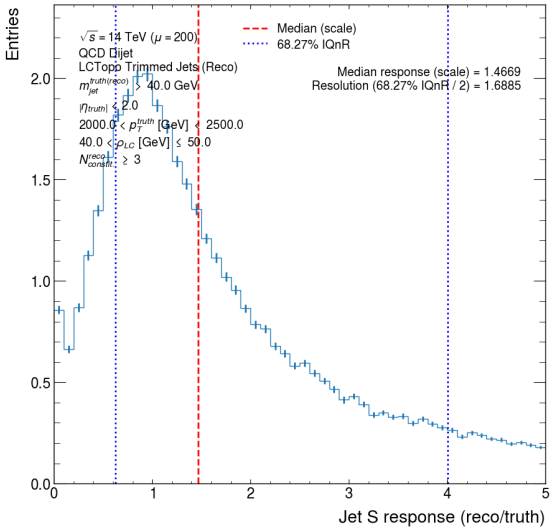

(r) $2000 < p_{\mathrm{T}}^{\mathrm{truth}}$ (GeV) < 2500 and $40 < \rho_{\mathrm{LCW}}$ (GeV) ≤ 50

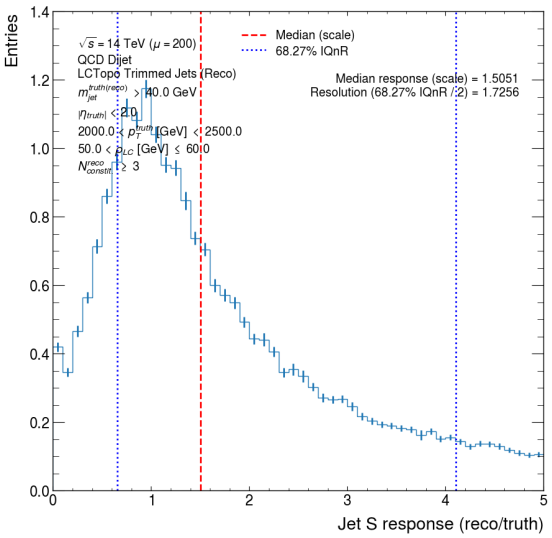

(s) $2000 < p_{\mathrm{T}}^{\mathrm{truth}}$ (GeV) < 2500 and $50 < \rho_{\mathrm{LCW}}$ (GeV) ≤ 60

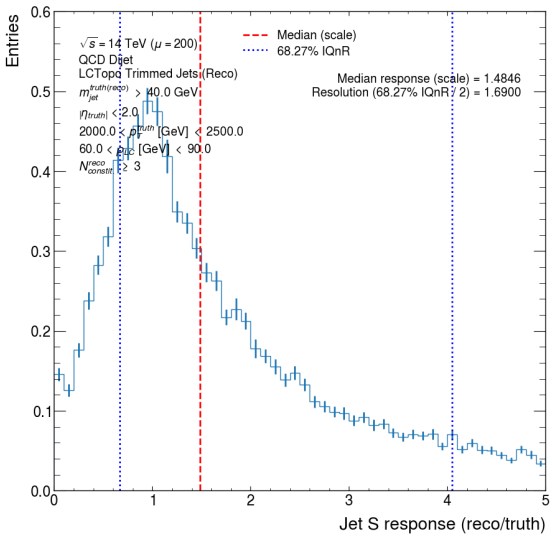

(t) $2000 < p_{\mathrm{T}}^{\mathrm{truth}}$ (GeV) < 2500 and $60 < \rho_{\mathrm{LCW}}$ (GeV) < 90

Figure H.2 (cont.): Trimmed jet S response distributions binned in the truth trimmed jet p_{T} and ρ_{LCW}.

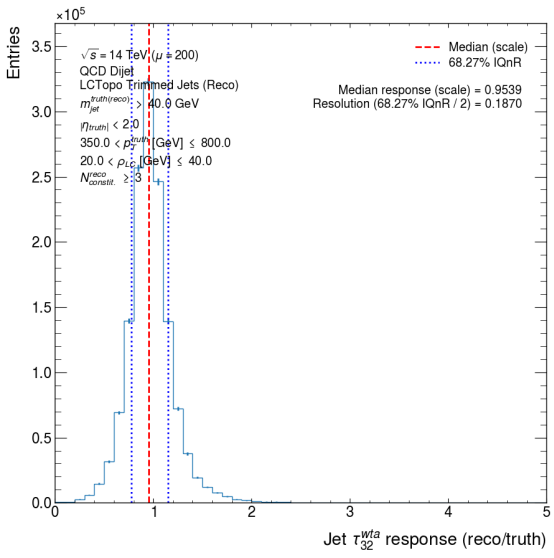

(a) $350 < p_{\mathrm{T}}^{\mathrm{truth}}$ (GeV) ≤ 800 and $20 < \rho_{\mathrm{LCW}}$ (GeV) ≤ 40

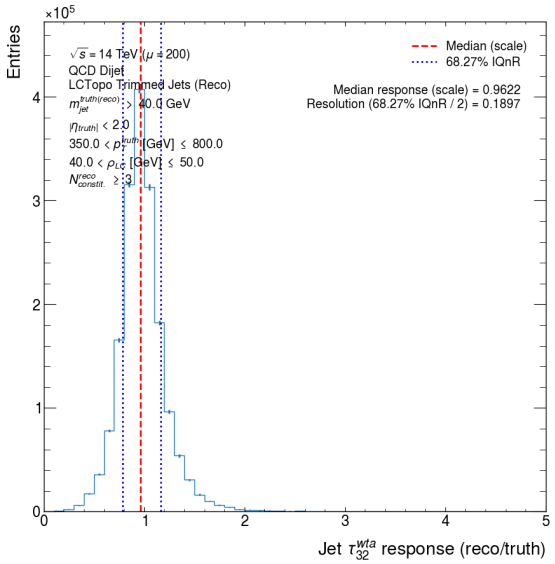

(b) $350 < p_{\mathrm{T}}^{\mathrm{truth}}$ (GeV) ≤ 800 and $40 < \rho_{\mathrm{LCW}}$ (GeV) ≤ 50

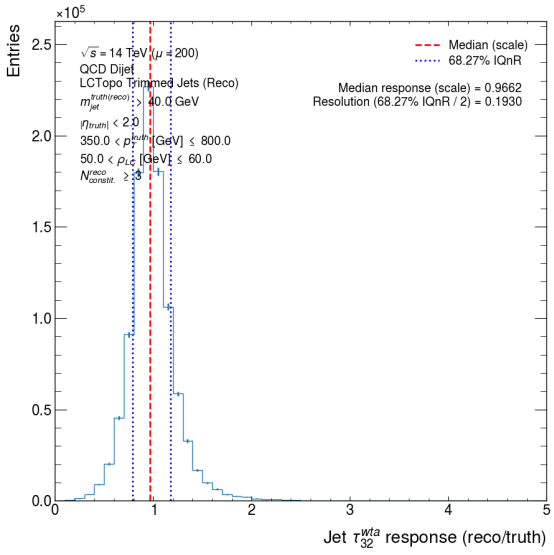

(c) $350 < p_{\mathrm{T}}^{\mathrm{truth}}$ (GeV) ≤ 800 and $50 < \rho_{\mathrm{LCW}}$ (GeV) ≤ 60

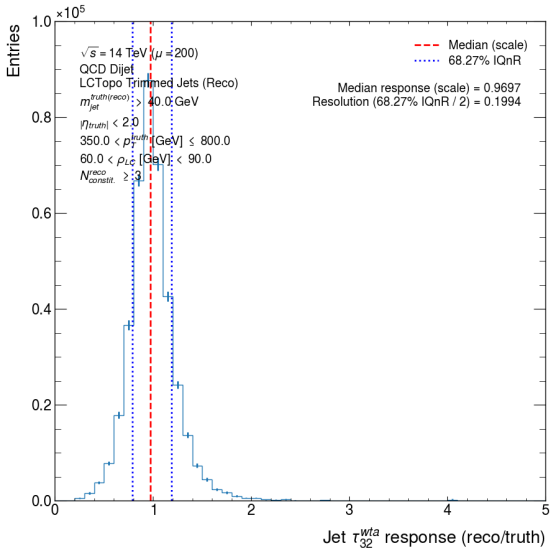

(d) $350 < p_{\mathrm{T}}^{\mathrm{truth}}$ (GeV) ≤ 800 and $60 < \rho_{\mathrm{LCW}}$ (GeV) < 90

Figure H.3: Trimmed jet τ_{32}^{wta} response distributions binned in the truth trimmed jet p_{T} and ρ_{LCW}.

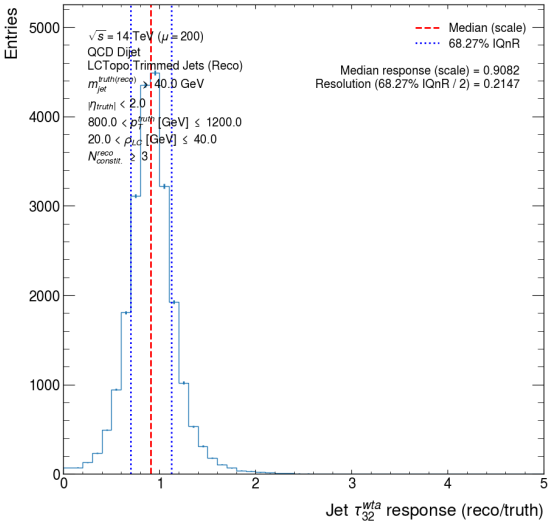

(e) $800 < p_{\mathrm{T}}^{\mathrm{truth}}$ (GeV) ≤ 1200 and $20 < \rho_{\mathrm{LCW}}$ (GeV) ≤ 40

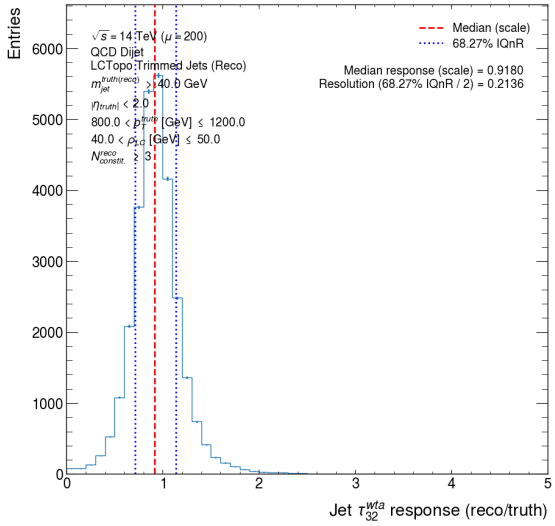

(f) $800 < p_{\mathrm{T}}^{\mathrm{truth}}$ (GeV) ≤ 1200 and $40 < \rho_{\mathrm{LCW}}$ (GeV) ≤ 50

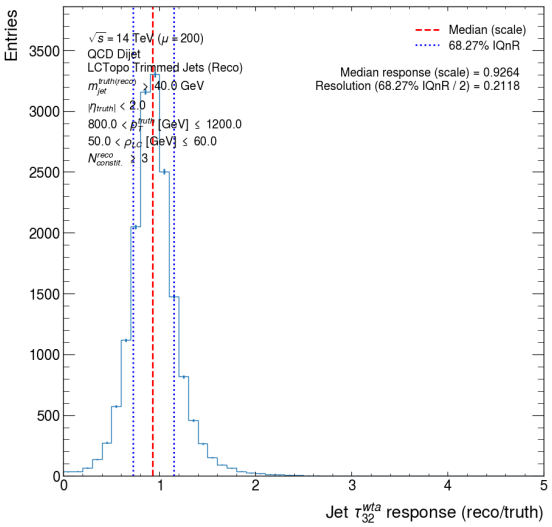

(g) $800 < p_{\mathrm{T}}^{\mathrm{truth}}$ (GeV) ≤ 1200 and $50 < \rho_{\mathrm{LCW}}$ (GeV) ≤ 60

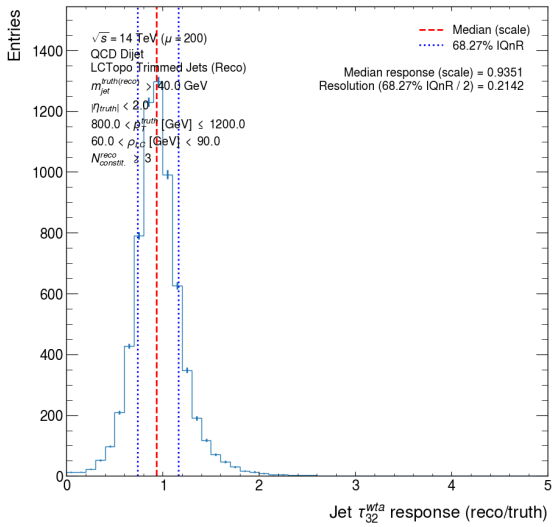

(h) $800 < p_{\mathrm{T}}^{\mathrm{truth}}$ (GeV) ≤ 1200 and $60 < \rho_{\mathrm{LCW}}$ (GeV) < 90

Figure H.3 (cont.): Trimmed jet τ_{32}^{wta} response distributions binned in the truth trimmed jet p_{T} and ρ_{LCW}.

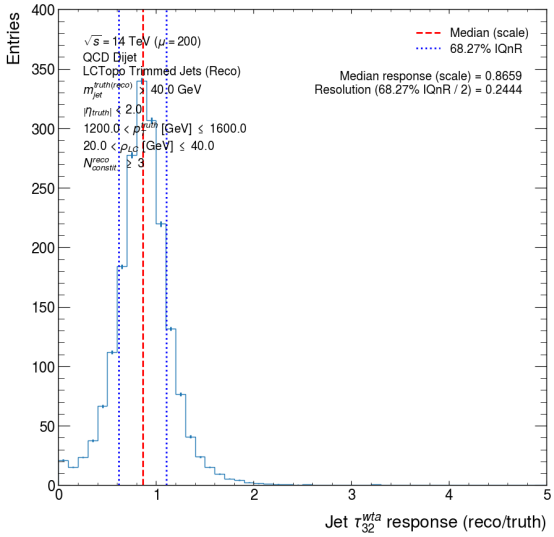

(i) $1200 < p_{\mathrm{T}}^{\mathrm{truth}}$ (GeV) ≤ 1600 and $20 < \rho_{\mathrm{LCW}}$ (GeV) ≤ 40

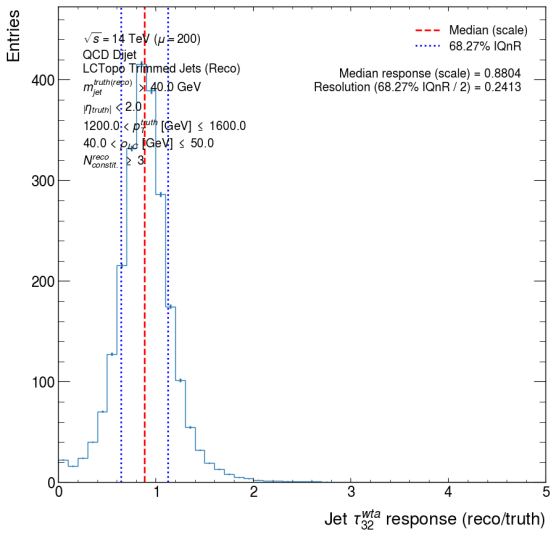

(j) $1200 < p_{\mathrm{T}}^{\mathrm{truth}}$ (GeV) ≤ 1600 and $40 < \rho_{\mathrm{LCW}}$ (GeV) ≤ 50

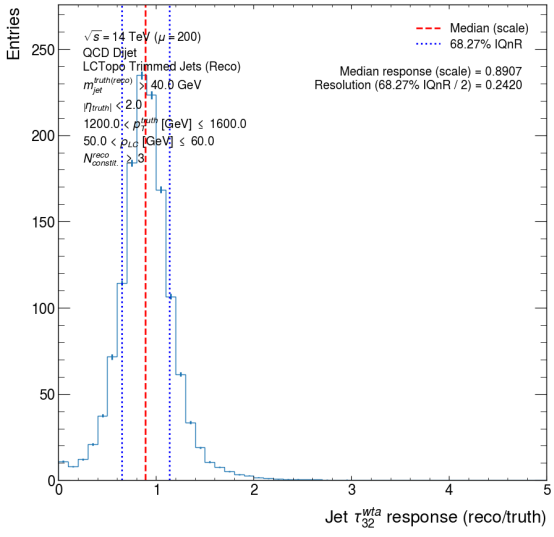

(k) $1200 < p_{\mathrm{T}}^{\mathrm{truth}}$ (GeV) ≤ 1600 and $50 < \rho_{\mathrm{LCW}}$ (GeV) ≤ 60

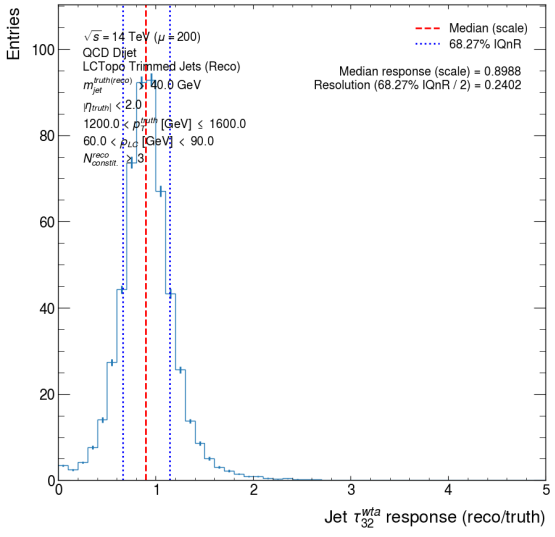

(l) $1200 < p_{\mathrm{T}}^{\mathrm{truth}}$ (GeV) ≤ 1600 and $60 < \rho_{\mathrm{LCW}}$ (GeV) < 90

Figure H.3 (cont.): Trimmed jet τ_{32}^{wta} response distributions binned in the truth trimmed jet p_{T} and ρ_{LCW}.

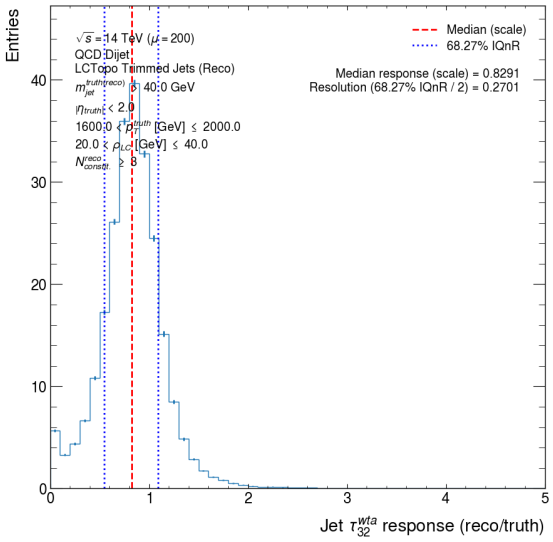

(m) $1600 < p_{\mathrm{T}}^{\mathrm{truth}}$ (GeV) ≤ 2000 and $20 < \rho_{\mathrm{LCW}}$ (GeV) ≤ 40

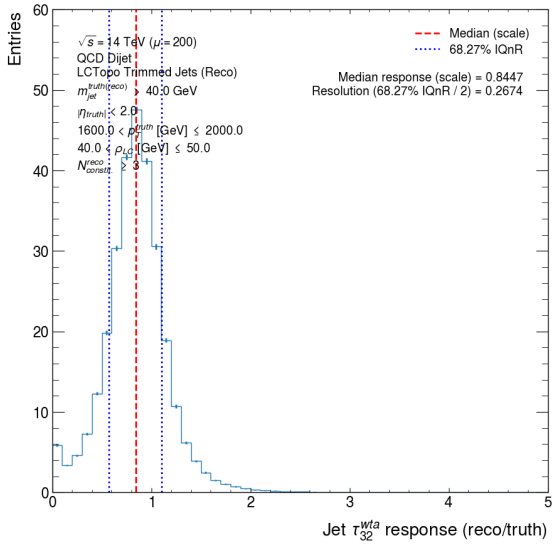

(n) $1600 < p_{\mathrm{T}}^{\mathrm{truth}}$ (GeV) ≤ 2000 and $40 < \rho_{\mathrm{LCW}}$ (GeV) ≤ 50

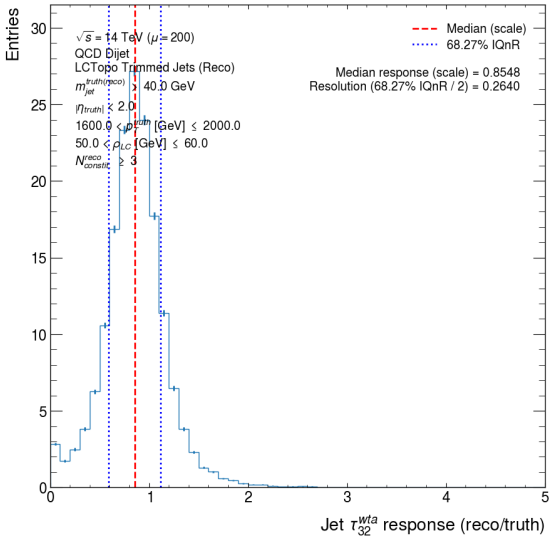

(o) $1600 < p_{\mathrm{T}}^{\mathrm{truth}}$ (GeV) ≤ 2000 and $50 < \rho_{\mathrm{LCW}}$ (GeV) ≤ 60

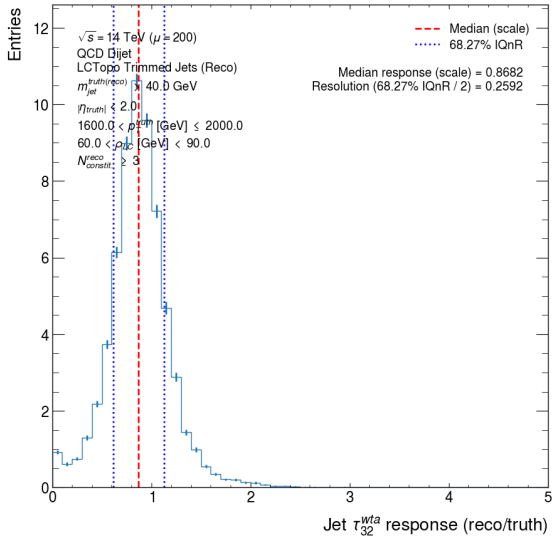

(p) $1600 < p_{\mathrm{T}}^{\mathrm{truth}}$ (GeV) ≤ 2000 and $60 < \rho_{\mathrm{LCW}}$ (GeV) < 90

Figure H.3 (cont.): Trimmed jet τ_{32}^{wta} response distributions binned in the truth trimmed jet p_{T} and ρ_{LCW}.

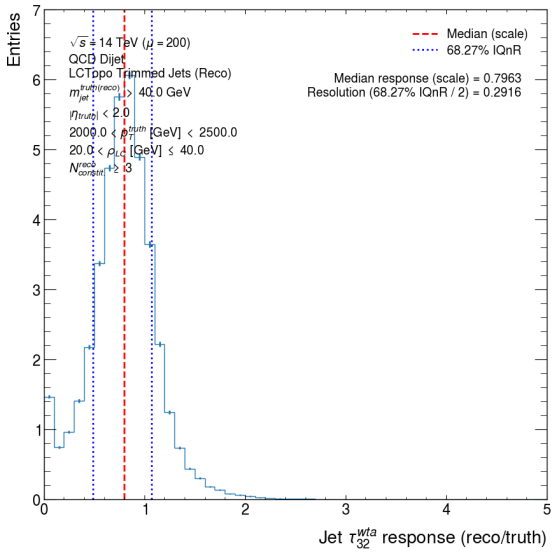

(q) $2000 < p_{\mathrm{T}}^{\mathrm{truth}}$ (GeV) < 2500 and $20 < \rho_{\mathrm{LCW}}$ (GeV) ≤ 40

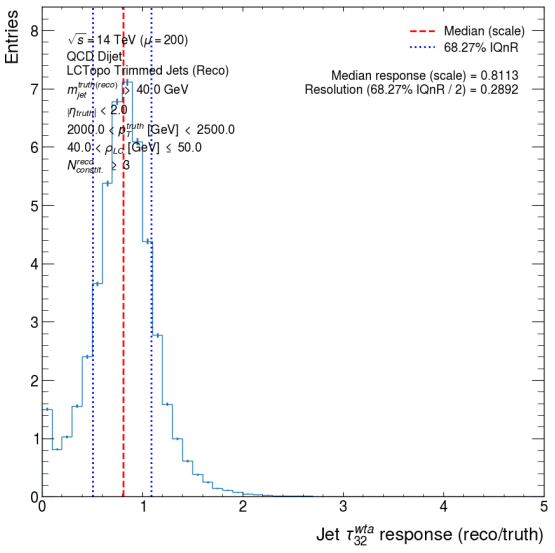

(r) $2000 < p_{\mathrm{T}}^{\mathrm{truth}}$ (GeV) < 2500 and $40 < \rho_{\mathrm{LCW}}$ (GeV) ≤ 50

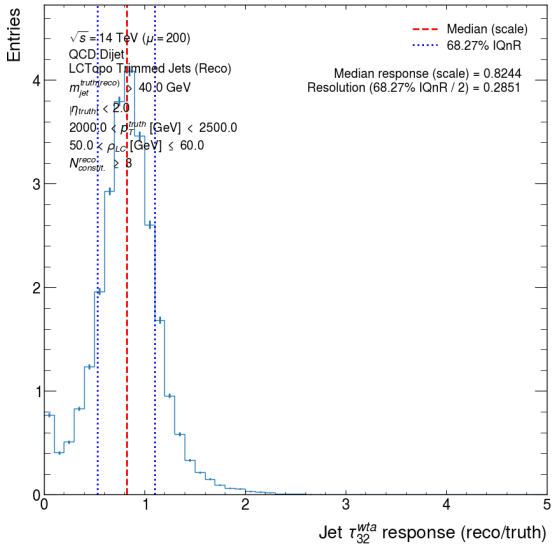

(s) $2000 < p_{\mathrm{T}}^{\mathrm{truth}}$ (GeV) < 2500 and $50 < \rho_{\mathrm{LCW}}$ (GeV) ≤ 60

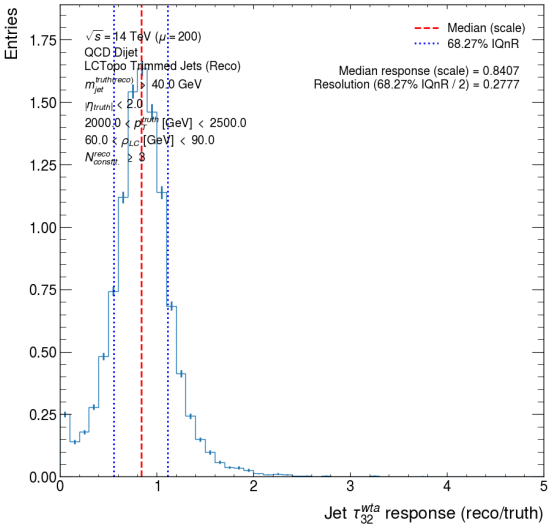

(t) $2000 < p_{\mathrm{T}}^{\mathrm{truth}}$ (GeV) < 2500 and $60 < \rho_{\mathrm{LCW}}$ (GeV) < 90

Figure H.3 (cont.): Trimmed jet τ_{32}^{wta} response distributions binned in the truth trimmed jet p_{T} and ρ_{LCW}.

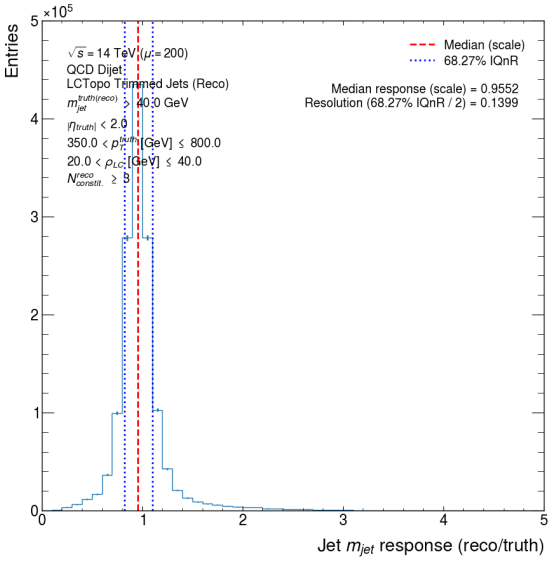

(a) $350 < p_{\mathrm{T}}^{\mathrm{truth}}$ (GeV) ≤ 800 and $20 < \rho_{\mathrm{LCW}}$ (GeV) ≤ 40

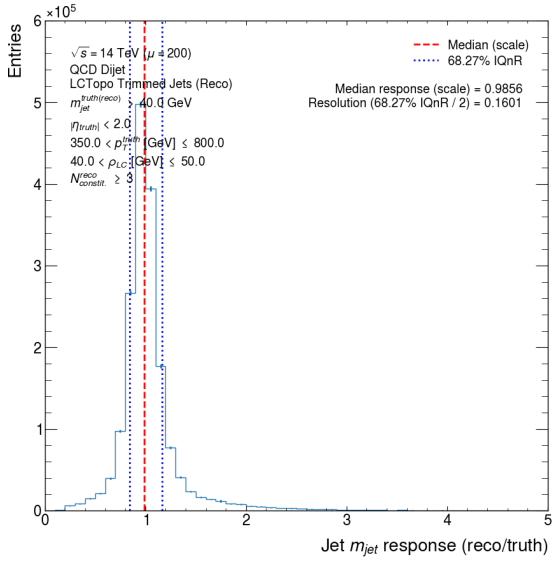

(b) $350 < p_{\mathrm{T}}^{\mathrm{truth}}$ (GeV) ≤ 800 and $40 < \rho_{\mathrm{LCW}}$ (GeV) ≤ 50

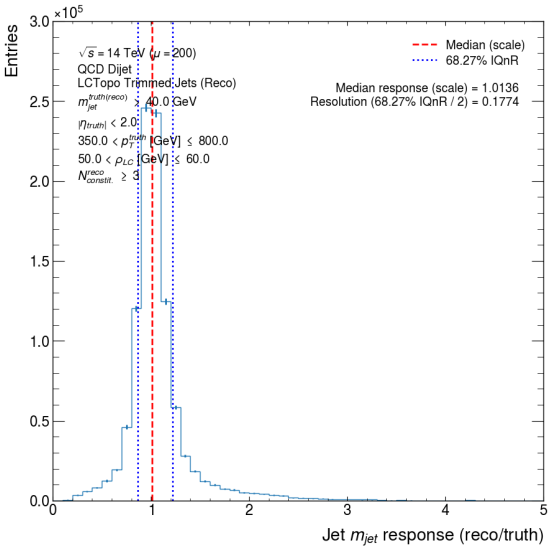

(c) $350 < p_{\mathrm{T}}^{\mathrm{truth}}$ (GeV) ≤ 800 and $50 < \rho_{\mathrm{LCW}}$ (GeV) ≤ 60

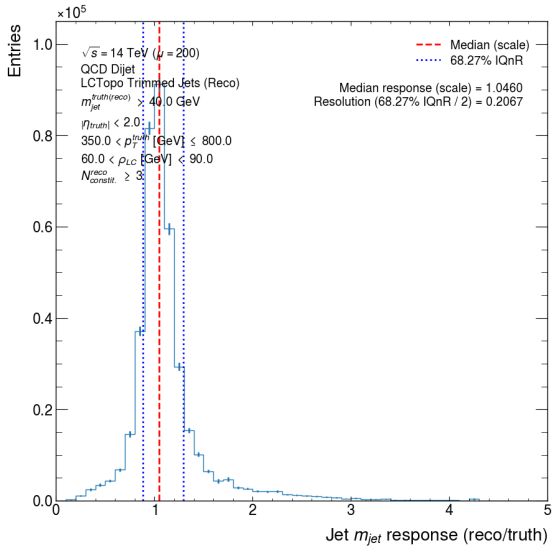

(d) $350 < p_{\mathrm{T}}^{\mathrm{truth}}$ (GeV) ≤ 800 and $60 < \rho_{\mathrm{LCW}}$ (GeV) < 90

Figure H.4: Trimmed jet m_{jet} response distributions binned in the truth trimmed jet p_{T} and ρ_{LCW}.

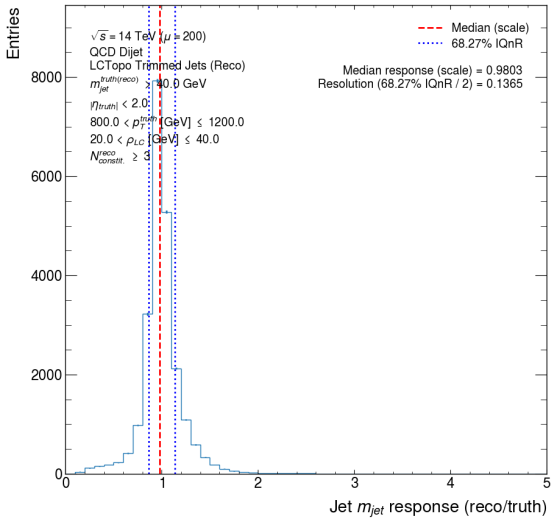

(e) $800 < p_{\mathrm{T}}^{\mathrm{truth}}$ (GeV) ≤ 1200 and $20 < \rho_{\mathrm{LCW}}$ (GeV) ≤ 40

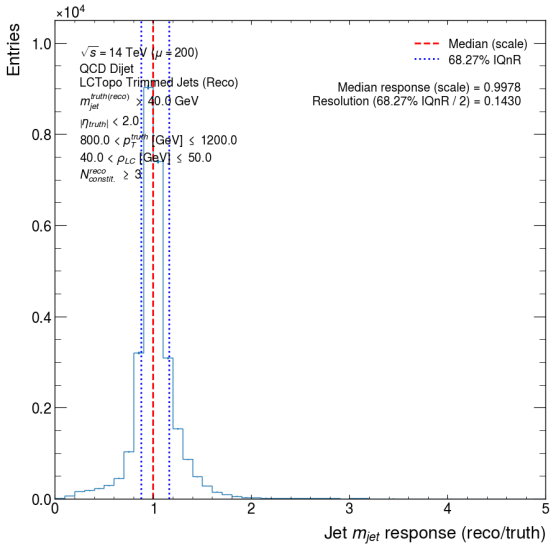

(f) $800 < p_{\mathrm{T}}^{\mathrm{truth}}$ (GeV) ≤ 1200 and $40 < \rho_{\mathrm{LCW}}$ (GeV) ≤ 50

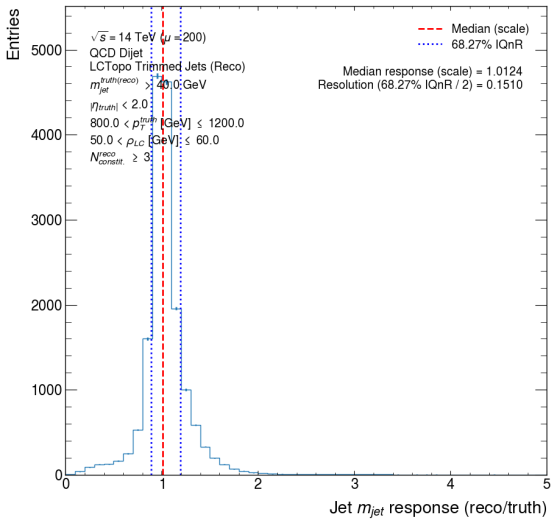

(g) $800 < p_{\mathrm{T}}^{\mathrm{truth}}$ (GeV) ≤ 1200 and $50 < \rho_{\mathrm{LCW}}$ (GeV) ≤ 60

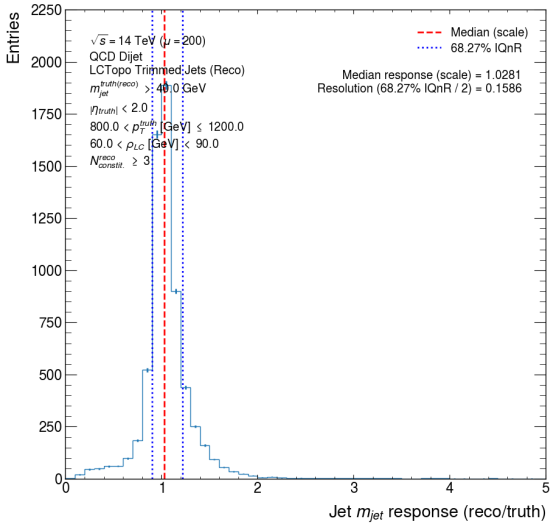

(h) $800 < p_{\mathrm{T}}^{\mathrm{truth}}$ (GeV) ≤ 1200 and $60 < \rho_{\mathrm{LCW}}$ (GeV) < 90

Figure H.4 (cont.): Trimmed jet m_{jet} response distributions binned in the truth trimmed jet p_{T} and ρ_{LCW}.

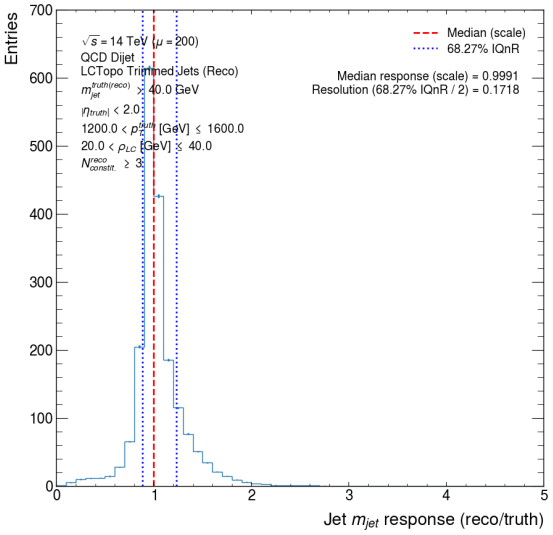

(i) $1200 < p_{\mathrm{T}}^{\mathrm{truth}}$ (GeV) ≤ 1600 and $20 < \rho_{\mathrm{LCW}}$ (GeV) ≤ 40

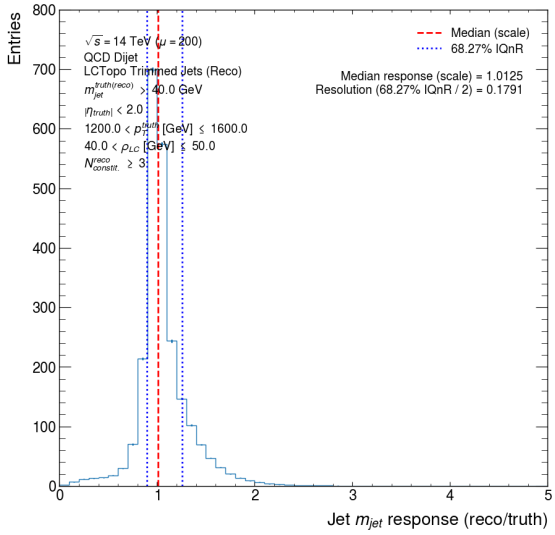

(j) $1200 < p_{\mathrm{T}}^{\mathrm{truth}}$ (GeV) ≤ 1600 and $40 < \rho_{\mathrm{LCW}}$ (GeV) ≤ 50

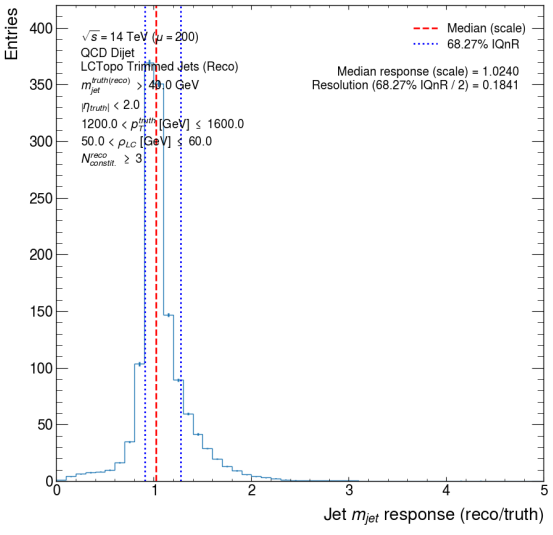

(k) $1200 < p_{\mathrm{T}}^{\mathrm{truth}}$ (GeV) ≤ 1600 and $50 < \rho_{\mathrm{LCW}}$ (GeV) ≤ 60

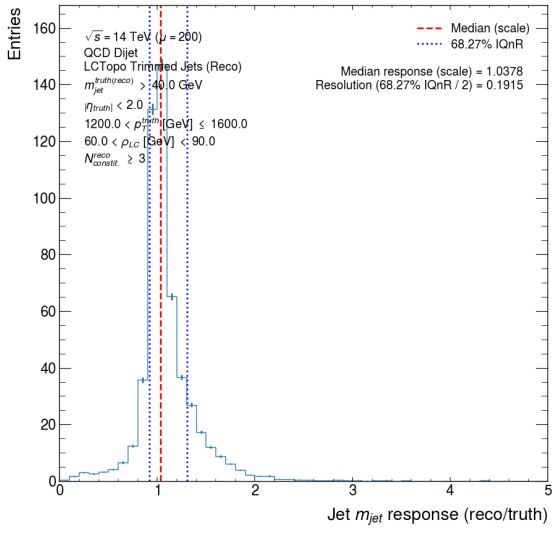

(l) $1200 < p_{\mathrm{T}}^{\mathrm{truth}}$ (GeV) ≤ 1600 and $60 < \rho_{\mathrm{LCW}}$ (GeV) < 90

Figure H.4 (cont.): Trimmed jet m_{jet} response distributions binned in the truth trimmed jet p_{T} and ρ_{LCW}.

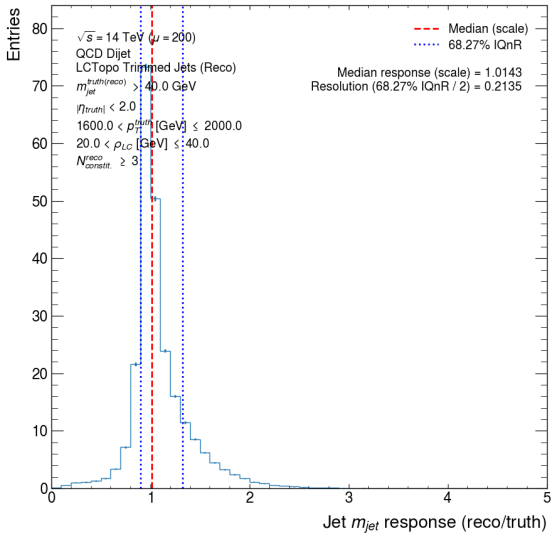

(m) $1600 < p_{\mathrm{T}}^{\mathrm{truth}}$ (GeV) ≤ 2000 and $20 < \rho_{\mathrm{LCW}}$ (GeV) ≤ 40

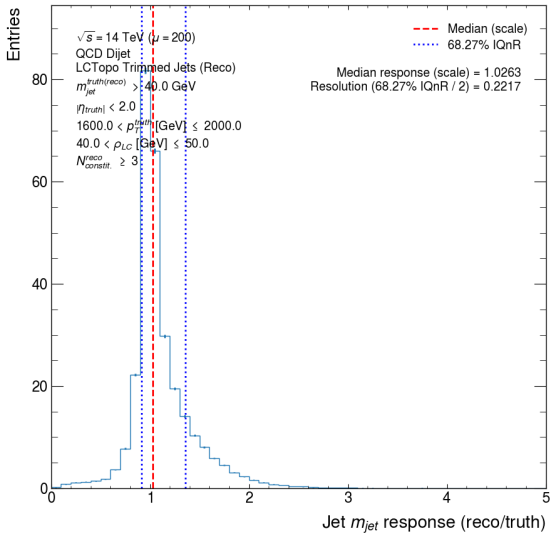

(n) $1600 < p_{\mathrm{T}}^{\mathrm{truth}}$ (GeV) ≤ 2000 and $40 < \rho_{\mathrm{LCW}}$ (GeV) ≤ 50

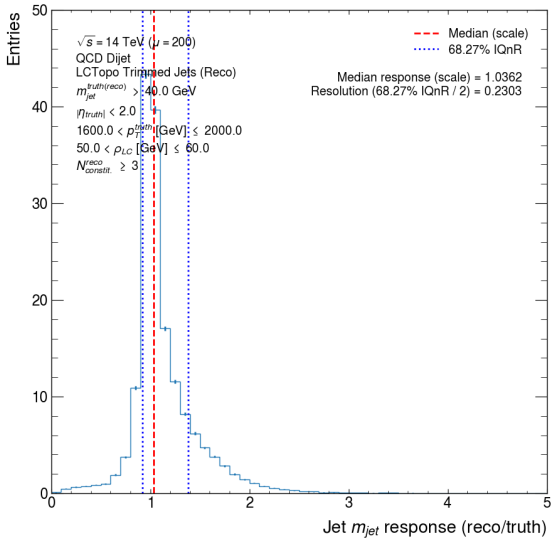

(o) $1600 < p_{\mathrm{T}}^{\mathrm{truth}}$ (GeV) ≤ 2000 and $50 < \rho_{\mathrm{LCW}}$ (GeV) ≤ 60

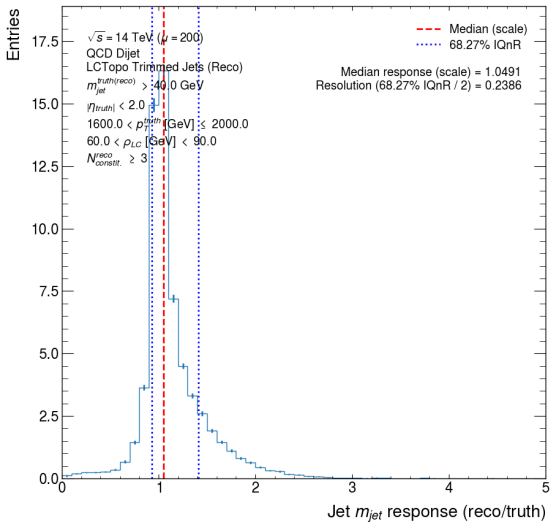

(p) $1600 < p_{\mathrm{T}}^{\mathrm{truth}}$ (GeV) ≤ 2000 and $60 < \rho_{\mathrm{LCW}}$ (GeV) < 90

Figure H.4 (cont.): Trimmed jet m_{jet} response distributions binned in the truth trimmed jet p_{T} and ρ_{LCW}.

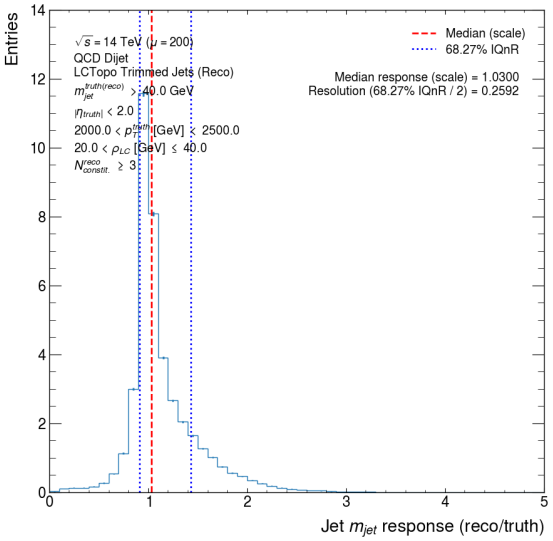

(q) $2000 < p_{\mathrm{T}}^{\mathrm{truth}}$ (GeV) < 2500 and $20 < \rho_{\mathrm{LCW}}$ (GeV) ≤ 40

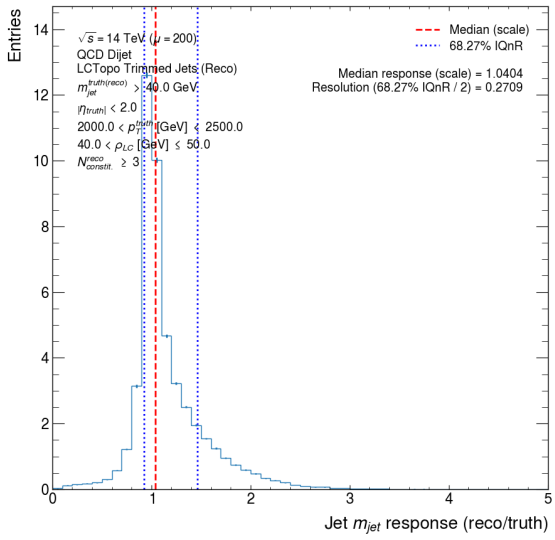

(r) $2000 < p_{\mathrm{T}}^{\mathrm{truth}}$ (GeV) < 2500 and $40 < \rho_{\mathrm{LCW}}$ (GeV) ≤ 50

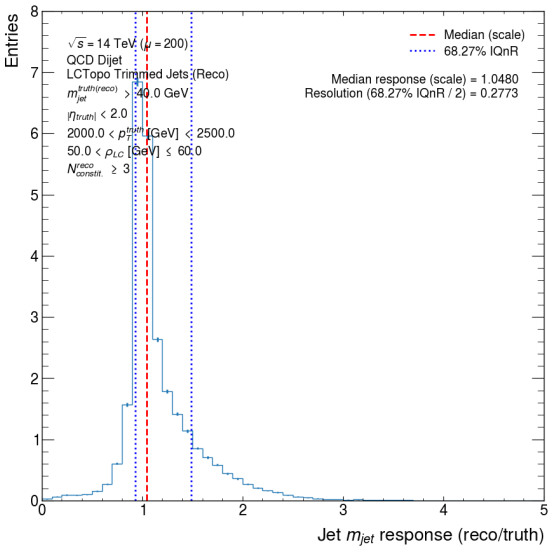

(s) $2000 < p_{\mathrm{T}}^{\mathrm{truth}}$ (GeV) < 2500 and $50 < \rho_{\mathrm{LCW}}$ (GeV) ≤ 60

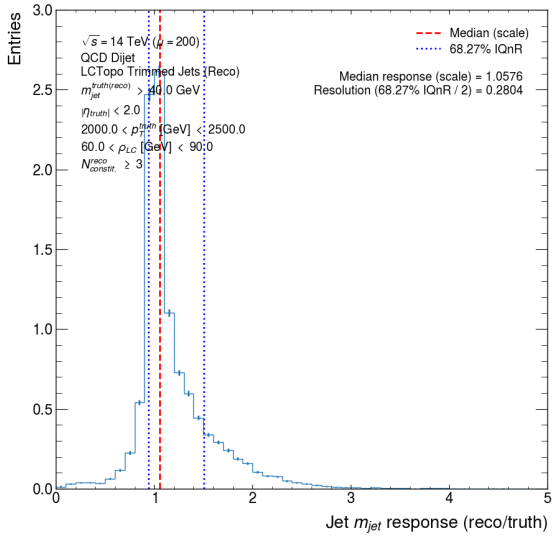

(t) $2000 < p_{\mathrm{T}}^{\mathrm{truth}}$ (GeV) < 2500 and $60 < \rho_{\mathrm{LCW}}$ (GeV) < 90

Figure H.4 (cont.): Trimmed jet m_{jet} response distributions binned in the truth trimmed jet p_{T} and ρ_{LCW}.

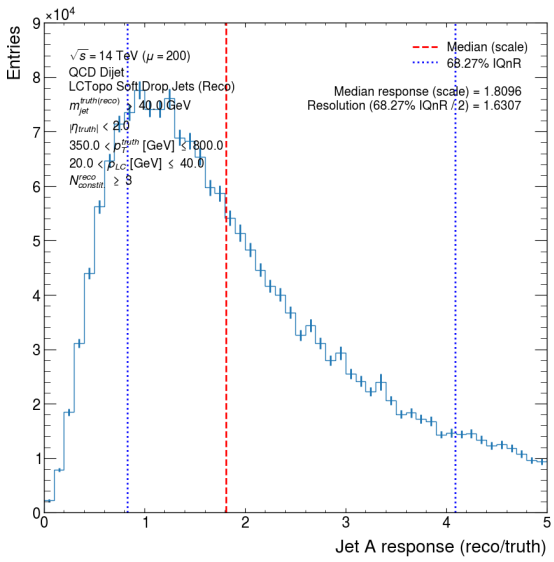

(a) $350 < p_{\mathrm{T}}^{\mathrm{truth}}$ (GeV) ≤ 800 and $20 < \rho_{\mathrm{LCW}}$ (GeV) ≤ 40

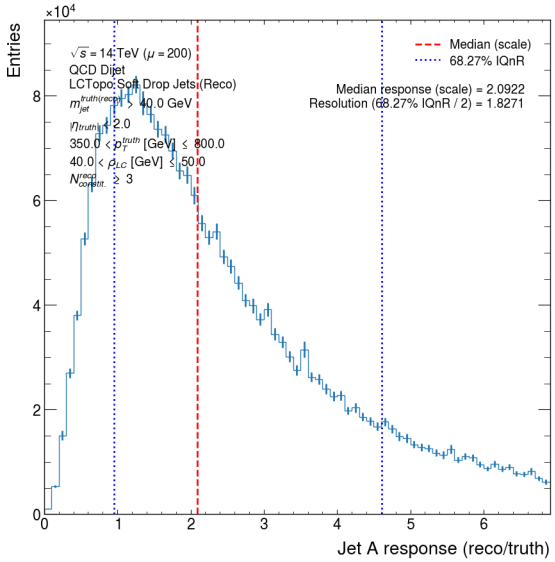

(b) $350 < p_{\mathrm{T}}^{\mathrm{truth}}$ (GeV) ≤ 800 and $40 < \rho_{\mathrm{LCW}}$ (GeV) ≤ 50

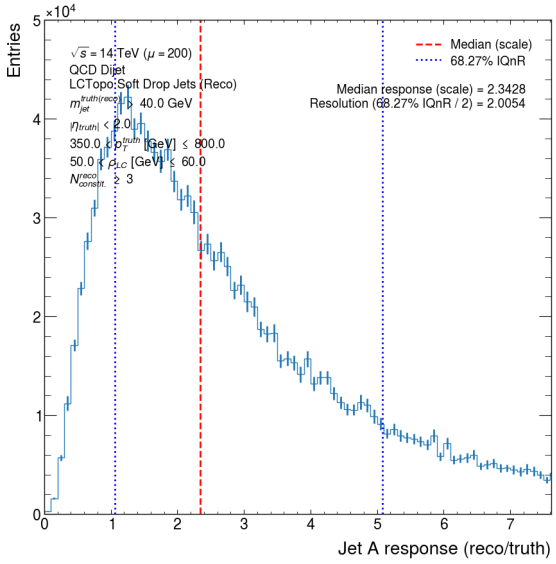

(c) $350 < p_{\mathrm{T}}^{\mathrm{truth}}$ (GeV) ≤ 800 and $50 < \rho_{\mathrm{LCW}}$ (GeV) ≤ 60

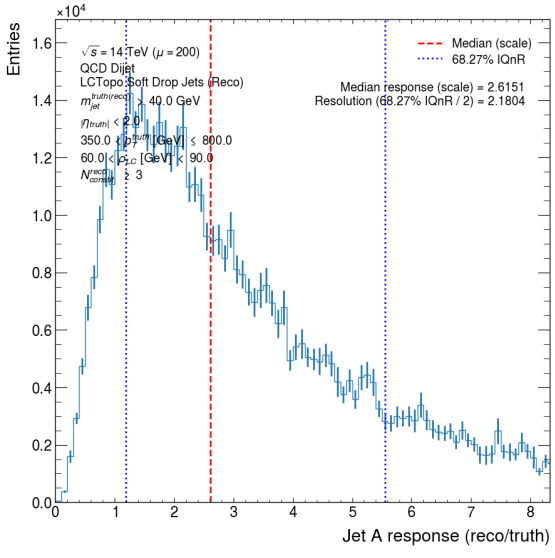

(d) $350 < p_{\mathrm{T}}^{\mathrm{truth}}$ (GeV) ≤ 800 and $60 < \rho_{\mathrm{LCW}}$ (GeV) < 90

Figure H.5: Soft-drop jet A response distributions binned in the truth soft-drop jet p_{T} and ρ_{LCW}.

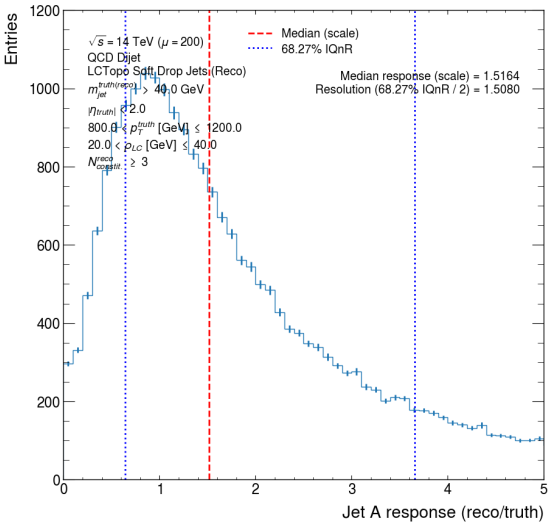

(e) $800 < p_{\mathrm{T}}^{\mathrm{truth}}$ (GeV) ≤ 1200 and $20 < \rho_{\mathrm{LCW}}$ (GeV) ≤ 40

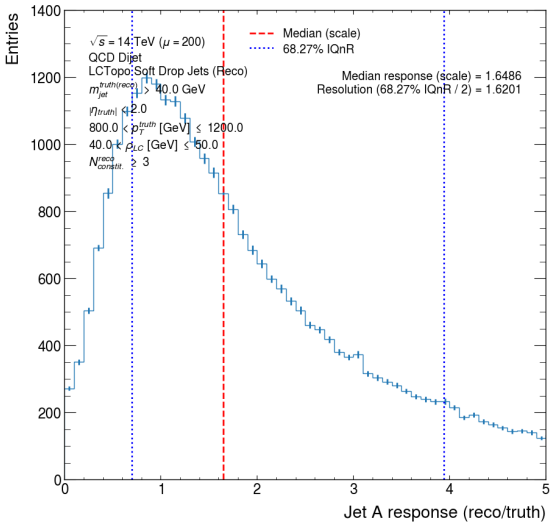

(f) $800 < p_{\mathrm{T}}^{\mathrm{truth}}$ (GeV) ≤ 1200 and $40 < \rho_{\mathrm{LCW}}$ (GeV) ≤ 50

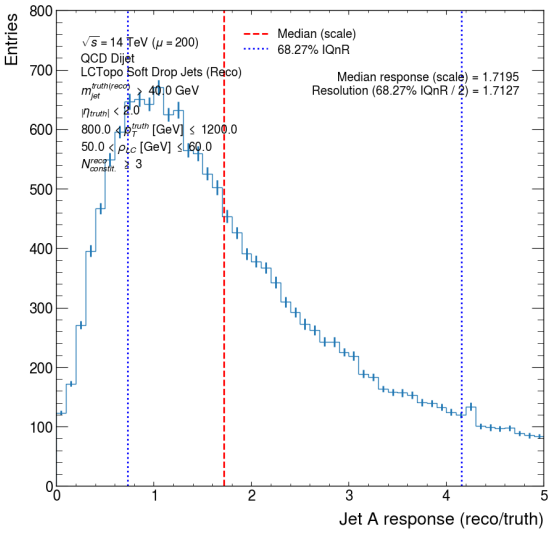

(g) $800 < p_{\mathrm{T}}^{\mathrm{truth}}$ (GeV) ≤ 1200 and $50 < \rho_{\mathrm{LCW}}$ (GeV) ≤ 60

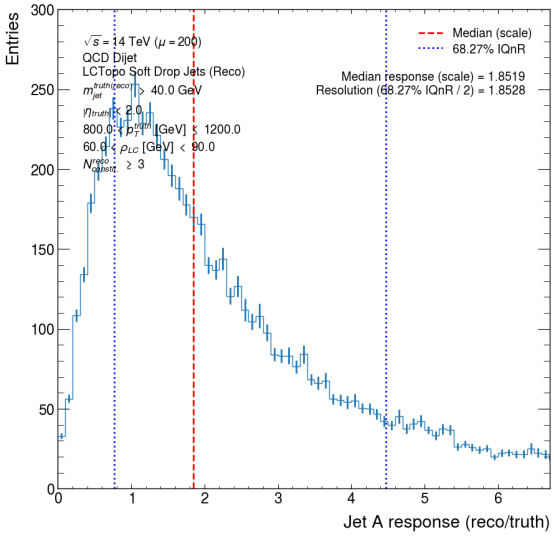

(h) $800 < p_{\mathrm{T}}^{\mathrm{truth}}$ (GeV) ≤ 1200 and $60 < \rho_{\mathrm{LCW}}$ (GeV) < 90

Figure H.5 (cont.): Soft-drop jet A response distributions binned in the truth soft-drop jet p_{T} and ρ_{LCW}.

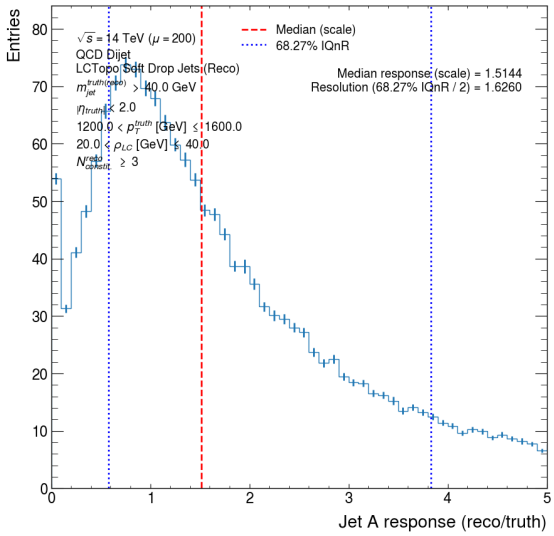

(i) $1200 < p_{\mathrm{T}}^{\mathrm{truth}}$ (GeV) ≤ 1600 and $20 < \rho_{\mathrm{LCW}}$ (GeV) ≤ 40

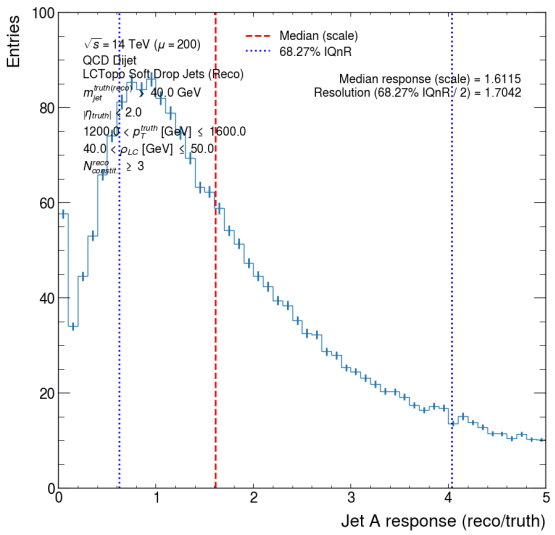

(j) $1200 < p_{\mathrm{T}}^{\mathrm{truth}}$ (GeV) ≤ 1600 and $40 < \rho_{\mathrm{LCW}}$ (GeV) ≤ 50

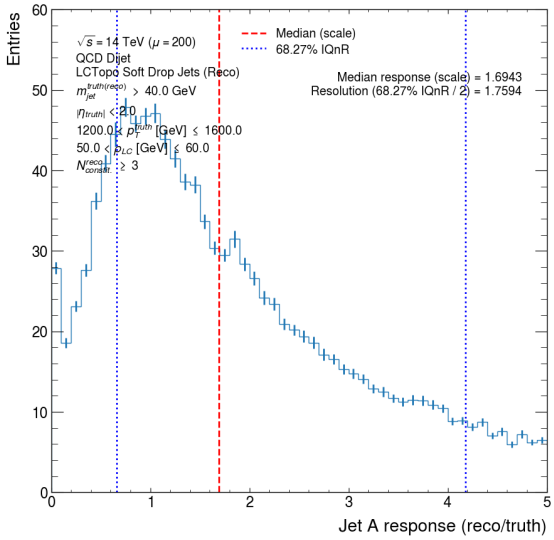

(k) $1200 < p_{\mathrm{T}}^{\mathrm{truth}}$ (GeV) ≤ 1600 and $50 < \rho_{\mathrm{LCW}}$ (GeV) ≤ 60

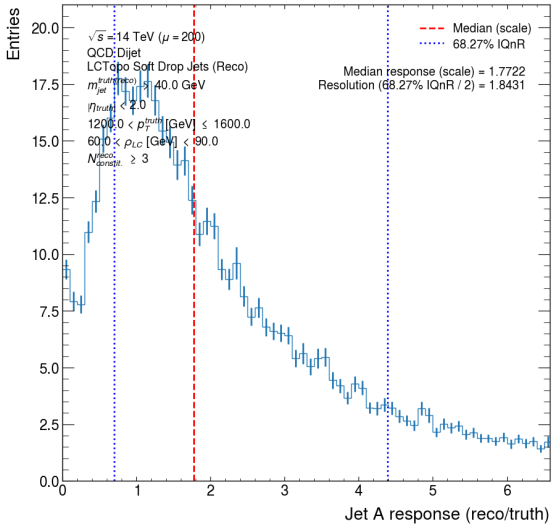

(l) $1200 < p_{\mathrm{T}}^{\mathrm{truth}}$ (GeV) ≤ 1600 and $60 < \rho_{\mathrm{LCW}}$ (GeV) < 90

Figure H.5 (cont.): Soft-drop jet A response distributions binned in the truth soft-drop jet p_{T} and ρ_{LCW}.

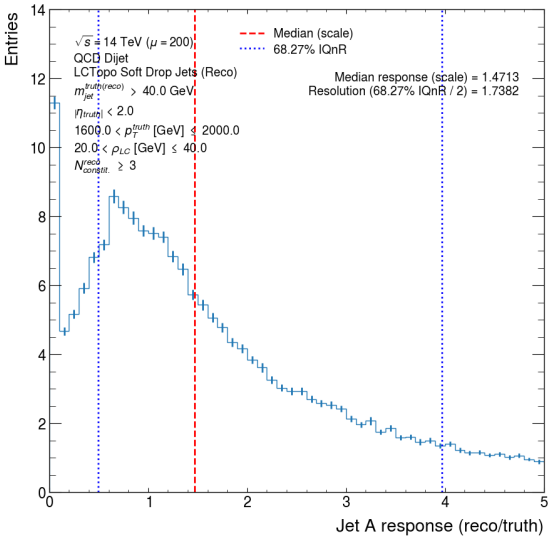

(m) $1600 < p_{\mathrm{T}}^{\mathrm{truth}}$ (GeV) ≤ 2000 and $20 < \rho_{\mathrm{LCW}}$ (GeV) ≤ 40

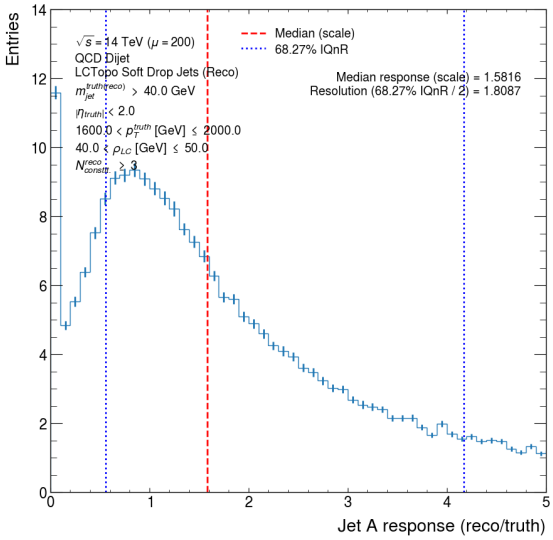

(n) $1600 < p_{\mathrm{T}}^{\mathrm{truth}}$ (GeV) ≤ 2000 and $40 < \rho_{\mathrm{LCW}}$ (GeV) ≤ 50

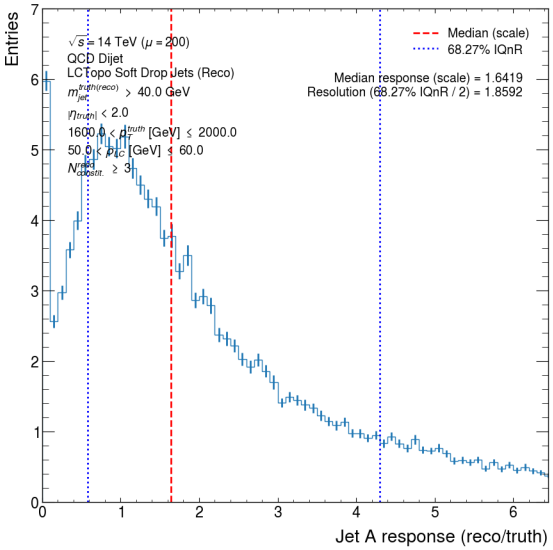

(o) $1600 < p_{\mathrm{T}}^{\mathrm{truth}}$ (GeV) ≤ 2000 and $50 < \rho_{\mathrm{LCW}}$ (GeV) ≤ 60

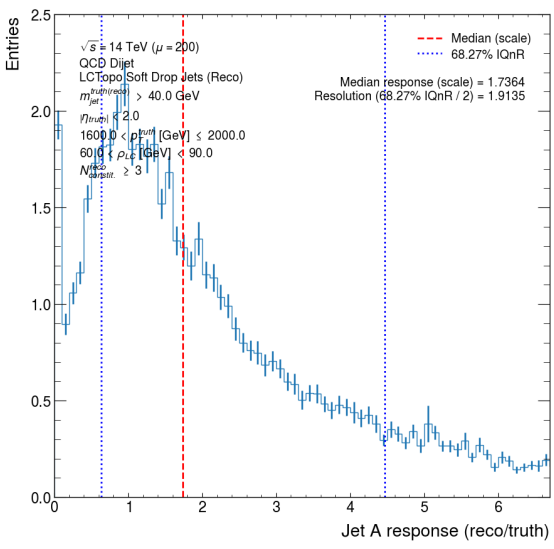

(p) $1600 < p_{\mathrm{T}}^{\mathrm{truth}}$ (GeV) ≤ 2000 and $60 < \rho_{\mathrm{LCW}}$ (GeV) < 90

Figure H.5 (cont.): Soft-drop jet A response distributions binned in the truth soft-drop jet p_{T} and ρ_{LCW}.

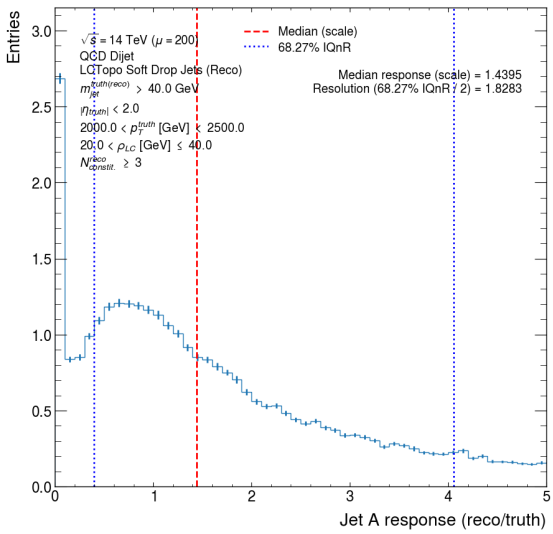

(q) $2000 < p_{\mathrm{T}}^{\mathrm{truth}}$ (GeV) < 2500 and $20 < \rho_{\mathrm{LCW}}$ (GeV) ≤ 40

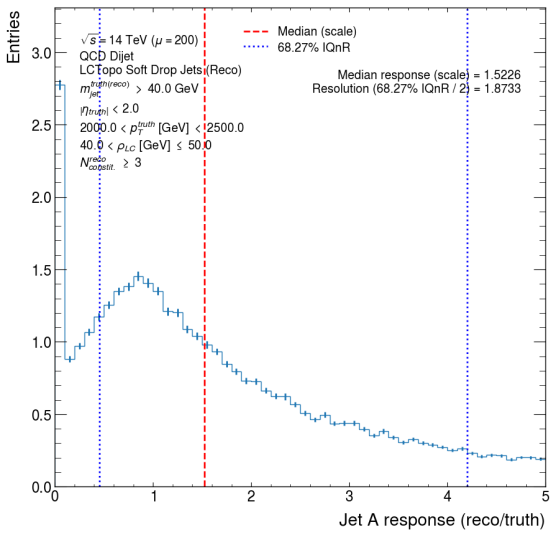

(r) $2000 < p_{\mathrm{T}}^{\mathrm{truth}}$ (GeV) < 2500 and $40 < \rho_{\mathrm{LCW}}$ (GeV) ≤ 50

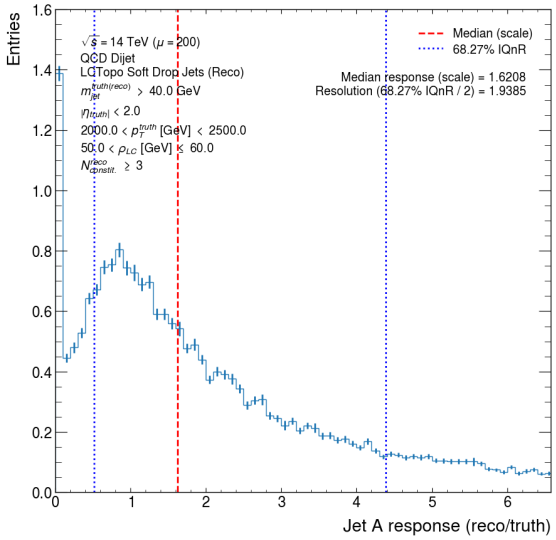

(s) $2000 < p_{\mathrm{T}}^{\mathrm{truth}}$ (GeV) < 2500 and $50 < \rho_{\mathrm{LCW}}$ (GeV) ≤ 60

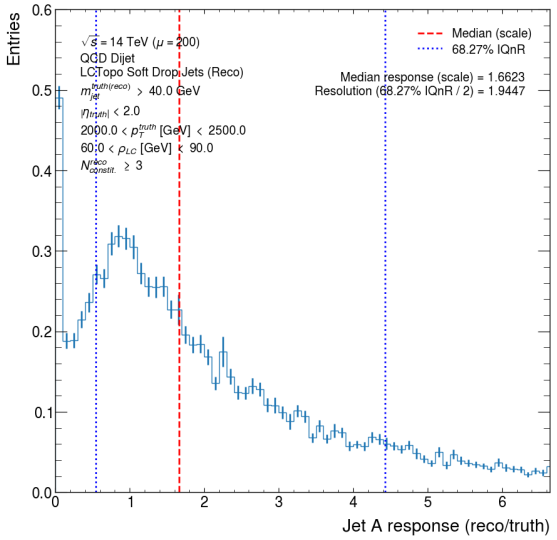

(t) $2000 < p_{\mathrm{T}}^{\mathrm{truth}}$ (GeV) < 2500 and $60 < \rho_{\mathrm{LCW}}$ (GeV) < 90

Figure H.5 (cont.): Soft-drop jet A response distributions binned in the truth soft-drop jet p_{T} and ρ_{LCW}.

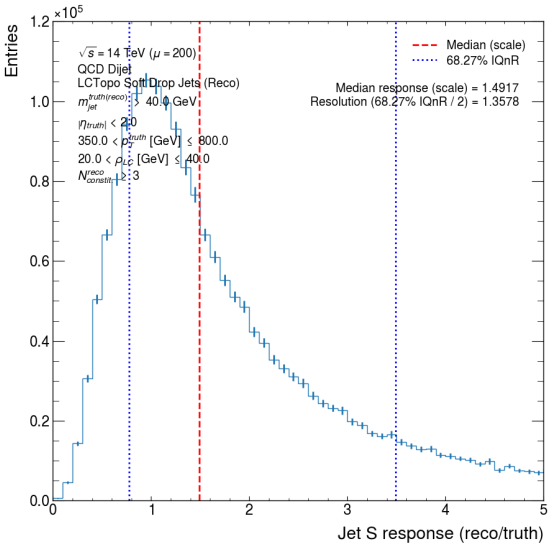

(a) $350 < p_{\mathrm{T}}^{\mathrm{truth}}$ (GeV) ≤ 800 and $20 < \rho_{\mathrm{LCW}}$ (GeV) ≤ 40

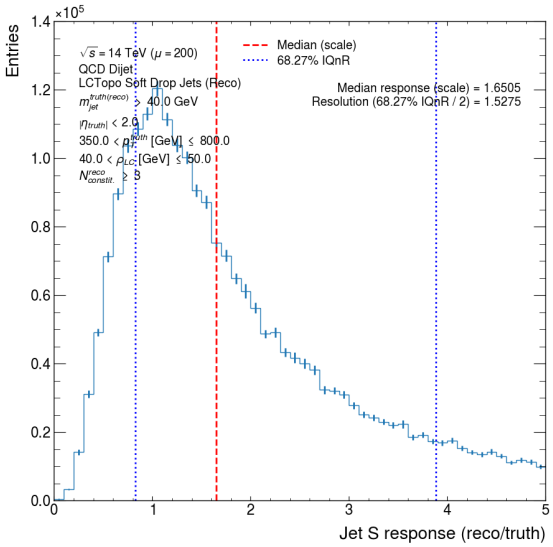

(b) $350 < p_{\mathrm{T}}^{\mathrm{truth}}$ (GeV) ≤ 800 and $40 < \rho_{\mathrm{LCW}}$ (GeV) ≤ 50

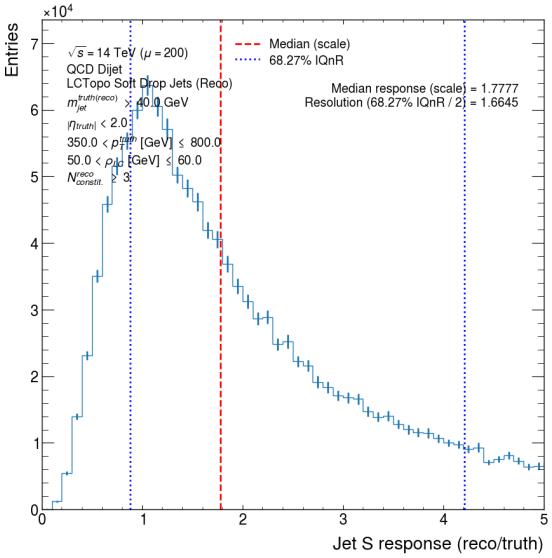

(c) $350 < p_{\mathrm{T}}^{\mathrm{truth}}$ (GeV) ≤ 800 and $50 < \rho_{\mathrm{LCW}}$ (GeV) ≤ 60

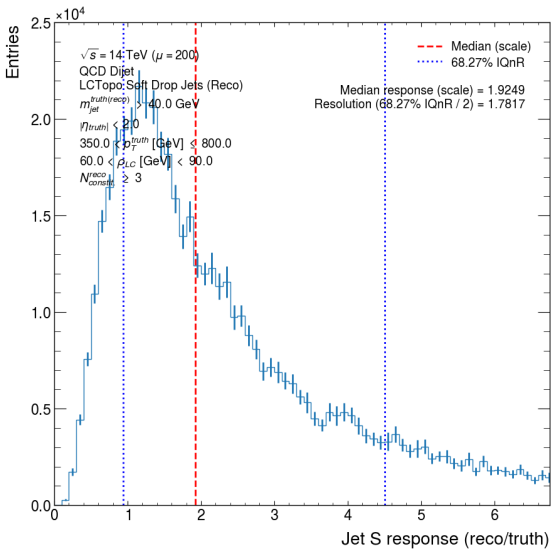

(d) $350 < p_{\mathrm{T}}^{\mathrm{truth}}$ (GeV) ≤ 800 and $60 < \rho_{\mathrm{LCW}}$ (GeV) < 90

Figure H.6: Soft-drop jet S response distributions binned in the truth soft-drop jet p_{T} and ρ_{LCW}.

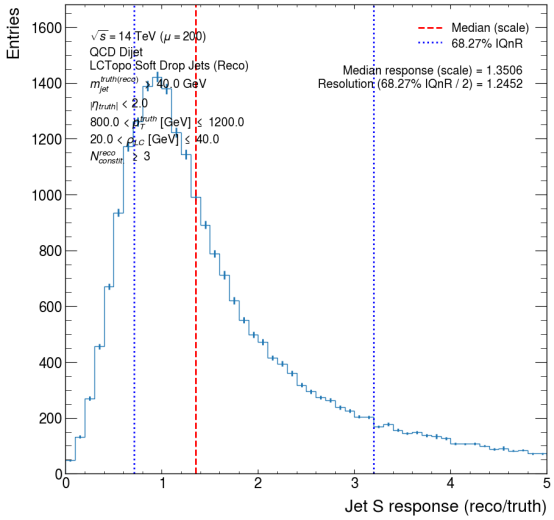

(e) $800 < p_{\mathrm{T}}^{\mathrm{truth}}$ (GeV) ≤ 1200 and $20 < \rho_{\mathrm{LCW}}$ (GeV) ≤ 40

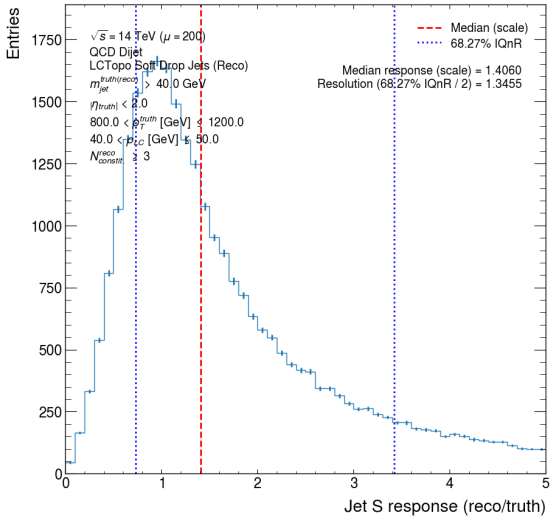

(f) $800 < p_{\mathrm{T}}^{\mathrm{truth}}$ (GeV) ≤ 1200 and $40 < \rho_{\mathrm{LCW}}$ (GeV) ≤ 50

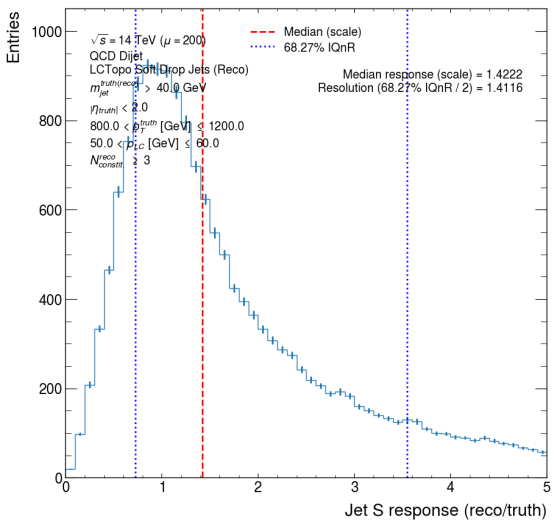

(g) $800 < p_{\mathrm{T}}^{\mathrm{truth}}$ (GeV) ≤ 1200 and $50 < \rho_{\mathrm{LCW}}$ (GeV) ≤ 60

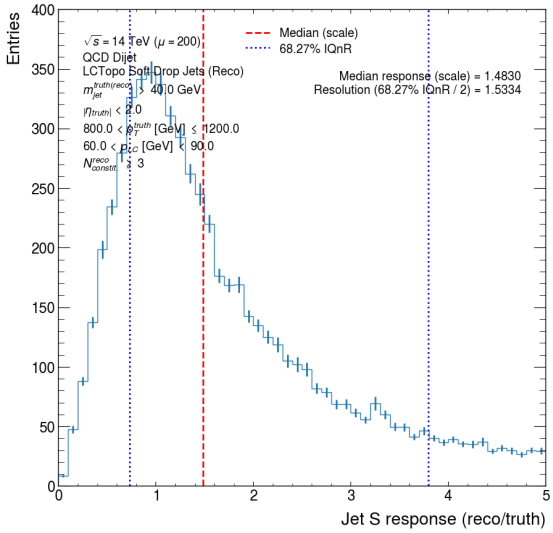

(h) $800 < p_{\mathrm{T}}^{\mathrm{truth}}$ (GeV) ≤ 1200 and $60 < \rho_{\mathrm{LCW}}$ (GeV) < 90

Figure H.6 (cont.): Soft-drop jet S response distributions binned in the truth soft-drop jet p_{T} and ρ_{LCW}.

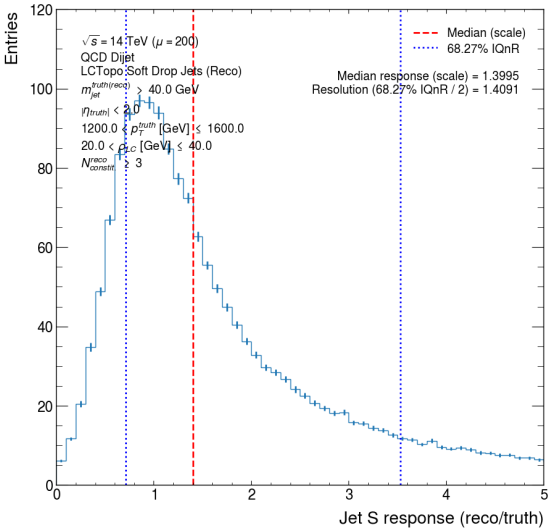

(i) $1200 < p_{\mathrm{T}}^{\mathrm{truth}}$ (GeV) ≤ 1600 and $20 < \rho_{\mathrm{LCW}}$ (GeV) ≤ 40

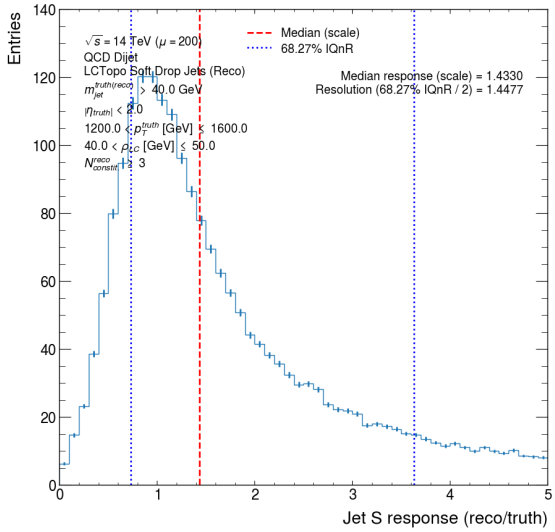

(j) $1200 < p_{\mathrm{T}}^{\mathrm{truth}}$ (GeV) ≤ 1600 and $40 < \rho_{\mathrm{LCW}}$ (GeV) ≤ 50

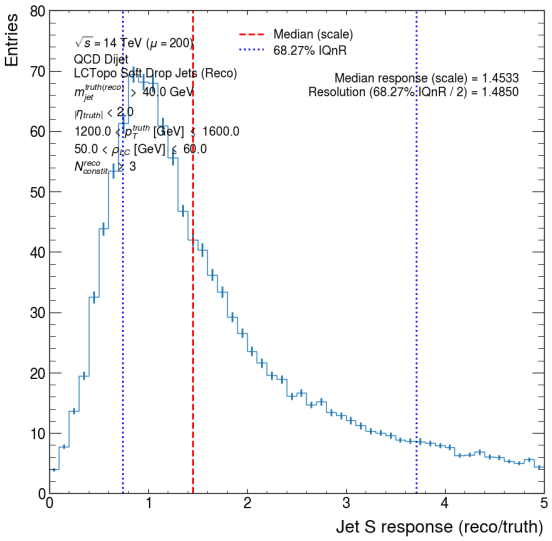

(k) $1200 < p_{\mathrm{T}}^{\mathrm{truth}}$ (GeV) ≤ 1600 and $50 < \rho_{\mathrm{LCW}}$ (GeV) ≤ 60

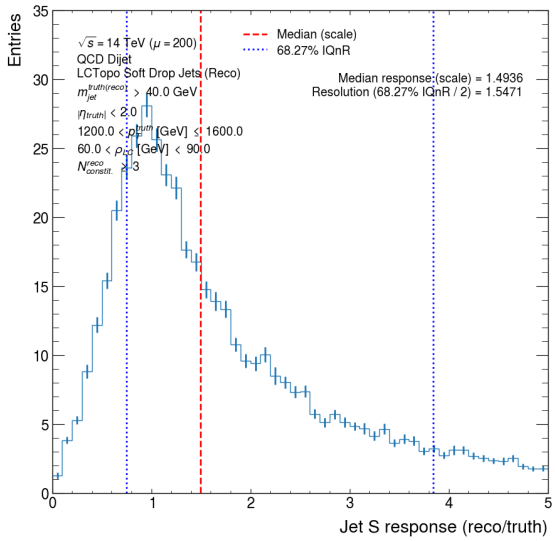

(l) $1200 < p_{\mathrm{T}}^{\mathrm{truth}}$ (GeV) ≤ 1600 and $60 < \rho_{\mathrm{LCW}}$ (GeV) < 90

Figure H.6 (cont.): Soft-drop jet S response distributions binned in the truth soft-drop jet p_{T} and ρ_{LCW}.

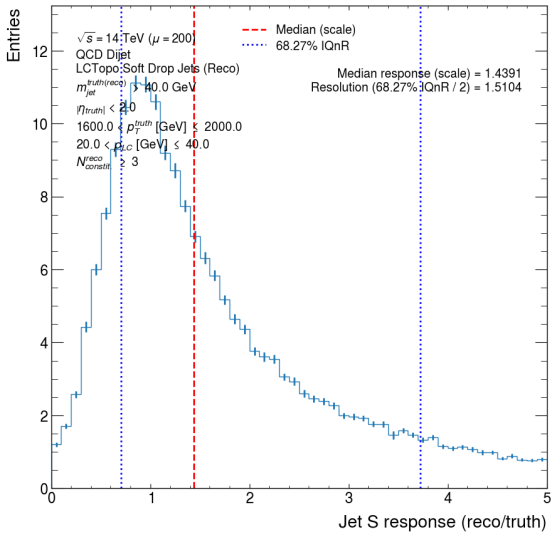

(m) $1600 < p_{\mathrm{T}}^{\mathrm{truth}}$ (GeV) ≤ 2000 and $20 < \rho_{\mathrm{LCW}}$ (GeV) ≤ 40

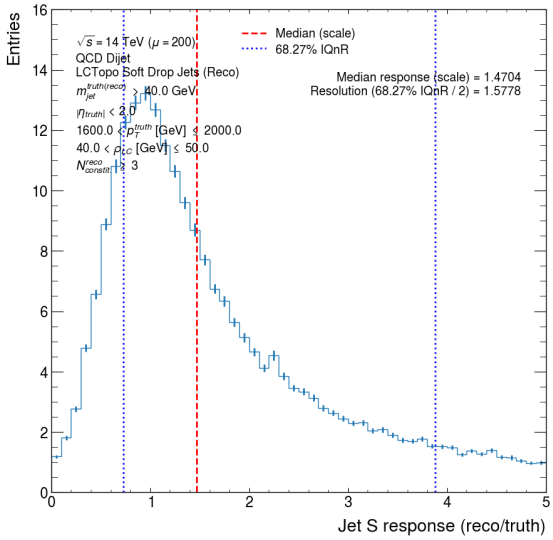

(n) $1600 < p_{\mathrm{T}}^{\mathrm{truth}}$ (GeV) ≤ 2000 and $40 < \rho_{\mathrm{LCW}}$ (GeV) ≤ 50

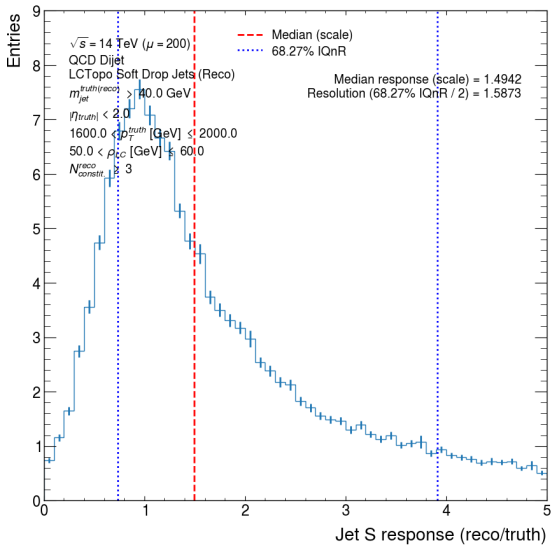

(o) $1600 < p_{\mathrm{T}}^{\mathrm{truth}}$ (GeV) ≤ 2000 and $50 < \rho_{\mathrm{LCW}}$ (GeV) ≤ 60

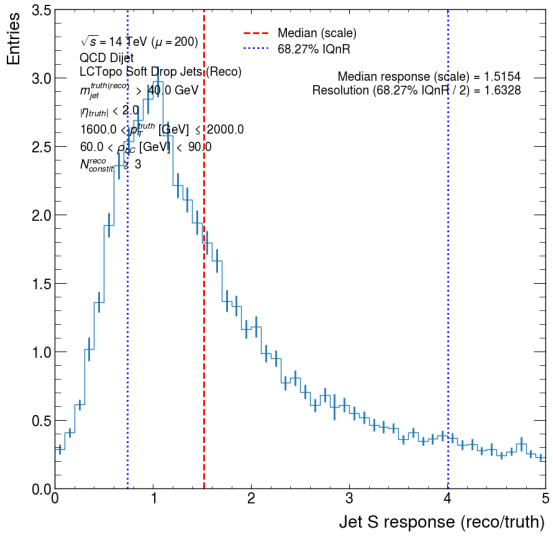

(p) $1600 < p_{\mathrm{T}}^{\mathrm{truth}}$ (GeV) ≤ 2000 and $60 < \rho_{\mathrm{LCW}}$ (GeV) < 90

Figure H.6 (cont.): Soft-drop jet S response distributions binned in the truth soft-drop jet p_{T} and ρ_{LCW}.

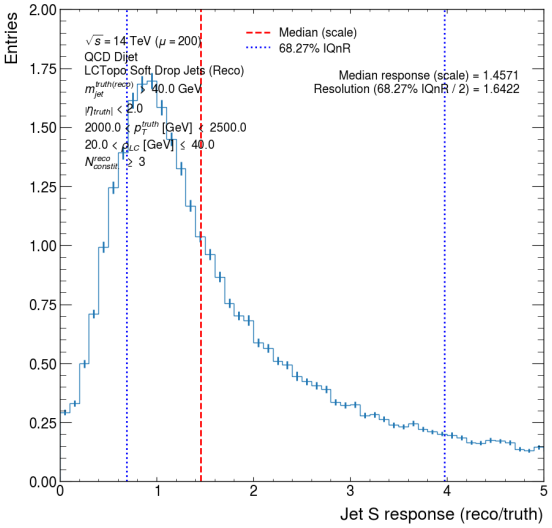

(q) $2000 < p_{\mathrm{T}}^{\mathrm{truth}}$ (GeV) < 2500 and $20 < \rho_{\mathrm{LCW}}$ (GeV) ≤ 40

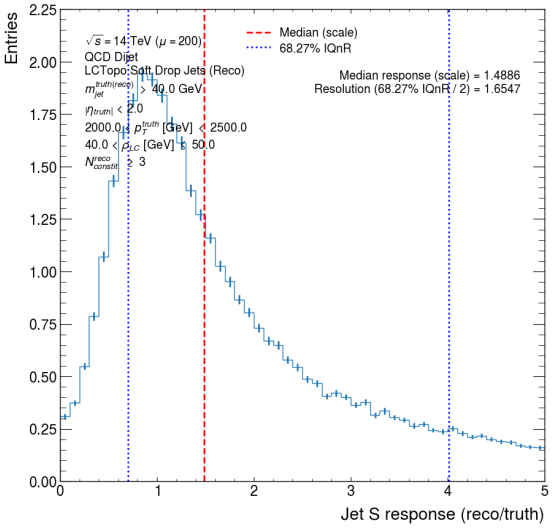

(r) $2000 < p_{\mathrm{T}}^{\mathrm{truth}}$ (GeV) < 2500 and $40 < \rho_{\mathrm{LCW}}$ (GeV) ≤ 50

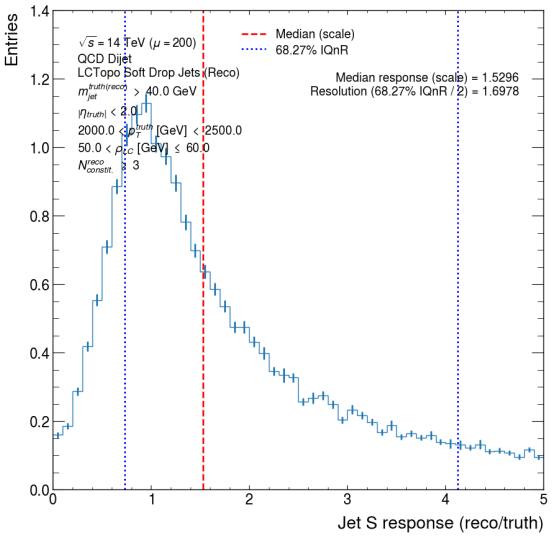

(s) $2000 < p_{\mathrm{T}}^{\mathrm{truth}}$ (GeV) < 2500 and $50 < \rho_{\mathrm{LCW}}$ (GeV) ≤ 60

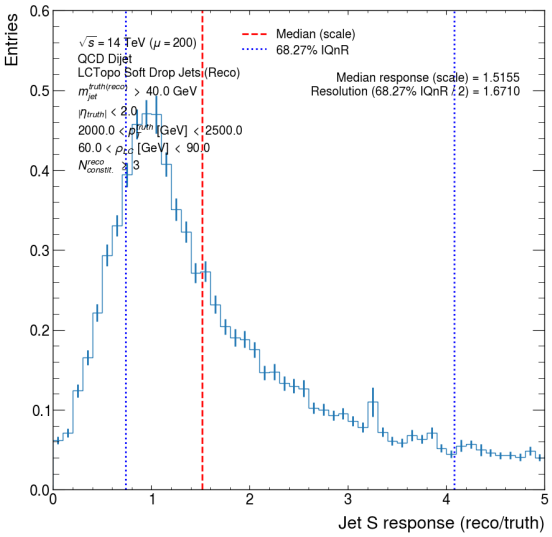

(t) $2000 < p_{\mathrm{T}}^{\mathrm{truth}}$ (GeV) < 2500 and $60 < \rho_{\mathrm{LCW}}$ (GeV) < 90

Figure H.6 (cont.): Soft-drop jet S response distributions binned in the truth soft-drop jet p_{T} and ρ_{LCW}.

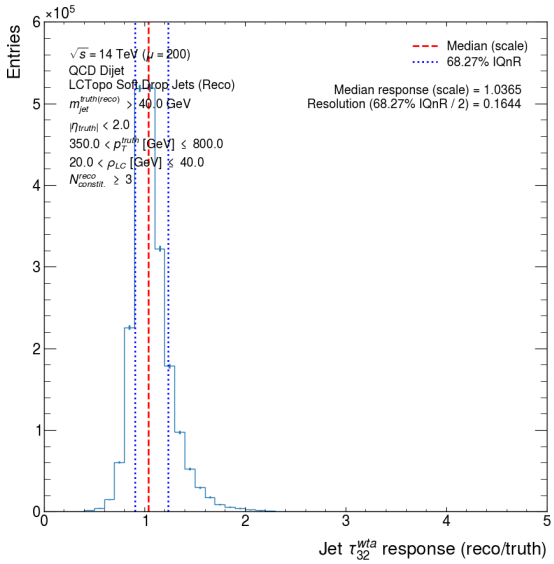

(a) $350 < p_{\mathrm{T}}^{\mathrm{truth}}$ (GeV) ≤ 800 and $20 < \rho_{\mathrm{LCW}}$ (GeV) ≤ 40

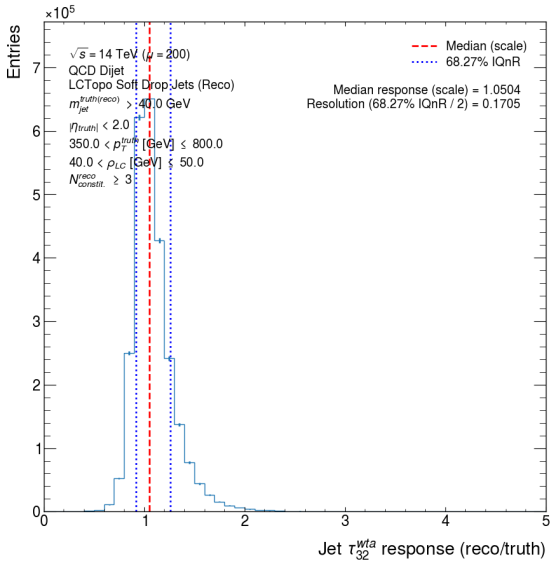

(b) $350 < p_{\mathrm{T}}^{\mathrm{truth}}$ (GeV) ≤ 800 and $40 < \rho_{\mathrm{LCW}}$ (GeV) ≤ 50

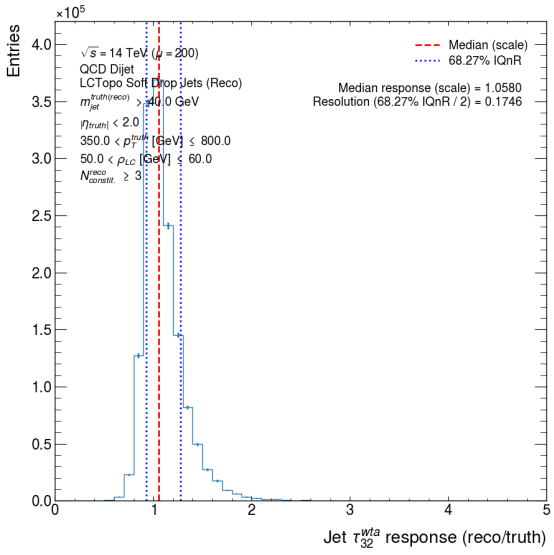

(c) $350 < p_{\mathrm{T}}^{\mathrm{truth}}$ (GeV) ≤ 800 and $50 < \rho_{\mathrm{LCW}}$ (GeV) ≤ 60

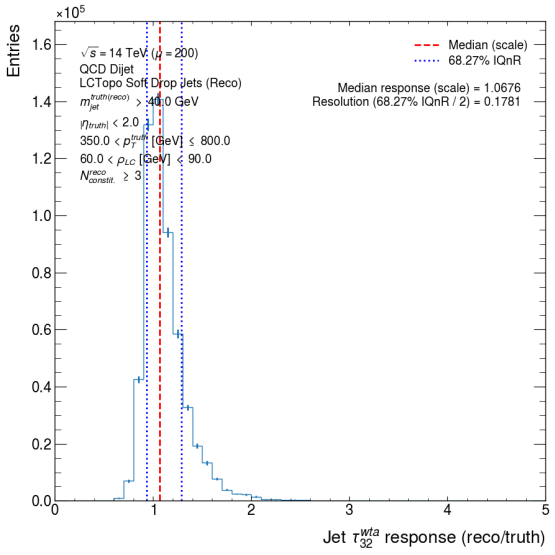

(d) $350 < p_{\mathrm{T}}^{\mathrm{truth}}$ (GeV) ≤ 800 and $60 < \rho_{\mathrm{LCW}}$ (GeV) < 90

Figure H.7: Soft-drop jet τ_{32}^{wta} response distributions binned in the truth soft-drop jet p_{T} and ρ_{LCW}.

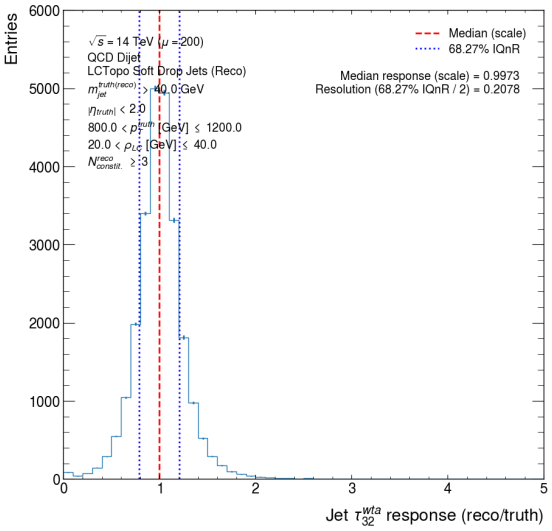

(e) $800 < p_{\mathrm{T}}^{\mathrm{truth}}$ (GeV) ≤ 1200 and $20 < \rho_{\mathrm{LCW}}$ (GeV) ≤ 40

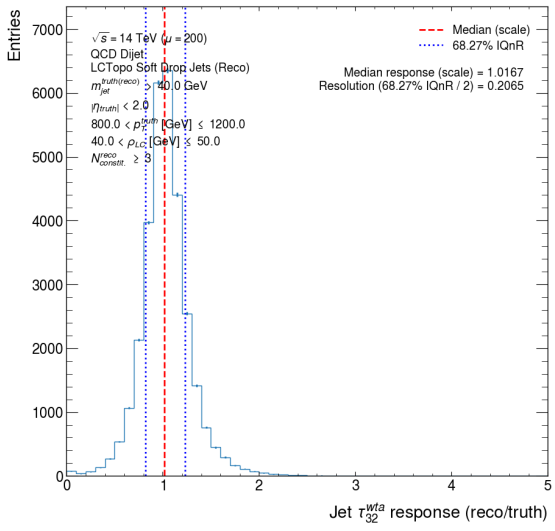

(f) $800 < p_{\mathrm{T}}^{\mathrm{truth}}$ (GeV) ≤ 1200 and $40 < \rho_{\mathrm{LCW}}$ (GeV) ≤ 50

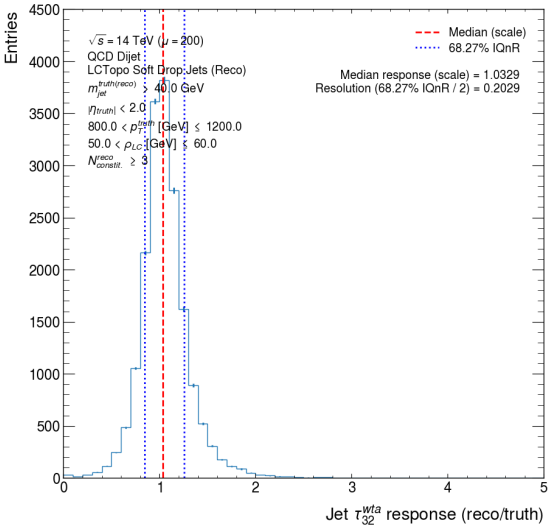

(g) $800 < p_{\mathrm{T}}^{\mathrm{truth}}$ (GeV) ≤ 1200 and $50 < \rho_{\mathrm{LCW}}$ (GeV) ≤ 60

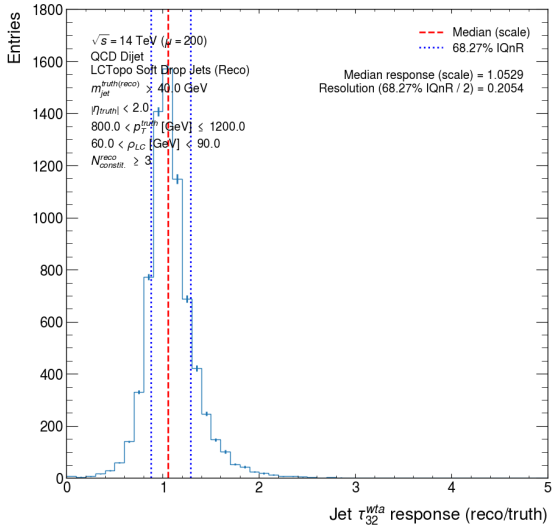

(h) $800 < p_{\mathrm{T}}^{\mathrm{truth}}$ (GeV) ≤ 1200 and $60 < \rho_{\mathrm{LCW}}$ (GeV) < 90

Figure H.7 (cont.): Soft-drop jet τ_{32}^{wta} response distributions binned in the truth soft-drop jet p_{T} and ρ_{LCW}.

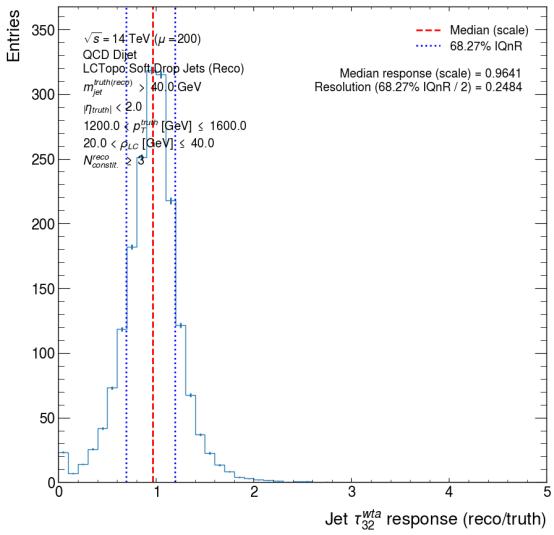

(i) $1200 < p_{\mathrm{T}}^{\mathrm{truth}}$ (GeV) ≤ 1600 and $20 < \rho_{\mathrm{LCW}}$ (GeV) ≤ 40

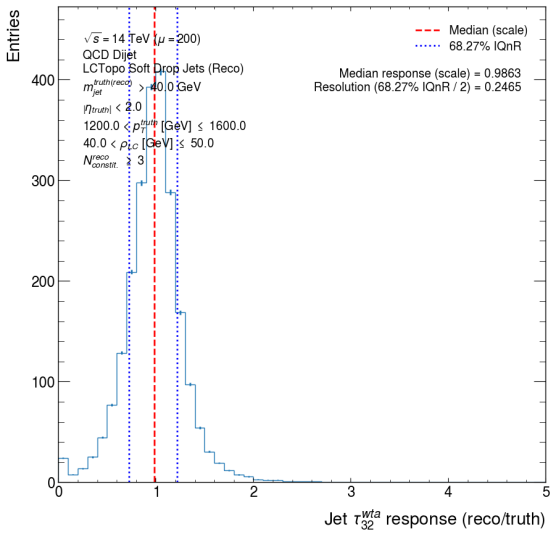

(j) $1200 < p_{\mathrm{T}}^{\mathrm{truth}}$ (GeV) ≤ 1600 and $40 < \rho_{\mathrm{LCW}}$ (GeV) ≤ 50

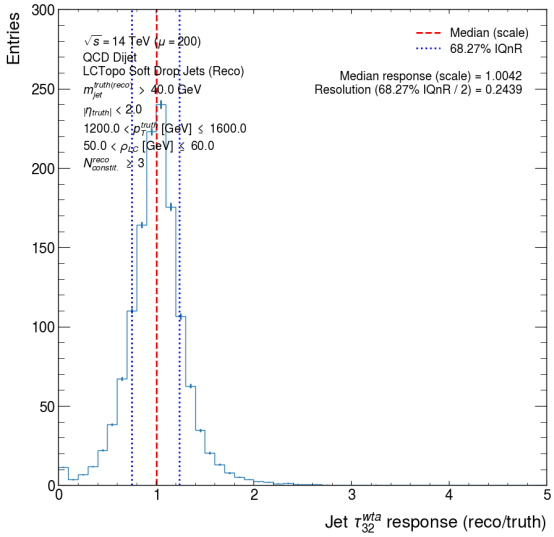

(k) $1200 < p_{\mathrm{T}}^{\mathrm{truth}}$ (GeV) ≤ 1600 and $50 < \rho_{\mathrm{LCW}}$ (GeV) ≤ 60

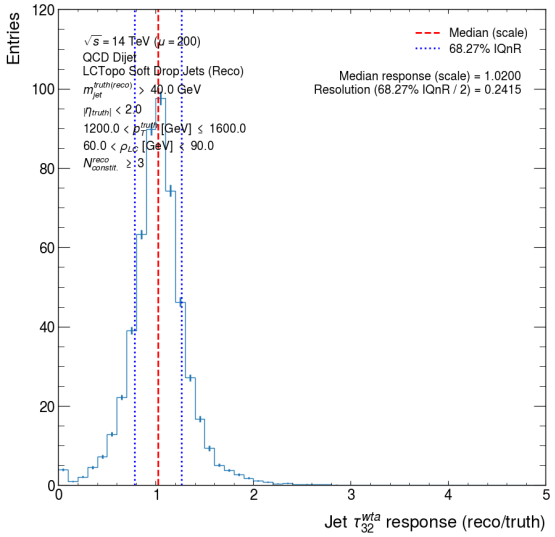

(l) $1200 < p_{\mathrm{T}}^{\mathrm{truth}}$ (GeV) ≤ 1600 and $60 < \rho_{\mathrm{LCW}}$ (GeV) < 90

Figure H.7 (cont.): Soft-drop jet τ_{32}^{wta} response distributions binned in the truth soft-drop jet p_{T} and ρ_{LCW}.

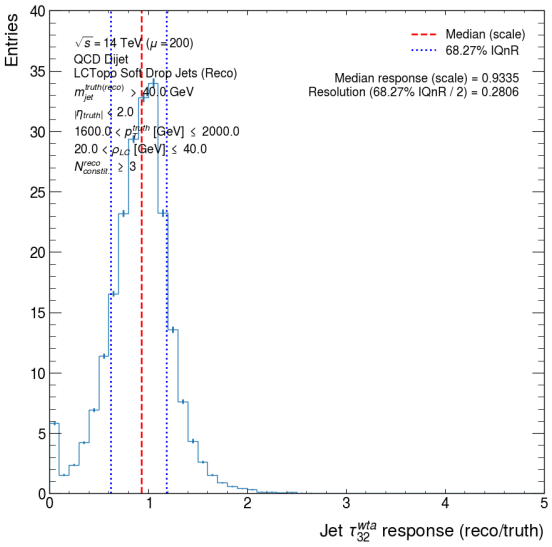

(m) $1600 < p_{\mathrm{T}}^{\mathrm{truth}}$ (GeV) ≤ 2000 and $20 < \rho_{\mathrm{LCW}}$ (GeV) ≤ 40

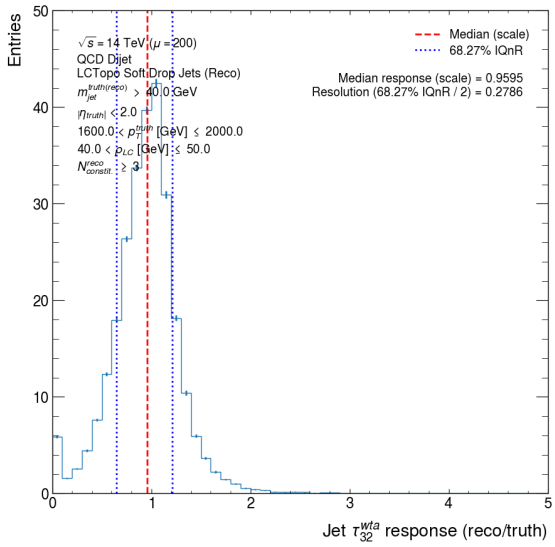

(n) $1600 < p_{\mathrm{T}}^{\mathrm{truth}}$ (GeV) ≤ 2000 and $40 < \rho_{\mathrm{LCW}}$ (GeV) ≤ 50

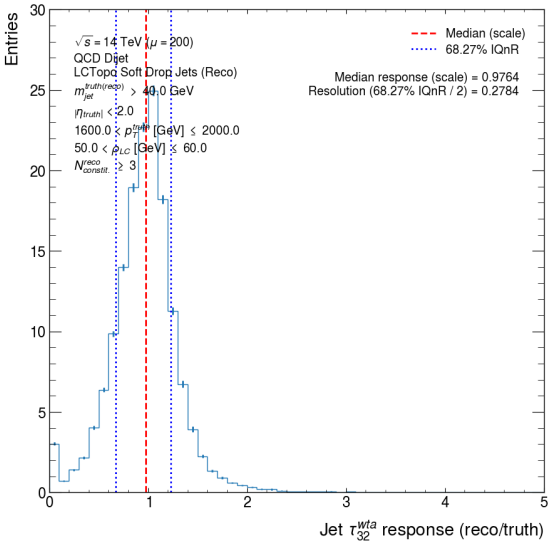

(o) $1600 < p_{\mathrm{T}}^{\mathrm{truth}}$ (GeV) ≤ 2000 and $50 < \rho_{\mathrm{LCW}}$ (GeV) ≤ 60

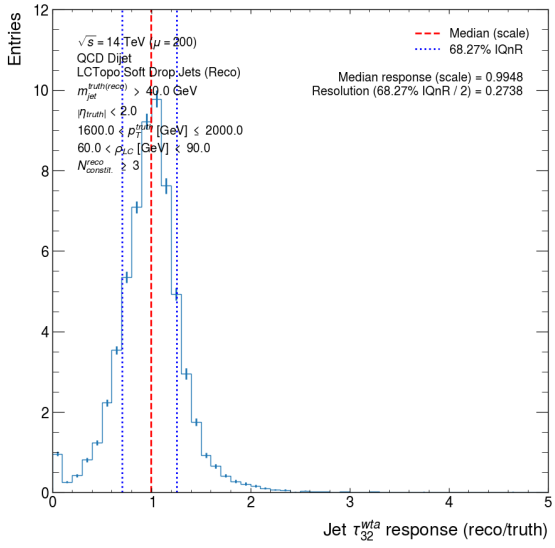

(p) $1600 < p_{\mathrm{T}}^{\mathrm{truth}}$ (GeV) ≤ 2000 and $60 < \rho_{\mathrm{LCW}}$ (GeV) < 90

Figure H.7 (cont.): Soft-drop jet τ_{32}^{wta} response distributions binned in the truth soft-drop jet p_{T} and ρ_{LCW}.

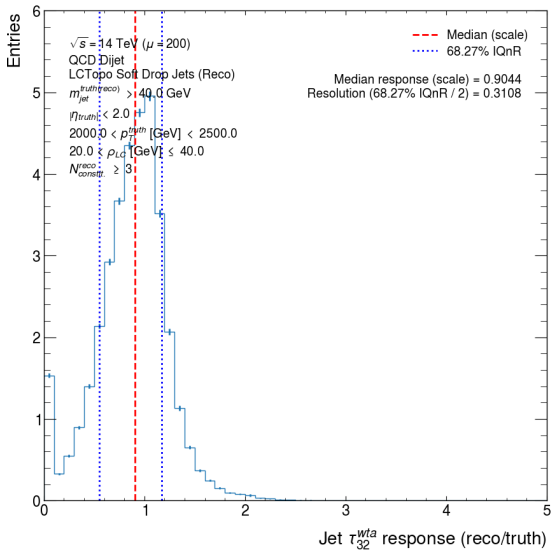

(q) $2000 < p_{\mathrm{T}}^{\mathrm{truth}}$ (GeV) < 2500 and $20 < \rho_{\mathrm{LCW}}$ (GeV) ≤ 40

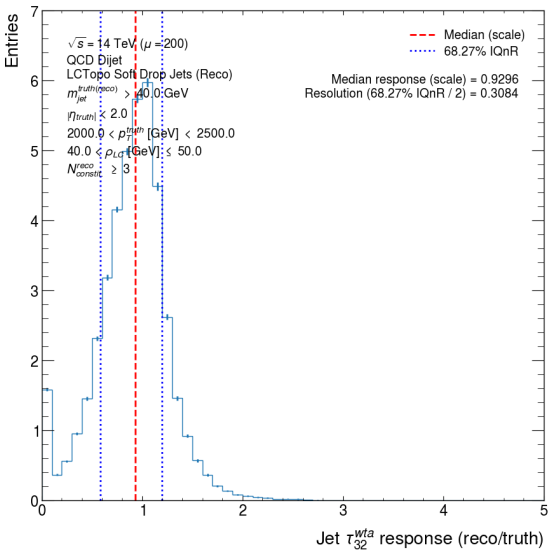

(r) $2000 < p_{\mathrm{T}}^{\mathrm{truth}}$ (GeV) < 2500 and $40 < \rho_{\mathrm{LCW}}$ (GeV) ≤ 50

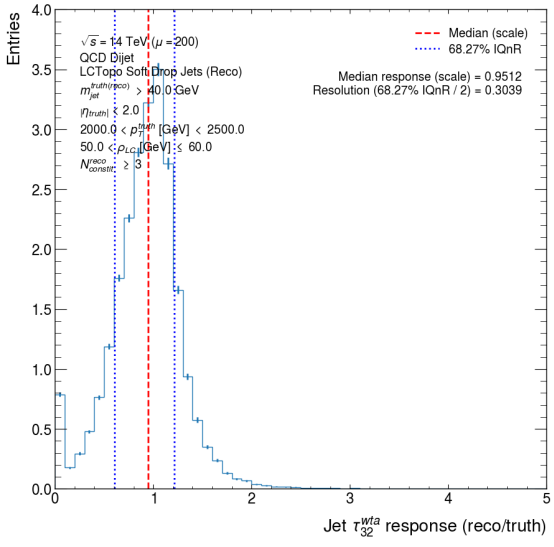

(s) $2000 < p_{\mathrm{T}}^{\mathrm{truth}}$ (GeV) < 2500 and $50 < \rho_{\mathrm{LCW}}$ (GeV) ≤ 60

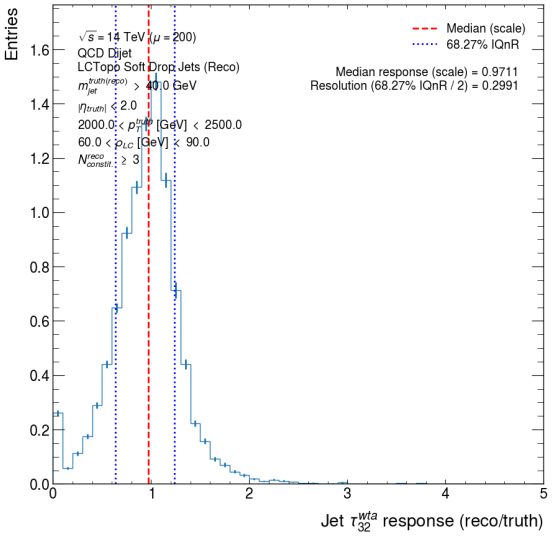

(t) $2000 < p_{\mathrm{T}}^{\mathrm{truth}}$ (GeV) < 2500 and $60 < \rho_{\mathrm{LCW}}$ (GeV) < 90

Figure H.7 (cont.): Soft-drop jet τ_{32}^{wta} response distributions binned in the truth soft-drop jet p_{T} and ρ_{LCW}.

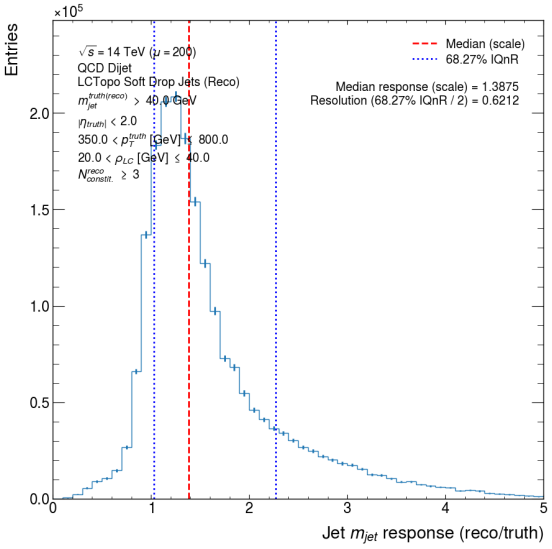

(a) $350 < p_{\mathrm{T}}^{\mathrm{truth}}$ (GeV) ≤ 800 and $20 < \rho_{\mathrm{LCW}}$ (GeV) ≤ 40

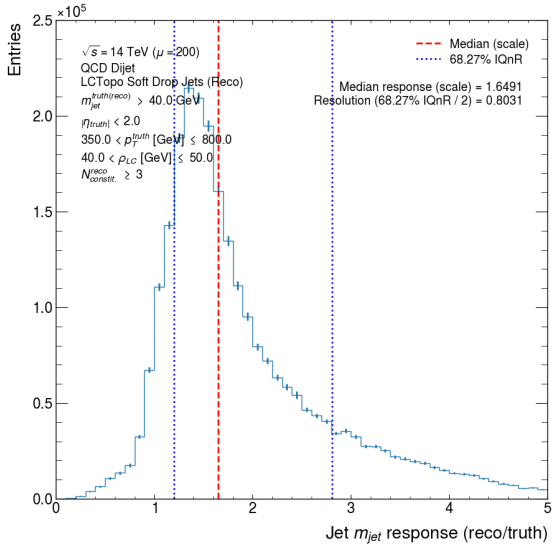

(b) $350 < p_{\mathrm{T}}^{\mathrm{truth}}$ (GeV) ≤ 800 and $40 < \rho_{\mathrm{LCW}}$ (GeV) ≤ 50

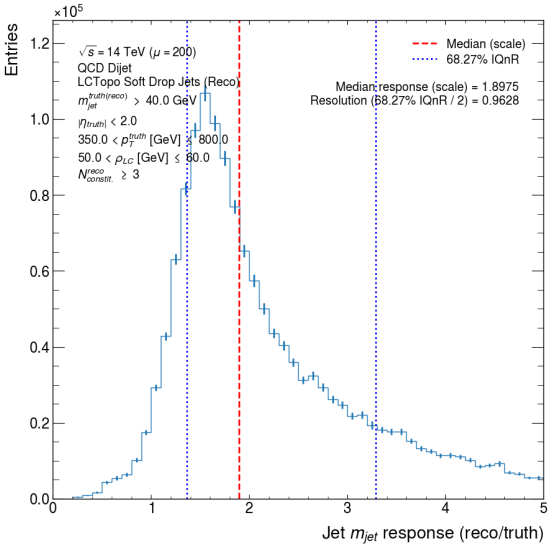

(c) $350 < p_{\mathrm{T}}^{\mathrm{truth}}$ (GeV) ≤ 800 and $50 < \rho_{\mathrm{LCW}}$ (GeV) ≤ 60

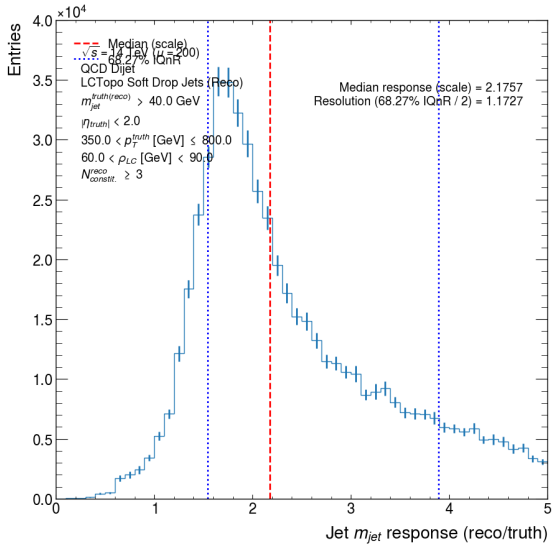

(d) $350 < p_{\mathrm{T}}^{\mathrm{truth}}$ (GeV) ≤ 800 and $60 < \rho_{\mathrm{LCW}}$ (GeV) < 90

Figure H.8: Soft-drop jet m_{jet} response distributions binned in the truth soft-drop jet p_{T} and ρ_{LCW}.

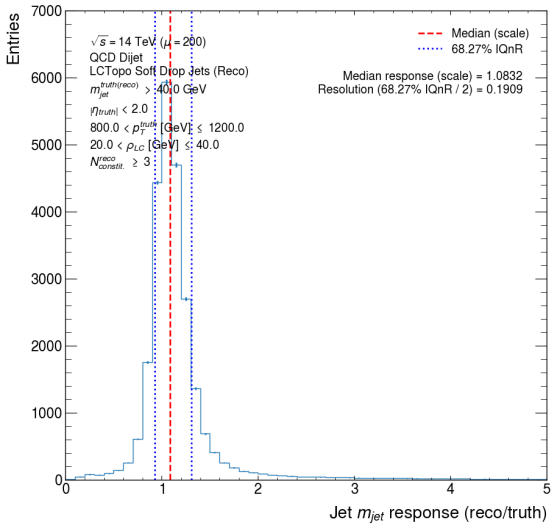

(e) $800 < p_{\mathrm{T}}^{\mathrm{truth}}$ (GeV) ≤ 1200 and $20 < \rho_{\mathrm{LCW}}$ (GeV) ≤ 40

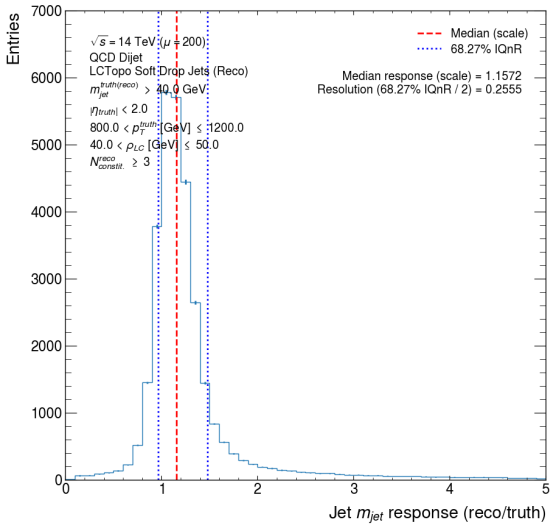

(f) $800 < p_{\mathrm{T}}^{\mathrm{truth}}$ (GeV) ≤ 1200 and $40 < \rho_{\mathrm{LCW}}$ (GeV) ≤ 50

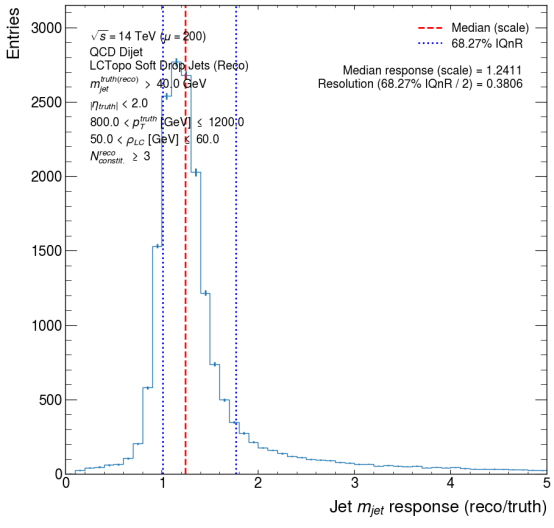

(g) $800 < p_{\mathrm{T}}^{\mathrm{truth}}$ (GeV) ≤ 1200 and $50 < \rho_{\mathrm{LCW}}$ (GeV) ≤ 60

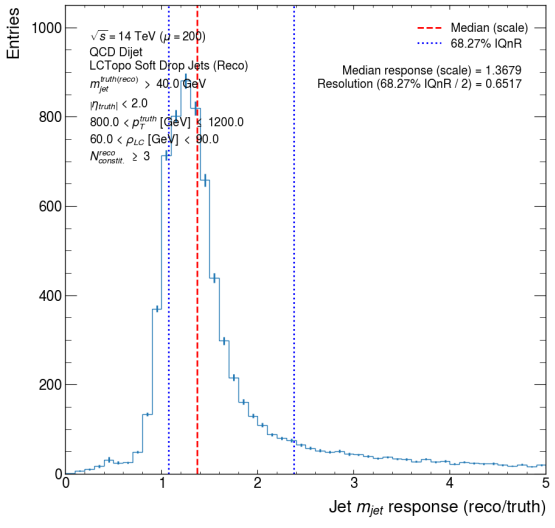

(h) $800 < p_{\mathrm{T}}^{\mathrm{truth}}$ (GeV) ≤ 1200 and $60 < \rho_{\mathrm{LCW}}$ (GeV) < 90

Figure H.8 (cont.): Soft-drop jet m_{jet} response distributions binned in the truth soft-drop jet p_{T} and ρ_{LCW}.

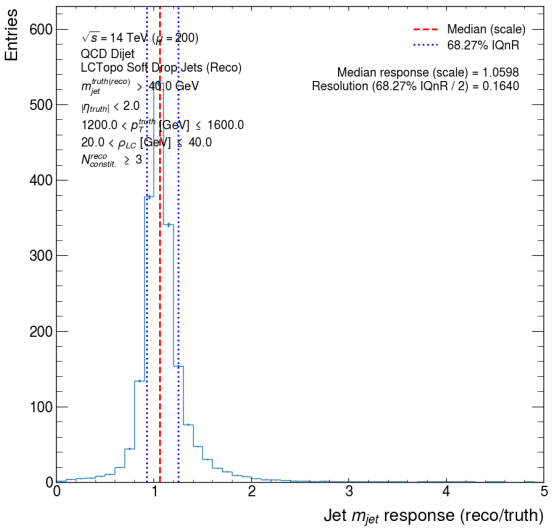

(i) $1200 < p_{\mathrm{T}}^{\mathrm{truth}}$ (GeV) ≤ 1600 and $20 < \rho_{\mathrm{LCW}}$ (GeV) ≤ 40

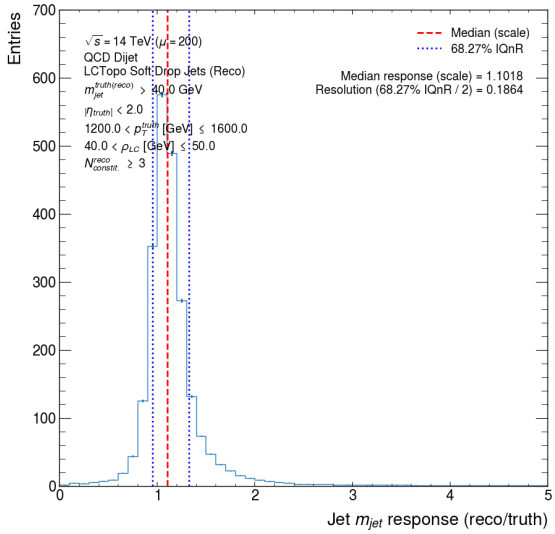

(j) $1200 < p_{\mathrm{T}}^{\mathrm{truth}}$ (GeV) ≤ 1600 and $40 < \rho_{\mathrm{LCW}}$ (GeV) ≤ 50

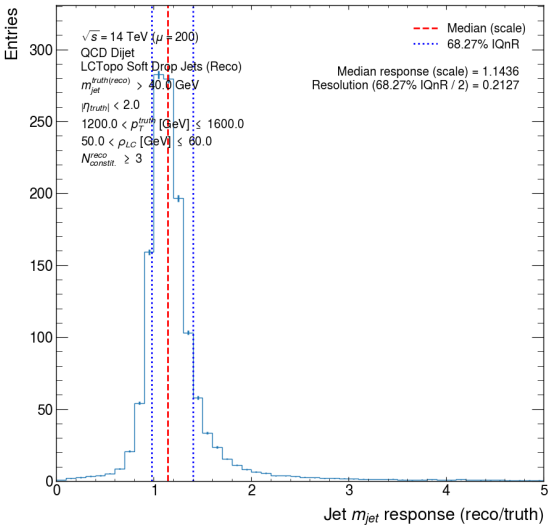

(k) $1200 < p_{\mathrm{T}}^{\mathrm{truth}}$ (GeV) ≤ 1600 and $50 < \rho_{\mathrm{LCW}}$ (GeV) ≤ 60

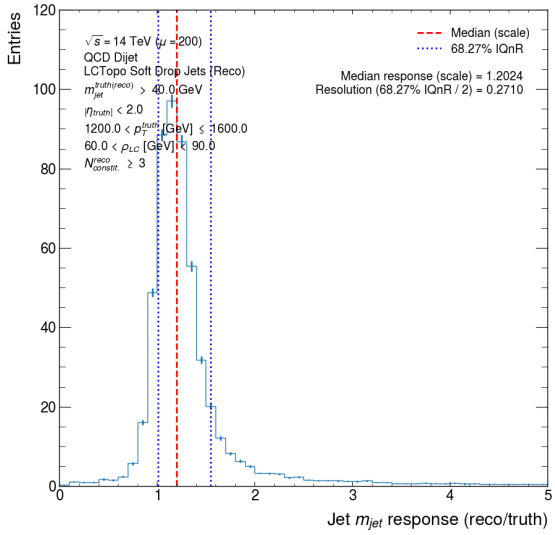

(l) $1200 < p_{\mathrm{T}}^{\mathrm{truth}}$ (GeV) ≤ 1600 and $60 < \rho_{\mathrm{LCW}}$ (GeV) < 90

Figure H.8 (cont.): Soft-drop jet m_{jet} response distributions binned in the truth soft-drop jet p_{T} and ρ_{LCW}.

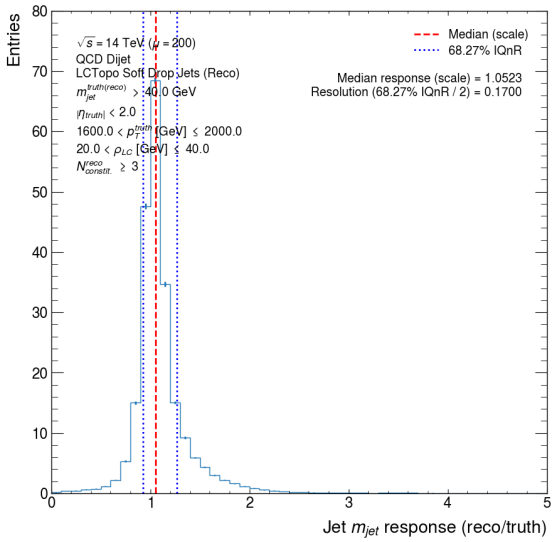

(m) $1600 < p_{\mathrm{T}}^{\mathrm{truth}}$ (GeV) ≤ 2000 and $20 < \rho_{\mathrm{LCW}}$ (GeV) ≤ 40

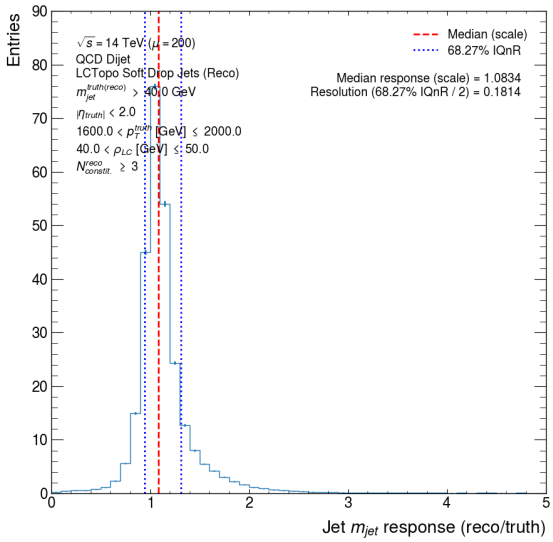

(n) $1600 < p_{\mathrm{T}}^{\mathrm{truth}}$ (GeV) ≤ 2000 and $40 < \rho_{\mathrm{LCW}}$ (GeV) ≤ 50

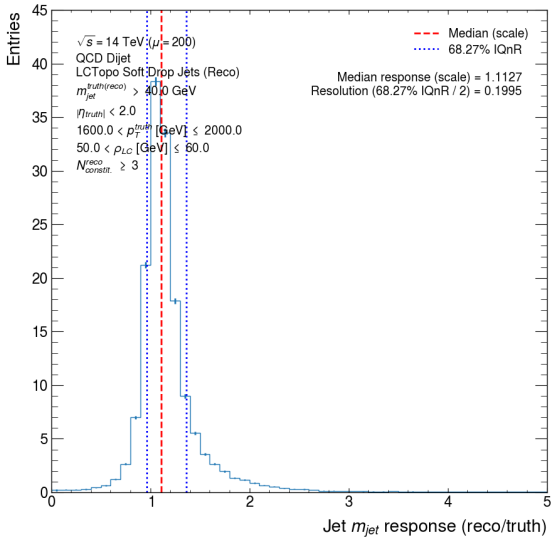

(o) $1600 < p_{\mathrm{T}}^{\mathrm{truth}}$ (GeV) ≤ 2000 and $50 < \rho_{\mathrm{LCW}}$ (GeV) ≤ 60

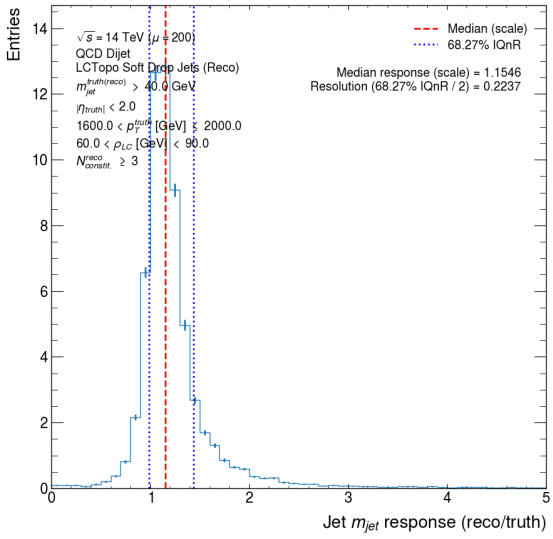

(p) $1600 < p_{\mathrm{T}}^{\mathrm{truth}}$ (GeV) ≤ 2000 and $60 < \rho_{\mathrm{LCW}}$ (GeV) < 90

Figure H.8 (cont.): Soft-drop jet m_{jet} response distributions binned in the truth soft-drop jet p_{T} and ρ_{LCW}.

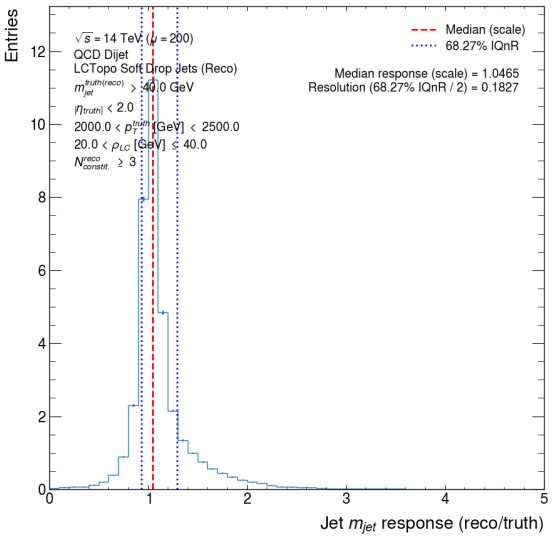

(q) $2000 < p_{\mathrm{T}}^{\mathrm{truth}}$ (GeV) < 2500 and $20 < \rho_{\mathrm{LCW}}$ (GeV) ≤ 40

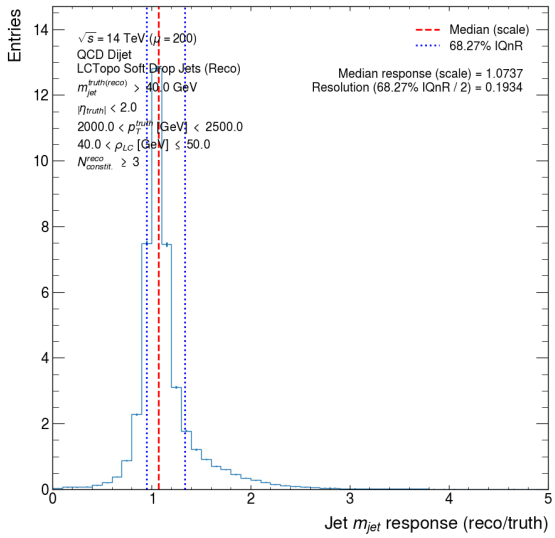

(r) $2000 < p_{\mathrm{T}}^{\mathrm{truth}}$ (GeV) < 2500 and $40 < \rho_{\mathrm{LCW}}$ (GeV) ≤ 50

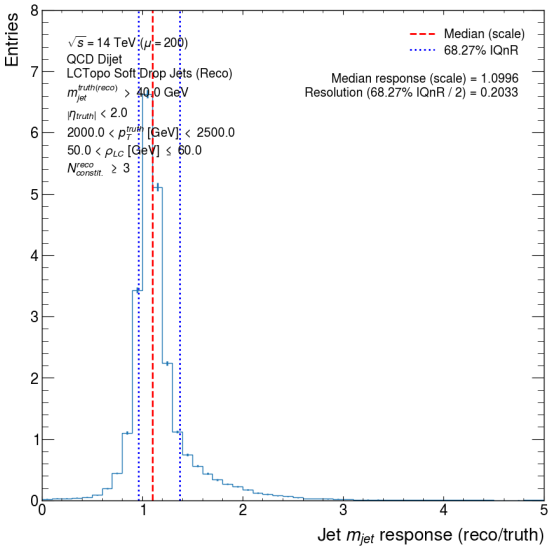

(s) $2000 < p_{\mathrm{T}}^{\mathrm{truth}}$ (GeV) < 2500 and $50 < \rho_{\mathrm{LCW}}$ (GeV) ≤ 60

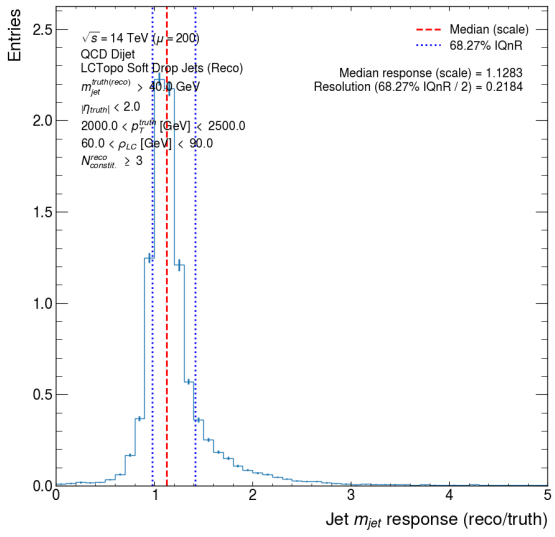

(t) $2000 < p_{\mathrm{T}}^{\mathrm{truth}}$ (GeV) < 2500 and $60 < \rho_{\mathrm{LCW}}$ (GeV) < 90

Figure H.8 (cont.): Soft-drop jet m_{jet} response distributions binned in the truth soft-drop jet p_{T} and ρ_{LCW}.

Bibliography

[1] Langacker, P 2017, The Standard Model and Beyond, Series in High Energy Physics, Cosmology, and Gravitation, CRC Press, 2 ed.

[2] LIGO Scientific Collaboration and Virgo Collaboration 2016, 'Observation of Gravitational Waves from a Binary Black Hole Merger', *Phys. Rev. Lett.*, vol. 116, p. 061102, doi:10.1103/PhysRevLett.116.061102, URL https://link.aps.org/doi/10.1103/PhysRevLett.116.061102.

[3] de Rham, C, Deskins, JT, Tolley, AJ & Zhou, SY 2017, 'Graviton mass bounds', *Reviews of Modern Physics*, vol. 89, no. 2, doi:10.1103/revmodphys.89.025004, URL https://doi.org/10.1103%2Frevmodphys.89.025004.

[4] Schwartz, MD 2013, Quantum Field Theory and the Standard Model, Cambridge University Press, United States of America.

[5] Sakurai, JJ & Napolitano, J 2017, Modern Quantum Mechanics, Cambridge University Press, 2 ed., doi:10.1017/9781108499996.

[6] Griffiths, D 2008, Introduction to Elementary Particles, Wiley-VCH, 1. aufl. ed., ISBN 0471603864.

[7] Murayama, H & Riesselmann, K 2022, 'DOE explains...The Standard Model of Particle Physics', Accessed on 22/01/2022, URL https://www.energy.gov/science/doe-explainsthe-standard-model-particle-physics.

[8] Zyla, PA *et al.* (Particle Data Group) 2020, 'Review of Particle Physics', *Progress of Theoretical and Experimental Physics*, vol. 2020, no. 8, ISSN 2050-3911, doi:10.1093/ptep/ptaa104, 083C01, https://academic.oup.com/ptep/article-pdf/2020/8/083C01/34673722/ptaa104.pdf, URL https://doi.org/10.1093/ptep/ptaa104.

[9] Higgs, PW 1964, 'Broken Symmetries and the Masses of Gauge Bosons', *Phys. Rev. Lett.*, vol. 13, pp. 508–509, doi:10.1103/PhysRevLett.13.508, URL https://link.aps.org/doi/10.1103/PhysRevLett.13.508.

[10] The CMS Collaboration 2012, 'Observation of a new boson at a mass of 125 GeV with the CMS experiment at the LHC', *Physics Letters B*, vol. 716, no. 1, pp. 30–61, ISSN 0370-2693, doi:10.1016/j.physletb.2012.08.021, URL https://www.sciencedirect.com/science/article/pii/S0370269312008581.

[11] The ATLAS Collaboration 2012, 'Observation of a new particle in the search for the Standard Model Higgs boson with the ATLAS detector at the LHC', *Physics Letters B*, vol. 716, no. 1, pp. 1–29, ISSN 0370-2693, doi:10.1016/j.physletb.2012.08.020, URL https://www.sciencedirect.com/science/article/pii/S037026931200857X.

[12] Ellis, J & You, T 2013, 'Updated global analysis of Higgs couplings', *Journal of High Energy Physics*, vol. 2013, no. 6, p. 103, ISSN 1029-8479, doi:10.1007/JHEP06(2013)103, URL https://doi.org/10.1007/JHEP06(2013)103.

[13] Englert, F & Brout, R 1964, 'Broken Symmetry and the Mass of Gauge Vector Mesons', *Phys. Rev. Lett.*, vol. 13, pp. 321–323, doi:10.1103/PhysRevLett.13.321, URL https://link.aps.org/doi/10.1103/PhysRevLett.13.321.

[14] Pich, A 2005, 'The Standard Model of Electroweak Interactions; rev. version', in 'European School of High-Energy Physics', doi:10.5170/CERN-2006-003.1, URL https://cds.cern.ch/record/819632.

[15] Ellis, J 2012, 'Outstanding questions: physics beyond the Standard Model', *Phil. Trans. R. Soc. A*, vol. 370, pp. 818–830, doi:10.1098/rsta.2011.0452, URL https://cds.cern.ch/record/1457821.

[16] Baer, H, Choi, KY, Kim, JE & Roszkowski, L 2015, 'Dark matter production in the early Universe: Beyond the thermal WIMP paradigm', *Physics Reports*, vol. 555, pp. 1–60, ISSN 0370-1573, doi:10.1016/j.physrep.2014.10.002, URL https://dx.doi.org/10.1016/j.physrep.2014.10.002.

[17] Schumann, M 2019, 'Direct detection of WIMP dark matter: concepts and status', *Journal of Physics G: Nuclear and Particle Physics*, vol. 46, no. 10, p. 103003, ISSN 1361-6471, doi:10.1088/1361-6471/ab2ea5, URL https://dx.doi.org/10.1088/1361-6471/ab2ea5.

[18] Condon, JJ & Matthews, AM 2018, 'ΛCDM Cosmology for Astronomers', *Publications of the Astronomical Society of the Pacific*, vol. 130, no. 989, p. 073001, ISSN 1538-3873, doi:10.1088/1538-3873/aac1b2, URL https://dx.doi.org/10.1088/1538-3873/aac1b2.

[19] Bertone, G & Hooper, D 2018, 'History of dark matter', *Reviews of Modern Physics*, vol. 90, no. 4, ISSN 1539-0756, doi:10.1103/revmodphys.90.045002, arXiv:1605.04909, URL https://dx.doi.org/10.1103/RevModPhys.90.045002.

[20] Carroll, BW & Ostlie, DA 2017, An Introduction to Modern Astrophysics, Cambridge University Press, 2 ed., doi:10.1017/9781108380980.

[21] Roberts, M & Rots, A 1973, 'Comparison of Rotation Curves of Different Galaxy Types', *Astronomy and Astrophysics*, vol. 26, pp. 483–485, URL https://ui.adsabs.harvard.edu/abs/1973A&A....26..483R.

[22] Penning, B 2018, 'The pursuit of dark matter at colliders—an overview', *Journal of Physics G: Nuclear and Particle Physics*, vol. 45, no. 6, p. 063001, doi:10.1088/1361-6471/aabea7, URL https://doi.org/10.1088/1361-6471/aabea7.

[23] Buchmueller, O, Doglioni, C & Wang, LT 2017, 'Search for dark matter at colliders', *Nature Physics*, vol. 13, no. 3, pp. 217–223, ISSN 1745-2481, doi:10.1038/nphys4054, URL https://dx.doi.org/10.1038/nphys4054.

[24] Barbier, R, Bérat, C, Besançon, M, Chemtob, M, Deandrea, A, Dudas, E, Fayet, P, Lavignac, S, Moreau, G, Perez, E & Sirois, Y 2005, 'R-Parity-violating supersymmetry', *Physics Reports*, vol. 420, no. 1, pp. 1–195, ISSN 0370-1573, doi:10.1016/j.physrep.2005.08.006, URL https://www.sciencedirect.com/science/article/pii/S0370157305003327.

[25] Martin, SP 1998, 'A SUPERSYMMETRY PRIMER', in 'Perspectives on Supersymmetry', WORLD SCIENTIFIC, pp. 1–98, doi:10.1142/9789812839657_0001, arXiv:hep-ph/9709356v7, URL https://doi.org/10.1142%2F9789812839657_0001.

[26] Canepa, A 2019, 'Searches for supersymmetry at the Large Hadron Collider', *Reviews in Physics*, vol. 4, p. 100033, ISSN 2405-4283, doi:10.1016/j.revip.2019.100033, URL https://www.sciencedirect.com/science/article/pii/S2405428318300091.

[27] Pettersson, NE (ATLAS, CMS) 2015, 'R-Parity Violating SUSY Results from ATLAS and CMS', in '3rd Annual Large Hadron Collider Physics Conference', ATL-PHYS-PROC-2015-198, URL https://cds.cern.ch/record/2117091.

[28] Fox, PJ 2019, 'TASI Lectures on WIMPs and Supersymmetry', in 'Theoretical Advanced Study Institute Summer School 2018 "Theory in an Era of Data"', vol. TASI2018, p. 005, doi:10.22323/1.333.0005.

[29] The ATLAS Collaboration 2008, 'The ATLAS Experiment at the CERN Large Hadron Collider', *Journal of Instrumentation*, vol. 3, no. 08, pp. S08003–S08003, doi:10.1088/1748-0221/3/08/s08003, URL https://doi.org/10.1088/1748-0221/3/08/s08003.

[30] Evans, L & Bryant, P 2008, 'LHC Machine', *Journal of Instrumentation*, vol. 3, no. 08, pp. S08001–S08001, doi:10.1088/1748-0221/3/08/s08001, URL https://doi.org/10.1088/1748-0221/3/08/s08001.

[31] Wenninger, J 2017, 'Approaching the Nominal Performance at the LHC', in '8th International Particle Accelerator Conference', p. MOYAA1. 6 p, doi:10.18429/JACoW-IPAC2017-MOYAA1, URL https://cds.cern.ch/record/2289717.

[32] Mobs, E 2019, 'The CERN accelerator complex – 2019. Complexe des accélérateurs du CERN – 2019', General Photo, URL https://cds.cern.ch/record/2684277.

[33] Wenninger, J 2015, 'The LHC collider', *Comptes Rendus Physique*, vol. 16, no. 4, pp. 347–355, ISSN 1631-0705, doi:10.1016/j.crhy.2015.03.005, Highlights of the LHC run 1 / Résultats marquants de la première période d'exploitation du GCH, URL https://www.sciencedirect.com/science/article/pii/S1631070515000560.

[34] Taylor, T 2000, 'Superconducting Magnets and RF Cavities for the LHC', in '38th INFN Eloisatron Project Workshop : Superconducting Materials for High Energy Colliders "Ettore Majorana"', URL https://cds.cern.ch/record/442755.

[35] The ATLAS Collaboration 2019, 'Luminosity determination in pp collisions at $\sqrt{s} = 13$ TeV using the ATLAS detector at the LHC', Tech. Rep. ATLAS-CONF-2019-021, CERN, Geneva, URL https://cds.cern.ch/record/2677054.

[36] Edwards, DA 1993, An introduction to the physics of high energy accelerators, Wiley series in beam physics and accelerator technology, Wiley, New York, ISBN 1-282-01049-2.

[37] The ATLAS Collaboration 2020, 'ATLAS data quality operations and performance for 2015–2018 data-taking', *JINST*, vol. 15, no. 04, p. P04003, doi:10.1088/1748-0221/15/04/P04003, arXiv:1911.04632, URL https://doi.org/10.1088/1748-0221/15/04/p04003.

[38] Pequenao, J 2008, 'Computer generated image of the whole ATLAS detector', URL https://cds.cern.ch/record/1095924.

[39] Schwartz, MD 2017, 'TASI Lectures on Collider Physics', in 'Proceedings of 2016 Theoretical Advanced Study Institute in Elementary Particle Physics', arXiv:1709.04533, URL https://doi.org/10.48550/arXiv.1709.04533.

[40] Mitsou, VA (ATLAS, CMS) 2020, 'SUSY searches in ATLAS and CMS', in 'Proceedings of Corfu Summer Institute 2019 "School and Workshops on Elementary Particle Physics and Gravity" — PoS(CORFU2019)', vol. 376, p. 050, doi:10.22323/1.376.0050.

[41] The ATLAS Collaboration 2014, 'Tagging and suppression of pileup jets with the ATLAS detector', Tech. Rep. ATLAS-CONF-2014-018, CERN, Geneva, URL https://cds.cern.ch/record/1700870.

[42] Belyaev, A, Prestel, S, Rojas-Abatte, F & Zurita, J 2021, 'Probing dark matter with disappearing tracks at the LHC', *Physical Review D*, vol. 103, no. 9, ISSN

2470-0029, doi:10.1103/physrevd.103.095006, URL https://dx.doi.org/10.1103/PhysRevD.103.095006.

[43] Schwaller, P, Stolarski, D & Weiler, A 2015, 'Emerging jets', *Journal of High Energy Physics*, vol. 2015, no. 5, ISSN 1029-8479, doi:10.1007/jhep05(2015)059, URL https://dx.doi.org/10.1007/JHEP05(2015)059.

[44] The ATLAS Collaboration 2019, 'ATLAS b-jet identification performance and efficiency measurement with $t\bar{t}$ events in pp collisions at $\sqrt{s} = 13$ TeV', *Eur. Phys. J. C*, vol. 79, p. 970. 36 p, doi:10.1140/epjc/s10052-019-7450-8, arXiv:1907.05120, URL https://cds.cern.ch/record/2682119.

[45] The ATLAS Collaboration 2017, 'Technical Design Report for the Phase-II Upgrade of the ATLAS TDAQ System', Tech. Rep. CERN-LHCC-2017-020, ATLAS-TDR-029, CERN, Geneva, URL https://cds.cern.ch/record/2285584.

[46] Pequenao, J 2008, 'Computer generated image of the ATLAS inner detector', URL https://cds.cern.ch/record/1095926.

[47] Wigmans, R 2017, Calorimetry: Energy Measurement in Particle Physics, Oxford University Press, 2nd ed.

[48] Pequenao, J 2008, 'Computer Generated image of the ATLAS calorimeter', URL https://cds.cern.ch/record/1095927.

[49] Kawamoto, T, Vlachos, S, Pontecorvo, L, Dubbert, J, Mikenberg, G, Iengo, P, Dallapiccola, C, Amelung, C, Levinson, L, Richter, R & Lellouch, D 2013, 'New Small Wheel Technical Design Report', Tech. Rep. CERN-LHCC-2013-006, ATLAS-TDR-020, CERN, URL https://cds.cern.ch/record/1552862.

[50] Pequenao, J 2008, 'Computer generated image of the ATLAS Muons subsystem', URL https://cds.cern.ch/record/1095929.

[51] The ATLAS Collaboration 2020, 'Operation of the ATLAS trigger system in Run 2', *Journal of Instrumentation*, vol. 15, no. 10, pp. P10004–P10004, ISSN 1748-0221, doi:10.1088/1748-0221/15/10/p10004, URL https://dx.doi.org/10.1088/1748-0221/15/10/P10004.

[52] The ATLAS Collaboration 2017, 'Performance of the ATLAS trigger system in 2015', *European Physical Journal C: Particles and Fields*, vol. 77, no. 5, pp. 1–53, ISSN 1434-6052, doi:10.1140/epjc/s10052-017-4852-3, URL https://link.springer.com/article/10.1140/epjc/s10052-017-4852-3.

[53] The ATLAS Collaboration 2021, 'The ATLAS Fast TracKer system', *JINST*, vol. 16, p. P07006. 64 p, doi:10.1088/1748-0221/16/07/P07006, arXiv:2101.05078, URL https://cds.cern.ch/record/2749130.

[54] Bernius, C 2012, 'The ATLAS Trigger Menu: Design and Performance', Tech. Rep. ATL-DAQ-PROC-2012-065, CERN, Geneva, URL https://cds.cern.ch/record/1494548.

[55] Sfyrla, Anna 2013, 'ATLAS Triggering on SUSY in 2012', *EPJ Web of Conferences*, vol. 49, p. 18014, doi:10.1051/epjconf/20134918014, URL https://doi.org/10.1051/epjconf/20134918014.

[56] The ATLAS Collaboration 2016, 'Trigger monitoring and rate predictions using Enhanced Bias data from the ATLAS Detector at the LHC', Tech. rep., CERN, Geneva, URL https://cds.cern.ch/record/2223498.

[57] Salam, GP 2010, 'Towards jetography', *The European Physical Journal C*, vol. 67, no. 3-4, pp. 637–686, ISSN 1434-6052, doi:10.1140/epjc/s10052-010-1314-6, arXiv:0906.1833v2, URL https://dx.doi.org/10.1140/epjc/s10052-010-1314-6.

[58] Banfi, A 2016, Hadronic Jets, 2053-2571, Morgan & Claypool Publishers, ISBN 978-1-6817-4073-7, doi:10.1088/978-1-6817-4073-7, URL https://dx.doi.org/10.1088/978-1-6817-4073-7.

[59] Loch, P & Haley, J 2021, 'US-ATLAS mini-course on Jets', Online, URL https://indico.cern.ch/event/1054786.

[60] Huth, John E. and others 1990, 'Toward a standardization of jet definitions', in '1990 DPF Summer Study on High-energy Physics: Research Directions for the Decade (Snowmass 90)', pp. 0134–136.

[61] Cacciari, M, Salam, GP & Soyez, G 2011, 'FastJet user manual', *Eur. Phys. J. C*, vol. 72, p. 1896. 69 p, doi:10.1140/epjc/s10052-012-1896-2, arXiv:1111.6097, URL https://cds.cern.ch/record/1402449.

[62] Cacciari, M & Salam, GP 2006, 'Dispelling the N^3 myth for the k_t jet-finder', *Physics Letters B*, vol. 641, no. 1, pp. 57–61, ISSN 0370-2693, doi:10.1016/j.physletb.2006.08.037, arXiv:hep-ph/0512210v2, URL https://dx.doi.org/10.1016/j.physletb.2006.08.037.

[63] The ATLAS Collaboration 2017, 'Jet reconstruction and performance using particle flow with the ATLAS Detector', *The European Physical Journal C*, vol. 77, no. 7, ISSN 1434-6052, doi:10.1140/epjc/s10052-017-5031-2, URL https://dx.doi.org/10.1140/epjc/s10052-017-5031-2.

[64] The ATLAS Collaboration 2017, 'Topological cell clustering in the ATLAS calorimeters and its performance in LHC Run 1', *The European Physical Journal C*, vol. 77, no. 7, p. 490, ISSN 1434-6052, doi:10.1140/epjc/s10052-017-5004-5, URL https://doi.org/10.1140/epjc/s10052-017-5004-5.

[65] The ATLAS Collaboration 2017, 'Performance of the ATLAS Track Reconstruction Algorithms in Dense Environments in LHC run 2', *Eur. Phys. J. C*, vol. 77, p. 673. 44 p, doi:10.1140/epjc/s10052-017-5225-7, arXiv:1704.07983, URL https://cds.cern.ch/record/2261156.

[66] The ATLAS Collaboration 2020, 'Optimisation of large-radius jet reconstruction for the ATLAS detector in 13 TeV proton-proton collisions', *Eur. Phys. J. C*, vol. 81, p. 334. 47 p, doi:10.1140/epjc/s10052-021-09054-3, arXiv:2009.04986, URL https://cds.cern.ch/record/2730141.

[67] The ATLAS Collaboration 2020, 'Jet energy scale and resolution measured in proton–proton collisions at $\sqrt{s} = 13$ TeV with the ATLAS detector', *Eur. Phys. J. C*, vol. 81, p. 689. 73 p, doi:10.1140/epjc/s10052-021-09402-3, arXiv:2007.02645, URL https://cds.cern.ch/record/2722869.

[68] Galea, C (The ATLAS Collaboration) 2016, 'Tau Lepton Reconstruction in ATLAS', in 'The 14th International Workshop on Tau Lepton Physics (Tau2016), Beijing, China, 18–23 Sep 2016', ATL-PHYS-PROC-2016-231, pp. 111–114, doi:10.1016/j.nuclphysbps.2017.03.056, URL https://cds.cern.ch/record/2233110.

[69] Rettie, S (The ATLAS Collaboration) 2018, 'Muon identification and performance in the ATLAS experiment', in 'XXVI International Workshop on Deep Inelastic Scattering and Related Subjects (DIS2018), Kobe, Hyogo, Japan, 16–20 Apr 2018', ATL-PHYS-PROC-2018-052, p. 097, doi:10.22323/1.316.0097, URL https://cds.cern.ch/record/2626330.

[70] The ATLAS Collaboration 2020, 'Muon reconstruction and identification efficiency in ATLAS using the full Run 2 *pp* collision data set at $\sqrt{s} = 13$ TeV', *Eur. Phys. J., C*, vol. 81, p. 578. 44 p, doi:10.1140/epjc/s10052-021-09233-2, arXiv:2012.00578, URL https://cds.cern.ch/record/2746302.

[71] Vannicola, D (The ATLAS Collaboration) 2019, 'Reconstruction and identification of high-pT muons in $\sqrt{s} = 13$ TeV proton-proton collisions with the ATLAS detector', in '7th Edition of the Large Hadron Collider Physics Conference (LHCP), Puebla, Mexico, 20 May 2019', ATL-PHYS-PROC-2019-110, doi:10.22323/1.350.0041, URL https://cds.cern.ch/record/2691453.

[72] The ATLAS Collaboration 2019, 'Electron and photon performance measurements with the ATLAS detector using the 2015-2017 LHC proton-proton collision data', *JINST*, vol. 14, p. P12006. 70 p, doi:10.1088/1748-0221/14/12/P12006, arXiv:1908.00005, URL https://cds.cern.ch/record/2684552.

[73] The ATLAS Collaboration 2018, '$E_{\mathrm{T}}^{\mathrm{miss}}$ performance in the ATLAS detector using 2015-2016 LHC p-p collisions', Tech. Rep. ATLAS-CONF-2018-023, CERN, Geneva, URL https://cds.cern.ch/record/2625233.

[74] The ATLAS Collaboration 2017, 'Jet energy scale measurements and their systematic uncertainties in proton-proton collisions at $\sqrt{s} = 13$ TeV with the ATLAS detector', *Phys. Rev. D*, vol. 96, p. 072002. 36 p, doi:10.1103/PhysRevD.96.072002, arXiv:1703.09665, URL https://cds.cern.ch/record/2257300.

[75] The ATLAS Collaboration 2011, 'Jet energy measurement with the ATLAS detector in proton-proton collisions at $\sqrt{s} = 7$ TeV', *Eur. Phys. J. C*, vol. 73, p. 2304. 100 p, doi:10.1140/epjc/s10052-013-2304-2, arXiv:1112.6426, URL https://cds.cern.ch/record/1409965.

[76] Achenbach, R *et al.* 2008, 'The ATLAS Level-1 Calorimeter Trigger', *Journal of Instrumentation*, vol. 3, no. 03, pp. P03001–P03001, doi:10.1088/1748-0221/3/03/p03001, URL https://doi.org/10.1088/1748-0221/3/03/p03001.

[77] Okumura, Y (The ATLAS Collaboration) 2022, 'Triggering in ATLAS in Run 2 and Run 3', in 'Proceedings of European Physics Society conference on High Energy Physics 2021, Online, 26–30 Jul 2021', vol. EPS-HEP2021, p. 788, doi:10.22323/1.398.0788, URL https://cds.cern.ch/record/2783645.

[78] The ATLAS Collaboration 2013, 'Performance of jet substructure techniques for large-R jets in proton-proton collisions at $\sqrt{s} = 7$ TeV using the ATLAS detector. Performance of jet substructure techniques for large-R jets in proton-proton collisions at sqrt(s) = 7 TeV using the ATLAS detector', *JHEP*, vol. 09, p. 076. 83 p, doi:10.1007/JHEP09(2013)076, arXiv:1306.4945, URL https://cds.cern.ch/record/1556999.

[79] The ATLAS Collaboration 2018, 'In situ calibration of large-R jet energy and mass in 13 TeV proton-proton collisions with the ATLAS detector', *Eur. Phys. J. C*, vol. 79, p. 135. 70 p, doi:10.1140/epjc/s10052-019-6632-8, submitted to Eur.Phys.J., arXiv:1807.09477, URL https://cds.cern.ch/record/2632341.

[80] The ATLAS Collaboration 2019, 'Performance of top-quark and W-boson tagging with ATLAS in Run 2 of the LHC', *Eur. Phys. J. C*, vol. 79, no. 5, p. 375, doi:10.1140/epjc/s10052-019-6847-8, arXiv:1808.07858.

[81] Larkoski, AJ, Neill, D & Thaler, J 2014, 'Jet shapes with the broadening axis', *Journal of High Energy Physics*, vol. 2014, no. 4, ISSN 1029-8479, doi:10.1007/jhep04(2014)017, URL https://dx.doi.org/10.1007/JHEP04(2014)017.

[82] Kogler, R 2021, Advances in Jet Substructure at the LHC: Algorithms, Measurements and Searches for New Physical Phenomena, Springer tracts in modern physics, Springer International Publishing, ISBN 9783030728588, doi:10.1007/978-3-030-72858-8, URL https://books.google.com.au/books?id=n5AtEAAAQBAJ.

[83] Thaler, J & Van Tilburg, K 2011, 'Identifying boosted objects with N-subjettiness', *Journal of High Energy Physics*, vol. 2011, no. 3, ISSN 1029-8479, doi:10.1007/jhep03(2011)015, URL https://dx.doi.org/10.1007/JHEP03(2011)015.

[84] Larkoski, AJ, Salam, GP & Thaler, J 2013, 'Energy correlation functions for jet substructure', *Journal of High Energy Physics*, vol. 2013, no. 6, ISSN 1029-8479, doi:10.1007/jhep06(2013)108, URL https://dx.doi.org/10.1007/JHEP06(2013)108.

[85] Moult, I, Necib, L & Thaler, J 2016, 'New angles on energy correlation functions', *Journal of High Energy Physics*, vol. 2016, no. 12, ISSN 1029-8479, doi:10.1007/jhep12(2016)153, URL https://dx.doi.org/10.1007/JHEP12(2016)153.

[86] Chen, C 2012, 'New approach to identifying boosted hadronically decaying particles using jet substructure in its center-of-mass frame', *Physical Review D*, vol. 85, no. 3, ISSN 1550-2368, doi:10.1103/physrevd.85.034007, arXiv:1112.2567v3, URL https://dx.doi.org/10.1103/PhysRevD.85.034007.

[87] Thaler, J & Wang, LT 2008, 'Strategies to identify boosted tops', *Journal of High Energy Physics*, vol. 2008, no. 07, pp. 092–092, ISSN 1029-8479, doi:10.1088/1126-6708/2008/07/092, arXiv:0806.0023v2, URL https://dx.doi.org/10.1088/1126-6708/2008/07/092.

[88] The ATLAS Collaboration 2013, 'Measurement of k_T splitting scales in $W \to l\nu$ events at $\sqrt{s} = 7$ TeV with the ATLAS detector', *The European Physical Journal C*, vol. 73, no. 5, ISSN 1434-6052, doi:10.1140/epjc/s10052-013-2432-8, URL https://dx.doi.org/10.1140/epjc/s10052-013-2432-8.

[89] Halkiadakis, E, Redlinger, G & Shih, D 2014, 'Status and Implications of BSM Searches at the LHC', doi:10.48550/ARXIV.1411.1427, URL https://arxiv.org/abs/1411.1427.

[90] Mukherjee, S 2020, 'Data scouting and data parking with the CMS high level trigger', in 'Proceedings of European Physical Society Conference on High Energy Physics — PoS(EPS-HEP2019)', vol. EPS-HEP2019, p. 139, doi:10.22323/1.364.0139.

[91] Benson, S, Gligorov, V, Vesterinen, MA & Williams, JM 2015, 'The LHCb Turbo Stream', *Journal of Physics: Conference Series*, vol. 664, no. 8, p. 082004, doi:10.1088/1742-6596/664/8/082004, URL https://doi.org/10.1088/1742-6596/664/8/082004.

[92] The ATLAS Collaboration 2018, 'Search for low-mass dijet resonances using trigger-level jets with the ATLAS detector in pp collisions at $\sqrt{s} = 13$ TeV', *Phys. Rev. Lett.*, vol. 121, p. 081801. 20 p, doi:10.1103/PhysRevLett.121.081801, arXiv:1804.03496, URL https://cds.cern.ch/record/2312376.

[93] The ATLAS Collaboration 2017, 'Trigger-object Level Analysis with the ATLAS detector at the Large Hadron Collider: summary and perspectives', Tech. Rep. ATL-DAQ-PUB-2017-003, CERN, URL https://cds.cern.ch/record/2295739.

[94] The ATLAS Collaboration 2015, 'Search for massive supersymmetric particles decaying to many jets using the ATLAS detector in pp collisions at $\sqrt{s} = 8$ TeV', *Phys. Rev. D*, vol. 91, p. 112016. 37 p, doi:10.1103/PhysRevD.93.039901, arXiv:1502.05686, URL https://cds.cern.ch/record/1993236.

[95] The ATLAS Collaboration 2012, 'Search for pair production of massive particles decaying into three quarks with the ATLAS detector in $\sqrt{s} = 7$ TeV pp collisions at the LHC', *JHEP*, vol. 12, p. 086. 50 p, doi:10.1007/JHEP12(2012)086, arXiv:1210.4813, URL https://cds.cern.ch/record/1485557.

[96] The ATLAS Collaboration 2018, 'Search for R-parity-violating supersymmetric particles in multi-jet final states produced in p-p collisions at $\sqrt{s} = 13$ TeV using the ATLAS detector at the LHC', *Physics Letters B*, vol. 785, pp. 136–158, ISSN 0370-2693, doi:10.1016/j.physletb.2018.08.021, URL https://www.sciencedirect.com/science/article/pii/S0370269318306270.

[97] Alwall, J, Frederix, R, Frixione, S, Hirschi, V, Maltoni, F, Mattelaer, O, Shao, HS, Stelzer, T, Torrielli, P & Zaro, M 2014, 'The automated computation of tree-level and next-to-leading order differential cross sections, and their matching to parton shower simulations', *Journal of High Energy Physics*, vol. 2014, no. 7, p. 79, ISSN 1029-8479, doi:10.1007/JHEP07(2014)079, URL https://doi.org/10.1007/JHEP07(2014)079.

[98] Sjöstrand, T, Mrenna, S & Skands, P 2008, 'A brief introduction to PYTHIA 8.1', *Computer Physics Communications*, vol. 178, no. 11, pp. 852–867, ISSN 0010-4655, doi:10.1016/j.cpc.2008.01.036, URL https://www.sciencedirect.com/science/article/pii/S0010465508000441.

[99] Lange, DJ 2001, 'The EvtGen particle decay simulation package', *Nucl. Instrum. Meth. A*, vol. 462, pp. 152–155, doi:10.1016/S0168-9002(01)00089-4.

[100] Ball, RD, Bertone, V, Carrazza, S, Debbio, LD, Forte, S, Guffanti, A, Hartland, NP & Rojo, J 2013, 'Parton distributions with QED corrections', *Nuclear Physics B*, vol. 877, no. 2, pp. 290–320, doi:10.1016/j.nuclphysb.2013.10.010, URL https://doi.org/10.1016%2Fj.nuclphysb.2013.10.010.

[101] South, D & Gingrich, D 2018 [Online], 'ATLAS MC Production Workflow', Accessed 10 May 2022, URL https://indico.cern.ch/event/692124/contributions/2898693/attachments/1610808/2557701/mccoord_050318.pdf.

[102] The ATLAS Collaboration 2022, 'Performance of the ATLAS Level-1 topological trigger in Run 2', *The European Physical Journal C*, vol. 82, no. 1, p. 7, ISSN 1434-6052, doi:10.1140/epjc/s10052-021-09807-0, URL https://doi.org/10.1140/epjc/s10052-021-09807-0.

[103] The ATLAS Collaboration 2020, 'Search for phenomena beyond the Standard Model in events with large b-jet multiplicity using the ATLAS detector at the LHC', *Eur. Phys. J. C*, vol. 81, p. 11. 29 p, doi:10.1140/epjc/s10052-020-08730-0, arXiv:2010.01015, URL https://cds.cern.ch/record/2739342.

[104] The ATLAS Collaboration 2018, 'A search for pair-produced resonances in four-jet final states at $\sqrt{s} = 13$ TeV with the ATLAS detector', *The European Physical Journal C*, vol. 78, no. 3, ISSN 1434-6052, doi:10.1140/epjc/s10052-018-5693-4, URL https://dx.doi.org/10.1140/epjc/s10052-018-5693-4.

[105] The ATLAS Collaboration 2017, 'Search for new phenomena with large jet multiplicities and missing transverse momentum using large-radius jets and flavour-tagging at ATLAS in 13 TeV pp collisions.', *JHEP*, vol. 12, p. 034. 53 p, doi:10.1007/JHEP12(2017)034, arXiv:1708.02794, URL https://cds.cern.ch/record/2277363.

[106] The ATLAS Collaboration 2016, 'Search for new phenomena in final states with large jet multiplicities and missing transverse momentum with atlas using $\sqrt{s} = 13$ TeV proton-proton collisions', *Physics Letters B*, vol. 757, pp. 334–355, ISSN 0370-2693, doi:10.1016/j.physletb.2016.04.005, URL https://dx.doi.org/10.1016/j.physletb.2016.04.005.

[107] The ATLAS Collaboration 2020, 'Search for new phenomena in final states with large jet multiplicities and missing transverse momentum using $\sqrt{s} = 13$ TeV proton-proton collisions recorded by ATLAS at Run-2 of the LHC', *JHEP*, vol. 2010, p. 062. 49 p, doi:10.1007/JHEP10(2020)062, arXiv:2008.06032, URL https://cds.cern.ch/record/2728000.

[108] Stark, G *et al.* 2020, 'xAODAnaHelpers, v1.0.0', doi:10.5281/zenodo.3743307, URL https://doi.org/10.5281/zenodo.3743307.

[109] The CMS Collaboration 2019, 'Search for pair-produced three-jet resonances in proton-proton collisions at $\sqrt{s} = 13$ TeV', *Physical Review D*, vol. 99, no. 1, ISSN 2470-0029, doi:10.1103/physrevd.99.012010, arXiv:1810.10092v2, URL https://dx.doi.org/10.1103/PhysRevD.99.012010.

[110] Buckley, A, Ferrando, J, Lloyd, S, Nordström, K, Page, B, Rüfenacht, M, Schönherr, M & Watt, G 2015, 'LHAPDF6: parton density access in the LHC precision era', *The European Physical Journal C*, vol. 75, no. 3, ISSN

1434-6052, doi:10.1140/epjc/s10052-015-3318-8, URL https://dx.doi.org/10.1140/epjc/s10052-015-3318-8.

[111] The ATLAS Collaboration 2022, 'SimpleAnalysis: Truth-level Analysis Framework', Tech. Rep. ATL-PHYS-PUB-2022-017, CERN, Geneva, URL https://cds.cern.ch/record/2805991.

[112] Soper, DE 1997, 'Parton distribution functions', *Nuclear Physics B - Proceedings Supplements*, vol. 53, no. 1-3, pp. 69–80, ISSN 0920-5632, doi:10.1016/s0920-5632(96)00600-7, URL https://dx.doi.org/10.1016/S0920-5632(96)00600-7.

[113] Buckley, A, 'Discussion regarding PDF re-weighting of monte-carlo samples', personal communication, 23 September 2021.

[114] Borschensky, C, Krämer, M, Kulesza, A, Mangano, M, Padhi, S, Plehn, T & Portell, X 2014, 'Squark and gluino production cross sections in pp collisions at $\sqrt{s}$ = 13, 14, 33 and 100 TeV', *The European Physical Journal C*, vol. 74, no. 12, doi:10.1140/epjc/s10052-014-3174-y, URL https://doi.org/10.1140%2Fepjc%2Fs10052-014-3174-y.

[115] Borschensky, C, Gecse, Z, Kraemer, M, van der Leeuw, R, Kulesza, A, Mangano, M, Padhi, S, Plehn, T, Portell, X & Sekmen, S 2021, 'LHC SUSY Cross Section Working Group', Accessed Online 12 May 2022, URL https://twiki.cern.ch/twiki/bin/view/LHCPhysics/SUSYCrossSections.

[116] The ATLAS Collaboration 2014, 'ATLAS Pythia 8 tunes to 7 TeV data', Tech. Rep. ATL-PHYS-PUB-2014-021, CERN, Geneva, URL https://cds.cern.ch/record/1966419.

[117] Carrazza, S, Forte, S & Rojo, J 2013, 'Parton Distributions and Event Generators', doi:10.48550/ARXIV.1311.5887, URL https://arxiv.org/abs/1311.5887.

[118] Kar, D 2019, Experimental Particle Physics, 2053-2563, IOP Publishing, ISBN 978-0-7503-2112-9, doi:10.1088/2053-2563/ab1be6, URL https://dx.doi.org/10.1088/2053-2563/ab1be6.

[119] Nason, P 2004, 'A New Method for Combining NLO QCD with Shower Monte Carlo Algorithms', *Journal of High Energy Physics*, vol. 2004, no. 11, pp. 040–040, doi:10.1088/1126-6708/2004/11/040, URL https://doi.org/10.1088%2F1126-6708%2F2004%2F11%2F040.

[120] Alioli, S, Nason, P, Oleari, C & Re, E 2010, 'A general framework for implementing NLO calculations in shower Monte Carlo programs: the POWHEG BOX', *Journal of High Energy Physics*, vol. 2010, no. 6, doi:10.1007/jhep06(2010)043, URL https://doi.org/10.1007%2Fjhep06%282010%29043.

[121] Frixione, S, Ridolfi, G & Nason, P 2007, 'A positive-weight next-to-leading-order Monte Carlo for heavy flavour hadroproduction', *Journal of High Energy Physics*, vol. 2007, no. 09, pp. 126–126, doi:10.1088/1126-6708/2007/09/126, URL https://doi.org/10.1088%2F1126-6708%2F2007%2F09%2F126.

[122] The CMS Collaboration 2012, 'Search for three-jet resonances in pp collisions at $\sqrt{s} = 7$ TeV', *Physics Letters B*, vol. 718, no. 2, pp. 329–347, ISSN 0370-2693, doi:10.1016/j.physletb.2012.10.048, URL https://www.sciencedirect.com/science/article/pii/S0370269312011021.

[123] The CMS Collaboration 2014, 'Searches for light- and heavy-flavour three-jet resonances in pp collisions at $\sqrt{s} = 8$ TeV', *Physics Letters B*, vol. 730, pp. 193–214, doi:10.1016/j.physletb.2014.01.049, URL https://doi.org/10.1016%2Fj.physletb.2014.01.049.

[124] The CDF Collaboration 2011, 'First Search for Multijet Resonances in $\sqrt{s} = 1.96$ TeV $p\bar{p}$ Collisions', *Phys. Rev. Lett.*, vol. 107, p. 042001, doi:10.1103/PhysRevLett.107.042001, URL https://link.aps.org/doi/10.1103/PhysRevLett.107.042001.

[125] Kang, Y, Kim, J, Choi, J & Yun, S 2020, 'Implementation of a search for pair-produced resonances decaying each into a trijet system (36 fb^{-1}; CMS-EXO-17-030)', doi:10.14428/DVN/GAZACQ, URL https://doi.org/10.14428/DVN/GAZACQ.

[126] Halser, L, 'Discussion regarding truth-matching for RPV SUSY gluino pair-production multi-jet signals', personal communication, January and March 2022.

[127] The ATLAS Collaboration 2015, 'Selection of jets produced in 13 TeV proton-proton collisions with the ATLAS detector', Tech. Rep. ATLAS-CONF-2015-029, CERN, Geneva, URL https://cds.cern.ch/record/2037702.

[128] Hoecker, A *et al.* 2007, 'TMVA - Toolkit for Multivariate Data Analysis', doi:10.48550/ARXIV.PHYSICS/0703039, URL https://arxiv.org/abs/physics/0703039.

[129] Newville, M, Stensitzki, T, Allen, DB & Ingargiola, A 2014, 'LMFIT: Non-Linear Least-Square Minimization and Curve-Fitting for Python', doi:10.5281/zenodo.11813, URL https://doi.org/10.5281/zenodo.11813.

[130] The ATLAS Collaboration 2021, 'Identification of hadronically-decaying top quarks using UFO jets with ATLAS in Run 2', Tech. Rep. ATL-PHYS-PUB-2021-028, CERN, Geneva, URL https://cds.cern.ch/record/2776782.

[131] The ATLAS Collaboration 2021, 'Athena', doi:10.5281/zenodo.4772550, URL https://doi.org/10.5281/zenodo.4772550.

[132] Almeida, LG, Lee, SJ, Perez, G, Sung, I & Virzi, J 2009, 'Top quark jets at the LHC', *Physical Review D*, vol. 79, no. 7, ISSN 1550-2368, doi:10.1103/physrevd.79.074012, arXiv:0810.0934v1, URL https://doi.org/10.48550/arXiv.0810.0934.

[133] The ATLAS Collaboration 2015, 'Boosted hadronic top identification at ATLAS for early 13 TeV data', Tech. Rep. ATL-PHYS-PUB-2015-053, CERN, Geneva, URL https://cds.cern.ch/record/2116351.

[134] The ATLAS Collaboration 2018, 'Jet Mass Resolutions in ATLAS using Run 2 Monte Carlo Simulation', Tech. Rep. ATL-PHYS-PUB-2018-015, CERN, Geneva, URL https://cds.cern.ch/record/2631339.

[135] The ATLAS Collaboration 2019, 'Measurement of jet-substructure observables in top quark, W boson and light jet production in proton-proton collisions at $\sqrt{s} = 13$ TeV with the ATLAS detector', *JHEP*, p. 47 p, doi:10.1007/JHEP08(2019)033, arXiv:1903.02942, URL https://cds.cern.ch/record/2665903.

[136] Wackerly, DD, Mendenhall, W & Scheaffer, RL 2008, Mathematical Statistics with Applications, Cengage, Mason, OH, 7th ed. ed.

[137] Virtanen, P *et al.* 2020, 'SciPy 1.0: Fundamental Algorithms for Scientific Computing in Python', *Nature Methods*, vol. 17, pp. 261–272, doi:10.1038/s41592-019-0686-2.